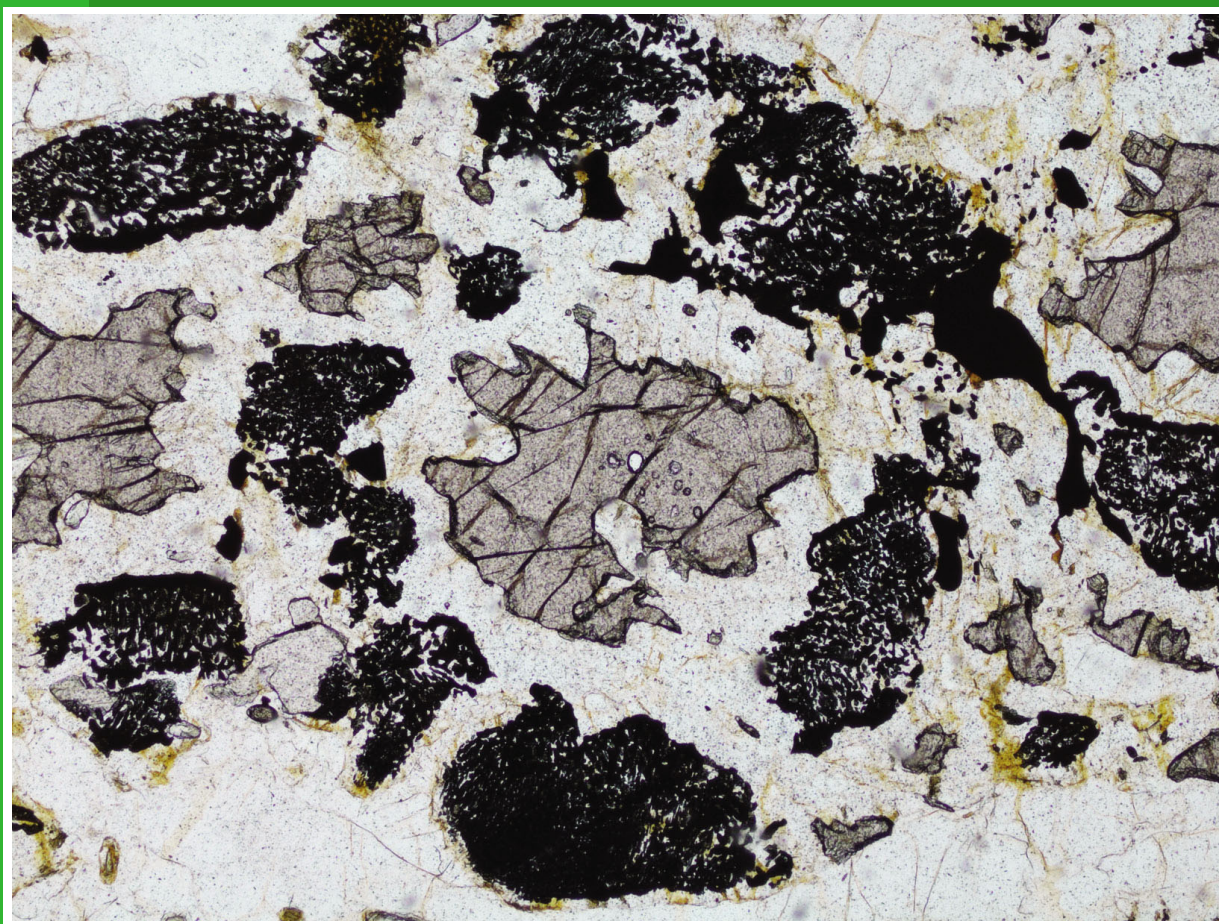


**REPORT  
166**

# **THERMO-MECHANICAL EVOLUTION OF OROGENY IN THE MUSGRAVE PROVINCE**

**by A Walsh**





Government of **Western Australia**  
Department of **Mines and Petroleum**

**REPORT 166**

# **THERMO-MECHANICAL EVOLUTION OF OROGENY IN THE MUSGRAVE PROVINCE**

**by**

**A Walsh**

Geology and Geophysics  
School of Physical Sciences  
The University of Adelaide

**Perth 2017**



**Geological Survey of  
Western Australia**

**MINISTER FOR MINES AND PETROLEUM**  
**Hon. Sean K L'Estrange MLA**

**ACTING DIRECTOR GENERAL, DEPARTMENT OF MINES AND PETROLEUM**  
**Tim Griffin**

**EXECUTIVE DIRECTOR, GEOLOGICAL SURVEY OF WESTERN AUSTRALIA**  
**Rick Rogerson**

#### **REFERENCE**

**The recommended reference for this publication is:**

Walsh, A 2017, Thermo-mechanical evolution of orogeny in the Musgrave Province: Geological Survey of Western Australia, Report 166, 188p.

#### **National Library of Australia Cataloguing-in-Publication entry**

**Creator:** Walsh, Alec, author.  
**Title:** Thermo-mechanical evolution of orogeny in the Musgrave province / Alec Walsh.  
**ISBN:** 9781741687361 (ebook)  
**Subjects:** Orogeny--Western Australia--Musgrave Province.  
Metamorphism (Geology)--Western Australia—Musgrave Province.  
Musgrave Province (WA).  
**Other Authors/Contributors:** Geological Survey of Western Australia, issuing body.  
**ISSN 0508–4741**

Grid references in this publication refer to the Geocentric Datum of Australia 1994 (GDA94). Locations mentioned in the text are referenced using Map Grid Australia (MGA) coordinates, Zone 50. All locations are quoted to at least the nearest 100 m.

#### **Disclaimer**

This product was produced using information from various sources. The Department of Mines and Petroleum (DMP) and the State cannot guarantee the accuracy, currency or completeness of the information. DMP and the State accept no responsibility and disclaim all liability for any loss, damage or costs incurred as a result of any use of or reliance whether wholly or in part upon the information provided in this publication or incorporated into it by reference.

#### **Published 2017 by Geological Survey of Western Australia**

This Report is published in digital format (PDF) and is available online at <[www.dmp.wa.gov.au/GSWApublications](http://www.dmp.wa.gov.au/GSWApublications)>.

#### **Further details of geological publications and maps produced by the Geological Survey of Western Australia are available from:**

Information Centre  
Department of Mines and Petroleum  
100 Plain Street | EAST PERTH WESTERN AUSTRALIA 6004  
Telephone: +61 8 9222 3459 Facsimile: +61 8 9222 3444  
[www.dmp.wa.gov.au/GSWApublications](http://www.dmp.wa.gov.au/GSWApublications)

**Cover photograph:** Photomicrograph of metapelite from Cohn Hill, showing a resorbed garnet porphyroblast surrounded by a multilayer corona of cordierite–plagioclase and spinel–magnetite–cordierite

**Notice to the reader**

This Report is an accepted PhD research thesis submitted by the author to the Centre of Tectonics, Resources and Exploration (TRaX), The University of Adelaide and was partially funded by the Geological Survey of Western Australia (GSWA) as part of an Australian Research Council Linkage project (LP100200127). The scientific content of the Report, and the drafting of figures, has been the responsibility of the author. No editing has been undertaken by GSWA.

All work carried out in the west Musgrave region was done so within the framework of a collaborative project involving GSWA, the traditional owners of the region and the Ngaanyatjarra Council. The considerable efforts of the traditional owners and of the Ngaanyatjarra Council in facilitating this work, is gratefully acknowledged.

**Permission statement**

Permission was granted from Elsevier to republish the following articles in chapters 1 and 2:

Walsh, AK, Raimondo, T, Kelsey, DE, Hand, M, Pfitzner, HL and Clark, C 2013, Duration of high-pressure metamorphism and cooling during the intraplate Petermann Orogeny: *Gondwana Research*, vol. 24, iss. 3–4, November 2013, p. 969–983, doi:org/10.1016/j.gr.2012.09.006.

Walsh, AK, Kelsey, DE, Kirkland, CL, Hand, M, Smithies, RH, Clark, C and Howard, HM 2014, P–T–t evolution of a large, long-lived, ultrahigh-temperature Grenvillian belt in central Australia: *Gondwana Research*, 27 June 2014, doi:org/10.1016/j.gr.2014.05.012.

Permission was granted from Wiley to republish the following article in chapter 3:

Walsh, AK, Hand, M and Kelsey, DE, 2015. A metamorphic perspective on foreland flexure during intraplate orogeny: evidence for the involvement of weak lithosphere: *TerraNova*, vol. 27, issue 5, p. 329–337, doi:10.1111/ter.12164.

Chapter 4 was submitted and reviewed for publication in *Journal of the Geological Society of London* but was not published as the required revisions were not completed.







# Thermo-mechanical evolution of orogeny in the Musgrave Province

ALEC WALSH

Geology and Geophysics  
School of Physical Sciences  
University of Adelaide

This thesis is submitted in fulfillment of the  
requirements for the degree of Doctor of Philosophy

June 2015

---



---

---

# Table of contents

---

Table of contents	v
Abstract	v
Declaration	vi
Publications arising from this thesis	vii
Acknowledgements	ix
Significance and aims of this thesis	xi
Chapter Outlines	xiv
<b>Chapter 1: P–T–t evolution of a large, long-lived, ultrahigh-temperature Grenvillian belt in central Australia</b>	
Introduction	3
Regional geology	6
Sample description	10
Garnet and spinel chemistry	18
Mineral equilibria modelling	18
Zr-in rutile thermometry	30
U-Pb geochronology	33
Discussion	37
<i>Interpretation of U-Pb monazite geochronology</i>	37
<i>Implications for monazite behaviour during UHT metamorphism</i>	40
<i>P–T–t evolution of the Musgrave Orogeny</i>	42
<i>Tectonic setting of UHT metamorphism during the Musgrave Orogeny</i>	43
Conclusions	45
References	46
Supporting information	57
<b>Chapter 2: Duration of high pressure metamorphism and cooling during the intraplate Petermann Orogeny</b>	
Introduction	63
Regional geology	66
Petrography	68
U-Pb SHRIMP geochronology	71
Trace element thermometry	74
Discussion	76
<i>Duration of tectonism and cooling</i>	76
<i>‘Cold’ vs. ‘hot’: the mechanical environment of the Petermann Orogeny</i>	80
Conclusions	81
References	82

---

---

### **Chapter 3: A metamorphic perspective on foreland flexure during intraplate orogeny: evidence for the involvement of weak lithosphere**

Introduction	89
Geological setting	89
Metamorphic constraints on burial in the Petermann orogenic foreland	93
Discussion	95
Conclusions	97
References	98
Supporting information	101

### **Chapter 4: Crustal thickening in the Petermann Orogeny prior to 600 Ma; evidence from $^{40}\text{Ar}/^{39}\text{Ar}$ geochronology and implications for spatial patterns of reworking in intraplate orogens**

Introduction	107
Geological setting	108
Geology of the foreland fold-thrust belt (Petermann Nappe Complex)	112
Petrography	112
$^{40}\text{Ar}/^{39}\text{Ar}$ geochronology	114
<i>Results</i>	116
<i>Summary of <math>^{40}\text{Ar}/^{39}\text{Ar}</math> results</i>	117
Discussion	119
<i>Interpretation of <math>^{40}\text{Ar}/^{39}\text{Ar}</math> ages</i>	119
<i>Foreland fold-thrust belt samples</i>	120
<i>Deformation history of the Petermann Orogeny</i>	123
Conclusions	125
References	126
Supporting information	133

### **Chapter 5: Duration of elevated thermal conditions in the deep crust during intracratonic orogeny**

Introduction	143
Geological setting	146
Geology of the Amata region	148
Petrography	150
Phase equilibria modelling	151
<i>A325-535</i>	152
<i>A325-907Q</i>	154
<i>A325-672</i>	154
<i>Summary</i>	155
U-Pb geochronology	155
<i>LA-ICP-MS methods</i>	155
<i>SHRIMP methods</i>	155
<i>Results</i>	156
<i>Monazite</i>	156
<i>Rutile</i>	158
Diffusion modelling	158



---

---

Discussion	159
<i>Timing of metamorphism and footprint of elevated temperatures</i>	159
<i>Duration of metamorphism</i>	160
<i>Drivers for metamorphism</i>	161
<i>Thermo-mechanical evolution of the Petermann Orogen</i>	162
Conclusions	163
References	163
Supporting information	172
 <b>Chapter 6</b>	
Summary and conclusions	185



---

---

# Abstract

---

The architecture of orogens, the physical record of deformation and metamorphism, and the duration and rates at which orogeny progresses is intimately linked with thermomechanical state of the lithosphere and its evolution and modification during orogenesis in polymetamorphic terrains. This thesis presents an integrated study that investigates the structural, metamorphic and geodynamic features of the Musgrave Province to understand the interplay between orogenesis and the temporal and spatial changes in lithospheric rheology.

The metamorphic record in the Musgrave Province is dominated by Grenvillian-aged (1270–1100 Ma) ultra-high-temperature metamorphism which was characterised by > 80 Myr of metamorphic temperatures of approximately 1000 °C. The duration of such extreme conditions resulted in extremely residual crust which had major implications for the style of reworking in the younger Ediacaran–Cambrian intraplate Petermann Orogeny.

Crustal thickening during intraplate orogeny occurred at ~ 600 Ma and resulted in the development of a thick-skinned foreland fold-thrust belt. Loading of the lithosphere caused the development of an extremely deep and narrow flexural foreland basin in which syn-orogenic sequences were buried to depths of ~10 km. The architecture of the foreland implies that intraplate deformation was localised into a region of dramatically weakened lithosphere, which could have developed in response to the initial distribution (and burial) of heat producing layers in the mid-crust.

In the deep-crustal core of the orogen, migmatites from the western part of the orogenic system which record peak metamorphism between 600 and 570 Ma and long-lived pervasive deformation (> 40 Myr), represent a comparatively warm and weak portion of crust. To the east, discrete and brittle deformation occurred in comparatively strong lithosphere and but is accompanied by a similar record of elevated metamorphic temperatures (>600 °C) which span 590 to 530 Ma. Observed variations in deformational response independent of temperature or duration highlights the important role of other factors, such as availability of fluids, might have in facilitating reduction in strength and localise deformation in residual lithosphere. Ultimate re-strengthening of the Petermann Orogen lithosphere was achieved during progressive removal of the orogenic heat production during erosion, enabling the preservation of a puzzling record of intraplate orogeny.

---

---

## Declaration

---

I certify that this work contains no material which has been accepted for the award of any other degree or diploma in my name, in any university or other tertiary institution and, to the best of my knowledge and belief, contains no material previously published or written by another person, except where due reference has been made in the text. In addition, I certify that no part of this work will, in the future, be used in a submission in my name, for any other degree or diploma in any university or other tertiary institution without the prior approval of the University of Adelaide and where applicable, any partner institution responsible for the joint-award of this degree.

I give consent to this copy of my thesis when deposited in the University Library, being made available for loan and photocopying, subject to the provisions of the Copyright Act 1968.

The author acknowledges that copyright of published works contained within this thesis resides with the copyright holder(s) of those works.

I also give permission for the digital version of my thesis to be made available on the web, via the University's digital research repository, the Library Search and also through web search engines, unless permission has been granted by the University to restrict access for a period of time.

ALEC WALSH

DATE

---

---

## Publications arising from this thesis

---

### *Journal articles*

**Walsh, A. K.**, T. Raimondo, D. E. Kelsey, M. Hand, H. L. Pfitzner, and C. Clark. 2013. Duration of high-pressure metamorphism and cooling during the intraplate Petermann Orogeny. *Gondwana Research*, Volume 24, Issues 3–4, November 2013, Pages 969-983, ISSN 1342-937X, <http://dx.doi.org/10.1016/j.gr.2012.09.006>.

**Walsh, A. K.**, D. E. Kelsey, C.L. Kirkland, M Hand, R. Hugh Smithies, C Clark, and H.M. Howard. in press. P–T–t evolution of a large, long-lived, ultrahigh-temperature Grenvillian belt in central Australia. *Gondwana Research*, Available online 27 June 2014, ISSN 1342-937X, <http://dx.doi.org/10.1016/j.gr.2014.05.012>.

**Walsh, A. K.**, Hand, M. & Kelsey, D. E., in review. A metamorphic perspective on foreland flexure during intraplate orogeny: evidence for the involvement of weak lithosphere. *Terra Nova*.

**Walsh, A. K.**, Kelsey, D. E., Hand, M. & Jourdan, F. in review. Crustal thickening prior to 600 Ma; evidence from <sup>40</sup>Ar–<sup>39</sup>Ar thermochronology and implications for spatial patterns of reworking and exhumation in intraplate orogens. *Journal of the Geological Society of London*.

### *Conference abstracts*

**Walsh, A. K.**, D. E. Kelsey, C.L. Kirkland, M Hand, R. Hugh Smithies, C Clark, and H.M. Howard. A long-lived UHT Grenvillian belt in central Australia. Granulites and Granulites conference 2013.

**Walsh, A. K.**, D. E. Kelsey, C.L. Kirkland, M Hand, R. Hugh Smithies, C Clark, and H.M. Howard. A long-lived UHT Grenvillian belt in central Australia. International Geological Congress, Abstracts 2012

**Walsh, A. K.**, Kelsey, D. E., Hand, M. Duration of high-pressure metamorphism and cooling during the intraplate Petermann Orogeny. Specialist Group for Geochemistry, Mineralogy and Petrology conference, Abstracts 2011

**Walsh, A. K.**, Kelsey, D. E., Hand, M. Constraining the thermal evolution of a large intracontinental orogen. Australian Earth Sciences Convention, Abstracts 2010





---

---

## Acknowledgements

---

Upon reflection, i've been pretty lucky throughout my Phd and even luckier to have the people around me i did and still have. To begin, Dave Kelsey deserves my endless gratitude for his supervisory role which he performed to aplomb. My PhD was a great experience largely because he had the humility to allow me to direct my own project. I can't think of a better supervisor and a pretty good friend at the end of it all! Thanks to my other supervisor Martin who always made metamorphic geology exhilarating and was never short of outrageous anecdotes around the fire. Hugh, Chris, Roland, Mario, Kieran, Raphael and Dave were great people and geologists which made 12-odd weeks of field work in the Musgraves memorable. On the analytical side; Ben and Angus at Adelaide Microscopy have been incredibly helpful and comical in our attempts to get data that doesn't look like a complete pile of ... out of the Musgraves; Fred for his hospitality at Curtin University and showing me how a world-class lab runs, Chris and Rich for their SHRIMP lessons and data processing skills, and Chris Kirkland for his positivity and ability to generate an amazing array of data tables and explanations that were a huge part of getting the UHT paper through.

Thanks to all the CERG tank crew inc. Dan, Laura, Naomi, Kieran, Lachy, Cesco, Katnip and Morgan, my upstairs running mates Jade and Bonnie, Rowan for sharing the Liverpool FC burden and Justin, who all made more difference than they think.

Enormous thanks to all my family and friends, Dad and Deb, Mum and Jon, Hannah, Maz, Jules, Devin, Jen and my extended family, who always make the effort to support me with all they can, take an interest in what i do and provide me with a wonderful foil to work which i am always grateful. Thanks lastly to my lovely, wonderful Kelly who gives me incentive to wake up and come home and supports every aspect of my life.



---

## Literature, significance and aims of this thesis

---

The physical architecture of orogens and the duration and rates at which orogeny progresses is a function of the inherited thermomechanical state of the lithosphere and its evolution through orogenesis. Furthermore metamorphism and deformation will result in modification of the thermal and mechanical properties of lithosphere and seek to dramatically affect the future reworking of a terrane. It follows then that the investigating the time-integrated record of metamorphism and deformation of a terrane will provide insight into the cause of orogeny and the effect of orogenic processes in modifying the physical properties of lithosphere.

The Musgrave Province in central Australia preserves a polymetamorphic and deformational record which spans at least 1330–520 Ma. Therefore, the Musgrave Province provides an excellent natural laboratory to examine the thermal and mechanical evolution of lithosphere through multiple orogenic cycles.

The metamorphic and deformational record is dominated by the 1220–1150 Ma Musgrave Orogeny predominantly involved the emplacement of voluminous felsic magmatism expressed as the orthopyroxene-bearing (charnockitic, ‘A-type’) granitic rocks of the Pitjantjatjara Supersuite (Maboko, et al., 1992; White, et al., 1999; Edgoose, et al., 2004; Evins, et al., 2010; Smithies, et al., 2011). These granitic rocks typically have an anhydrous primary mineralogy, are ferroan and enriched in titanium and phosphorus, and had extremely high intrusive temperatures >900°C (Smithies, et al., 2010; Smithies, et al., 2011). Mafic magmatism was rare and of low volume during the Musgrave Orogeny (Smithies, et al., 2011). Although it is established that temperatures were high (~900 °C) during Grenvillian metamorphism (Clarke & Powell, 1991; Glikson, et al., 1996; White, et al., 1999; White, et al., 2002; Wade, et al., 2008; Smithies, et al., 2011), the duration and footprint of the event are unknown. Therefore, investigating the time-integrated thermal structure of the crust is crucial, as metamorphic rocks provide a primary record of the temporal thermal state of the Earth (Brown, 2007) and such information can provide insight into the tectonic setting of such high-T metamorphism— which is debated, and the mechanisms by which the crust is able to reach high temperatures. The need to characterise and understand high-T events in a polymetamorphic terrane becomes crucial as it has major implications for future crustal reworking.

Reworking of the Musgrave Province occurred during the Ediacaran–Cambrian (600–520 Ma) intraplate Petermann Orogeny (e.g. Scrimgeour & Close, 1999; Scrimgeour, et al., 1999; Camacho & McDougall, 2000; Buick, et al., 2001; Flöttmann, et al., 2004; Wade, et al., 2005; Aitken, et al., 2009; Camacho, et al., 2009; Gregory, et al., 2009; Raimondo, et al., 2009; Raimondo, et al., 2010). The Petermann Orogeny involves magnitudes of crustal thickening, shortening and exhumation comparable to both plate margin orogenic systems, and intraplate systems such as Tien Shan in central Asia (Flöttmann, et al., 2004; Raimondo, et al., 2014). the Petermann Orogen has been the focus of numerous studies to understand the thermal and mechanical evolution of the system by investigating the timing, duration and physical conditions of metamorphism and deformation (Camacho, et al., 1997; e.g. Camacho, et al., 2001; Camacho, et al., 2009; Gregory, et al., 2009; Raimondo, et al., 2009; Raimondo, et al., 2010; Walsh, et al., 2013; Walsh, et al., in review). It is evident from these studies that the orogen preserves a spatially and temporally complex record of the thermal and mechanical evolution. Initial deformation and crustal thickening is argued to have developed in comparatively weak lithosphere, reflecting a regionally elevated thermal regime (Sandiford & Hand, 1998; Hand & Sandiford, 1999; Walsh, et al., in review), potentially caused by sedimentary cover creating thermal blanketing of high-heat-producing granitic crust (approximately 4  $\mu\text{W m}^{-3}$ ) that was localised in the mid-upper crust (Sandiford & Hand, 1998; Hand & Sandiford, 1999; Sandiford

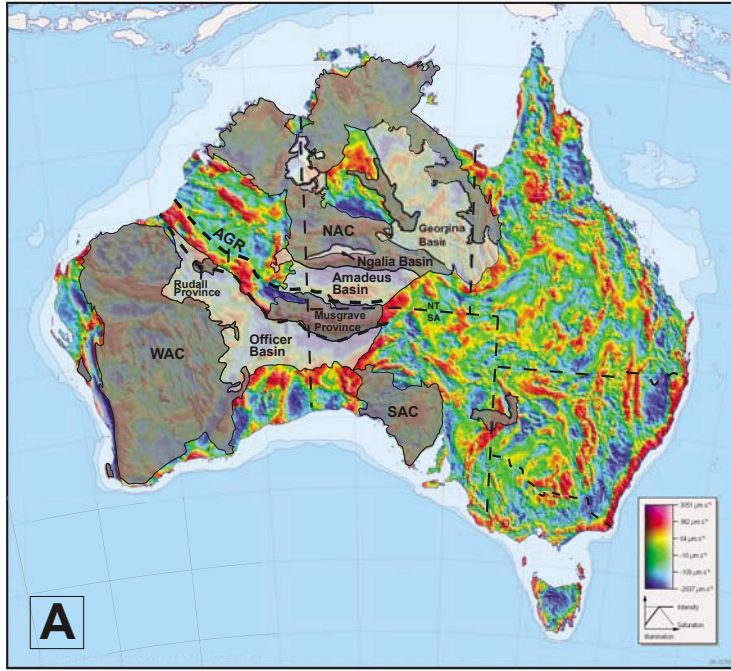
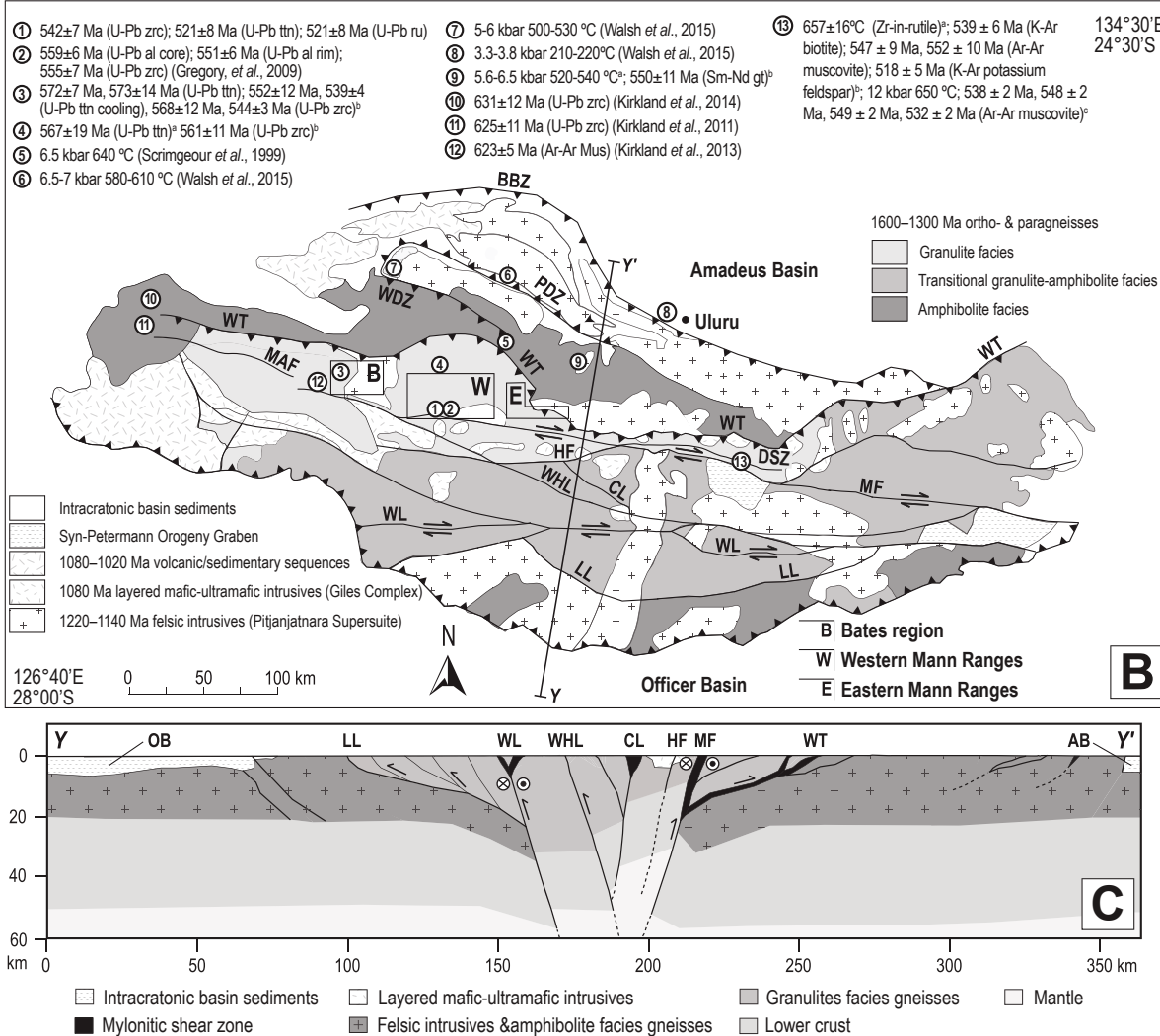


Figure 1. (a) Gravity map of Australia overlain with distribution of Proterozoic and early Phanerozoic basement provinces and sedimentary basins. Interpreted continuity of Ediacaran intraplate orogenic belt outlined in association with the Ankettell Gravity Ridge (AGR). (b) Regional solid geology map of the Musgrave Province. The locations of key E-W trending fault structures of the Petermann Orogen and previously collected geochronological and  $P-T$  data are shown. 1. (Walsh et al., 2013); 3. (Raimondo et al., 2009, 2010); 4a. (Walsh et al., 2013); 5. (Scrimgeour et al., 1999); 9. a (Walsh et al., in review) b (Scrimgeour et al., 1999); 13. a (Camacho et al., 2009), b (Camacho et al., 1997), c (Camacho and McDougall, 2000). Figure modified from Edgoose et al. (2004), Raimondo et al. (2010) and Aitken et al. (2009). (c) Schematic cross section (Y-Y') across the central Musgrave Block. Highlights the overall crustal-scale dextral transpressive shear system, involving significant Moho displacement and deep exhumation along the Woodroffe Thrust/Mann Fault. Modified from Aitken et al. (2009). Abbreviations: AB, Amadeus Basin; BBZ, Bloods Back Thrust Zone; CL, Caroline Lineament; HF, Hinckley Fault; LL, Lindsay Lineament; MAF, Mount Aloysius Fault; MF, Mann Fault; NAC, North Australian Craton OB, Officer Basin; PDZ, Piltardi Detachment Zone; SAC, South Australian Craton; WAC, West Australian Craton WDZ, Wankari Detachment Zone ; WHL, Wintigninna-Hinckley Lineament; WL, Wintigninna lineament; WT, Woodroffe Thrust.





& McLaren, 2002; McLaren, et al., 2003). The development of a deep (~10 km) and narrow foreland basin, a thick ( $\geq 20$  km) basement-involved (thick-skinned) foreland fold-thrust belt and the exhumation of the core of the orogen via lateral extrusion (channel flow) reflect continued orogenic evolution in a mechanically weak lithosphere associated with elevated temperatures (Raimondo, et al., 2009; Raimondo, et al., 2010; Walsh, et al., in review).

However, in contrast to this notion of a (hot/warm) weak lithosphere across the Petermann Orogen is the presence of comparatively low geothermal gradient rocks ( $\sim 9^\circ\text{C km}^{-1}$ ;  $350^\circ\text{C}$ , 12 kbar) in the axial core, in which low temperatures are deduced based on the interpretation that Ar–Ar isotopic systems have failed to reset (Camacho, et al., 1997; Camacho & McDougall, 2000). Within this core, mylonitic shear zones that host transitional-eclogite facies rocks and voluminous pseudotachylites (Lin, et al., 2005) define Petermann-aged metamorphism. Mesoproterozoic granulites to the south of the orogenic core are largely unaffected by Petermann-aged reworking. To explain the presence of ‘cold’, transitional eclogite facies rocks and pseudotachylites as well as their spatially restricted occurrence, the heat source for Petermann-aged tectonism has been argued to be shear heating (Camacho, et al., 2001). Tectonism (i.e. burial, metamorphism and exhumation) associated with shear heating is argued to be rapid—of the order of 1 Myr—within regionally cold and strong lithosphere (Camacho, et al., 2009). Such an interpretation has been reinforced through using compositional zoning profiles in garnet from the core of the orogen to estimate/constrain cooling rates and the preservation of pre orogenic ages in low-T thermochronometers (Camacho, et al., 2001; Camacho, et al., 2009). Therefore, the Petermann Orogen preserves a seemingly paradoxical record of tectonism in warm, weak lithosphere as well as in cold, strong lithosphere.

The currently established views on the tectonic and metamorphic evolution of the Petermann Orogeny imply opposing views on the thermomechanical state of the central Australian lithosphere. This has significance as it has implications for the initiation and localisation of deformation and the development of orogeny in the interior of the Australian plate.

The general aim of this thesis is to characterise the metamorphic and structural evolution of the Musgrave Province with the aim of understanding how the physical properties of crustal lithosphere change through time in response to the metamorphic processes which occur during orogenesis. This is firstly achieved by investigating the Grenvillian-aged high temperature metamorphic event to understand the effects of high-T crustal processes and establish the lithospheric framework in which to assess younger Ediacaran–Cambrian reworking. Secondly, it focusses on the mechanical response of lithosphere to Ediacaran–Cambrian reworking in an intraplate setting to assess the importance of inherited lithospheric thermal and mechanical properties and more broadly, the thermo-mechanical evolution of intraplate orogeny.

The specific aims of this thesis are:

1. Determine the physical conditions and duration of high-T Grenvillian-aged metamorphism and investigate the crustal and tectonic processes leading to high temperatures in the Musgrave Province
2. To obtain precise geochronological constraints on deformation, metamorphism and exhumation/cooling from both the orogenic foreland and hinterland to evaluate the spatial and temporal patterns of deformation during intraplate reworking.
3. To investigate the mechanical strength of the pre-Petermann Orogeny lithosphere
4. Assess drivers for metamorphism by investigating the duration, timing and spatial footprint of high-grade metamorphism in the core of the orogen.
5. To critically evaluate the thermomechanical state of the lithosphere prior to, during and post Petermann orogeny.

## Chapter Outlines

**Chapter 1** provides an assessment of the  $P$ – $T$ – $t$  evolution of Grenvillian-aged high- $T$  metamorphism in the Musgrave Province. It presents an application of modern metamorphic analysis ( $P$ – $T$  pseudosections) and high-precision U–Pb monazite geochronology to high-grade metamorphic rocks across the orogen in order to constrain the timing, duration, physical conditions and spatial distribution of high- $T$  metamorphism in the Musgrave Province. More broadly, these datasets allow discussion of the ability of the crust to generate and maintain high temperatures, the use of monazite as a geochronometer in high- $T$  terrains, the tectonic setting of the Musgrave Province during the Grenvillian and the spatial footprint of high- $T$  metamorphism. This chapter describes and discusses high- $T$  metamorphic processes which dramatically modify the thermal and mechanical properties of the lithosphere. Therefore the outcomes of this study have major implications for future reworking of the Musgrave Province.

**Chapter 2** shifts the focus of the thesis to the younger Ediacaran–Cambrian intraplate Petermann Orogeny. It investigates the timing of high- $P$  metamorphism and the rate of cooling during intraplate reworking in the Mann Ranges region, central Musgrave Province. Titanite, zircon and rutile geochronology is collected from partially migmatised meta-igneous rocks from shear zones. This data allows the temperature–time history of orogeny to be constructed and the applicability of previously suggested models for the thermal evolution of the Petermann Orogeny to be tested. Additionally partially migmatised zones represent volumetrically minor Petermann-aged deformation in an otherwise anhydrous orogenic core and therefore requiring mechanisms additional to elevated temperatures in order to localise metamorphism and deformation during intraplate reworking.

**Chapter 3** builds on the previous chapter by assessing the thermomechanical state of the lithosphere during orogeny by examining the large scale architecture of the foreland fold-thrust belt and foreland basin system. The record of deep burial metamorphism of syn-orogenic sediments in the foreland basin and thick-skinned fold-thrust is used to measure the flexural (burial) response of the foreland basin and fold-thrust belt. The architecture of the foreland is a direct function of the mechanical strength of the lithosphere in which the Petermann Orogen developed, therefore this innovative approach allows the lithospheric strength to be measured and the mechanisms by which intraplate orogeny develops to be examined.

**Chapter 4** builds on the previous chapter in that it constrains the timing of deep burial of the foreland of the Petermann Orogeny, therefore placing the localisation of deformation in the foreland in an absolute time context in the history of the orogen.  $^{40}\text{Ar}/^{39}\text{Ar}$  muscovite and biotite geochronology is used to constrain the timing of metamorphism in fold-thrust belt sequences and therefore the burial of the foreland of the orogen. Integration of geochronological data from the foreland allows the spatial and temporal patterns of deformation to be assessed and provides insight into the processes by which intraplate orogens develop and how lithosphere evolves rheologically during orogenesis.

**Chapter 5** builds on the previous chapters by investigating the record of metamorphism in the lower crust of the Petermann Orogeny. U–Pb geochronology and metamorphic  $P$ – $T$  pseudosections are used to assess the physical conditions of metamorphism, the duration of elevated temperatures and cooling, and the spatial distribution of metamorphism in lower crustal shear zones and their host country rocks in Amata region of the Musgrave Province. This study specifically seeks to address whether metamorphism during intraplate orogeny was pervasively developed or localised in zones of high-strain. The study discusses the drivers for metamorphism of the Petermann Orogeny, the ability of the crust to record multiple cycles of metamorphism and highlights that the inherited composition of the crust plays a fundamental role in the thermal and mechanical evolution of the orogen.

**Chapter 6** concludes the thesis by providing a concise discussion of the current views regarding the thermomechanical evolution of the central Australian lithosphere during the intraplate Petermann Orogeny and the significant role Grenvillian-aged metamorphism played in modifying the crust. It assimilates the key results and interpretations of the previous chapters and highlights questions that future research might pursue.



# Chapter 1

This chapter is published as:

A.K. Walsh, D.E. Kelsey, C.L. Kirkland, M. Hand, R.H. Smithies, C. Clark, H.M. Howard,  
P–T–t evolution of a large, long-lived, ultrahigh-temperature Grenvillian belt in central  
Australia, *Gondwana Research*, Available online 27 June 2014, ISSN 1342-937X, <http://dx.doi.org/10.1016/j.gr.2014.05.012>.





---

# ***P–T–t* evolution of a large, long-lived, ultrahigh-temperature Grenvillian belt in central Australia**

---

## **ABSTRACT**

The ~120,000 km<sup>2</sup> Musgrave Province forms part of a continuous Musgrave–Albany–Fraser mid-late Mesoproterozoic orogenic system that transects central and southern Australia, and continues into formerly contiguous Antarctica. Voluminous felsic magmatic rocks that intruded over the interval 1330–1150 Ma, corresponding globally to the Grenvillian timeline, dominate the Musgrave Province. However, rare but widely distributed metapelitic granulites contain peak metamorphic mineral assemblages comprising garnet + sillimanite ± quartz ± spinel. These are variably overprinted by coronae and/or symplectites of cordierite-bearing assemblages such as cordierite + spinel + magnetite ± plagioclase ± garnet. Petrologic forward modelling and Zr-in-rutile thermometry indicates these peak mineral assemblages developed at thermally extreme conditions of approximately 1000 °C and ca. 7–8 kbar. These ultra-high temperature (UHT) conditions appear to have prevailed throughout the Musgrave Province, across an approximate 600 km strike distance. The retrograde *P–T* evolution was characterised by modest decreases in pressure during the initial high temperature segment of the cooling path, suggesting that the crust was not significantly thickened as a result of tectonism. Combined SIMS (SHRIMP) and LA–ICP–MS U–Pb geochronology constrains the total range of metamorphic monazite growth/recrystallisation ages span 1263–1111 Ma with most individual samples spanning an age range of ≥ 80 Myr. The total age span implies approximately 150 Myr of perturbed thermal conditions during the Musgrave Orogeny. Our data requires that monazite is extremely resistive to isotopic resetting, even when exposed to extreme thermal conditions for long (≥80 Myr) periods. The thermal conditions, large regional footprint and long timescale of metamorphism and magmatism classify the Musgrave Province as a large, hot orogen.

---

## **1. INTRODUCTION**

The Musgrave–Albany–Fraser Orogen represents the Australian component of the global Grenvillian-aged orogenic system (Fig. 1). The Musgrave–Albany–Fraser system has been widely used as a ‘piercing point’ for Proterozoic reconstructions linking Laurentia and Antarctica to Australia (Moore, 1991; Karlstrom et al., 2001; Duebendorfer, 2002; Wingate et al., 2002). The Grenville belt in Laurentia is well documented as reflecting predominantly collisional tectonics (e.g. Hoffman, 1991; Davidson, 1995; Cawood and Pisarevsky, 2006). However, for the Australian Grenvillian-aged belts it is much less clear what the prevailing tectonic regime was (Myers et al., 1996; Wingate et al., 2002; Wade et al., 2008; Aitken and Betts, 2009a; Morrissey et al., 2011). In older continental

reconstructions of Proterozoic Australia there was a tacit assumption that the Grenvillian-aged tectonism in the Musgrave Province (Fig. 1) reflected amalgamation (Maboko et al., 1991). However, subsequent work demonstrated that the high-pressure rocks upon which this assertion was made are not Grenvillian-aged, but rather the product of late Neoproterozoic (Ediacaran) to Cambrian intracontinental compressional reworking (Maboko et al., 1992; Camacho and Fanning, 1995; Scrimgeour and Close, 1999; Gregory et al., 2009; Raimondo et al., 2009; Raimondo et al., 2010; Walsh et al., 2013). More recent work on the Western Australian portion of the Musgrave Province (Fig. 2) has demonstrated that voluminous and comparatively juvenile felsic magmatism during the middle of three Grenvillian-aged events to have formed and shaped the Musgrave Province, the

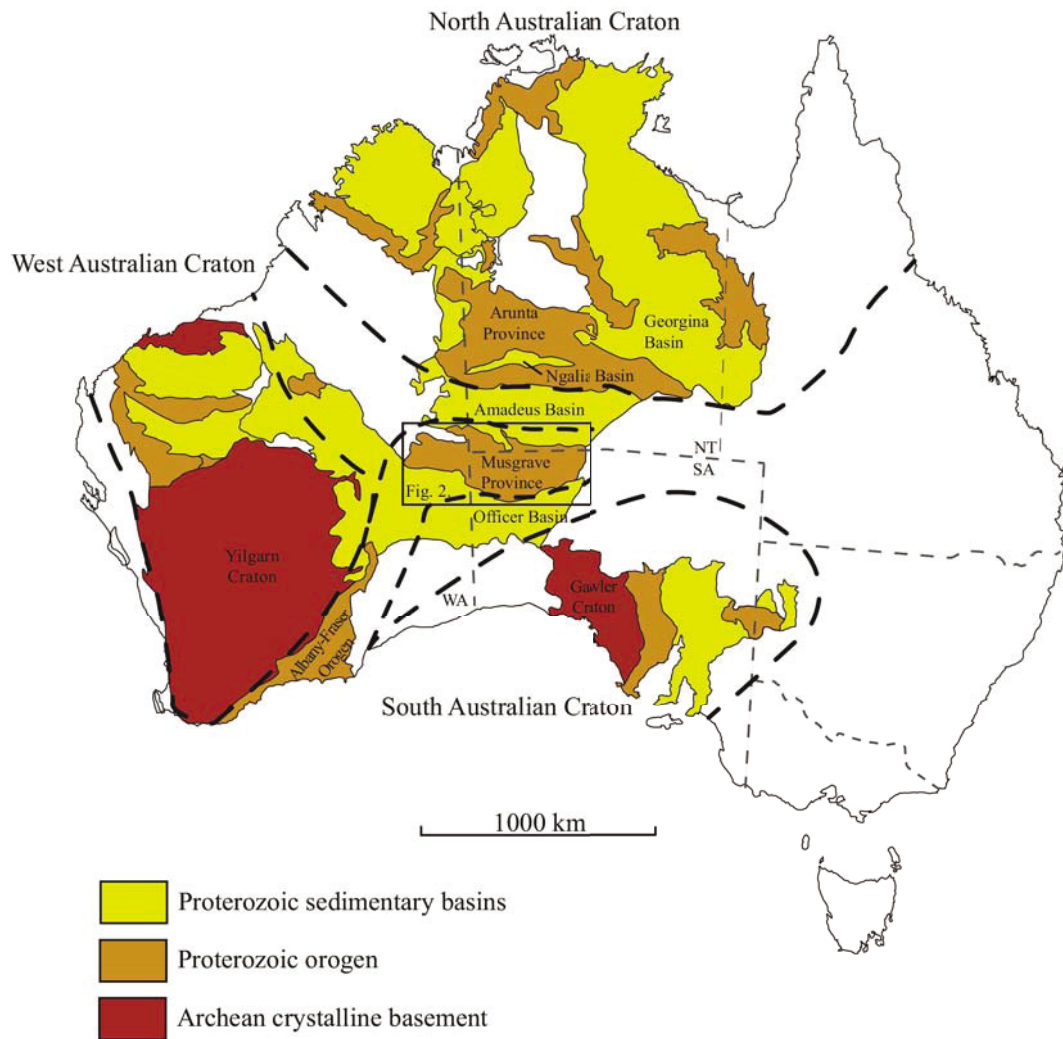


**Figure 1.** Map of Australia showing the location of the Musgrave Province with respect to the major cratonic basement and basin regions.

1220–1150 Ma Musgrave Orogeny, has geochemical characteristics more akin to ‘within-plate’ magmatism rather than arc-related affinities (Smithies et al., 2011). Ultimately, the prevailing tectonic setting during the Musgrave Orogeny remains poorly understood.

This study focuses on the Musgrave Orogeny as it is the most pervasive Grenvillian-aged events to have formed and shaped the Musgrave Province. One approach to investigating the possible tectonic setting of the 1220–1150 Ma Musgrave Orogeny is to study the time-integrated thermal structure of the crust, as metamorphic rocks provide a primary record of the temporal thermal state of the Earth (Brown, 2007), which in turn can

be characteristic of different tectonic settings. As the number of studies investigating the metamorphic evolution of rocks in the Musgrave Province is small (Maboko, 1988; Clarke and Powell, 1991; Maboko et al., 1991; Camacho and Fanning, 1995; Clarke et al., 1995; Glikson et al., 1996; White and Clarke, 1997; Scrimgeour and Close, 1999; White et al., 2002; Kelly et al., 2006; Gregory et al., 2009; Smithies et al., 2011) relative to the size of the province, there is considerable scope to provide new and useful constraints on the thermo-physical conditions of the Musgrave Orogeny. The purpose of this study is to present a broad regional foundation for the thermal structure of the crust at the time of the Musgrave Orogeny by investigating samples from widely separated locations

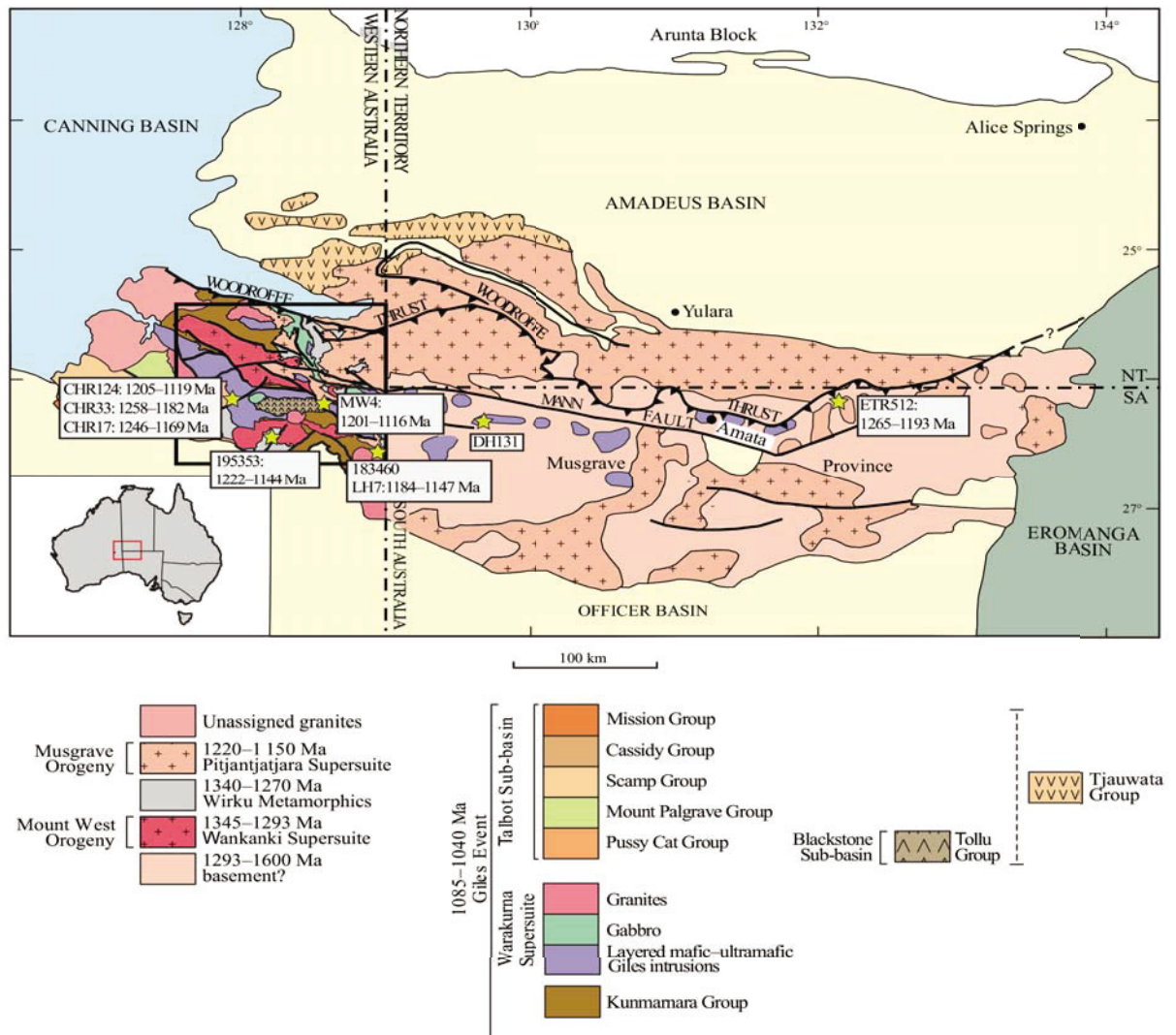


**Figure 2.** Interpreted solid geology map of the Musgrave Province, showing location of west Musgrave Province (boxed, Fig. 3). The difference in detail between the western Australian portion and the remainder of the Musgrave Province reflects the large difference in amount of detailed work conducted either side of the Western Australian border. Modified from Howard et al. (2011).

in the province. UHT metamorphism in the Musgrave Province has been suggested by recent workers (e.g. Smithies et al., 2011; Smithies et al., 2014), however, these studies utilise magmatic crystallisation temperatures in addition to limited constraints from phase equilibria. This paper combines quantitative metamorphic phase equilibria (calculated pseudosections) and Zr-in-rutile thermometry with accessory mineral U–Pb geochronology, to demonstrate that the Musgrave Orogeny was regionally characterised by elevated thermal gradients ( $\geq 40$  °C km<sup>-1</sup>) and ultrahigh-temperature (UHT) conditions over a timescale potentially as long as 150 Myr. The regionally extreme thermal conditions

identify the Musgrave Province as an ancient large, hot and long-lived terrain. In conjunction with the existing and extensive dataset on magmatic rocks produced during the Musgrave Orogeny (Smithies et al., 2010; Smithies et al., 2011), we infer that protracted metamorphism and magmatism occurred in hot, probably thin crust, and possibly occurred within an extensional setting. Our findings have implications for: 1) the ability of Earth's crust to generate and sustain extreme thermal conditions for long periods of time; 2) the interpretation of U–Pb monazite geochronology in high-grade gneiss terrains; 3) the ability of monazite to resist isotopic resetting during prolonged exposure to high



temperatures; 4) the ability of high-Fe–Al metapelitic rocks to reliably record evidence of UHT metamorphic conditions; 5) the tectonic setting of the Musgrave Province during the Musgrave Orogeny; and 6) the ‘spatial footprint’ of regional UHT metamorphism.

## 2. REGIONAL GEOLOGY

The Musgrave Province is an east–west trending Mesoproterozoic basement province that outcrops over ~120,000 km<sup>2</sup>, straddling

the Northern Territory, South Australian and Western Australian borders (Camacho and McDougall, 2000; Aitken and Betts, 2008; Wade et al., 2008) (Figs. 1, 2). The external east–west orientation of the outcropping Musgrave Province is a strong function of the overprinting intraplate Ediacaran- to Cambrian-aged Petermann Orogeny (Camacho et al., 1997; Wade et al., 2008). The Petermann-aged structures have dissected the older rocks such that granulite facies gneisses are exposed to the south (hangingwall) and amphibolite

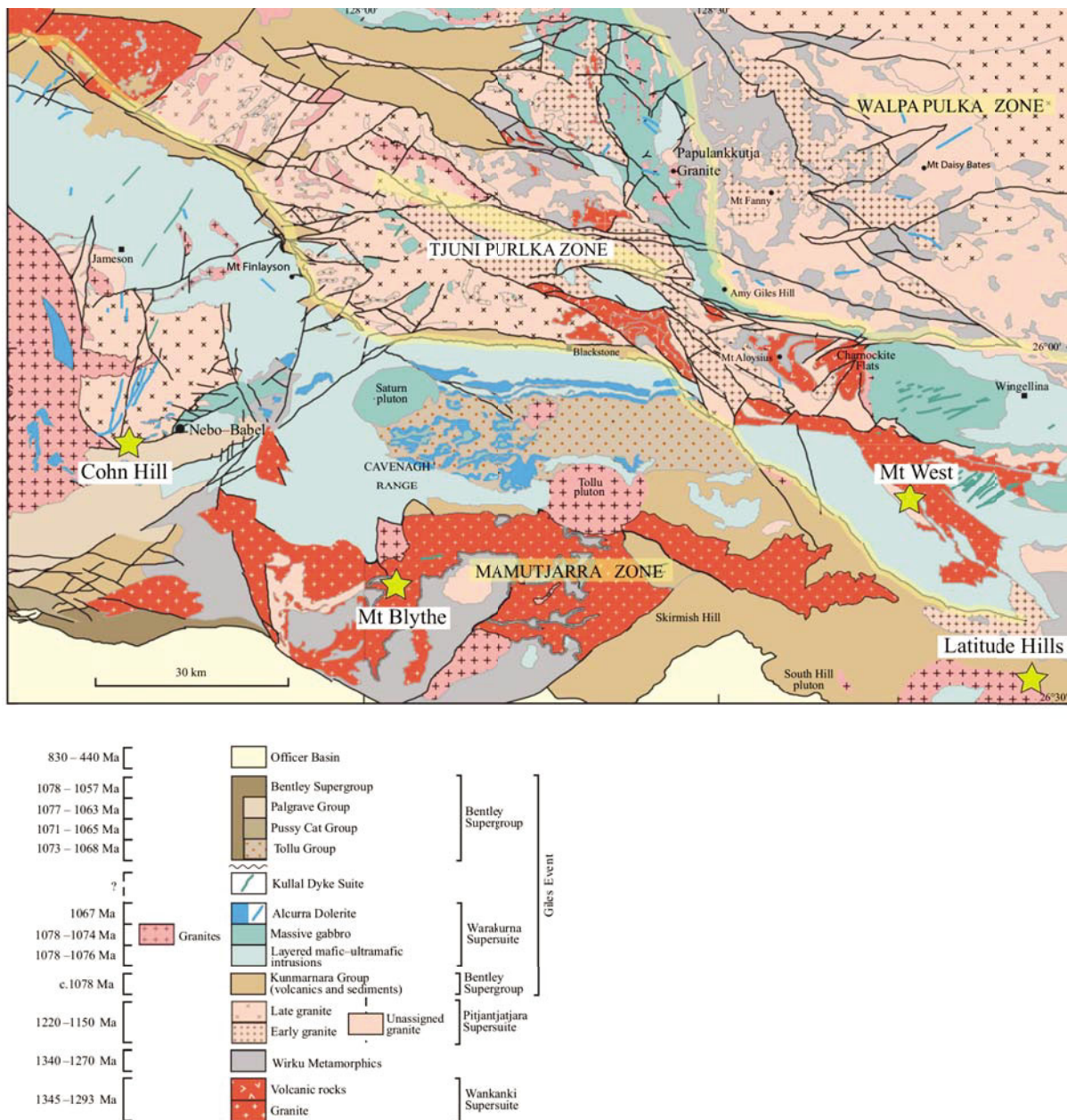


**Figure 3.** Simplified solid geology map of the west Musgrave Province showing the three main lithotectonic zones. Modified from Smithies et al. (2011).



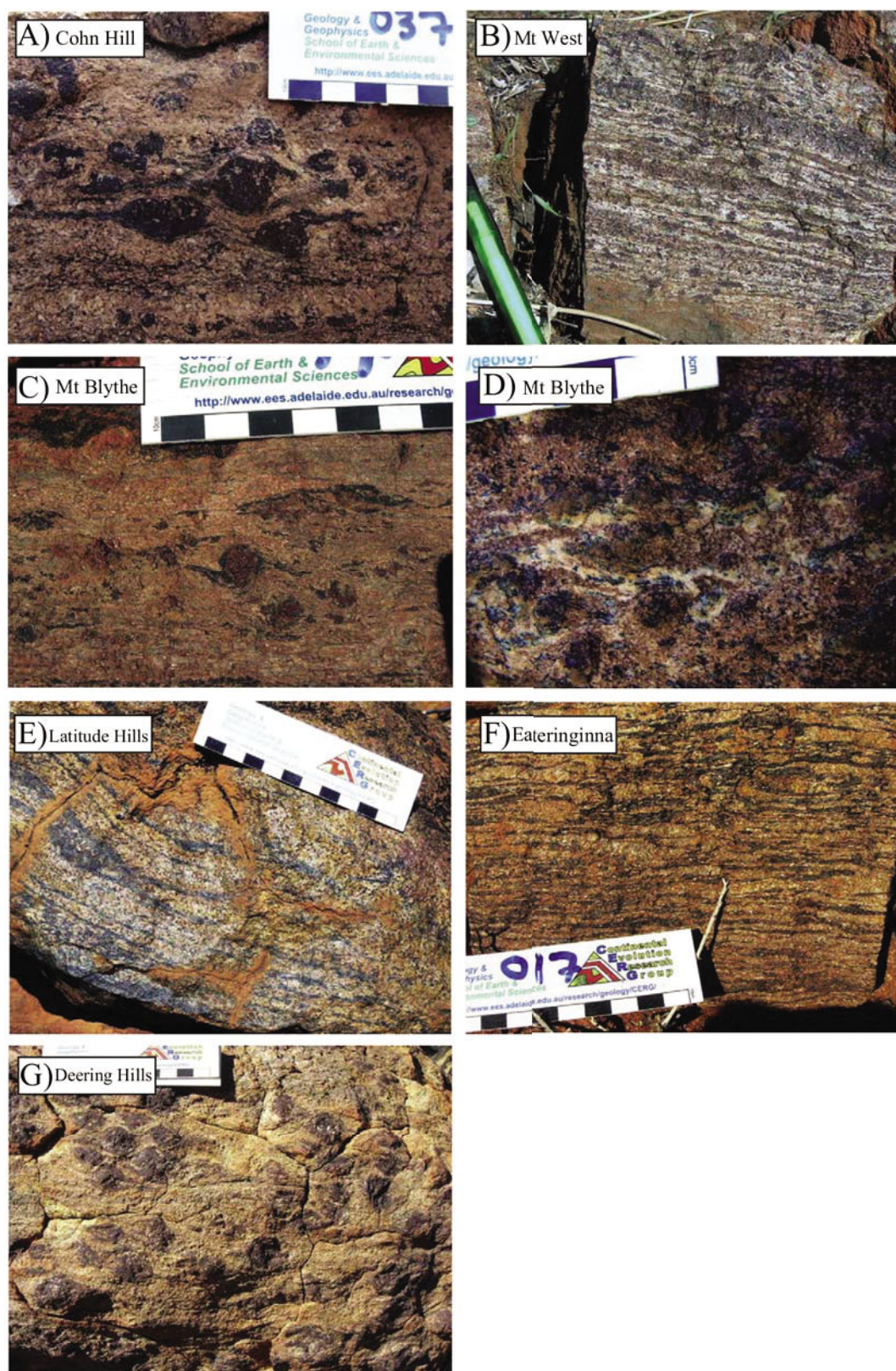


**Figure 4.** Outcrop photos from sample localities. (A) Cohn Hill locality, showing garnet porphyroblasts in amigmatitic quartz + feldspar matrix. Note the garnet in the centre defines a sigma clast in the XZ plane (prominent sillimanite-bearing lineation is parallel to long edge of photo), and the tails of the clast are comprised of  $cd + sp + mt \pm pl$ . The breakdown of garnet (with sillimanite) to produce symplectites is linked to the deformation of the rock. Portion of scale bar shown is 7 cm long. (B) Mt West locality, showing garnet porphyroblasts in a highly strained and migmatitic quartz + feldspar matrix. Spinel and sillimanite are not obvious at this scale. Our locality is the 'Northern metapelite' locality in White et al. (2002). Portion of pencil

**Table 1.** Summary of information and results for each sample discussed in this paper.

Sample	Region	GPS Location (UTM)	Peak metamorphic assemblage	U–Pb monazite age range (Ma)	Peak metamorphic conditions
CHR124	Cohn Hill, WA	52 J 363718 mE 7112335 mS	G–sill–pl–ksp–ilm–q	1263–1163	920–1000 °C at >7 kbar
CHR33	Cohn Hill, WA	52 J 362653 mE 7115111 mS	G–sill–pl–ksp–ilm	1234–1162	–
CHR17	Cohn Hill, WA	52 J 363245 mE 7118060 mS	G–sill–pl–ksp–ilm	1246–1155	–
MW4	Mt West, WA	52 J 478131 mE 7101875 mS	G–sill–sp–pl–ksp–ilm–q	1219–1116	920–1040 °C at 6.7–8 kbar
195353	Mt Blythe, WA	52 J 401298 mE 7085212 mS	G–sill–sp–pl–ksp–ilm–q	1244–1152	950–1050 °C at 6.5–7 kbar
183460	Latitude Hills, WA	52 J 495916 mE 7080309 mS	G–sill–sp–ilm–q	–	>1000 °C at 6.5–8 kbar
LH7	Latitude Hills, WA	52 J 496800 mE 7077616 mS	G–sill–sp–ksp–ilm–q	1147–1111	980–1050 °C at 6.8–7.8 kbar
ETR512	Eateringenina, SA	53 J 297480 mE 7113893 mS	G–sill–sp–pl–ksp–ilm–q	1251–1193	950–1050 °C at 7–9 kbar
DH131	Deering Hills, SA	52 J 592261 mE 7081433 mS	G–sill–ksp–ilm–q–ru	–	900–980 °C

facies and lower-grade mid- to upper-crustal basement and cover rocks are exposed to the north (including north of the Woodroffe Thrust) (Fig. 2). The trends of structural fabrics related to older events such as the Grenvillian-aged Musgrave Orogeny have a NW to NE trend (Wade et al., 2008; Aitken and Betts, 2009a, 2009b; Smithies et al., 2011).

The outcropping Musgrave Province exposes predominantly granulite-facies gneisses that preserve a complex deformational, metamorphic and magmatic history (Glikson et al., 1995; Sun et al., 1996; Edgoose et al., 2004; Wade et al., 2008; Evins et al., 2010; Smithies et al., 2011). Magmatic and volcanic rocks were intruded and extruded during numerous Mesoproterozoic events outlined below and dominate outcrop throughout the Musgrave Province (Figs. 2, 3). The composition and structure of the basement to the province is cryptic although Nd- and Hf-isotopic data from the west Musgrave Province (the Western Australian portion of the Musgrave Province is herein referred to as ‘west Musgrave Province’) implies three components including c. 1500–1600 Ma Mesoproterozoic to Paleoproterozoic juvenile basement (Wade et al., 2006; Kirkland et al., 2013), dominant 1900 Ma juvenile

basement (possibly an underplate) and minor unradiogenic Archean component (Kirkland et al., 2013). An unnamed event involved the emplacement of felsic calc-alkaline magmas comprising the Papulankutja Supersuite in the west Musgrave Province, which represents a basement component with age c. 1400 Ma, and its contemporaneous erosion and deposition into sedimentary basins (Howard et al., 2011). The Papulankutja Supersuite may represent magmatism during initial stages of subduction associated with the amalgamation of the South Australian and North Australian Craton (Kirkland et al., 2013). All three Grenvillian-aged events, spanning the total age range of c. 1345 Ma to 1050 Ma, involved the emplacement and extrusion of voluminous magmatic (many now gneissic) and volcanic rocks that dominate outcrop (~ 50–60% of total outcrop) throughout the province (Glikson et al., 1996; Camacho et al., 2002; Wade et al., 2008; Evins et al., 2010; Smithies et al., 2010; Howard et al., 2011; Smithies et al., 2011).

The majority of our understanding of the Grenvillian-aged events comes from the west Musgrave Province (Smithies et al., 2010; Smithies et al., 2011). The 1345–1293 Ma Mt West Orogeny is the oldest and least

shown is 7 cm long. (C) Mt Blythe locality, showing coarse very coarse garnet porphyroblasts/poikiloblasts (inclusions of quartz and K-feldspar) wrapped by sillimanite in a migmatitic quartz+ feldsparmatrix. Garnet is separated from sillimanite by cordierite+spinel bearing symplectites. Portion of scale bar shown is 6 cm long. (D) Mt Blythe locality showing a close-up view of another, more sillimanite- and spinel-rich portion (still with garnet and still migmatitic) of the metapelitic gneisses. The dark mineral is spinel+/- magnetite. Portion of scale bar shown is 4 cm long. (E) Latitude Hills locality, showing a quartz-garnet-rich metapelitic gneiss. The dark layers are sillimanite-, spinel, cordierite-rich. Scale bar is 11 cm long. (F) Eateringenina. This gneiss in this photo is cordierite- and sillimanite-rich, with abundant leucosomes of K-feldspar and quartz. Garnet is not abundant in this particular photo. However, visitation to the legacy sample site of sample ETR512 was not done by any of the authors. Portion of scale bar shown is 9 cm long. (G) Deering Hills locality, showing garnet and sillimanite-rich layers, with abundant leucosomes of K-feldspar and quartz.



well-known Grenvillian event. It involved the emplacement of calc-alkaline granitic rocks of the Wankanki Supersuite (Evinset al., 2010; Smithies et al., 2011), which, thus far, have only been identified in the west Musgrave Province. These granitic rocks are typically metaluminous, calc-alkaline granodiorites and monzogranites that are compositionally similar to the Phanerozoic granites of the Andean continental arc (Smithies et al., 2010). Therefore, the Mt West Orogeny could be linked to the final accretionary event during amalgamation of the South Australian, North Australian and West Australian Cratons (Giles et al., 2004; Betts and Giles, 2006; Smithies et al., 2011; Kirkland et al., 2013) (Fig. 1).

The 1220–1150 Ma Musgrave Orogeny predominantly involved the emplacement of voluminous felsic magmatism expressed as the orthopyroxene-bearing (charnockitic, ‘A-type’) granitic rocks of the Pitjantjatjara Supersuite (Maboko et al., 1992; White et al., 1999; Edgoose et al., 2004; Evinset al., 2010; Smithies et al., 2011). These granitic rocks typically have an anhydrous primary mineralogy, are ferroan and enriched in titanium and phosphorus, and had extremely high intrusive temperatures N 900 °C (Smithies et al., 2010; Smithies et al., 2011). Mafic magmatism was rare and of low volume during the Musgrave Orogeny (Smithies et al., 2011).

The c. 1085–1050 Ma Giles Event first resulted in the emplacement of layered mafic and ultramafic rocks (Evinset al., 2010; Smithies et al., 2011). Extrusion and deposition of bimodal volcanic sequences of the Bentley Supergroup subsequently occurred between 1075 and 1026 Ma (Sun et al., 1996; Wade et al., 2008; Evinset al., 2010). The Bentley supergroup unconformably overlies deformed Giles-aged layered mafic intrusions, indicating that deformation and exhumation to the surface was a part of the Giles Event. The Giles Event has been interpreted to result from a mantle plume (Wingate et al., 2004) although a more complex geodynamic

setting is probably required (Evinset al., 2010; Smithies et al., 2013). The Giles event could represent a long-lived, failed rift occurring in an intracontinental setting, called the Ngaanyatjarra Rift (Evinset al., 2010).

In the west Musgrave Province, magmatic rocks emplaced during the three consecutive Grenvillian-aged events are distributed between three lithotectonic zones; the Tjuni–Purlka, Walpa–Pulka and Mamutjarra zones (Fig. 3) (Smithies et al., 2010; Smithies et al., 2011). Felsic meta-igneous rocks generated during the Musgrave Orogeny dominate outcrop in the northeastern Walpa Pulka Zone (Fig. 3). By contrast, meta-igneous rocks of the Mt West Orogeny and Giles Event dominate outcrop in the southwestern Mamutjarra Zone (Fig. 3). Between these zones, the Tjuni Purlka Tectonic Zone (Fig. 3) is a broad northwest-trending zone that was a focus for deformation from at least c. 1220 Ma to c. 1050 Ma (Smithies et al., 2010). The Tjuni Purlka Tectonic Zone contains meta-igneous rocks from all three Grenvillian-aged events, as well as volcanic rocks of the Bentley Supergroup.

The Wirku Metamorphics, which are gneissic metasedimentary rocks in the west Musgrave Province, are interpreted to have protoliths of sedimentary and lesser volcanoclastic and volcanic origin, based on locally continuous layering (Fig. 4a, b) and the presence of pelitic, arkosic, and near-orthoquartzitic interlayers (Smithies et al., 2010). Their maximum depositional age is constrained by detrital zircon U–Pb data to between c. 1360 and 1307 Ma, whereas intrusive contacts with granites of the Mount West Orogeny provide a minimum depositional age of 1345–1293 Ma (Smithies et al., 2010). Elsewhere in the Musgrave Province, metasedimentary gneisses are termed the ‘Birksgate Complex’ (Major and Connor, 1993) or ‘Musgravian gneisses’ (Edgoose et al., 2004) and depositional age information is poorly constrained. It is not known if the metasediments of the Wirku Metamorphics



and Birksgate Complex/Musgravian Gneisses are equivalents of each other.

The dominant metamorphic imprint on the Musgrave Province is a result of the Musgrave Orogeny (Smithies et al., 2011). Regionally extensive granulite-facies conditions of  $N$  850–900 °C and 7–8 kbar were reached (Clarke and Powell, 1991; Glikson et al., 1996; White et al., 1999; White et al., 2002; Wade et al., 2008; Smithies et al., 2011) by rocks outcropping south of the Mann Fault (Fig. 2). Modern metamorphic (i.e. pseudosection) analysis has been used in one study (White et al., 2002); however, no existing metamorphic study has derived accessory mineral age data from the same rocks used for metamorphic analysis (cf. preliminary results in Smithies et al., 2011). Corundum and quartz assemblages in anhydrous sillimanite–magnetite quartzites from the Latitude Hills (R. W. White, pers. comm.) and biotite-absent garnet–corundum–quartz–K-feldspar magmatic rocks from Amata, south Australia (Collerson) provide circumstantial support for high temperature granulite facies metamorphism.

### 3. SAMPLE DESCRIPTION

Metapelitic rocks are sensitive recorders of metamorphic conditions due to the large number of mineralogical changes such rocks experience as they travel through the crust (i.e.  $P$ – $T$  space). As such, metapelitic rocks are ideal for interrogating the thermal structure of the crust. Whereas there is a paucity of metapelitic rocks across the Musgrave Province, rare occurrences containing garnet, sillimanite, spinel and cordierite with or without quartz outcrop in a number of locations across the Province (Figs. 2, 3; Table 1) and are here used to constrain the time-integrated thermal structure. Metapelitic rocks of the Wirku Metamorphics comprise seven of the nine samples of this study, with the eighth and ninth metapelites being from the Birksgate Complex in the central and eastern Musgrave Province in South Australia (Fig. 2). In

outcrop, metapelitic rocks are strongly foliated and lineated and commonly highly migmatitic (Fig. 4). Typically, foliation is defined by alternating Al-rich (sillimanite–garnet–spinel–cordierite-bearing) layers and leucosome and/or psammitic layers (Fig. 4). A pronounced, usually NE- or SW-plunging, lineation is defined by coarse-grained sillimanite, but may also be defined by elongate, plastically deformed garnet porphyroblasts as well as quartz ribbons. In rare examples, dark symplectites (which can be identified in thin section as cordierite + spinel + magnetite  $\pm$  plagioclase) define  $\sigma$ - and  $\delta$ -tails on garnet porphyroblasts (Fig. 4a) implying ductile deformation was synchronous with or post-dates the breakdown of garnet and development of symplectic coronae mineral assemblages. The metamorphic reactions inferred from microstructures in the metapelitic rocks are very similar across the entire Province, though the morphology of the reaction products differs from location to location. Overall, a peak mineral assemblage of garnet + sillimanite  $\pm$  spinel  $\pm$  quartz  $\pm$  K-feldspar  $\pm$  plagioclase (+ silicate melt) is overprinted to varying degrees by coronae and/or symplectitic coronae of cordierite-bearing assemblages such as cordierite  $\pm$  spinel + magnetite  $\pm$  plagioclase  $\pm$  garnet (Fig. 5, Table 2). Silicate melt is interpreted as part of the peak assemblage in all samples due to the migmatitic and ksp-qtz-rich nature of the samples at outcrop scale (Fig. 4). One of the striking features of the metapelitic rocks of the Musgrave Province is the total, or near total, absence of biotite. Any biotite that is present is either as (very) rare inclusions in garnet, or as tiny, ragged, poorly shaped grains that comprise  $\leq 2\%$  area of thin sections.

Samples CHR124 (UTM 52J 363718 mE 7112335 mS), CHR 33 (UTM 52 J 362653 mE 7115111 mS) and CHR17 (UTM 52J 363242 mE 7118060 mS), from the Cohn Hill region (Figs. 2, 3) in the west Musgrave Province, contain porphyroblastic garnet grains

(1–3 mm in diameter) and sillimanite ( $\leq 2$  mm in length), surrounded by a matrix comprising fine-grained (approximately 0.5 mm in diameter), plagioclase, quartz (absent in CHR33 and CHR17), K-feldspar and ilmenite (Fig. 5a, b). Well-developed symplectitic coronae separate garnet from sillimanite and from the matrix minerals (Fig. 5c, d). These coronae around garnet may be up to 1 mm wide, and mostly consist of cordierite and spinel<sub>ss</sub> (ss = solid solution with magnetite), with some minor plagioclase and ilmenite (Figs. 5a–d, 6a). The timing of exsolution of magnetite from spinel is unclear. Spinel<sub>ss</sub> and cordierite intergrowths are interpreted to be pseudomorphing coarse-grained sillimanite (Fig. 5a–d), as there are cases where relict sillimanite remains in the centre of well-developed symplectites (Figs. 5c, d). In places, sillimanite is only partially mantled by narrow cordierite or spinel coronas (Fig. 5b). Ilmenite occurs in the matrix, commonly in contact with quartz and rarely included in garnet and biotite. Biotite occurs in low (c. 5% total area of thin section) abundance, commonly as fine-grained, anhedral and poorly formed grains in the matrix, in contact with plagioclase and K-feldspar or as fine-grained rounded inclusions in garnet, interpreted to be retrograde, and relict prograde inclusions respectively (Fig. 5a–d). In sample CHR124 the peak assemblage is interpreted to be garnet + sillimanite + silicate melt + K-feldspar + plagioclase + ilmenite + quartz and the post-peak/retrograde mineral assemblage is interpreted to involve cordierite + spinel<sub>ss</sub> + plagioclase and biotite.

Sample MW4 (52 J 478131 mE 7101875 mS) is from Mt West (Figs. 2, 3) in the West Musgrave Province. This sample is from the ‘Northern metapelite’ outcrop in (White et al., 2002). As such, the petrography of this sample is well documented by White et al. (2002). The sample comprises a coarse-grained assemblage of garnet, sillimanite, spinel<sub>ss</sub>, ilmenite, K-feldspar, plagioclase and quartz. Coarse-grained sillimanite (up to 3 mm in length) is abundant and symplectitic corona tex-

tures are not extensively developed. Coarse-grained sillimanite and garnet are uncommonly in direct contact (Fig. 5f). Coarse-grained, blocky (1–2 mm) spinel<sub>ss</sub> (e.g. Fig. 5e) occurs in contact with, and included within, coarse-grained garnet grains and is therefore interpreted to form part of the peak assemblage (Fig. 5e, f). Fine-grained coronae of garnet and sillimanite are developed on spinel (Figs. 5e, f, 6b) and each of these coronae typically separate spinel from quartz (Fig. 5e, f). Cordierite is only present in very minor amounts, is commonly pinnitised and occurs as fine-grained corona on garnet, separating garnet from sillimanite and spinel. Rare fine-grained biotite is included in coarse-grained garnet and occurs as poorly formed, ragged anhedral grains either at grain boundaries of garnet or in the matrix. Ilmenite occurs in low abundance in the matrix, in contact with quartz and K-feldspar; and rarely, included in garnet. In sample MW4 the peak assemblage is interpreted to be garnet + sillimanite + spinel<sub>ss</sub> + silicate melt + K-feldspar + plagioclase + quartz + ilmenite and the post-peak/retrograde mineral assemblage is interpreted to involve cordierite + garnet + sillimanite + biotite.

Sample 195353 (52 J 401298 mE 7085212 mS) is from the Mt Blythe region (Figs. 2, 3) of the West Musgrave Province. This sample comprises a coarse-grained (interpreted peak) assemblage of garnet, K-feldspar, sillimanite, spinel<sub>ss</sub>, ilmenite and quartz (Fig. 5g, h, i). Spinel, garnet, sillimanite and quartz are commonly separated by a simple corona of cordierite  $\pm$  plagioclase (Fig. 5i). Coarse-grained spinel<sub>ss</sub> (1–2 mm) occurring in the matrix is enclosed by either coronae of fine-grained garnet (Fig. 5g), analogous to the sample from Mt West. Spinel<sub>ss</sub> is also included in coarse-grained garnet (Fig. 5h) and this spinel is separated from quartz by narrow garnet coronae (Fig. 5g). Rare anhedral, fine-grained biotite occurs at grain boundaries of coarse-grained garnet and is commonly ragged and poorly formed. Ilmenite occurs in the matrix, in contact with quartz, K-feldspar



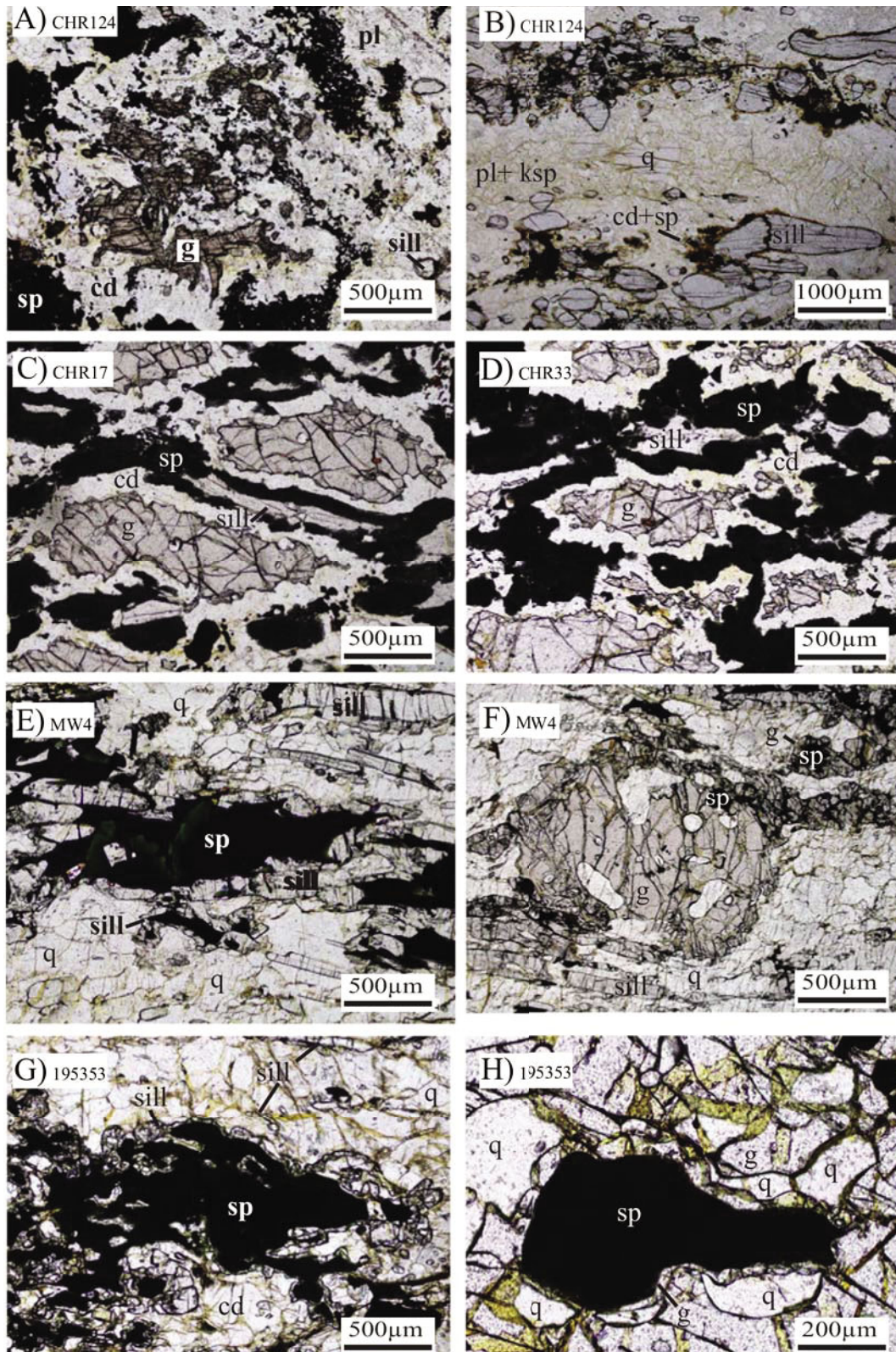
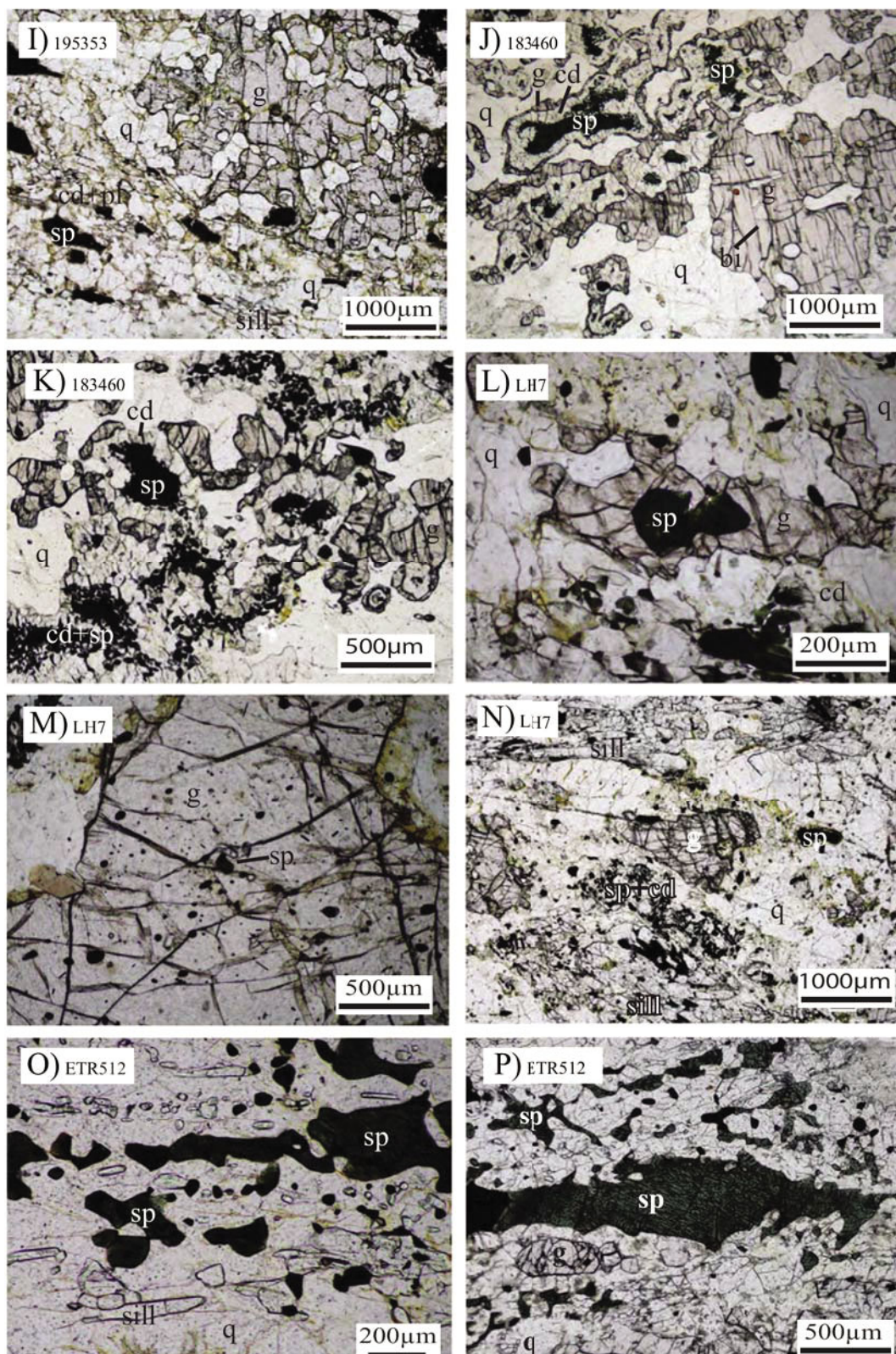


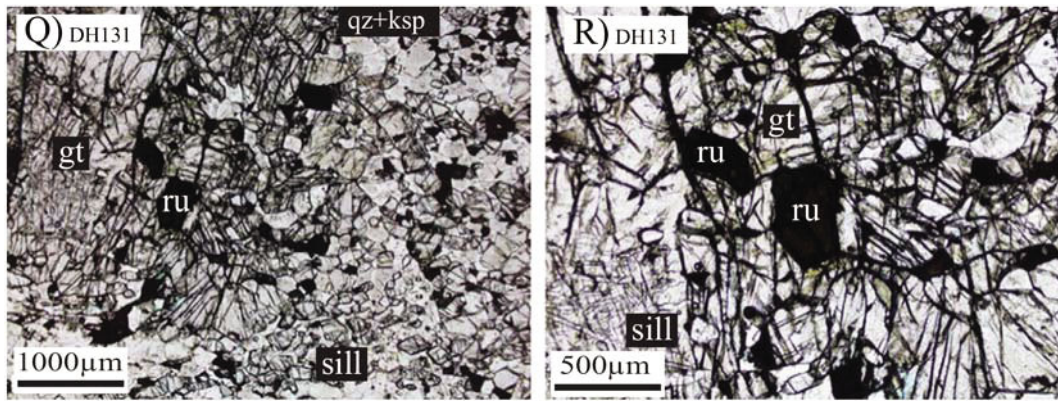
**Figure 5.** Photos of thin sections showing the main reaction microstructures and key mineralogical observations in metapelitic rock samples. (A) Sample CHR124: Garnet is surrounded by a double corona of cordierite immediately adjacent to garnet and a fine-grained spinel + magnetite + cordierite  $\pm$  plagioclase symplectite further away. There are places where relict sillimanite can be seen within the symplectite. (B) Sample CHR124: Coarse-grained matrix minerals sillimanite, quartz, plagioclase and K-feldspar. The layer quartz, K-feldspar and minor plagioclase is interpreted as a leucosome. Fine-grained symplectites of spinel, partially pinitised cordierite  $\pm$  magnetite mantle sillimanite. (C) Sample CHR17: Coarse-grained





garnet and sillimanite porphyroblasts consistently separated by a double corona of cordierite adjacent to garnet and very fine-grained symplectites of spinel+magnetite+cordierite  $\pm$  plagioclase adjacent to sillimanite. Sample CHR17 is quartz absent. (D) Sample CHR33: Coarse-grained garnet and sillimanite porphyroblasts consistently separated by a double corona of cordierite adjacent to garnet and very fine-grained symplectites of spinel+magnetite+ cordierite  $\pm$  plagioclase adjacent to sillimanite. Sample CHR33 is quartz absent. (E) Sample MW4: Coarse-grained garnet, spinel, sillimanite and quartz, interpreted to comprise part of the peak metamorphic mineral assemblage. Spinel remains in direct contact with sillimanite, whereas spinel is separated from quartz by a narrow corona of garnet. (F) Sample MW4: at





the top right of the photo is an example of coarse-grained (peak) spinel that is separated from quartz by a corona of garnet. The coarse grain of garnet contains an inclusion of spinel at its rim. Small grains of spinel in the EW-trending 'layer' in the middle-top of the photo are also surrounded by a corona of garnet. (G) Sample 195353: Coarse-grained spinel separated from quartz by thin coronas of garnet. Spinel is also rarely in contact with sillimanite. (H) Sample 195353: Inclusions of spinel and quartz in coarse-grained garnet. The spinel and quartz are separated by a fine-grained corona of garnet. (I) Sample 195353: Coarse-grained garnet porphyroblast in contact with quartz. Spinel is separated from sillimanite and garnet by thin, very fine-grained symplectites of pinnitised cordierite+plagioclase. (J) Sample 183460: Coarse-grained garnet, spinel and quartz (interpreted to form part of the peak assemblage). Coarse spinel and quartz are consistently separated by a double corona of cordierite directly adjacent to spinel and garnet directly adjacent to quartz. Rare fine-grained biotite occurs only as inclusions in garnet. Plagioclase and K-feldspar are completely absent from the matrix and coronas. (K) Sample 183460: Zoomed in view to highlight the consistent separation of coarse-grained spinel from quartz by a double-layered corona of cordierite and garnet. Plagioclase and K-feldspar are absent from the matrix. (L) Sample LH7: Coarse-grained spinel included inside coarse-grained garnet, which are interpreted to form part of the peak assemblage with sillimanite, plagioclase, quartz and ilmenite. (M) Sample LH7: Fine-grained spinel and ilmenite included in coarse-grained garnet. This observation suggests spinel was stable during (a part of) the prograde evolution of these rocks. (N) Sample LH7: Coarse-grained garnet is separated from quartz by a corona of fine-grained cordierite. Sillimanite is separated from garnet by a symplectite of fine-grained spinel and cordierite. Fine-grained spinel is associated with coarse-grained sillimanite aggregates (top of photo) and matrix quartz. (O) Fine-grained elongate sillimanite occurs in contact with quartz and rarely with spinel. (P) Sample ETR512: Coarse-grained spinel (ss=solid solution with magnetite) occurs in the matrix with quartz, K-feldspar, plagioclase and ilmenite. (Q) Sample DH131: Fine-grained sillimanite and rutile included in coarse-grained garnet porphyroblast within a matrix of medium-coarse grained sillimanite, quartz, rutile and K-feldspar matrix. (R) Sample DH131: Prismatic rutile grains included within garnet.

and plagioclase. In sample 195353 the peak assemblage is interpreted to be garnet + sillimanite + spinel<sub>ss</sub> + silicate melt + K-feldspar + plagioclase + quartz + ilmenite and the post-peak/retrograde mineral assemblage is interpreted to involve cordierite + garnet + sillimanite + biotite.

Sample 183460 (52°J 495916 mE 7080309 mS) is from the Latitude Hills region (Figs.

2, 3) of the west Musgrave Province. It contains coarse-grained garnet, spinel, and quartz (Fig. 5j) interpreted as part of the peak assemblage. Double coronae present in this sample comprise coronal cordierite immediately adjacent to coarse spinel (up to 1.5 mm) and coronal garnet adjacent to quartz (Figs. 5j, 6c). Inclusions of spinel in coarse-grained garnet (1–2 mm) are common (Fig. 5j, k). Sillimanite is rare in this sample. It is restricted to rare

inclusions in coarse-grained garnet (Fig. 6c) and as tiny inclusions in matrix quartz (Fig. 6c). As such, sillimanite is not considered part of the peak mineral assemblage in this sample, but is interpreted as being stable during the (earlier) prograde evolution. Biotite is present in this sample only as small, rounded and rare inclusions in coarse garnet (Fig. 5j), and these inclusions are interpreted as relict prograde biotite. K-feldspar and plagioclase are absent from this sample. In sample 183460 the peak assemblage is interpreted to be garnet + spinel<sub>ss</sub> + silicate melt + quartz + ilmenite and the post-peak/retrograde mineral assemblage is interpreted to involve cordierite + garnet ± spinel.

Sample LH7 (52 J 496800 mE 7077616 mS) is from the Latitude Hills region (Figs. 2, 3) of the west Musgrave Province. It contains coarse grains of garnet, spinel, sillimanite, quartz, ilmenite and K-feldspar (Fig. 5n). Coarse-grained porphyroblastic garnet (~1–3 mm) is generally inclusion-free although spinel (~200 µm) and quartz are occasionally included (Fig. 5l, m). Coarse-grained, bladed sillimanite forms aggregates that are in contact with quartz and isolated from garnet by symplectites of spinel and cordierite, and cordierite and plagioclase (Fig. 5n, 6d). Coarse-grained spinel (up to 1 mm) is separated from garnet by symplectites of cordierite and plagioclase, and is in contact with sillimanite and quartz (Fig. 6d). Cordierite and plagioclase occur exclusively in symplectites that separate garnet from spinel and

sillimanite (Fig. 6d). Biotite occurs in minor amounts and is observed as fine-grained ragged, anhedral grains that occur at grain boundaries of garnet and in the quartz–K-feldspar matrix, or as rounded inclusions in garnet (Fig. 5m). These biotite inclusions are interpreted as relict prograde biotite. In sample LH7 the peak assemblage is interpreted to be garnet + spinel + sillimanite + K-feldspar + silicate melt + quartz + ilmenite and the post-peak/retrograde mineral assemblage is interpreted to involve cordierite + plagioclase + spinel + biotite.

Sample ETR512 (53J 297480 mE 7113893 mS) is from the Eateringinna region of the eastern Musgrave Province in South Australia. Between Eateringinna and the Western Australian border there are as yet no known outcrops of spinel–cordierite-bearing metapelite. This sample contains coarse-grained garnet, spinel<sub>ss</sub> and quartz (Fig. 5o, p). Sillimanite occurs in the sample with a finer grain size (100–200 µm) compared to other samples but is consistently separated from garnet, quartz and usually spinel<sub>ss</sub> by a simple cordierite corona (Fig. 6e). In addition, spinel<sub>ss</sub>, garnet, sillimanite and quartz are isolated by a simple corona of cordierite (Fig. 6e). Biotite occurs in very minor amounts and is only observed as ragged fine grains that occur at grain boundaries of garnet and rarely in the matrix. In sample ETR512 the peak assemblage is interpreted to be garnet + sillimanite + spinel<sub>ss</sub> + silicate melt + K-feldspar + plagioclase + quartz + ilmenite and the post-peak/retrograde mineral assemblage is

**Table 2.** Petrographic summary of iron-rich metapelites from the Musgrave Province. Abbreviations and subscripts are as follows: P = peak mineral; S = post peak, retrograde mineral; ph porphyroblast; p prism; ix inclusion in mineral x; s within symplectite; c corona; m within matrix; rt relict. Spss (ss = solid solution with magnetite).

Sample	CHR124	CHR33	CHR17	MW4	195353	183460	LH7	ETR512	DH131
g	P <sub>ph</sub>	P <sub>ph</sub>	P <sub>ph</sub>	P <sub>ph</sub> , S <sub>c</sub>	P <sub>ph</sub> , S <sub>c</sub>	P <sub>ph</sub> , S <sub>c</sub>	P <sub>ph</sub>	P <sub>ph</sub>	P <sub>ph</sub>
cd	S <sub>s, c</sub>	S <sub>s, c</sub>	S <sub>s, c</sub>	S	S	S <sub>s, c</sub>	S <sub>c</sub>	S <sub>c</sub>	S <sub>c</sub>
sill	P <sub>p</sub>	P <sub>p</sub>	P <sub>p</sub>	P <sub>p</sub> , S	P <sub>p</sub> , S <sub>c</sub>	—	P <sub>p</sub>	P <sub>p</sub>	P <sub>m, Igt</sub>
sp <sub>ss</sub>	S <sub>s, c</sub>	S <sub>s, c</sub>	S <sub>s, c</sub>	P <sub>p</sub> , I <sub>g</sub>	P <sub>p</sub> , I <sub>g</sub>	P <sub>p</sub> , I <sub>g</sub>	P <sub>p</sub> , S <sub>s</sub>	P <sub>p</sub>	—
bi	I <sub>gt</sub> , S <sub>m</sub>	I <sub>gt</sub> , S <sub>m</sub>	I <sub>gt</sub> , S <sub>m</sub>	I <sub>gt</sub> , S <sub>m</sub>	I <sub>gt</sub> , S <sub>m</sub>	I <sub>gt</sub> , S <sub>m</sub>	I <sub>gt</sub> , S <sub>m</sub>	I <sub>gt</sub> , S <sub>m</sub>	—
q	P <sub>m, Igt</sub>	—	—	P <sub>m, Igt</sub>	P <sub>m, Igt</sub>	P <sub>m</sub>	P <sub>m, Igt</sub>	P <sub>m, Igt</sub>	P <sub>m, Igt</sub>
ksp	P <sub>m</sub>	P <sub>m</sub>	P <sub>m</sub>	P <sub>m</sub>	P <sub>m</sub>	—	P <sub>m</sub>	P <sub>m</sub>	P <sub>m</sub>
pl	P <sub>m</sub> , S <sub>s</sub>	P <sub>m</sub> , S <sub>s</sub>	P <sub>m</sub> , S <sub>s</sub>	P <sub>m</sub>	P <sub>m</sub>	—	S <sub>s</sub>	P <sub>m</sub>	P <sub>m</sub>
ru	—	—	—	—	—	—	—	—	P <sub>m, Igt</sub>
ilm	P <sub>m</sub>	P <sub>m</sub>	P <sub>m</sub>	P <sub>m</sub>	P <sub>m</sub>	P <sub>m</sub>	P <sub>m</sub>	P <sub>m</sub>	P <sub>m</sub>



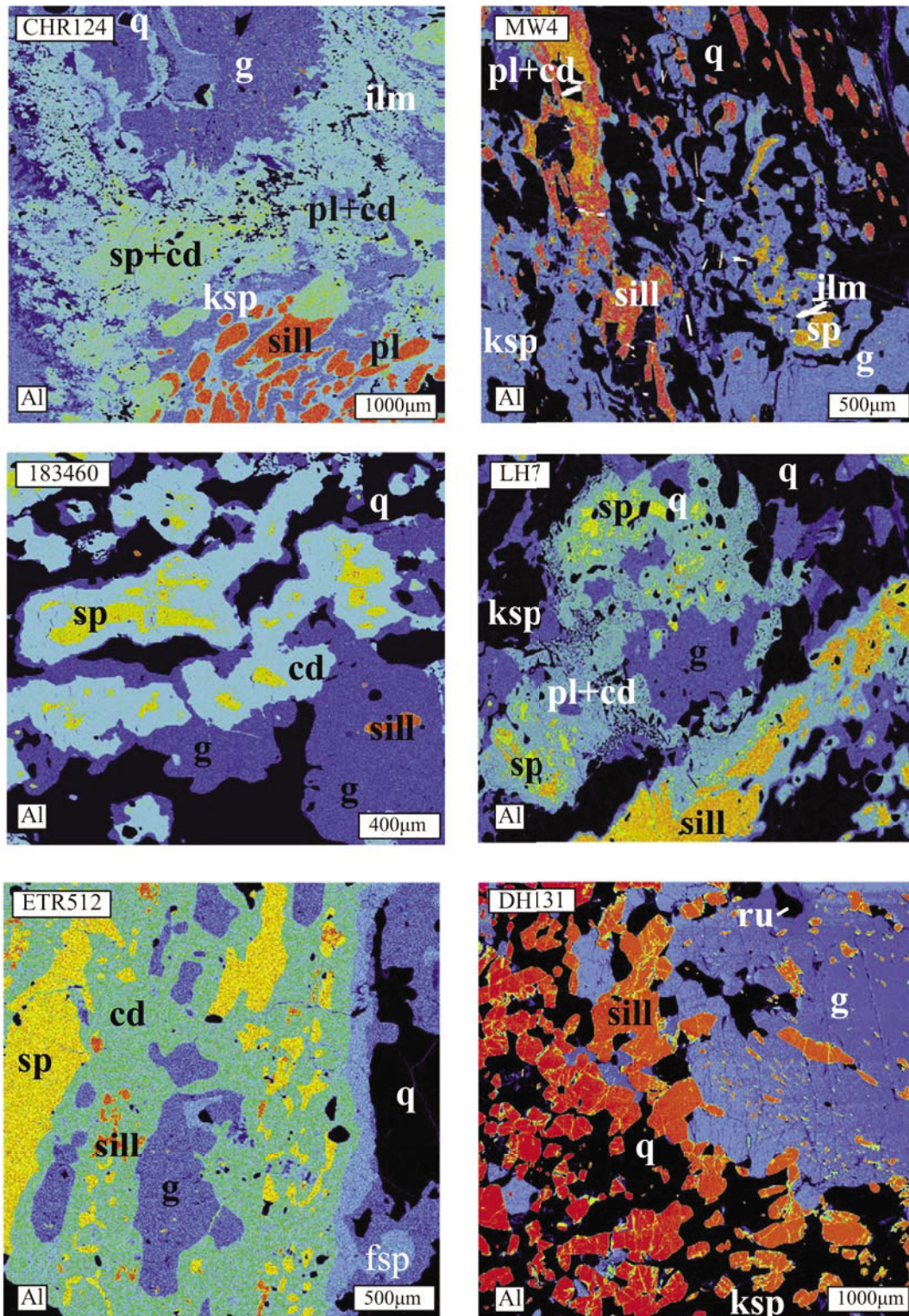


**Figure 6.** Electron microprobe (EMP) maps of Al illustrating the spatial distribution of interpreted peak and retrograde minerals in a number of samples. Red/orange colours represent high relative concentration of Al and blue colours represent low relative concentration. Black indicates zero concentration of Al. The whole suite of element maps (Na, Ca, K, Fe, Mg, Al, Si, Ti) for each sample have been used in conjunction with representative, measured mineral compositions to quantify the effective bulk composition used for P–T pseudosection calculation. The black lower left-hand corner of the Al map for ETR512 is the edge of the thin section, i.e. glass, not quartz.

interpreted to involve cordierite + biotite.

Sample DH131 (52J 592261 mE 7081433 mS) is from the Deering Hills in the central Musgrave Province in South Australia. This sample comprises a coarse-grained assemblage of garnet, sillimanite, rutile, K-feldspar and quartz, and zircon is additionally present (Fig. 5q). All coarse-grained minerals are observed in contact with one another and no symplectitic or coronal microstructures occur (Fig. 5q). Rutile occurs as prismatic grains up to 500  $\mu\text{m}$  (Fig. 5r) and is observed in contact with matrix quartz and k-feldspar and included within coarse-grained garnet in contact with quartz. Fine to medium-grained ( $\sim 200\text{--}400\ \mu\text{m}$ ) sillimanite is included within garnet (Fig. 5r); whereas sillimanite observed in the matrix can be much coarser (up to 3 mm). Fine-grained ilmenite (100–200  $\mu\text{m}$ ) is observed included in garnet, but occurs in much lower abundances than in other metapelitic samples (b1%). Biotite is not observed in this sample. In sample DH131 the peak assemblage is interpreted to be garnet + sillimanite + K-feldspar + rutile + silicate melt + quartz  $\pm$  ilmenite + zircon. There is no petrographic evidence for the growth of post-peak/retrograde minerals.

In summary, several samples are characterised by interpreted peak garnet + sillimanite + spinel + quartz bearing assemblages (MW4, 195353, ETR512, LH7). The presence of peak spinel will be key to constraining the P–T conditions of metamorphism. One sample, 183460, does not contain peak sillimanite, but does contain a peak garnet + spinel + quartz bearing assemblage. Samples from Cohn Hill (CHR124, CHR17, CHR33) and Deering Hills (DH131) do not contain peak spinel; their peak mineral assemblage is garnet + sillimanite bearing (CHR124 and DH131 additionally contain peak qz). Cordierite is present in all samples except DH131 and always occurs within coronae (simple or symplectitic) that consistently separate (relict) peak minerals and is therefore interpreted to be a retrograde mineral. Spinel occurs (additionally) as an interpreted retrograde mineral in the three Cohn Hills samples (CHR124, CHR17, CHR33) as well as in sample LH7. Retrograde garnet occurs additionally in samples MW4, 195353 and 183460. Retrograde sillimanite occurs additionally in MW4 and 195353. In all samples where it occurs in the matrix, biotite is interpreted as retrograde in origin. Spinel

**Table 3.** Representative garnet analyses. XMg assumes no Fe<sup>3+</sup>.

Sample no.	CHR124	CHR124	MW4	MW4	195353	195353	183460	183460	LH7	LH7	ETR512	ETR512	DH131	DH131
Analysis no.	L1_8_core	L1_1_rim	gt_3_core	gt_3_rim	gt1_3_core	gt1_3_rim	L1_10_core	L1_2_rim	L3_core	L3_rim	L4_6_core	L6_14_rim	L2_3_core	L3_12_rim
Mineral	Garnet	Garnet	Garnet	Garnet	Garnet	Garnet	Garnet	Garnet	Garnet	Garnet	Garnet	Garnet	Garnet	Garnet
SiO <sub>2</sub>	36.686	38.101	38.323	37.389	37.773	37.517	37.470	37.856	36.609	36.749	37.690	37.426	37.127	38.079
TiO <sub>2</sub>	0.038	0.030	0.021	0.000	0.001	0.020	0.010	0.019	0.000	0.017	0.000	0.018	0.075	0.076
Al <sub>2</sub> O <sub>3</sub>	21.806	21.382	21.896	21.506	21.755	21.606	21.450	21.778	21.162	21.274	21.812	21.813	21.703	22.251
Cr <sub>2</sub> O <sub>3</sub>	0.000	0.022	0.000	0.000	0.000	0.000	0.000	0.000	0.011	0.030	0.000	0.000	0.000	0.027
FeO	28.305	29.458	29.080	30.555	30.361	30.312	30.508	29.960	32.748	32.715	23.712	23.861	28.348	29.373
MnO	2.167	2.400	0.889	1.076	1.048	1.009	0.696	0.475	0.577	0.448	6.499	6.403	0.416	0.582
MgO	8.296	7.524	8.700	7.995	8.119	8.221	7.467	7.799	6.176	6.574	8.933	9.118	9.413	9.646
ZnO	0.000	0.000	0.058	0.000	0.028	0.119	0.000	0.155	0.038	0.099	0.000	0.087	0.139	0.061
CaO	0.972	1.052	0.841	0.878	0.846	0.843	0.896	0.902	1.109	1.266	1.020	0.945	1.203	1.156
Na <sub>2</sub> O	0.052	0.046	0.013	0.043	0.011	0.021	0.000	0.000	0.020	0.018	0.023	0.003	0.034	0.000
K <sub>2</sub> O	0.000	0.005	0.000	0.026	0.010	0.000	0.002	0.000	0.000	0.002	0.000	0.000	0.147	0.000
Total	98.493	100.096	99.953	99.548	99.985	99.939	98.504	99.035	98.550	99.248	99.791	99.747	98.604	98.604
No. Oxygens	12.000	12.000	12.000	12.000	12.000	12.000	12.000	12.000	12.000	12.000	12.000	12.000	12.000	12.000
Si	2.914	2.985	2.976	2.948	2.956	2.943	2.976	2.980	2.947	2.936	2.941	2.925	2.923	2.905
Ti	0.002	0.002	0.001	0.000	0.000	0.001	0.001	0.001	0.000	0.001	0.000	0.001	0.004	0.000
Al	2.041	1.974	2.004	1.998	2.006	1.997	2.008	2.020	2.008	2.003	2.006	2.009	2.014	2.027
Cr	0.000	0.001	0.000	0.000	0.000	0.000	0.000	0.000	0.001	0.002	0.000	0.000	0.000	0.001
Fe <sup>2+</sup>	1.880	1.930	1.889	2.014	1.987	1.988	2.026	1.972	2.205	2.186	1.547	1.559	1.867	1.872
Mn <sup>2+</sup>	0.146	0.159	0.058	0.072	0.069	0.067	0.047	0.032	0.039	0.030	0.430	0.424	0.028	0.030
Mg	0.982	0.879	1.007	0.940	0.947	0.961	0.884	0.915	0.741	0.783	1.039	1.062	1.105	1.139
Zn	0.000	0.000	0.003	0.000	0.002	0.007	0.000	0.009	0.002	0.006	0.000	0.005	0.008	0.004
Ca	0.083	0.088	0.070	0.074	0.071	0.071	0.076	0.076	0.096	0.108	0.085	0.079	0.101	0.096
Na	0.008	0.007	0.002	0.007	0.002	0.003	0.000	0.000	0.003	0.003	0.003	0.000	0.005	0.002
K	0.000	0.001	0.000	0.003	0.001	0.000	0.000	0.000	0.000	0.000	0.000	0.000	0.015	0.001
Total Cations (S)	8.065	8.029	8.016	8.058	8.041	8.050	8.019	8.008	8.047	8.061	8.056	8.069	8.071	8.071
X(alim)	0.608	0.631	0.624	0.650	0.646	0.644	0.668	0.658	0.716	0.703	0.499	0.499	0.602	0.597
X(py)	0.318	0.288	0.333	0.303	0.308	0.311	0.291	0.306	0.241	0.252	0.335	0.340	0.356	0.363
X(grs)	0.027	0.029	0.023	0.024	0.023	0.023	0.025	0.025	0.031	0.035	0.027	0.025	0.002	0.001
X(spss)	0.047	0.052	0.019	0.023	0.023	0.022	0.015	0.011	0.013	0.010	0.139	0.136	0.009	0.010



**Table 4.** Representative spinel analyses.

Sample no.	CHR124	MW4	195353	183460	LH7	ETR512
Analysis no.	124_P34	MW1a_sp2	353_P12	460_56	LH7_51	512_P14
Mineral	Spinel	Spinel	Spinel	Spinel	Spinel	Spinel
SiO <sub>2</sub>	0.144	0.019	0.271	0.015	0.433	0.045
TiO <sub>2</sub>	0.059	0.032	0.006	0.000	0.030	0.000
Al <sub>2</sub> O <sub>3</sub>	56.211	59.353	59.900	60.031	56.675	61.186
Cr <sub>2</sub> O <sub>3</sub>	0.047	0.101	0.113	0.032	0.670	0.222
FeO	36.367	30.950	30.948	29.235	34.405	26.869
MnO	0.645	0.061	0.021	0.072	0.064	0.908
MgO	4.914	8.854	8.465	8.559	5.186	10.149
ZnO	0.647	0.270	0.199	0.403	0.750	1.003
CaO	0.000	0.000	0.019	0.000	0.000	0.000
Na <sub>2</sub> O	0.042	0.011	0.030	0.000	0.027	0.034
K <sub>2</sub> O	0.018	0.000	0.000	0.000	0.012	0.007
V <sub>2</sub> O <sub>3</sub>	0.000	0.062	0.046	0.157	0.231	0.034
ZrO <sub>2</sub>	0.000	0.000	0.034	0.000	0.000	0.000
Total	99.10	99.71	100.53	98.51	98.51	100.50
No. oxygens	4	4	4	4	4	4
Si	0.004	0.001	0.007	0.000	0.012	0.001
Ti	0.001	0.001	0.000	0.000	0.001	0.000
Al	1.887	1.917	1.919	1.957	1.906	1.939
Cr	0.001	0.002	0.002	0.001	0.015	0.005
Fe <sup>3+</sup> +	0.105	0.078	0.064	0.038	0.050	0.055
Fe <sup>2+</sup> +	0.762	0.631	0.640	0.638	0.771	0.549
Mn <sup>2+</sup> +	0.016	0.001	0.000	0.002	0.002	0.021
Mg	0.209	0.362	0.359	0.353	0.221	0.407
Zn	0.014	0.005	0.004	0.008	0.016	0.020
Ca	0.000	0.000	0.001	0.000	0.000	0.000
Na	0.002	0.001	0.002	0.000	0.002	0.002
K	0.001	0.000	0.000	0.000	0.000	0.000
V <sup>3+</sup> +	0.000	0.001	0.001	0.003	0.005	0.001
Zr	0.000	0.000	0.000	0.000	0.000	0.000
Total cations (Σ)	3	3	3	3	3	3
X <sub>hrc</sub>	0.700	0.587	0.600	0.615	0.729	0.533
X <sub>sp</sub>	0.192	0.336	0.337	0.340	0.209	0.395
X <sub>gah</sub>	0.012	0.005	0.004	0.008	0.015	0.019
X <sub>mt</sub>	0.096	0.072	0.060	0.037	0.047	0.053

and magnetite commonly coexist (CHR124, MW4, 195353). Spinel is observed to contain exsolved magnetite (e.g. ETR512), and so spinel–magnetite coexistence is most probably the result of exsolution from spinel<sub>ss</sub>.

#### 4. GARNET AND SPINEL CHEMISTRY

Garnet is an almandine rich, almandine-pyrope-dominated solid solution with minor grossular and spessartine. X<sub>Mg</sub> (Mg/(Mg + Fe)) (g) displays a range between 0.24 and 0.33 within the samples (Table. 3). In most samples, garnets display rimward zoning to typically lower X<sub>Mg</sub> (g) values; however, the range never exceeds 0.03. X<sub>gr</sub> Ca/(Ca + Mg + Fe<sup>2+</sup> + Mn) is typically 0.01–0.03 and never exceeds 0.04. X<sub>sps</sub> = Mn/(Ca + Mg + Fe<sup>2+</sup> + Mn) typically ranges from 0.01 to 0.05 and X<sub>sps</sub> zoning profiles in all samples are flat. Sample ETR512 typically has much higher X<sub>sps</sub>, with values 0.14–0.16.

Exsolved spinel is a spinel-hercynite solid solution (Table. 4). Fe<sup>3+</sup> was estimated on the basis of stoichiometric constraints. Fe<sup>3+</sup>

contents in spinel with magnetite exsolution are low, with X<sub>mt</sub> = (Fe<sup>3+</sup>/(Fe<sup>2+</sup> + Fe<sup>3+</sup> + Zn + Mg)) ranging between 0.05 and 0.11. X<sub>hrc</sub> = (Fe<sup>2+</sup>/(Fe<sup>2+</sup> + Fe<sup>3+</sup> + Zn + Mg)) ranges between 0.52 and 0.74. Spinel has low wt% ZnO, with values ranging between 0.102 and 1.081 wt.%. Spinel has low wt% Cr<sub>2</sub>O<sub>3</sub>, with values ranging between 0.041 and 0.682 wt.% but typically b 0.2 wt.%.

#### 5. MINERAL EQUILIBRIA MODELLING

Phase diagram calculations were performed using Theriak-Domino software (De Capitani and Petrakakis, 2010) in the geologically realistic NCKFMASHTO (Na<sub>2</sub>O–CaO–K<sub>2</sub>O–FeO–MgO–Al<sub>2</sub>O<sub>3</sub>–SiO<sub>2</sub>–H<sub>2</sub>O–TiO<sub>2</sub>–Fe<sub>2</sub>O<sub>3</sub>) chemical system, using the internally consistent thermodynamic dataset of Holland and Powell (1998; dataset tcds55 November 2003 update), compiled as tcdb55c2d for use in Theriak-Domino, and the most recently available a–x models: garnet, biotite and silicate melt (White et al., 2007), orthopyroxene, spinel and magnetite (White et al., 2002), cordierite (Holland and

**Table 5.** Representative electron microprobe analyses of minerals from metapelitic samples from the Musgrave Province

Sample	CHR124	CHR124	CHR124	CHR124	CHR124	CHR124	CHR124	CHR124	CHR124	CHR124
Mineral	gt	gt	pl	cd	sp	bi	ilm	ksp	sill	q
Analysis	8_Core	8_Rim	14	53	62	41	p8	51	69	45
SiO <sub>2</sub>	36.686	38.101	58.25	47.98	0.05	36.49	0.03	63.99	36.50	99.36
TiO <sub>2</sub>	0.038	0.030	0.02	0.00	0.03	5.02	52.04	0.04	0.02	0.02
Al <sub>2</sub> O <sub>3</sub>	21.806	21.382	24.50	32.05	54.52	13.45	0.00	18.59	61.70	0.05
Cr <sub>2</sub> O <sub>3</sub>	0.000	0.022	0.00	0.03	0.04	0.00	0.04	0.01	0.04	0.04
FeO	28.305	29.458	0.09	6.48	32.17	13.00	44.51	0.00	1.00	0.00
MnO	2.167	2.400	0.00	0.31	0.58	0.05	1.49	0.03	0.01	0.00
MgO	8.296	7.524	0.00	9.58	4.63	15.50	0.39	0.01	0.02	0.00
ZnO	0.000	0.000	0.08	0.00	0.52	0.03	0.02	0.00	0.02	0.02
CaO	0.972	1.052	6.86	0.01	0.00	0.00	0.03	0.19	0.00	0.01
Na <sub>2</sub> O	0.052	0.046	7.58	0.01	0.08	0.14	0.00	2.36	0.03	0.02
K <sub>2</sub> O	0.000	0.005	0.14	0.02	0.00	9.59	0.00	13.02	0.01	0.00
Total	98.493	100.096	97.53	96.46	92.62	93.28	98.55	98.24	99.37	99.51
Si	2.914	2.985	2.66	5.00	0.00	2.77	4.92	2.97	1.00	1.00
Ti	0.002	0.002	0.00	0.00	0.00	0.29	0.00	0.00	0.00	0.00
Al	2.041	1.974	1.32	3.94	1.84	1.20	3.94	1.02	1.98	0.00
Cr	0.000	0.001	0.00	0.00	0.00	0.00	0.00	0.00	0.00	0.00
Fe <sup>3+</sup>				0.16	0.16	0.83	0.41	0.00	0.00	0.00
Fe <sup>2+</sup>	1.880	1.930	0.00	0.56	0.77	0.83	0.41	0.00	0.00	0.00
Mn <sup>2+</sup>	0.146	0.159	0.00	0.03	0.01	0.00	0.03	0.00	0.00	0.00
Mg	0.982	0.879	0.00	1.49	0.20	1.75	1.45	0.00	0.00	0.00
Zn	0.000	0.000	0.00	0.00	0.01	0.00	0.00	0.00	0.00	0.00
Ca	0.083	0.088	0.34	0.00	0.00	0.00	0.00	0.01	0.00	0.00
Na	0.008	0.007	0.67	0.00	0.00	0.02	0.01	0.21	0.00	0.00
K	0.000	0.001	0.01	0.00	0.00	0.93	0.00	0.77	0.00	0.00
Sum	8.065	8.029	5.01	11.02	3.00	7.80	11.00	4.99	3.02	1.00
Sample	195353	195353	195353	195353	195353	195353	195353	195353	195353	195353
Mineral	gt	gt	pl	cd	sp	ilm	ksp	sill	q	
Analysis	12_3 Core	12_4 Rim	45	31	6	51	12	65	70	
SiO <sub>2</sub>	37.773	37.517	59.5771	49.056	0.433	0.044	64.432	36.251	99.205	
TiO <sub>2</sub>	0.001	0.020	0.0273	0.000	0.030	51.477	0.043	0.030	0.070	
Al <sub>2</sub> O <sub>3</sub>	21.755	21.606	24.753	34.129	56.675	0.000	18.773	61.686	0.039	
Cr <sub>2</sub> O <sub>3</sub>	0.000	0.000	0.0051	0.010	0.670	0.056	0.004	0.060	0.009	
FeO	30.361	30.312	0.0917	3.995	34.405	46.154	0.000	0.760	0.105	
MnO	1.048	1.009	0.6665	0.325	0.064	0.180	0.000	0.000	0.000	
MgO	8.119	8.221	0.0003	11.677	5.186	0.484	0.008	0.027	0.009	
ZnO	0.028	0.119	0.0002	0.000	0.750	0.077	0.000	0.000	0.000	
CaO	0.846	0.843	6.4523	0.011	0.000	0.013	0.012	0.000	0.000	
Na <sub>2</sub> O	0.011	0.021	7.7152	0.000	0.027	0.013	0.845	0.000	0.000	
K <sub>2</sub> O	0.010	0.000	0.123	0.013	0.012	0.002	14.967	0.028	0.000	
Total	99.95	99.67	99.41	99.22	98.25	98.50	99.09	98.84	99.44	
Si	2.956	2.943	2.676	4.918	0.012	0.001	2.987	0.991	0.998	
Ti	0.000	0.001	0.001	0.000	0.001	0.966	0.001	0.001	0.001	
Al	2.006	1.997	1.310	4.032	1.906	0.000	1.026	1.987	0.000	
Cr	0.000	0.000	0.000	0.001	0.015	0.001	0.000	0.001	0.000	
Fe <sup>3+</sup>					0.050	0.021		0.029		
Fe <sup>2+</sup>	1.987	1.988	0.003	0.335	0.771	0.942	0.000	0.000	0.001	
Mn <sup>2+</sup>	0.069	0.067	0.025	0.028	0.002	0.004	0.000	0.000	0.000	
Mg	0.947	0.961	0.000	1.745	0.221	0.018	0.001	0.001	0.000	
Zn	0.002	0.007	0.000	0.000	0.016	0.001	0.000	0.000	0.000	
Ca	0.071	0.071	0.310	0.001	0.000	0.000	0.001	0.000	0.000	
Na	0.002	0.003	0.672	0.000	0.002	0.001	0.076	0.000	0.000	
K	0.001	0.000	0.007	0.002	0.000	0.000	0.885	0.001	0.000	
Sum	8.04	8.050	5.00	11.06	2.99	1.96	4.98	3.01	1.00	
Sample	MW4	MW4	MW4	MW4	MW4	MW4	MW4	MW4	MW4	MW4
Mineral	gt	gt	pl	cd	sp	ilm	ksp	sill	q	
Analysis	34_core	35_core	51	24	16	29	54	42	11	
SiO <sub>2</sub>	38.323	37.389	61.04	48.23	0.27	0.00	63.97	36.55	100.01	
TiO <sub>2</sub>	0.021	0.000	0.03	0.02	0.01	49.33	0.03	0.03	0.03	
Al <sub>2</sub> O <sub>3</sub>	21.896	21.506	23.79	32.19	59.90	0.00	18.52	62.48	0.01	
Cr <sub>2</sub> O <sub>3</sub>	0.000	0.000	0.00	0.02	0.11	0.01	0.00	0.00	0.00	
FeO	29.080	30.555	0.12	6.53	30.95	47.24	0.25	1.19	0.31	
MnO	0.889	1.076	0.00	0.06	0.02	0.12	0.01	0.00	0.04	
MgO	8.700	7.995	0.00	9.65	8.86	1.02	0.00	0.01	0.00	
ZnO	0.058	0.000	0.05	0.00	0.20	0.00	0.15	0.03	0.03	
CaO	0.841	0.878	5.53	0.00	0.02	0.00	0.03	0.02	0.00	
Na <sub>2</sub> O	0.013	0.043	8.52	0.02	0.03	0.00	0.97	0.00	0.00	
K <sub>2</sub> O	0.000	0.026	0.17	0.00	0.00	0.02	15.49	0.00	0.00	
Total	99.953	99.548	99.25	96.72	100.37	97.74	99.43	100.29	100.43	

(continued on next page)

Powell, 1998), K-feldspar and plagioclase (Holland and Powell, 2003) and ilmenite (White et al., 2000). Mn is not considered for the reasons given by White et al. (2007).

## 5.1. Bulk compositions

Bulk compositions for the calculation of P–T pseudosection for samples CHR124, MW4, 183460, LH7, ETR512 and DH131 were

Table 5. (continued)

Sample	195353	195353	195353	195353	195353	195353	195353	195353	195353
Mineral	gt	gt	pl	cd	sp	ilm	ksp	sill	q
Analysis	L2_3 Core	L2_4 Rim	45	31	6	51	12	65	70
Si	2.976	2.948	2.73	1.51	0.01	0.00	2.97	0.99	1.00
Ti	0.001	0.000	0.00	0.00	0.00	0.95	0.00	0.00	0.00
Al	2.004	1.998	1.25	0.95	1.92	0.00	1.01	1.98	0.00
Cr	0.000	0.000	0.00	0.00	0.00	0.00	0.00	0.00	0.00
Fe3+					0.06	0.10		0.03	
Fe2+	1.889	2.014	0.00	0.09	0.70	1.01	0.01	0.00	0.00
Mn2+	0.058	0.072	0.00	0.00	0.00	0.00	0.00	0.00	0.00
Mg	1.007	0.940	0.00	0.24	0.36	0.04	0.00	0.00	0.00
Zn	0.003	0.000	0.00	0.00	0.00	0.00	0.01	0.00	0.00
Ca	0.070	0.074	0.27	0.00	0.00	0.00	0.00	0.00	0.00
Na	0.002	0.007	0.74	0.00	0.00	0.00	0.09	0.00	0.00
K	0.000	0.003	0.01	0.00	0.00	0.00	0.92	0.00	0.00
Sum	8.016	8.058	5.01	2.89	3.06	2.10	5.00	3.00	1.00
Sample	183460	183460	183460	183460	183460	183460	183460	183460	183460
Mineral	gt	gt	pl	cd	sp	ilm	ksp	sill	q
Analysis	L1_4_core	L1_4_rim	45	L3_5	54	25	51	32	60
SiO2	37.470	37.856	60.19	49.19	0.02	0.00	62.66	36.01	98.53
TiO2	0.010	0.019	0.01	0.00	0.00	50.68	0.02	0.05	0.00
Al2O3	21.450	21.778	24.48	32.58	60.03	0.00	18.15	60.98	0.04
Cr2O3	0.000	0.000	0.00	0.00	0.03	0.08	0.00	0.02	0.07
FeO	30.508	29.960	0.08	4.99	29.24	44.97	0.06	0.67	0.16
MnO	0.696	0.475	0.00	0.00	0.07	0.24	0.00	0.02	0.05
MgO	7.467	7.799	0.00	10.70	8.56	0.67	0.02	0.01	0.03
ZnO	0.000	0.155	0.00	0.00	0.40	0.00	0.11	0.00	0.08
CaO	0.896	0.902	6.90	0.02	0.00	0.02	0.03	0.03	0.00
Na2O	0.000	0.000	7.92	0.02	0.00	0.00	0.79	0.00	0.00
K2O	0.002	0.000	0.09	0.00	0.00	0.01	14.64	0.03	0.00
Total	98.504	99.035	99.68	97.51	98.35	96.66	96.47	97.83	98.96
Si	2.976	2.980	2.69	0.00	0.00	0.00	2.97	0.99	1.00
Ti	0.001	0.001	0.00	0.00	0.00	0.96	0.00	0.00	0.00
Al	2.008	2.020	1.29	8.56	1.96	0.00	1.02	1.98	0.00
Cr	0.000	0.000	0.00	0.01	0.00	0.00	0.00	0.00	0.00
Fe3+					0.04	0.02		0.02	
Fe2+	2.026	1.972	0.00	3.39	0.64	0.93	0.00	0.00	0.00
Mn2+	0.047	0.032	0.00	0.00	0.00	0.01	0.00	0.00	0.00
Mg	0.884	0.915	0.00	1.57	0.35	0.03	0.00	0.00	0.00
Zn	0.000	0.009	0.00	0.03	0.01	0.00	0.00	0.00	0.00
Ca	0.076	0.076	0.33	0.00	0.00	0.00	0.00	0.00	0.00
Na	0.000	0.000	0.69	0.00	0.00	0.00	0.07	0.00	0.00
K	0.000	0.000	0.01	0.00	0.00	0.00	0.89	0.00	0.00
Sum	8.019	8.008	5.01	13.57	3.00	1.94	4.96	3.01	1.00
Sample	LH7	LH7	LH7	LH7	LH7	LH7	LH7	LH7	LH7
Mineral	gt	gt	pl	cd	sp	ilm	ksp	sill	q
Analysis	L7_1_3_core	L7_1_4_rims	LH7_61	L4_1_1	L5_2_2	LH7_11	LH7_65	LH7_65	LH7_63
SiO2	36.609	36.749	57.23	48.48	0.04	0.05	64.86	36.21	99.99
TiO2	0.000	0.017	0.01	0.02	0.00	50.70	0.02	0.02	0.02
Al2O3	21.162	21.274	25.87	32.53	57.04	0.00	18.65	62.00	0.05
Cr2O3	0.011	0.030	0.00	0.00	0.58	0.00	0.00	0.07	0.04
FeO	32.748	32.715	0.13	6.91	33.99	46.41	0.06	1.10	0.00
MnO	0.577	0.448	0.02	0.04	0.03	0.16	0.00	0.02	0.00
MgO	6.176	6.574	0.00	9.51	5.38	0.26	0.00	0.00	0.00
ZnO	0.038	0.099	0.01	0.00	0.76	0.03	0.02	0.00	0.02
CaO	1.109	1.266	8.31	0.03	0.02	0.04	0.05	0.00	0.01
Na2O	0.020	0.018	6.94	0.03	0.02	0.02	1.33	0.03	0.02
K2O	0.000	0.002	0.05	0.00	0.02	0.00	14.38	0.02	0.00
Total	98.45	99.19	98.57	97.55	97.88	97.67	99.38	99.46	100.14
Si	2.947	2.936	2.60	5.00	0.00	0.00	2.99	0.98	1.00
Ti	0.000	0.001	0.00	0.00	0.00	0.96	0.00	0.00	0.00
Al	2.008	2.003	1.39	3.95	1.92	0.00	1.01	1.99	0.00
Cr	0.001	0.002	0.00	0.00	0.01	0.00	0.00	0.00	0.00
Fe3+					0.06	0.03		0.05	
Fe2+	2.205	2.186	0.00	0.60	0.75	0.95	0.00	0.00	0.00
Mn2+	0.039	0.030	0.00	0.00	0.00	0.00	0.00	0.00	0.00
Mg	0.741	0.783	0.00	1.46	0.23	0.01	0.00	0.00	0.00
Zn	0.002	0.006	0.00	0.00	0.02	0.00	0.00	0.00	0.00
Ca	0.096	0.108	0.40	0.00	0.00	0.00	0.00	0.00	0.00
Na	0.003	0.003	0.61	0.01	0.00	0.00	0.12	0.00	0.00
K	0.000	0.000	0.00	0.00	0.00	0.00	0.85	0.00	0.00

estimated by integrating the abundances of minerals from x-ray element maps (e.g. Fig. 6) with representative compositions of minerals measured using the SX51 electron microprobe (Table 5). This is an established method for estimating bulk composition for

compositionally heterogeneous rocks (e.g. Marmo et al., 2002; Kelsey et al., 2003; Boger and Hansen, 2004; Tinkham and Ghent, 2005). The region of a thin section chosen for the location of element mapping was such that the map area would incorporate a portion of



Table 5. (continued)

Sample	195353	195353	195353	195353	195353	195353	195353	195353	195353
Mineral	gt	gt	pl	cd	sp	ilm	ksp	sill	q
Analysis	L2_3 Core	L2_4 Rim	45	31	6	51	12	65	70
Sum	8.047	8.061	5.01	11.02	2.99	1.96	4.98	3.02	1.00
Sample	ETR512	ETR512	ETR512	ETR512	ETR512	ETR512	ETR512	ETR512	ETR512
Mineral	gt	gt	pl	cd	sp	ilm	ksp	sill	q
Analysis	512_L2 core	512_L5_rim	512_32	512_L3_l	512_4	512_38	512_43	512_47	512_35
SiO <sub>2</sub>	37.690	37.426	59.97	50.01	0.05	0.03	64.70	36.51	99.72
TiO <sub>2</sub>	0.000	0.018	0.00	0.02	0.00	41.23	0.02	0.00	0.05
Al <sub>2</sub> O <sub>3</sub>	21.812	21.813	25.14	34.03	60.61	0.00	19.01	62.05	0.04
Cr <sub>2</sub> O <sub>3</sub>	0.000	0.000	0.00	0.00	0.07	0.00	0.00	0.00	0.00
FeO	23.712	23.861	0.00	3.92	26.46	52.71	0.04	0.99	0.00
MnO	6.499	6.403	0.05	0.32	1.00	2.05	0.00	0.03	0.00
MgO	8.933	9.118	0.03	11.75	10.72	0.41	0.02	0.04	0.02
ZnO	0.000	0.087	0.15	0.00	1.01	0.00	0.00	0.00	0.13
CaO	1.020	0.945	6.70	0.03	0.00	0.00	0.18	0.00	0.02
Na <sub>2</sub> O	0.023	0.003	7.79	0.06	0.06	0.00	2.34	0.01	0.00
K <sub>2</sub> O	0.000	0.000	0.09	0.01	0.00	0.00	13.20	0.01	0.00
Total	99.69	99.67	99.93	100.15	99.98	96.42	99.50	99.65	99.99
Si	2.941	2.925	2.67	4.96	0.00	0.00	2.97	0.99	1.00
Ti	0.000	0.001	0.00	0.00	0.00	0.78	0.00	0.00	0.00
Al	2.006	2.009	1.32	3.98	1.92	0.00	1.03	1.99	0.00
Cr	0.000	0.000	0.00	0.00	0.00	0.00	0.00	0.00	0.00
Fe <sup>3+</sup>					0.07	0.39		0.02	
Fe <sup>2+</sup>	1.547	1.559	0.00	0.33	0.52	0.72	0.00	0.00	0.00
Mn <sup>2+</sup>	0.430	0.424	0.00	0.03	0.02	0.04	0.00	0.00	0.00
Mg	1.039	1.062	0.00	1.74	0.43	0.02	0.00	0.00	0.00
Zn	0.000	0.005	0.01	0.00	0.02	0.00	0.00	0.00	0.00
Ca	0.085	0.079	0.32	0.00	0.00	0.00	0.01	0.00	0.00
Na	0.003	0.000	0.67	0.01	0.00	0.00	0.21	0.00	0.00
K	0.000	0.000	0.01	0.00	0.00	0.00	0.77	0.00	0.00
Sum	8.056	8.069	5.00	11.05	3.00	1.95	5.00	3.01	1.00
Sample	DH131	DH131	DH131	DH131	DH131	DH131	DH131	DH131	DH131
Mineral	gt	gt	ru	ilm	ksp	sill	q		
Analysis	core	rim	DH131B_7	DH131B_13	DH131B_21	DH131B_15	DH131B_2		
SiO <sub>2</sub>	37.1271	38.0792	0.000	0.05	64.393	36.700	98.298		
TiO <sub>2</sub>	0.075	0.0763	98.018	49.70	0.032	0.004	0.040		
Al <sub>2</sub> O <sub>3</sub>	21.7028	22.2509	0.000	0.00	19.229	62.587	0.008		
Cr <sub>2</sub> O <sub>3</sub>	0.0002	0.0273	0.034	0.00	0.000	0.030	0.010		
FeO	28.348	29.3733	0.145	47.32	0.000	0.760	0.027		
MnO	0.4157	0.5817	0.000	0.16	0.000	0.005	0.000		
MgO	9.4132	9.6458	0.000	0.26	0.000	0.003	0.006		
ZnO	0.1385	0.0607	0.198	0.03	0.089	0.045	0.027		
CaO	1.2027	1.1559	0.007	0.04	0.644	0.001	0.004		
Na <sub>2</sub> O	0.0338	0.0003	0.000	0.02	2.561	0.007	0.000		
K <sub>2</sub> O	0.1467	0.0001	0.000	0.00	12.111	0.000	0.002		
Total	98.604	98.604	98.40	97.67	99.29	100.14	98.42		
Si	2.923	2.905	0.001	0.00	2.963	0.990	0.999		
Ti	0.004	0.000	0.934	0.96	0.001	0.000	0.000		
Al	2.014	2.027	0.000	0.00	1.043	1.989	0.000		
Cr	0.000	0.001	0.000	0.00	0.000	0.001	0.000		
Fe <sup>3+</sup>			0.000	0.03	0.000	0.017	0.000		
Fe <sup>2+</sup>	1.867	1.872	0.000	0.95	0.000	0.000	0.000		
Mn <sup>2+</sup>	0.028	0.030	0.000	0.00	0.000	0.000	0.000		
Mg	1.105	1.139	0.001	0.01	0.000	0.001	0.000		
Zn	0.008	0.004	0.000	0.00	0.003	0.000	0.000		
Ca	0.101	0.096	0.000	0.00	0.032	0.000	0.000		
Na	0.005	0.002	0.001	0.00	0.228	0.000	0.000		
K	0.015	0.001	0.000	0.00	0.711	0.000	0.000		
Sum	8.071	8.071	0.94	1.96	4.98	3.00	1.00		

the coarse-grained minerals as well as the reaction microstructures; therefore the total area of the map is dependent on the grain size of the sample and scale of the mineral reaction microstructures (Fig. 6). Fe<sub>2</sub>O<sub>3</sub> was estimated by recasting the analysed compositions of spinel, ilmenite, magnetite, sillimanite in terms of Fe<sup>3+</sup> cations (and Fe<sub>2</sub>O<sub>3</sub> wt.%) following the procedure of Droop (1987). The amount of H<sub>2</sub>O in the bulk composition was estimated on the basis of the abundance and composition of hydrous minerals biotite and cordierite.

The estimation of low H<sub>2</sub>O abundance in the samples (Table. 6) is substantiated by the field out-crop and thin section observation that these granulite facies gneisses contain (very) little biotite, e.g. typically b1% modal biotite. The bulk composition for sample 195353 was measured via whole-rock X-ray fluorescence at Amdel Laboratories, Adelaide. As the rocks have undergone partial melting and inevitable melt loss (White and Powell, 2002), as suggested by the abundance of anhydrous leucosomes in outcrop (Fig. 4), the bulk composition for each sample

**Table 6.** NCKFMASHTO bulk composition (wt% oxide) used in P-T pseudosection calculations.

	Si	Ti	Al	Fe3	Fe2	Mg	Ca	Na	K	H
CHR124	46.02	1.15	28.90	2.41	10.91	6.40	0.78	1.02	2.23	0.18
195355	49.07	1.54	23.51	1.28	17.21	5.21	0.40	0.10	1.62	0.06
MW4	60.80	0.70	20.00	0.45	7.35	2.50	0.45	0.64	2.35	0.08
183460	43.35	1.57	27.87	0.81	19.79	5.64	0.30	0.12	0.44	0.12
LH7	60.80	1.08	17.64	0.40	8.85	4.10	0.31	0.25	1.72	0.12
ETR512	39.67	0.77	29.20	3.70	17.75	6.88	0.54	0.61	0.78	0.09
DH131	59.81	3.08	24.56	0.57	5.59	2.02	0.41	0.67	3.16	0.02
Fig. 15 LHS	60.80	0.70	20.00	0.45	7.35	2.50	0.45	0.64	2.35	0.08
Fig. 15 RHS	60.80	0.70	20.00	3.90	3.90	2.50	0.45	0.64	2.35	0.08
Fig. 16 LHS	43.51	1.57	27.97	0.00	20.31	5.66	0.30	0.12	0.44	0.12
Fig. 16 RHS	43.51	1.57	27.97	10.15	10.15	5.66	0.30	0.12	0.44	0.12

represents a residual composition. Therefore it is not possible to obtain any reliable quantitative information regarding the prograde P–T path trajectory for the modelled rocks; the bulk compositions are appropriate for modelling the peak and post-peak/retrograde evolution of the rocks due to the scale of the sampled (mapped) portion of the thin section for most samples.

## 5.2. P–T pseudosections

The interpreted peak mineral assemblage of garnet + sillimanite + spinel<sub>ss</sub> ± quartz ± plagioclase ± K-feldspar + ilmenite + silicate melt is stable at minimum 930–980 °C and 6.5–7.2 kbar, in samples MW4, 195353, 183460, LH7 and ETR512, extending to a maximum of 1030–1080 °C and 7.4–9.5 kbar for samples MW4, 195353, LH7 and ETR512 (Figs. 8, 9, 10, 11, 12). The stability of the peak assemblage field for sample 183460 is open-ended to higher temperatures (Fig. 10), but is presumably limited to a max of ~1100 °C, which represents the approximate upper temperature limit of dry melting of crustal rocks. The stability of the garnet + sillimanite + quartz (+melt) peak assemblage in sample CHR124 has a large P–T range of N 7.1 kbar and 1060 N T N 940 °C (Fig. 7). The stability of garnet + sillimanite + quartz in sample DH131 has a large P–T range of N 7.2 kbar and N 900 °C (Fig. 13). The coronae and/or symplectic coronae of cordierite + spinel<sub>ss</sub> ± plagioclase ± garnet that overprint the peak assemblage define fields with minimum pressures and temperature bounds, depending on the sample, of approximately

950 °C and 6 kbar (Figs. 7–13). The presence of peak (coarse) spinel in samples MW4, 195353, 183460, LH7 and ETR512 provides the primary constraint on the upper bound of pressure and lower bound of temperature for the peak of metamorphism (nb: we are not suggesting that the maximum temperature, i.e. ‘peak’ of metamorphism, necessarily corresponded to maximum pressures). Fig. 14 summarises the P–T locations for the peak assemblage stability fields for all the samples (e.g. Kelsey et al., 2003; Halpin et al., 2007; Phillips et al., 2010). Samples containing peak spinel provide the tightest constraint on peak conditions, by contrast to the large P–T window/range offered by spinel-absent garnet + sillimanite-bearing assemblages (Fig. 14). The peak P–T conditions summarised in Fig. 14 illustrates that the peak assemblage developed at similar conditions for all rocks containing peak spinel but does not imply that all the samples have recorded an identical or synchronous P–T evolution.

As samples CHR124 and DH131 do not contain spinel that can obviously or easily be interpreted as part of the peak assemblage, these samples lack definitive constraints on the pressure and temperature corresponding to peak (thermal) metamorphism. The absence of peak biotite implies that temperatures must have been in excess of terminal biotite stability, i.e. N ~900 °C (Figs. 7, 13). Constraints on the peak metamorphic conditions for samples CHR124 and DH131 are problematic since there are no identified samples from Cohn Hill or Deering Hills that contain coarse-grained, peak spinel. Unfortunately, peak metamorphic conditions recorded by

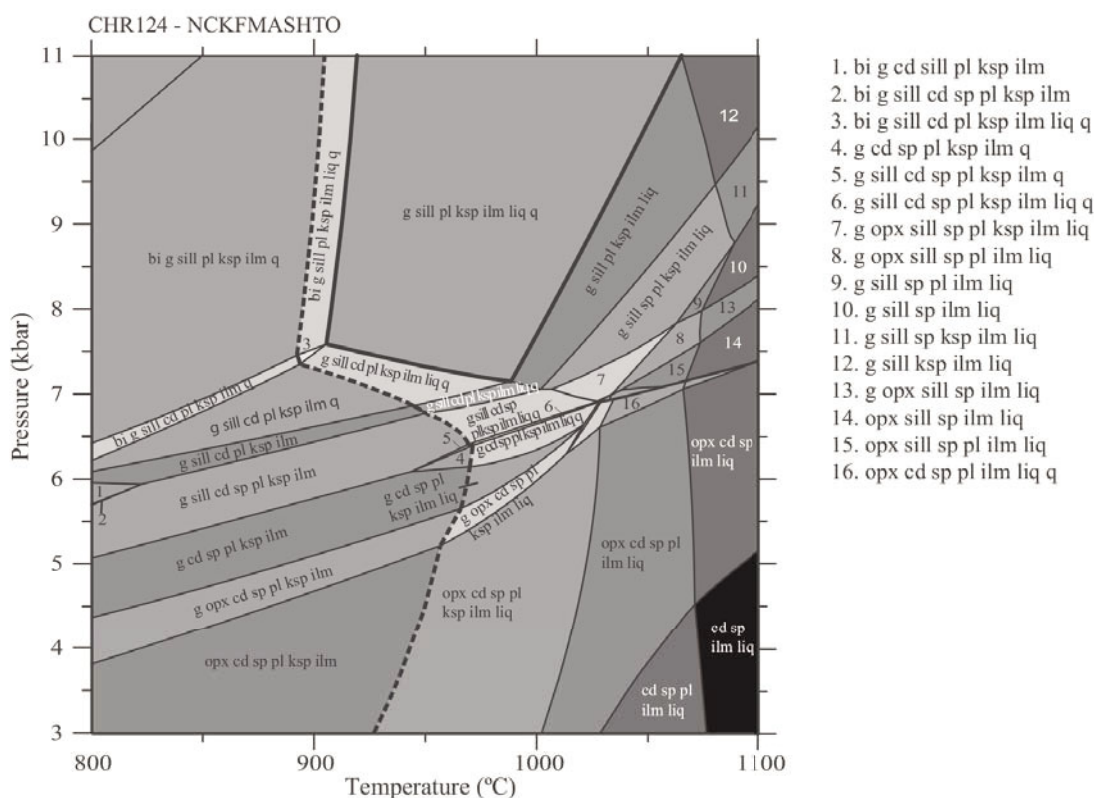


**Figure 7.** NCKFMASHTO P–T pseudosection for sample CHR124. The stability of the peak assemblage  $g+sill+pl+ksp+ilm+liq+q$  occurs above the solidus (dashed bold line) and at pressures higher than cordierite stability. As spinel cannot be unequivocally classified as part of the peak assemblage the constraints are not precise for this sample. The bulk composition is given in Table 6.

the Cohn Hill samples and DH131 cannot be tightly constrained, as it is not a requirement that all the Wirkku Metamorphics and the Birksgate Complex rocks in the Musgrave Province record near-identical conditions of metamorphism.

The coronal reaction microstructures preserved in all samples except DH131 provide the best constraint on the retrograde P–T path (Vernon, 1996). In sample 183460, for example, the consumption of the peak assemblage garnet + spinel + quartz + ilmenite, which is stable at  $\sim 1000^\circ\text{C}$  and 6.5–8 kbar, and the development of cordierite + garnet + quartz coronas, requires decompression and cooling along a P–T path that intersects cordierite-stable equilibria, which occurs at lower pressure and temperatures of approximately  $980\text{--}1000^\circ\text{C}$  and 6.5 kbar (Fig. 10). The preservation of much of the coarse-grained garnet and sillimanite (Figs. 5 and 6) could

support the interpretation that the amount of decompression was quite minor ( $\sim 1\text{--}2$  kbar). An identical approach is taken when predicting the retrograde P–T path for all samples and the high-temperature section of the retrograde P–T path is characterised by a minor decrease in pressure (1–2 kbar) and between 50 and  $70^\circ\text{C}$  in all samples except CHR124. As the constraints on peak metamorphic conditions are poorly defined for sample CHR124 it is difficult to identify the actual trajectory of a retrograde P–T path.

Variations in the amount of ferric iron estimated to be the bulk composition for a rock can have a significant influence on phase equilibria (e.g. White et al., 2000; Diener et al., 2008; Johnson et al., 2008; Diener and Powell, 2010; Johnson and White, 2011; Boger et al., 2012). Of particular relevance to the rocks studied here is that spinel stability is sensitive to the ferric iron

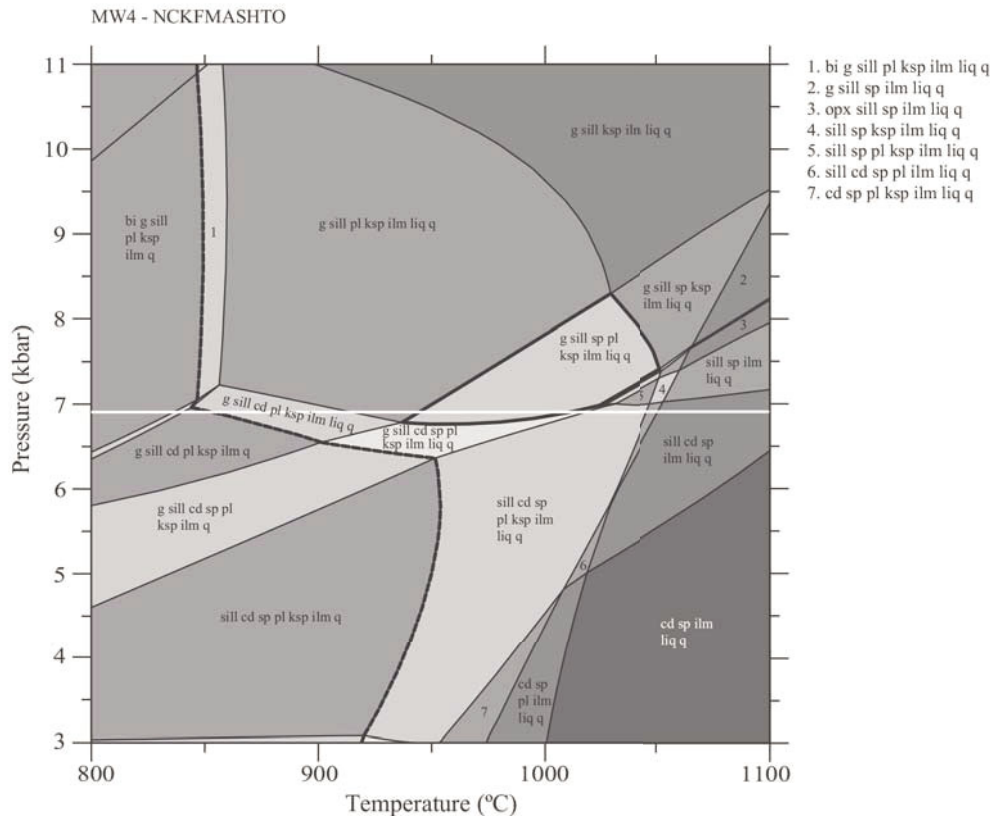


**Figure 8.** NCKFMASHTO P–T pseudosection for sample MW4. The peak assemblage  $g + sill + sp + pl + ksp + ilm + liq + q$  (in bold) is constrained to the highlighted field, at pressures lower than spinel-out boundary and temperatures lower than the sillimanite-out boundary. Retrogression into cordierite-bearing assemblages and towards the solidus (dashed bold line) along a shallow P–T path is consistent with the development of the  $cd$ – $spss$  ( $ss$  = solid solution with magnetite) symplectites. The bulk composition is given in Table 6.

(and  $ZnO$  and  $Cr_2O_3$ , see later) content of a rock (Vielzeuf, 1983; Hensen, 1986; Powell and Sandiford, 1988; Waters, 1991). In order to explore the sensitivity and/or robustness of our estimations of peak metamorphic conditions on the basis of coarse-grained spinel in peak mineral assemblages, Fig. 15 shows an isobaric (6.9 kbar) T– $X_{ferric}$  pseudosection calculated for sample MW4. The section illustrates the effect of varying  $X_{ferric} = Fe_2O_3 / (Fe_2O_3 + FeO)$  on the stability of the peak assemblage. Increasing  $X_{ferric}$  over the narrow interval 0–0.18 very rapidly stabilises spinel-bearing assemblages from  $\sim 1015^\circ C$  down to  $\sim 915^\circ C$ ; however, the stabilisation of spinel to lower temperatures by increasing  $X_{ferric}$  results in cordierite-bearing assemblages. There is no peak cordierite interpreted in any of the rocks in this study, as cordierite, when it occurs, is

only found in coronae that consistently separate peak (‘coarse-grained’) minerals. Therefore, it seems probable, on the basis of this T–X section for MW4, that the amount of ferric iron in the sample is relatively low—certainly low enough to prevent cordierite and spinel both comprising part of the peak mineral assemblage—and that the peak metamorphic temperatures were indeed higher than  $900^\circ C$ . It is possible, on the basis of the T–X section, that peak temperatures could be approximately  $20^\circ C$  lower than indicated by the P–T pseudosection (Fig. 8), if the amount of ferric iron was slightly higher ( $\sim 0.15$  along x-axis in Fig. 15). However, such temperatures still correspond to thermally extreme, UHT metamorphic conditions. If there is an approximate  $20^\circ C$  leeway (down-temperature) in the temperature estimation for these rocks, a pertinent question



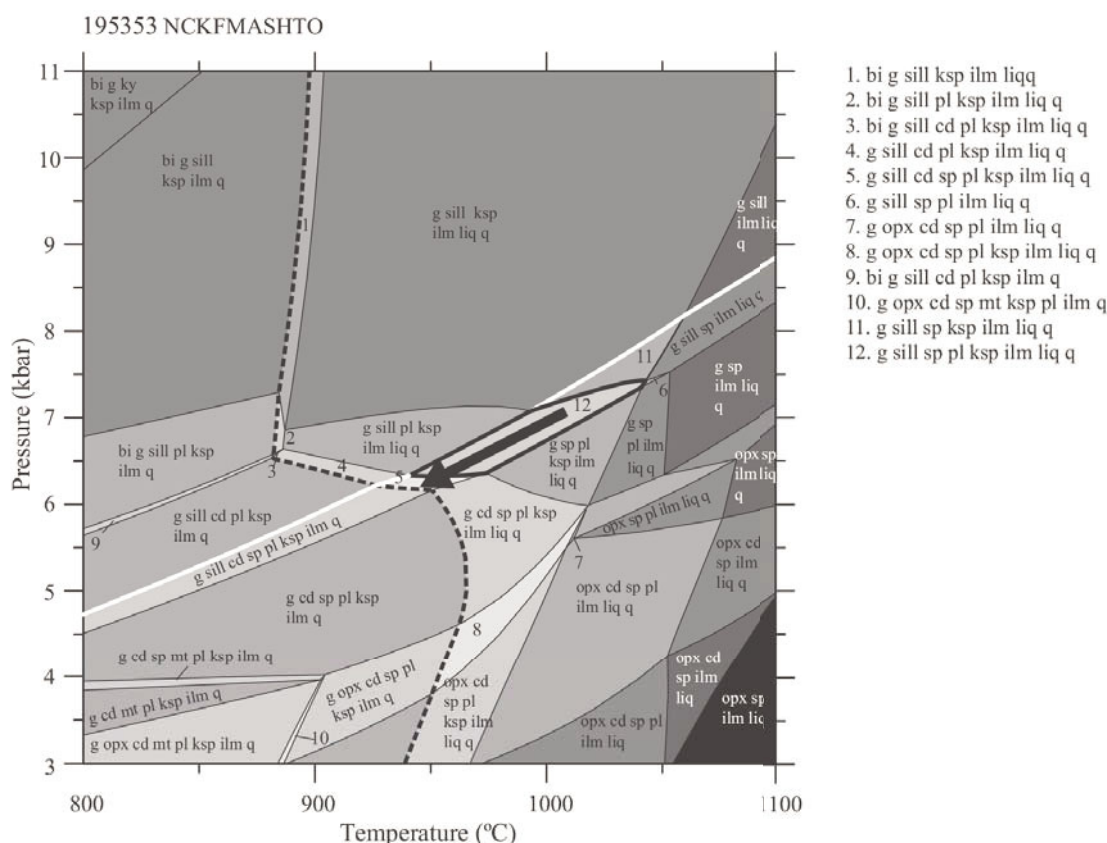


**Figure 9.** NCKFMASHTO P–T pseudosection for sample 195353. The peak assemblage of g + sill + sp + pl + ksp + ilm + liq + q is constrained to the highlighted field (in bold), at pressures lower than spinel-out boundary and temperatures higher than cordierite stability. Retrogression into cordierite-bearing assemblages and towards the solidus (dashed bold line) along a shallow P–T path is consistent with the development of gt-cd coronas. The bulk composition is given in Table 6.

to then ask is what impact does a lower peak temperature (e.g. 920 °C) have on the estimations of pressure? This is critical to address as it impacts on estimations of crustal thickness and also estimations of the apparent thermal gradient in the crust to the depth of the UHT metamorphism. If it is assumed that the (sp)-out field boundary in Fig. 8 maintains the same gradient but is translated 20 °C down-temperature as a consequence of higher  $\text{Fe}^{3+}$  in the rock composition, the estimation of pressure for the peak metamorphic assemblage remains unchanged (Fig. 8). However, the apparent thermal gradient undergoes a minor decrease from approximately 52 °C km<sup>-1</sup> (in Fig. 8) to approximately 49 °C km<sup>-1</sup>. This still clearly indicates that the metamorphic conditions recorded by sample MW4 (and by inference, the others) are extreme, and that by undertaking this sensitivity analysis, estimations for the peak metamorphic

conditions and apparent thermal gradient are not greatly affected by changes to the ferric iron content of the rock. A second sensitivity analysis, conducted to reinforce the above conclusion, was conducted using sample 183460 (Fig. 16). The T–X<sub>ferric</sub> section shows that this rock could be significantly more  $\text{Fe}^{3+}$ -rich before cordierite enters the assemblage (at ~ X = 22). This rock is relatively insensitive to increasing  $\text{Fe}^{3+}$  over the interval 0 to ~22 because the sillimanite boundary (lower-T bound of peak field) is sub-horizontal. Therefore, the peak P–T conditions determined for this rock are robust. The two T–X sections together validate and justify that the high temperatures estimated for these rocks are reliable.

Spinel stability is also known to be enhanced by Zn and Cr (e.g. Hensen,



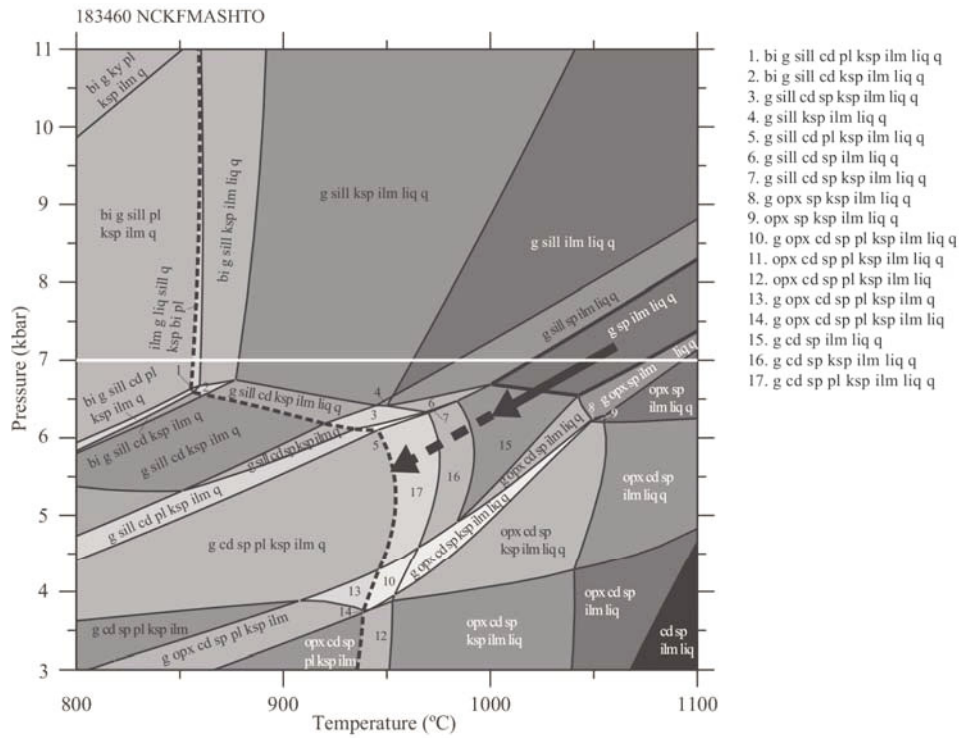


**Figure 10.** NCKFMASHTO P–T pseudosection for sample 183460. The peak assemblage of g + sp + ilm + liq + q is constrained to the highlighted field (in bold), at pressures lower than quartz-out boundary and temperatures higher than cordierite stability. Retrogression into cordierite-bearing assemblages and towards the solidus (dashed bold line) along a shallow P–T path is consistent with the development of the cd–gt coronas. The bulk composition is given in Table 6.

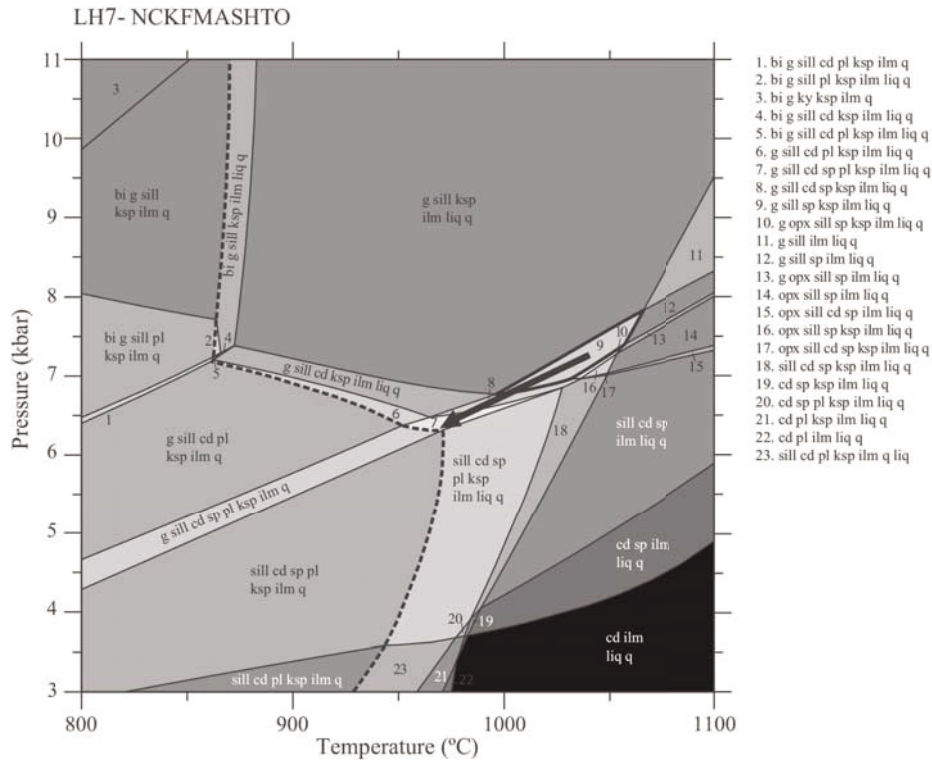


**Figure 11.** NCKFMASHTO P–T pseudosection for sample LH7. The peak assemblage of g + sill + sp + ksp + ilm + liq + q is constrained to the highlighted field (in bold), at pressures lower than spinel-out boundary and temperatures and pressures higher than cordierite stability. Retrogression into cordierite + plagioclase-bearing assemblages and towards the solidus (dashed bold line) along a shallow P–T path is consistent with the development of the cd–pl symplectites. The bulk composition is given in Table 6.

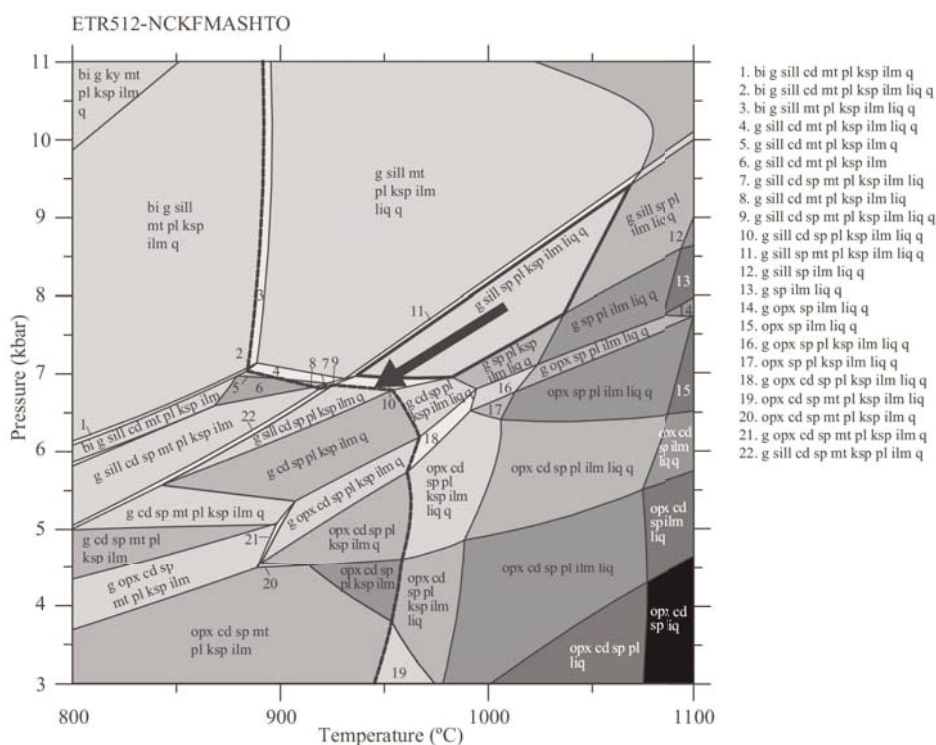


**Figure 12.** NCKFMASHTO P–T pseudosection for sample ETR512. The peak assemblage of g + sill + sp + pl + ksp + ilm + liq + q is constrained to the highlighted field (in bold), at pressures lower than quartz-out boundary and temperatures higher than cordierite stability. The bulk composition is given in Table 6.

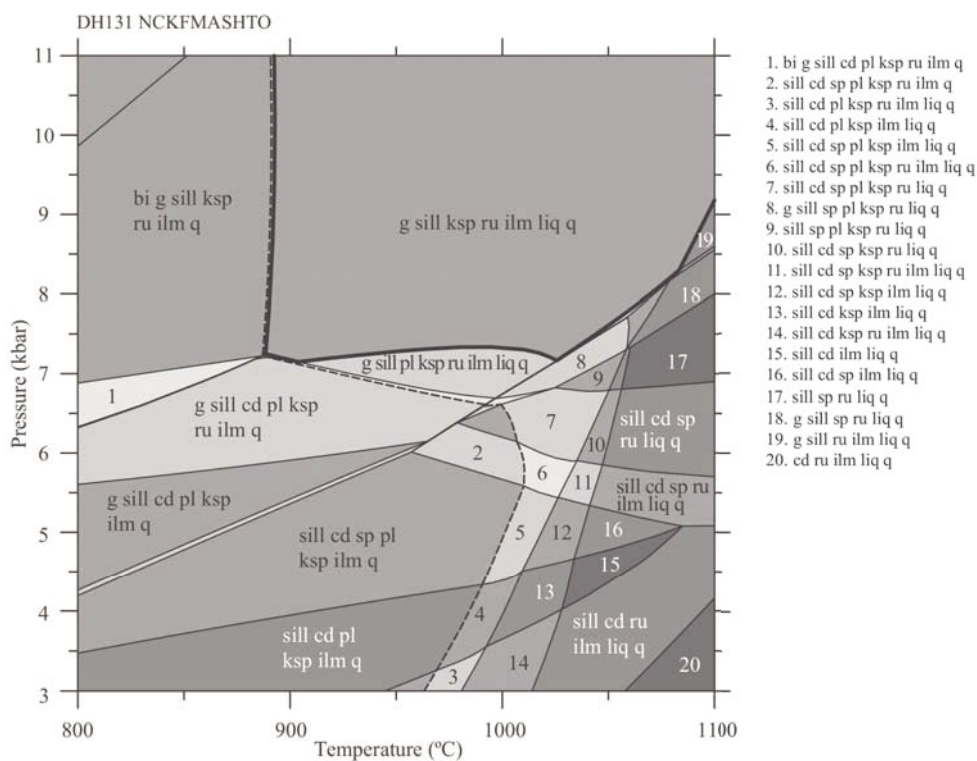


**Figure 13.** NCKFMASHTO P–T pseudosection for sample ETR512. The peak assemblage of g + sill + ksp + ru + ilm + liq + q is constrained to the highlighted field (in bold). The bulk composition is given in Table 6.

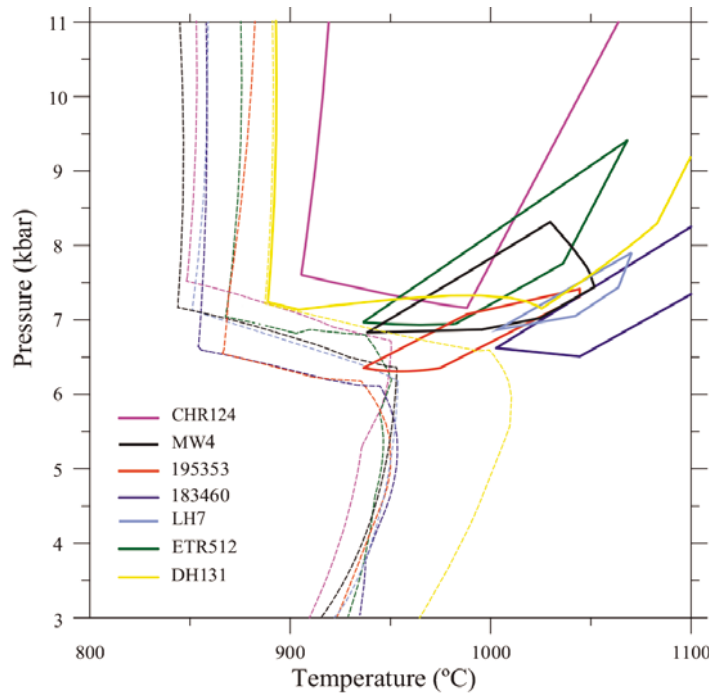


**Figure 14.** ‘Venn diagram’ summarising the stability fields of peak metamorphic assemblages modelled for each sample. There is no requirement that the peak assemblage fields need to overlap (except LH7 and 183460) as the samples are from widely separated locations. Dashed lines represent the variation of the modelled solidii.

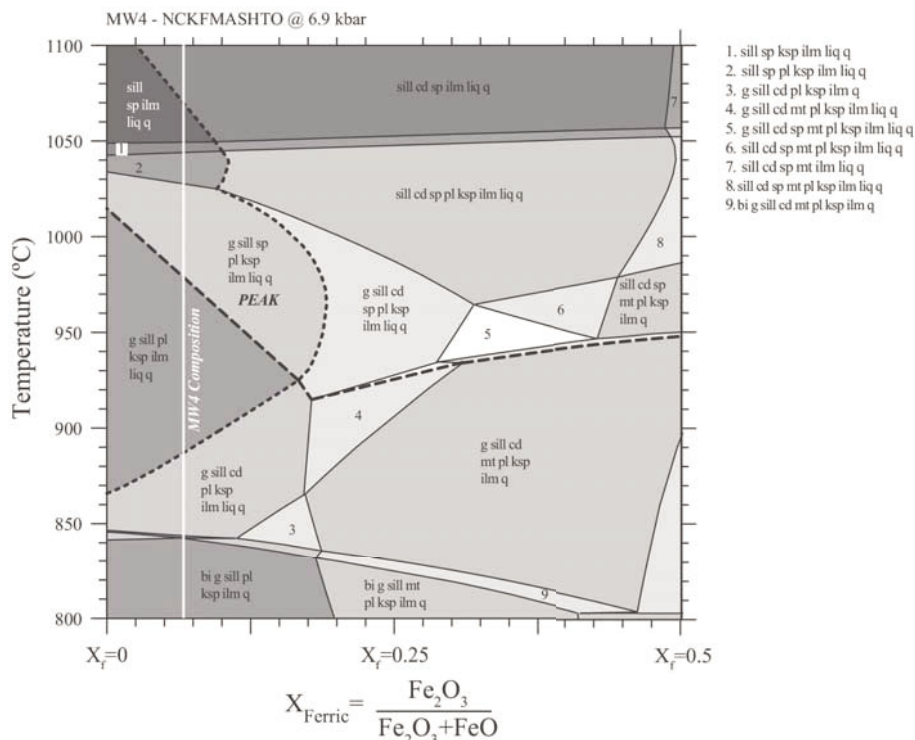


**Figure 15.** Isobaric (6.9 kbar) T–X<sub>ferric</sub> pseudosection for sample MW4, where  $X_{\text{ferric}} = \text{Fe}_2\text{O}_3 / (\text{Fe}_2\text{O}_3 + \text{FeO})$ . Increasing  $X_{\text{ferric}}$  increases the stability of the spinel bearing assemblages to lower temperatures although cordierite is stabilised to higher temperatures constraining maximum  $X_{\text{ferric}}$  values and minimum temperatures for sample MW4, the peak assemblage requires temperatures above ~920 °C. White line indicates  $X_{\text{ferric}}$  used to calculate P–T pseudosection for sample MW4. Bulk composition at the LHS and RHS are presented in Table 6. The righthand axis ( $X = 0.5$ ) corresponds to  $X_{\text{ferric}} = 0.5$ .

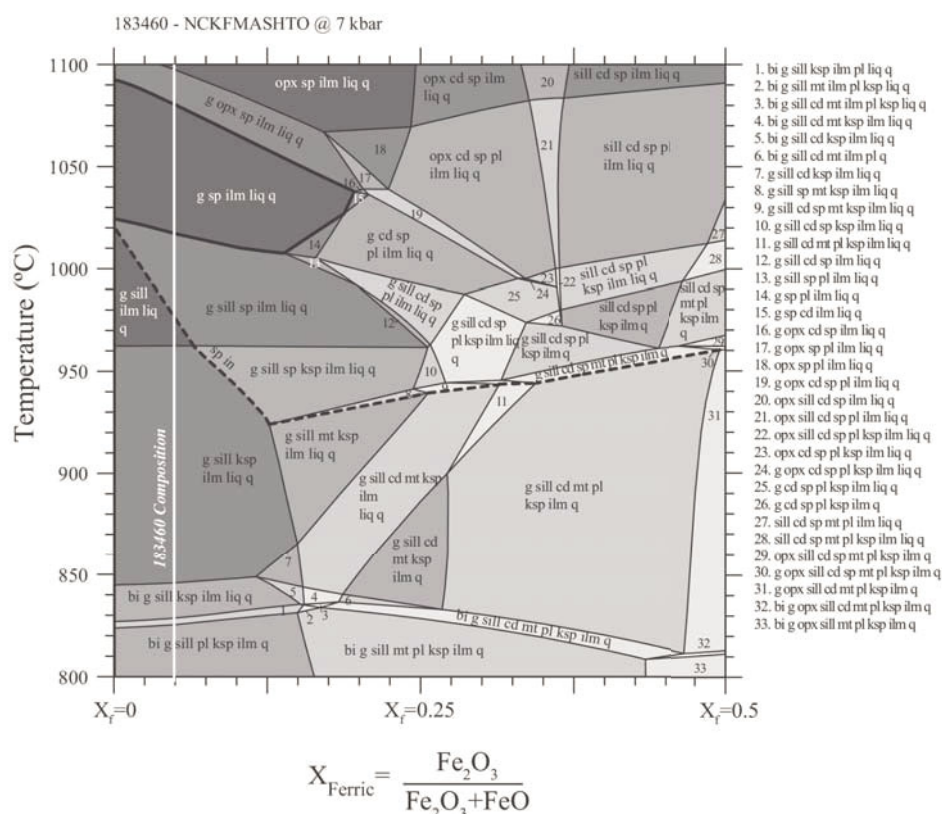


**Figure 16.** Isobaric (7 kbar) T–X<sub>ferric</sub> pseudosection for sample 183460, where X<sub>ferric</sub>=Fe<sub>2</sub>O<sub>3</sub>/(Fe<sub>2</sub>O<sub>3</sub> + FeO). Increasing X<sub>ferric</sub> increases the stability of the spinel bearing assemblages to lower temperatures, although cordierite is stabilised to higher temperatures constraining maximum X<sub>ferric</sub> values to below ~0.2 and minimum temperatures to be above ~1020 °C. White line indicates X<sub>ferric</sub> used to calculate P–T pseudosection for sample 183460. Bulk composition at the LHS and RHS are presented in Table 6. The right-hand axis (X=0.5) corresponds to X<sub>ferric</sub>=0.5.

1986; Nichols et al., 1992; Dasgupta et al., 1995; Guiraud et al., 1996; Tajčmanová et al., 2009), such that spinel is stabilised to lower temperatures and higher pressures. The absolute down-temperature shift as a result of incorporation of Zn and/or Cr is not possible to quantify with phase equilibria modelling. However, given that the amount of ZnO and Cr<sub>2</sub>O<sub>3</sub> wt.% in spinel across all studied samples is low, it is possible that the enhancement of spinel stability is not great. Nevertheless, if the lower-temperature bound of the peak stability fields (containing spinel) were shifted to temperatures less than ~900 °C by the presence of Zn and/or Cr, we consider it improbable that the entire peak assemblage filed would shift to temperatures below 900 °C.

The paragenesis of matrix biotite can be difficult to interpret from thin section

petrography, if it is fine-grained, ragged and low in abundance. We have interpreted biotite to comprise part of the retrograde assemblage as it is rarely oriented, in addition to the above mentioned physical characteristics. However, there is the possibility that the biotite could be relict prograde/peak. At granulite-facies conditions, biotite can be stabilised to very high temperatures by fluorine and titanium (Sankar et al., 2005; Tajčmanová et al., 2009). If the biotite in the studied rocks contains appreciable fluorine, it is possible that the stability field of biotite (as a peak mineral in this case) could overlap with the peak stability fields involving spinel. Again, the absolute temperature effect of fluorine in biotite is unquantifiable within the modelling realm. Therefore, on the basis of ferric iron sensitivity analysis for two of the eight studied rocks, as well as consideration of Zn, Cr and F, we infer that



UHT conditions are definitively recorded by the entire suite of rocks studied here.

These rocks represent an unusual case in the history of documenting UHT metamorphism. Our global recognition of UHT rocks and terrains has almost universally been restricted to high-Mg–Al rocks that contain mineral assemblages such as sapphirine + quartz or osumilite or orthopyroxene + sillimanite + quartz (Hensen and Green, 1971; Hensen and Green, 1973; Ellis, 1980; Annersten and Seifert, 1981; Sandiford, 1985; Audibert et al., 1995; Carrington and Harley, 1995; Harley, 1998, 2004; Kelsey, 2008). The rocks documented here are all high-Fe–Al rocks, many with spinel ± quartz assemblages. Spinel + quartz assemblages are regarded as only being ‘indicative’, rather than ‘diagnostic’, of UHT metamorphism if spinel has low Zn and Cr (Harley, 2008; Kelsey, 2008). Above, we have demonstrated that if rigorous analysis is performed for spinel-bearing granulite-facies metapelites, robust and reliable UHT conditions can be retrieved. Therefore, this opens the possibility that UHT conditions may be recorded in a great many more terrains where high-Mg–Al diagnostic rocks and minerals are absent.

P–T conditions for the Mt West metapelitic rocks have previously been estimated at approximately 850 °C and 6 kbar (White et al., 2002). The calculated phase equilibria in this study indicate a similar apparent thermal gradient of  $\geq 40$  °C km<sup>-1</sup> for the peak metamorphic conditions, but more thermally extreme conditions of approximately 930–1000 °C at about 7–8 kbar. We are unable to reconcile the approximately 80–150 °C difference between our estimate of the peak temperature from Mt West (and elsewhere in the Musgrave Province) with that of White et al. (2002). Our Mt West sample MW4 was collected from one of the same locations as those in the White et al. (2002) study. Whereas we have derived our bulk composition using a methodology involving the combination of

a mapped area of a thin section with (spot) compositional analyses, White et al. (2002) do not provide the methodology for how they attained their original (pre-melt loss) bulk rock composition.

## 6. ZR-IN-RUTILE THERMOMETRY

The incorporation of zirconium (Zr) into rutile provides a robust single-mineral thermometer when rutile grows in equilibrium with quartz and zircon (Zack et al., 2004; Watson et al., 2006; Ferry and Watson, 2007; Tomkins et al., 2007). Rutile has been shown to be retentive of its Zr signature and yield robust estimates at high temperatures in excess of approximately 900 °C (Zack et al., 2004; Baldwin and Brown, 2008b; Luvizotto and Zack, 2009; Kotková and Harley, 2010; Jiao et al., 2011; Kooijman et al., 2012; Ewing et al., 2013). The reason for this is that zirconium can be expelled from rutile by exsolution, rather than lost by diffusion (Bingen et al., 2001; Schmitz and Bowring, 2003; Kooijman et al., 2012; Ewing et al., 2013). Zr-in-rutile thermometry is utilised here to provide an estimate of metamorphic temperatures during the Musgrave Orogeny that is independent of the results obtained from calculated P–T pseudosections (Figs. 7–13).

Zr-in-rutile analysis of in situ rutile was performed for sample DH131. Sample DH131 contains a peak metamorphic assemblage of garnet, sillimanite, K-feldspar, quartz and rutile (with zircon), that is stable at temperatures  $\geq 900$  °C (Fig. 13). Based on these observations and results it is interpreted that rutile from sample DH131 developed during Grenvillian-aged granulite-facies metamorphism.

The distribution of zirconium in rutile was observed via high-magnification back-scattered electron (BSE) imaging and is shown to vary between rutile grains in sample DH131 (Fig. 17). Many rutiles have ‘flat’ Zr contents (Fig. 17a) which could suggest that

the Zr remains evenly distributed, effectively disseminated, within the crystal lattice of the rutile grain. There are rare examples of rutile grains that feature zirconium exsolution (Fig. 17b, c).

### 6.1. Methods

Zr-in-rutile analysis of in situ rutile for sample DH131 was conducted using a New Wave 213 nm Nd-YAG laser in a He-ablation atmosphere connected to an Agilent 7500cs ICP-MS at the University of Adelaide. Ablation of rutile was done with a frequency of 5 Hz and a spot size of 60  $\mu\text{m}$  was used. The total acquisition time of each analysis was 120 s. This included 60 s of background measurement, 10 s of the laser firing with the shutter closed to allow for beam stabilisation and 50 s of sample ablation. Trace element concentrations were normalised to NIST-610 synthetic glass and accuracy was monitored with repeated analysis

of the NIST 612 synthetic glass and the R10 and R19 rutile standards (Luvizotto et al., 2009). Internal standardisation was to  $\text{TiO}_2 = 100 \text{ wt.}\%$ .

### 6.2. Thermometry

Zr-in-rutile temperatures were calculated using the calibration of Tomkins et al. (2007). Rutile is presumed to have grown in the presence of quartz given the abundance in quartz in the sample (Figs. 5q, r). Rutile is additionally assumed to have grown in equilibrium with zircon since zircon is present in the rocks (Fig. 17b), although equilibrium is difficult to assess given the paucity of examples of zircon in direct contact with rutile grains. Where zircon does not stably coexist with rutile, Zr-in-rutile thermometry yields minimum temperatures (Zack et al., 2004). An uncertainty of  $\sim 4.2\%$  was assigned of the Zr-in-rutile temperatures and was calculated by summing in quadrature the

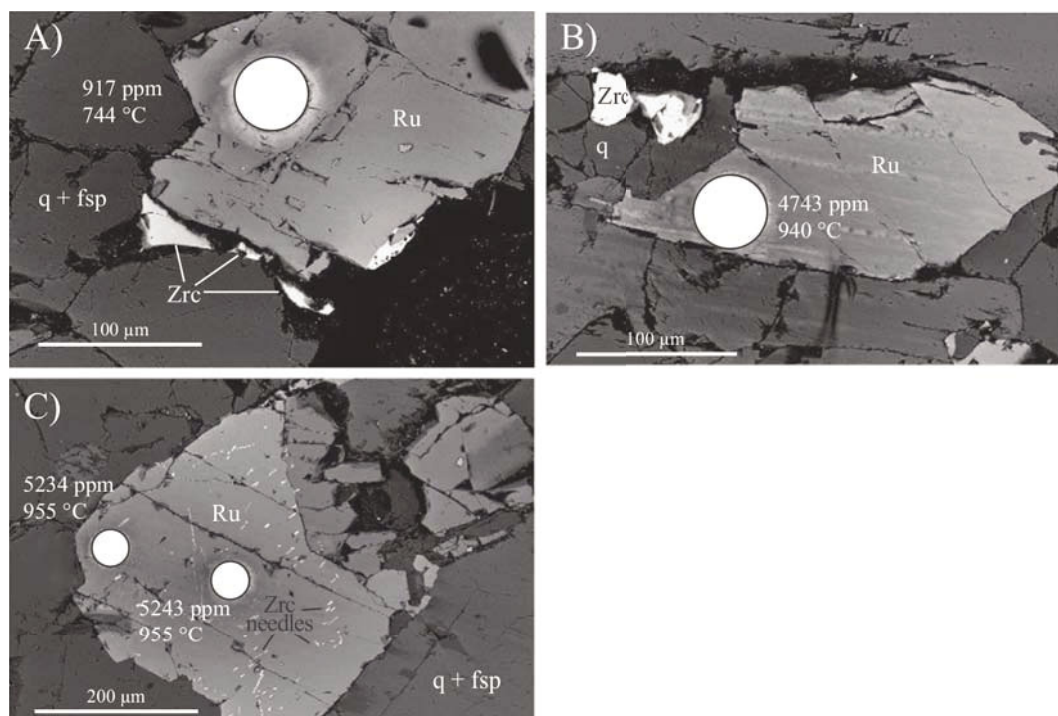


**Figure 17.** Back scattered electron (BSE) images for thin section sample DH131 for which Zr-in-rutile analysis was performed. Locations of spot analyses are illustrated by filled-white circles. (a) Rutile in contact with quartz that displays no Zr expulsion and preserves high concentrations of Zr (b) Small zircon grains at the edge of a rutile grain which records low concentrations of Zr. (c) Rutile grain, which records high-Zr concentrations, showing intragranular exsolution of zircon/baddeleyite needles.

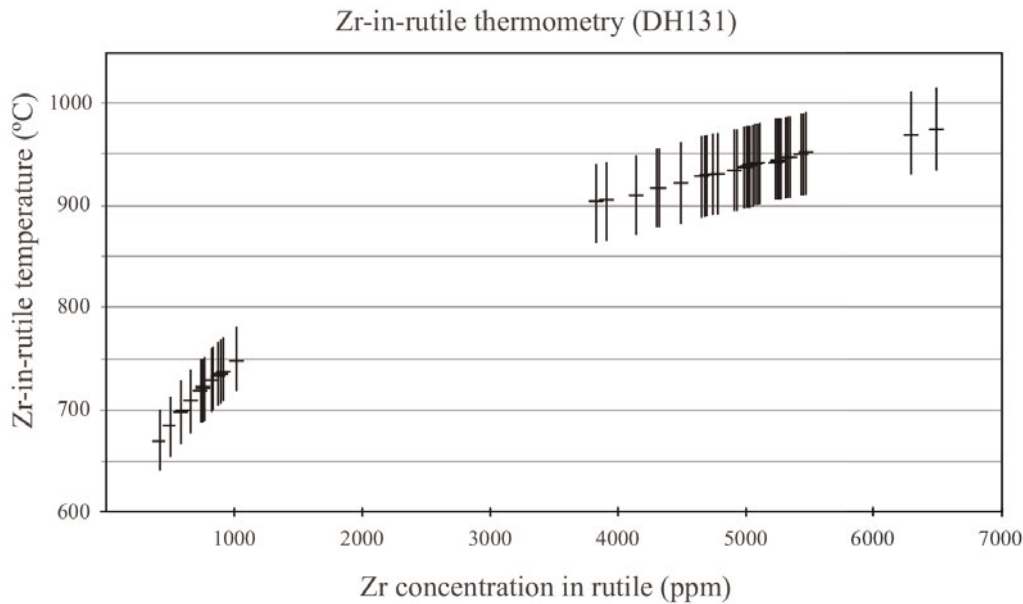


**Figure 18.** Zr-in-rutile temperature estimates (y-axis) plotted versus Zr concentration in rutile grains from sample DH131. Plot illustrates bi-modal distribution of Zr-in-rutile concentrations and temperatures. Individual error bars show total  $2\sigma$  uncertainty calculated for Zr-in-rutile temperatures. Error calculation is discussed in text.

relative errors contributing to the calculations by: 1) the pressure estimate; 2) the analytical uncertainty on the measurement of Zr; and 3) the analytical uncertainty inherent in the calibration (e.g. Ewing et al., 2013). The pressure estimates, provided in this study, are arbitrarily assigned an uncertainty of  $\pm 1$  kbar. The analytical uncertainty on measurement of Zr concentrations is  $\pm 3\%$ . The uncertainty inherent in the calibration of the Zr-in-rutile thermometer is not quantified in Tomkins et al. (2007) and therefore an uncertainty of  $\pm 3\%$  is used, calculated for the Zr-in-rutile thermometer of Watson et al. (2006).

The trace element concentration was measured by LA-ICP-MS for twenty-three rutile grains. None of the sixty analyses were discarded from the data set as there were no irregular signals in any trace element concentrations that indicated contamination by inclusion of other minerals. The Zr concentration of rutiles in sample DH131 ranges from 450 to 6500 ppm (Fig. 18). The large range in Zr concentration is strongly bimodal, a characteristic that is additionally found within single rutile grains and is

commonly observed by other researchers (e.g. Kooijman et al., 2012; Ewing et al., 2013). The lowest Zr concentrations define a range between 450 and 1200 ppm, corresponding to Zr-in-rutile temperatures of 680–770 °C (Fig. 18). The highest Zr concentrations define a band between 3900 and 6800 ppm, corresponding to Zr-in-rutile temperatures of 900–990 °C (Fig. 18).

The strongly bi-modal distribution of Zr concentration and therefore Zr-in-rutile temperature estimates shows no systematic relationship with grain size, microstructural location, or with the position of the laser spot analysis with respect to the center or edge of a rutile grain. Therefore the variability of Zr content is not considered to be significantly affected by diffusive exchange, as might be expected at temperatures  $\sim 900$  °C (Cherniak et al., 2007).

Rutile grains with the lowest Zr concentrations and Zr-in-rutile temperatures could be explained by post-peak exsolution/expulsion of Zr as zircon in (or adjacent to) rutile or by growth during lower temperatures either during the prograde or (less likely) retrograde

evolution. Small zircons ( $\sim 20 \mu\text{m}$ ) are observed around the edge of rutile grains (Fig. 17a) that record low temperatures and are interpreted to have formed either as a result of the expulsion of Zr from the rutile grain (e.g. Bingen et al., 2001; Baldwin and Brown, 2008a; Ewing et al., 2013) or by intragranular exsolution (Kooijman et al., 2012). This observation supports resetting via recrystallisation during the post-peak evolution rather than growth during prograde or retrograde conditions (Ewing et al., 2013). Rutile grains that record temperatures of 680–770 °C are interpreted to record the temperature of cooling-driven zirconium expulsion during post-peak resetting.

Electron microprobe X-ray element maps and BSE images indicate that rutile grains which preserve high Zr concentrations are characterised by both ‘flat’ Zr distribution and less commonly by fine-grained needles of baddelyite (Fig. 17b, c). Exsolution of baddelyite or zircon in rutile is interpreted to occur during cooling (Schmitz and Bowring, 2003; Watson et al., 2006; Cherniak et al., 2007; Kooijman et al., 2012). The preservation of high Zr concentrations suggest that significant net loss of Zr has not occurred during cooling-driven exsolution and therefore whilst the distribution of the exsolved baddelyite is heterogeneous in rutile grains, high concentrations of Zr will likely be measured due the large laser spot size (60  $\mu\text{m}$ ) and high temperatures reflecting formation of rutile will be preserved rather irrespective of the temperature of exsolution of Zr phases (Ewing et al., 2013). It is interpreted that if samples which preserve exsolution of baddelyite and/or zircon have undergone no net loss of Zr, then they provide an accurate constraint on the highest temperatures of rutile crystallisation in sample DH131. It is interpreted that the Zr in rutile grains that do not display any exsolution features is effectively disseminated throughout the rutile grain and does not appear to have been modified by cooling-driven processes and therefore will preserve Zr concentrations reflecting crystallisation during

high temperatures.

Temperatures of 900–980 °C calculated via the Zr-in-rutile thermometer (Fig. 18) for sample DH131 are in agreement with the UHT temperatures (930–1000 °C) predicted from the P–T pseudosection analysis of metapelitic samples (Figs. 7–14). Therefore the results of the two independent approaches combined increases the robustness and reliability of the estimated UHT temperatures.

## 7. U–Pb GEOCHRONOLOGY

### 7.1. Methods

#### 7.1.1. U–Pb SHRIMP geochronology

U–Th–Pb analysis of monazite was undertaken using the SHRIMP-II facility at the John De Laeter Centre for Mass Spectrometry, Curtin University, Perth. For all samples except CHR124 and MW4, monazite grains were separated from crush rock and mounted in 25 mm epoxy discs. For samples CHR124 and MW4, pieces of thin section containing a high abundance of monazite were mounted in 25 mm epoxy discs so that monazite could be analysed in situ. All monazite grains were imaged with a back-scattered electron (BSE) detector and compositionally mapped using the electron microprobe, and then the disc was coated with a thin membrane of gold that produced a resistivity of 10–20  $\Omega$  across the disc. Detailed SHRIMP operating procedures for monazite are outlined in Foster et al. (2000). A 5–10  $\mu\text{m}$  diameter primary beam was employed, dependent on the grain size, with an intensity of  $\sim 0.5 \text{ nA}$ . Ion microprobe analyses of monazite are affected by an uneven background spectrum of scattered ions (Kinny, 1997), which can be reduced effectively by use of the SHRIMP retardation lens system, which is set at  $\sim 10 \text{ kV}$ . This discriminates against low-energy ions entering the collector. Each analysis consists of six cycles through the isotopic masses in the following sequence: 202 (species [ $^{139}\text{La}^{31}\text{P}^{16}\text{O}_2$ ] $^+$ , count time 2 s), 203 ([ $^{140}\text{Ce}^{31}\text{P}^{16}\text{O}_2$ ] $^+$ , 2 s), 204 ( $^{204}\text{Pb}$  +10 s), 204.1 (background, 10 s), 206 ( $^{206}\text{Pb}$



+ , 10 s), 207 ( $^{207}\text{Pb}+$ , 30 s), 208 ( $^{208}\text{Pb}+$ , 5 s), 232 ( $^{232}\text{Th}+$ , 5 s), 254 ( $^{238}\text{U}^{16}\text{O}_2$ ] + , 5 s), 264 ( $^{232}\text{Th}^{16}\text{O}_2$ ] + , 2 s), and 270 ( $^{238}\text{U}^{16}\text{O}_2$ ] + , 3 s). The monazite standard “India” was used for concentration calibration (509 Ma; 2890 ppm  $^{238}\text{U}$ ;  $^{206}\text{Pb}/^{238}\text{U} = 0.082133$  (Korhonen et al., 2011)) and also U–Pb calibration. Ratios of  $^{206}\text{Pb}+/^{238}\text{U} +$  in monazite are calibrated to the known  $^{206}\text{Pb}/^{238}\text{U}$  of the monazite standard using a linear relationship between  $^{206}\text{Pb}+/^{207}\text{Pb} +$  and  $^{206}\text{Pb}+/^{238}\text{U} +$  (Kinny, 1997). Monazite generates an unresolvable isobaric interference on  $^{204}\text{Pb} +$ , which may be ( $^{232}\text{Th}^{144}\text{Nd}^{16}\text{O}_2$ )++ (Kirkland et al., 2009). This interference has been observed to correlate with thorium content (Kinny, 1997). Excess  $^{204}\text{Pb} +$  counts are corrected against the India monazite standard assuming  $^{206}\text{Pb}/^{238}\text{U}$ – $^{207}\text{Pb}/^{235}\text{U}$  age-concordance of the standard at a known thorium concentration. Fractionation of the  $^{207}\text{Pb}/^{206}\text{Pb}$  ratio is typically observed when the retardation lens system is at operating voltage during monazite analysis. Fractionation of the  $^{207}\text{Pb}/^{206}\text{Pb}$  ratio was monitored and corrections were applied, if necessary, by reference to the GM3 monazite standard which was run as an unknown. Uncertainties associated with this correction are added in quadrature to the uncertainties of  $^{207}\text{Pb}*/^{206}\text{Pb}*$  ratios and dates. The common Pb correction was based on measured  $^{204}\text{Pb}$  and Stacey and Kramers (1975) crustal Pb composition appropriate for the age of the sample (Stacey and Kramers, 1975). Data was reduced using SQUID 2 software and plotted using Isoplot 3.66 (Ludwig, 2001; Ludwig, 2003).

### 7.1.2. U–Pb LA-ICP-MS geochronology

U–Pb analysis of in situ monazite for sample 195353 was conducted using a New Wave 213 nm Nd–YAG laser in a He-ablation atmosphere connected to an Agilent 7500cs ICP-MS at the University of Adelaide following the method of Payne et al. (2008). Ablation of monazites was done with a frequency of 5 Hz and a spot size of 15

$\mu\text{m}$  was used. The total acquisition time of each analysis was 90 s. This included 40 s of background measurement, 10 s of the laser firing with the shutter closed to allow for beam stabilisation and 40 s of sample ablation. Iso- topes measured were  $^{204}\text{Pb}$ ,  $^{206}\text{Pb}$ ,  $^{207}\text{Pb}$  and  $^{238}\text{U}$  for 10, 15, 30 and 15 ms, respectively.

Monazite data were reduced using ‘Glitter’ (Van Achterbergh et al., 2001; Griffin et al., 2008). The monazite standard MADEL (TIMS normalisation data:  $^{207}\text{Pb}/^{206}\text{Pb} = 491.0 \pm 2.7$  Ma,  $^{206}\text{Pb}/^{238}\text{U} = 518.37 \pm 0.99$  Ma and  $^{207}\text{Pb}/^{235}\text{U} = 513.13 \pm 0.19$  Ma; updated from Payne et al. (2008) with additional TIMS analyses). The accuracy of the corrected data was verified using in-house standards 94-222/Bruna-NW (c. 450 Ma; Payne et al., 2008). Within Glitter an uncertainty of 1% is assigned to the age of the normalising standard.

### 7.2. Microstructural location of monazite

Monazite is common in all metapelitic samples in the Musgrave Province. In samples CHR124 and MW4, monazite is ubiquitous in all microstructural locations. Monazite occurs as well-armoured inclusions in coarse-grained garnet as well along fractures and less commonly in coarse-grained sillimanite (Fig. 17a, b). Monazite is also abundant in cordierite-spinel-plagioclase symplectites/coronas in sample CHR124, commonly included in cordierite or plagioclase and rarely at grain boundaries in matrix minerals (Fig. 17a). Monazites that are located in cordierite corona mantling garnet in CHR124 (Fig. 20a) could be interpreted to represent monazite former inclusions in garnet, but have been ‘stranded’ outside of garnet as a consequence of retrograde consumption of garnet by cordierite (and spinel). In either sample monazite is not included or in contact with rare fine-grained anhedral biotite.

### 7.3. Results

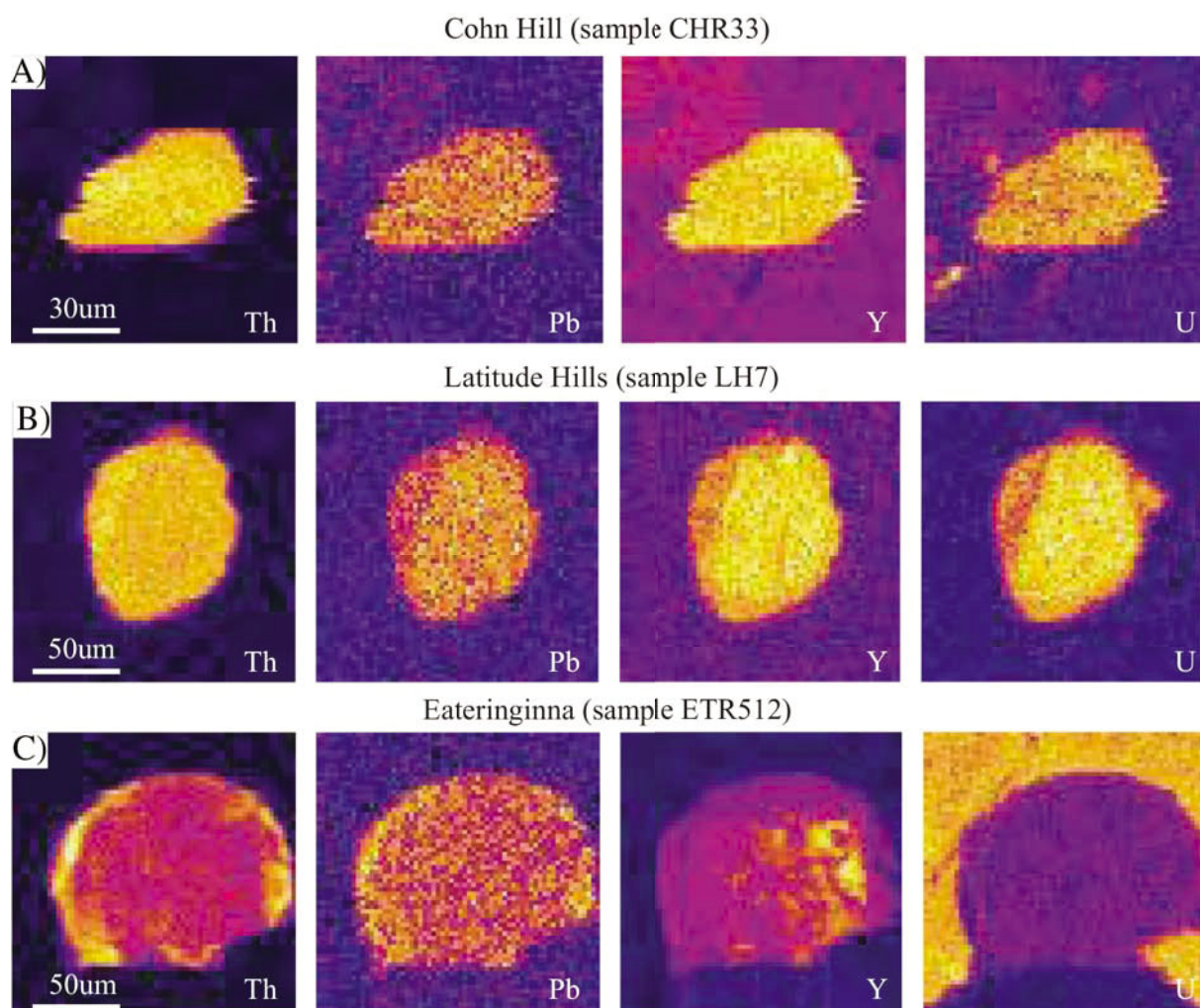


**Figure 19.** Representative EMP element maps of monazite grains for samples CHR33, LH7 and ETR512. Elements are thorium(Th), lead (Pb), yttrium (Y) and uranium(U). Yellow represents highest concentrations and purple represents lowest concentrations.

Age data for all samples are presented in Fig. 21 and analytical data is provided in supplementary data Tables 1 and 2. All age errors are quoted in the text at 2 sigma ( $2\sigma$ ) level. Representative element (Th, Pb, Y, U) probe maps of monazite grains from samples CHR33, ETR512 and LH7 are presented in Fig. 16. We define data that is within  $2\sigma$  analytical uncertainty of the concordia curve as concordant. Discordant data may have suffered some degree of radiogenic Pb-loss and is not used to constrain the timing of monazite growth within the samples. Concordia ages (Ludwig, 1998), which make optimum use of both  $^{207}\text{Pb}^*/^{206}\text{Pb}^*$  and  $^{238}\text{U}/^{206}\text{Pb}^*$  ratios, are also reported along with  $^{207}\text{Pb}^*/^{206}\text{Pb}^*$  and  $^{238}\text{U}/^{206}\text{Pb}^*$  dates in supplementary data. Concordia ages will typically yield a more

precise age than can be obtained using either ratio alone. Weighted mean ages are calculated based on concordia ages to demonstrate the high degree of dispersion (e.g. potentially due to prolonged growth) within the dataset.

### 7.3.1. Sample CHR124

Thirty analyses were collected from twenty monazite grains. Monazite grains are subhedral, up to 150  $\mu\text{m}$  long and display irregular zoning patterns in BSE with some grains containing core domains (Fig. 20a). Six discordant analyses are discounted. Twenty-four analyses yield concordia ages that range from 1263 to 1163 Ma (Fig. 21a). A weighted mean of these ages yields an age of  $1195 \pm 10$  Ma (MSWD = 8.2,  $n = 24$ ), which clearly indicates scatter in excess of that which

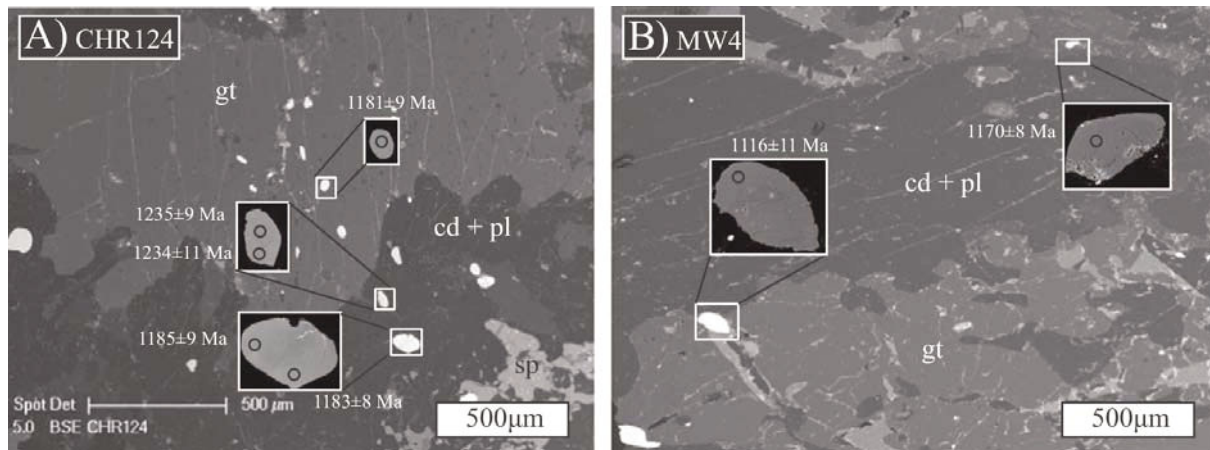


**Figure 20.** Back scattered electron (BSE) images for thin section samples CHR124 (a) and MW4 (b) for which monazites were analysed in-situ. Inset photos are BSE images of monazite grains illustrating spot locations and accompanying concordia age data. Individual spot age data errors are  $1\sigma$ . Spot size is  $\sim 30\ \mu\text{m}$  for (a) and (b).

can be accounted for by analytical errors. U + Th concentrations range between 8000 and 27,000 ppm but have no correlation with age. There is no detectable age difference between the microstructural location of grains, with monazite grains in the matrix and those included in garnet grains showing no systematic age dissimilarity (Fig. 20a).

### 7.3.2. Sample CHR33

Twenty-three analyses were collected from twelve monazite grains. Monazite grains are subhedral and up to  $100\ \mu\text{m}$  long and display flat REE zoning patterns (Fig. 19a). Two discordant analyses are excluded. Twenty-one analyses yield ages that range from 1234 to 1162 Ma (Fig. 21b). The weighted average of the concordia ages yields an age of  $1201 \pm 10$  (MSWD = 3.5,  $n = 21$ ). The large MSWD indicates that there are reasons other than analytical uncertainty for the dispersion in the dataset. U + Th concentrations range between 17,000 and 52,000 ppm but do not correlate with age.

### 7.3.3. Sample CHR17

Seventeen analyses were collected from fifteen monazite grains. Monazite grains are subhedral and up to  $150\ \mu\text{m}$  long. 17 analyses yield concordia ages that range from 1246 to 1155 Ma (Fig. 21c). A

weighted mean of these ages yields an age of  $1180 \pm 15$  Ma (MSWD = 27,  $n = 17$ ), which also indicates scatter in excess of that attributable to analytical uncertainty. U + Th concentrations range between 20,000 and 50,000 ppm but do not correlate with age.

### 7.3.4. Sample MW4

Twenty four analyses were collected from twelve monazite grains. Monazite grains are subhedral and up to  $150\ \mu\text{m}$  long. Two discordant analyses are not considered further. Twenty analyses yield concordia ages that range from 1219 to 1116 Ma (Fig. 21d). Two significantly younger analyses at  $1040 \pm 8$  and  $1020 \pm 10$  Ma ( $1\sigma$ ) are not considered to be relevant to the timing of the Musgrave Orogeny and are not included in the weighted average calculation (Fig. 21d). A weighted mean of eighteen analysis yields an age of  $1189 \pm 14$  Ma (MSWD = 9.8), with indubitable scatter. U + Th concentrations range between 8000 and 18,000 ppm but have no correlation with age. There is no detectable age difference between microstructural location of grains, with monazite in the matrix and those included in garnet having no systematic age dissimilarity (Fig. 20b).



### 7.3.5. Sample 195353 (LA-ICP-MS)

Twenty-four analyses were collected from twenty-one monazite grains. Monazite grains are subhedral and up to 150  $\mu\text{m}$  long. Seven discordant analyses are discounted. Seventeen analyses yield concordia dates that range from 1222 to 1144 Ma (Fig. 21e), with a weighted mean age of  $1181 \pm 12$  Ma (MSWD = 2.3,  $n = 17$ ). One analysis has a significantly older age of  $1318 \pm 12$  Ma ( $1\sigma$ ) and is not included in the mean age calculation (Fig. 21e). In any case, the degree of dispersion implies that there are geological reasons for the scatter in the dataset.

### 7.3.6. Sample LH7

Seventeen analyses were collected from fourteen monazite grains. Monazite grains are subhedral and up to 100  $\mu\text{m}$  long, and display irregular REE zoning, with elevated thorium values in the thin rims (Fig. 19b). Four discordant analyses are not considered to be geologically significant. Thirteen analyses yield concordia ages that range from 1147 to 1111 Ma (Fig. 21f). The calculated mean concordia age yields a date of  $1130 \pm 8$  (MSWD = 9). The elevated MSWD indicates that analytical uncertainties cannot explain the scatter alone. U + Th concentrations range between 10,000 and 72,000 ppm but have no correlation with age. There is no apparent correlation between ages and REE distribution.

### 7.3.7. Sample ETR512

Twenty-three analyses were collected from fifteen monazite grains. Monazite grains are subhedral and up to 150  $\mu\text{m}$  long and irregular REE zoning, with elevated thorium values in rims and distinctively higher yttrium in cores of some grains (Fig. 19c). Three discordant analyses are discounted. Fifteen analyses yield concordia ages that range from 1251 to 1193 Ma, with three additional analyses significantly older (N 1300 Ma) than the majority of the data and not included in weighted mean calculations (Fig. 21g). A weighted mean of the ages yields

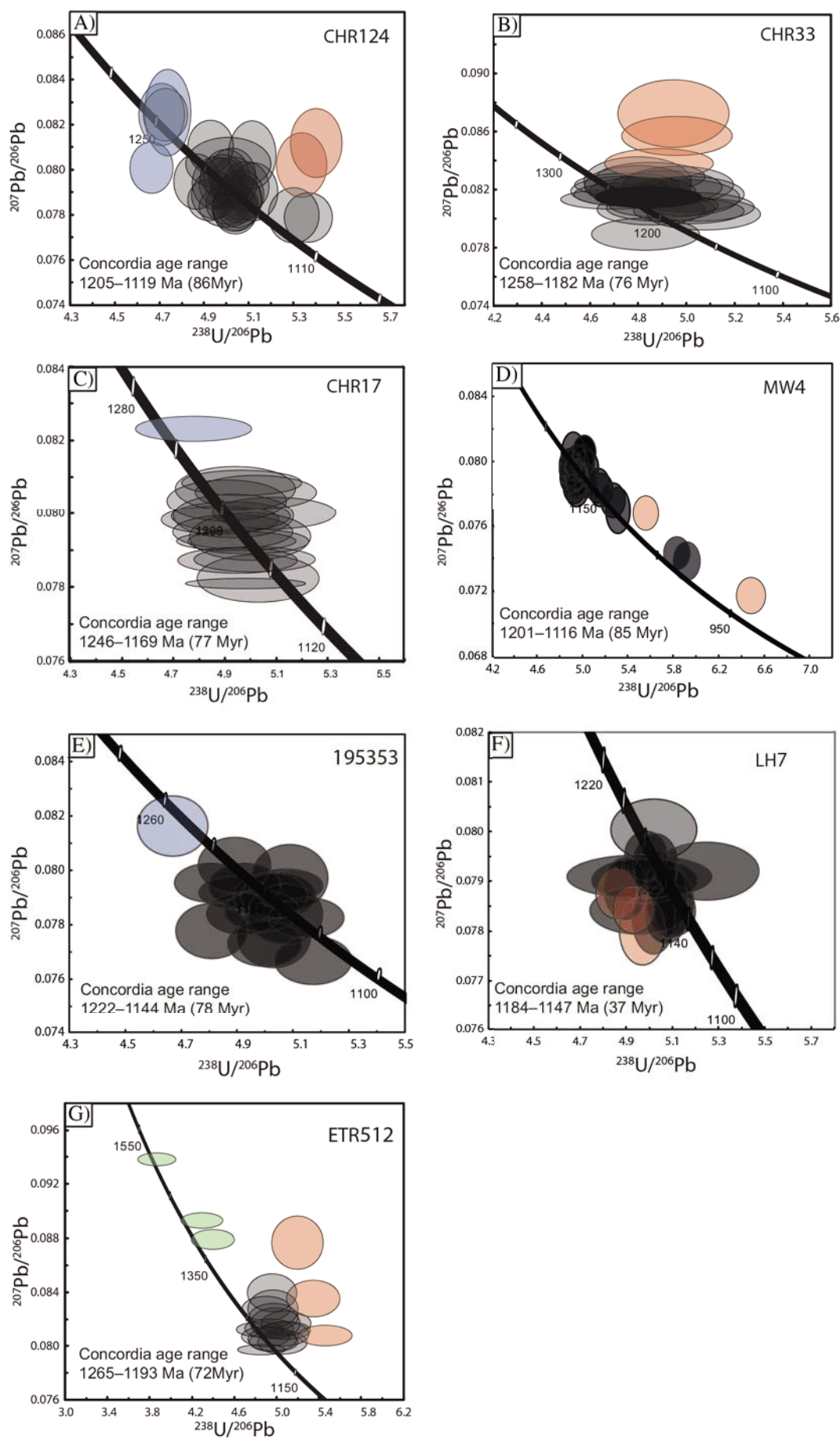
an age of  $1211 \pm 9$  Ma (MSWD = 2.6,  $n = 13$ ), with scatter in excess of that attributable to analytical uncertainties. U + Th concentrations range between 15,000 and 30,000 ppm but have no correlation with age. There is no apparent correlation between ages and REE distribution.

In summary, all of the samples are dominated by monazite ages corresponding to the prolonged 1220–1150 Ma Musgrave Orogeny (Smithies et al., 2010). Four samples (CHR124, CHR17, ETR512 and 195353) have a small number (b4) of older monazite ages, and one sample (MW4) has two age analyses younger than the Musgrave Orogeny.

## 8. DISCUSSION

### 8.1. Interpretation of U–Pb monazite geochronology

Constraining timescales of UHT metamorphism via conventional chronometers, e.g. monazite and zircon, in any terrain is potentially complicated by the extreme temperatures ( $\geq 900$  °C) reached (e.g. Halpin et al., 2012). These temperatures approach or exceed temperatures at which the Pb isotopic system in monazite and zircon is typically accepted to be open to diffusion (Cherniak and Watson, 2001; Cherniak et al., 2004). Furthermore, at such high temperatures, monazite and zircon dissolution (into melt) may be well advanced and as a result, zircon and monazite ages from UHT rocks and terrains do not necessarily record the timing of peak metamorphism (e.g. Fraser et al., 1997; Roberts and Finger, 1997; Kelsey et al., 2008; Stepanov et al., 2012). However, recent work has demonstrated that the U–Th–Pb closure temperature of monazite and zircon can be in excess of 1050 °C, implying the preservation of crystallisation/growth ages through/during UHT conditions is possible, at least in ‘dry’ systems (Sajeev et al., 2010).





U–Pb monazite geochronology from metapelitic samples in the Musgrave Province is commonly characterised by spread of concordant analyses along the Concordia curve, spanning 100 Myr in CHR124, 72 Myr in CHR33, 89 Myr in CHR17, 103 Myr in MW4, 78 Myr in 195353, 36 Myr in LH7 and 78 Myr in ETR512 (Fig. 21). The age span in each sample is considerable, with seven of eight samples characterised by monazite ages spanning  $\sim 70$  Myr. Due to this spread of concordant ages, the calculation of a single weighted mean age for each dataset is unfeasible as the analytical uncertainties are far too small to explain the observed scatter (MSWD  $\gg 1$ ). Therefore the scatter is interpreted to a result of geological processes. There are several potential explanations of this distribution of U–Th–Pb data that needs to be considered.

1) The array of ages could represent multiple discrete (and perhaps short-lived) thermal events recorded by each sample at each location. U–Pb age data under such a process would then reflect numerous single magmatic or metamorphic growth events, over geologically short crystallisation episodes (Fig. 21). If monazite growth is in response to numerous discrete short lived events, then the time scale of these events must be of shorter duration than the analytical resolution of the SIMS and LAICPMS techniques employed.

2) If the age data do not represent a series of discrete populations, the spread along concordia could perhaps reflect protracted isotopic disturbance (e.g. Halpin et al., 2012). If the younger concordant monazite ages were an artefact of Pb-diffusion then the

younger monazite grains should have higher radiation doses (McFarlane and Hamison, 2006). However, the lack of correlation between the concentration of U + Th and ages for all samples suggests that younger monazites do not show higher radiation doses. This may suggest that spread of younger monazite ages is not an artefact of radiogenic Pb diffusion. However, there are no unambiguous physical features in the analysed monazites observed that allow the distinction of growth or alteration processes. Therefore, it is possible that the observed data reflects a combination of growth and alteration (Pb diffusion) processes. As Pb diffusion in monazite at high temperatures ( $\sim 900$  °C) is considered to an effective process (Cherniak et al., 2004), it is plausible that Pb diffusion may have played a role given the very high temperatures (930–1000 °C) suggested in this study.

3) The spread of age data in each sample could reflect resetting of the U–Th–Pb system in monazite as a result of fluid–rock interactions (Teufel and Heinrich, 1997; Seydoux-Guillaume et al., 2002; Williams et al., 2011; Seydoux-Guillaume et al., 2012). In such a scenario some of the youngest ages could represent isotopic disturbance due to fluid interaction produced during crystallisation of silicate melts. Biotite in the rocks of the Musgrave Province provides some of the best evidence for a former fluid phase; however sample LH7 with the highest abundance of biotite ( $\sim 3$ –5%), of unknown age has the least spread of ages (36 Myr). This argues against a significant role for fluid–rock interaction. The remainder of the samples are much poorer in biotite ( $\sim 2\%$  by area) but contain the largest

**Figure 21.** U–Pb Tera-Wasserburg diagrams, plotting  $^{207}\text{Pb}/^{206}\text{Pb}$  (y-axis) Vs.  $^{238}\text{Pb}/^{206}\text{Pb}$ , for monazite samples: (A) CHR124; (B) CHR33; (C) CHR17; (D) MW4; (E) 195353; (F) LH7; and (G) ETR512. Red ellipses are not considered in age determination, blue ellipses are interpreted to represent prograde monazite growth and green ellipses represent detrital ages. All error ellipses are  $2\sigma$ .

spread of concordant ages.

4) The spread of ages along Concordia in each sample could perhaps indicate protracted, continuous growth of monazite (Korhonen et al., 2013). Above the solidus, growth of monazite can occur due to crystallisation of REE+U+Th+Y bearing silicate melt (Rapp and Watson, 1986; Rapp et al., 1987; Montel, 1993; Bea, 1996; Bea and Montero, 1999; Kelsey et al., 2008; Spear and Pyle, 2010; Stepanov et al., 2012). Crystallisation could be initiated by cooling (Kelsey et al., 2008) or by extraction of a melt that is LREE-depleted, which results in LREE-saturation of the remaining melt (Villaseca et al., 2003; Villaseca et al., 2007). The growth of monazite commences at a temperature above the solidus, which is governed by rock composition (including monazite-forming components such as LREE), melt abundance and peak metamorphic temperatures (Kelsey et al., 2008). Once supra-solidus monazite crystallisation has commenced, it is predicted to continue down-temperature until the solidus is reached, whereupon final melt and monazite crystallisation occurs (Kelsey et al., 2008). That is, monazite growth is predicted to occur over a temperature range as the rock cools from peak (or close to) metamorphic temperatures towards the solidus. As such, the protracted growth of monazite over a range of temperatures can potentially provide a mechanism to explain the spread of U–Pb monazite ages of this study.

Solid-state monazite growth (as opposed to crystallisation from melt) as temperatures continue to decrease below the solidus can only be predicted in the presence of apatite at present (e.g. Spear and Pyle, 2010). If the large span (N70 Myr for most samples) of concordant ages can be explained as the result of supra-solidus crystallisation, potentially plus some as-yet unrecognised

sub-solidus (retrograde) growth, then an implication is that cooling must have been very slow in these rocks to enable monazite growth to occur for so long. Such a process would then have implications for the tectonic setting of the Musgrave Orogeny.

If some of the monazite ages in the spread represent prograde ages, rather than (retrograde) crystallisation ages, then the implications are not significantly changed; in this scenario monazite growth was taking place from near peak conditions, through peak conditions, to post-peak conditions down to the solidus. The large span of ages then still supports a long-lived process, and is still an indicator on the tectonic setting of UHT metamorphism. Regardless of the specific (high-T) mechanism resulting in the monazite age distribution that's recorded, high temperatures were sustained for a prolonged period, approximately 70 Myr, at each sample location. Taking all the sample locations together, the total span of the monazite ages is approximately 150 Myr which represents an exceptionally long period over which high temperatures were sustained.

## 8.2. Implications for monazite behaviour during UHT metamorphism

The implication for our interpretation is that once monazite has crystallised, from crystallising melt, it resides within an essentially anhydrous environment. There is a perception that, in terms of diffusion, monazite is much less robust than zircon at withstanding high temperatures (Cherniak and Watson, 2001; Cherniak et al., 2004). However, in dry environments it has been demonstrated that monazite is capable of withstanding very high temperatures and not be reset through Pb diffusion processes (Sajeev et al., 2010). The very low abundance of biotite in the studied samples lends support to the rocks representing an essentially 'dry' system.

All samples except LH7 include concordant monazite ages that are statistically older

than c. 1220 Ma. The commencement of the Musgrave Orogeny, as established on the basis of U–Pb zircon ages of felsic magmatic rocks (Smithies et al., 2010, 2011), was at c. 1220 Ma. Therefore, the possible significance of these old monazite ages needs to be considered. Deposition of the Wirku Metamorphics has been constrained by U–Pb (detrital) zircon geochronology to between 1340 and 1270 Ma (Smithies et al., 2010; Evins et al., 2012). On this basis, the c. 1220–1265 Ma monazite ages cannot indicate detrital monazite. Therefore, the old monazite grains/ages likely preserve a record of the prograde history of the system. Whereas it is understood that supra-solidus monazite growth will occur during cooling and contemporaneous melt crystallisation (e.g. Kelsey et al., 2008), sub- and supra-solidus growth of prograde monazite would probably form through reactions involving the breakdown of minerals such as apatite (Parrish, 1990; Spear and Pyle, 2002; Pyle and Spear, 2003; Wing et al., 2003; Kohn and Malloy, 2004; Fitzsimons et al., 2005; Krenn and Finger, 2007; Spear and Pyle, 2010). The interpretation that the oldest ages (blue ellipses in Fig. 21a) represent prograde monazite growth can explain the large age gap between the onset of magmatism (1220 Ma) and the oldest monazite ages (1265 Ma). Monazite ages which are significantly older than 1270 Ma (e.g. Fig. 21e, green ellipses) are considered to be detrital ages. Remarkably, the oldest ages, as well as the spread of ages, from ETR512, a sample 600 km across strike from the other samples, are comparable to ages in the west Musgrave Province. This suggests that the onset of UHT metamorphism across the province was not diachronous and that the timescale of metamorphism was also extremely long-lived in the eastern part of the Musgrave Province.

The older monazite dates, interpreted to indicate prograde ages, have a cryptic relationship to microstructural features. Nonetheless, some important observations can be made. Some of the older ages are from

monazite that is located in cordierite corona mantling garnet (Fig. 20a). The monazite pictured in Fig. 20a with spot ages of  $1235 \pm 9$  and  $1234 \pm 11$  Ma is interpreted as a monazite grain that was formerly included in garnet, but has been ‘stranded’ outside of garnet as a consequence of retrograde consumption of garnet by cordierite (and spinel). If our interpretation is correct that this monazite grain did formerly reside inside garnet, then a clearer relationship between old ages and microstructural setting emerges. This has the major implication that monazite is extremely resistive to isotopic resetting, even when exposed to extreme thermal conditions for long ( $\geq 80$  Myr) periods (see also Sajeew et al., 2010).

The preservation of U–Pb monazite and zircon ages despite protracted ultra-high temperatures in the Musgrave Province is seemingly at odds with the current understanding of accessory phase behaviour during HT metamorphism. However, granulites ((Harley and Motoyoshi, 2000; Hokada, 2001) from the type locality of UHT metamorphism, the Napier Complex, commonly preserve U–Pb zircon ages older than the reported ages (N 2580–2550 Ma) for UHT metamorphism (Kelly and Harley, 2005; Horie et al., 2012). This suggests that U–Pb ages in accessory phase minerals may be in part resistive to resetting during long-lived ultra-high temperature metamorphism. The well-documented magmatic record during the Musgrave Orogeny supports our interpretation that metamorphism during the Musgrave Orogeny was thermally extreme and long-lived (Smithies et al., 2010; Smithies et al., 2011). Orthopyroxene-bearing granitic rocks of the Pitjantjatjara Supersuite outcrop throughout the Musgrave Province (Smithies et al., 2010; Smithies et al., 2011) and are mineralogically and compositionally equivalent to volcanic and intrusive rocks elsewhere established to have very-high (900–1000 °C) extrusion or emplacement temperatures (e.g. Kilpatrick & Ellis, 1992). Intrusive temperatures of N 870–1000 °C

have been calculated for the Pitjantjatjara Supersuite using both the apatite and zircon-saturation thermometers (Smithies et al., 2010; Smithies et al., 2011). In addition, an extensive dataset of U–Pb SHRIMP zircon ages from Pitjantjatjara Supersuite rocks in the west Musgrave Province span the range 1220–1150 Ma (Smithies et al., 2010; <http://www.dmp.wa.gov.au/geochron>). The span of ages is interpreted to reflect more or less continuous intrusion, for at least 70 Myr, of high-temperature granitic magmas into the mid-crust (Smithies et al., 2011). Thus, the combination of extreme intrusive temperatures with the large span of intrusive ages provides independent supporting evidence to the metamorphic rock record for a long-lived and very hot thermo-tectonic regime in the Musgrave Province during the Musgrave Orogeny (Smithies et al., 2010; Smithies et al., 2011). The interpretation that extreme thermal conditions occurred over a distance of at least 600 km across strike, places the Musgrave Province amongst the largest, if not the largest, exposed UHT terrain on Earth.

### 8.3. P–T–t evolution of the Musgrave Orogeny

Protracted growth of supra-solidus monazite is linked with the P–T evolution of rocks and can therefore provide information about the time-integrated thermal history of UHT metamorphism. The interpreted peak mineral assemblage of garnet + sillimanite + spinel  $\pm$  quartz  $\pm$  K-feldspar  $\pm$  plagioclase is stable at approximately 930–1000 °C and 6.5–8 kbar in all samples modelled, except CHR124 (Figs. 7–13). As a consequence of the metapelitic rocks having a residual bulk composition, the integration of P–T pseudosections and U–Pb geochronology can only be used to provide a time-integrated thermal record of the peak and retro-grade evolution of the rock.

In an attempt to constrain the duration of high-temperature metamorphism, whilst

allowing the possibility that not all monazite growth occurred at peak metamorphic temperatures and/or the high-temperature section of the retrograde evolution, varying proportions of the concordant monazite age dataset (discounting distinctly older ages or populations) are taken to represent growth during the retro-grade P–T evolution, conveying a plausible range of cooling rates. For example; if we assume that 80% of the monazite age data from sample 195353 (Fig. 21e) reflects monazite crystallisation from melt, then over a timescale of 62 Myr the rate of cooling from peak temperatures to the solidus is very slow, between 30 and 100 °C/63 Myr or  $\sim 0.5$ – $1.5$  °C/Myr. If we assume 40% of the monazite age data reflects crystallisation from melt, then over a timescale of 31 Myr the rate of cooling from peak temperatures to the solidus is between 30 and 100 °C/31 Myr or  $\sim 1$ – $3$  °C/Myr. As all of the samples have a range of ages 78–103 Myr (except LH7) and have been interpreted to follow a similar retrograde P–T evolution—and regardless of the proportion of the age range that is interpreted to represent crystallisation from melt during the peak–retrograde evolution (within reason)—cooling rates are very slow.

Peak metamorphic conditions of 930–1000 °C at 6.5–8 kbar (Fig. 9) define an apparent crustal thermal gradient of approximately 50 °C km<sup>−1</sup> (assuming crustal density of 3 kgm<sup>−3</sup>). Due to the high apparent thermal gradients predicted, small vertical (pressure) changes related to exhumation would result in drastic changes in temperature. If monazite crystallisation is controlled by melt crystallisation, the youngest monazite age in each sample's dataset will represent the final crystallisation of melt and monazite. The P–T pseudosections show that this will occur at approximately 950 °C in all samples along their retrograde P–T path (Figs. 7–13). Therefore, disparity between the youngest ages in each sample is more likely to reflect differential exhumation across the terrain



since the solidus is at more or less the same temperature in each sample (Fig. 14).

The flat trajectory of the retrograde P–T path described (Figs. 7–13) suggests that the high-temperature part of the retrograde path was dominated by (slow) cooling and did not involve significant decompression from ultra-high temperatures (N950 °C). Invoking a scenario where the system appears to have undergone minor decompression over a period ~60–30 Myr would suggest there is no major exhumation driver. This could imply that the crust was not overly thick or at least did not sustain significant topography. However, limited exhumation can be observed in regions of exceptionally thick crust and therefore the rate and total extent of exhumation is not unequivocally reflective of crustal thickness.

#### 8.4. Tectonic setting of UHT metamorphism during the Musgrave Orogeny

Extreme thermal conditions at relatively shallow depths (approximately 1000 °C at ~25–30 km) may be used to infer high (palaeo-) surface heat flow from the high apparent thermal gradient of ~50 °C km<sup>-1</sup>, probably synchronously across the Musgrave Province given the apparently very low cooling rates. Smithies et al. (2011) inferred the presence of a MASH (Melting-Assimilation-Storage-Homogenisation) zone below the crustal level at which UHT metamorphism was occurring. The presence of a MASH zone implies that the crust is thicker than the depth at which UHT metamorphism is occurring, additionally implying that the apparent thermal gradient we have calculated is only applicable to the depth at which UHT metamorphism was occurring. As a consequence, the apparent thermal gradient cannot be used directly to make inferences about crustal thickness during the Musgrave Orogeny. REE signatures in the Pitjantjatjara Supersuite rocks suggest that crustal melting of an isotopically homogeneous source occurred at depths shallower than garnet stability (>10 kbar)

(Smithies et al., 2011). On this basis, it is plausible that the thickness of crust below the depth of UHT metamorphism during the Musgrave Orogeny was not greater than the equivalent of approximately 3 kbar (~8.5–10 km). Therefore, the total crustal thickness during the Musgrave Orogeny was probably of the order of ~30–40 km. Since the (geo)thermal gradient in the MASH zone will be essentially adiabatic, the temperature at the 30–40 km base of the crust will be in the close vicinity of the UHT temperatures recorded by the metapelitic rocks. If we assume a temperature of 1000 °C at the UHT rocks depth, then the temperature at the base of the crust will be approximately 1020 °C. This translates to the crust overall having an apparent thermal gradient of approximately 25–35 °C km<sup>-1</sup>.

Concurrent with the acceptance of UHT metamorphic conditions as common throughout the Precambrian part of Earth history (Brown, 2006, 2007; Harley, 2008; Kelsey, 2008). There has been an increase in trying to understand the large-scale thermo-tectonic mechanisms by which thermally extreme (high thermal gradient/UHT) metamorphic conditions can be generated and sustained in the crust. Our understanding of mechanisms and possible tectonic settings for UHT metamorphism has been greatly enhanced by numerous recent studies (Hyndman et al., 2005; Brown, 2006; Currie and Hyndman, 2006; Brown, 2007; Sizova et al., 2010; Sizova et al., 2014). A common tectonic setting has emerged from these studies, that UHT metamorphism appears to be related to subduction–collision processes. Back-arc environments, where crust is relatively thin and the mantle is consequently shallow (and possibly partially melted), have been widely invoked for the tectonic setting of UHT metamorphism (e.g. Brown, 2006, 2007; Clark et al., 2009; Bose et al., 2011; Cutts et al., 2011; Cutts et al., 2013). This has particularly been the case since the studies of Hyndman et al., 2005 and

Currie and Hyndman (2006) documented high surface heat flow and thin crust in modern pan-Pacific back-arc environments. Indeed, Collins (2002a, 2002b) earlier proposed that extension in a back-arc setting, was the setting in which formation of the majority of granulite facies rocks/ belts occurred. More recent studies using geodynamic modelling tools have reinforced the notion that UHT conditions require shallow mantle in regions of thin crust, generated in back-arcs (e.g. Sizova et al., 2010, 2014). Sizova et al. (2010, 2014) and Clark et al. (2011) have invoked collisional thickening of (former) back-arc environments as an additional mechanism by which UHT conditions can be generated. Elevated crustal heat production is stated as a necessity to attain UHT conditions (Sizova et al., 2010; Clark et al., 2011; Sizova et al., 2014). Because crustal heat production provides a long-lived, conductive heat source, UHT metamorphic conditions generated in a back-arc are expected to last for as long as the heat production remains sufficiently buried.

If UHT conditions require a subduction–collision setting, then in the case of the Musgrave Province it would be helpful to identify evidence for the actual subduction–collision processes itself. Subduction in the context of the Musgrave Province is not well constrained. However, the magmatic rocks of the c. 1300 Ma Mt West Orogeny (the first of the three Grenvillian-aged events) do carry arc-like geochemical signatures (Smithies et al., 2010). It remains an open question as to whether those magmatic rocks are actually indicative of an arc, and therefore subduction (Smithies et al., 2010; Kirkland et al., 2013), in the early stages of Grenvillian-aged tectonism in the Musgrave Province, or whether they inherited their arc-like signature from their magmatic source (Smithies et al., 2010, 2011). A compressional regime that pre-dates the Musgrave Orogeny does appear to have existed, at least locally (Aitken and Betts, 2008; Smithies et al., 2011), and is considered to involve the formation of a deformational fabric after the

intrusion of the Papulankutja Supersuite (c. 1400 Ma), but before the Mt West Orogeny (1345–1293 Ma) and the production of major NE–SW oriented folding in the west Musgrave Province (Howard et al., 2011).

If the magmatic rocks of the Mt West Orogeny are indicative of subduction–collision, it follows that the province evolved into an extensional-type setting. Smithies et al. (2010) states that the onset of UHT metamorphism coincided with significant thinning of the crust, which was sustained throughout the orogeny. The expanded metamorphic/P–T results we have presented here (cf. Smithies et al., 2011), including estimations of crustal thickness, apparent thermal gradients, cooling rates from UHT conditions and timescales of extreme thermal conditions in the crust, indicate the Musgrave Orogeny was likely extensional, and a back-arc environment. In the eastern end of the Musgrave Province sub-horizontal seismic reflectors have been detected in the deep crust, consistent with extensional fabrics (Korsch and Kositsin, 2010). The Musgrave Province was an extensional environment in the early part of the Giles Event, the youngest of the three Grenvillian-aged events, as vast tracts of mafic to ultramafic layered intrusions were rapidly emplaced at c. 1076 Ma (Evins et al., 2010). Compressional tectonics involving substantial exhumation followed after the emplacement of these mafic to ultramafic intrusions because thick volcanic sequences of the Bentley Supergroup (Giles Event-aged) were deposited directly onto deformed (folded) Giles-aged magmatic rocks.

The North and South Australian cratonic blocks are usually considered to have amalgamated prior to the Musgrave Orogeny (cf. Morrissey et al., 2011), either during an earlier Grenvillian event corresponding to the early evolution of the Albany–Fraser Orogeny and the Mount West Orogeny at c. 1345–1290 Ma (Myers et al., 1996; Clark et al., 2000; Giles et al., 2004; Betts and Giles, 2006) or during older tectonism (c. 1800–1500) (Giles et al., 2004;

Wade et al., 2008). Felsic magmatic rocks of the Pitjantjatjara Supersuite, emplaced between 1220 and 1150 Ma in the Musgrave Province, are interpreted to be within-plate ‘anorogenic’ type (Smithies et al., 2010). In light of the results presented in this study and Smithies et al. (2011) it is plausible that the Pitjantjatjara Supersuite were emplaced in an extensional setting. The juvenile nature of Musgrave Province crust compared to surrounding cratons, and the presence of older source material in the felsic magmatic rocks supports the notion that the Musgrave Orogeny occurred at or close to an active margin (Smithies et al., 2010; Kirkland et al., 2013). Despite major mantle input inferred in the Pitjantjatjara Supersuite, there is a paucity of mafic magmatic rocks from the Musgrave Orogeny at the current exposure level.

On the basis of the above, we propose that the entire Grenvillian-aged history of the Musgrave Province reflects early subduction–collision (Mt West Orogeny), followed by a transition into a long (at least 70–80 Myr) period of elevated and extreme thermal conditions (Musgrave Orogeny). This period of evolution of the Musgrave Province was characterised by voluminous, relatively juvenile felsic magmatism (Smithies et al., 2011) and long-lived UHT metamorphism with extremely slow cooling in crust that was at most 40 km thick which did not support substantial topography to allow erosion and exhumation. Shallow (asthenospheric) mantle that contributed to the juvenile isotopic signature of the felsic magmatic rocks was the driver for the production of such voluminous magmatism coincident with UHT metamorphism. This major period of crustal evolution was followed by the (extensional) emplacement of large mafic to ultramafic bodies, granites and volcanics (the ‘back-arc’ stage) and then compressional inversion of the extensional environment (Giles Event). The system may have ‘relaxed’ back to a now intracontinental extensional setting to ultimately result in the initiation of the Neoproterozoic

Centralian Superbasin. The Australian example, the Musgrave Province, can be considered a distinct and exceptional type of large, hot orogen due to the long timescale over which magmatism and thermally extreme metamorphism was sustained.

## 9. CONCLUSIONS

The Musgrave Province in central Australia is an ancient, large, hot orogen. Our study shows that: 1) Earth’s crust is able to generate and sustain extreme thermal conditions for long periods ( $\geq 85$  Myr) of time. UHT metamorphism in the Musgrave Province is characterised by apparent thermal gradients well in excess of the conductive limit for crustal metamorphism in crust that had a maximum thickness of 40 km; 2) monazite is able to grow and preserve a long ( $\geq 85$  Myr) record of elevated ( $\geq 950$  °C) thermal conditions in Earth’s crust; 3) Monazite is extremely resistive to isotopic resetting, even when exposed to extreme thermal conditions for long ( $\geq 80$  Myr) periods; 4) UHT conditions can be reliably retrieved from high-Fe–Al metapelitic rocks; 5) the Grenvillian-aged Musgrave Orogeny was most probably reflective of an extensional setting, involving voluminous and comparatively juvenile felsic magmatism coincident with UHT metamorphism that reached temperatures of approximately 1000 °C. Tectonism involved very slow rates of cooling from high temperatures, as well as very slow exhumation in topographically neutral crust; and 6) the spatial footprint of extreme thermal conditions is at least 600 km across strike, thus placing the Musgrave Province amongst the largest, if not the largest, exposed UHT terrain on Earth.

Supplementary data to this article can be found online at <http://dx.doi.org/10.1016/j.gr.2014.05.012>.

## ACKNOWLEDGEMENTS

The following are thanked: Primary Industries & Resources of South Australia (PIRSA), now

Department for Manufacturing, Innovation, Trade, Resources and Energy (DMITRE) – in particular Dr Justin Gum, Ailsa Woodhouse and Colin Connor – for access to parts of the South Australian portion of the Musgrave Province; Traditional Owners of the Anangu Pitjantjatjara Yankunytjatjara (APY) lands and the Warburton–Wingellina regions; the Ngaanyatjarra Council; Colin Connor (of DMITRE) for the use of his sample ETR512; Marion Marshall for SHRIMP mount preparation; Prof. Ian Fitzsimons for covering part of the SHRIMP data collection costs (through ARC project DP06694679); Angus Netting, Dr Ben Wade and Laura Morrissey for assistance with the laser and electron microprobe analyses. Constructive reviews by Ian Fitzsimons, Jacqui Halpin, Pavel Pitra, Steve Boger and one anonymous reviewer improved the manuscript greatly. DEK was funded by ARC projects DP0665094 and LP100200127 and CC was funded through DE120103067. CLK, RHS and HMH publish with the permission of the Executive Director of the Geological Survey of Western Australia.

## REFERENCES

- Aitken, A.R.A., Betts, P.G., 2008. High-resolution aeromagnetic data over central Australia assist Grenville-era (1300;1100 Ma) Rodinia reconstructions. *Geophysical Research Letters* 35 (1), L01306.
- Aitken, A.R.A., Betts, P.G., 2009a. Constraints on the Proterozoic supercontinent cycle from the structural evolution of the south-central Musgrave Province, central Australia. *Precambrian Research* 168 (3–4), 284–300.
- Aitken, A.R.A., Betts, P.G., 2009b. Multi-scale integrated structural and aeromagnetic analysis to guide tectonic models: An example from the eastern Musgrave Province, Central Australia. *Tectonophysics* 476 (3–4), 418–435.
- Annersten, H., Seifert, F., 1981. Stability of the assemblage orthopyroxene-sillimanite-quartz in the system  $\text{MgO-FeO-Fe}_2\text{O}_3\text{-Al}_2\text{O}_3\text{-SiO}_2\text{-H}_2\text{O}$ . *Contributions to Mineralogy and Petrology* 77 (2), 158–165.
- Audibert, N., Hensen, B.J., Bertrand, P., 1995. Experimental study of phase relations involving osumilite in the system  $\text{K}_2\text{O-FeO-MgO-Al}_2\text{O}_3\text{-SiO}_2\text{-H}_2\text{O}$  at high pressure and temperature. *Journal of Metamorphic Geology* 13 (3), 331–344.
- Baldwin, J., Brown, M., 2008a. Age and duration of ultrahigh-temperature metamorphism in the Anápolis–Itaçu Complex, Southern Brasília Belt, central Brazil—constraints from U–Pb geochronology, mineral rare earth element chemistry and trace-element thermometry. *Journal of Metamorphic Geology* 26 (2), 213–233.
- Baldwin, J.A., Brown, M., 2008b. Age and duration of ultrahigh-temperature metamorphism in the Anápolis–Itaçu Complex, Southern Brasília Belt, central Brazil—constraints from U–Pb geochronology, mineral rare earth element chemistry and trace-element thermometry. *Journal of Metamorphic Geology* 26 (2), 213–233.
- Bea, F., 1996. Controls on the trace element composition of crustal melts. *Transactions of the Royal Society of Edinburgh–Earth Sciences* 87 (1), 33–42.
- Bea, F., Montero, P., 1999. Behavior of accessory phases and redistribution of Zr, REE, Y, Th, and U during metamorphism and partial melting of metapelites in the lower crust: An example from the Kinzigite Formation of Ivrea-Verbano, NW Italy. *Geochimica et Cosmochimica Acta* 63, 1133–1153.
- Betts, P.G., Giles, D., 2006. The 1800–1100 Ma tectonic evolution of Australia. *Precambrian Research* 144 (1–2), 92–125.
- Bingen, B., Austerheim, H., Whitehouse, M., 2001. Ilmenite as a source for zirconium during high-grade metamorphism? Textural evidence from the Caledonides of



- Western Norway and implications for zircon geochronology. *Journal of Petrology* 42 (2), 355–375.
- Boger, S.D., Hansen, D., 2004. Metamorphic evolution of the Georgetown Inlier, northeast Queensland, Australia; evidence for an accreted Palaeoproterozoic terrane? *Journal of Metamorphic Geology* 22, 511–527.
- Boger, S., White, R., Schulte, B., 2012. The importance of iron speciation ( $\text{Fe}^{+2}/\text{Fe}^{+3}$ ) in determining mineral assemblages: an example from the high- $\square$  grade aluminous metapelites of southeastern Madagascar. *Journal of Metamorphic Geology* 30 (9), 997–1018.
- Bose, S., Dunkley, D.J., Dasgupta, S., Das, K., Arima, M., 2011. India–Antarctica–Australia–Laurentia connection in the Paleoproterozoic–Mesoproterozoic revisited: Evidence from new zircon U–Pb and monazite chemical age data from the Eastern Ghats Belt, India. *Geological Society of America Bulletin* 123 (9–10), 2031–2049.
- Brown, M., 2006. Duality of thermal regimes is the distinctive characteristic of plate tectonics since the Neoproterozoic. *Geology* 34 (11), 961–964.
- Brown, M., 2007. Metamorphic conditions in orogenic belts: a record of secular change. *International Geology Review* 49, 193–234.
- Camacho, A., Fanning, C.M., 1995. Some isotopic constraints on the evolution of the granulite and upper amphibolite facies terranes in the eastern Musgrave Block, central Australia. *Precambrian Research* 71 (1–4), 155–181.
- Camacho, A., McDougall, I., 2000. Intracratonic, strike-slip partitioned transpression and the formation and exhumation of eclogite facies rocks: An example from the Musgrave Block, central Australia. *Tectonics* 19 (5), 978–996.
- Camacho, A., Compston, W., McCulloch, M., McDougall, I., 1997. Timing and exhumation of eclogite facies shear zones, Musgrave Block, central Australia. *Journal of Metamorphic Geology* 15 (6), 735–751.
- Camacho, A., Hensen, B.J., Armstrong, R., 2002. Isotopic test of a thermally driven intraplate orogenic model, Australia. *Geology* 30 (10), 887–890.
- Carrington, D.P., Harley, S.L., 1995. The stability of osumilite in metapelitic granulites. *Journal of Metamorphic Geology* 13, 613–625.
- Cawood, P.A., Pisarevsky, S.A., 2006. Was Baltica right-way-up or upside-down in the Neoproterozoic? *Journal of the Geological Society* 163 (5), 753–759.
- Cherniak, D.J., Watson, E.B., 2001. Pb diffusion in zircon. *Chemical Geology* 172 (1–2), 5–24.
- Cherniak, D.J., Watson, E.B., Grove, M., Harrison, T.M., 2004. Pb diffusion in monazite: a combined RBS/SIMS study. *Geochimica et Cosmochimica Acta* 68 (4), 829–840.
- Cherniak, D.J., Manchester, J., Watson, E.B., 2007. Zr and Hf diffusion in rutile. *Earth and Planetary Science Letters* 261 (1–2), 267–279.
- Clark, D.J., Hensen, B.J., Kinny, P.D., 2000. Geochronological constraints for a two-stage history of the Albany-Fraser Orogen, Western Australia. *Precambrian Research* 102 (3–4), 155–183.
- Clark, C., Collins, A.S., Santosh, M., Taylor, R., Wade, B.P., 2009. The PTt architecture of a Gondwanan suture: REE, U–Pb and Ti-in-zircon thermometric constraints from the Palghat Cauvery shear system, South India. *Precambrian Research* 174 (1), 129–144.
- Clark, C., Fitzsimons, I.C.W., Healy, D., Harley, S.L., 2011. How does the continental crust get really hot? *Elements* 7 (4), 235–240.
- Clarke, G.L., Powell, R., 1991.

- Decompressional coronas and symplectites in granulites of the Musgrave Block, central Australia. *Journal of Metamorphic Geology* 9, 441–450.
- Clarke, G.L., Buick, I.S., Glikson, A.Y., Stewart, A.J., 1995. Structural and pressure-temperature evolution of host rocks of the Giles Complex, central Australia: evidence for multiple high pressure events. *AGSO Journal of Australian Geology & Geophysics* 16, 127–146.
- Collins, W.J., 2002a. Hot orogens, tectonic switching, and creation of continental crust. *Geology* 30 (6), 535–538.
- Collins, W.J., 2002b. Nature of extensional accretionary orogens. *Tectonics* 21 (4) (Art. No. 1024).
- Currie, C.A., Hyndman, R.D., 2006. The thermal structure of subduction zone back arcs. *Journal of Geophysical Research* 111 (B8), B08404.
- Cutts, K., Hand, M., Kelsey, D.E., 2011. Evidence for early Mesoproterozoic (ca. 1590 Ma) ultrahigh-temperature metamorphism in southern Australia. *Lithos* 124 (1), 1–16.
- Cutts, K., Kelsey, D.E., Hand, M., 2013. Evidence for late Paleoproterozoic (ca 1690–1665 Ma) high-to ultrahigh-temperature metamorphism in southern Australia: Implications for Proterozoic supercontinent models. *Gondwana Research* 23 (2), 617–640.
- Dasgupta, S., Sengupta, P., Ehl, J., Raith, M., Bardhan, S., 1995. Reaction textures in a suite of spinel granulites from the Eastern Ghats Belt, India: Evidence for polymetamorphism, a partial petrogenetic grid in the system KFMASH and the roles of ZnO and Fe<sub>2</sub>O<sub>3</sub>. *Journal of Petrology* 36 (2), 435–461.
- Davidson, A., 1995. A review of the Grenvillian orogen in its North American type area. *AGSO Journal of Australian Geology & Geophysics* 16, 3–24.
- De Capitani, C., Petrakakis, K., 2010. The computation of equilibrium assemblage diagrams with Theriak/Domino software. *American Mineralogist* 95 (7), 1006–1016.
- Diener, J., Powell, R., 2010. Influence of ferric iron on the stability of mineral assemblages. *Journal of Metamorphic Geology* 28 (6), 599–613.
- Diener, J., Powell, R., White, R., 2008. Quantitative phase petrology of cordierite–orthoamphibole gneisses and related rocks. *Journal of Metamorphic Geology* 26 (8), 795–814.
- Droop, G., 1987. A general equation for estimating Fe<sup>3+</sup> concentrations in ferromagnesian silicates and oxides from microprobe analyses, using stoichiometric criteria. *Mineralogical Magazine* 51 (361), 431–435.
- Duebendorfer, E.M., 2002. Regional correlation of Mesoproterozoic structures and deformational events in the Albany–Fraser orogen, Western Australia. *Precambrian Research* 116 (1), 129–154.
- Edgoose, C.J., Scrimgeour, I.R., Close, D.F., 2004. Geology of the Musgrave Block, Northern Territory. Northern Territory Geological Survey. Report 15.
- Ellis, D.J., 1980. Osumilite–sapphirine–quartz granulites from Enderby Land, Antarctica — P-T conditions of metamorphism, implications for garnet–cordierite equilibria and the evolution of the deep crust. *Contributions to Mineralogy and Petrology* 74 (2), 201–210.
- Evins, P.M., Smithies, R.H., Howard, H.M., Kirkland, C.L., Wingate, M.T.D., Bodorkos, S., 2010. Devil in the detail; The 1150–1000 Ma magmatic and structural evolution of the Ngaanyatjarra Rift, west Musgrave Province, Central Australia. *Precambrian Research* 183 (3), 572–588.
- Evins, P.M., Kirkland, C.L., Wingate, M.T.D.,

- Smithies, R.H., Howard, H.M., Bodorkos, S., 2012. Provenance of the 1340–1270 Ma Ramarama Basin in the West Musgrave Province, Central Australia. Report 2012/116.
- Ewing, T.A., Hermann, J., Rubatto, D., 2013. The robustness of the Zr-in-rutile and Ti-in-zircon thermometers during high-temperature metamorphism (Ivrea–Verbano Zone, northern Italy). *Contributions to Mineralogy and Petrology* 1–23.
- Ferry, J.M., Watson, E.B., 2007. New thermodynamic models and revised calibrations for the Ti-in-zircon and Zr-in-rutile thermometers. *Contributions to Mineralogy and Petrology* 154, 429–437.
- Fitzsimons, I.C.W., Kinny, P.D., Wetherley, S., Hollingsworth, D.A., 2005. Bulk chemical control on metamorphic monazite growth in pelitic schists and implications for U–Pb age data. *Journal of Metamorphic Geology* 23, 261–277.
- Foster, G., Kinny, P., Vance, D., Prince, C., Harris, N., 2000. The significance of monazite U–Th–Pb age data in metamorphic assemblages; a combined study of monazite and garnet chronometry. *Earth and Planetary Science Letters* 181 (3), 327–340.
- Fraser, G., Ellis, D., Eggins, S., 1997. Zirconium abundance in granulite-facies minerals, with implications for zircon geochronology in high-grade rocks. *Geology* 25, 607–610.
- Giles, D., Betts, P.G., Lister, G.S., 2004. 1.8–1.5-Ga links between the North and South Australian Cratons and the Early-Middle Proterozoic configuration of Australia. *Tectonophysics* 380, 27–41.
- Glikson, A.Y., Ballhaus, C.G., Clarke, G.L., Sheraton, J.W., Stewart, A.J., Sun, S.-S., 1995. Geological framework and crustal evolution of the Giles mafic–ultramafic complex and environs, western Musgrave Block, central Australia. *AGSO Journal of Australian Geology & Geophysics* 16, 41–67.
- Glikson, A.Y., Stewart, A.J., Ballhaus, C.G., Clarke, G.L., Feeken, E.H.J., Leven, J.H., Sheraton, J.W., Sun, S.-S., 1996. Geology of the western Musgrave Block, central Australia, with particular reference to the mafic–ultramafic Giles complex. *AGSO Bulletin* 239, 41–68.
- Gregory, C.J., Buick, I.S., Hermann, J., Rubatto, D., 2009. Mineral-scale trace element and U–Th–Pb age constraints on metamorphism and melting during the Petermann Orogeny (central Australia). *Journal of Petrology* 50 (2), 251–287.
- Griffin, W., Powell, W., Pearson, N., O'Reilly, S., 2008. GLITTER: data reduction software for laser ablation ICP-MS. *Laser Ablation-ICP-MS in the Earth Sciences. Mineralogical Association of Canada Short Course Series*, 40, pp. 204–207.
- Guiraud, M., Kienast, J.R., Rahmani, A., 1996. Petrological study of high-temperature granulites from In Ouzzal, Algeria: some implications on the phase relationships in the FMAS/TOCr system. *European Journal of Mineralogy* 8 (1375–1390).
- Halpin, J.A., White, R.W., Clarke, G.L., Kelsey, D.E., 2007. The Proterozoic P–T–t evolution of the Kemp Land coast, east Antarctica; constraints from Si-saturated and Si-undersaturated metapelites. *Journal of Petrology* 48, 1321–1349.
- Halpin, J., Daczko, N., Milan, L., Clarke, G., 2012. Decoding near-concordant U–Pb zircon ages spanning several hundred million years: recrystallisation, metamictisation or diffusion? *Contributions to Mineralogy and Petrology* 163 (1), 67–85.
- Harley, S.L., 1998. On the occurrence and characterization of ultrahigh-temperature crustal metamorphism. In: Treloar, P.J., O'Brien, P.J. (Eds.), *What Drives Metamorphism and Metamorphic Relations? Special Publications. Geological Society, London*, pp. 81–107.

- Harley, S.L., 2004. Extending our understanding of ultrahigh temperature crustal metamorphism. *Journal of Mineralogical and Petrological Sciences* 99, 140–158.
- Harley, S., 2008. Refining the P–T records of UHT crustal metamorphism. *Journal of Metamorphic Geology* 26 (2), 125–154.
- Harley, S.L., Motoyoshi, Y., 2000. Al zoning in orthopyroxene in a sapphirine quartzite: evidence for N 1120 degrees C UHT metamorphism in the Napier Complex, Antarctica, and implications for the entropy of sapphirine. *Contributions to Mineralogy and Petrology* 138 (4), 293–307.
- Hensen, B.J., 1986. Theoretical phase relations involving cordierite and garnet revisited: the influence of oxygen fugacity on the stability of sapphirine and spinel in the system Mg–Fe–Al–Si–O. *Contributions to Mineralogy and Petrology* 92 (3), 362–367.
- Hensen, B.J., Green, D.H., 1971. Experimental study of the stability of cordierite and garnet in pelitic compositions at high pressures and temperatures; I, Compositions with excess alumino-silicate. *Contributions to Mineralogy and Petrology* 33 (4), 309–330.
- Hensen, B.J., Green, D.H., 1973. Experimental study of the stability of cordierite and garnet in pelitic compositions at high pressures and temperatures III. Synthesis of experimental data and geological applications. *Contributions to Mineralogy and Petrology* 38, 151–166.
- Hoffman, P., 1991. Did the breakout of Laurentia turn Gondwanaland inside-out? *Science* 252, 1409–1412.
- Hokada, T., 2001. Feldspar thermometry in ultrahigh-temperature metamorphic rocks: Evidence of crustal metamorphism attaining similar to 1100 degrees C in the Archean Napier Complex, East Antarctica. *American Mineralogist* 86 (7–8), 932–938.
- Holland, T.J.B., Powell, R., 1998. An internally consistent thermodynamic data set for phases of petrological interest. *Journal of Metamorphic Geology* 16 (3), 309–343.
- Holland, T., Powell, R., 2003. Activity–composition relations for phases in petrological calculations: an asymmetric multicomponent formulation. *Contributions to Mineralogy and Petrology* 145 (4), 492–501.
- Horie, K., Hokada, T., Hiroi, Y., Motoyoshi, Y., Shiraishi, K., 2012. Contrasting Archean crustal records in western part of the Napier Complex, East Antarctica: New constraints from SHRIMP geochronology. *Gondwana Research* 21 (4), 829–837.
- Howard, H.M., Werner, M., Smithies, R.H., Kirkland, C.L., Kelsey, D.L., Hand, M., Collins, A., Pirajno, F., Wingate, M.T.D., Maier, W.D., Raimondo, T., 2011. The geology of the west Musgrave Province and the Bentley Supergroup. — a field guide. *Geological Survey of Western Australia Record*, 2011/4 978-1-74168-379-0, p. 119.
- Hyndman, R.D., Currie, C.A., Mazzotti, S., 2005. Subduction zone backarcs, mobile belts, and orogenic heat. *GSA Today* 15, 4–10.
- Jiao, S., Guo, J., Mao, Q., Zhao, R., 2011. Application of Zr-in-rutile thermometry: a case study from ultrahigh-temperature granulites of the Khondalite belt, North China Craton. *Contributions to Mineralogy and Petrology* 162 (2), 379–393.
- Johnson, T., White, R., 2011. Phase equilibrium constraints on conditions of granulite-facies metamorphism at Scourie, NW Scotland. *Journal of the Geological Society* 168 (1), 147–158.
- Johnson, T.E., White, R., Powell, R., 2008. Partial melting of metagreywacke: a calculated mineral equilibria study. *Journal of Metamorphic Geology* 26 (8), 837–853.
- Karlstrom, K.E., Ahall, K.I., Harlan, S.S.,



- Williams, M.L., McLelland, J., Geissman, J.W., 2001. Long-lived (1.8–1.0 Ga) convergent orogen in southern Laurentia, its extensions to Australia and Baltica, and implications for refining Rodinia. In: Bartley Julie, K., Kah Linda, C. (Eds.), *Rodinia and the Mesoproterozoic Earth–ocean system*.
- Kelly, N.M., Harley, S.L., 2005. An integrated microtextural and chemical approach to zircon geochronology: refining the Archaean history of the Napier Complex, east Antarctica. *Contributions to Mineralogy and Petrology* 149, 57–84.
- Kelly, N.M., Clarke, G.L., Harley, S.L., 2006. Monazite behaviour and age significance in poly-metamorphic high-grade terrains: A case study from the western Musgrave Block, central Australia. *Lithos* 88 (1–4), 100–134.
- Kelsey, D.E., 2008. On ultrahigh-temperature crustal metamorphism. *Gondwana Research* 13, 1–29.
- Kelsey, D.E., White, R.W., Powell, R., Wilson, C.J.L., Quinn, C.D., 2003. New constraints on metamorphism in the Rauer Group, Prydz Bay, east Antarctica. *Journal of Metamorphic Geology* 21, 739–759.
- Kelsey, D.E., Clark, C., Hand, M., 2008. Thermobarometric modeling of zircon and monazite growth in melt-bearing systems: examples using model metapelitic and metapsammitic granulites. *Journal of Metamorphic Geology* 26, 199–212.
- Kilpatrick, J.A., Ellis, D.J., 1992. C-type magmas: igneous charnockites and their extrusive equivalents. *Geological Society of America Special Papers* 272, 155–164.
- Kinny, P.D., 1997. Users guide to U–Th–Pb dating of titanite, perovskite, monazite and baddeleyite using the W.A. SHRIMP. School of Physical Sciences Curtin University of Technology, Perth, WA.
- Kirkland, C.L., Whitehouse, M.J., Slagstad, T., 2009. Fluid-assisted zircon and monazite growth within a shear zone: a case study from Finnmark, Arctic Norway. *Contributions to Mineralogy and Petrology* 158 (5), 637–657.
- Kirkland, C.L., Smithies, R.H., Woodhouse, A.J., Howard, H.M., Wingate, M.T., Belousova, E.A., Cliff, J., Murphy, R., Spaggiari, C.V., 2013. Constraints and deception in the isotopic record; the crustal evolution of the west Musgrave Province, central Australia. *Gondwana Research* 23 (2), 759–781.
- Kohn, M.J., Malloy, M.A., 2004. Formation of monazite via prograde metamorphic reactions among common silicates: implications for age determinations. *Geochimica et Cosmochimica Acta* 68 (1), 101–113.
- Kooijman, E., Smit, M., Mezger, K., Berndt, J., 2012. Trace element systematics in granulite facies rutile: implications for Zr geothermometry and provenance studies. *Journal of Metamorphic Geology* 30 (4), 397–412.
- Korhonen, F., Saw, A., Clark, C., Brown, M., Bhattacharya, S., 2011. New constraints on UHT metamorphism in the Eastern Ghats Province through the application of phase equilibria modelling and in situ geochronology. *Gondwana Research* 20 (4), 764–781.
- Korhonen, F.J., Clark, C., Brown, M., Bhattacharya, S., Taylor, R., 2013. How long-lived is ultrahigh temperature (UHT) metamorphism? Constraints from zircon and monazite geochronology in the Eastern Ghats orogenic belt, India. *Precambrian Research* 234, 322–350.
- Korsch, R.J., Kositsin, N., 2010. GOMA (Gawler Craton–Officer Basin–Musgrave Province–Amadeus Basin) Seismic and MT Workshop 2010. Geoscience Australia record, 2010/39.
- Kotková, J., Harley, S.L., 2010. Anatexis during high-pressure crustal metamorphism: evidence from Garnet–Whole-rock REE Relationships

- and Zircon–Rutile Ti–Zr Thermometry in Leucogranulites from the Bohemian Massif. *Journal of Petrology* 51 (10), 1967–2001.
- Krenn, E., Finger, F., 2007. Formation of monazite and rhabdophane at the expense of allanite during Alpine low temperature retrogression of metapelitic basement rocks from Crete, Greece: Microprobe data and geochronological implications. *Lithos* 95 (1), 130–147.
- Ludwig, K.R., 2001. User's manual for ISOPLOT/Ex, rev. Version 2.49. A Geochronological Toolkit for Microsoft Excel. Special Publication No.1a. Berkeley Geochronology Centre, Berkeley, CA.
- Ludwig, K.R., 1998. On the treatment of concordant uranium-lead ages. *Geochimica et Cosmochimica Acta* 62 (4), 665–676.
- Ludwig, K.R., 2003. Users Manual for Isoplot/Ex, Version 3.00. A Geochronological Toolkit for Microsoft Excel. Special Publication No.4. Berkeley Geochronology Centre, Berkeley, CA.
- Luvizotto, G., Zack, T., 2009. Nb and Zr behavior in rutile during high-grade metamorphism and retrogression: an example from the Ivrea–Verbano Zone. *Chemical Geology* 261 (3), 303–317.
- Luvizotto, G., Zack, T., Meyer, H., Ludwig, T., Triebold, S., Kronz, A., Münker, C., Stockli, D., Prowatke, S., Klemme, S., 2009. Rutile crystals as potential trace element and isotope mineral standards for microanalysis. *Chemical Geology* 261 (3), 346–369.
- Maboko, M. A. H., 1988. Metamorphic and Geochronological Evolution in the Musgrave Ranges, Central Australia. Unpub. Ph.D. Thesis, Australian National University.
- Maboko, M.A.H., Williams, I.S., Compston, W., 1991. Zircon U–Pb chronometry of the pressure and temperature history of granulites in the Musgrave Ranges, central Australia. *Journal of Geology* 99 (5), 675–697.
- Maboko, M.A.H., McDougall, I., Zeitler, P.K., Williams, I.S., 1992. Geochronological evidence for ~530–550 Ma juxtaposition of two Proterozoic metamorphic terranes in the Musgrave Ranges, central Australia. *Australian Journal of Earth Sciences* 39 (4), 457–471.
- Major, R.B., Connor, C.H.H., 1993. The Musgrave Block. In: Drexel, J.F., Preiss, W.P., Parker, A. J. (Eds.), *The Geology of South Australia, Vol.1. The Precambrian*. Geol. Surv. South. Aust. Bull., pp. 156–167.
- Marmo, B., Clarke, G., Powell, R., 2002. Fractionation of bulk rock composition due to porphyroblast growth: effects on eclogite facies mineral equilibria, Pam Peninsula, New Caledonia. *Journal of Metamorphic Geology* 20 (1), 151–165.
- McFarlane, C.R.M., Hamison, T.M., 2006. Pb-diffusion in monazite: Constraints from a high-T contact aureole setting. *Earth and Planetary Science Letters* 250 (1–2), 376–384.
- Montel, J.-M., 1993. A model for monazite/melt equilibrium and application to the generation of granitic magmas. *Chemical Geology* 110, 127–146.
- Moores, E.M., 1991. Southwest U.S.–East Antarctic (SWEAT) connection: A hypothesis. *Geology* 19, 425–428.
- Morrissey, L., Payne, J.L., Kelsey, D.E., Hand, M., 2011. Grenvillian-aged reworking in the North Australian Craton, central Australia: Constraints from geochronology and modelled phase equilibria. *Precambrian Research* 191 (3–4), 141–165.
- Myers, J.S., Shaw, R.D., Tyler, I.M., 1996. Tectonic evolution of Proterozoic Australia. *Tectonics* 15, 1431–1446.
- Nichols, G.T., Berry, R.F., Green, D.H., 1992. Internally consistent gahnitic spinel–cordierite–

- garnet equilibria in the  $\text{Fmashzn}$  System — geothermobarometry and applications. *Contributions to Mineralogy and Petrology* 111 (3), 362–377.
- Parrish, R.R., 1990. U-Pb dating of monazite and its application to geological problems. *Canadian Journal of Earth Sciences* 27 (11), 1431–1450.
- Payne, J.L., Hand, M., Barovich, K.M., Wade, B.P., 2008. Temporal constraints on the timing of high-grade metamorphism in the northern Gawler Craton: implications for assembly of the Australian Proterozoic. *Australian Journal of Earth Sciences* 55 (5), 623–640.
- Phillips, G., Hand, M., Offler, R., 2010. P–T–X controls on phase stability and composition in LTMP metabasite rocks – a thermodynamic evaluation. *Journal of Metamorphic Geology* 28 (5), 459–476.
- Powell, R., Sandiford, M.J., 1988. Sapphirine and spinel phase relationships in the system  $\text{FeO-MgO-Al}_2\text{O}_3\text{-TiO}_2\text{-O}_2$  in the presence of quartz and hypersthene. *Contributions to Mineralogy and Petrology* 98, 64–71.
- Pyle, J.M., Spear, F.S., 2003. Four generations of accessory-phase growth in low pressure migmatites from SW New Hampshire. *American Mineralogist* 88, 338–351.
- Raimondo, T., Collins, A.S., Hand, M., Walker-Hallam, A., Smithies, R.H., Evins, P.M., Howard, H.M., 2009. Ediacaran intracontinental channel flow. *Geology* 37 (4), 291–294.
- Raimondo, T., Collins, A.S., Hand, M., Walker-Hallam, A., Smithies, R.H., Evins, P.M., Howard, H.M., 2010. The anatomy of a deep intracontinental orogen. *Tectonics* 29 (4), TC4024.
- Rapp, R.P., Watson, E.B., 1986. Monazite solubility and dissolution kinetics — implications for the thorium and light rare-Earth chemistry of felsic magmas. *Contributions to Mineralogy and Petrology* 94 (3), 304–316.
- Rapp, R.P., Ryerson, F.J., Miller, C.F., 1987. Experimental-evidence bearing on the stability of monazite during crustal anatexis. *Geophysical Research Letters* 14 (3), 307–310.
- Roberts, M.P., Finger, F., 1997. Do U–Pb zircon ages from granulites reflect peak metamorphic conditions? *Geology* 25, 319–322.
- Sajeev, K., Williams, I., Osanai, Y., 2010. Sensitive high-resolution ion microprobe U–Pb dating of prograde and retrograde ultrahigh-temperature metamorphism as exemplified by Sri Lankan granulites. *Geology* 38 (11), 971–974.
- Sandiford, M., 1985. The metamorphic evolution of granulites at Fyfe Hills — Implications for Archean crustal thickness in Enderby Land, Antarctica. *Journal of Metamorphic Geology* 3 (2), 155–178.
- Sankar, B., Kaushik, D., Fukuoka, M., 2005. Fluorine content of biotite in granulite-grade metapelitic assemblages and its implications for the Eastern Ghats granulites. *European Journal of Mineralogy* 17 (5), 665–674.
- Schmitz, M.D., Bowring, S.A., 2003. Ultrahigh-temperature metamorphism in the lower crust during Neoarchean Ventersdorp rifting and magmatism, Kaapvaal Craton, southern Africa. *Geological Society of America Bulletin* 115 (5), 533–548.
- Scrimgeour, I.R., Close, D.F., 1999. Regional high-pressure metamorphism during intracratonic deformation: the Petermann Orogeny, central Australia. *Journal of Metamorphic Geology* 17 (5), 557–572.
- Seydoux-Guillaume, A.-M., Paquette, J.-L., Wiedenbeck, M., Montel, J.-M., Heinrich, W., 2002. Experimental resetting of the U–Th–Pb systems in monazite. *Chemical Geology* 191 (1), 165–181.

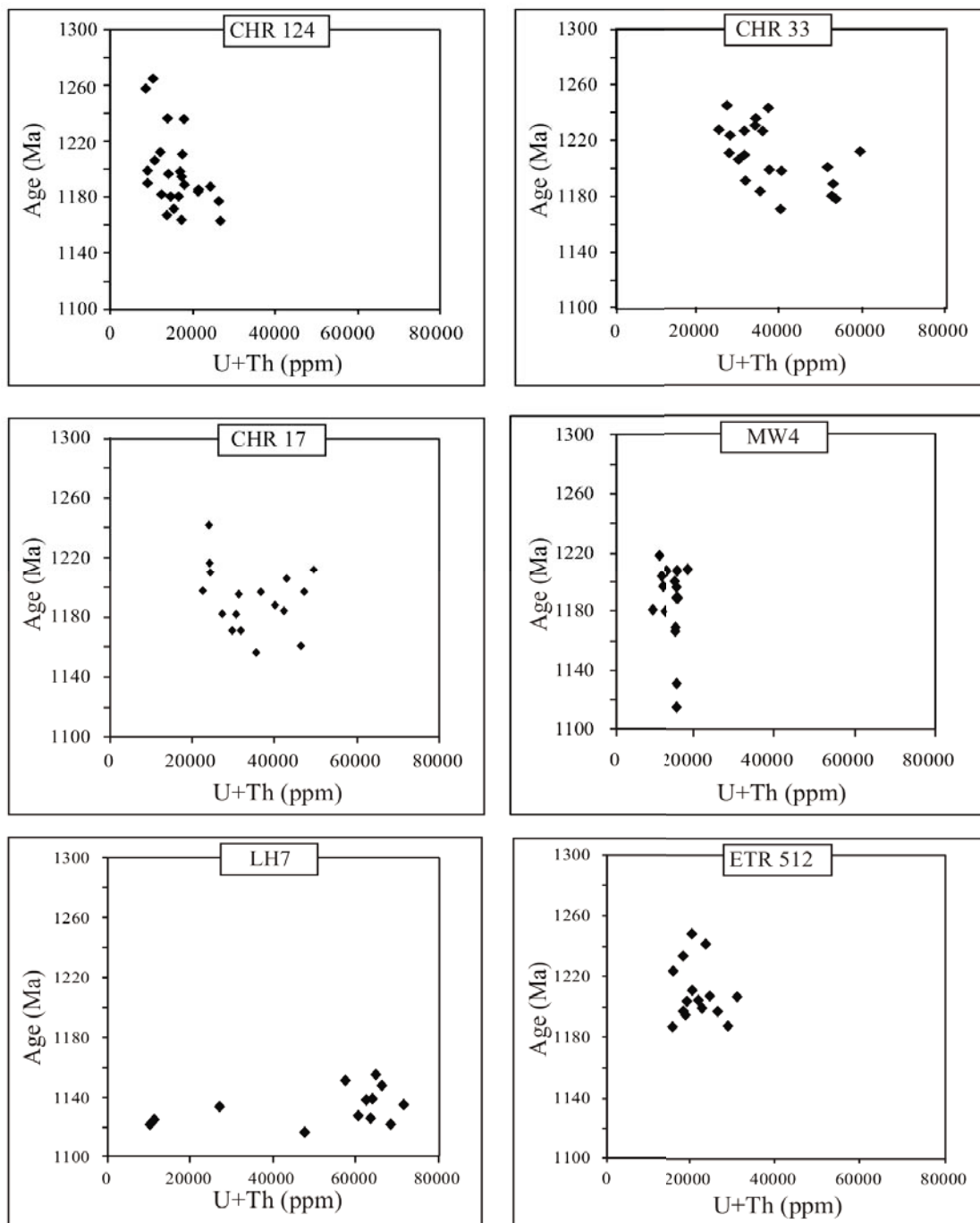
- Seydoux-Guillaume, A.-M., Montel, J.-M., Bingen, B., Bosse, V., De Parseval, P., Paquette, J.-L., Janots, E., Wirth, R., 2012. Low-temperature alteration of monazite: Fluid mediated coupled dissolution-precipitation, irradiation damage, and disturbance of the U–Pb and Th–Pb chronometers. *Chemical Geology*
- Sizova, E., Gerya, T., Brown, M., Perchuk, L., 2010. Subduction styles in the Precambrian: Insight from numerical experiments. *Lithos* 116 (3), 209–229.
- Sizova, E., Gerya, T., Brown, M., 2014. Contrasting styles of Phanerozoic and Precambrian continental collision. *Gondwana Research* 25 (2), 522–545.
- Smithies, R.H., Howard, H.M., Evins, P.M., Kirkland, C.L., Kelsey, D.E., Hand, M., Wingate, M.T.D., Collins, A.S., Belousova, E., Allchurch, S., 2010. Geochemistry, geochronology and petrogenesis of Mesoproterozoic felsic rocks in the western Musgrave Province of central Australia and implication for the Mesoproterozoic tectonic evolution of the region. *Geological Survey of Western Australia Record* 2011/4, Report 106 73.
- Smithies, R.H., Howard, H.M., Evins, P.M., Kirkland, C.L., Kelsey, D.E., Hand, M., Wingate, M.T.D., Collins, A.S., Belousova, E., 2011. High-temperature granite magmatism, crust–mantle interaction and the Mesoproterozoic intracontinental evolution of the Musgrave Province, Central Australia. *Journal of Petrology* 52 (5), 931–958.
- Smithies, R.H., Howard, H.M., Kirkland, C.L., Werner, M., Medlin, C.C., Wingate, M.T.D., Cliff, J.B., 2013. Geochemical evolution of rhyolites of the Talbot Sub-basin and associated felsic units of the Warakurna Supersuite. *Geological Survey of Western Australia Record* 2011/4, Report 118 (74 pp.).
- Smithies, R.H., Kirkland, C.L., Korhonen, F.J., Aitken, A.R.A., Howard, H.M., Maier, W.D., Wingate, M.T.D., Quentin de Gromard, R., Gessner, K., 2015. The Mesoproterozoic thermal evolution of the Musgrave Province in central Australia—plume vs. the geological record. *Gondwana Research* 27 (4), 1419–1429.
- Spear, F.S., Pyle, J.M., 2002. Apatite, monazite, and xenotime in metamorphic rocks. In: Kohn Matthew, J., Rakovan, J., Hughes John, M. (Eds.), *Phosphates; geochemical, geobiological, and materials importance*.
- Spear, F.S., Pyle, J.M., 2010. Theoretical modeling of monazite growth in a low-Ca metapelite. *Chemical Geology* 273, 111–119.
- Stacey, J.S., Kramers, J.D., 1975. Approximation of terrestrial lead isotope evolution by a two-stage model. *Earth and Planetary Science Letters* 26 (2), 207–221.
- Stepanov, A.S., Hermann, J., Rubatto, D., Rapp, R.P., 2012. Experimental study of monazite/melt partitioning with implications for the REE, Th and U geochemistry of crustal rocks. *Chemical Geology* 300, 200–220.
- Sun, S.-S., Sheraton, J.W., Glikson, A.Y., Stewart, A.J., 1996. A major magmatic event during 1050–1080 in central Australia and an emplacement age for the Giles Complex. *AGSO Research Newsletter* 17, 9–10.
- Tajčmanova, L., Connolly, J.A.D., Cesare, B., 2009. A thermodynamic model for titanium and ferric iron solution in biotite. *Journal of Metamorphic Geology* 27 (2), 153–165.
- Tajčmanová, L., Konopásek, J., Košler, J., 2009. Distribution of zinc and its role in the stabilization of spinel in high-grade felsic rocks of the Moldanubian domain (Bohemian Massif). *European Journal of Mineralogy* 21 (2), 407–418.
- Teufel, S., Heinrich, W., 1997. Partial resetting of the U–Pb isotope system in monazite through hydrothermal experiments: An SEM and U–Pb isotope study. *Chemical Geology* 137 (3), 273–281.



- Tinkham, D.K., Ghent, E.D., 2005. Estimating P–T conditions of garnet growth with isochemical phase diagram sections and the problem of effective bulk composition. *The Canadian Mineralogist* 43 (1), 35–50.
- Tomkins, H.S., Powell, R., Ellis, D.J., 2007. The pressure dependence of the zirconium-in-rutile thermometer. *Journal of Metamorphic Geology* 25, 703–713.
- Van Achtebergh, E., Ryan, C.G., Jackson, S.E., Griffin, W.L., 2001. Data reduction software for LA-ICP-MS. In: Sylvester Paul, J. (Ed.), *Laser-ablation-ICPMS in the earth sciences; principles and applications*. Mineralogical Association of Canada, Ottawa, ON, Canada.
- Vernon, R.H., 1996. Problems with inferring P–T–t paths in low-P granulite facies rocks. *Journal of Metamorphic Geology* 14, 143–153.
- Vielzeuf, D., 1983. The spinel and quartz associations in high-grade xenoliths from Tallante (SE Spain) and their potential use in geothermometry and barometry. *Contributions to Mineralogy and Petrology* 82 (4), 301–311.
- Villaseca, C., Martín Romera, C., De la Rosa, J., Barbero, L., 2003. Residence and redistribution of REE, Y, Zr, Th and U during granulite-facies metamorphism: behaviour of accessory and major phases in peraluminous granulites of central Spain. *Chemical Geology* 200 (3), 293–323.
- Villaseca, C., Orejana, D., Paterson, B.A., 2007. Zr–LREE rich minerals in residual peraluminous granulites, another factor in the origin of low Zr–LREE granitic melts? *Lithos* 96 (3), 375–386.
- Wade, B.P., Barovich, K.M., Hand, M., Scrimgeour, I.R., Close, D.F., 2006. Evidence for early Mesoproterozoic arc magmatism in the Musgrave Block, central Australia: Implications for Proterozoic crustal growth and tectonic reconstructions of Australia. *Journal of Geology*, 114, 43–63.
- Wade, B.P., Kelsey, D.E., Hand, M., Barovich, K.M., 2008. The Musgrave Province; Stitching North, West and South Australia. *Precambrian Research* 166, 370–386.
- Walsh, A.K., Raimondo, T., Kelsey, D.E., Hand, M., Pfitzner, H.L., Clark, C., 2013. Duration of high-pressure metamorphism and cooling during the intraplate Petermann Orogeny. *Gondwana Research* 24 (3–4), 969–983.
- Waters, D.J., 1991. Hercynite-quartz granulites: phase relations, and implications for crustal processes. *European Journal of Mineralogy* 3 (2), 367–386.
- Watson, E.B., Wark, D.A., Thomas, J.B., 2006. Crystallization thermometers for zircon and rutile. *Contributions to Mineralogy and Petrology* 151, 413–433.
- White, R.W., Clarke, G.L., 1997. The role of deformation in aiding recrystallization: an example from a high-pressure Shear Zone, Central Australia. *Journal of Petrology* 38 (10), 1307–1329.
- White, R.W., Powell, R., 2002. Melt loss and the preservation of granulite facies mineral assemblages. *Journal of Metamorphic Geology* 20 (7), 621–632.
- White, R.W., Clarke, G.L., Nelson, D.R., 1999. SHRIMP U–Pb zircon dating of Grenville-age events in the western part of the Musgrave Block, central Australia. *Journal of Metamorphic Geology* 17, 465–481.
- White, R.W., Powell, R., Holland, T.J.B., Worley, B.A., 2000. The effect of TiO<sub>2</sub> and Fe<sub>2</sub>O<sub>3</sub> on metapelitic assemblages at greenschist and amphibolite facies conditions: mineral equilibria calculations in the system K<sub>2</sub>O–FeO–MgO–Al<sub>2</sub>O<sub>3</sub>–SiO<sub>2</sub>–H<sub>2</sub>O–TiO<sub>2</sub>–Fe<sub>2</sub>O<sub>3</sub>. *Journal of Metamorphic Geology* 18, 497–511.
- White, R.W., Powell, R., Clarke, G.L., 2002. The interpretation of reaction textures in Fe-rich metapelitic granulites of the Musgrave Block, central Australia: constraints from

- mineral equilibria calculations in the system K<sub>2</sub>O–FeO–MgO–Al<sub>2</sub>O<sub>3</sub>–SiO<sub>2</sub>–H<sub>2</sub>O–TiO<sub>2</sub>–Fe<sub>2</sub>O<sub>3</sub>. *Journal of Metamorphic Geology* 20, 41–55.
- White, R.W., Powell, R., Holland, T.J.B., 2007. Progress relating to calculation of partial melting equilibria for metapelites. *Journal of Metamorphic Geology* 25 (5), 511–527.
- Williams, M., Jercinovic, M., Harlov, D., Budzyń, B., Hetherington, C., 2011. Resetting monazite ages during fluid-related alteration. *Chemical Geology* 283 (3), 218–225.
- Wing, B.A., Ferry, J.M., Harrison, T.M., 2003. Prograde destruction and formation of monazite and allanite during contact and regional metamorphism of pelites; petrology and geochronology. *Contributions to Mineralogy and Petrology* 145 (2), 228–250.
- Wingate, M.T.D., Pisarevsky, S.A., Evans, D.A.D., 2002. Rodinia connection between Australia and Laurentia; no SWEAT, no AUSWUS? *Terra Nova* 14 (2), 121–128.
- Wingate, M.T.D., Pirajno, F., Morris, P.A., 2004. Warakurna large igneous province: A new Mesoproterozoic large igneous province in west-central Australia. *Geology* 32 (2), 105–108.
- Zack, T., Moraes, R., Kronz, A., 2004. Temperature dependence of Zr in rutile: empirical calibration of a rutile thermometer. *Contributions to Mineralogy and Petrology* 148, 471–488.

## Supporting information



**Supplementary Figure 1.** U+Th Vs. Concordia age data for the samples: (a) CHR124; (b) CHR33; (c) CHR17; (d) MW4; (e) LH7; and (f) ETR512. A plot is not provided for sample 195353 as Th was not measured during LA-ICP-MS analysis. ellipses represent detrital ages. All error ellipses are 2 $\sigma$ .

**Supplementary Table 1.** Ion microprobe U–Th–Pb data. All errors are quoted at the 1 $\sigma$  level. Spot name refers to the individual grain and analysis identification. \*: Displayed ratio is corrected for common Pb based on measured  $^{204}\text{Pb}$  and crustal Pb composition appropriate for the age of the sample (Stacey and Kramers, 1975). a: Overcount corrected isotope value.

Grain	$^{238}\text{U}$	$^{232}\text{Th}$	$f^{204}$	$^{238}\text{U}/^{206}\text{Pb}^*$	$^{207}\text{Pb}/^{206}\text{Pb}^*$	$^{207}\text{Pb}/^{235}\text{U}$	$\delta$ Disc. %	$^{238}\text{U}/^{206}\text{Pb}^*$	$^{207}\text{Pb}/^{206}\text{Pb}^*$	Concordia Age	$^{207}\text{corr } ^{238}\text{U}/^{206}\text{Pb}$							
Spot	(ppm)	(ppm)	(%)	$\pm 1\sigma$	$\pm 1\sigma$	$\pm 1\sigma$	2s lim	date (Ma) $\pm 1\sigma$	date (Ma) $\pm 1\sigma$	date (Ma) $\pm 1\sigma$	date (Ma) $\pm 1\sigma$							
124-21.1	693	12782	-0.06	4.6560	1.3597	0.0811	0.5904	2.4180	1.5055	1254	15	1224	12	1235	9	1256	16	
124-21.2	395	16996	-0.30	4.7385	1.4259	0.0815	0.7746	2.4542	1.9831	1234	16	1234	15	1234	11	1234	17	
124-3.1	689	16801	-0.14	5.0141	1.3502	0.0800	0.5801	2.2373	1.5328	1172	14	1198	11	1188	9	1171	15	
124-3.2	672	16341	-0.12	4.9962	2.4594	0.0808	0.5774	2.2596	2.5520	1176	26	1215	11	1209	10	1174	28	
124-3.3	641	15484	-0.09	5.0490	1.3359	0.0796	0.5395	2.1965	1.4689	1165	14	1188	11	1180	9	1164	15	
124-20.1	479	9557	-0.09	4.7176	1.3596	0.0833	0.5854	2.4567	1.5108	1239	15	1275	11	1263	9	1237	16	
124-19.1	527	13172	-0.08	4.9678	1.3451	0.0803	0.5670	2.2471	1.4865	1182	14	1204	11	1196	9	1181	15	
124-19.2	813	22857	-0.10	4.9326	1.3191	0.0795	0.4805	2.2489	1.4304	1190	14	1186	9	1187	8	1190	15	
124-19.3	434	14620	-0.07	4.9163	1.3591	0.0819	0.6076	2.3164	1.5176	0.03	1194	15	1243	12	1224	9	1191	16
124-4.1	789	14185	-0.10	5.0288	1.3153	0.0790	0.4649	2.1912	1.4214	1169	14	1172	9	1171	8	1169	15	
124-4.2	839	24830	-0.10	5.0439	1.3120	0.0794	0.4620	2.1945	1.4219	1166	14	1181	9	1177	8	1165	15	
124-6.1	1319	10739	0.00	5.0217	1.2944	0.0797	0.6070	2.1892	1.4303	1171	14	1189	12	1181	9	1170	15	
124-8.1	554	14841	-0.19	5.3868	1.3894	0.0811	0.7208	2.1213	1.7301	6.31	1098	14	1223	14	1159	10	1091	15
124-10.1	617	20245	-0.13	5.0212	1.3353	0.0798	0.5402	2.2251	1.4829	1171	14	1193	11	1185	9	1170	15	
124-10.2	660	20102	-0.10	5.0705	1.3290	0.0799	0.5236	2.1978	1.4581	1160	14	1195	10	1183	8	1159	15	
124-11.1	550	15934	-0.09	4.9844	1.3467	0.0805	0.5721	2.2497	1.4962	1179	14	1208	11	1197	9	1177	15	
124-9.1	724	13510	-0.04	5.0197	1.3249	0.0795	0.4960	2.1923	1.4254	1171	14	1184	10	1180	8	1170	15	
124-5.1	2169	6569	-0.02	4.9904	1.2789	0.0798	0.2778	2.2099	1.3168	1177	14	1191	5	1189	5	1177	14	
124-5.2	2056	6673	-0.01	4.9068	1.2806	0.0801	0.2875	2.2520	1.3135	1196	14	1198	6	1198	5	1196	15	
124-1.1	304	7990	-0.14	4.7042	1.4117	0.0828	0.7145	2.4657	1.6626	1243	16	1266	14	1256	11	1241	17	
124-1.2	2343	10988	0.02	4.9808	1.5883	0.0784	0.7611	2.2104	1.6132	1179	17	1157	15	1167	11	1179	18	
124-1.3	1184	10580	-0.04	4.9664	1.2954	0.0809	0.3666	2.2559	1.3530	1183	14	1218	7	1211	6	1181	15	
124-13.1	395	16409	-0.18	5.1114	1.3688	0.0790	0.6543	2.1758	1.5961	1152	14	1173	13	1164	10	1151	15	
124-13.2	526	15070	-0.24	5.1066	1.3508	0.0802	0.5656	2.2242	1.6957	0.21	1153	14	1201	11	1183	9	1150	15
124-13.3	612	25440	-0.19	5.0412	1.3420	0.0785	0.5824	2.1957	1.5331	1167	14	1160	12	1163	9	1167	15	
124-13.4	580	16273	-0.11	4.9381	1.3434	0.0800	0.5639	2.2617	1.4954	1189	14	1197	11	1194	9	1188	15	
124-13.5	507	22310	-0.30	5.3280	1.3517	0.0792	0.6198	2.1211	1.6503	1.81	1109	14	1177	12	1147	9	1105	14
124-15.1	395	10038	-0.08	4.8550	1.3792	0.0803	0.6561	2.3015	1.5652	1207	15	1204	13	1205	10	1208	16	
124-17.1	334	16653	-0.03	5.2780	1.3900	0.0792	0.7300	2.0761	1.5869	0.44	1118	14	1178	14	1148	10	1115	15
124-17.2	734	21904	-0.12	5.3478	1.3199	0.0783	0.5058	2.0483	1.4488	0.83	1105	13	1156	10	1138	8	1103	14
33-1.1	215	32191	-0.41	4.8151	3.0627	0.0794	0.8189	2.3756	3.3371	1216	33	1182	16	1188	15	1218	36	
33-2.1	328	25664	-0.12	4.8204	3.0423	0.0810	0.6532	2.3465	3.1391	1215	33	1221	13	1220	12	1215	36	
33-4.1	369	28829	-0.03	4.7518	3.0403	0.0815	0.6174	2.3718	3.1084	1231	33	1233	12	1233	11	1231	36	
33-5.1	527	25616	-0.15	4.7595	3.0282	0.0812	0.5137	2.3897	3.0956	1229	33	1225	10	1225	10	1230	36	
33-5.2	566	45096	-0.22	5.0177	3.0265	0.0788	0.5419	2.2187	3.1084	1172	32	1168	11	1169	10	1172	34	
33-6.1	310	18823	-0.16	4.8593	3.0429	0.0817	0.6433	2.3565	3.1438	1206	33	1238	13	1234	12	1205	35	
33-6.2	333	23301	0.13	4.8278	3.0471	0.0790	0.9264	2.2558	3.1848	1214	33	1172	18	1182	16	1216	36	
33-7.1	301	23064	-0.15	4.7435	3.0462	0.0807	0.6616	2.3847	3.1547	1233	33	1214	13	1217	12	1234	36	
33-7.2	241	27572	-0.15	4.9210	3.1023	0.0810	0.7490	2.3066	3.2341	1193	33	1221	15	1216	13	1191	36	
33-8.1	256	43365	-0.35	4.8134	3.0530	0.0795	0.7709	2.3653	3.2494	1217	33	1186	15	1191	14	1219	36	
33-8.2	611	19269	-0.10	4.6949	3.0239	0.0806	0.4660	2.3921	3.0735	1245	33	1211	9	1213	9	1247	36	
33-9.1	201	44777	-1.01	4.9927	3.0707	0.0793	0.8961	2.4339	3.5386	1177	32	1180	18	1179	16	1177	35	
33-9.2	249	29183	-0.21	4.9985	3.0568	0.0798	0.7769	2.2528	3.2196	1176	32	1192	15	1189	14	1175	35	
33-9.3	239	19584	0.06	4.8836	3.0590	0.0838	0.8106	2.3667	3.1646	0.21	1201	33	1289	16	1274	14	1196	35
33-9.4	254	21456	0.29	4.9584	3.0562	0.0857	1.0419	2.3835	3.2289	4.27	1184	32	1332	20	1295	17	1176	35
33-10.1	510	16654	-0.08	4.8435	3.0273	0.0809	0.5076	2.3226	3.0853	1210	32	1218	10	1217	10	1209	35	
33-10.2	320	31863	-0.22	5.0813	3.0426	0.0786	0.6885	2.1848	3.1735	1158	31	1162	14	1162	13	1158	34	
33-11.1	433	21523	-0.12	4.9114	3.0321	0.0800	0.5607	2.2758	3.1047	1195	32	1197	11	1196	10	1195	35	
33-11.2	326	26887	-0.23	4.8627	3.0434	0.0789	0.6671	2.2927	3.1672	1206	33	1169	13	1174	13	1208	35	
33-11.3	473	44198	-0.24	5.0543	3.0932	0.0790	0.5939	2.2110	3.1938	1164	32	1172	12	1171	11	1163	35	
33-11.4	281	51267	-0.25	4.9746	3.0497	0.0804	0.7685	2.2883	3.2172	1181	32	1206	15	1202	14	1179	35	
33-12.1	315	19370	-0.07	4.8940	3.0435	0.0802	0.6538	2.2762	3.1291	1199	32	1201	13	1201	12	1198	35	
33-12.2	230	23147	-0.17	5.0100	3.1111	0.0803	0.7956	2.2527	3.2704	1173	32	1205	16	1200	14	1171	35	
17-1.1	2989	22587	-0.02	4.9409	3.0062	0.0793	0.2153	2.2163	3.0144	1188	32	1178	4	1179	4	1189	34	
17-2.1	1019	45093	-0.10	5.0230	3.0150	0.0782	0.5358	2.1727	3.0718	1170	31	1153	11	1155	10	1171	34	
17-3.1	1240	34404	-0.05	4.9203	3.0131	0.0799	0.3435	2.2528	3.0361	1193	32	1195	7	1195	7	1193	35	
17-3.2	3165	27263	-0.01	4.9457	3.0059	0.0787	0.2917	2.1985	3.0204	1187	32	1166	6	1166	6	1188	34	
17-4.1	1278	28609	-0.02	4.8807	3.0112	0.0798	0.3225	2.2599	3.0295	1202	32	1193	6	1193	6	1202	35	
17-5.1	643	48810	-0.18	4.9367	3.0234	0.0807	0.4963	2.2987	3.0878	1189	32	1214	10	1212	9	1188	35	
17-6.1	1012	38337	-0.10	4.9273	3.0144	0.0795	0.3811	2.2499	3.0464	1191	32	1185	8	1185	7	1191	35	
17-7.1	1929	20189	0.04	4.7813	3.0147	0.0820	0.2824	2.3656	3.0279	1224	33	1246	6	1246	5	1223	36	
17-7.2	655	41728	-0.09	4.9050	3.0210	0.0804	0.4735	2.2820	3.0689	1196	32	1206	9	1205	9	1196	35	
17-8.1	1845	27350	-0.07	4.9873	3.0089	0.0792	0.2799	2.2080	3.0251	1178	32	1178	6	1178	5	1178	34	
17-9.1	12622	21805	-0.01	4.9761	3.0034	0.0781	0.1192	2.1660	3.0058	1180	32	1150	2	1150	2	1182	34	
17-10.1	614	46348	-0.19	4.9304	3.0237	0.0799	0.5032	2.2824	3.0902	1190	32	1196	10	1195	9	1190	35	
17-11.1	1754	26419	-0.04	5.0099	3.0091	0.0788	0.2854	2.1768	3.0245	1173	31	1166	6	1166	6	1174	34	
17-12.1	1022	40657	-0.12	4.9936	3.0201	0.0794	0.5343	2.2199	3.0762	1177	32	1181	11	1181	10	1176	34	
17-13.1	1902	20373																



Supplementary Table 1. (continued)

MW4-6.1	767	11538	0.00	5.0121	1.3343	0.0821	0.5150	2.2581	1.4307	2.67	1173	14	1247	10	1223	8	1169	15
MW4-6.2	873	10021	-0.02	4.9499	1.3256	0.0802	0.4880	2.2396	1.4178		1186	14	1203	10	1198	8	1185	15
MW4-6.3	726	17089	-0.05	4.9457	1.3418	0.0810	0.5436	2.2706	1.4639		1187	14	1221	11	1209	9	1185	15
MW4-6.4	775	13938	0.05	4.9467	1.3360	0.0784	0.5616	2.2244	1.4493		1187	14	1156	11	1167	9	1187	15
MW4-11.2	972	9567	-0.02	4.9249	1.3161	0.0805	0.4513	2.2582	1.3953		1192	14	1209	9	1205	8	1191	15
MW4-11.3	826	9973	-0.02	5.1357	1.3285	0.0798	0.5098	2.1487	1.4295	0.28	1147	14	1193	10	1177	8	1144	15
MW4-11.4	1409	8553	-0.02	4.8914	1.3000	0.0811	0.3828	2.2934	1.3594		1199	14	1225	8	1219	7	1198	15
lh7-1.1	5454	57982	0.05	5.1161	2.7688	0.0774	0.6723	2.1854	1.2776		1151	28	1130	13	1134	12	1179	14
lh7-1.2	5598	55409	0.08	5.0492	1.1133	0.0764	0.6795	2.1679	2.8604	-1.11	1165	12	1105	14	1138	9	1187	32
lh7-2.1	3378	53442	0.07	5.1166	1.1753	0.0777	0.7786	2.1853	2.5011		1151	12	1140	15	1147	10	1171	28
lh7-3.1	2420	7601	0.12	5.2066	1.2369	0.0761	0.8667	2.1368	1.3793		1133	13	1097	17	1120	10	1173	14
lh7-4.1	6437	56369	0.11	5.0322	1.1868	0.0764	0.6815	2.1791	1.2636	-0.79	1168	13	1106	14	1139	9	1193	14
lh7-4.2	6260	59498	0.04	5.0729	1.1039	0.0771	0.6448	2.1741	3.0449		1160	12	1123	13	1143	9	1181	34
lh7-5.1	5383	57609	0.08	5.2011	1.1447	0.0763	0.6976	2.1024	1.2516		1134	12	1103	14	1121	9	1153	13
lh7-6.1	2703	6274	0.18	5.2534	1.2407	0.0763	0.9211	2.1271	1.4006		1123	13	1103	18	1117	10	1162	14
lh7-7.1	4161	57776	0.03	5.1864	3.0831	0.0774	0.7266	2.1628	1.3606		1137	31	1133	14	1133	13	1170	14
lh7-8.1	2718	56997	0.12	5.1867	1.2375	0.0753	0.8808	2.1503	1.4518	-0.05	1137	13	1076	18	1115	10	1185	15
lh7-9.1	5456	55344	0.03	4.9822	1.2415	0.0766	0.6799	2.2208	1.2959	-1.42	1179	13	1111	14	1145	9	1209	14
lh7-10.1	3937	60340	0.11	4.9768	1.2946	0.0767	0.7821	2.2063	1.3617		1180	14	1114	16	1151	10	1200	15
lh7-10.2	10859	60244	0.04	5.0674	3.9673	0.0772	0.6308	2.1857	4.1858		1161	41	1127	13	1130	12	1186	48
lh7-11.1	3875	56102	0.08	5.1858	1.1717	0.0762	0.7666	2.1159	1.2959		1137	12	1101	15	1123	9	1161	13
lh7-12.1	2792	44062	0.02	5.3036	1.2323	0.0765	0.7987	2.1155	1.4470		1114	12	1108	16	1111	10	1157	15
lh7-13.1	7079	18930	0.09	5.1993	1.1931	0.0771	0.6660	2.1577	1.2625		1134	12	1123	13	1129	9	1171	13
lh7-14.1	4623	63298	0.00	5.3340	1.1634	0.0773	0.7021	2.0686	2.9077		1108	12	1129	14	1117	9	1123	31
512-1.1	481	19074	0.02	5.3971	3.0380	0.0808	0.6352	2.0651	3.1037	4.33	1096	30	1217	12	1202	11	1090	32
512-2.1	237	35720	-0.69	5.1777	3.0750	0.0824	0.8611	2.3518	3.4127	8.88	1138	31	1254	17	1231	14	1132	34
512-3.1	621	18841	-0.04	5.0329	3.0275	0.0809	0.5093	2.2262	3.0753		1168	31	1220	10	1216	9	1165	34
512-4.1	615	24359	-0.07	5.0220	3.0269	0.0804	0.6882	2.2241	3.1136		1171	32	1208	14	1202	12	1169	34
512-5.1	804	22455	-0.13	5.0446	3.0236	0.0808	0.4656	2.1928	3.0762		1166	31	1216	9	1212	9	1163	34
512-6.1	448	17078	-0.07	4.8501	3.0318	0.0802	0.5501	2.2375	3.1097		1208	33	1202	11	1203	10	1209	35
512-7.1	436	26769	-0.09	4.9123	3.0452	0.0798	0.6269	2.2976	3.0926		1194	32	1193	12	1193	12	1195	35
512-1.2	292	20086	-0.22	5.2978	3.0867	0.0818	0.7936	2.2635	3.1283	6.04	1115	31	1241	16	1219	13	1108	33
512-8.1	219	17265	-0.25	4.9181	3.0732	0.0821	0.8230	2.1798	3.2686		1193	33	1247	16	1237	14	1190	35
512-8.2	383	17621	0.09	5.0033	3.0449	0.0803	0.7342	2.3611	3.2696		1175	32	1205	14	1200	13	1173	34
512-8.3	624	17679	-0.11	4.8857	3.0267	0.0805	0.4970	2.2136	3.1322		1200	32	1210	10	1209	9	1200	35
512-8.4	332	19047	-0.04	4.8546	3.0494	0.0825	0.6721	2.2987	3.0831		1207	33	1258	13	1251	12	1205	35
512-9.1	133	22251	0.05	4.9144	3.1126	0.0828	1.1145	2.3539	3.1329		1194	33	1265	22	1245	18	1190	36
512-10.1	269	28924	-0.12	4.9440	3.0661	0.0808	0.7780	2.3238	3.3061		1187	32	1217	15	1212	14	1186	35
512-11.1	700	14625	0.00	4.7984	3.0233	0.0813	0.4522	2.2827	3.2003		1220	33	1228	9	1228	9	1220	36
512-12.1	465	18832	-0.02	4.3596	3.0348	0.0878	0.5209	2.3361	3.0571		1331	36	1378	10	1375	9	1328	39
512-12.2	751	17761	-0.03	4.2597	3.0224	0.0891	0.4081	2.7822	3.0817		1359	36	1407	8	1405	7	1356	40
512-13.1	404	20380	-0.21	4.9312	3.0411	0.0806	0.6167	2.8976	3.0520		1190	32	1212	12	1209	11	1189	35
512-14.1	1538	13648	0.03	4.8105	3.0113	0.0798	0.3210	2.3038	3.1463		1217	33	1192	6	1193	6	1219	35
512-14.2	818	20766	0.28	4.9203	3.0248	0.0804	0.6089	2.2868	3.0283		1193	32	1206	12	1205	11	1192	35
512-15.1	905	16838	0.01	3.8409	3.0176	0.0939	0.3391	2.2522	3.0854		1492	39	1505	6	1505	6	1491	44

\* Age discordance at closest approach of error ellipse to concordia (2 sigma level).

\* denotes common Pb correction using measured  $^{204}\text{Pb}$  where 204 counts are statistically significantSupplementary Table 2. LA-ICP-MS U-Pb data for sample 195353. All errors are quoted at the 1 $\sigma$  level. Spot name refers to the individual grain and analysis identification.

Spot Name	$^{207}\text{Pb}/^{206}\text{Pb}$	1 $\sigma$ %	$^{206}\text{Pb}/^{238}\text{U}$	1 $\sigma$ %	$^{207}\text{Pb}/^{235}\text{U}$	1 $\sigma$ %	$^{207}\text{Pb}/^{206}\text{Pb}$ Age	1 $\sigma$	$^{206}\text{Pb}/^{238}\text{U}$ Age	1 $\sigma$	$^{207}\text{Pb}/^{235}\text{U}$ Age	1 $\sigma$	% conc.	Age	1 $\sigma$
1A	0.0776	0.00121	0.19964	0.00339	2.13585	0.04173	1137	31	1173	18	1161	14	1.01	1156	13
3A	0.07843	0.00121	0.19806	0.00338	2.14156	0.04162	1158	30	1165	18	1162	13	1.00	1161	13
4A	0.07921	0.00098	0.20526	0.00342	2.24153	0.03892	1177	24	1204	18	1194	12	1.01	1183	9
5A	0.07946	0.00098	0.19798	0.00331	2.16903	0.0379	1184	24	1165	18	1171	12	0.99	1179	9
6A	0.07829	0.00101	0.1952	0.00328	2.10689	0.03776	1154	25	1150	18	1151	12	1.00	1152	10
7A	0.07909	0.00106	0.20005	0.00338	2.18122	0.03991	1174	26	1176	18	1175	13	1.00	1175	11
9A	0.07948	0.00105	0.20376	0.00343	2.23267	0.04053	1184	26	1196	18	1191	13	1.00	1188	11
10A	0.08024	0.00116	0.2052	0.00349	2.26977	0.04299	1203	28	1203	19	1203	13	1.00	1203	12
8A	0.08588	0.00114	0.22134	0.00376	2.6207	0.04798	1335	25	1289	20	1307	13	0.99	—	—
8B	0.08553	0.00118	0.22366	0.0038	2.63739	0.049	1328	26	1301	20	1311	14	0.99	1318	12
11A	0.07975	0.00127	0.19749	0.00341	2.17142	0.04348	1191	31	1162	18	1172	14	0.99	1175	14
11B	0.0883	0.00154	0.22854	0.00401	2.78223	0.0587	1389	33	1327	21	1351	16	0.98	—	—
12A	0.07957	0.00105	0.20884	0.00354	2.29142	0.04111	1186	26	1223	19	1210	13	1.01	1197	10
12B	0.07779	0.00117	0.20858	0.00357	2.2374	0.04277	1142	30	1221	19	1193	13	1.02	—	—
13A	0.07849	0.00115	0.21341	0.0037	2.30973	0.04448	1159	29	1247	20	1215	14	1.03	—	—
14A	0.07909	0.0011	0.19902	0.0034	2.17074	0.03988	1174	27	1170	18	1172	13	1.00	1173	11
14B	0.07841	0.00107	0.20394	0.00347	2.20538	0.04004	1157	27	1196	19	1183	13	1.01	1170	11
15A	0.07658	0.00107	0.20216	0.00345	2.13505	0.03934	1110	28	1187	19	1160	13	1.02	—	—
15B	0.07853	0.00105	0.20131	0.00344	2.18002	0.03966	1160	26	1182	18	1175	13	1.01	1168	10
16A	0.07733	0.00107	0.20082	0.00343	2.14136	0.03953	1130	27	1180	18	1162	13	1.01	—	—
17A	0.08157	0.00125	0.21469	0.00371	2.41483	0.04704	1235	30	1254	20	1247	14	1.01	1244	13
18A	0.08595	0.00118	0.20593	0.00358	2.44053	0.0457	1337	26	1207	19	1255	13	0.96	—	—
20A	0.0767	0.0011	0.19431	0.00334	2.05529	0.03858	1114	28	1145	18	1134	13	1.01	1127	13
21A	0.07502	0.00113	0.19424	0.00335	2.00955	0.03865	1069	30	1144	18	1119	13	1.02	—	—



# Chapter 2

This chapter is published as:

Walsh, A. K., Raimondo, T., Kelsey, D. E., Hand, M., Pfitzner, H. L., Clark, C. (2013) Duration of high-pressure metamorphism and cooling during the intraplate Petermann Orogeny, *Gondwana Research*, Volume 24, Issues 3–4, Pages 969–983, ISSN 1342-937X, <http://dx.doi.org/10.1016/j.gr.2012.09.006>.





---

# Duration of high-pressure metamorphism and cooling during the intraplate Petermann Orogeny

---

## ABSTRACT

The Ediacaran–Cambrian Petermann Orogeny, central Australia, is an exceptional example of intraplate orogenesis. It involved sub-eclogite facies metamorphism and extreme basin inversion during the exhumation of Musgrave Province basement from beneath the formerly contiguous Centralian Superbasin. Sensitive High Resolution Ion Microprobe (SHRIMP) U–Pb geochronology of zircon, titanite and rutile, along with Ti-in-zircon thermometry from meta-igneous samples, have been used to determine the timing and duration of high-pressure metamorphism and subsequent cooling associated with this orogenic event. Peak metamorphic temperatures of 720–760 °C were attained at  $544 \pm 7$  Ma (U–Pb zircon). Subsequent cooling to 600–660 °C by ~521 Ma occurred at a rate of ~2.6–7.0 °C Myr<sup>-1</sup>, as recorded by the closure of Pb diffusion in titanite. Further cooling to 585–560 °C by 498–472 Ma occurred at a rate of 0.9–4.8 °C Myr<sup>-1</sup>, as recorded by Pb closure in rutile. The duration of tectonism was long-lived (>40 Myr) across the central and western parts of the orogenic system, and deformation occurred in a comparatively warm and weak portion of crust, characterised by regional thermal gradients of 17–26 °C km<sup>-1</sup>. This proposed duration of tectonism is much longer than that permitted by a shear heating mechanism, which requires an exceptionally short duration of tectonism, and additionally, an overall cold lithosphere characterised by geothermal gradients of ~9 °C km<sup>-1</sup>.

---

## 1. INTRODUCTION

Weakening, failure and deformation in continental interiors, ultimately leading to orogeny, are significant because they are the most obvious exceptions to the main tenet of plate tectonics: that plates are rigid and deform only at their margins. Central Australia records two exceptional examples of intraplate orogenesis. The Ediacaran–Cambrian Petermann Orogeny and the Ordovician–Carboniferous Alice Springs Orogeny are both large-scale intraplate events that define the modern-day geophysical architecture of the Australian continental interior (Goleby et al., 1989; Lambeck and Burgess, 1992; Korsch et al., 1998; Flöttmann et al., 2004; Aitken and Betts, 2009a, 2009b). The former was responsible for the exhumation of the crystalline basement of the Musgrave Province from beneath the formerly contiguous Centralian Superbasin (Fig. 1) (Walter et al., 1995; Hand and Sandiford, 1999; Sandiford et al., 2001).

The Petermann Orogen (Fig. 2) is a ~700 km long transpressive belt that involved the development of >100 km-scale basement-cored nappes and thick-skinned thrust sheets that transported the orogenic core toward a deeply depressed foreland (Fig. 2B) (Camacho and McDougall, 2000; Flöttmann et al., 2004). It is moderately well-exposed from its high-pressure core to foreland nappe and basin, incorporating a near-complete crustal section, but has been the subject of relatively few studies for its size (e.g. Maboko et al., 1992; Camacho et al., 1997; White and Clarke, 1997; Scrimgeour and Close, 1999; Camacho et al., 2001, 2009; Gregory et al., 2009; Raimondo et al., 2009; Aitken and Betts, 2009a, 2009b; Raimondo et al., 2010). The evolution of the Petermann Orogeny thus remains contentious and relatively poorly understood due to a paucity of empirical data, particularly with regard to the duration, rate, and physical and thermal conditions of this event.

Two contrasting views concerning the

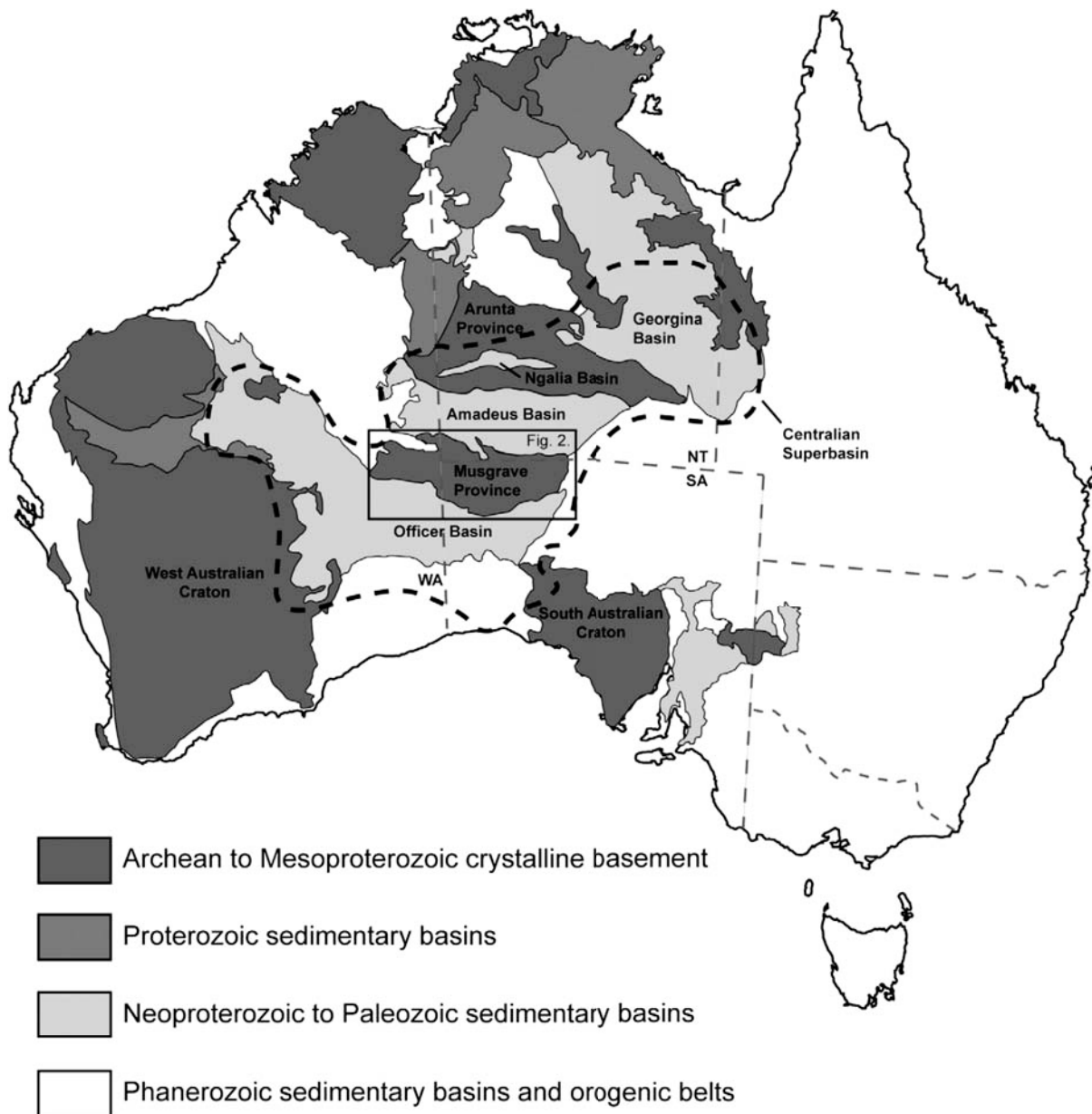


**Figure 1.** Map of Australia highlighting its major basement and basin regions, including the proposed extent of formerly contiguous Centralian Superbasin that is now divided into the remnant structural Officer, Amadeus, Ngalia and Georgina Basins. Figure modified from Walter et al. (1995).

duration and rate of metamorphism and cooling during the Petermann Orogeny have been proposed by Camacho et al. (2001, 2009) and Raimondo et al. (2009, 2010). These perspectives impose dramatically different conditions on the mechanical environment in which deformation occurred. Camacho et al. (2001) suggested that sub-eclogite facies rocks in the eastern parts of the Petermann Orogen formed at ~40 km depth by localised shear heating over a very short duration (b1 Myr). Elevated temperatures were confined

to discrete mylonitic shear zones alone, and did not impact the surrounding basement rocks. Camacho et al. (2009) expanded on this concept to suggest that shear heating was the driving mechanism for sub-eclogite facies metamorphism (~650 °C; ~12 kbar) in generally cold (~9 °C km<sup>-1</sup>) and strong crust. By inference, both thickening and formation of the high-pressure metamorphic overprint, followed by exhumation of the orogenic core, must have occurred in rapid succession.

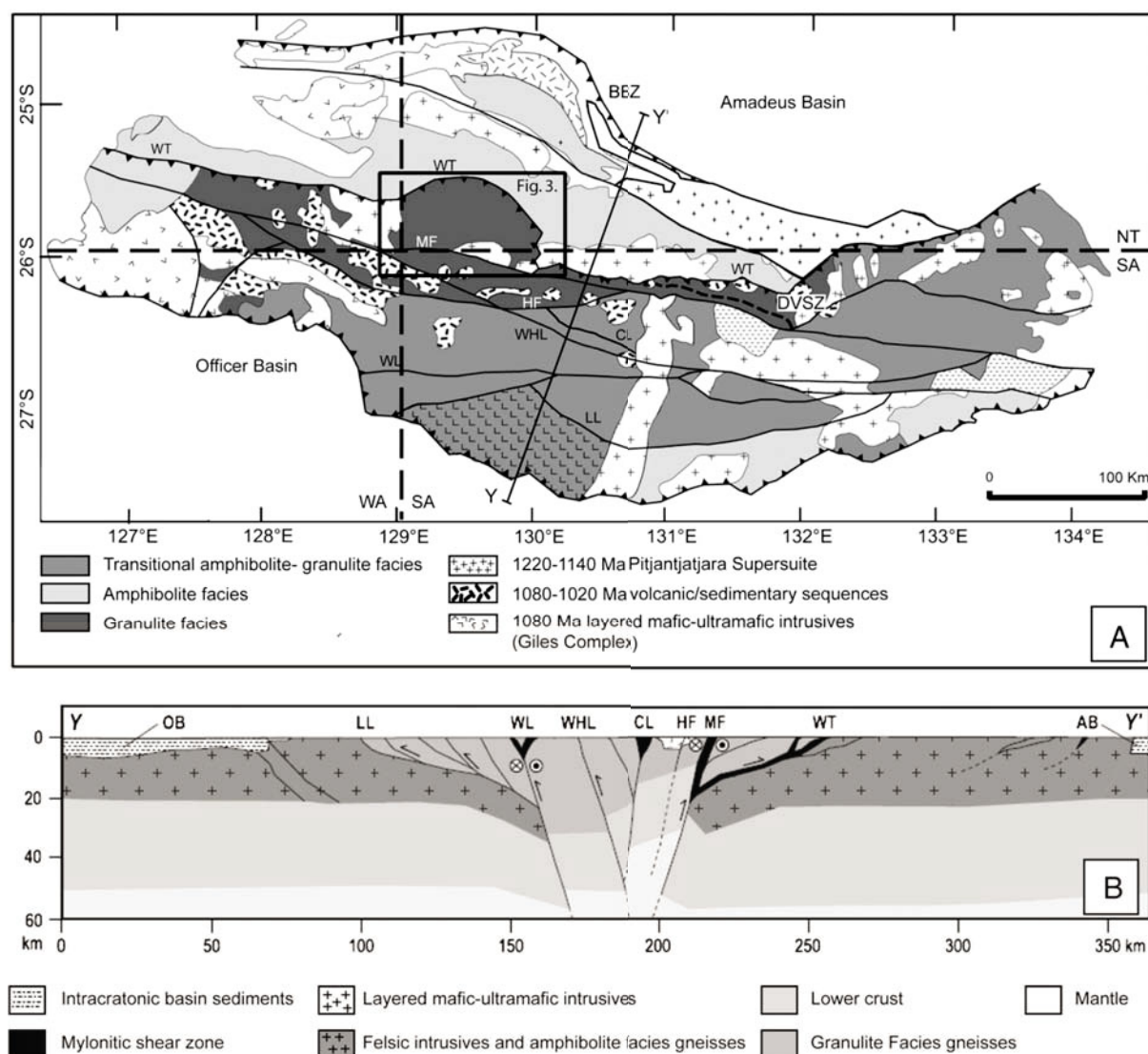


**Figure 2.** (A) Regional geology map of the Musgrave Province showing its position relative to the Amadeus and Officer Basins. East–west-trending Petermann structures are highlighted. Modified from Aitken and Betts (2009b) and Edgoose et al. (2004). Bold black box highlights the study area (refer to Fig. 3). (B) A geophysical magnetic/gravity joint model (Y–Y') across the central Musgrave block, showing arrangement of structures and lithological blocks, and particularly emphasising the deep-crustal 'core' of the orogen. Modified from (Aitken et al., 2009b). BBZ, Bloods Back Thrust Zone; CL, Caroline Lineament; DVSZ, Davenport Shear Zone; HF, Hinckley Fault; Lindsay Lineament; MF, Mann Fault; WHL, Wintiginna-Hinckley Lineament; WL, Wintiginna Lineament; WT, Woodroffe Thrust.

Unlike the 'cold' view of the crust advocated by Camacho et al. (2001, 2009), Raimondo et al. (2009, 2010) proposed that the western domain of the Petermann Orogen was characterised by hot (~750 °C) and weak mid-to lower-crust capable of deforming via large-scale channel flow (Bird, 1991; Nelson et al., 1996; Beaumont et al., 2001, 2006; Flament et al., 2011). This argument is supported by the preservation of regional-scale, low angle shear

fabrics with opposing shear senses, which bound the northern and southern margins of the migmatitic orogenic core. The existence of pervasive mylonitic deformation and partial melting in this domain, coupled with its apparent extrusive behaviour, necessitates that the crust experienced regionally elevated temperatures and prolonged burial at depth. Furthermore, SHRIMP dating of synkinematic titanite and zircon within the proposed

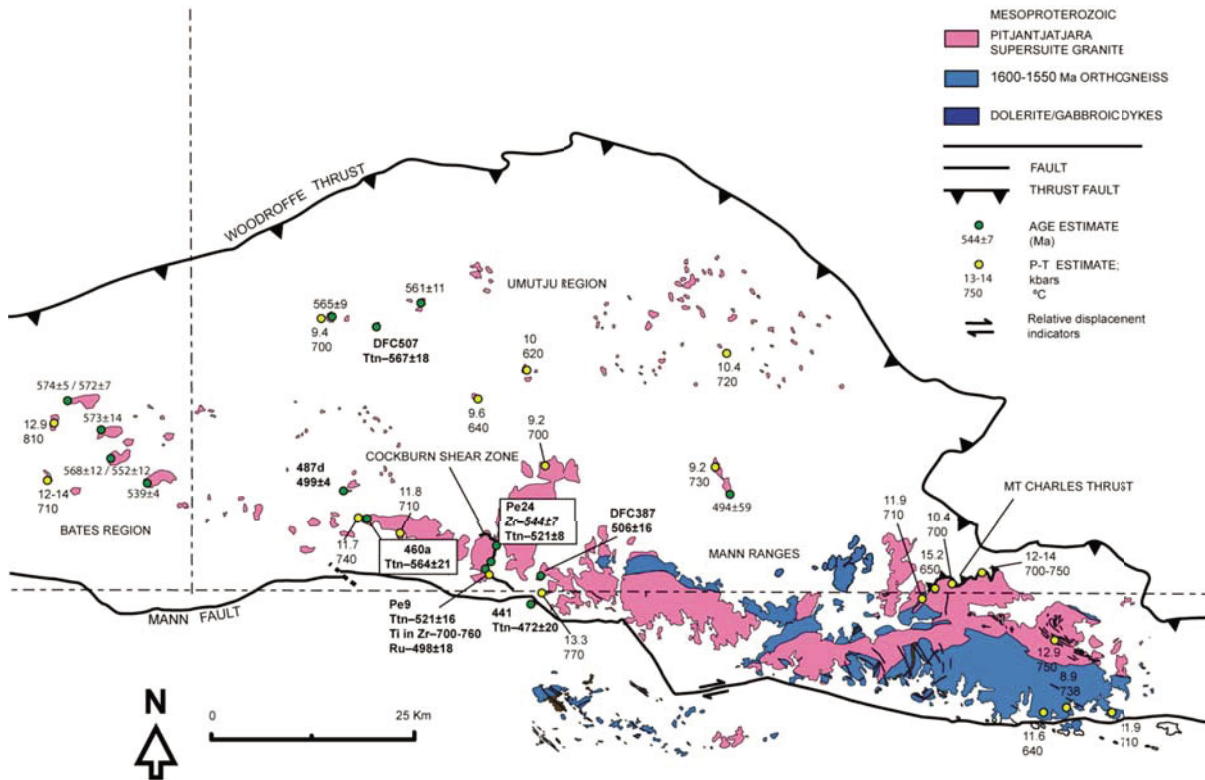


**Figure 3.** Simplified geology of the central Musgrave Province, highlighting the high-grade metamorphic rocks situated in the orogenic core between the Mann Fault and the Woodroffe Thrust, the focus of this study. The locations of geochronology samples and accompanying data are shown, and data sources are listed in Table 1. Thermobarometric estimates are sourced from White and Clarke (1997), Scrimgeour and Close (1999) and Raimondo et al. (2010). Map is adapted from Scrimgeour et al., 1999; Raimondo et al., 2009, the Bates 1:100,000 map sheet (Howard et al., 2006) and the Petermann Ranges 1:250,000 map sheet (Scrimgeour et al., 1999). Ttn, titanite; Zr, Zircon; Ru, rutile; Ti in Zr, Ti in zircon thermometry estimate.

channel suggests that tectonism was active for approximately 30 Myr between 570 and 540 Ma (Raimondo et al., 2009, 2010), a much longer duration than that permitted by the shear heating mechanism.

In this contribution, we present zircon, titanite and rutile U–Pb geochronology from the core and proximal foreland of the central Petermann Orogen (Fig. 3). Together with published data from the flanking western and eastern parts of the orogen, our findings are used to assess the duration of tectonism and prevailing thermal regime of the orogenic system as a whole. This provides an important link between the spatially restricted study areas of previous contributions, allowing the apparent disagreement between ‘hot’ vs. ‘cold’ models of the Petermann Orogen to be reconciled.

## 2. REGIONAL GEOLOGY

The Musgrave Province is an east–west trending Mesoproterozoic basement inlier that straddles the Northern Territory, South Australian and Western Australian borders (Wade et al., 2008) (Fig. 1). It is bounded to the north and south by remnant structural basins (the Amadeus and Officer Basins, respectively) that once comprised the Centralian Superbasin (Fig. 1) (Lindsay et al., 1987; Walter et al., 1995).

The Musgrave Province exposes rocks that preserve a complex deformational, metamorphic and magmatic history (Glikson et al., 1995; Sun et al., 1996; Edgoose et al., 2004; Wade et al., 2008; Evins et al., 2010;



**Table 1.** Summary of Ediacaran–Cambrian geochronological data from the western and central Musgrave Province. Sample UTM locations use coordinate system WGS 84, all coordinates were derived from the Map Grid Australia Zone 52J (MGA94).

Age (Ma)	Method	Location	Reference
565 ± 9	K–Ar hornblende	Umutju region	Scrimgeour et al. (1999)
561 ± 11	SHRIMP U–Pb zircon (rim)	Umutju region	Scrimgeour et al. (1999)
494 ± 59	Sm–Nd mineral isochron	Eastern Mann Ranges	Scrimgeour et al. (1999)
559 ± 6	SHRIMP Th–Pb allanite (core)	Western Mann Ranges	Gregory et al. (2009)
551 ± 6	SHRIMP Th–Pb allanite (rim)	Western Mann Ranges	Gregory et al. (2009)
555 ± 7	SHRIMP U–Pb zircon (rim)	Western Mann Ranges	Gregory et al. (2009)
572 ± 7	SHRIMP U–Pb titanite	Bates region	Raimondo et al. (2009)
573 ± 14	SHRIMP U–Pb titanite	Bates region	Raimondo et al. (2009)
552 ± 12	SHRIMP U–Pb titanite (cooling)	Bates region	Raimondo et al. (2009)
539 ± 4	SHRIMP U–Pb titanite (cooling)	Bates region	Raimondo et al. (2009)
568 ± 12	SHRIMP U–Pb zircon (rim)	Bates region	Raimondo et al. (2010)
574 ± 5	SHRIMP U–Pb zircon (rim)	Bates region	Raimondo et al. (2010)
544 ± 7	SHRIMP U–Pb zircon (rim)	543137E 7127755N	This study
521 ± 8	SHRIMP U–Pb titanite	543137E 7127755N	This study
551 ± 21	SHRIMP U–Pb titanite	543128E 7127326N	This study
567 ± 18	SHRIMP U–Pb titanite	524127E 7165281N	This study
564 ± 22	SHRIMP U–Pb titanite	530550E 7134650N	This study
496 ± 4	SHRIMP U–Pb titanite	522360E 7139140N	This study
472 ± 20	SHRIMP U–Pb rutile (cooling)	546600E 7124275N	This study
519 ± 15	SHRIMP U–Pb rutile (cooling)	550625E 7125847N	This study
498 ± 18	SHRIMP U–Pb rutile (cooling)	543128E 7127326N	This study

Smithies et al., 2011). The oldest rocks in the Musgrave Province (c. 1600 Ma orthogneisses) appear to be confined to its eastern margin, while 1345–1290 Ma magmatism and metamorphism is currently known only in the western Musgrave Province as the Mt West Orogeny (Evins et al., 2010; Smithies et al., 2011). The dominant metamorphic imprint on the Musgrave Province is a result of the Musgrave Orogeny (1230–1140 Ma), during which temperature–pressure conditions of >850–900 °C and 7–8 kbar were reached, causing regionally extensive granulite facies metamorphism (Glikson et al., 1996; White et al., 1999, 2002; Wade et al., 2008; Smithies et al., 2011). Coeval with the Musgrave Orogeny was voluminous felsic magmatism expressed as the Pitjantjatjara Supersuite granitoids (Maboko et al., 1992; White et al., 1999; Edgoose et al., 2004; Evins et al., 2010; Smithies et al., 2011).

The Giles Event (c. 1080 Ma) resulted in the

emplacement of layered mafic and ultramafic rocks (Glikson et al., 1996; Sun et al., 1996; Evins et al., 2010) and the emplacement and extrusion of felsic granitoids and volcanic rocks subsequently occurred between 1075 and 1026 Ma (Sun et al., 1996; Wade et al., 2008; Evins et al., 2010). The emplacement of the Alcurra and Amata mafic dike swarms occurred at ~1000 Ma and ~830 Ma (Zhao, 1994; Glikson et al., 1996; Sun et al., 1996).

The Petermann Orogeny (600–530 Ma) led to the present-day structural architecture of the Musgrave Province (Wade et al., 2008; Aitken and Betts, 2009a, 2009b). Deformation produced a series of major E–W trending fault structures that extend up to 40 km deep (Korsch et al., 1998). The most significant of these structures are the Mann Fault and the Woodroffe Thrust, between which lies the exposed high-pressure core of the Petermann Orogen (Fig. 2). The Woodroffe Thrust is a shallowly south-dipping mylonite and pseudotachylyte zone up to 3 km thick that offsets the Moho by ~20 km (Lambeck and Burgess, 1992; Camacho and Fanning, 1995; Aitken et al., 2009a; Korsch and Kositsin, 2010), and created an exceptionally large intracontinental gravitational gradient that is maintained today (Sandiford and Hand, 1998; Sandiford, 2002; Aitken et al., 2009a). Top-to-the-north thrusting along the Woodroffe Thrust facilitated the exhumation of high-grade lower-crustal rocks from approximately 40 km depth and the emplacement of a broad crustal wedge (Camacho et al., 1997; Scrimgeour and Close, 1999; Raimondo et al., 2010). Reworking is expressed as discrete shear zones such as the Davenport Shear Zone (Fig. 2) and the Cockburn Shear Zone (Fig. 3), which reach kilometre-scale widths and strike lengths up to hundreds of kilometres (Camacho et al., 1997; Wade et al., 2008). In regions such as the western Mann Ranges, including the Cockburn Shear Zone (Fig. 3), Petermann-aged deformation is expressed as a large-scale pervasive migmatitic fabric that has overprinted earlier structural fabrics

(Buick et al., 2001; Edgoose et al., 2004). Syn-kinematic low-angle shear fabrics, which record opposing kinematics along a north–south transect across the orogenic core, occur on a regional scale throughout the western Musgrave Province (Raimondo et al., 2010).

Sequential cross-section restorations indicate that north-directed shortening during the Petermann Orogeny exceeded 100 km and was accommodated by significant crustal thickening (Flöttmann et al., 2004). This is supported by thermobarometric constraints from the exposed orogenic core between the Woodroffe Thrust and the Mann Fault, with the highest pressure–temperature (P–T) conditions of 12–14 kbar and 700–750 °C attained immediately north of the Mann Fault in the western Mann Ranges (Camacho et al., 1997; White and Clarke, 1997; Scrimgeour and Close, 1999; Gregory et al., 2009; Raimondo et al., 2010). The eastern part of the orogenic core records sub-eclogitic facies mineral assemblages in the Davenport Shear Zone (Fig. 2) that formed at 12–14 kbar and temperatures of 600–650 °C (Ellis and Maboko, 1992; Camacho et al., 1997). Metamorphic grade decreases toward the foreland to the north, with P–T conditions of 6–7 kbar and 600–650 °C recorded north of the Woodroffe thrust (Scrimgeour and Close, 1999).

The age of Petermann orogenesis is relatively well constrained in selected regions (Fig. 3; Table 1). U–Pb dating of metamorphic zircon and titanite from the BATES 1:100 k map region (Howard et al., 2006) suggests that peak conditions occurred at ~570 Ma (Raimondo et al., 2009, 2010). In the western Mann Ranges, Gregory et al. (2009) report U–Pb allanite core and rim ages of 559±6 and 551±6 Ma, respectively, and a zircon age of 555±7 Ma, which are consistent with other estimates from this region (Table 1). Further to the east, age estimates for peak metamorphism are sparse. Syn-kinematic biotite and muscovite growth from the Woodroffe Thrust at 530 Ma is the

youngest recorded deformation and defines an age close to the cessation of exhumation (Camacho and Fanning, 1995).

### 3. PETROGRAPHY

Seven samples from the central Petermann Orogen, encompassing spatial coverage from the core towards the foreland (Fig. 3, Table 1), were selected for geochronology. Samples were selected from the legacy collections of the Northern Territory Geological Survey. Petrographic analysis of the thin sections assumed that early-formed minerals were typically coarser than finer-grained minerals. The identification of accessory minerals as peak or post-peak is typically difficult, but is crucial for the interpretation of age data.

#### 3.1. Pe9

Sample Pe9 is ameta-granite from the Cockburn Shear Zone (Fig. 3). Coarse-grained poikiloblastic garnet (up to 5 mm) has common inclusions of hornblende, plagioclase, quartz, rutile isolated from cracks. Garnet grains occur in direct contact with matrix plagioclase and have coronae of hornblende (Fig. 4A). Euhedral clinopyroxene grains have inclusions of rutile and quartz. Coarse-grained garnet, clinopyroxene, quartz, plagioclase and hornblende grains commonly occur in contact and are interpreted to form the peak mineral assemblage. Titanite growth is interpreted to be texturally late with respect to the peak mineral assemblage and forms coronas around rutile and ilmenite grains (Fig. 4B). The petrogenesis of rutile is difficult to constrain although it must be earlier than titanite growth based on the previous observation. Large, euhedral titanite grains (up to 300 µm), similar to those observed in sample Pe24 (Fig. 4c), were observed during mineral separation and subsequently analysed (Fig. 5A). Titanite grains of this morphology are not observed in thin section, therefore the relative timing of their growth in the petrogenetic sequence is unclear.



### 3.2. Pe24

Sample Pe24 is a non-mylonitic meta-granite adjacent to the Cockburn Shear Zone (Fig. 3). Coarse-grained garnet (up to 18 mm) and hornblende occur in a fine-grained

matrix of quartz, K-feldspar and fine-grained elongate biotite grains that define a weak foliation. Titanite and less common rutile and zircon comprise the accessory phases in the assemblage. Garnet poikiloblasts include quartz, K-feldspar and occasional rutile and titanite. Coarse-grained euhedral hornblende

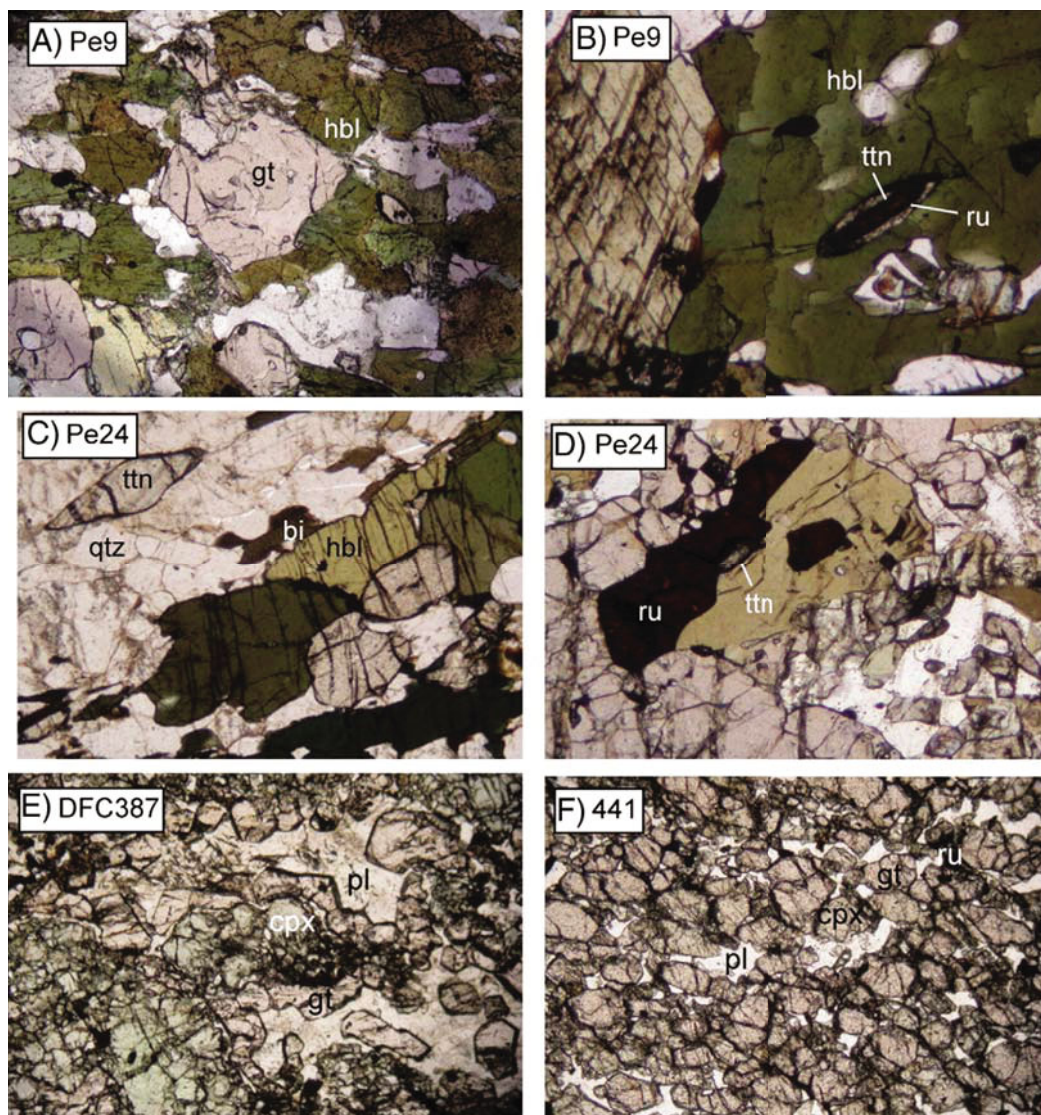


**Figure 4.** A) Sample Pe9. Porphyroblastic garnet with hornblende. Width of view is 3.5 mm. B) Sample Pe9. Thin titanite corona around rutile, in hornblende. Width of view is 2 mm. C) Sample Pe24. Euhedral titanite grains occurring in the matrix, aligned with the foliation, with hornblende and biotite. D) Sample Pe24. Rutile and zircon in contact. Width of view is 2 mm. E) Sample DFC 387. Garnet and plagioclase double corona around relict clinopyroxene. F) Sample 441. Fine-grained groundmass of clinopyroxene, garnet and metamorphic plagioclase. G) Sample DFC 507. Titanite corona on ilmenite with garnet, biotite and K-feldspar matrix. H) Sample DFC 507. Poikiloblastic garnet with biotite and titanite. I) Sample 460a. Relict clinopyroxene with hornblende coronas, with matrix garnet and plagioclase. J) Sample 460a. Rutile grains occurring along grain boundaries of matrix plagioclase, garnet, hornblende and clinopyroxene. K) Sample 487d. Gneissic layering of ferro-magnesian minerals; garnet, magnetite and clinopyroxene, and quartz-feldspathic minerals. L) Sample 487d. Magnetite grains with coronas of feldspar and garnet.



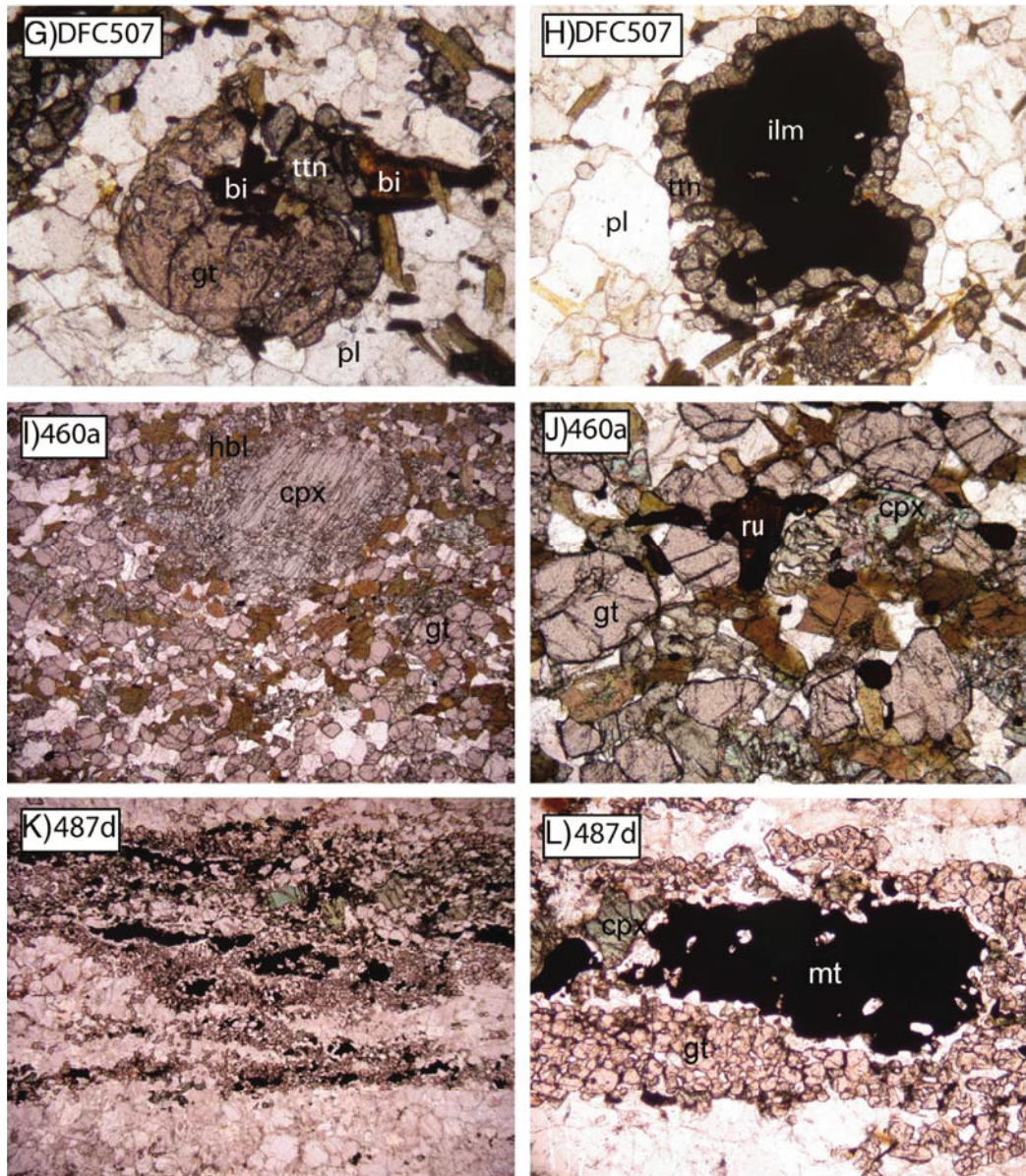


**Figure 4.** (continued)

grains (up to 8 mm) contain inclusions of quartz and K-feldspar and minor titanite and rutile. Titanite inclusions in both garnet and hornblende are randomly orientated (long axis), whereas those in the matrix are orientated parallel to the structural fabric (Fig. 4C). It is not clear whether the different microstructural settings of titanite correspond to two distinct titanite (growth) generations. Rutile occurs along fractures and grain boundaries of garnet and hornblende grains and is commonly in contact with titanite (Fig. 4D). Zircon occurs predominantly at grain boundaries of poikiloblastic garnet as well as hornblende although uncommonly occurs in the matrix,

generally orientated parallel to the foliation. Elongate hornblende and/or biotite grains occur in strain shadows around garnet grains. Garnet, hornblende, biotite, K-feldspar and quartz comprise the peak mineral assemblage with accessory rutile, zircon and titanite.

### 3.3. DFC387

Sample DFC387 is a mylonitic mafic dyke from the western Mann Ranges (Fig. 3). The rock is dominated by a very fine-grained matrix of garnet and clinopyroxene (Fig. 4E). Sub-angular to angular porphyroblastic garnet grains up to 1 mm in diameter are commonly



surrounded by a corona of plagioclase. Fine-grained (b1.5 mm) euhedral clinopyroxene grains are commonly in contact with plagioclase and more rarely with garnet. Fine grained (>0.5 mm) angular rutile is the dominant accessory phase and occurs within the matrix and at grain boundaries and along fractures of porphyroblastic garnet and clinopyroxene. The peak mineral assemblage is interpreted to comprise garnet, clinopyroxene, plagioclase and rutile.

### 3.4. 441

Sample 441 is a mylonitic mafic dyke from the western Mann Ranges (Fig. 3). A fine-grained matrix of garnet, clinopyroxene, quartz and rutile dominates the rock (Fig. 4F). Euhedral garnet and clinopyroxene grains are generally inclusion-free and commonly in direct contact with each other. Anhedral plagioclase grains occur in both in the matrix as well as coronae separating garnet and clinopyroxene. Clinozoisite occurs at grain boundaries of garnet and/or clinopyroxene, and is also commonly in contact with plagioclase. The peak mineral assemblage is interpreted to comprise garnet, quartz, rutile and clinopyroxene, with plagioclase and clinozoisite comprising the post-peak mineral assemblage.

### 3.5. DFC507

Sample DFC507 is a meta-granite located ~40 km north of the Mann Ranges (Fig. 3). Poikiloblastic garnet grains (up to 3 mm) occur in a fine-grained matrix of biotite, K-feldspar, quartz, clinozoisite and plagioclase, with titanite and ilmenite occurring as accessory minerals. Garnet is always in contact with plagioclase, and inclusions are commonly plagioclase and quartz and occasionally ilmenite (Fig. 4G). Porphyroclastic K-feldspar grains are up to 5 mm in diameter, far larger than the surrounding matrix. Titanite growth commonly occurs as coronae on ilmenite and occasionally at the grain boundaries of garnet grains (Fig. 4H, G).

### 3.6. 460a

Sample 460a is a mylonitic mafic dyke from the western Mann Ranges (Fig. 3). Interpreted relict clinopyroxene grains (up to 5 mm) commonly have inclusions of rutile. The matrix is defined by fine-grained hornblende and plagioclase and inclusion-free garnet, (Fig. 3i). Garnet grains commonly have coronae of hornblende. Rutile and titanite commonly occur at grain boundaries of garnet and hornblende, rather than as inclusions (Fig. 3j).

### 3.7. 487d

Sample 487d is a felsic gneiss from a shear zone in the western Mann Ranges (Fig. 3). Gneissic layering is defined by alternating perthitic alkali feldspar grains and quartz, and fine-grained euhedral garnet and coarse-grained magnetite and clinopyroxene (Fig. 4K). Magnetite and garnet are commonly separated by plagioclase (Fig. 4L). Large euhedral zircon and fine-grained titanite commonly occur aligned in the fabric in both the quartzofeldspathic and ferro-magnesian layers of the sample.

## 4. U–Pb SHRIMP GEOCHRONOLOGY

### 4.1. Methods

Rutile, titanite and zircon grains were separated from crushed rock samples by conventional heavy liquid and magnetic methods. Approximately 100 rutile, titanite and zircon grains of varying morphologies (titanite was typically euhedral and prismatic/well faceted) were hand-picked for each sample and mounted in epoxy resin discs. The grains were then ground to approximately half their diameter to expose a representative section through the grain using a combination of polishing cloths. Prior to SHRIMP analysis the mounts were cleaned and coated with 500 nm of high purity gold that produced a resistivity of 10–20  $\Omega$  across the disc. Imaging

of the mounts was undertaken using a Phillips XL20 scanning electron microscope fitted with a Gatan CL detector. Titanite and rutile grains were imaged with a backscattered electron (BSE) detector, whereas the internal morphology of zircon grains was imaged using cathodoluminescence (CL).

U–Pb–Th analysis of rutile, titanite and zircon was conducted using the SHRIMP-II facility at the John De Laeter Centre for Mass Spectrometry, Curtin University, Perth. Detailed SHRIMP operating procedures for zircon are outlined by Williams (1998), for titanite by Kinny (1997), and for rutile by Taylor et al. (2012). For all analyses a beam diameter of 30  $\mu\text{m}$  was used. Prior to each analysis, the spot was rastered for 2 min at 120 nA to remove the gold coating and reduce surficial common lead and other sources of contamination. The  $^{204}\text{Pb}$  component was modelled on the Stacey–Kramers crustal Pb composition appropriate for the age of the sample (Stacey and Kramers, 1975). U–Pb fractionation was corrected using the

covariation between  $\text{Pb}^{+}/\text{U}^{+}$  and  $\text{UO}^{+}/\text{U}^{+}$  determined by analyses of: (1) titanite standard Kahn, with an ID-TIMS concordant U–Pb age of  $518 \pm 2$  Ma; (2) rutile standard WHQ with an age of 2625 Ma (Taylor et al., 2012); and (3) zircon standard BR266, with an age of  $559 \pm 0.3$  Ma, a  $^{206}\text{Pb}/^{238}\text{U}$  ratio of 0.09059 and U and Th content of 909 ppm (Stern, 2001). Data was reduced using SQUID 2 software and plotted using Isoplot 3.66 (Ludwig, 2001, 2003).

Titanite analyses from all samples showed low concentrations of  $^{235}\text{U}$  (10–35 ppm), and consequently, low radiogenic components. Concentrations of common lead (PbC) were detected for all titanite samples, with  $f_{206}$  (%  $^{206}\text{PbC}$ ) ranging from 0.1 to 0.6%. These values are significantly higher than can be attributed to other sources such as remnant gold-coating or contamination from the mount surface, which were estimated from the measured PbC in the Khan standard (Kinny et al., 1994). Extremely low precision is recorded for  $^{207}\text{Pb}/^{206}\text{Pb}$  isotope ratios, reflecting the high concentrations of PbC.

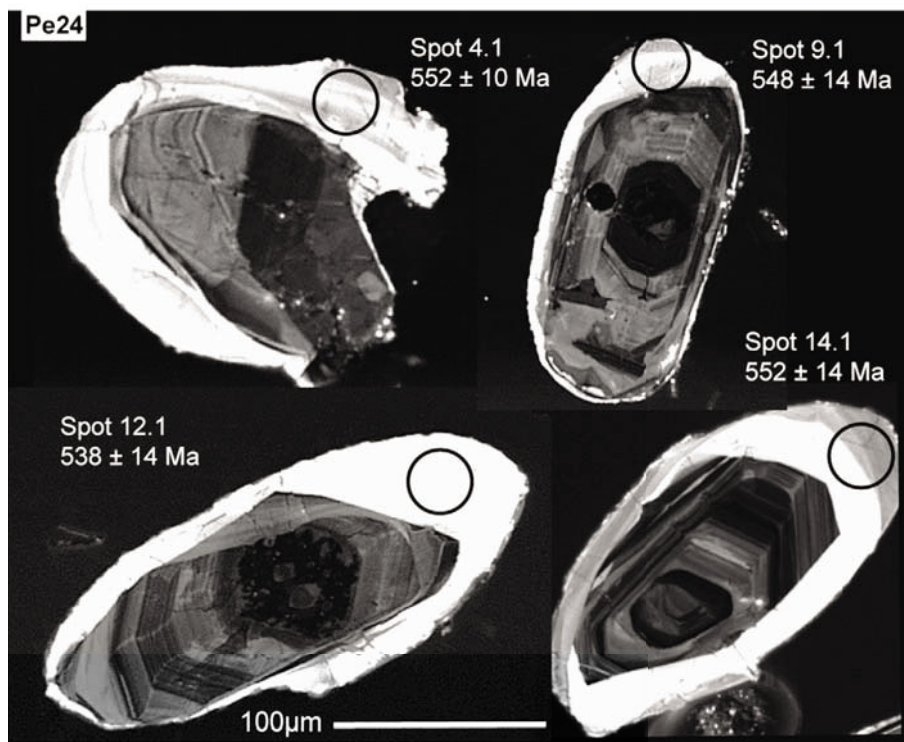


**Figure 5.** Cathodoluminescence images of representative zircon grains from geochronology sample Pe24, showing the range of textural features observed. See text for discussion. Individual spot ages are  $^{204}\text{Pb}$ -corrected  $^{206}\text{Pb}/^{238}\text{U}$  ages, and spot errors are quoted at the  $2\sigma$  level. Spot size shown is 30  $\mu\text{m}$ .

Rutile analyses from all samples showed very low U concentrations (<10 ppm) and consequently also had low radiogenic components. Because  $^{238}\text{Th}$  counts are negligible,  $^{208}\text{Pb}$  values are assumed to be representative of PbC components in all rutile samples analysed.

## 4.2. Results

Age data for all samples are summarised in Table 1 and presented in Fig. 7. All analytical data are provided in Tables 2, 3 and 4. All errors in data tables are quoted at 2 sigma ( $2\sigma$ ) level, whereas intercept and concordia ages are quoted at 95% confidence. Representative CL images of zircon and BSE images of titanite and rutile grains are presented in Figs. 5 and 6, respectively, along with individual analysis locations and corresponding age data. The location of each sample and corresponding age estimates is shown in Fig. 3. Age data for all zircon, titanite and rutile samples are plotted on Tera–Wasserburg diagrams.

### 4.2.1. Zircon — Pe24

Eighteen zircon analyses were performed on meta-granite sample Pe24, of which only two were >10% discordant. Outliers were identified and eliminated from age calculations based on weighted residuals ( $\pm 2$ ). Twelve analyses yielded  $^{238}\text{U}/^{206}\text{Pb}$  ages ranging between ca. 565 and 533 Ma. Twelve analyses yielded a single concordant age of  $544 \pm 7$  Ma (MSWD=0.91), (Fig. 7A).

### 4.2.2. Titanite

There is no evidence for chemical zoning in titanite grains from any sample in BSE imaging (Fig. 6). All analysed grains are typically between 75 and 200  $\mu\text{m}$  in diameter. Grains of varying morphology and size were analysed in order to account for possible volume diffusion effects. All concordia intercept ages are calculated using a free linear regression through uncorrected  $^{238}\text{U}/^{206}\text{Pb}$

vs.  $^{207}\text{Pb}/^{206}\text{Pb}$  isotope ratios. Outliers were identified and eliminated from age calculations based on weighted residuals ( $\pm 2$ ). The variability in PbC and U concentrations between titanite samples is consistently reflected in the array of  $^{238}\text{U}/^{206}\text{Pb}$  ages, where higher PbC and lower U concentrations result in significantly older  $^{238}\text{U}/^{206}\text{Pb}$  ages and lower levels of precision and accuracy.

#### 4.2.2.1. Pe24.

Seventeen titanite analyses were performed on sample Pe24. Analyses yielded uncorrected  $^{238}\text{U}/^{206}\text{Pb}$  ages ranging between ca. 562 and 517 Ma. Fifteen analyses yielded an intercept age of  $521 \pm 8$  Ma (95% confidence; MSWD=0.68) (Fig. 7B).

#### 4.2.2.2. 460a.

Thirteen titanite analyses were performed on metagranite sample 460a. Analyses yielded uncorrected  $^{238}\text{U}/^{206}\text{Pb}$  ages ranging between ca. 1103 and 631 Ma. Twelve analyses yielded an intercept age of  $564 \pm 22$  Ma (95% confidence; MSWD=0.64) (Fig. 7C).

#### 4.2.2.3. Pe9.

Twenty-seven titanite analyses were performed on metagranite sample Pe9. Analyses yielded uncorrected  $^{238}\text{U}/^{206}\text{Pb}$  ages ranging between ca. 620 and 522 Ma. Twenty two analyses yielded an intercept age of  $551 \pm 21$  Ma (95% confidence; MSWD = 0.90) (Fig. 7D).

#### 4.2.2.4. DFC507.

Twelve titanite analyses were performed on metagranite sample DFC507. Analyses yielded uncorrected  $^{238}\text{U}/^{206}\text{Pb}$  ages ranging between ca. 904 and 665 Ma. All analyses yielded an intercept age of  $567 \pm 18$  Ma (95% confidence; MSWD = 0.80) (Fig. 7E).

#### 4.2.2.5. 487d.

**Table 2.** SHRIMP zircon U–Pb age data for sample Pe24.

Spot name	Th/U	Isotopic ratios <sup>a</sup>						Rho <sup>b</sup>	Age estimates			
		<sup>207</sup> Pb/ <sup>206</sup> Pb	± 1σ (%)	<sup>206</sup> Pb/ <sup>238</sup> U	± 1σ (%)	<sup>207</sup> Pb/ <sup>235</sup> U	± 1σ (%)		<sup>206</sup> Pb/ <sup>238</sup> U	± 1σ	<sup>207</sup> Pb/ <sup>206</sup> Pb	± 1σ
PE-1.1	0.025	0.05556	6.2769	0.0888	1.9780	0.6804	6.5811	0.301	549	10	435	140
PE-2.1	0.022	0.06382	4.7014	0.0890	1.7741	0.7831	5.0250	0.353	550	9	736	100
PE-3.1	0.008	0.05596	6.6538	0.0878	1.6251	0.6772	6.8494	0.237	542	8	451	148
PE-4.1	0.020	0.05854	3.6428	0.0895	2.0157	0.7225	4.1633	0.484	553	11	550	80
PE-5.1	0.024	0.05397	9.1479	0.0885	2.0840	0.6588	9.3823	0.222	547	11	370	206
PE-6.1	0.120	0.11330	57.9672	0.0951	6.9405	1.4859	58.3812	0.119	586	39	1853	1048
PE-7.1	0.305	0.08089	9.5325	0.1207	3.7359	1.3462	10.2384	0.365	735	26	1219	187
PE-8.1	0.041	0.06461	16.1751	0.0856	1.8990	0.7623	16.2862	0.117	529	10	762	341
PE-9.1	0.024	0.05178	16.3336	0.0887	2.5849	0.6335	16.5368	0.156	548	14	276	374
PE-10.1	0.078	0.06908	24.4789	0.0837	3.1624	0.7976	24.6823	0.128	518	16	901	505
PE-11.1	0.118	0.05182	24.7876	0.1010	2.5129	0.7218	24.9147	0.101	620	15	278	568
PE-12.1	0.023	0.07805	12.5447	0.0871	2.7010	0.9376	12.8321	0.210	539	14	1148	249
PE-13.1	0.375	0.08913	4.3306	0.1509	1.4430	1.8543	4.5647	0.316	906	12	1407	83
PE-14.1	0.161	0.03499	41.3399	0.0864	2.6094	0.4166	41.4222	0.063	534	13	709	1150
PE-15.1	0.610	0.07614	2.0568	0.1719	1.5606	1.8051	2.5819	0.604	1023	15	1099	41
PE-16.1	0.021	0.08890	12.5983	0.0916	2.3225	1.1229	12.8106	0.181	565	13	1402	241
PE-17.1	0.108	0.04002	70.1503	0.0693	4.1272	0.3823	70.2716	0.059	432	17	349	1811
PE-18.1	0.037	0.04385	16.5151	0.0867	2.4048	0.5240	16.6893	0.144	536	12	119	407

<sup>a</sup> Displayed ratios and ages are corrected for common Pb following the method of Stacey and Kramers (1975).<sup>b</sup> Error correlation; defined as [(err. <sup>206</sup>Pb/<sup>238</sup>U)/(measured <sup>206</sup>Pb/<sup>238</sup>U)]/[(err. <sup>207</sup>Pb/<sup>235</sup>U)/(measured <sup>207</sup>Pb/<sup>235</sup>U)].

Fifteen titanite analyses were performed on metagranite sample 487d. Analyses yielded uncorrected <sup>238</sup>U/<sup>206</sup>Pb ages ranging between ca. 528 and 470 Ma. Ten analyses yielded an intercept age of 496 ± 4 Ma (95% confidence; MSWD = 0.94) (Fig. 7F).

#### 4.2.3. Rutile

All rutile grains had very low U and radiogenic Pb, with concentration values between 2.8 and 8 ppm and <sup>208</sup>Pb-corrected <sup>206</sup>Pb values ranging between 0.177 and 0.546 ppm. Consequently, individual isotope ratio errors are commonly in the range of 10–20% in all ages.

##### 4.2.3.1. 441.

Fifteen rutile analyses were performed on sample 441. Analyses yielded <sup>238</sup>U/<sup>206</sup>Pb ages ranging between ca. 745 and 472 Ma. Ten analyses yielded an intercept age of 472 ± 20 Ma (95% conf; MSWD=0.23), calculated by linear regression through the uncorrected <sup>238</sup>U/<sup>206</sup>Pb vs. <sup>207</sup>Pb/<sup>206</sup>Pb isotope ratios (Fig. 7G).

##### 4.2.3.2. Pe9.

Fifteen rutile analyses were performed on sample Pe9. Analyses yielded <sup>238</sup>U/<sup>206</sup>Pb ages ranging between ca. 602 and 476 Ma.

Eight analyses yielded an intercept age of 498 ± 18 Ma (95% conf; MSWD=0.93), calculated by linear regression through the uncorrected <sup>238</sup>U/<sup>206</sup>Pb vs. <sup>207</sup>Pb/<sup>206</sup>Pb isotope ratios (Fig. 7H).

##### 4.2.3.3. DFC387.

Fifteen rutile analyses were performed on sample DFC387. Analyses yielded <sup>238</sup>U/<sup>206</sup>Pb ages ranging between ca. 602 and 476 Ma. Eleven analyses yielded an intercept age of 519 ± 15 Ma (95% conf; MSWD = 1.2), calculated by linear regression through the uncorrected <sup>238</sup>U/<sup>206</sup>Pb vs. <sup>207</sup>Pb/<sup>206</sup>Pb isotope ratios (Fig. 7I).

## 5. TRACE ELEMENT THERMOMETRY

Zircon trace element thermometry provides an independent means of estimating the temperatures associated with the growth or recrystallisation of accessory minerals, and allows the timing of their growth to be placed within a specific metamorphic context. We performed Ti-in-zircon thermometry on rim domains of zircon in sample Pe24. Petrographic information related to Pe24 is discussed in Section 3.3, and related geochronology is discussed in Section 4.2.1 and presented in Table 2.

Laser ablation inductively coupled plasma



mass spectrometry (LA-ICP-MS) trace element analysis was performed at the University of Adelaide using an Agilent 7500cs ICP-MS with a NewWave 213 nm Nd-YAG laser. Zircon grains were analysed using a 50  $\mu\text{m}$  diameter beam, with a repetition rate of 5 Hz. The total acquisition time per analysis was 100 seconds (s), with 30 s of background measurement, 10 s of beam stabilisation and 60 s of sample ablation and acquisition.  $^{49}\text{Ti}$

**Table 3.** SHRIMP titanite U–Pb age data for samples 460a, Pe24, 487d, DFC507 and Pe9.

Spot name	U (ppm)	Th (ppm)	Th/U	<sup>204</sup> Pb/ <sup>206</sup> Pb	±1σ (%)	Isotopic ratios				Age estimates					
						<sup>208</sup> Pb/ <sup>206</sup> Pb	±1σ (%)	<sup>238</sup> U/ <sup>206</sup> Pb	±1σ (%)	<sup>207</sup> Pb/ <sup>206</sup> Pb	±1σ (%)	<sup>206</sup> Pb/ <sup>238</sup> U	±1σ	<sup>207</sup> Pb/ <sup>206</sup> Pb	±1σ
Sample Pe24															
PE24-1.1	141	98	0.70	0.0058	7.24	0.4963	0.85	10.3388	0.87	0.1532	0.86	538	6	933	200
PE24-1.2	82	54	0.66	0.0089	6.52	0.5463	0.93	9.9024	2.85	0.1827	0.91	524	16	305	449
PE24-1.3	88	21	0.24	0.0065	8.52	0.3519	1.20	10.2841	0.87	0.1647	1.04	534	7	962	263
PE24-1.4	134	42	0.31	0.0051	7.46	0.3140	1.01	10.6895	2.25	0.1388	0.88	527	12	768	202
PE24-1.5	96	37	0.38	0.0053	43.59	0.3764	1.06	10.4014	2.15	0.1511	0.96	541	25	1080	965
PE24-1.6	74	24	0.33	0.0081	7.85	0.4348	1.14	9.9542	0.89	0.1820	1.02	533	8	760	358
PE24-1.7	91	40	0.44	0.0085	7.66	0.4927	1.10	9.7053	0.90	0.1894	1.02	544	8	870	339
PE24-1.8	97	23	0.23	0.0063	7.84	0.3310	1.17	10.3737	0.85	0.1507	1.01	529	7	564	306
PE24-1.9	94	23	0.25	0.0104	7.89	0.4404	1.27	10.1854	0.92	0.1945	1.11	490	10	−397	1024
PE24-1.10	42	19	0.45	0.0153	25.80	0.7362	1.16	8.1420	1.23	0.2933	1.07	563	49	1115	1959
PE24-1.11	103	54	0.53	0.0050	8.20	0.3889	0.99	10.5292	0.82	0.1357	3.91	536	6	730	290
PE24-1.12	69	29	0.42	0.0124	6.26	0.5598	1.02	9.2281	0.90	0.2275	0.92	516	10	−78	830
PE24-1.13	114	50	0.44	0.0074	7.08	0.4211	0.99	10.3467	0.83	0.1601	0.92	518	7	294	393
PE24-1.14	94	21	0.22	0.0067	8.51	0.3652	1.22	10.3410	0.88	0.1661	1.06	529	7	915	281
PE24-1.15	139	42	0.30	0.0059	6.73	0.3286	0.96	10.4464	0.79	0.1456	0.84	529	6	578	243
PE24-1.16	71	18	0.25	0.0082	8.29	0.4370	1.27	9.8113	0.92	0.1951	1.10	543	8	1159	291
PE24-1.17	107	40	0.37	0.0071	7.33	0.3942	1.08	10.5813	0.84	0.1572	0.98	510	7	329	383
Sample 460a															
60-1.1	45	163	3.64	0.0189	27.73	1.7423	4.30	7.1983	3.97	0.4132	1.08	631	63	2676	785
60-2.1	59	101	1.71	0.0110	12.63	1.1608	1.70	7.6797	1.73	0.3202	1.76	677	18	2713	185
60-3.1	15	124	8.48	0.0297	5.53	2.5079	4.36	3.5836	5.90	0.6492	1.12	1104	66	3886	91
60-4.1	24	320	13.19	0.0200	5.81	3.5204	0.92	5.1390	1.57	0.5294	5.05	905	20	3683	165
60-5.1	26	68	2.55	0.0225	5.49	1.7123	4.76	5.0491	1.58	0.5447	1.02	885	20	3624	81
60-6.1	20	132	6.53	0.0318	4.76	2.3454	1.00	4.1403	1.65	0.6145	1.03	893	28	3389	151
60-7.1	35	155	4.46	0.0237	5.49	1.9704	1.02	5.2177	1.57	0.5333	1.04	828	21	3417	108
60-8.1	15	107	6.95	0.0308	5.20	2.4324	1.07	3.6232	1.75	0.6596	1.09	1073	32	3889	90
60-9.1	31	69	2.24	0.0258	4.77	1.6151	3.81	5.0091	3.93	0.5310	0.93	812	35	3148	141
60-10.1	32	115	3.57	0.0250	4.73	1.8629	0.91	5.1130	1.53	0.5286	0.92	815	20	3231	122
60-11.1	26	136	5.29	0.0221	5.47	2.1409	0.99	4.6301	1.59	0.5598	1.01	971	22	3754	68
60-12.1	26	17	0.66	0.0195	7.29	1.1863	6.96	6.0464	1.60	0.4670	1.14	760	20	3211	135
60-13.1	27	134	4.90	0.0200	24.31	2.0495	4.17	5.5440	1.60	0.4982	1.06	830	60	3446	342
Sample Pe9															
PE9-1.1	30.6	56	1.82	0.017	7.79	0.332	1.21	7.78	1.53	0.332	1.21	548	20	1417	596
PE9-1.2	29.7	42	1.42	0.013	9.11	0.294	1.26	8.41	1.51	0.294	1.26	561	17	1889	339
PE9-2.1	57.9	28	0.48	0.012	7.97	0.281	1.79	8.65	1.41	0.281	1.79	567	14	2065	230
PE9-3.1	30.7	38	1.25	0.007	13.75	0.214	1.56	9.71	1.52	0.214	1.56	552	14	1865	258
PE9-4.1	19.4	70	3.60	0.016	17.98	0.359	1.40	7.26	1.67	0.359	1.40	610	42	2424	549
PE9-5.1	33.7	48	1.43	0.013	8.31	0.304	1.13	7.99	1.47	0.304	1.13	591	17	2090	264
PE9-6.1	44.3	36	0.82	0.015	6.70	0.280	1.01	8.56	1.43	0.280	1.01	530	14	786	642
PE9-7.1	22.5	72	3.18	0.013	10.12	0.353	1.25	7.69	1.57	0.353	1.25	620	19	2849	164
PE9-8.1	13.3	53	4.00	0.019	9.08	0.488	1.35	5.57	1.84	0.488	1.35	722	34	3387	163
PE9-9.1	36.3	40	1.11	0.012	7.90	0.271	1.11	8.49	1.43	0.271	1.11	565	14	1585	343
PE9-10.1	35.9	33	0.92	0.016	7.11	0.323	1.08	8.15	1.45	0.323	1.08	537	17	1545	457
PE9-11.1	37.6	42	1.13	0.014	7.95	0.314	1.11	8.39	1.45	0.314	1.11	553	16	2094	272
PE9-12.1	15.6	48	3.09	0.021	7.97	0.404	1.29	6.90	1.65	0.404	1.29	561	27	2014	523
PE9-13.1	30.2	51	1.69	0.020	7.24	0.342	1.20	7.81	1.52	0.342	1.20	502	22	−573	2615
PE9-14.1	28.7	42	1.45	0.016	7.93	0.354	1.16	7.86	1.51	0.354	1.16	560	19	2291	283
PE9-15.1	25.3	60	2.37	0.017	7.85	0.344	1.20	7.52	1.53	0.344	1.20	575	20	1938	390
PE9-16.1	19.0	51	2.66	0.022	8.05	0.422	1.26	6.91	1.65	0.422	1.26	540	29	2054	561
PE9-17.1	38.1	32	0.84	0.013	7.26	0.297	1.04	8.14	1.42	0.297	1.04	578	15	1919	268
PE9-18.1	23.1	107	4.64	0.013	17.75	0.317	1.31	8.17	1.55	0.317	1.31	574	32	2250	502
PE9-19.1	16.5	67	4.09	0.022	7.54	0.400	1.24	6.92	1.62	0.400	1.24	547	26	1656	684
PE9-20.1	43.0	45	1.04	0.015	6.91	0.291	1.04	8.27	1.42	0.291	1.04	545	15	1088	549
PE9-21.1	43.2	34	0.78	0.013	6.42	0.281	0.89	8.20	1.37	0.281	0.89	584	13	1804	238
PE9-22	35.0	54	1.54	0.015	7.07	0.320	1.06	7.94	1.45	0.320	1.06	563	16	1791	351
PE9-23.1	43.2	32	0.74	0.013	12.13	0.290	1.01	8.30	1.41	0.290	1.01	576	21	1964	396
PE9-24.1	18.2	42	2.30	0.011	12.73	0.302	1.69	8.45	1.68	0.302	1.69	580	20	2399	267
PE9-25.1	23.6	48	2.02	0.021	7.30	0.380	1.23	7.30	1.58	0.380	1.23	525	24	1156	919
PE9-26.1	38.9	43	1.10	0.005	14.18	0.187	1.40	10.37	1.42	0.187	1.40	542	10	1950	163
PE9-27.1	19.7	92	4.66	0.013	9.22	0.337	1.26	7.75	1.56	0.337	1.26	609	19	2598	195
Sample DFC507															
507-1.1	15.8	2.1	0.13	0.026	7.60	0.518	1.27	4.91	1.86	0.518	1.27	665	44	2824	384
507-2.1	19.2	4.1	0.21	0.025	6.54	0.523	1.08	4.58	1.72	0.523	1.08	727	38	3092	238
507-3.1	6.2	0.8	0.12	0.044	5.85	0.719	1.15	2.24	2.40	0.719	1.15	618	120	2584	1417
507-4.1	23.7	1.8	0.07	0.022	6.66	0.445	1.08	5.70	1.62	0.445	1.08	650	29	2459	341
507-5.1	4.2	3.0	0.70	0.047	6.88	0.777	1.39	1.53	3.32	0.777	1.39	688	217	3342	1188
507-6.1	12.2	4.3	0.35	0.031	6.38	0.598	1.13	3.34	1.92	0.598	1.13	732	53	3266	290
507-7.1	22.4	5.3	0.24	0.012	11.61	0.370	1.39	6.90	1.68	0.370	1.39	703	23	3104	137

(continued on next page)

**Table 3.** (continued)

Spot name	U (ppm)	Th (ppm)	Th/U	<sup>204</sup> Pb/ <sup>206</sup> Pb	±1σ	Isotopic ratios						Age estimates					
						<sup>208</sup> Pb/ <sup>206</sup> Pb	±1σ	<sup>238</sup> U/ <sup>206</sup> Pb	±1σ	<sup>207</sup> Pb/ <sup>206</sup> Pb	±1σ	<sup>206</sup> Pb/ <sup>238</sup> U	±1σ	<sup>207</sup> Pb/ <sup>206</sup> Pb	±1σ		
Sample DFC507																	
507-9.1	20.3	2.5	0.12	0.021	7.27	0.481	1.82	5.21	1.69	0.481	1.82	733	32	3123	206		
507-8.1	16.4	2.8	0.17	0.024	7.80	0.518	1.26	5.03	1.88	0.518	1.26	704	40	3199	234		
507-10.1	7.9	4.4	0.56	0.033	6.95	0.663	1.20	2.80	2.27	0.663	1.20	904	83	3661	254		
507-11.1	12.5	2.2	0.17	0.030	7.66	0.618	1.31	3.54	2.17	0.618	1.31	821	66	3580	239		
Sample 487d																	
487d-1.1	40	29	0.72	0.0025	15.84	0.2705	1.41	12.4483	0.83	0.0779	1.48	475	5	−356	416		
487d-1.2	91	49	0.54	0.0007	17.19	0.2066	0.96	12.1391	0.73	0.0782	0.89	505	4	882	56		
487d-1.3	101	52	0.52	0.0008	14.32	0.2012	0.93	12.1421	1.39	0.0788	0.85	503	7	832	58		
487d-1.4	75	44	0.58	0.0011	14.17	0.2250	5.32	11.9038	2.10	0.0789	0.97	511	10	725	79		
487d-1.5	197	117	0.59	0.0006	12.01	0.2265	0.63	12.3121	0.70	0.0783	0.62	498	3	919	34		
487d-1.6	92	65	0.71	0.0011	17.88	0.2755	1.05	12.9580	0.72	0.0779	0.94	471	4	692	99		
487d-1.7	137	70	0.51	0.0005	16.48	0.1967	0.79	12.2902	1.64	0.0788	0.71	500	8	992	35		
487d-1.8	284	142	0.50	0.0004	11.28	0.1921	0.55	11.6200	1.41	0.0789	0.49	529	7	1021	21		
487d-1.9	45	44	0.97	0.0026	11.93	0.3735	1.09	12.1989	0.80	0.0783	1.34	484	5	−425	341		
487d-1.10	87	47	0.54	0.0012	61.02	0.2067	0.96	11.8497	0.73	0.0792	0.88	512	7	682	362		
487d-1.11	40	27	0.66	0.0010	23.07	0.2516	8.96	11.5503	0.80	0.0776	1.32	526	5	712	119		
487d-1.12	184	92	0.50	0.0006	12.66	0.1860	0.68	11.8275	0.71	0.0774	0.60	518	4	896	36		
487d-1.13	100	59	0.59	0.0008	85.72	0.2243	0.86	12.0159	1.87	0.0781	0.83	509	11	831	309		
487d-1.14	44	38	0.85	0.0024	12.20	0.3263	1.11	11.8685	2.25	0.0805	1.24	499	11	−54	251		
487d-1.15	56	38	0.68	0.0019	12.67	0.2614	1.08	12.0304	0.78	0.0793	1.11	498	4	280	164		

was the measured isotope rather than  $^{48}\text{Ti}$  in order to avoid interference issues. Internal calibration was performed using the NIST 612 glass standard, and accuracy was monitored using the NIST 614 glass standard. Internal calibration for zircon was completed using stoichiometrically determined  $^{178}\text{Hf}$  values. Data reduction was completed using GLITTER software (Van Achterbergh et al., 2001).

Temperatures estimated from trace element concentrations in this study employ the updated Ti-in-zircon thermometer of Ferry and Watson (2007). Ti substitution in zircon, at the pressures relevant to this study (b15 kbar), is assumed to be largely independent of pressure (Ferriss et al., 2008). This implies that analytical and thermometer calibration uncertainties are the dominant source of error associated with temperature estimates (Ferry and Watson, 2007; Fu et al., 2008; Watson et al., 2006). The application of the Ti-in-zircon thermometer is based on a weighted average Ti content. The quoted error is based on the variation in Ti content, which yields a temperature range.  $2\sigma$  errors are associated with an uncertainty of  $\pm 18^\circ\text{C}$ , reflecting low titanium concentrations (b20 ppm). Uncertainties associated with calibration of the thermometer are also included in the calculations and contribute errors of  $\pm 4^\circ\text{C}$ . An equilibrium mineral assemblage in Pe24

contains rutile, zircon and quartz (Fig. 4D), allowing  $\alpha\text{TiO}_2$  and  $\alpha\text{SiO}_2$  to be fixed at 1.

Ti-in-zircon temperature estimates from sample Pe24 are presented in Table 5. Each individual LA-ICP-MS spot location overprinted existing SHRIMP pits that yielded Petermann-aged U-Pb data. The calculated average temperature from recrystallised zircon rims is  $738 \pm 18^\circ\text{C}$ . Several analyses yielded concentrations that are an order of magnitude higher than the quoted average Ti concentrations. The observed spectrometry signals for these analyses were highly variable and it was difficult to isolate a significant part of the signal that would produce a representative rim analysis. This signal variability is attributed to ablation through a thin recrystallised rim and subsequent analysis of the core, which may preserve a chemical signature reflecting a previous thermal event. On this basis, these analyses were discounted from weighted average calculations.

## 6. DISCUSSION

### 6.1. Duration of tectonism and cooling

U-Pb geochronology collected in this study from recrystallised zircon rims in sample Pe24 yields an age of  $544 \pm 7$  Ma. Ti-in-zircon thermometry from these zircon rims yield



**Table 4.** SHRIMP rutile U–Pb age data for samples 441, DFC 387 and Pe9.

Spot	U	Th	<sup>206</sup> Pb (ppm)	Isotopic ratios										Age estimates <sup>a</sup>						
				<sup>207</sup> Pb/ <sup>206</sup> Pb	± 1σ	<sup>238</sup> U/ <sup>206</sup> Pb	± 1σ	<sup>207</sup> Pb/ <sup>206</sup> Pb	± 1σ	<sup>238</sup> U/ <sup>206</sup> Pb <sup>a</sup>	± 1σ	<sup>207</sup> Pb <sup>a</sup> / <sup>206</sup> Pb <sup>a</sup>	±1σ	<sup>207</sup> Pb <sup>a</sup> / <sup>235</sup> U	±1σ	<sup>206</sup> Pb <sup>a</sup> / <sup>238</sup> U	±1σ	Rho <sup>b</sup>	<sup>206</sup> Pb/ <sup>238</sup> U	±1σ
				(%)	(%)	(%)	(%)	(%)	(%)	(%)	(%)	(%)	(%)	(%)	(%)	(%)	(%)	(%)	(%)	(%)
Sample 441																				
441-1.1	3.2	0.008	0.233	0.588	6.1	3.92	13.8	0.588	6.1	11.99	97	0.013	873	0.15	830	0.083	97	0.39	516	480
441-2.1	4.0	0.005	0.416	0.675	3.2	1.97	14.6	0.675	3.2	8.16	204	0.055	305	0.93	162	0.123	204	0.38	745	1439
441-3.1	5.6	0.003	0.420	0.220	6.8	9.23	3.9	0.220	6.8	11.54	9	0.056	29	0.67	33	0.087	9	0.60	536	45
441-4.1	6.9	0.060	0.448	0.159	12.2	11.34	3.2	0.159	12.2	13.18	8	0.044	48	0.46	51	0.076	8	0.48	472	34
441-5.1	2.4	0.006	0.177	0.260	12.1	8.66	3.9	0.260	12.1	11.52	18	0.057	66	0.68	73	0.087	18	0.51	537	92
441-6.1	4.1	0.007	0.309	0.476	6.2	5.56	9.4	0.476	6.2	11.46	57	0.049	122	0.59	124	0.087	57	0.26	540	294
441-7.1	4.6	0.020	0.297	0.170	4.7	11.36	3.7	0.170	4.7	13.16	10	0.058	14	0.61	16	0.076	10	0.48	472	47
441-8.1	4.5	0.002	0.315	0.163	15.4	10.54	6.0	0.163	15.4	12.23	45	0.050	65	0.56	59	0.082	45	0.24	507	221
441-9.1	5.6	0.006	0.373	0.200	4.0	10.52	4.5	0.200	4.0	12.86	11	0.051	16	0.55	20	0.078	11	0.55	483	51
441-10.1	3.9	0.007	0.264	0.195	8.7	10.72	3.3	0.195	8.7	12.66	9	0.072	24	0.79	28	0.079	9	0.55	490	42
441-11.1	3.0	0.014	0.195	0.254	7.4	9.88	5.7	0.254	7.4	13.00	21	0.059	36	0.63	42	0.077	21	0.53	478	99
441-12.1	4.8	0.007	0.376	0.557	1.8	3.56	8.3	0.557	1.8	10.92	122	0.123	136	1.55	26	0.092	122	0.47	565	661
441-13.1	3.6	0.001	0.259	0.294	8.6	8.52	3.6	0.294	8.6	11.86	84	0.066	65	0.77	53	0.084	84	0.63	522	421
441-14.1	3.2	0.003	0.212	0.431	8.1	6.80	10.8	0.431	8.1	12.77	71	0.043	135	0.47	152	0.078	71	0.46	486	334
441-15.1	3.5	0.011	0.266	0.601	4.9	4.17	17.5	0.601	4.9	11.36	89	0.118	78	1.43	70	0.088	89	0.54	544	467
Sample DFC387																				
387-1.1	3.0	0.006	0.252	0.250	9.2	7.98	3.6	0.250	9.2	10.22	18	0.073	32	0.99	41	0.098	18	0.63	602	105
387-2.1	6.6	0.012	0.439	0.191	9.0	10.83	3.3	0.191	9.0	12.86	11	0.064	28	0.68	32	0.078	11	0.52	483	52
387-3.1	3.4	0.007	0.259	0.192	4.7	9.33	3.5	0.192	4.7	11.12	11	0.061	16	0.76	18	0.090	11	0.47	555	60
387-4.1	3.0	0.003	0.212	0.222	5.0	9.32	6.4	0.222	5.0	12.14	28	0.026	54	0.29	57	0.082	28	0.36	510	139
387-5.1	4.0	0.003	0.277	0.180	7.8	10.38	3.3	0.180	7.8	12.27	12	0.055	26	0.61	31	0.081	12	0.56	505	59
387-6.1	8.0	−0.002	0.546	0.188	9.9	10.69	3.0	0.188	9.9	12.60	6	0.066	30	0.72	33	0.079	6	0.58	492	30
387-7.1	6.2	−0.007	0.429	0.659	2.8	3.09	11.2	0.659	2.8	12.49	73	0.022	384	0.24	346	0.080	73	0.45	496	349
387-8.1	2.9	0.009	0.223	0.191	11.1	9.29	3.5	0.191	11.1	11.17	19	0.053	45	0.65	49	0.090	19	0.39	553	101
387-9.1	4.0	0.016	0.303	0.224	11.9	9.19	3.4	0.224	11.9	11.34	14	0.072	40	0.88	46	0.088	14	0.54	545	72
387-10.1	5.1	−0.001	0.379	0.161	10.4	9.98	3.1	0.161	10.4	11.52	35	0.052	39	0.62	37	0.087	35	0.43	537	180
387-11.1	3.6	0.014	0.284	0.185	12.8	9.40	7.0	0.185	12.8	10.76	12	0.085	30	1.09	32	0.093	12	0.41	573	66
387-12.1	4.1	0.005	0.309	0.191	7.8	9.45	6.0	0.191	7.8	11.25	13	0.061	27	0.75	30	0.089	13	0.42	549	68
387-13.1	2.8	0.007	0.193	0.226	9.9	9.72	3.5	0.226	9.9	12.28	14	0.056	44	0.63	51	0.081	14	0.61	505	69
387-14.1	4.4	−0.003	0.288	0.179	10.1	11.07	5.5	0.179	10.1	13.01	8	0.058	35	0.62	37	0.077	8	0.37	477	36
387-15.1	6.8	0.008	0.450	0.156	10.1	11.65	3.6	0.156	10.1	13.05	10	0.070	22	0.74	25	0.077	10	0.50	476	45
Sample Pe9																				
PE9-1.1	6.4	−0.003	0.425	0.118	15.0	11.91	2.7	0.118	15.0	12.96	3	0.052	36	0.55	37	0.077	3	0.28	479	±16
PE9-1.2	5.0	0.015	0.368	0.207	9.8	9.55	4.8	0.207	9.8	11.59	14	0.065	32	0.78	38	0.086	14	0.60	534	±71
PE9-3.1	16.2	0.014	1.123	0.140	9.2	11.30	2.4	0.140	9.2	12.43	5	0.067	20	0.74	21	0.080	5	0.43	499	±25
PE9-4.1	11.0	−0.004	0.825	0.085	4.7	10.78	2.5	0.085	4.7	11.46	3	0.036	12	0.43	12	0.087	3	0.23	540	±15
PE9-5.1	5.8	0.002	0.433	0.135	7.4	10.55	2.5	0.135	7.4	11.53	10	0.066	18	0.79	17	0.087	10	0.20	536	±52
PE9-6.1	6.3	0.001	0.438	0.105	4.7	11.67	2.5	0.105	4.7	12.31	7	0.063	9	0.70	9	0.081	7	0.36	503	±33
PE9-7.1	5.1	0.023	0.394	0.118	4.7	10.18	2.8	0.118	4.7	11.11	4	0.048	12	0.60	13	0.090	4	0.27	555	±24
PE9-9.1	5.0	0.016	0.357	0.133	13.3	10.88	4.7	0.133	13.3	11.97	8	0.059	32	0.69	33	0.084	8	0.24	517	±38
PE9-10.1	10.5	0.007	0.644	0.086	4.2	13.43	2.4	0.086	4.2	13.94	3	0.057	7	0.56	7	0.072	3	0.35	447	±14
PE9-11.1	5.3	0.019	0.412	0.513	7.1	4.67	9.1	0.513	7.1	11.15	72	0.004	2091	0.05	2126	0.090	72	0.49	554	±382
PE9-12.1	7.2	0.045	0.569	0.128	4.1	10.07	2.5	0.128	4.1	10.89	4	0.067	7	0.85	9	0.092	4	0.52	566	±22
PE9-13.1	6.2	0.007	0.418	0.136	4.6	11.43	4.1	0.136	4.6	12.70	8	0.054	12	0.59	13	0.079	8	0.42	489	±36
PE9-14.1	4.5	0.006	0.320	0.162	4.3	10.77	3.1	0.162	4.3	12.09	8	0.075	10	0.86	11	0.083	8	0.48	512	±42
PE9-15.1	4.3	0.012	0.331	0.139	9.8	10.12	2.8	0.139	9.8	11.20	7	0.061	23	0.75	25	0.089	7	0.43	551	±36

<sup>a</sup> Isotope ratios and ages are corrected for common Pb using the measured <sup>208</sup>Pb values.<sup>b</sup> Error correlation; defined as [(err. <sup>206</sup>Pb/<sup>238</sup>U)/(measured <sup>206</sup>Pb/<sup>238</sup>U)]/[(err. <sup>207</sup>Pb/<sup>235</sup>U)/(measured <sup>207</sup>Pb/<sup>235</sup>U)].

temperature estimates of 738±18 °C (Table 5), well below the closure temperature of Pb diffusion in zircon (~900 °C) (Cherniak and Watson, 2007). The earliest record of peak Petermann Orogeny metamorphism in the western Musgrave Province is constrained at ~570 Ma by U–Pb zircon and titanite (Fig. 3) (Raimondo et al., 2009, 2010). In the Cockburn Shear Zone, geochronology from zircon and allanite indicate that peak metamorphism and partial melting occurred between 559±6 and 551±6 Ma, at temperatures of 720–750 °C (Gregory et al., 2009). This is complemented by a U–Pb zircon age of 561±11 Ma from a migmatitic shear zone ~40 km further north (Fig. 3) (Scrimgeour et al., 1999).

Temperature estimates in this study for zircon crystallisation are in close agreement with previous thermobarometric studies, which indicate peak metamorphic temperatures in the range 700–760 °C (Camacho et al., 1997; Scrimgeour and Close, 1999; Gregory et al., 2009; Raimondo et al., 2010).

Zircons from sample Pe24 commonly display poorly luminescent, featureless to convolutedly zoned cores that are mantled by oscillatory zoned regions with low to moderate luminescence (Fig. 5). Highly luminescent rims either truncate or form concentric zoning patterns around concentrically zoned domains (Fig. 5). The rim zoning characteristics from

sample Pe24 are similar to those discussed by Raimondo et al. (2010) and Gregory et al. (2009), where zircon rim crystallisation is interpreted to have formed at  $\sim 700^\circ\text{C}$  in migmatitic rocks. This suggests that metamorphic zircon rims across the core of the orogen formed under similar high-temperature conditions associated with a single long-lived event, rather than episodic deformational events. Moreover, an absence of magmatism or overprinting metamorphic assemblages during the Petermann Orogeny indicates zircon growth is associated with a single deformational event.

Ages obtained from titanite samples from the western Mann Ranges vary between  $567 \pm 18$  Ma and  $499 \pm 4$  Ma (Fig. 3). The timing of titanite crystallisation will not necessarily be preserved by the U–Pb isotopic system. If peak temperatures associated with metamorphism are above the closure temperature for Pb diffusion in titanite ( $\sim 600$ – $660^\circ\text{C}$ ), then the possibility arises that age estimates will reflect the timing of U–Pb diffusive closure during cooling, rather than the prograde or peak evolution (Cherniak, 2006; Frost et al., 2001). As the peak metamorphic temperatures

associated with the Petermann Orogeny are  $>700^\circ\text{C}$ , it is interpreted that the titanite ages from the core of the orogen will reflect cooling of the orogen through the closure temperature of Pb diffusion.

Titanite-bearing samples analysed show petrographic and/or mineral separate evidence for one (DFC507, ?460a) or two (Pe9 and Pe24) generations of titanite growth, either euhedral titanite grains aligned with the foliation, or those that occur as coronae and therefore late with respect to the fabric/peak assemblage (Fig. 4B). However, sample Pe9 in which there is petrographic evidence for titanite occurring exclusively as coronas (e.g. Fig. 4B), show evidence of far larger, euhedral titanite grains in mineral separation (Fig. 5a). This provides strong evidence that there is in fact multiple generations of titanite growth. If this interpretation is correct then the disparity in titanite ages could reflect the continual growth/resetting of titanite during long-lived tectonism. However, due to access restrictions, structural and lithological relationships in the western Mann Ranges are not well understood. Therefore, based on the available information, there are limitations

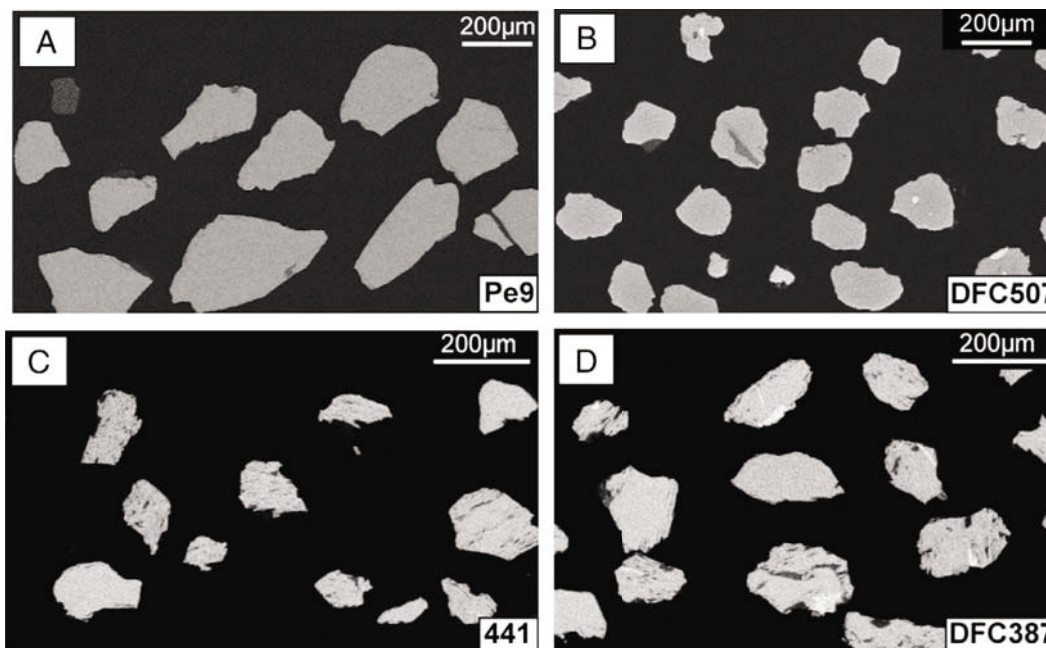


**Figure 6.** A, B) Backscattered electron images of representative titanite from samples Pe9 and DFC507. C, D) Backscattered electron images of representative rutile from samples 441 and DFC387.



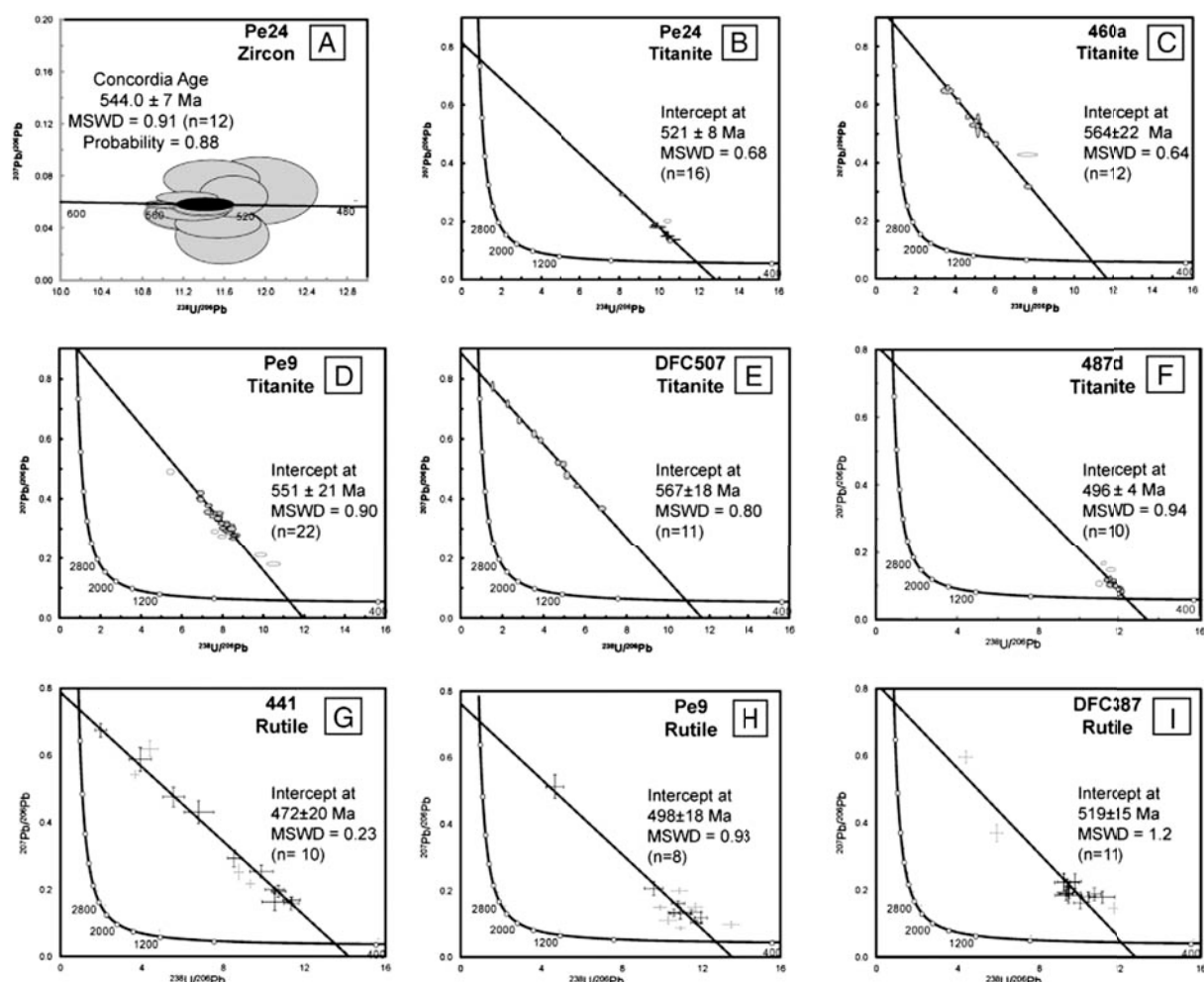


**Figure 7.** A) Tera–Wasserburg plots of  $^{204}\text{Pb}$ -corrected  $^{238}\text{U}/^{206}\text{Pb}$  vs.  $^{207}\text{Pb}/^{235}\text{U}$  isotope ratios of Sensitive High Resolution Ion Microprobe (SHRIMP) zircon data for sample Pe24. Concordia age is quoted at the 95% confidence level. B–F) Tera–Wasserburg plots of uncorrected  $^{238}\text{U}/^{206}\text{Pb}$  vs.  $^{207}\text{Pb}/^{235}\text{U}$  isotope ratios of titanite data for samples Pe24, 460a Pe9, DFC 507, and 487d. G–I) Tera–Wasserburg plots of the uncorrected  $^{238}\text{U}/^{206}\text{Pb}$  vs.  $^{207}\text{Pb}/^{235}\text{U}$  isotope ratios of rutile data from samples DFC 387 and 441. Age uncertainties are quoted at 95% confidence level. MSWD; mean square of weighted deviates. Grey data points represent those not included in the age calculations.

that prevent an unequivocal solution to the apparent diachroneity of the titanite age data.

Titanite grains containing higher amounts of common lead and lower concentrations of uranium show relatively older U–Pb ages and are associated with greater errors (Fig. 7). Samples Pe24 and 487d have the lowest concentrations of common Pb and the highest concentration of U and radiogenic Pb. These analyses are more concordant and produce a far more accurate and precise population. Statistically, titanite samples Pe24 and 487d present the most robust age calculations and

are considered to most accurately represent the timing of closure of the Pb systematics in titanite. These samples are therefore used for the interpretation of the duration and rate of cooling.

Frost et al. (2001) and Cherniak & Watson (2001) estimate closure temperatures of 600–660 °C for titanite grains with a radius of 100  $\mu\text{m}$  and a cooling rate of 10 °C Myr. Analysed titanite grains from all samples have diffusional radii in the range 60–100  $\mu\text{m}$ . Therefore, it is expected that closure temperatures should be approximately 600–660 °C. A U–Pb

**Table 5.** Titanium concentrations, errors and calculated temperatures for zircon sample Pe24.

Spot name	Ti conc. $\pm 1\sigma$ (ppm)	Position	T °C $\pm$ calibration uncertainty	T °C $\pm$ calibration and analytical uncertainties
Spot 1	7.8 $\pm$ 0.4	Rim	720 $\pm$ 3	720 $\pm$ 19
Spot 2	5.8 $\pm$ 0.32	Rim	698 $\pm$ 4	698 $\pm$ 15
Spot 3	8.33 $\pm$ 0.57	Rim	729 $\pm$ 3	729 $\pm$ 18
Spot 4	29.2 $\pm$ 1.3	Core	858 $\pm$ 2	858 $\pm$ 10
Spot 5	129 $\pm$ 6.1	Core	1061 $\pm$ 3	1061 $\pm$ 8
Spot 6	13.9 $\pm$ 1.1	Rim	779 $\pm$ 2	779 $\pm$ 18
Spot 7	9.47 $\pm$ 0.67	Rim	741 $\pm$ 2	741 $\pm$ 17
Spot 8	16.4 $\pm$ 2.1	Rim	795 $\pm$ 3	795 $\pm$ 20
Spot 9	6.46 $\pm$ 0.98	Rim	685 $\pm$ 3	685 $\pm$ 43
Spot 10	7.97 $\pm$ 1.12	Rim	725 $\pm$ 2	725 $\pm$ 15
Spot 11	12.0 $\pm$ 1.32	Rim	764 $\pm$ 2	764 $\pm$ 28
Spot 12	14.3 $\pm$ 1.21	Rim	783 $\pm$ 2	783 $\pm$ 10
Spot 13	8.82 $\pm$ 0.76	Rim	734 $\pm$ 2	734 $\pm$ 11
Spot 14	8.85 $\pm$ 0.64	Rim	735 $\pm$ 2	735 $\pm$ 11
Spot 15	32.1 $\pm$ 2.86	Core	869 $\pm$ 3	869 $\pm$ 12
Spot 16	5.9 $\pm$ 0.68	Rim	699 $\pm$ 2	699 $\pm$ 15
Spot 17	8.22 $\pm$ 1.14	Rim	728 $\pm$ 2	728 $\pm$ 15
Spot 18	17.1 $\pm$ 1.96	Core	799 $\pm$ 3	799 $\pm$ 12
Spot 19	6.62 $\pm$ 1.03	Rim	709 $\pm$ 2	709 $\pm$ 14
Spot 20	14.3 $\pm$ 1.31	Rim	781 $\pm$ 3	781 $\pm$ 9
Spot 21	16.0 $\pm$ 1.36	Rim	794 $\pm$ 3	792 $\pm$ 9
Wtd. ave.	9.2 $\pm$ 1.8	Rims	738 $\pm$ 3	738 $\pm$ 18

titanite age of  $521 \pm 8$  Ma (Table 1) from the Cockburn Shear Zone (Fig. 3) is considered to correspond to the timing of cessation of Pb diffusion. This allows a constraint of  $\sim 660$ – $600$  °C to be placed at c. 521 Ma. If this logic is correct this implies cooling from  $720$ – $760$  °C to  $600$ – $660$  °C between c. 544 Ma and c. 521 Ma, at an average rate of  $\sim 2.6$ – $7.0$  °C Myr $^{-1}$ .

Similar to titanite, the closure temperature for Pb diffusion in rutile will influence the interpretation of U–Pb age data. This parameter is considered to be strongly dependent on grain size, where it is expected that diffusion of Pb in the cores of smaller grains will occur for longer durations and at lower temperatures as opposed to the cores of larger rutile grains. Therefore, a spread of rutile ages may reflect different closure temperatures as a result of variations in diffusive volumes. Kooijman et al. (2010) report closure temperatures of  $563$  °C for the cores of rutile grains with a radius of  $63$   $\mu\text{m}$ . Analysed rutile grains from samples 441 and Pe9 typically have diffusive radii between  $40$  and  $60$   $\mu\text{m}$  (Fig. 6C, D) and therefore, based on the modelling of Kooijman et al. (2010), it can be expected that they will have closure temperatures in the range  $550$ – $560$  °C. U–Pb geochronology from samples 441

and Pe9 correspond to age estimates of  $472 \pm 20$  and  $498 \pm 18$  Ma, respectively (Table 1). These estimates are younger than those obtained from zircon and titanite samples from this study due to progressively later Pb closure. This allows a further constraint on cooling from  $600$ – $660$  °C at  $\sim 521$  Ma to  $550$ – $560$  °C at  $\sim 498$ – $472$  Ma, at an average rate of  $0.9$ – $4.8$  °C Myr $^{-1}$ . The cooling rates are consistent with those from the Bates Region (Fig. 3), obtained using the temporal and thermal separation of titanite crystallisation and subsequent Pb closure, which are  $\sim 1.8$ – $5.8$  °C Myr $^{-1}$  (Raimondo et al., 2010); and those from the Musgrave Ranges using the difference in garnet (Sm–Nd) and muscovite/biotite/K-feldspar ( $40\text{Ar}$ – $39\text{Ar}$ ) closure, which estimate an average cooling rate of  $\sim 3$  °C Myr $^{-1}$  between  $630$  and  $520$  Ma, and  $\sim 4$  °C Myr $^{-1}$  between  $525$  and  $490$  Ma (Camacho et al., 1997). These constraints imply that the duration of tectonism and cooling during the Petermann Orogeny occurred for  $\sim 95$  Myr between c.  $567$  and  $472$  Ma and was associated with slow average rates of cooling.

## 6.2. ‘Cold’ vs. ‘hot’: the mechanical environment of the Petermann Orogeny

Recent studies of the core of the Petermann Orogen present contrasting views of its thermal regime, and by inference, the mechanical environment in which deformation occurred. Camacho et al. (2001) suggested that deformation occurred over a very short duration (c. 1 Myr). Elevated temperatures during the Petermann Orogeny were confined to discrete shear zones and did not affect surrounding basement rocks, which were characterised by temperatures of  $350$ – $400$  °C at depths of  $40$  km. This implies that the crustal section of the lithosphere was characterised by average thermal gradients of  $\sim 9$  °C km $^{-1}$ . Based on diffusion profiles developed in garnet porphyroclasts from mylonites, Camacho et al. (2009) suggested that localised heating within shear zones allowed sub-eclogite facies metamorphism ( $\sim 650$  °C;  $\sim 12$  kbar) to occur in overall cold and strong crust. In order to develop and preserve thermal

gradients of  $\sim 9^{\circ}\text{C km}^{-1}$  in crust with elevated heat production, thickening and formation of high-pressure metamorphic assemblages, followed by exhumation of the orogenic core, must have occurred in rapid succession. At present, the structures that could have accommodated this thickening have not been identified. The requirement for the lithosphere to be comparatively cold and by inference strong during intraplate deformation, is seemingly at odds with the accepted notion that strain is focused into areas of weakness in the lithosphere, generally as a result of high crustal heat production (Sandiford and Hand, 1998; Hand and Sandiford, 1999; Stephenson et al., 2009).

An alternative hypothesis of Raimondo et al. (2009) is that the core of the orogen reflects a channel-flow regime involving lateral flow of ductile lower crustal material. This style of deformation typically necessitates a weak and hot lithosphere, and time scales associated with deformation are considered to be comparatively long ( $>20$  Myr) (Beaumont et al., 2001, 2004; Flament et al., 2011). The existence of pervasive mylonitic deformation and partial melting in this domain, coupled with its apparent extrusive behaviour, necessitates that the crust experienced regionally elevated temperatures and prolonged burial at depth. SHRIMP dating of syn-kinematic titanite and zircon within the proposed channel suggests that tectonism was active for at least 30 Myr between 570 and 540 Ma (Raimondo et al., 2009, 2010).

The interpretation of new U–Pb geochronology from this study is somewhat hindered as there is no unequivocal explanation of the diachroneity of titanite ages throughout the orogen, and therefore, it is difficult to resolve the duration or cooling rates with absolute certainty. Nevertheless, taken holistically, robust SHRIMP zircon, titanite and rutile geochronology from high-pressure rocks in the core of the orogen suggests that this domain experienced elevated temperatures ( $>550^{\circ}\text{C}$ )

deep in the crust for a duration of c. 95 Myr between 567 and 472 Ma, and was associated with slow rates of cooling during this period. The proposed duration of tectonism during the Petermann Orogeny is far longer than permitted by a shear heating model ( $\sim 1$  Myr). Furthermore, conventional thermobarometric estimates from the core of the orogen indicate that the regional thermal gradient during the Petermann Orogeny was  $17\text{--}26^{\circ}\text{C km}^{-1}$  (Scrimgeour and Close, 1999; Raimondo et al., 2010). These estimates suggest that the central and western parts of the orogen were characterised by an elevated thermal regime during tectonism, and lend support to the notion that the lithosphere was hot and by inference mechanically weak, rather than strong and cold. These observations permit, but do not require, the development of a channel flow system. This model is also compatible with the above average level of crustal heat production in the orogen, and provides a mechanism for the long-lived evolution of the Petermann Orogeny.

## 7. CONCLUSIONS

In the core of the Petermann Orogen, peak metamorphic temperatures of  $720\text{--}760^{\circ}\text{C}$  were obtained at 567–544 Ma, followed by slow cooling to  $\sim 600\text{--}660^{\circ}\text{C}$  by 521 Ma at a rate of  $\sim 2.6\text{--}7.0^{\circ}\text{C Myr}^{-1}$ , and further cooling to  $585\text{--}560^{\circ}\text{C}$  at c. 498–472 Ma at a rate of  $0.9\text{--}4.8^{\circ}\text{C Myr}^{-1}$ . Tectonism in the central and western parts of the orogen occurred for an interval of  $>40$  Myr in a mechanically weak lithosphere, which was characterised by regional thermal gradients of  $17\text{--}26^{\circ}\text{C km}^{-1}$ . The proposed duration of tectonism is much longer than that permitted by a shear heating mechanism, which requires an exceptionally short duration of tectonism, and additionally, an overall cold crustal lithosphere characterised by geothermal gradients of  $\sim 9^{\circ}\text{C km}^{-1}$ . The duration of the Petermann Orogeny thermal regime is comparable to that of typical collisional orogens, suggesting that the rheological development and

thermal evolution of intraplate orogens may be comparable to those developed at plate margins.

## ACKNOWLEDGEMENTS

Thanks to Dorothy Close, Ian Scrimgeour and Ian Buick for providing the samples used in this study. Research is funded by ARC LP100200127 to DEK and MH. Thanks to Richard Taylor for assistance in acquiring the SHRIMP data. Constructive and thorough comments from two anonymous reviewers improved the final manuscript considerably. This publication is TRaX record 246.

## REFERENCES

- Aitken, A.R.A., Betts, P.G., 2009a. Constraints on the Proterozoic supercontinent cycle from the structural evolution of the south-central Musgrave Province, central Australia. *Precambrian Research* 168, 284–300.
- Aitken, A.R.A., Betts, P.G., 2009b. Multi-scale integrated structural and aeromagnetic analysis to guide tectonic models: an example from the eastern Musgrave Province, Central Australia. *Tectonophysics* 476, 418–435.
- Aitken, A.R.A., Betts, P.G., Ailleres, L., 2009a. The architecture, kinematics, and lithospheric processes of a compressional intraplate orogen occurring under Gondwana assembly: the Petermann Orogeny, central Australia. *Lithosphere* 1, 343–357.
- Aitken, A.R.A., Betts, P.G., Weinberg, R.F., Gray, D., 2009b. Constrained potential field modeling of the crustal architecture of the Musgrave Province in central Australia: evidence for lithospheric strengthening due to crust–mantle boundary uplift. *Journal of Geophysical Research B: Solid Earth* 114.
- Beaumont, C., Jamieson, R.A., Nguyen, M.H., Lee, B., 2001. Himalayan tectonics explained by extrusion of a low-viscosity crustal channel coupled to focused surface denudation. *Nature* 414, 738–742.
- Beaumont, C., Jamieson, R.A., Nguyen, M.H., Medvedev, S., 2004. Crustal channel flows: 1. Numerical models with applications to the tectonics of the Himalayan–Tibetan orogen. *Journal of Geophysical Research — Solid Earth* 109, B06406.
- Beaumont, C., Nguyen, M.H., Jamieson, R.A., Ellis, S., 2006. Crustal flow modes in large hot orogens. In: Law, R.D., Searle, M.P., Godin, L. (Eds.), *Channel Flow, Ductile Extrusion and Exhumation in Continental Collision Zones*. Geological Society, London, pp. 91–145.
- Bird, P., 1991. Lateral extrusion of lower crust from under high topography in the isostatic limit. *Journal of Geophysical Research* 96, 10275–10286.
- Buick, I.S., Close, D., Scrimgeour, I.R., Miller, J., Harris, C., Cartwright, I., 2001. High-pressure melting and fluid flow during the Petermann Orogeny, central Australia. *Water–Rock Interaction*, 10.
- Camacho, A., Fanning, C.M., 1995. Some isotopic constraints on the evolution of the granulite and upper amphibolite facies terranes in the eastern Musgrave Block, central Australia. *Precambrian Research* 71, 155–181.
- Camacho, A., McDougall, I., 2000. Intracratonic, strike–slip partitioned transpression and the formation and exhumation of eclogite facies rocks: an example from the Musgrave Block, central Australia. *Tectonics* 19, 978–996.
- Camacho, A., Compston, W., McCulloch, M., McDougall, I., 1997. Timing and exhumation of eclogite facies shear zones, Musgrave Block, central Australia. *Journal of Metamorphic Geology* 15, 735–751.
- Camacho, A., McDougall, I., Armstrong, R., Braun, J., 2001. Evidence for shear heating, Musgrave Block, central Australia. *Journal of Structural Geology* 23, 1007–1013.
- Camacho, A., Yang, P., Frederiksen, A., 2009. Constraints from diffusion profiles on the duration of high-strain deformation in thickened crust. *Geology* 37, 755–758.
- Cherniak, D.J., 2006. Zr diffusion in titanite. *Contributions to Mineralogy and Petrology* 152



- (5), 639–647.
- Cherniak, D.J., Watson, E.B., 2001. Pb diffusion in zircon. *Chemical Geology* 172 (1–2), 5–24.
- Cherniak, D.J., Watson, E.B., 2007. Ti diffusion in zircon. *Chemical Geology* 242 (3–4), 470–483.
- Edgoose, C.J., Scrimgeour, I.R., Close, D.F., 2004. Geology of the Musgrave Block, Northern Territory. Northern Territory Geological Survey. Report 15.
- Ellis, D.J., Maboko, M.A.H., 1992. Precambrian tectonics and the physiochemical evolution of the continental crust. Part I: The gabbro–eclogite transition. *Precambrian Research* 55, 491–506.
- Evins, P.M., Smithies, R.H., Howard, H.M., Kirkland, C.L., Wingate, M.T.D., Bodorkos, S., 2010. Devil in the detail; the 1150–1000 Ma magmatic and structural evolution of the Ngaanyatjarra Rift, west Musgrave Province, central Australia. *Precambrian Research* 183, 572–588.
- Ferriss, E.D.A., Essene, E.J., Becker, U., 2008. Computational study of the effect of pressure on the Ti-in-zircon geothermometer. *European Journal of Mineralogy* 20, 745–755.
- Ferry, J.M., Watson, E.B., 2007. New thermodynamic models and revised calibrations for the Ti-in-zircon and Zr-in-rutile thermometers. *Contributions to Mineralogy and Petrology* 154 (4), 429–437.
- Flament, N., Rey, P.F., Coltice, N., Dromart, G., Olivier, N., 2011. Lower crustal flow kept Archean continental flood basalts at sea level. *Geology* 39, 1159–1162.
- Flöttmann, T., Hand, M., Close, D., Edgoose, C., Scrimgeour, I.R., 2004. Thrust tectonic styles of the intracratonic Alice Springs and Petermann Orogenies, central Australia. In: McClay, K. (Ed.), *Thrust Tectonics and Hydrocarbon Systems*. American Association of Petroleum Geologists Memoir, pp. 538–557.
- Frost, B.R., Chamberlain, K.R., Schumacher, J.C., 2001. Sphene (titanite): phase relations and role as a geochronometer. *Chemical Geology* 172 (1–2), 131–148.
- Fu, B., Page, F.Z., Cavosie, A.J., Fournelle, J., Kita, N.T., Lackey, J.S., Wilde, S.A., Valley, J.W., 2008. Ti-in-zircon thermometry: applications and limitations. *Contributions to Mineralogy and Petrology* 156 (2), 197–215.
- Glikson, A.Y., Ballhaus, C.G., Clarke, G.L., Sheraton, J.W., Stewart, A.J., Sun, S.-S., 1995. Geological framework and crustal evolution of the Giles mafic–ultramafic complex and environs, western Musgrave Block, central Australia. *AGSO Journal of Australian Geology and Geophysics* 16, 41–67.
- Glikson, A.Y., Stewart, A.J., Ballhaus, C.G., Clarke, G.L., Feecken, E.H.J., Leven, J.H., Sheraton, J.W., Sun, S.-S., 1996. Geology of the western Musgrave Block, central Australia, with particular reference to the mafic–ultramafic Giles complex. *AGSO Bulletin* 239, 41–68.
- Goleby, B.R., Shaw, R.D., Wright, C., Kennett, B.L.N., Lambeck, K., 1989. Geophysical evidence for ‘thick-skinned’ crustal deformation in central Australia. *Nature* 337, 325–330.
- Gregory, C.J., Buick, I.S., Hermann, J., Rubatto, D., 2009. Mineral-scale trace element and U–Th–Pb age constraints on metamorphism and melting during the Petermann Orogeny (central Australia). *Journal of Petrology* 50 (2), 251–287.
- Hand, M., Sandiford, M., 1999. Intraplate deformation in central Australia, the link between subsidence and fault reactivation. *Tectonophysics* 305, 121–140.
- Howard, H.M., Smithies, R.H., Pirajno, F., Skwarnecki, M.S., 2006. Bates, W.A. Sheet 4646. Western Australia Geological Survey 1:100,000 Geological Series.
- Kinny, P.D., 1997. Users guide to U–Th–Pb dating of titanite, perovskite, monazite and baddeleyite using the W.A. SHRIMP, School of Physical Sciences. Curtin University of Technology, Perth, WA.
- Kinny, P.D., McNaughton, N.J., Fanning, C.M., Maas, R., 1994. 518 Ma sphene (titanite) from the Khan pegmatite, Namibia, southwest Africa: A potential ion-microprobe standard, Eighth International Conference on Geochronology, Cosmochronology and Isotope Geology

- Abstracts. Berkeley, US Geological Survey Circular 1107, p. 171.
- Kooijman, E., Mezger, K., Berndt, J., 2010. Constraints on the U-Pb systematics of metamorphic rutile from in situ LA-ICP-MS analysis. *Earth and Planetary Science Letters* 293 (3–4), 321–330.
- Korsch, R.J., Kositsin, N., 2010. GOMA (Gawler Craton–Officer Basin–Musgrave Province–Amadeus Basin) Seismic and MT Workshop 2010. *Geoscience Australia Record* 2010/39.
- Korsch, R.J., Goleby, B.R., Leven, J.H., Drummond, B.J., 1998. Crustal architecture of central Australia based on deep seismic reflection profiling. *Tectonophysics* 288, 57–69.
- Lambeck, K., Burgess, G., 1992. Deep crustal structure of the Musgrave Block, central Australia: results from teleseismic travel-time anomalies. *Australian Journal of Earth Sciences: An International Geoscience Journal of the Geological Society of Australia* 39, 1–19.
- Lindsay, J.F., Korsch, R.J., Wilford, J.R., 1987. Timing the breakup of a Proterozoic supercontinent: evidence from Australian intracratonic basins. *Geology* 15, 1061–1064.
- Ludwig, K.R., 2003. Users Manual for Isoplot/Ex, Version 3.00, A Geochronological Toolkit for Microsoft Excel. Berkeley Geochronology Centre, Berkeley, CA. Special Publication No.4.
- Ludwig, K.R., 2001. Users manual for Isoplot/Ex: a geochronological toolkit for Microsoft excel. Berkeley Geochronology Centre Special Publication No. 1a.
- Maboko, M.A.H., McDougall, I., Zeitler, P.K., Williams, I.S., 1992. Geochronological evidence for 530–550 Ma juxtaposition of two Proterozoic metamorphic terranes in the Musgrave Ranges, central Australia. *Australian Journal of Earth Sciences* 39, 457–471.
- Nelson, K.D., Zhao, W., Brown, L.D., Kuo, J., Che, J., Liu, X., Klemperer, S.L., Makovsky, Y., Meissner, R., Mechie, J., Kind, R., Wenzel, F., Ni, J., Nabelek, J., Leshou, C., Tan, H., Wei, W., Jones, A.G., Booker, J., Unsworth, M., Kidd, W.S.F., Hauck, M., Alsdorf, D., Ross, A., Cogan, M., Wu, C., Sandvol, E., Edwards, M., 1996. Partially molten middle crust beneath southern Tibet: synthesis of project INDEPTH results. *Science* 274, 1684–1688.
- Raimondo, T., Collins, A.S., Hand, M., Walker-Hallam, A., Smithies, R.H., Evins, P.M., Howard, H.M., 2009. Ediacaran intracontinental channel flow. *Geology* 37, 291–294.
- Raimondo, T., Collins, A.S., Hand, M., Walker-Hallam, A., Smithies, R.H., Evins, P.M., Howard, H.M., 2010. The anatomy of a deep intracontinental orogen. *Tectonics* 29, TC4024.
- Sandiford, M., 2002. Low thermal Peclet number intraplate orogeny in central Australia. *Earth and Planetary Science Letters* 201, 309–320.
- Sandiford, M., Hand, M., 1998. Controls on the locus of intraplate deformation in central Australia. *Earth and Planetary Science Letters* 162, 97–110.
- Sandiford, M., Hand, M., McLaren, S., 2001. Tectonic feedback, intraplate orogeny and the geochemical structure of the crust; a central Australian perspective. In: Miller, J.A., Holdsworth, R.E., Buick Ian, S., Hand, M. (Eds.), *Continental Reactivation and Reworking*. Geological Society, London.
- Scrimgeour, I.R., Close, D.F., 1999. Regional high-pressure metamorphism during intracratonic deformation: the Petermann Orogeny, central Australia. *Journal of Metamorphic Geology* 17, 557–572.
- Scrimgeour, I.R., Close, D.F., Edgoose, C.J., 1999. Petermann Ranges, N.T. 1:250,000 Geological Series. Department of Mines and Energy, Northern Territory Geological Survey. Explanatory Notes SG52-7.
- Smithies, R.H., Howard, H.M., Evins, P.M., Kirkland, C.L., Kelsey, D.E., Hand, M., Wingate, M.T.D., Collins, A.S., Belousova, E., 2011. High-temperature granite magmatism, crust–mantle interaction and the Mesoproterozoic intracontinental evolution of the Musgrave Province, central Australia. *Journal of Petrology* 52, 931–958.
- Stacey, J.S., Kramers, J.D., 1975. Approximation

- of terrestrial lead isotope evolution by a two-stage model. *Earth and Planetary Science Letters* 26, 207–221.
- Stephenson, R., Egholm, D.L., Nielsen, S.B., Stovba, S.M., 2009. Role of thermal refraction in localizing intraplate deformation in southeastern Ukraine. *Nature Geosci* 2 (4), 290–293.
- Stern, R., 2001. A new isotopic and trace-element standard for the ion-microprobe: preliminary thermal ionisation mass spectrometry (TIMS) U–Pb and electron microprobe data. *Geological Survey of Canada Current Research* 2001-F1, 11 pages.
- Sun, S.-S., Sheraton, J.W., Glikson, A.Y., Stewart, A.J., 1996. A major magmatic event during 1050–1080 in central Australia and an emplacement age for the Giles Complex. *AGSO Research Newsletter* 17, 9–10.
- Taylor, R., Clark, C., Reddy, S.M., 2012. The effect of grain orientation on secondary ion mass spectrometry (SIMS) analysis of rutile. *Chemical Geology* 300–301, 81–87.
- Van Achtebergh, E., Ryan, C.G., Jackson, S.E., Griffin, W.L., 2001. Data reduction software for LA–ICPMS. *Laser-Ablation–ICPMS in the Earth Sciences; Principles and Applications*. Mineralogical Association of Canada, Ottawa, ON, Canada.
- Wade, B.P., Kelsey, D.E., Hand, M., Barovich, K.M., 2008. The Musgrave Province; stitching north, west and south Australia. *Precambrian Research* 166, 370–386.
- Walter, M.R., Veevers, J.J., Calver, C.R., Grey, K., 1995. Neoproterozoic stratigraphy of the Centralian Superbasin, Australia. *Precambrian Research* 73, 173–195.
- Watson, E.B., Wark, D.A., Thomas, J.B., 2006. Crystallization thermometers for zircon and rutile. *Contributions to Mineralogy and Petrology* 151, 413–433.
- White, R.W., Clarke, G.L., 1997. The role of deformation in aiding recrystallization: an example from a high-pressure shear zone, central Australia. *Journal of Petrology* 38, 1307–1329.
- White, R.W., Clarke, G.L., Nelson, D.R., 1999. SHRIMP U–Pb zircon dating of Grenville-age events in the western part of the Musgrave Block, central Australia. *Journal of Metamorphic Geology* 17, 465–481.
- White, R.W., Powell, R., Clarke, G.L., 2002. The interpretation of reaction textures in Fe-rich metapelitic granulites of the Musgrave Block, central Australia: constraints from mineral equilibria calculations in the system K<sub>2</sub>O–FeO–MgO–Al<sub>2</sub>O<sub>3</sub>–SiO<sub>2</sub>–H<sub>2</sub>O–TiO<sub>2</sub>–Fe<sub>2</sub>O<sub>3</sub>. *Journal of Metamorphic Geology* 20, 41–55.
- Williams, I.S., 1998. U–Th–Pb geochronology by ion microprobe. *Reviews in Economic Geology* 7, 1–35.
- Zhao, J.X., 1994. Geochemical and Sm–Nd isotopic study of amphibolites in the southern Arunta Inlier, central Australia: evidence for subduction at a Proterozoic continental margin. *Precambrian Research* 65, 71–94.





# Chapter 3

This chapter is submitted as:

Walsh, A. K., Hand, M. & Kelsey, D. E., 2014. A metamorphic perspective on foreland flexure during intraplate orogeny: evidence for the involvement of weak lithosphere. *Terra Nova*.



---

# A metamorphic perspective on foreland flexure during intraplate orogeny: evidence for the involvement of weak lithosphere.

---

## ABSTRACT

Constraining depth–temperature conditions of syn-orogenic burial metamorphism of syn-orogenic sediments in a foreland basin provides an innovative way to investigate the thermomechanical state of lithosphere. In central Australia, major intraplate deformation resulted in 10 km of synorogenic sedimentation in a basin approximately 70 km wide. The deep level of burial in the foreland of the intraplate orogen requires the involvement of weak lithosphere with an elastic thickness of  $\leq 20$  km. The profound flexural response of the foreland region indicates that major intraplate deformation in central Australia was localised into a region of dramatically weakened lithosphere.

---

## 1. INTRODUCTION

Crustal thickening associated with development of fold-thrust belts creates loads on the lithosphere that cause isostatic subsidence (Jordan, 1981; Flemings & Jordan, 1990; Watts, 2001). The depressions, which form away from the load due to the finite flexural rigidity of the lithosphere, represent the accommodation space where foreland basins develop (Beaumont, 1981; Jordan, 1981; Simpson, 2006).

A deep, narrow foreland basin requires lithosphere that has low flexural rigidity or low elastic thickness ( $T_e$ ) e.g. Focşani Depression, Carpathians (Tărăpoancă, *et al.*, 2003; Tărăpoancă, *et al.*, 2004), whereas a broad, shallow basin will develop in stronger lithosphere that has a higher flexural rigidity (Watts, 1992). Low flexural rigidity or  $T_e$  values may be associated with elevated regional temperatures (Hyndman, *et al.*, 2009). Therefore constraining the shape and burial of foreland basins, and their immediately adjacent hinterland provides information about the rheology and thermal regime of the lithosphere at an orogenic scale.

In this paper we document the deep burial of syn-orogenic sediments deposited in the proximal foreland to the intraplate Petermann Orogen in central Australia. This deep burial of the foreland region points to the involvement of weak lithosphere during intraplate orogeny, and unambiguously resolves debate about

the thermomechanical state of Australia's intraplate orogenic lithosphere.

## 2. GEOLOGICAL SETTING

The Ediacaran to Cambrian Petermann Orogeny (Fig. 1) was a major intraplate event that shaped the geophysical architecture of southern central Australia. It forms a  $>1000$  km long E-W trending transpressive belt that is characterised by high-pressure, near eclogite-facies (10–14 kbar; approx. 45 km) metamorphism (Ellis & Maboko, 1992; Camacho *et al.*, 1997; Scrimgeour & Close, 1999) and the development of  $>100$  km-scale basement-cored nappes and thick-skinned thrust sheets that transported the orogenic core toward the foreland (Flöttmann *et al.*, 2004). Sequential cross-section restorations indicate that north-directed shortening during the Petermann Orogeny exceeded  $\sim 150$  km and was accommodated by significant, but unquantified crustal thickening (Flöttmann *et al.*, 2004; Aitken *et al.*, 2009). Exhumation of the deep crust and upper mantle during the Petermann Orogeny produced one of the largest known gravity gradients ( $\sim 150$  mgal) within continental interiors (Lambeck *et al.*, 1988; Aitken *et al.*, 2009).

There are differing views on the thermomechanical state of the central Australian lithosphere during early Palaeozoic intraplate orogeny. Korsch *et al.* (1998) considered it a type example of deformation within strong

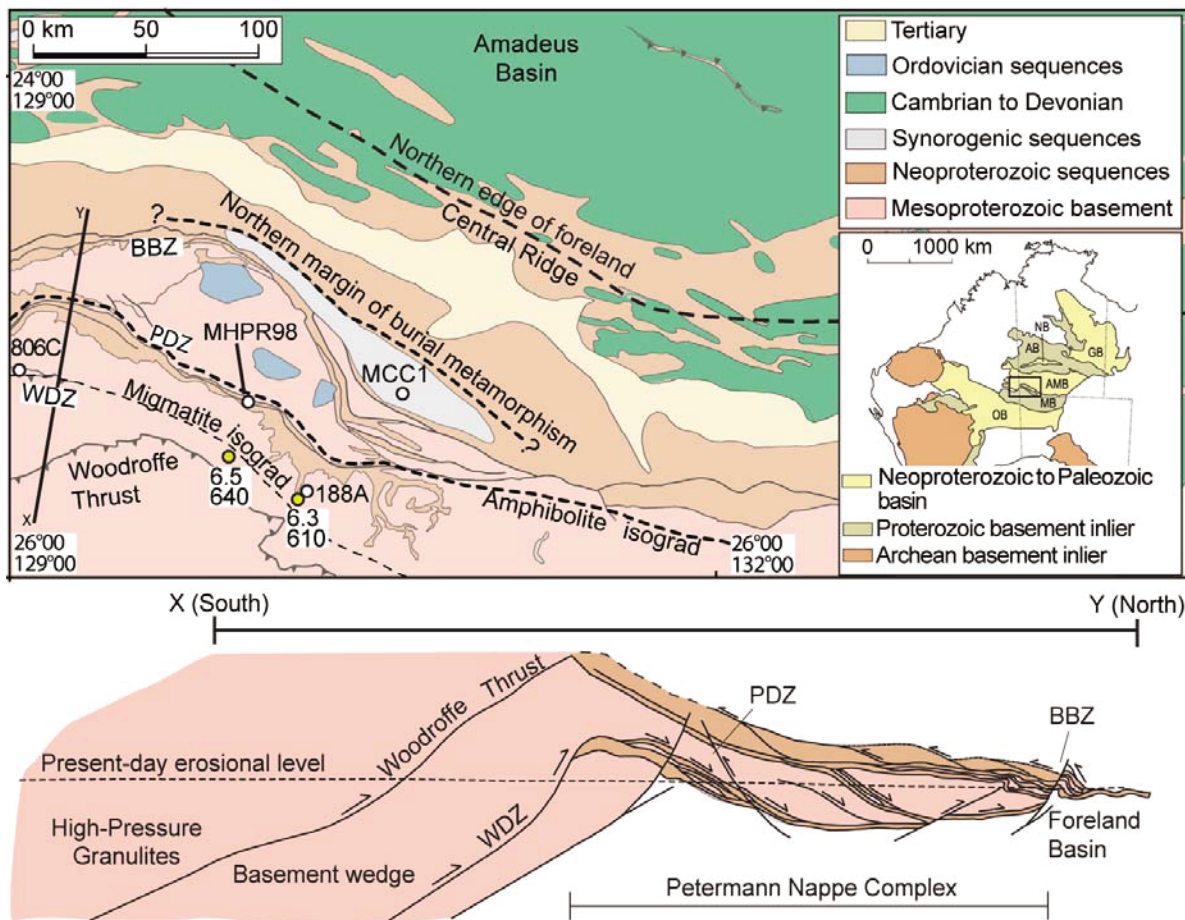


**Figure 1.** Simplified solid geology map of the fold-thrust belt and foreland basin system of the Petermann Orogen. P–T estimates (yellow circles) of metamorphism during the Petermann Orogeny are from Scrimgeour and Close (1999). Metamorphic isograds adapted from Scrimgeour and Close (1999). Sample locations of this study are shown by white circles. Northern extent of foreland basin is adapted from Korsch and Lindsay (1989). WDZ–Wankari Detachment Zone; PDZ–Piltardi Detachment Zone; BBZ–Bloods Back-thrust Zone. Inset: Intraplate basins and basement inliers in central and western Australia. AB–Arunta block, AMB–Amadeus Basin, GB–Georgina Basin, MB–Musgrave Block, NB–Ngalia Basin, OB–Officer Basin.

cold lithosphere. Similarly Camacho et al. (2001; 2002; 2009) argued that intraplate deformation was short-lived and occurred within cold crust. These views are in line with present day estimates of the elastic thickness of the central Australian region (e.g. Zuber et al., 1989; Simons et al., 2000; Swain & Kirby, 2006). In contrast, Sandiford & Hand (1998); Raimondo et al. (2009; 2010) and Walsh et al. (2013) suggested that intraplate deformation was long-lived and occurred within thermally weakened lithosphere. However, it is possible that divergent views reflect the varying deformational responses to intraplate stresses

during the Petermann Orogeny. The western part of the orogen records pervasive high-temperature metamorphism ( $\sim 700^\circ\text{C}$ , 10–14 kbar) and migmatitisation during channelised flow and development of a large nappe complex in the foreland (Scrimgeour & Close, 1999; Flöttmann et al., 2004; Raimondo et al., 2009; Raimondo et al., 2010; Walsh et al., 2013). In contrast, the eastern part of the orogen is characterised by comparatively discrete deformation where high-temperature metamorphism ( $\sim 700^\circ\text{C}$ , 12 kbar) is recorded in shear zones by the resetting of low-temperature isotopic systems (Maboko et



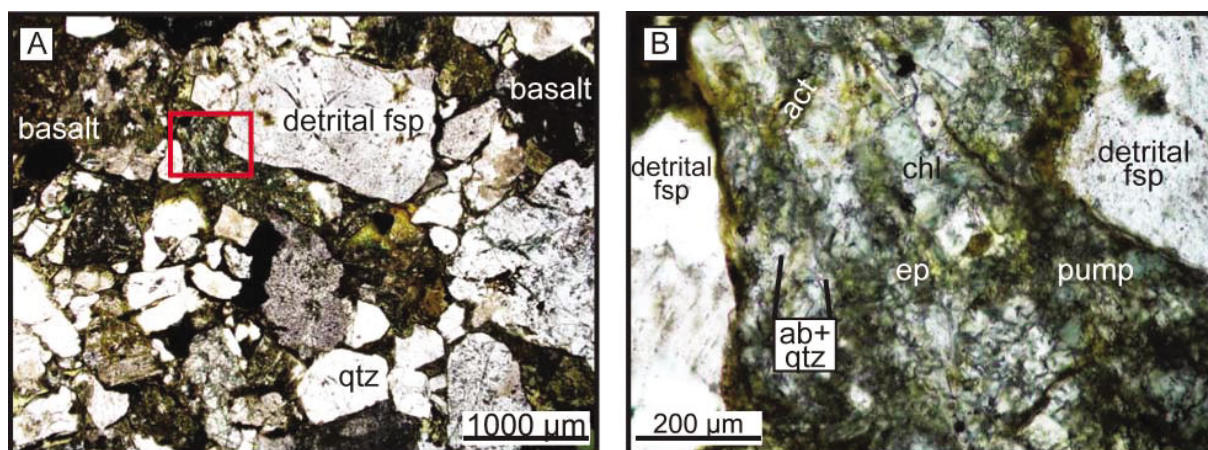


**Figure 2.** Thin section photos of the Mt Currie Conglomerate sample MCC1. A) Sedimentary nature of the conglomerate is shown by coarse-grained (~1 cm), angular to sub-angular detrital quartz and feldspar grains as well as clasts of basalt, separated by a fine-grained metamorphic matrix. Box refers to area of b. B) Fine-grained metamorphic assemblage of actinolite, epidote, pumpellyite, chlorite, feldspar and quartz occurs interstitially between grains/clasts of quartz, feldspar and basalt.

al., 1992; Camacho et al., 1997; Camacho et al., 2001). The absence of thick foreland successions or nappe development that requires basement–cover interaction indicates the degree of foreland development in the eastern part of the orogen is comparatively limited. Thermal heterogeneities, advection of fluids, strain softening or compositional variation could have contributed to the distribution of lithospheric weakening and subsequent deformation during the Petermann

orogeny (Raimondo et al., 2014).

Rather than focus on the orogen itself, another way to evaluate the mechanical state of lithosphere during deformation is to examine the response to orogenic loading that is recorded in the foreland region. The northern foreland of the orogen is well preserved; with a thick-skinned fold-thrust belt and a locally well exposed foreland basin succession (Fig. 1). In the fold thrust belt, late Mesoproterozoic sedimentary units and volcanics that are

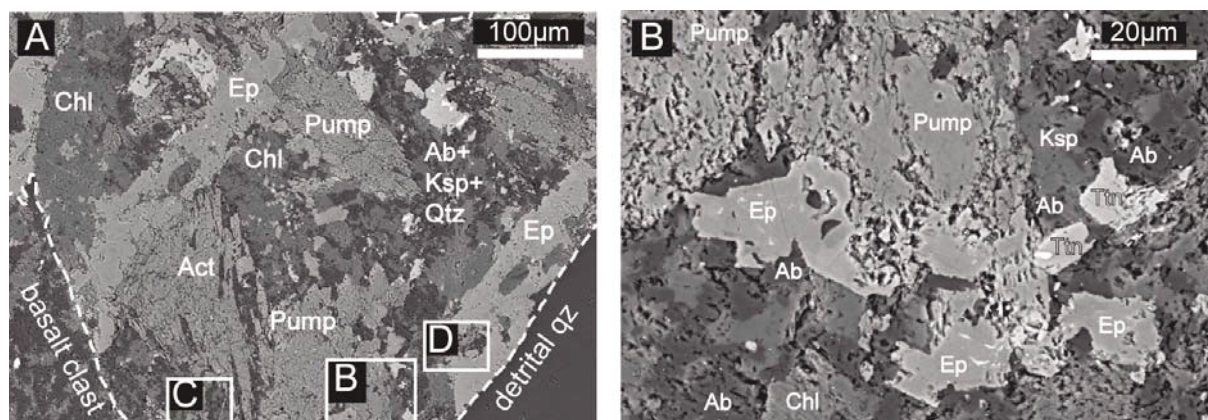


**Figure 3.** Back-scattered-electron (BSE) images collected on a Scanning Electron Microscope (SEM). A) Metamorphic mineral assemblage of chlorite–actinolite–pumpellyite–epidote–albite(ab)–quartz–titanite(ttn)–K-feldspar; developed interstitially between a basaltic clast (bottom left) and a detrital quartz grain (bottom right). Area used for bulk composition of sample MCC1 is effectively the interstitial region shown. Boxes B, C and D refer to Figs. 3b and Supplementary Figure 1a–b. B) Clots of pumpellyite in contact with epidote, titanite, potassium feldspar and plagioclase.



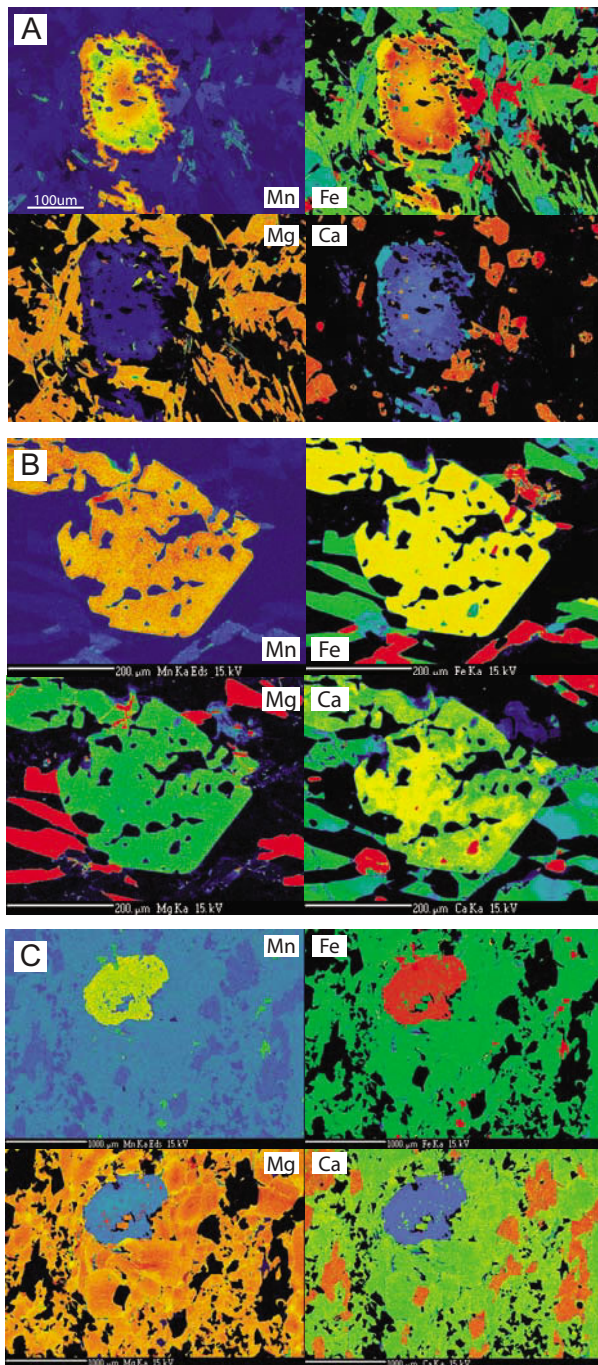


**Figure 4.** X-ray element maps collected on a Cameca SX-Five Electron Microprobe. Maps for manganese, iron, magnesium and calcium are presented for A) 188A; B) 806C and; C) MHPR98. Maps are used to estimate mineral proportions for the calculation of bulk compositions for metamorphic forward modelling.

overlain by early Neoproterozoic sequences belonging to the Amadeus Basin (Walter et al., 1995; Lindsay & Leven, 1996) are structurally imbricated with Mesoproterozoic granitic rocks produced during Grenvillian-aged orogenesis (Scrimgeour et al., 1999; Edgoose et al., 2004; Flöttmann et al., 2004). Metamorphism of these sedimentary units during the Petermann Orogeny reached amphibolite facies and produced locally coarse-grained kyanite. Within granitic units are mafic dykes that cross-cut the gneissic fabric (Zhao & McCulloch, 1993; Evins et al., 2010) and developed metamorphic garnet-bearing assemblages.

The foreland basin succession comprises coarse to extremely coarse-grained (up to 1m) conglomerate comprising clasts of well-rounded Mesoproterozoic granite, mafic and felsic volcanics, and Neoproterozoic sedimentary rocks derived from the orogen to the south (Wells et al., 1970; Camacho et al., 2002; Young et al., 2002; Sweet et al., 2012). The contact with the underlying successions is not exposed. However, the absence of high-grade metamorphic clasts (Young et al., 2002; Sweet et al., 2012), which characterise the exposed orogenic hinterland, suggests that the exposed foreland was deposited before deep denudation of the orogen had commenced and therefore it lies toward the base of the foreland-basin succession. The foreland basin succession is up to 6000 m thick (Sweet et al., 2012) and it has a preserved width of ~30 km, estimated to have been approximately 70 km in width based on onlap relationships (Lambeck, 1984; Korsch & Lindsay, 1989; Shaw et al., 1991). Despite the obviously sedimentary character of the syn-orogenic sequences, they are exceptionally lithified, with extensive development of epidote-bearing assemblages. In places the matrix of the conglomerate contains a metamorphic assemblage consisting of quartz-albite-epidote-actinolite-chlorite (Wells et al., 1970; Edgoose et al., 2004). The conglomerate is unconformably overlain by unmetamorphosed late-Cambrian–Ordovician sequences (Wells et al., 1970; Young et al., 2002), implying

	SiO <sub>2</sub>	TiO <sub>2</sub>	Al <sub>2</sub> O <sub>3</sub>	FeO	MnO	MgO	CaO	Na <sub>2</sub> O	K <sub>2</sub> O	H <sub>2</sub> O	O
MCC1	60.50	0.74	10.77	4.90	–	7.12	10.48	2.80	1.65	excess	1.00
188A	58.19	0.50	7.55	7.88	1.60	8.84	3.50	0.38	2.44	8.07	2.65
806C	62.73	1.25	9.64	8.18	0.63	7.81	5.42	1.91	1.37	excess	1.05
MHPR98	43.27	0.97	16.10	10.64	0.28	5.79	9.30	1.20	–	5	0.61

**Table 1.** Bulk compositions used for P–T pseudosection calculations in wt% oxides.

that burial occurred during the Petermann Orogeny. The apparent metamorphism of the syn-orogenic sediments near the base of the foreland basin provides an excellent opportunity to constrain the approximate basin thickness during intraplate orogenesis. Together with the metamorphosed sequences within the foreland fold-thrust belt, the metamorphism of the foreland region provides an avenue to evaluate the extent of lithospheric flexure during intraplate orogeny.

### 3. METAMORPHIC CONSTRAINTS ON BURIAL IN THE PETERMANN OROGENIC FORELAND

Bulk compositions for metamorphic modelling were determined by the combination of point counting and EMPA (Fig. 4, Supplementary Table. 1) and are presented in Table 1. P–T pseudosections were calculated using Theriak-Domino (De Capitani & Petrakakis, 2010) using the internally consistent thermodynamic dataset of Holland & Powell (1998; dataset tcds55 November 2003 update), compiled as tcd55c2d.bs for use in Theriak-Domino, and the most recently available a–x models: garnet (White et al., 2005), biotite (White et al., 2007), spinel and magnetite (White et al., 2002), K-feldspar and plagioclase (Holland & Powell, 2003), amphibole (Diener et al., 2007) and ilmenite (White et al., 2000). Samples MCC1, 188A and 806C used in this study were collected during regional geological survey work undertaken by Geoscience Australia and the Northern Territory Geological Survey (Scrimgeour et al., 1999; Young et al., 2002).

GPS coordinates for sample locations are presented in Table 2.

Sample MCC1 is a comparatively fine-grained sample of the syn-orogenic conglomerate. It contains angular fragments of fine-grained basalt, felsic volcanic as well as detrital K-feldspar and quartz (Fig. 2a). The matrix contains ubiquitous fine-grained epidote–chlorite–titanite with spatially variable sub-assemblages that contain some or all of actinolite, albite, quartz and pumpellyite (Fig. 2b). Metamorphic minerals commonly form small monomineralic clusters of ~50–200 microns (Fig. 3a). Fine-grained clots of pumpellyite occur predominantly in contact with epidote, albite and K-feldspar (Fig. 3b). A small region of the matrix containing the full assemblage chlorite–epidote–actinolite–pumpellyite–albite–K-feldspar–titanite–quartz + H<sub>2</sub>O was chosen for metamorphic forward modelling (Fig. 3a). For the modelled bulk composition, the matrix assemblage occurs at 2.6–4.1 kbar and 205–260 °C (Fig. 5a). Compositional isopleths for epidote  $Y(ep)=Al_3+$  p.f.u and chlorite  $X(chl)=Fe/Fe+Mg$  further constrain P–T conditions to 3.3–3.9 kbar and 205–220 °C (Fig. 5a).

Foreland Fold-Thrust Belt samples

Sample 188A is recrystallised Mesoproterozoic granite with a Sm–Nd garnet age of  $550 \pm 11$  Ma (Edgoose et al., 2004). It contains a metamorphic assemblage of biotite–garnet–epidote–plagioclase–hematite–quartz. This assemblage is modelled to occur between 500–560 °C and pressures of 4–7.5 kbar. The measured compositions of garnet rims further constrain the P–T conditions to 520–540 °C



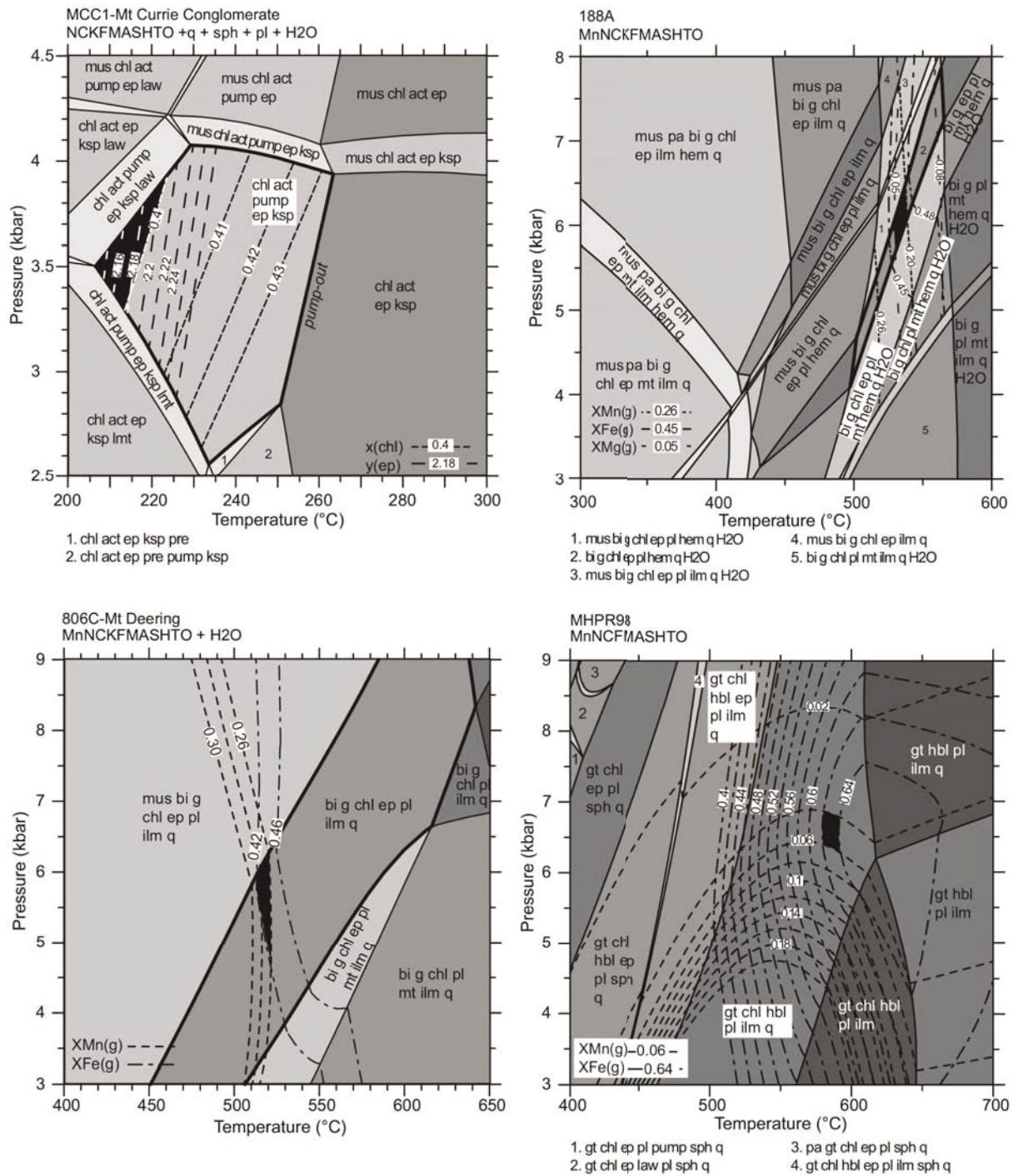


**Figure 5.** P-T pseudosections. A) NCKFMASHTO pseudosection for sample MCC1. Metamorphic assemblage of chlorite (chl)–actinolite (act)–pumpellyite (pump)–epidote (ep)–albite (pl)–quartz (q)–titianite (sph)–K-feldspar (ksp) + H<sub>2</sub>O is calculated to occur in the range 2.6–4.1 kbar and 205–260 °C. Peak field is contoured with isopleths of  $X(\text{chl}) = \text{Fe}/(\text{Fe}^{2+} + \text{Mg}^{2+})$  and  $Y(\text{ep}) = \text{Al}^{3+}$  per formula unit (p.f.u), which constrain P–T range to 3.3–3.8 kbar and 205–220 °C (black region) based on measured values of  $X(\text{chl}) = 0.39\text{--}0.40$  and  $Y(\text{ep}) = 2.16\text{--}2.19$ . B) MnNCKFMASHTO pseudosection for sample 188A. Interpreted peak assemblage of biotite (bi)–garnet (g)–chlorite–epidote–plagioclase–hematite (hem)–quartz (+H<sub>2</sub>O) is calculated to occur in the range 500–560 °C and pressures of 4–7.5 kbar. The measured compositions of  $X_{\text{spss}} = 0.20\text{--}0.26$ ,  $X_{\text{alm}} = 0.45\text{--}0.48$  and  $X_{\text{py}} = 0.05\text{--}0.08$  further constrain the P–T conditions to 520–540 °C and 5.6–6.5 kbar (black region). C) MnNCKFMASHTO pseudosection for sample 806C. Interpreted metamorphic assemblage is biotite–garnet–chlorite–epidote–plagioclase–



ilmenite (ilm)–quartz (+ H<sub>2</sub>O) is calculated to be stable at 450–600 °C and unconstrained pressures. Measured  $X_{\text{spss}} = 0.26\text{--}0.30$  and  $X_{\text{alm}} = 0.42\text{--}0.46$  compositions constrain the P–T conditions to between 500–530°C and 5–6 kbar (black region). D) MnNCFMASHTO pseudosection for sample MHPR98. Interpreted metamorphic assemblage of garnet–chlorite–hornblende (hbl)–plagioclase–ilmenite–quartz (+ H<sub>2</sub>O). This assemblage is calculated to occur at 450–600 °C and unconstrained pressures. The measured compositions of  $X_{\text{spss}} = 0.04\text{--}0.06$  and  $X_{\text{alm}} = 0.62\text{--}0.64$  constrain P–T conditions to 580–610 °C and 6.5–7 kbar (black region).  $X_{\text{alm}} = X_{\text{Fe}} / (X_{\text{Fe}} + X_{\text{Mg}} + X_{\text{Mn}} + X_{\text{Ca}})$ ;  $X_{\text{spss}} = X_{\text{Mn}} / (X_{\text{Fe}} + X_{\text{Mg}} + X_{\text{Mn}} + X_{\text{Ca}})$ ;  $X_{\text{grs}} = X_{\text{Ca}} / (X_{\text{Fe}} + X_{\text{Mg}} + X_{\text{Mn}} + X_{\text{Ca}})$ ;  $X_{\text{py}} = X_{\text{Py}} / (X_{\text{Fe}} + X_{\text{Mg}} + X_{\text{Mn}} + X_{\text{Ca}})$ ;  $\text{Fe\#} = X_{\text{Fe}} / (X_{\text{Fe}} + X_{\text{Mg}})$ .

and 5.6–6.5 kbar (Fig. 5b).

Sample 806C from the Mt Deering area (Fig. 1) comes from the Tjauwata Group sediments and volcanoclastics that overlie Mesoproterozoic granite basement which were unmetamorphosed clastics prior to the Petermann Orogeny (Scrimgeour et al., 1999; Edgoose et al., 2004). The metamorphic assemblage is biotite–garnet–chlorite–epidote–plagioclase–ilmenite–quartz + H<sub>2</sub>O. This assemblage is calculated to be stable at 450–600 °C and unconstrained pressures. Measured garnet compositions constrain P–T conditions to between 500–530°C and 5–6 kbar (Fig. 5c).

Sample MHPR98 is recrystallised Mesoproterozoic granite from the Piltardi Detachment Zone (Fig. 1) and contains the metamorphic assemblage garnet–chlorite–hornblende–plagioclase–ilmenite–quartz. This assemblage is calculated to occur at 450–600 °C and unconstrained pressures. The measured garnet compositions constrain P–T conditions to 580–610 °C and 6.5–7 kbar (Fig. 5d).

#### 4. DISCUSSION

The metamorphic evidence from the Petermann Nappe Complex and the Mt Currie Conglomerate indicate that they were deeply

Sample	Zone (UTM)	Northing	Easting
MCC1	52J	7202009	674182
188A	52J	7168068	622150
806C	52J	7221596	498368
MHPR98	52J	7213467	590578

**Table 2.** GPS locations for samples in this study.

buried. Pressures of 5–7 kbar in the Petermann Nappe Complex imply burial to depths of at least 15 km, consistent with the presence of coarse-grained kyanite in the (meta)sedimentary sequences and with previous estimates of P–T conditions within the fold-thrust belt (Scrimgeour & Close, 1999; Edgoose et al., 2004). Although sequences in the Petermann Nappe Complex may have resided at depth prior to orogeny, significant crustal thickening and mechanical interleaving of basement–cover sequences suggests lithospheric strength was low, albeit unquantifiable. In contrast, burial of the syn-orogenic conglomerate must have occurred during orogeny. Crustal thickening of 15–20 km accompanying at least 150 km of shortening in the north-western foreland fold-thrust belt (Flöttmann et al., 2004) suggests that loading of the foreland due to crustal thickening appears the most plausible burial mechanism. The metamorphic pressure range of 3.3–3.9 kbar from the syn-orogenic conglomerate corresponds to burial of the foreland basin sequence to at least 10 km. The location of the forebulge at approximately 70 km from the southern basin margin (Lambeck, 1984; Korsch & Lindsay, 1989; Shaw et al., 1991) constrains the width of Mt Currie sub-basin. The absence of gravity data of the northern Musgrave Province prevents the comparison of a more accurate foreland basin shape with flexural forward modelling. Nevertheless, considering the depth estimates from metamorphic mineral assemblage analysis i.e. the only dataset available to assess the degree of flexure in this ancient foreland basin, our results are significant. Simple 1D modelling was performed to

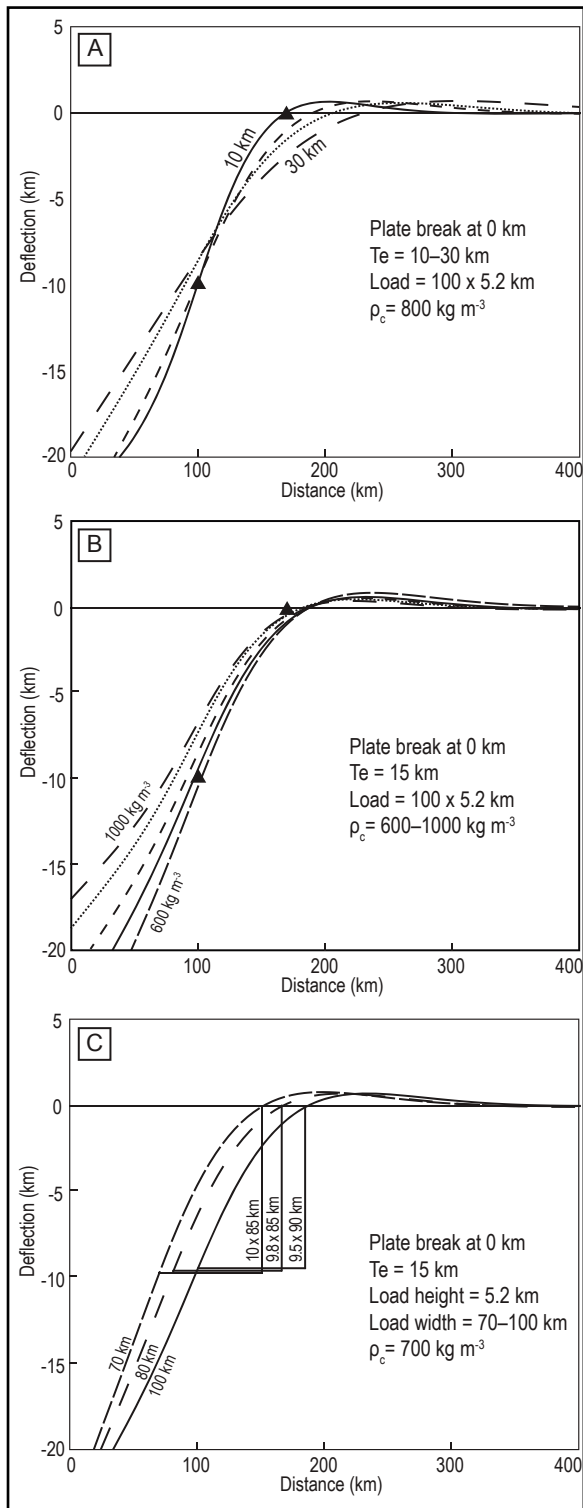


**Figure 6.** A) Flexural curves for  $T_e = 10, 15, 20$  and  $30$  km with a load distributed from  $x=0$  to  $100$  km on a broken plate with a density contrast of  $800 \text{ kg m}^{-3}$ . B) Flexural curves for  $T_e = 15$  km with a load distributed from  $x=0$  to  $100$  km on a broken plate with varying density contrast between  $600$  and  $1000 \text{ kg m}^{-3}$ . C) Flexural curves for  $T_e = 15$  km with a varying load width from  $70$  to  $100$  km on a broken plate with a density contrast of  $700 \text{ kg m}^{-3}$ .

m-3. Approximated best fit values are  $T_e = 15$  km,  $\rho_c = 700 \text{ kg m}^{-3}$  for a 2-D load of  $5200 \text{ m}^2$ .

determine the effective elastic thickness of lithosphere during loading and foreland basin development (Fig. 6). Flexural rigidity, density contrast, load size and infill density values were varied (Table 3), using a broken plate model to produce a flexural curve which best reproduces the measured basin dimensions.

The results show that an effective elastic thickness (EET) of approximately  $10$  km best reproduces the basin dimensions given the estimated density contrast and load size (Fig. 6). EET values up to  $20$  km can reproduce the basin shape although density contrast, flexural moment and load sizes become increasingly inconsistent with estimated values (Fig. 6). Inelastic yielding results in an unquantifiable amount of deformation, as a result EET values could be up to  $50\%$  lower (e.g. Burov, 2011) and a value of  $10$  km would be unrealistically low. In addition, for EET values approaching  $10$  km, lithosphere is unlikely to preserve mechanical integrity and would be in plate-breakup state (Burov, 2011). In absence of more thorough parametric analysis, EET values approaching  $20$  km are considered more appropriate and are consistent with the thick-skinned style of the foreland fold-thrust belt (Mouthereau et al., 2013). EET values  $\leq 20$  km are much lower than predicted for the elastic thickness of typical cratonic interiors (Watts, 1992; Hyndman et al., 2009; Audet & Bürgmann, 2011; Burov, 2011), and are significantly lower than the present day value inferred for central Australia (Zuber et al., 1989; Simons et al., 2000; Swain & Kirby, 2006).

The flexural response of the foreland implies that orogenesis was localised and developed in a region of very weak intraplate lithosphere. This view contrasts with suggestions (e.g. Korsch et al., 1998; Camacho et al., 2002) that the Petermann Orogen lithosphere was cold and strong, and is instead consistent with Sandiford & Hand (1998) and Raimondo et al. (2014) who suggested that intraplate deformation in central Australia was localised into a weakened region of lithosphere.

Density of Mantle ( $\rho_m$ )	3300 gm <sup>-3</sup>
Density of infilling sediments ( $\rho_i$ )	2300–2800 gm <sup>-3</sup>
Density of load	2700 gm <sup>-3</sup>
Elastic thickness ( $T_e$ )	10–30 km
Young's Modulus (E)	1x10 <sup>11</sup> Pa
Poisson's ratio	0.25

**Table 3.** Parameters for flexural modelling. Elastic thickness and density of infilling sediments are varied between models. Initial density of infilling sediments is 2500 gm<sup>-3</sup>.

The absence of significant fold-thrust belt and basin development in the foreland to the eastern part of the orogen suggests that weakening and deformation may have been initially localised in the western part of the orogen. This is consistent with comparatively pervasive high-temperature metamorphism (~700 °C, 10–14 kbar) and deformation via channelized flow during the earliest recorded stages of orogenesis > 570 Ma (Raimondo et al., 2009; Raimondo et al., 2010) and the development of the Petermann Nappe Complex (Flöttmann et al., 2004).

The mechanisms that led to lithospheric weakening are not clear, nor are the reasons why lithosphere appears to have become comparatively strong in the immediate aftermath of orogeny, as suggested by the shifting patterns of intraplate deformation and the preservation of extreme gravity gradients (Sandiford & Hand, 1998; Raimondo et al., 2014). One possible explanation is that the unusual distribution of heat production in the central Australian crust resulted in extreme thermomechanical sensitivity to burial and erosion (Sandiford et al., 2001).

Grenvillian-aged mid-crustal granites from the Petermann Nappe Complex (Fig. 1) and south of the Woodroffe Thrust in the western part of the orogen have average heat production values of  $4.13 \pm 0.55$  mW m<sup>-3</sup> (n=58) and 4.3 mW m<sup>-3</sup> respectively, at 575 Ma (Sandiford et al., 2001; Sandiford & McLaren, 2002). These values are ~40 % higher than average granite, and significantly higher than sedimentary sequences which overlie the Petermann Nappe

Complex. In contrast, average heat production in the deep crust is  $0.911 \pm 0.06$  mW-3 (n=430), implying that the heat production maxima was contained in mid–upper crustal basement granites. Therefore the presence of large high-heat producing granitic suites, might have caused long-term crustal heating of ~ 50 °C (Sandiford & McLaren, 2002) in regions of emplacement and promoted localised weakening in the western part of the orogen. This could suggest that orogeny was initiated in these weak regions with widespread orogeny occurring subsequently.

As a consequence of the stratification of the crustal heat production, denudation during the early stages of orogenesis would have removed the high-heat producing mid–upper crust of the orogenic lithosphere. Therefore, as erosion progressed, the lithosphere would have been dominated by an anhydrous, low heat-producing lower crust, resulting in a dramatic reduction in lithospheric heat production and an increase in lithospheric strength. Redistribution of orogenic heat production may have led to the development of strong orogenic lithosphere and facilitated the post-orogenic preservation of large gravitational gradients.

## 5. CONCLUSIONS

The Petermann Orogeny in Central Australia was a major intraplate contractional event that exhumed rocks from depths of up to 45 km. Syn-orogenic sediments deposited in the narrow foreland basin to the orogen underwent

burial metamorphism producing mineral assemblages that require rapid burial to depths of at least 10 km. This exceptionally deeply flexed and narrow foreland basin required the existence of very weak lithosphere during intraplate orogeny. Subsequent to orogeny, the lithosphere strengthened, perhaps as a result of erosional redistribution of the crustal heat production as orogenic denudation proceeded.

## ACKNOWLEDGEMENTS

Thanks are due to Dorothy Close and Ian Scrimgeour (Northern Territory Geological Survey) and Geoscience Australia for providing legacy samples used in this study. Thanks to two anonymous reviewers whose input improved this article significantly. Research was funded by ARC LP100200127.

## REFERENCES

- Aitken, A. R. A., Betts, P. G., Weinberg, R. F. & Gray, D., 2009. Constrained potential field modeling of the crustal architecture of the Musgrave Province in central Australia: Evidence for lithospheric strengthening due to crust-mantle boundary uplift. *Journal of Geophysical Research B: Solid Earth*, **114**(12).
- Audet, P. & Bürgmann, R., 2011. Dominant role of tectonic inheritance in supercontinent cycles. *Nature Geoscience*, **4**(3), 184-187.
- Beaumont, C., 1981. Foreland basins. *Geophysical Journal of the Royal Astronomical Society*, **65**(2), 291-329.
- Burov, E. B., 2011. Rheology and strength of the lithosphere. *Marine and Petroleum Geology*, **28**(8), 1402-1443.
- Camacho, A., Compston, W., McCulloch, M. & McDougall, I., 1997. Timing and exhumation of eclogite facies shear zones, Musgrave Block, central Australia. *Journal of Metamorphic Geology*, **15**(6), 735-751.
- Camacho, A., Hensen, B. J. & Armstrong, R., 2002. Isotopic test of a thermally driven intraplate orogenic model, Australia. *Geology*, **30**(10), 887-890.
- Camacho, A., McDougall, I., Armstrong, R. & Braun, J., 2001. Evidence for shear heating, Musgrave Block, central Australia. *Journal of Structural Geology*, **23**(6-7), 1007-1013.
- Camacho, A., Yang, P. & Frederiksen, A., 2009. Constraints from diffusion profiles on the duration of high-strain deformation in thickened crust. *Geology*, **37**(8), 755-758.
- De Capitani, C. & Petrakakis, K., 2010. The computation of equilibrium assemblage diagrams with Theriak/Domino software. *American Mineralogist*, **95**(7), 1006-1016.
- Edgoose, C. J., Scrimgeour, I. R. & Close, D. F., 2004. Geology of the Musgrave Block, Northern Territory. *Northern Territory Geological Survey. Report 15*.
- Ellis, D. J. & Maboko, M. A. H., 1992. Precambrian tectonics and the physiochemical evolution of the continental crust. Part I: The gabbro-eclogite transition. *Precambrian Research*, **55**, 491-506.
- Evins, P. M., Smithies, R. H., Howard, H. M., Kirkland, C. L., Wingate, M. T. D. & Bodorkos, S., 2010. Devil in the detail: The 1150–1000 Ma magmatic and structural evolution of the Ngaanyatjarra Rift, west Musgrave Province, Central Australia. *Precambrian Research*, **183**(3), 572-588.
- Flemings, P. B. & Jordan, T. E., 1990. Stratigraphic modeling of foreland basins: Interpreting thrust deformation and lithosphere rheology. *Geology*, **18**(5), 430-434.
- Flöttmann, T., Hand, M., Close, D., Edgoose, C. & Scrimgeour, I. R., 2004. Thrust tectonic styles of the intracratonic Alice Springs and Petermann Orogenies, central Australia. in *Thrust tectonics and hydrocarbon systems*, edited by K. McClay, pp. 538-557, *American Association of Petroleum Geologists Memoir*.
- Holland, T. & Powell, R., 2003. Activity–composition relations for phases in petrological calculations: an asymmetric multicomponent formulation. *Contributions to Mineralogy and Petrology*, **145**(4), 492-501.
- Holland, T. J. B. & Powell, R., 1998. An internally consistent thermodynamic data set for phases of petrological interest. *Journal of Metamorphic Geology*, **16**(3), 309-343.
- Hyndman, R. D., Currie, C. A., Mazzotti, S. & Frederiksen, A., 2009. Temperature control of continental lithosphere elastic thickness, Te vs Vs. *Earth and Planetary Science Letters*, **277**(3–4), 539-548.
- Jordan, T. E., 1981. Thrust loads and foreland basin evolution, Cretaceous, western United States. *Am. Assoc. Pet. Geol., Bull. (United States)*, **65**(12).



- Korsch, R. J., Goleby, B. R., Leven, J. H. & Drummond, B. J., 1998. Crustal architecture of central Australia based on deep seismic reflection profiling. *Tectonophysics*, **288**(1–4), 57–69.
- Korsch, R. J. & Lindsay, J. F., 1989. Relationships between deformation and basin evolution in the intracratonic Amadeus Basin, central Australia. *Tectonophysics*, **158**(1–4), 5–22.
- Lambeck, K., 1984. Structure and evolution of the Amadeus, officer and Ngalia basins of central Australia. *Australian Journal of Earth Sciences: An International Geoscience Journal of the Geological Society of Australia*, **31**(1), 25–48.
- Lambeck, K., Burgess, G. & Shaw, R., 1988. Teleseismic travel-time anomalies and deep crustal structure in central Australia. *Geophysical Journal International*, **94**(1), 105–124.
- Lindsay, J. F. & Leven, J. H., 1996. Evolution of a Neoproterozoic to Palaeozoic intracratonic setting, Officer Basin, South Australia. *Basin Research*, **8**(4), 403–424.
- Maboko, M. A. H., McDougall, I., Zeitler, P. K. & Williams, I. S., 1992. Geochronological evidence for ~530–550 Ma juxtaposition of two Proterozoic metamorphic terranes in the Musgrave Ranges, central Australia. *Australian Journal of Earth Sciences*, **39**(4), 457–471.
- Mouthereau, F., Watts, A. B. & Burov, E., 2013. Structure of orogenic belts controlled by lithosphere age. *Nature geoscience*, **6**(9), 785–789.
- Raimondo, T., Collins, A. S., Hand, M., Walker-Hallam, A., Smithies, R. H., Evins, P. M. & Howard, H. M., 2009. Ediacaran intracontinental channel flow. *Geology*, **37**(4), 291–294.
- Raimondo, T., Collins, A. S., Hand, M., Walker-Hallam, A., Smithies, R. H., Evins, P. M. & Howard, H. M., 2010. The anatomy of a deep intracontinental orogen. *Tectonics*, **29**(4), TC4024.
- Raimondo, T., Hand, M. & Collins, W. J., 2014. Compressional intracontinental orogens: Ancient and modern perspectives. *Earth-Science Reviews*, **130**, 128–153.
- Sandiford, M. & Hand, M., 1998. Controls on the locus of intraplate deformation in central Australia. *Earth and Planetary Science Letters*, **162**(1–4), 97–110.
- Sandiford, M., Hand, M. & McLaren, S., 2001. Tectonic feedback, intraplate orogeny and the geochemical structure of the crust: a central Australian perspective. *Special publication-Geological Society of London*, **184**, 195–218.
- Sandiford, M. & McLaren, S., 2002. Tectonic feedback and the ordering of heat producing elements within the continental lithosphere. *Earth and Planetary Science Letters*, **204**(1–2), 133–150.
- Scrimgeour, I. R. & Close, D. F., 1999. Regional high-pressure metamorphism during intracratonic deformation: the Petermann Orogeny, central Australia. *Journal of Metamorphic Geology*, **17**(5), 557–572.
- Scrimgeour, I. R., Close, D. F. & Edgoose, C. J., 1999. Petermann Ranges, N.T. 1:250000 Geological Series. *Department of Mines and Energy, Northern Territory Geological Survey. Explanatory Notes SG52-7*.
- Shaw, R., Etheridge, M. & Lambeck, K., 1991. Development of the Late Proterozoic to Mid-Paleozoic, intracratonic Amadeus Basin in central Australia: A key to understanding tectonic forces in plate interiors. *Tectonics*, **10**(4), 688–721.
- Simons, F. J., Zuber, M. T. & Korenaga, J., 2000. Isostatic response of the Australian lithosphere: Estimation of effective elastic thickness and anisotropy using multitaper spectral analysis. *Journal of Geophysical Research: Solid Earth* (1978–2012), **105**(B8), 19163–19184.
- Simpson, G. D. H., 2006. Modelling interactions between fold–thrust belt deformation, foreland flexure and surface mass transport. *Basin Research*, **18**(2), 125–143.
- Swain, C. & Kirby, J., 2006. An effective elastic thickness map of Australia from wavelet transforms of gravity and topography using Forsyth's method. *Geophysical research letters*, **33**(2).
- Sweet, I. P., Stewart, A. J. & Crick, I. H., 2012. *Uluru and Kata Tjuta : a geological guide*. Geoscience Australia, Canberra.
- Tărăpoancă, M., Bertotti, G., Mațenco, L., Dinu, C. & Cloetingh, S., 2003. Architecture of the Focșani depression: A 13 km deep basin in the Carpathians bend zone (Romania). *Tectonics*, **22**(6).
- Tărăpoancă, M., Garcia-Castellanos, D., Bertotti, G., Matenco, L., Cloetingh, S. & Dinu, C., 2004. Role of the 3-D distributions of load and lithospheric strength in orogenic arcs: polystage subsidence in the Carpathians foredeep. *Earth*

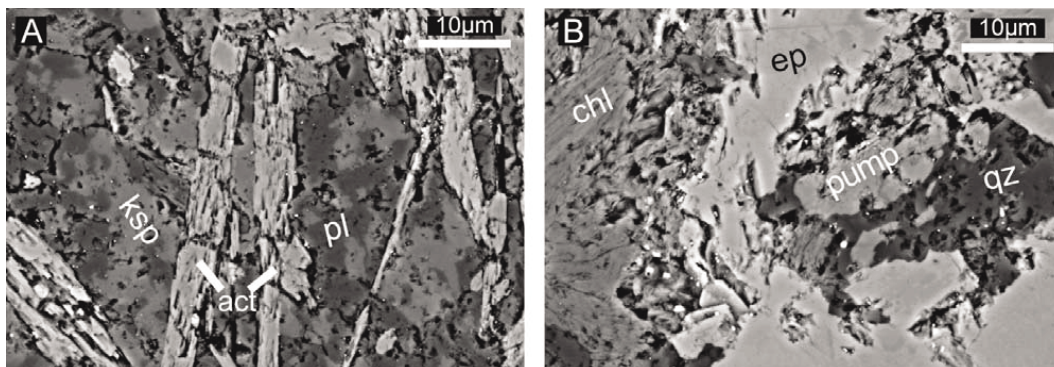
- and *Planetary Science Letters*, **221**(1), 163-180.
- Walsh, A. K., Raimondo, T., Kelsey, D. E., Hand, M., Pfitzner, H. L. & Clark, C., 2013. Duration of high-pressure metamorphism and cooling during the intraplate Petermann Orogeny. *Gondwana Research*, **24**(3-4), 969-983.
- Walter, M. R., Veevers, J. J., Calver, C. R. & Grey, K., 1995. Neoproterozoic stratigraphy of the Centralian Superbasin, Australia. *Precambrian Research*, **73**(1-4), 173-195.
- Watts, A. B., 1992. The effective elastic thickness of the lithosphere and the evolution of foreland basins. *Basin Research*, **4**(3-4), 169-178.
- Watts, A. B., 2001. *Isostasy and Flexure of the Lithosphere*. Cambridge University Press.
- Wells, A. T., Forman, D., Ranford, L. & Cook, P., 1970. *Geology of the Amadeus basin, central Australia*. Bureau of Mineral Resources, Geology and Geophysics.
- White, R. W., Powell, R. & Clarke, G. L., 2002. The interpretation of reaction textures in Fe-rich metapelitic granulites of the Musgrave Block, central Australia: constraints from mineral equilibria calculations in the system  $K_2O$ -FeO-MgO-Al<sub>2</sub>O<sub>3</sub>-SiO<sub>2</sub>-H<sub>2</sub>O-TiO<sub>2</sub>-Fe<sub>2</sub>O<sub>3</sub>. *Journal of Metamorphic Geology*, **20**, 41-55.
- White, R. W., Powell, R. & Holland, T. J. B., 2007. Progress relating to calculation of partial melting equilibria for metapelites. *Journal of Metamorphic Geology*, **25**(5), 511-527.
- White, R. W., Powell, R., Holland, T. J. B. & Worley, B. A., 2000. The effect of TiO<sub>2</sub> and Fe<sub>2</sub>O<sub>3</sub> on metapelitic assemblages at greenschist and amphibolite facies conditions: mineral equilibria calculations in the system  $K_2O$ -FeO-MgO-Al<sub>2</sub>O<sub>3</sub>-SiO<sub>2</sub>-H<sub>2</sub>O-TiO<sub>2</sub>-Fe<sub>2</sub>O<sub>3</sub>. *Journal of Metamorphic Geology*, **18**, 497-511.
- Young, D. N., Duncan, N., Camacho, A., Ferenczi, P. A. & Madigan, T. L. A., 2002. Ayers Rock, N.T. 1:250000 Geological Series. *Northern Territory Department of Business, Industry and Resource Development, Northern Territory Geological Survey. Explanatory Notes SG52-8*.
- Zhao, J.-X. & McCulloch, M. T., 1993. Sm-Nd mineral isochron ages of Late Proterozoic dyke swarms in Australia: evidence for two distinctive events of mafic magmatism and crustal extension. *Chemical Geology*, **109**, 341-354.
- Zuber, M. T., Bechtel, T. D. & Forsyth, D. W., 1989. Effective elastic thicknesses of the lithosphere and mechanisms of isostatic compensation in Australia. *Journal of Geophysical Research: Solid Earth (1978-2012)*, **94**(B7), 9353-9367.

## Supporting information

### SUPPLEMENTARY MATERIAL

#### Figure DR1

Additional back-scattered-electron (BSE) images collected on a Scanning Electron Microscope (SEM) for sample MCC1. A) Elongate actinolite grains with fine-grained, intergrown albite and potassium feldspar (ksp). B) Coarse-grained epidote, intergrown with chlorite, quartz and pumpellyite.



### SUPPLEMENTARY TABLES

#### Table 1

Mineral compositions collected on the SX-Five Electron Microprobe used for calculation of  $P$ – $T$  pseudosections and mineral compositional isopleth comparison for  $P$ – $T$  interpretation.

$$X_{\text{alm}} = X_{\text{Fe}} / (X_{\text{Fe}} + X_{\text{Mg}} + X_{\text{Mn}} + X_{\text{Ca}})$$

$$X_{\text{spss}} = X_{\text{Mn}} / (X_{\text{Fe}} + X_{\text{Mg}} + X_{\text{Mn}} + X_{\text{Ca}})$$

$$X_{\text{grs}} = X_{\text{Ca}} / (X_{\text{Fe}} + X_{\text{Mg}} + X_{\text{Mn}} + X_{\text{Ca}})$$

$$X_{\text{py}} = X_{\text{Py}} / (X_{\text{Fe}} + X_{\text{Mg}} + X_{\text{Mn}} + X_{\text{Ca}})$$

$$\text{Fe\#} = X_{\text{Fe}} / (X_{\text{Fe}} + X_{\text{Mg}})$$

Representative microprobe analyses from sample MCC1								
Mineral	ksp	hbl	pump	pl	ep	q	chl	ttn
SiO <sub>2</sub>	64.63	50.67	35.86	67.89	37.04	100.00	27.88	30.12
TiO <sub>2</sub>	0.03	0.25	0.19	0.04	0.09	0.00	0.02	38.43
Al <sub>2</sub> O <sub>3</sub>	18.09	5.54	20.41	20.12	20.73	0.00	18.30	1.01
Cr <sub>2</sub> O <sub>3</sub>	0.27	0.12	0.00	0.00	0.13	0.00	0.27	0.35
FeO	0.23	14.63	8.61	0.16	13.31	0.00	20.75	1.04
MnO	0.06	0.30	0.08	0.01	0.11	0.00	0.22	0.01
MgO	0.02	12.92	2.13	0.00	0.00	0.00	17.56	0.00
CaO	0.15	11.42	20.81	0.37	21.80	0.00	0.14	26.21
Na <sub>2</sub> O	1.19	0.53	0.00	11.14	0.04	0.00	0.02	0.00
K <sub>2</sub> O	12.20	0.22	0.02	0.09	0.04	0.00	0.02	0.02
Total	96.87	96.59	88.10	99.82	93.29	100.00	85.17	97.18
Si	3.02	7.46	6.24	2.97	3.32	3.33	2.93	1.01
Ti	0.00	0.03	0.02	0.00	0.01	0.00	0.00	0.97
Al	1.00	0.96	4.18	1.04	2.19	0.00	2.22	0.04
Cr	0.01	0.01	0.00	0.00	0.01	0.00	0.02	0.01
Fe <sup>2+</sup>	0.01	1.80	1.25	0.01	0.00	0.00	1.89	0.03
Fe <sup>3+</sup>	0.00	0.00	0.00	0.00	0.45	0.00	0.00	0.00
Mn	0.00	0.04	0.01	0.00	0.01	0.00	0.02	0.00
Mg	0.00	2.83	0.55	0.00	0.00	0.00	2.85	0.00
Ca	0.01	1.80	3.88	0.02	2.09	0.00	0.02	0.94
Na	0.11	0.15	0.00	0.94	0.01	0.00	0.00	0.00
K	0.73	0.04	0.01	0.01	0.00	0.00	0.00	0.00
Sum	4.89	15.12	16.15	4.98	8.08	3.33	9.95	3.00
<b>Al P.f.u</b>	<b>1.00</b>	<b>0.96</b>	<b>4.18</b>	<b>1.04</b>	<b>2.19</b>	<b>0.00</b>	<b>2.22</b>	<b>0.04</b>
<b>Fe#</b>	<b>0.88</b>	<b>0.39</b>	<b>0.69</b>	<b>1.00</b>	<b>1.00</b>	<b>0.00</b>	<b>0.40</b>	<b>1.00</b>

Representative microprobe analyses from sample 188A							
Mineral	gt	bi	hem	ep	q	pl	chl
SiO <sub>2</sub>	37.51	37.45	0.06	37.59	99.94	45.57	28.11
TiO <sub>2</sub>	0.07	1.64	0.01	0.18	0.00	0.00	0.05
Al <sub>2</sub> O <sub>3</sub>	20.12	16.16	0.05	23.96	0.00	32.54	18.52
Cr <sub>2</sub> O <sub>3</sub>	0.00	0.04	0.00	0.00	0.00	0.00	0.35
FeO	19.43	15.71	89.89	10.53	0.00	0.05	19.01
MnO	11.73	0.28	0.05	0.51	0.00	0.03	0.23
MgO	1.61	13.66	0.06	0.05	0.00	0.01	19.04
CaO	8.99	0.00	0.01	22.38	0.02	16.82	0.18
Na <sub>2</sub> O	0.03	0.29	0.03	0.06	0.00	1.66	0.02
K <sub>2</sub> O	0.00	9.32	0.00	0.03	0.00	0.00	0.07
Total	99.50	94.55	90.17	95.26	99.97	96.67	85.58
Si	3.02	2.83	0.00	3.11	1.00	2.17	2.93
Ti	0.00	0.09	0.00	0.01	0.00	0.00	0.00



Al	1.91	1.45	0.00	2.34	0.00	1.82	2.28
Cr	0.00	0.00	0.00	0.00	0.00	0.00	0.03
Fe2+	1.31	1.01	0.00	0.00	0.00	0.00	1.66
Fe3+	0.00	0.00	3.98	0.73	0.00	0.00	0.00
Mn	0.80	0.02	0.00	0.04	0.00	0.00	0.02
Mg	0.19	1.50	0.00	0.01	0.00	0.00	2.96
Ca	0.78	0.00	0.00	1.98	0.00	0.86	0.02
Na	0.01	0.03	0.00	0.01	0.00	0.15	0.00
K	0.00	0.88	0.00	0.00	0.00	0.00	0.01
Sum	8.02	7.81	3.99	8.22	1.00	5.00	9.92
<b>Xspss</b>	<b>0.26</b>						
<b>Xalm</b>	<b>0.44</b>						
<b>Xgrs</b>	<b>0.25</b>						
<b>Xpy</b>	<b>0.06</b>						

Representative microprobe analyses from sample 806C							
Mineral	gt	bi	chl	ep	pl	ilm	q
SiO <sub>2</sub>	37.66	37.18	27.62	37.33	63.57	0.05	97.89
TiO <sub>2</sub>	0.10	1.77	0.05	0.06	0.03	22.05	0.00
Al <sub>2</sub> O <sub>3</sub>	20.43	17.12	18.47	22.22	22.14	0.03	0.02
Cr <sub>2</sub> O <sub>3</sub>	0.00	0.00	0.00	0.00	0.00	0.00	0.00
FeO	20.12	16.16	20.23	13.08	0.12	67.11	0.10
MnO	12.26	0.19	0.30	0.30	0.01	1.30	0.01
MgO	1.91	12.69	19.66	0.00	0.00	0.03	0.00
CaO	7.62	0.02	0.02	22.16	4.53	0.04	0.00
Na <sub>2</sub> O	0.05	0.20	0.13	0.03	8.93	0.02	0.02
K <sub>2</sub> O	0.00	9.42	0.02	0.01	0.14	0.06	0.00
Total	100.15	94.74	86.49	95.18	99.33	90.64	98.04
Si	3.02	2.80	2.87	3.13	2.82	0.00	1.00
Ti	0.01	0.10	0.00	0.00	0.00	0.55	0.00
Al	1.93	1.52	2.26	2.20	1.16	0.00	0.00
Cr	0.00	0.00	0.00	0.00	0.00	0.00	0.00
Fe2+	1.35	1.02	1.76	0.00	0.00	1.86	0.00
Fe3+	0.00	0.00	0.00	0.92	0.00	0.00	0.00
Mn	0.83	0.01	0.03	0.02	0.00	0.04	0.00
Mg	0.23	1.42	3.05	0.00	0.00	0.00	0.00
Ca	0.65	0.00	0.00	1.99	0.22	0.00	0.00
Na	0.01	0.03	0.03	0.00	0.77	0.00	0.00
K	0.00	0.90	0.00	0.00	0.01	0.00	0.00
Sum	8.02	7.81	10.01	8.27	4.98	2.45	1.00
<b>Xspss</b>	<b>0.27</b>						
<b>Xalm</b>	<b>0.44</b>						

Representative microprobe analyses from sample MHP98									
Mineral	gt	gt	hbl	hbl	pl	pl	ilm	chl	q
SiO <sub>2</sub>	37.53	37.49	40.35	40.02	47.40	47.17	0.04	23.97	99.35
TiO <sub>2</sub>	0.01	0.01	0.76	0.55	0.00	0.00	51.60	0.04	0.00
Al <sub>2</sub> O <sub>3</sub>	20.83	21.10	16.78	16.06	33.11	33.30	0.02	17.46	0.01
Cr <sub>2</sub> O <sub>3</sub>	0.00	0.00	0.01	0.00	0.02	0.03	0.01	0.00	0.00
FeO	28.80	28.69	14.67	15.70	0.18	0.03	44.95	20.75	0.37
MnO	2.38	2.12	0.21	0.18	0.03	0.00	0.70	0.32	0.05
MgO	4.38	4.75	9.08	8.69	0.00	0.01	0.56	15.53	0.00
CaO	4.99	5.11	10.97	10.83	16.82	16.76	0.01	0.28	0.02
Na <sub>2</sub> O	0.02	0.02	1.61	1.59	1.65	1.65	0.00	6.21	0.00
K <sub>2</sub> O	0.00	0.00	0.68	0.64	0.02	0.01	0.01	0.18	0.00
Total	98.94	99.28	95.12	94.27	99.23	98.95	97.90	84.74	99.80
Si	3.00	2.99	6.14	6.17	2.19	2.18	0.00	2.66	1.00
Ti	0.00	0.00	0.09	0.06	0.00	0.00	1.00	0.00	0.00
Al	1.97	1.98	3.01	2.92	1.80	1.82	0.00	2.29	0.00
Cr	0.00	0.00	0.00	0.00	0.00	0.00	0.00	0.00	0.00
Fe <sup>2+</sup>	1.93	1.91	1.87	2.03	0.01	0.00	0.97	1.93	0.00
Mn	0.16	0.14	0.03	0.02	0.00	0.00	0.02	0.03	0.00
Mg	0.52	0.56	2.06	2.00	0.00	0.00	0.02	2.57	0.00
Ca	0.43	0.44	1.79	1.79	0.83	0.83	0.00	0.03	0.00
Na	0.00	0.00	0.48	0.48	0.15	0.15	0.00	1.34	0.00
K	0.00	0.00	0.13	0.13	0.00	0.00	0.00	0.03	0.00
Sum	8.01	8.02	15.58	15.60	4.98	4.98	2.00	10.87	1.00
<b>Xspss</b>	<b>0.05</b>								
<b>Xalm</b>	<b>0.63</b>								

# Chapter 4

This chapter is submitted as:

Walsh, A. K., Hand, M., Kelsey, D. E. & Jourdan, F., 2014. Crustal thickening in the Petermann Orogeny prior to 600 Ma; evidence from  $^{40}\text{Ar}/^{39}\text{Ar}$  geochronology and implications for spatial patterns of reworking in intraplate orogens. *Journal of the Geological Society*.





---

# Crustal thickening in the Petermann Orogeny prior to 600 Ma; evidence from $^{40}\text{Ar}/^{39}\text{Ar}$ geochronology and implications for spatial patterns of reworking in intraplate orogens

---

## ABSTRACT

Spatial and temporal patterns of deformation during intraplate orogeny provide insight into the processes by which intraplate orogens develop and how lithosphere evolves rheologically during orogenesis. Crustal thickening during the intraplate Petermann Orogeny in central Australia is recorded by greenschist/amphibolite facies metamorphism in the foreland fold-thrust belt. Metamorphic mica from lower grade flanks of the fold-thrust belt preserve  $^{40}\text{Ar}/^{39}\text{Ar}$  crystallisation ages of ca. 600 Ma whereas mica from amphibolite grade schists in deeper sequences record cooling ages between 560 and 545 Ma. The record of deformation in the foreland fold-thrust belt is at least 30 Myr older than is preserved in the high-grade orogenic core, and implies that crustal thickening in the Musgrave Province was near completion at 600 Ma. Converse to conventional contraction-dominated orogens, the locus of deformation migrated from the foreland, southward, toward the hinterland and orogenic core. Deformation was localised in strike-slip shear zones in the orogenic core during a shift from high-angle to low-angle transpression. The >600 Ma record of crustal thickening correlates with known ages in the Paterson Orogen, approximately 400 km to the northwest, providing a probable link which greatly increases the tectonic footprint of Ediacaran–Cambrian aged intraplate orogenesis in Australia.

---

## INTRODUCTION

Contractional orogens commonly develop at plate margins, in response to active plate collision (Burchfiel and Davis 1972; Burke and Dewey 1973; e.g. Dewey and Bird 1970; Dewey and Burke 1973; Jamieson and Beaumont 2013; Sengör 1976). Whereas deformation in plate interiors commonly accompanies plate margin orogenesis (Bull and Scrutton 1992; Cloetingh and Van Wees 2005; Kenner and Segall 2000; Marshak *et al.* 2000; Ziegler *et al.* 1995; Zoback 1992), the development of large contractional intraplate orogens is much less common.

The physical architecture of intraplate orogenic systems are increasingly compared and contrasted with their plate margin counterparts (Gorczyk *et al.* 2013; e.g. Raimondo *et al.* 2009; Raimondo *et al.* 2010; Raimondo *et al.* 2014), with much of the current knowledge derived from study of examples in modern Earth such as Tien Shan and Altai in central Asia (Buslov *et al.* 2007; e.g. Cunningham 2005; Van Hinsbergen *et*

*al.* 2008; Windley *et al.* 2007), the Sevier-Laramide Orogen, western North America (Bird 1998; e.g. Livaccari 1991; Marshak *et al.* 2000), Atlas Mountains, northern Africa (e.g. Beauchamp *et al.* 1999) and the Spanish Central System, Iberia (e.g. De Bruijne and Andriessen 2002). In addition, there are an increasing number of studies regarding the initiation of intraplate orogens and the thermal and rheological properties of lithosphere in which they develop (e.g. Holford *et al.* 2011; Neil and Houseman 1999; Pysklywec and Beaumont 2004; Raimondo *et al.* 2009, 2010; Sandiford and Hand 1998; Sandiford *et al.* 2001; Stephenson *et al.* 2009; Walsh *et al.* submitted). Quantifying the temporal and spatial distribution of deformation, exhumation and cooling is critical to increasing our understanding of the thermal, deformational and rheological evolution of intraplate orogens. To this end, here we investigate the temporal and spatial distribution of deformation during the Ediacaran–Cambrian aged Petermann Orogeny in central Australia, which is an exceptional large scale example of

ancient intraplate orogeny.

The Ediacaran–Cambrian Petermann Orogen in central Australia is one of the best preserved examples of intraplate orogeny and involves magnitudes of crustal thickening, shortening and exhumation comparable to both plate margin orogenic systems, and intraplate systems such as Tien Shan in central Asia (Flöttmann *et al.* 2004; Raimondo *et al.* 2014). The Petermann Orogen is best described as a dextral transpressive shear system that reworks mostly high-grade Mesoproterozoic gneisses of the Musgrave Province (Aitken *et al.* 2009a; Aitken *et al.* 2009b; Camacho and McDougall 2000; Flöttmann *et al.* 2004). Transpressional deformation resulted in north-vergent thrusting that was principally concentrated along the northern margin of the orogen and transported the orogenic core toward the foreland. Strike-slip deformation is recorded by Moho-penetrating shear zones in the central orogenic core (Aitken *et al.* 2009a; Fig. 1; Camacho and McDougall 2000). A near complete crustal section (Fig. 2) is preserved from transitional eclogite (12 to 14 kbar) facies deep crustal rocks in the core of the orogen (south), to pumpellyite to greenschist facies rocks in the northern foreland basin (Camacho *et al.* 2001; Raimondo *et al.* 2009, 2010; Scrimgeour *et al.* 1999; Walsh *et al.* submitted).

Despite excellent preservation there is a paucity of high-temperature geochronological data, partly due to the limited growth of high-temperature U–Pb geochronometers, such as zircon and monazite, in dry Mesoproterozoic gneisses. Previous researchers investigating the metamorphic and tectonic history of the Petermann Orogeny utilise U–Pb zircon, titanite and rutile geochronology and  $^{40}\text{Ar}/^{39}\text{Ar}$  K-feldspar, hornblende, muscovite and biotite thermochronology, from rare high-grade migmatitic rocks from the hinterland of the orogen (Fig. 1; Camacho *et al.* 1997; Camacho and McDougall 2000; Gregory *et al.* 2009; Raimondo *et al.* 2009, 2010; Scrimgeour and Close 1999; Scrimgeour *et al.* 1999; Walsh *et*

*al.* 2013). These researchers concluded that the metamorphic peak was achieved at 570 to 560 Ma and was followed by a protracted period of slow cooling and exhumation until *ca.* 500 Ma. The implication of this age dataset is that there is a pre-570 Ma history to the Petermann Orogeny that remains unconstrained.

The northern foreland fold-thrust belt of the Petermann Orogen preserves a record of deep burial metamorphism (up to amphibolite facies is exposed) and thick-skinned deformation in response to intraplate deformation in exceptionally weak lithosphere (Flöttmann *et al.* 2004; Walsh *et al.* submitted). In this contribution we utilise laser-step heating  $^{40}\text{Ar}/^{39}\text{Ar}$  geochronology on metamorphic sequences from this marginal foreland fold-thrust belt to investigate the pre-570 Ma history of crustal thickening, and, in concert with existing U–Pb geochronology, constrain the duration of metamorphism, deformation and post-peak cooling during intraplate orogeny. We propose that intraplate deformation progressively localised towards the orogenic core, similar to a transpressional flower structure with a centrally extruded core (cf. Goscombe *et al.* 2005).

## GEOLOGICAL SETTING

The Musgrave Province (Fig. 1) is an east-west trending Mesoproterozoic basement province that outcrops over approximately 120,000 km<sup>2</sup>, straddling the Northern Territory, South Australia and Western Australia borders in central Australia (Aitken and Betts 2008; Camacho and McDougall 2000). The Musgrave Province is bounded by the Neoproterozoic to Palaeozoic sedimentary rocks of the Amadeus, Officer, Canning and Perdilkas Basins (e.g. Walter *et al.* 1995).

The Musgrave Province exposes voluminous magmatic (many now gneissic) and volcanic rocks that dominate outcrop (approximately 50 to 60% of total outcrop) throughout the province (Camacho *et al.* 2002; Evins *et al.* 2010; Glikson *et al.* 1996;

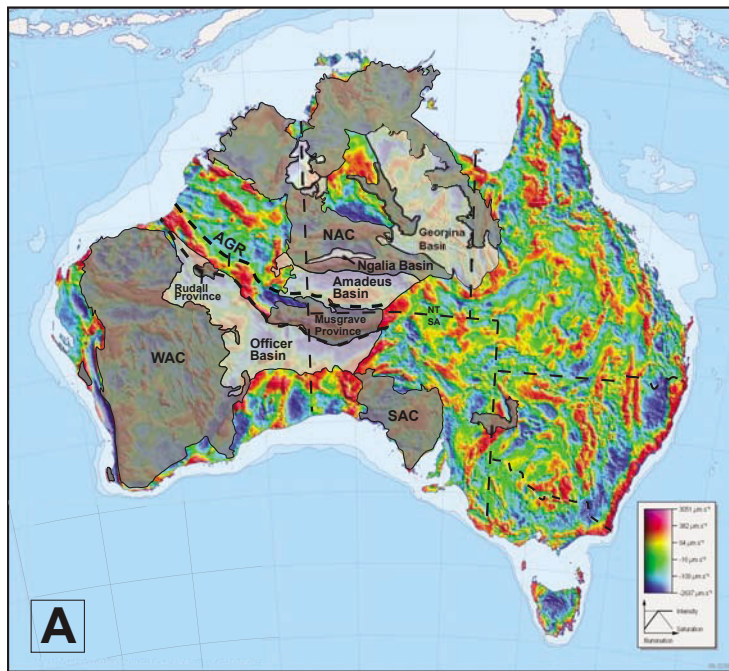
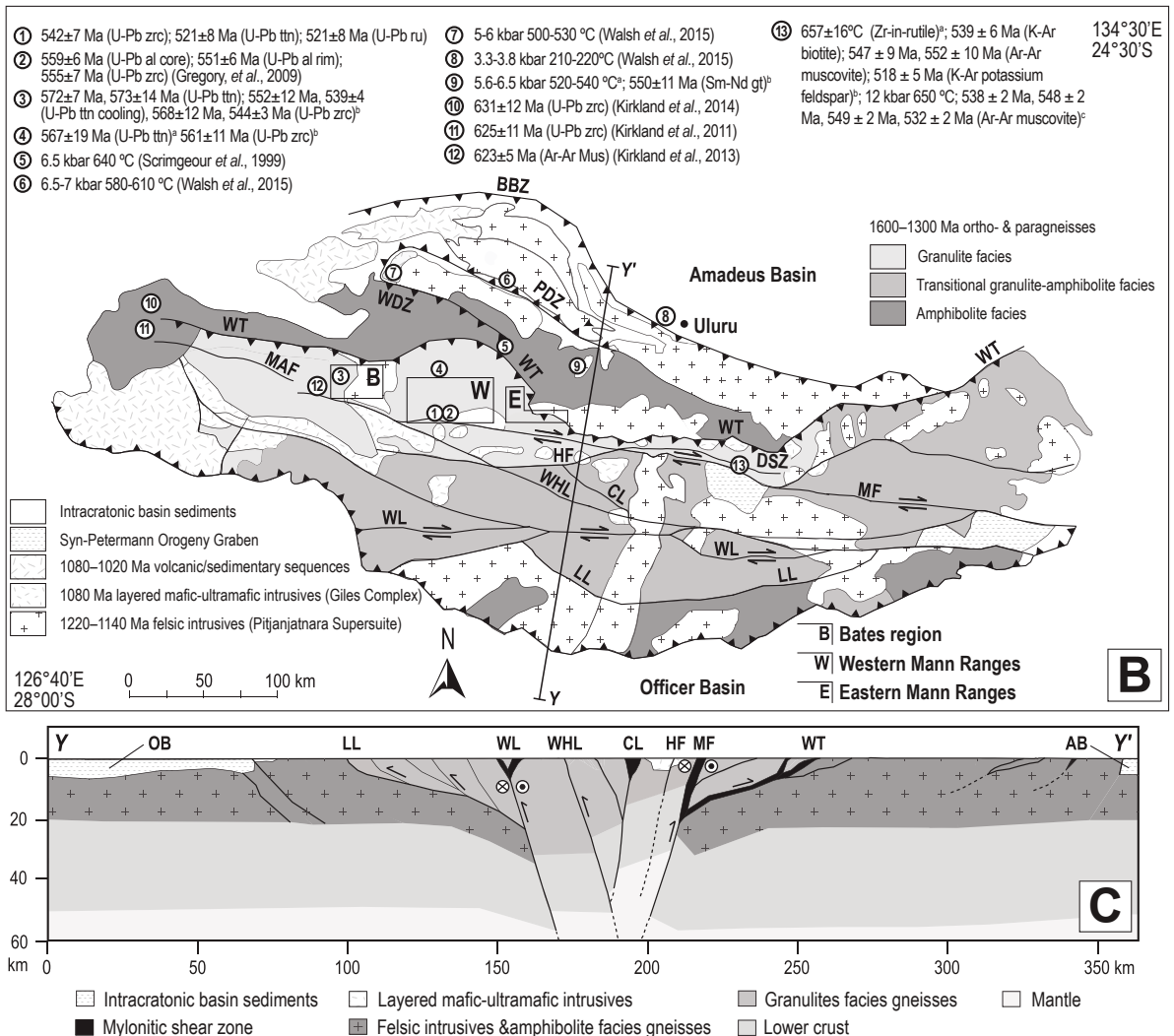


Figure 1. (a) Gravity map of Australia overlain with distribution of Proterozoic and early Phanerozoic basement provinces and sedimentary basins. Interpreted continuity of Ediacaran intraplate orogenic belt outlined in association with the Anketell Gravity Ridge (AGR). (b) Regional solid geology map of the Musgrave Province. The locations of key E-W trending fault structures of the Petermann Orogen and previously collected geochronological and  $P$ - $T$  data are shown. 1. (Walsh et al., 2013); 3. (Raimondo et al., 2009, 2010); 4a. (Walsh et al., 2013); 5. (Scrimgeour et al., 1999); 9. a (Walsh et al., in review) b (Scrimgeour et al., 1999); 13. a (Camacho et al., 2009), b (Camacho et al., 1997), c (Camacho and McDougall, 2000). Figure modified from Edgoose et al. (2004), Raimondo et al. (2010) and Aitken et al. (2009). (c) Schematic cross section (Y-Y') across the central Musgrave Block. Highlights the overall crustal-scale dextral transpressive shear system, involving significant Moho displacement and deep exhumation along the Woodroffe Thrust/Mann Fault. Modified from Aitken et al. (2009). Abbreviations: AB, Amadeus Basin; BBZ, Bloods Back Thrust Zone; CL, Caroline Lineament; HF, Hinckley Fault; LL, Lindsay Lineament; MAF, Mount Aloysius Fault; MF, Mann Fault; NAC, North Australian Craton; OB, Officer Basin; PDZ, Piltardi Detachment Zone; SAC, South Australian Craton; WAC, West Australian Craton; WDL, Wankari Detachment Zone; WHL, Wintiginna-Hinckley Lineament; WL, Wintiginna lineament; WT, Woodroffe Thrust.





Howard *et al.* 2011; Smithies *et al.* 2011; Smithies *et al.* 2010; Wade *et al.* 2008). The Musgrave Province records a complex deformational, metamorphic and magmatic history during the Grenvillian spanning *c.* 1345 to 1050 Ma (Edgoose *et al.* 2004; Evins *et al.* 2010; Glikson *et al.* 1995; Smithies *et al.* 2011; Sun *et al.* 1996; Wade *et al.* 2008; Walsh *et al.* 2014). The geochronological record is dominated by Grenvillian ages reflecting a prolonged period of high temperature, supra-solidus conditions between *ca.* 1250 and 1120 Ma, including multiple short-lived excursions to ultra-high temperatures ( $> 900^{\circ}\text{C}$ ) (Smithies *et al.* 2011; Tucker *et al.* 2015; Walsh *et al.* 2014), which accompanied the emplacement of large volumes of felsic magmatic rocks of the Pitjantjatjara Supersuite between *ca.* 1220 and 1120 Ma (Howard *et al.* 2015; Kirkland *et al.* 2013b; Smithies *et al.* 2014; Smithies *et al.* 2011; Smithies *et al.* 2010). Large volumes of mafic and felsic magma were emplaced into and erupted onto the crust of the Musgrave Province during the Giles Event, which spanned 1090 and 1040 Ma (Evins *et al.* 2010; Howard *et al.* 2015; Smithies *et al.* 2015; Smithies *et al.* 2011; Wingate *et al.* 2004). The modern day east-west orientation of the outcropping Musgrave Province is a strong function of the overprinting intraplate Ediacaran to Cambrian-aged Petermann Orogeny (Aitken *et al.* 2009a; Aitken *et al.* 2009b; Camacho *et al.* 1997; Raimondo *et al.* 2010; Wade *et al.* 2008). The Petermann Orogeny led to the present-day geophysical architecture of the Musgrave Province via the development of major E–W striking faults that penetrate the crust (Aitken *et al.* 2009a; Korsch *et al.* 1998). The most significant of these structures are the Mann Fault and the Woodroffe Thrust, between which lies the exposed high-pressure (12 to 14 kbar) core of the Petermann Orogen (Fig. 1). The Woodroffe Thrust is a shallow south-dipping mylonite and pseudotachylite zone up to 3 km thick that offsets the Moho by approximately 20 km (Aitken *et al.* 2009a; Camacho and Fanning 1995; Korsch and Kositsin 2010; Lambeck and Burgess 1992), and created one of the largest intracontinental

gravitational gradients on Earth.

Top-to-the-north tectonic transport along the Woodroffe Thrust, coupled with antithetic movement on the Mann Fault system facilitated the exhumation of lower-crustal granulite-facies gneisses from approximately 40 km depth and the emplacement of a broad crustal wedge (Camacho *et al.* 1997; Raimondo *et al.* 2010; Scrimgeour and Close 1999). This led to the development of  $>100$  km-scale basement-cored nappes and thick-skinned thrust sheets that transported the orogenic core towards a deeply depressed foreland (Flöttmann *et al.* 2004; Walsh *et al.* submitted).

Sequential cross-section restorations indicate that north-directed shortening during the Petermann Orogeny exceeded 150 km and was accommodated by significant crustal thickening (Flöttmann *et al.* 2004). Thermobarometric constraints from the exposed orogenic core show maximum pressure–temperature ( $P$ – $T$ ) conditions of 12–14 kbar and 700–750  $^{\circ}\text{C}$ , which are attained immediately north of the Mann Fault in the western Mann Ranges (Camacho *et al.* 1997; Gregory *et al.* 2009; Raimondo *et al.* 2009, 2010; Scrimgeour and Close 1999; White and Clarke 1997). More eastern parts of the orogenic core record transitional-eclogite facies mineral assemblages that formed at 12–14 kbar and 600–650  $^{\circ}\text{C}$  (Camacho *et al.* 1997; Ellis and Maboko 1992). Metamorphic grade decreases northward toward the foreland to the north (Figs. 1 & 2), with  $P$ – $T$  conditions of 6–7 kbar and 600–650  $^{\circ}\text{C}$  recorded north of the Woodroffe thrust in the foreland fold-thrust belt (Scrimgeour and Close 1999; Walsh *et al.* submitted). Syn-orogenic burial metamorphism in the foreland basin reached 3–4 kbar and 200–220  $^{\circ}\text{C}$ , reflecting the deep flexural response of weak lithosphere during orogeny (Walsh *et al.* submitted).

The timing of Petermann-aged ‘peak’ metamorphism, exhumation and cooling is relatively well constrained in the central western parts of the orogenic core (Fig. 1). However, there is a distinct paucity of



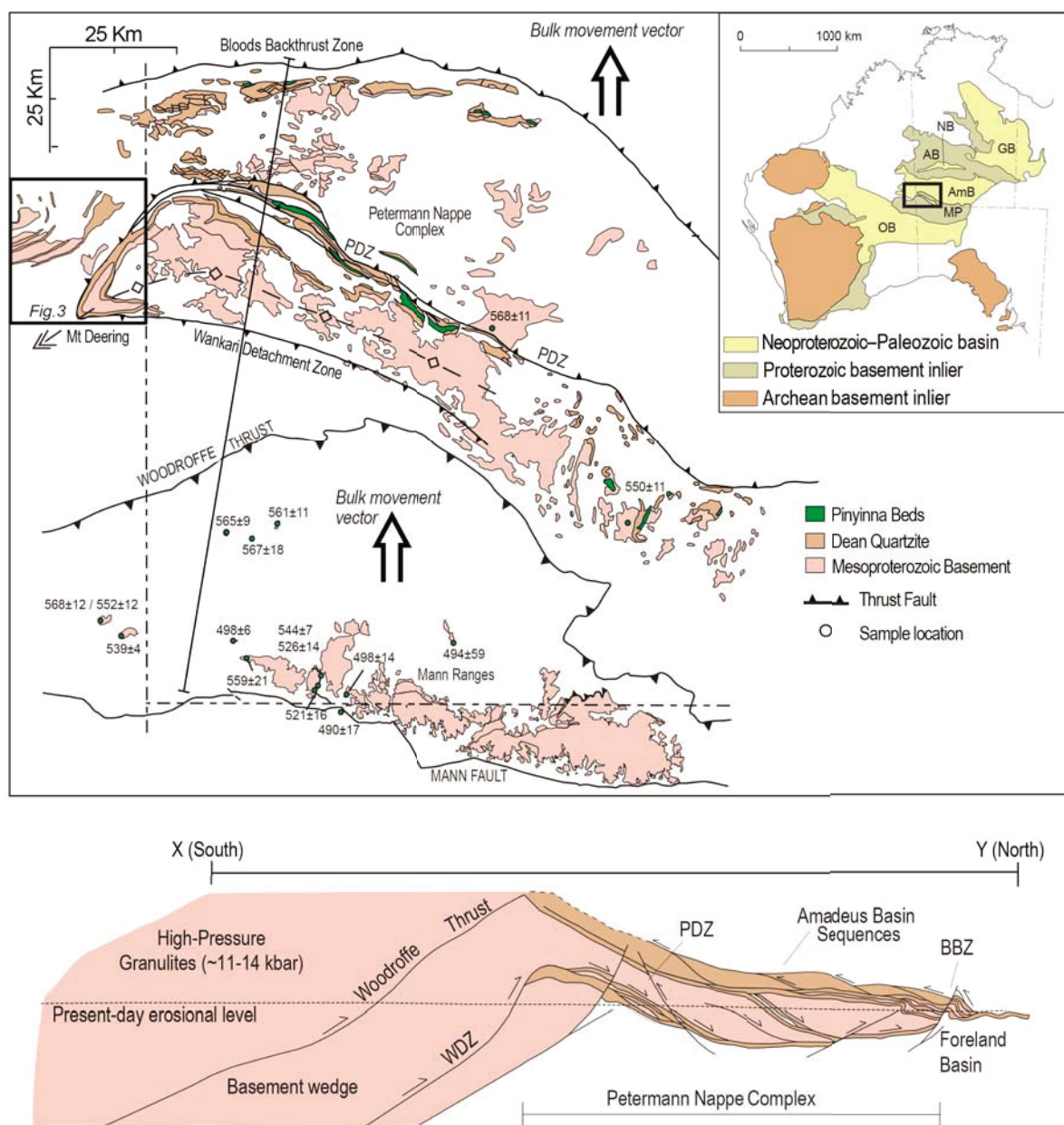


**Figure 2.** Simplified geology map showing the distribution of outcropping lithological units in the central and northern Musgrave Province. Previous geochronological data (green circles) and P–T estimates (yellow circles) from the Bates Region and Petermann Nappe Complex are shown. Adapted from Edgoose *et al.* (2004) and Raimondo *et al.* (2010).

geochronological data relative to the size of the orogen. The onset of the Petermann Orogeny was proposed to be *ca.* 600 Ma, based on the arrival of detritus from the 1345 to 1050 Ma rocks into the proximal sequences of the Officer Basin, located on the southern margin of the Musgrave Province (Fig. 1; Wade *et al.* 2006). In the western part of the orogenic core, the earliest U–Pb record of the Petermann Orogeny is constrained by transitional-eclogite

facies metamorphism (12–14 kbar, 670–730 °C), which has been dated by U–Pb zircon and titanite to have occurred at 575 to 560 Ma (Raimondo *et al.* 2009, 2010; Scrimgeour and Close 1999). Further to the east (Fig. 1b),  $^{40}\text{Ar}/^{39}\text{Ar}$  and K–Ar muscovite and biotite geochronology constrains the exhumation of deep crustal shear zones between *ca.* 550 and 530 Ma (Camacho *et al.* 1997; Camacho and McDougall 2000; Maboko *et al.* 1992).

The only temporal constraints on Petermann-aged deformation in the foreland of the orogen are a Sm–Nd garnet age of  $550 \pm 11$  Ma from a recrystallised Mesoproterozoic mafic dyke that transects basement granitic gneiss and K–Ar muscovite ages of  $586 \pm 5$  Ma and  $568 \pm 5$  Ma from imbricated Neoproterozoic sequences (Scrimgeour *et al.* 1999). It is now well established that the K–Ar method does not produce reliable results, therefore existing K–Ar ages are not taken into further consideration in this paper. The retrograde evolution (post-peak pressures), is dominated by north-vergent lower-crustal channel flow that facilitated exhumation of the high-grade core of the orogen (Raimondo *et al.* 2009, 2010). In response to regional exhumation and cooling, melt crystallisation in high-grade ductile shear zones is dated by U–Pb zircon and allanite to have occurred between  $559 \pm 6$  and  $542 \pm 7$  Ma (Gregory *et al.* 2009; Walsh *et al.* 2013). U–Pb titanite and rutile and  $^{40}\text{Ar}/^{39}\text{Ar}$  muscovite ages record further exhumation of the orogen, which was characterised by slow ( $0.9$  to  $4.8$  °C Ma<sup>-1</sup>), protracted cooling until ca. 500 Ma (Camacho *et al.* 1997; Camacho and Fanning 1995; Walsh *et al.* 2013). The overall thermal and deformational evolution of the Petermann Orogeny is therefore described as a slowly evolving continuous orogenic cycle, consistent with conventional models of collisional orogeny at plate margins (Raimondo *et al.* 2014).

Whereas the current geochronological dataset reflects the timing of ‘peak’ metamorphism, cooling and exhumation, the pre-570 Ma burial history of the orogen is poorly constrained. The most convincing evidence for early-Petermann-aged events in the Musgrave Province are from recent geochronological data, that shows: 1) a U–Pb zircon age of ca. 625 Ma from muscovite-tourmaline-bearing pegmatite in the central-western Musgrave Province (Kirkland *et al.* 2011); 2) an  $^{40}\text{Ar}/^{39}\text{Ar}$  muscovite age of ca. 623 from a greenschist facies micaceous quartzite in the MacDougall Formation, from the far north western Musgrave Province (Kirkland *et al.* 2013a)

and; 3) U–Pb zircon ages of ca. 628 Ma and ca. 631 Ma from garnet–staurolite–kyanite-bearing rocks of the MacDougall Formation (Kirkland *et al.* 2014).

## GEOLOGY OF THE FORELAND FOLD-THRUST BELT (PETERMANN NAPPE COMPLEX)

North of the Woodroffe thrust is the crustal-scale, thick-skinned fold-thrust belt, referred to here as the Petermann Nappe Complex (Figs. 2, 3). The highly deformed core of the Petermann Nappe Complex is characterised by the structural imbrication of basement and cover sequences (Flöttmann *et al.* 2004). The basement sequences include late Mesoproterozoic volcanics, volcanoclastics and sediments of the ca. 1064 Ma Bentley Supergroup (Howard *et al.* 2011) and quartz-rich sequences of the Bloods Range Beds (Fig. 2, 3). Basement is overlain by the lowermost sequences of the Amadeus Basin (Fig. 2), including the early Neoproterozoic (ca. 830 Ma) Dean Quartzite and the shale-rich Pinyinna Beds (Lindsay and Leven 1996; Walter *et al.* 1995). Mineral stretching lineations throughout the Petermann Nappe Complex range between down-dip, interpreted to be related to north-vergent thrusting, and sub-horizontal to gently southeast plunging in mylonites, interpreted to be related to later strike-slip deformation within the Wankari Detachment Zone (Scrimgeour *et al.* 1999). Metamorphism of basement and Neoproterozoic sedimentary sequences during the Petermann Orogeny reached mid-amphibolite facies, with maximum conditions of 6–7 kbar and 550–600 °C reached in the Mt Deering and Olia Chain regions (Fig. 1, 2), consistent with deep burial of the foreland region (Scrimgeour and Close 1999; Walsh *et al.* submitted).

## PETROGRAPHY

All muscovite and three biotite samples were collected in the Mt. Deering region immediately west of the western Australia/northern Territory border (Fig. 3). In the Mt.

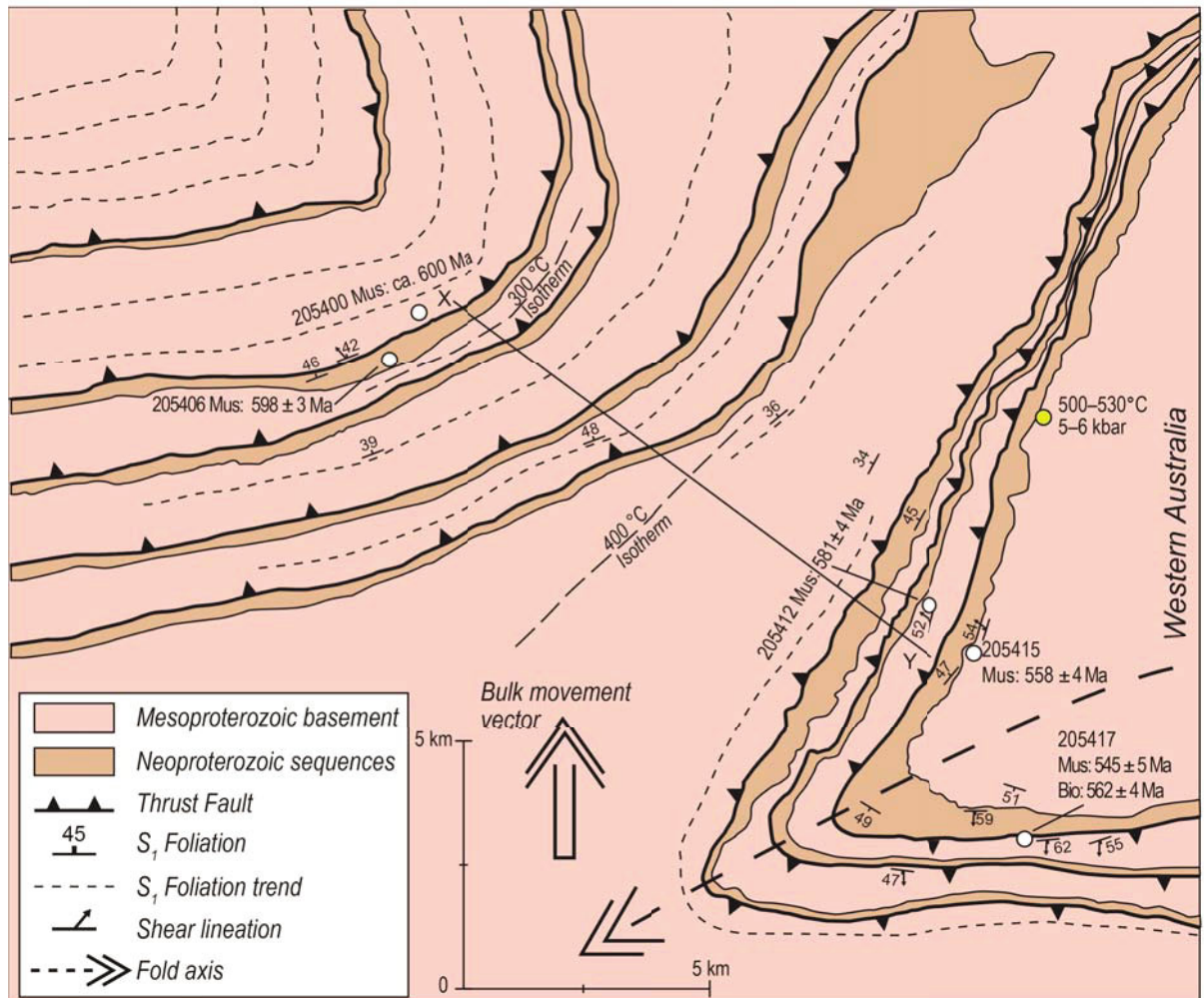


**Figure 3.** The interpreted solid geology of the Mt Deering region of the Petermann Nappe Complex (PNC) highlights scale of thick-skinned deformation observed in the fold-thrust belt. Location of samples (white circles) and accompanying  $^{40}\text{Ar}$ – $^{39}\text{Ar}$  ages are shown. Not all thrusts outcrop but are inferred to be located at the structural base of each layer of Dean Quartzite based on field observations. The autochthonous sequence of basement outcrops in the core of the anticline structure. North of the fold hinge, thrusts give apparent normal shear sense (top to the north/north side down) as a result of later folding and rotation during the development of the nappe structure. The implication of this is that samples further to the northwest are structurally higher and lower grade, relative to samples proximal to the core of the anticline.  $P$ – $T$  estimates for the PNC sample from Walsh *et al.* (2014b) is shown (yellow circle) and is used in this study to infer the metamorphic conditions for  $^{40}\text{Ar}/^{39}\text{Ar}$  samples (Y–X line is distance used).

Deering area the Petermann Nappe Complex is folded into a broad (approximately 40 km across) southwest-plunging anticline (Figs. 2, 3). The consequence of this folding is to cause the pre-folding thrusts located to the north of the fold axis appear to have extensional rather than thrust shear sense (e.g. Figs. 2, 3, e.g. Bloods Backthrust Zone). All hornblende samples and two biotite samples were collected from the Bates region (Fig. 2).

Samples 205400 [52J 7231936 mN 483648 mE], 205412 [52J 7226617 mN 494465 mE] and 205415 [52J 7226011 mN 495170 mE] are Mesoproterozoic basement-derived orthoschists that form part of the (thick-skinned) interleaved cover–basement sequence in the Petermann Nappe Complex (Fig. 3). Medium-grained (200 to 400  $\mu\text{m}$ ) prismatic muscovite defines a well-developed foliation within a matrix that consists of biotite (150 to 300  $\mu\text{m}$ ) and medium-grained



(200 to 600  $\mu\text{m}$ ) quartz and feldspar. Coarser potassium feldspar grains (2000 to 5000  $\mu\text{m}$ ) occur uncommonly and are interpreted as relic from the Mesoproterozoic granitic protolith. Ilmenite and rutile grains occur in the matrix; however, their petrogenesis is difficult to establish.

Sample 205406 [52J 7232589 mN 483761 mE] is from the Dean Quartzite, which forms an approximately 15 m thick sequence that occurs structurally above the basement sequence of sample 205400 (Fig. 3). The sample is dominated by fine-medium-grained quartz (Fig. 4b). Muscovite is fine-grained (100 to 200  $\mu\text{m}$ ) and strongly orientated.

Sample 205414 [52J 7226011 mN 495170 mE] is a biotite schist from the Mesoproterozoic basement (Bloods Beds). Medium-coarse-grained prismatic biotite (150 to 800  $\mu\text{m}$ ) defines a well-developed foliation in a matrix with fine to medium grained quartz (Fig. 4e).

Sample 205417 [52J 7222104 mN 496610 mE] is a kyanite-biotite-muscovite schist derived from the Mesoproterozoic basement (Bloods Beds) approximately 2.5 km ESE of Mt Deering (Fig. 2). Prismatic grains of biotite of  $\leq 400$   $\mu\text{m}$  define a strong foliation (Fig. 4f). Fine-grained quartz and plagioclase commonly occur as matrix forming minerals (Fig. 4f). Medium to coarse-grained prismatic muscovite is variably orientated and truncates oriented matrix biotite (Fig. 4f). Ilmenite and rutile grains occur in the matrix; however, their petrogenesis is difficult to establish.

Samples 195373 [52J 7134216 mN 476358 mE], 195377 [52J 7146470 mN 460840 mE] and 195379 [52J 7154440 mN 458237 mE], 195316 [52J 7142766 mN 456634 mE] and 195365 [52J 7161716 mN 484817 mE] are recrystallised/retrogressed Mesoproterozoic mafic rocks which outcrop in the central Bates region of the orogenic hinterland (Fig. 1 & 2). Outcrops of meta-dolerite and gabbro are variably cut by randomly orientated narrow shear zones (1–10 m) which caused

recrystallised and grain size reduction and homogenisation (c.f. White & Clarke 1997). Metadolerite samples rarely preserve coarse-grained clinopyroxene which might represent relict igneous phenocrysts. Hornblende is most commonly euhedral-subhedral and defines a foliation in a medium-grained matrix with fine-medium grained garnet, plagioclase and minor quartz and biotite (Fig. 5). Biotite is more abundant in sample 195365 and tabular to elongate grains weakly define a foliation (Fig. 5a).

#### <sup>40</sup>Ar/<sup>39</sup>Ar GEOCHRONOLOGY

Three hornblende and two biotite sample from the Bates region (Fig. 2) and five muscovite samples and two biotite samples from the Mt Deering region (Fig. 2, 3) of the foreland fold-thrust belt of the Petermann Orogen were prepared for <sup>40</sup>Ar/<sup>39</sup>Ar geochronology. Metamafic rocks from shear zones in the Bates region preserve a record of recrystallization as a result of high-pressure metamorphism during the Petermann Orogeny (White and Clarke 1997) and therefore were sampled to investigate the timing of exhumation and/or cooling of the deep crust of the orogen. The selection of samples from the fold-thrust belt aims to cover the widest (and accessible) across-strike section possible, to assess the effect of variation in crustal burial depths (Fig. 3). Muscovite was primarily targeted for <sup>40</sup>Ar/<sup>39</sup>Ar geochronology as it is more resistant to alteration than biotite and therefore is most likely to preserve a meaningful age. Muscovite and biotite were analysed for sample 205417 as petrographic observations indicate muscovite texturally overprints the biotite defined foliation (Fig. 4f).

Muscovite, biotite and hornblende were separated from a 450 to 150  $\mu\text{m}$  size fraction using a Frantz magnetic separator and hand-picked using a binocular microscope. Optically unaltered grains, free of inclusions were selected for all samples where possible.

Samples were loaded into large wells of



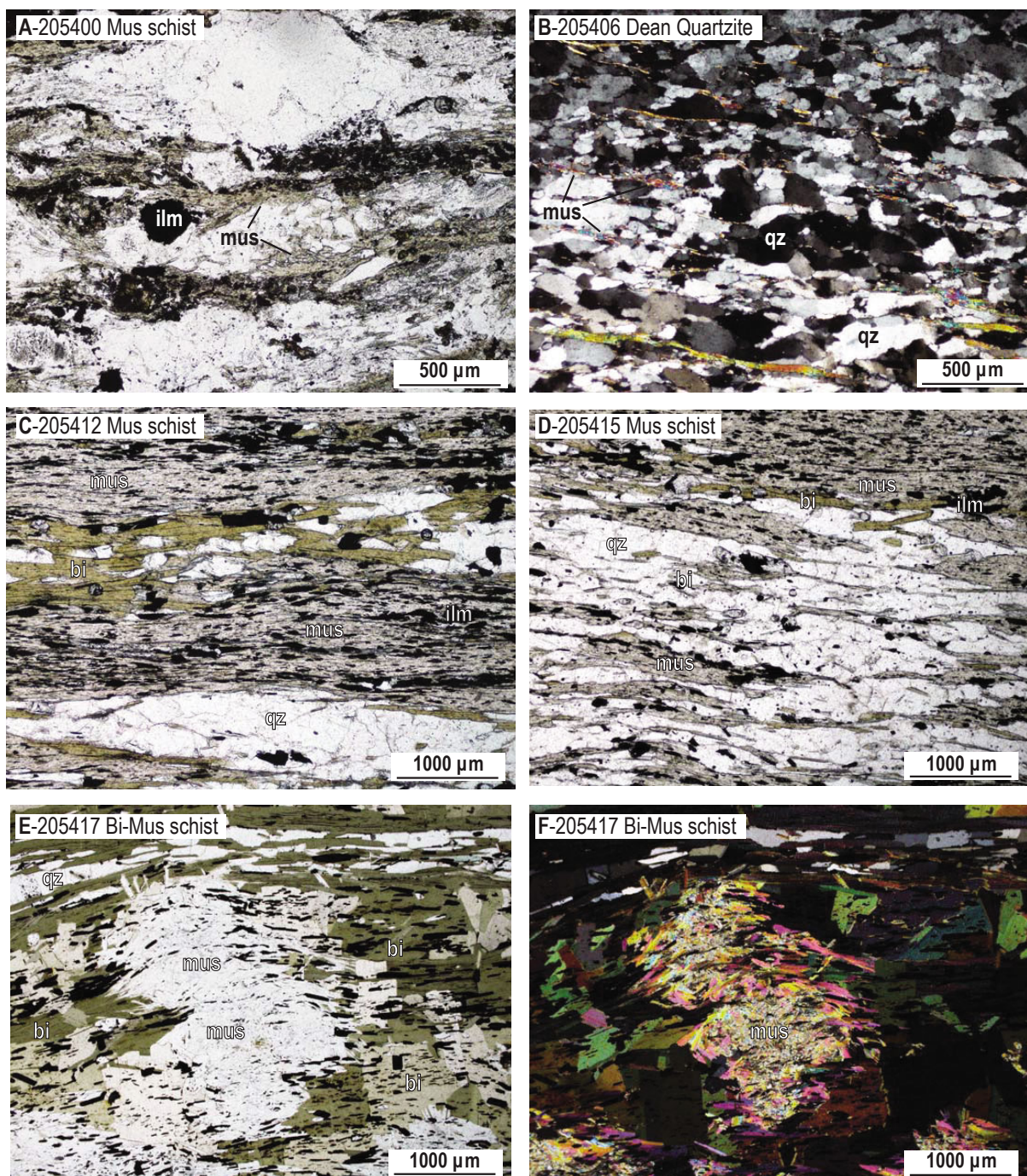


**Figure 4.** Thin section photos of samples from the Petermann Nappe Complex. A) sample 205400. Medium-grained (200 to 400  $\mu\text{m}$ ) elongate muscovite defines a foliation within a matrix which includes medium-grained (200 to 600  $\mu\text{m}$ ) quartz and feldspar. Muscovite is interpreted to have undergone alteration and is consequently slightly brown/yellow in plane polarised light. B) Sample 205406. Sub to angular to angular, fine to medium grained quartz is truncated by fine-grained muscovite (200 to 300  $\mu\text{m}$ ) which defines a weak foliation. C) Sample 205412. Medium to coarse grained (200 to 500  $\mu\text{m}$ ) altered muscovite defines a strong foliation within a matrix containing medium-grained (200 to 500  $\mu\text{m}$ ), biotite, quartz, feldspar and ilmenite. D) Sample 205415 Medium-coarse grained (200 to 500  $\mu\text{m}$ ) muscovite defines a strong foliation within a matrix which includes medium-grained (200 to 500  $\mu\text{m}$ ) biotite, quartz and feldspar. E) Coarse biotite grains, up to 400  $\mu\text{m}$ , are overprinted by variably oriented medium-coarse-grained muscovite. Ilmenite is commonly included in muscovite grains.



an aluminium disc measuring 1.9 cm in diameter and 0.3 cm in depth. These wells were bracketed by small wells containing Fish Canyon sanidine (FCs), used as a neutron flux monitor and for which an age of  $28.294 \pm 0.037$  Ma ( $1\sigma$ ) (Renne *et al.* 2010) was adopted. To minimise nuclear interference reactions, the discs was Cd-shielded. The disc was irradiated for 40 hours in the USGS TRIGA nuclear reactor (Oregon, USA) in a central position.

$^{40}\text{Ar}/^{39}\text{Ar}$  analyses were done at the Western Australian Argon Isotope Facility at Curtin University. The samples were step-heated using a 110 W Spectron Laser Systems, with a continuous Nd-YAG (IR; 1064 nm) laser rastered during 1 min over the sample ensuring a homogenously distributed temperature. The gas was purified in a stainless steel extraction line using three getters. Ar isotopes were measured in static mode using a MAP 215–50 mass spectrometer with a Balze electron multiplier mostly using 9 to 10 cycles of peak-hopping. The data acquisition was performed with the Argus program and was run under a LabView environment. The raw data were processed using ArArCALC software (Koppers 2002). Raw Ar isotopic data are given in Supplementary Data Table S1. Individual errors are given at the  $1\sigma$  level. The mean J-value computed from the standard FCs grains within the small pits is  $0.008215 \pm 0.000016$  (0.195%), calculated as the average and standard deviation of J-values of the standard FCs grains within each irradiation disc. An automated air pipette was used to monitor mass discrimination, which had a mean value of  $1.005413 \pm 0.003619$  (0.36%) per Dalton (atomic mass unit) relative to an air ratio of  $298.56 \pm 0.31$  (Lee *et al.* 2006). The correction factors for interfering isotopes were:  $(^{39}\text{Ar}/^{37}\text{Ar})_{\text{Ca}} = 7.60 \times 10^{-4}$  ( $\pm 7\%$ );  $(^{36}\text{Ar}/^{37}\text{Ar})_{\text{Ca}} = 2.81 \times 10^{-4}$  ( $\pm 3\%$ ); and  $(^{40}\text{Ar}/^{39}\text{Ar})_{\text{K}} = 6.76 \times 10^{-4}$  ( $\pm 10\%$ ). Blanks were monitored every 3 to 4 steps, and typical  $^{40}\text{Ar}$  blanks range from  $1 \times 10^{-16}$  to  $2 \times 10^{-16}$  mol. Individual errors are given at the  $1\sigma$  level. Our criteria for the determination of plateaus are as follows: 1)

plateaus must include at least 70% of  $^{39}\text{Ar}$ ; and 2) the plateau should be distributed over a minimum of three consecutive steps agreeing at the 95% confidence level and satisfying a probability of fit (P) of at least 0.05. Plateau ages are given at the  $2\sigma$  level and are calculated using the mean of all plateau steps, each weighted by the inverse variance of their individual analytical error. Unless otherwise stated, uncertainties on the  $^{40}\text{Ar}/^{39}\text{Ar}$  ratios of the monitors are included in the calculation of the integrated and plateau age uncertainties.

## Results

Twelve analyses were performed on three hornblende, five muscovite and four biotite samples. All hornblende samples and two biotite samples did not yield plateau ages and were highly perturbed (Fig. 7). Muscovite sample 205400 did not yield a plateau age albeit it suggests an age around 590 Ma (Fig. 6a). The perturbations could be due a complex thermal history, incomplete resetting, alteration or  $^{39}\text{Ar}$  recoil. Raw  $^{40}\text{Ar}/^{39}\text{Ar}$  data can be found in Supplementary Data Table S1.

Muscovite sample 205406 displays a plateau which incorporates 70% of the  $^{39}\text{Ar}$  and yields an age of  $598 \pm 3$  Ma (MSWD = 1.3, P = 0.23). The first 20% of  $^{39}\text{Ar}$  released records larger variability and errors (Fig. 6b). The concave up curve of the  $^{39}\text{Ar}$  data indicates the initial steps could be affected by recoil.

Muscovite sample 205412 displays a flat plateau with step ages between (Fig. 6c). A plateau age of  $581 \pm 4$  Ma (MSWD = 1.1, P = 0.33) is calculated from 100% of the  $^{39}\text{Ar}$ .

Muscovite sample 205415 displays a flat plateau (Fig. 6e). A plateau age of  $558 \pm 4$  Ma (MSWD = 0.27, P = 0.99) is calculated from incorporating 95% of the  $^{39}\text{Ar}$ . The first 5% of  $^{39}\text{Ar}$  released records larger variability and errors. These apparently older steps could represent some excess  $^{39}\text{Ar}$  or could be a result of minor amounts of recoil.

Biotite sample 205417 displays a flat plateau

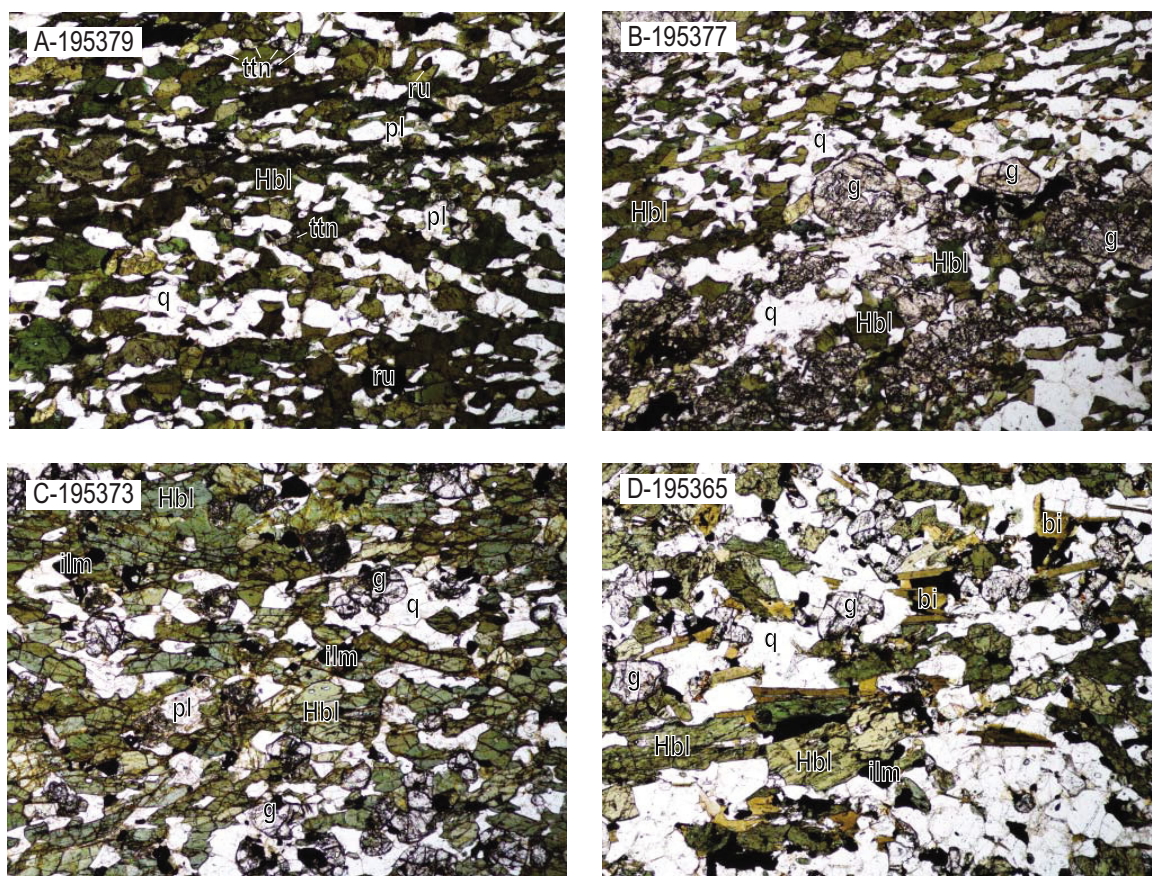


**Figure 5.** Thin section photos of samples from the Bates Region. A) sample 195379. Euhedral–Subhedral prismatic hornblende defines a strong foliation (east–west in photo) with anhedral quartz and plagioclase. Significant grain size reduction is not observed. Euhedral–subhedral titanite and rutile are common accessory matrix minerals and rarely included in hornblende and quartz. B) Sample 195377. Medium–coarse-grained poikiloblastic garnet includes quartz and plagioclase and is commonly in contact with fine-grained anhedral hornblende. Subhedral hornblende defines a strong foliation. C) Sample 195373. Euhedral garnet and euhedral–subhedral hornblende define a matrix with anhedral plagioclase, quartz and ilmenite. D) Sample 195365. Elongate biotite and anhedral hornblende define a strong foliation in a matrix of subhedral quartz and plagioclase and euhedral garnet. Ilmenite commonly occurs in contact with biotite.

(Fig. 6f). A plateau age of  $562 \pm 4$  Ma (MSWD = 0.1,  $P = 1$ ) incorporates 100% of the  $^{39}\text{Ar}$ . Muscovite sample 205417 displays a flat plateau (Fig. 6g). An age of  $545 \pm 5$  Ma (MSWD = 1.3,  $P = 0.21$ ) is calculated from 100% of the  $^{39}\text{Ar}$ .

Biotite sample 195316 displays a perturbed signal with step ages between 1000 and 1600 Ma (Fig. 7x). A plateau age of  $1086 \pm 7$  Ma (MSWD = 1.7,  $P = 0.21$ ) is calculated from 65% of the  $^{39}\text{Ar}$  released.

Biotite sample 195365 displays a perturbed signal with ages between 650 and 550 Ma

indicating significant resetting, but a plateau age cannot be calculated due to the variability of age steps (Fig. 7e). An age between 600 and 550 Ma likely reflects the true age.

#### *Summary of $^{40}\text{Ar}/^{39}\text{Ar}$ results*

$^{40}\text{Ar}/^{39}\text{Ar}$  biotite and muscovite ages from the Petermann Nappe Complex range between  $598 \pm 3$  and  $545 \pm 4$  Ma (Fig. 6). Metamorphic muscovite from the Dean Quartzite in the north-western-most sequences of the Petermann Nappe Complex preserves the oldest  $^{40}\text{Ar}/^{39}\text{Ar}$  age of  $598 \pm 3$  Ma (Fig. 6b). Schists closer to the core of the Petermann



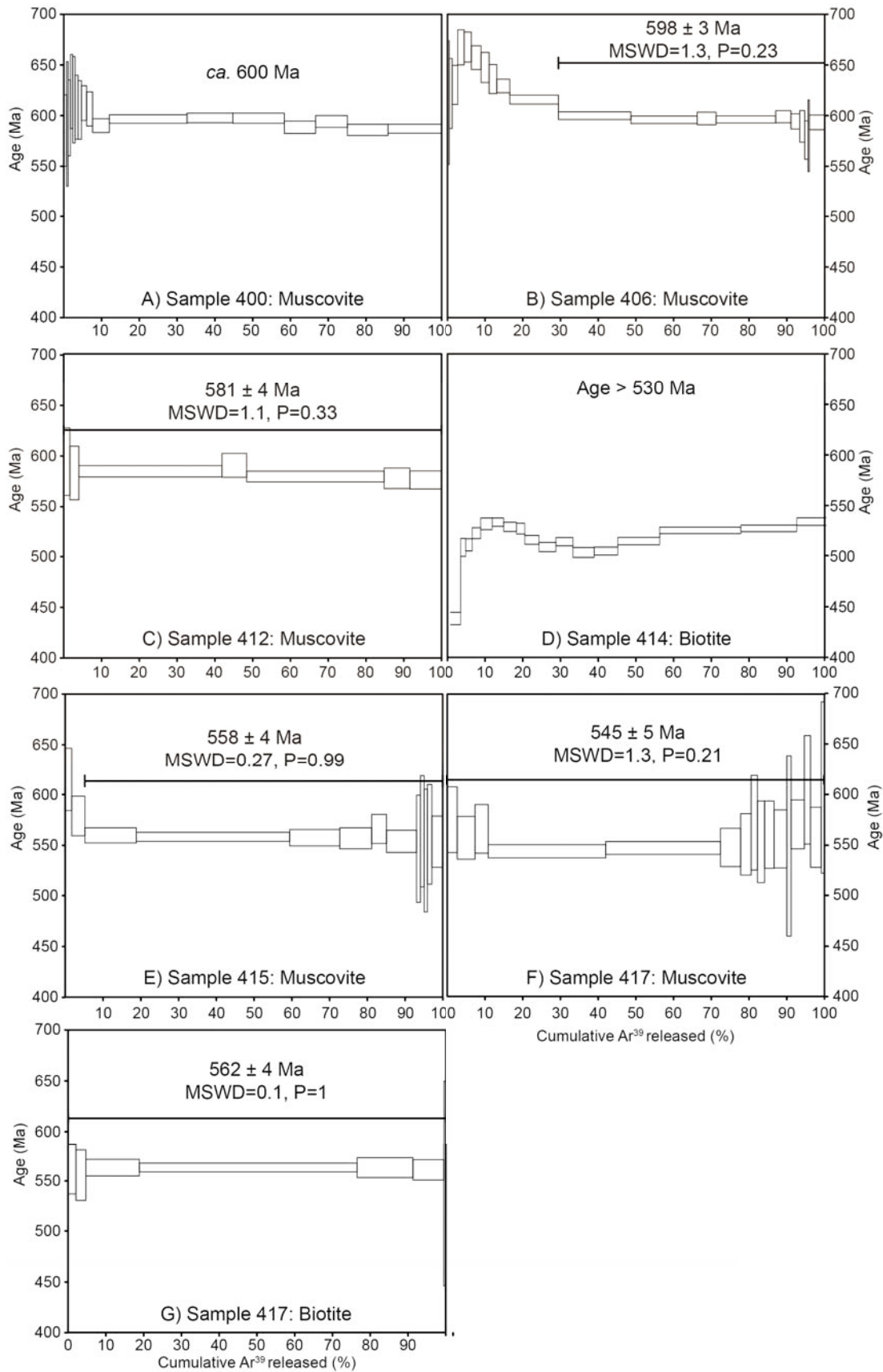


**Figure 6.** Plots of  $^{39}\text{Ar}$  released (%) Vs. age for each muscovite or biotite sample from the Petermann Nappe Complex. Solid line on each plot represents the section of the  $^{39}\text{Ar}$  signal is used to calculate the plateau age shown. Individual age errors are  $\pm 2$  sigma.



Nappe Complex preserve the youngest  $^{40}\text{Ar}/^{39}\text{Ar}$  ages;  $581 \pm 4$  Ma for sample 205412,  $558 \pm 4$  Ma for muscovite in sample 205415 and  $562 \pm 4$  Ma for biotite and  $545 \pm 5$  Ma for muscovite in sample 205417 (Fig. 6).  $^{40}\text{Ar}/^{39}\text{Ar}$  ages from hornblende samples from the Bates region preserve an array of ages between 1200 and 1050 Ma (Fig. 7). Biotite samples 195365 (Fig. 7e) and 205414 (Fig. 6c) preserve ages between 650 and 530 Ma although precise plateau ages cannot be calculated.

## DISCUSSION

### *Interpretation of $^{40}\text{Ar}/^{39}\text{Ar}$ ages*

In general terms  $^{40}\text{Ar}/^{39}\text{Ar}$  ages from muscovite, biotite and hornblende can represent the timing of: 1) primary mineral growth during prograde up to peak metamorphism, provided temperatures of metamorphism are below the closure temperature of Ar diffusion (e.g. Gray and Foster 2004; Warren *et al.* 2012); 2) recrystallisation or neocrystallisation during retrograde metamorphism (e.g. Gray and Foster 2004); or 3) closure of intergranular argon diffusion in response to cooling through the mineral's 'closure temperature' (Gray and Foster 2004; Harrison *et al.* 2009; Warren *et al.* 2012; Xu *et al.* 2000). Determining the significance of the  $^{40}\text{Ar}/^{39}\text{Ar}$  ages requires knowledge of the approximate closure temperature of the mineral,  $P$ – $T$  evolution and relationship between mineral growth and deformation (Warren *et al.* 2012).

### *Bates region (orogenic hinterland) samples*

Hornblende and biotite samples from late Mesoproterozoic (*ca.* 1080–1047 Ma) metadolerite in the Bates region do not yield plateau ages indicative of resetting during the Ediacaran–Cambrian-aged Petermann Orogeny (Fig. 7). Biotite sample 195316 yields a plateau age of  $1086 \pm 7$  Ma (Fig. 7x) that is consistent with the age of emplacement of the mafic–ultramafic Giles Complex. Biotite sample 195365 represents the most convincing evidence for Petermann-aged resetting with the entire spectra yielding ages between 650 and

550 Ma (Fig. 7e). Hornblende samples 195373, 195377, 195379 yield similar spectra (Fig. 7) and invoke similar interpretations. Early steps (first 5% of spectra) are significantly older than crystallisation age of the rocks ( $> 1080$  Ma) and suggest the incorporation of excess argon into the system. Step ages in hornblende samples are most commonly between 1100 and 1000 Ma although sample 195379 records a highly perturbed signal with ages as young as 700 Ma (Fig. 7c). The perturbed nature of the signal and incorporation of excess argon make interpretation difficult but none of the hornblende or biotite samples represent complete resetting of the argon isotope system during the Petermann Orogeny.

Incomplete resetting in hornblende and biotite is difficult to reconcile with the recognition of protracted ( $> 20$  Myr) high-pressure metamorphism (12–14 kbar, 700 °C) and pervasive recrystallization in the Bates region during the Petermann Orogeny (Gregory *et al.* 2009; Raimondo *et al.* 2009, 2010; Scrimgeour and Close 1999; Walsh *et al.* 2013; White and Clarke 1997). Specifically, shear zone-hosted metadolerites from the Bates region (Figs. 1 & 2) present recrystallised metamorphic mineral assemblages that developed at elevated metamorphic temperatures ( $\sim 750$  °C) during the Petermann Orogeny (White and Clarke 1997). If calculated metamorphic temperatures are significantly greater than the commonly proposed closure temperature of argon diffusion in hornblende or biotite i.e.  $> 400$  °C (e.g. Baldwin *et al.* 1990; Copeland *et al.* 1987; Grove and Harrison 1996; Harrison *et al.* 1985) resetting and/or diffusion is not solely dependent on temperature in this case. Fluid-rock interaction, strain variation, composition and grain size reduction are additional variables which affect the ability of isotopic systematics to reset or become 'open' to diffusion (e.g. Glodny *et al.* 2002; Glodny *et al.* 2008; Kühn *et al.* 2000). It is unclear what the limiting variable is but biotite-bearing shear zones present ages more consistent with resetting (Fig. 7e), therefore, a higher  $\text{H}_2\text{O}$ /fluid activity could have promoted more complete

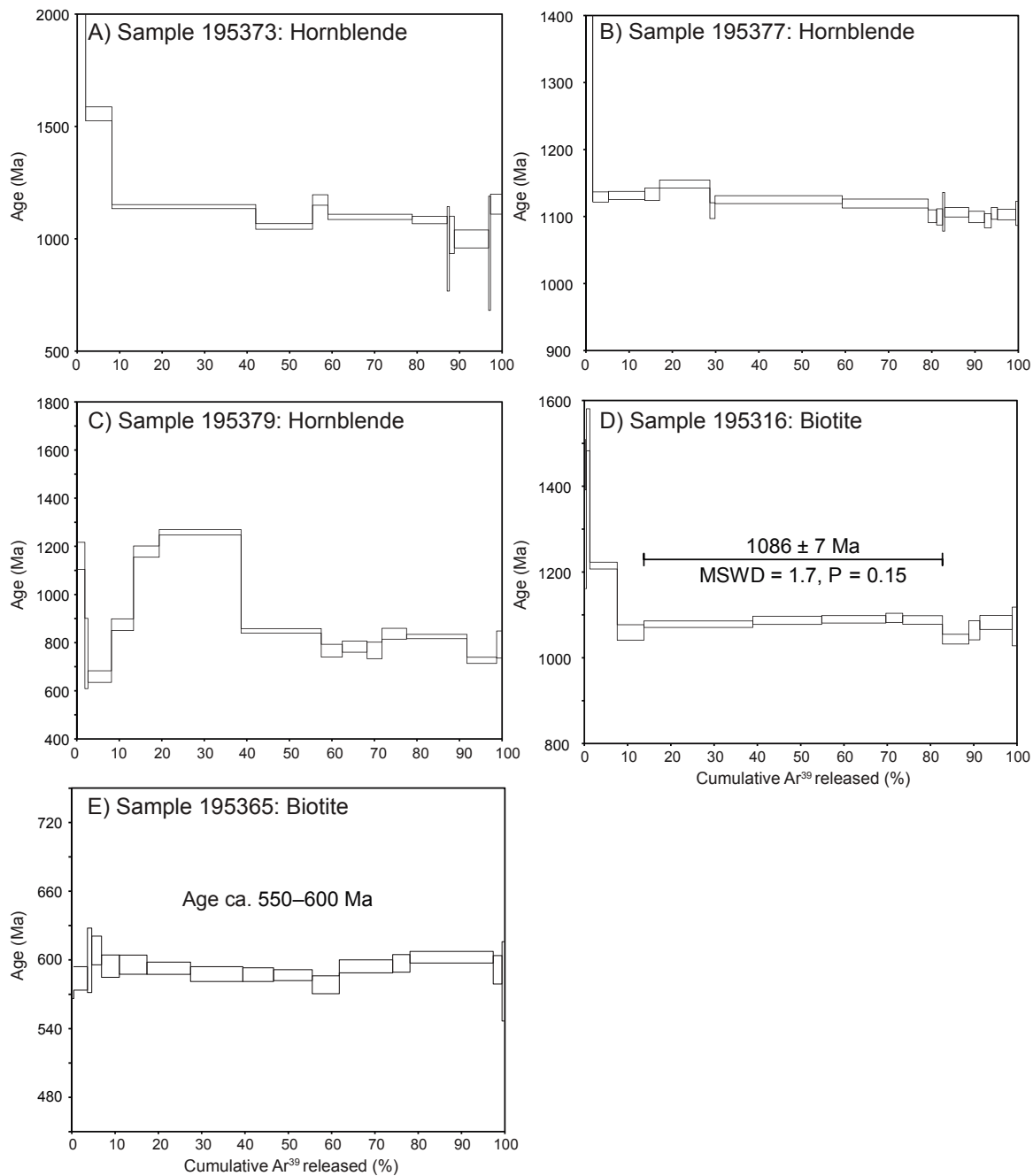


**Figure 7.** Plots of  $^{39}\text{Ar}$  released (%) Vs. age for each hornblende or biotite sample from the Bates Region. Solid line on each plot represents the section of the  $^{39}\text{Ar}$  signal is used to calculate the plateau age shown. Individual age errors are  $\pm 2$  sigma.

isotopic resetting during metamorphism of otherwise largely anhydrous rocks.

#### *Foreland fold-thrust belt samples*

Harrison *et al.* (2009) predicts the closure temperature of argon diffusion in muscovite to be approximately 425 °C for a 100  $\mu\text{m}$  diameter grain cooling at 10 °C  $\text{Ma}^{-1}$  at 10 kbar and approximately 530 °C for a 1 mm grain

cooling at 100 °C  $\text{Ma}^{-1}$  at 10 kbar. The apparent closure temperature of argon diffusion in biotite is lower than in muscovite but is less well defined. Nevertheless, it is considered to be approximately  $350 \pm 50$  °C (e.g. Copeland *et al.* 1987; Dahl 1996; Grove and Harrison 1996; Harrison *et al.* 1985). There are no existing cooling rates from the foreland of the Petermann orogen. Existing estimates

from the hinterland of the Petermann Orogen based on integrating U–Pb zircon, titanite and rutile and  $^{40}\text{Ar}/^{39}\text{Ar}$  ages suggest slow cooling rates of 1 to 5 °C Ma<sup>-1</sup> (Camacho *et al.* 2002; Raimondo *et al.* 2010; Walsh *et al.* 2013). It is unlikely that cooling rates are uniform across the orogen but for the purpose of this study we have assumed cooling rates in the foreland to be similar to those in the hinterland. Therefore, for 200 to 500 µm diameter grains (Fig. 4), temperatures of approximately 420 ± 50 °C and 350 ± 50 °C might be expected for the closure of argon diffusion in muscovite and biotite respectively.

Schists from the deepest exposed parts of the Petermann Nappe Complex (in the interior parts of the large E–W anticline) record *P–T* conditions of 5.5–7 kbar and 550–600 °C (Walsh *et al.* submitted). These temperatures are far higher than the predicted closure temperatures for the open-system diffusion of argon in both muscovite and biotite. Therefore it is unlikely that the ages preserved by either muscovite or biotite in the structurally deepest samples 205415 or 205417 will record the timing of crystallisation during prograde/burial metamorphism.

Sample 205415 is from autochthonous basement sequences and preserves an  $^{40}\text{Ar}/^{39}\text{Ar}$  age of 558 ± 4 Ma (Fig. 6e). Muscovite occurs exclusively in association with quartz and plagioclase and defines the strong foliation (Fig. 4d). There is no microstructural evidence for multiple generations of muscovite. Muscovite is interpreted to form part of the peak assemblage during amphibolite-facies metamorphism. Therefore, the  $^{40}\text{Ar}/^{39}\text{Ar}$  age of 558 ± 4 Ma recorded by muscovite is interpreted to represent the timing of cooling through the closure temperature of argon diffusion (approximately 420 °C).

Biotite in sample 205417 occurs exclusively as coarse tabular grains that define the strong foliation along with quartz and plagioclase (Fig. 4f). Biotite is interpreted to have formed during prograde to peak metamorphic conditions in

the fold-thrust belt. Therefore, biotite would have been ‘open’ to argon diffusion at the thermal peak of metamorphism and the age of 562 ± 4 Ma records the timing of closure of diffusion i.e. cooling through approximately 400 °C during the post-peak evolution. This is consistent with the interpretation of the age from muscovite sample 205415 above.

Muscovite grains in sample 205417 are fine-grained relative to biotite and are almost exclusively unorientated with respect to the foliation. Muscovite in the same sample commonly forms mono-mineralic clusters that overprint the biotite-quartz-plagioclase-ilmenite fabric (Fig. 4f). Based on these observations muscovite is interpreted to have crystallised after biotite and additionally, after foliation development. The exact relationship between the development of the foliation and the *P–T* history of the rock is impossible to decipher, given the high-variance of the mineral assemblage, but fine-grained, unorientated mica that overgrows the metamorphic foliation are commonly interpreted to have grown during the post-peak metamorphic (retrograde) evolution (e.g. Cruciani *et al.* 2008; Kunk *et al.* 2005; Stüwe 1997).

The temperature of muscovite crystallisation during the retrograde part of the *P–T* evolution is unknown and therefore it is difficult to unequivocally determine whether the  $^{40}\text{Ar}/^{39}\text{Ar}$  age of 545 ± 5 Ma records the timing of retrograde crystallisation or cooling. However, diffusion parameters for biotite suggest that diffusion of argon is more efficient at lower temperatures than in muscovite (Harrison *et al.* 1985), implying that biotite should record younger ages in a slow cooling terrain (~10 °C Myr<sup>-1</sup>). As muscovite preserves an age 8 to 26 Myr younger than biotite, which records cooling through approximately 400 °C at 562 ± 4 Ma in the same rock, the preserved age of 545 ± 5 Ma from muscovite is interpreted to record the timing of retrograde crystallisation at *T* < 400 °C during cooling. Alternatively, as the chemical composition of muscovite

and biotite are proposed to affect the closure temperature, which are additionally imprecisely quantified ( $\pm 50$  °C), the age difference recorded could arise if the closure temperature of biotite was greater than the closure temperature of muscovite.

Sample 205412 is from a sequence of muscovite schists that occur structurally above the autochthonous basement–cover sequence. Muscovite preserves an  $^{40}\text{Ar}/^{39}\text{Ar}$  age of  $581 \pm 4$  Ma. Muscovite almost exclusively occurs as elongate grains in contact with quartz and plagioclase and defines the dominant foliation (Fig. 4c). Therefore, muscovite is interpreted to have formed during prograde to peak metamorphic conditions. The schist sample occurs immediately structurally above the deepest layer of Dean Quartzite (Fig. 3) and would therefore have reached metamorphic conditions similar to the maximum  $P$ – $T$  estimates of 550–600 °C and 5.5–7 kbar (Fig. 3). Therefore the age of  $581 \pm 4$  Ma is interpreted to represent the timing of cooling through the closure temperature of approximately 420 °C. This age is 11 to 31 Myr older than the cooling ages from muscovite and biotite samples 205415 and 205417. As the incorporation of excess  $^{39}\text{Ar}$  into muscovite is generally negligible (De Jong *et al.* 2001), the age difference may be real. Variations in cooling ages from proximal locations are commonly interpreted to be an artefact of variable grain size. This interpretation is difficult to assert as muscovite grains in sample 205412 are commonly 100 to 200  $\mu\text{m}$  smaller than muscovite and biotite in sample 205417 but similar size to muscovite in sample 205415. Therefore there is no clear relationship between the cooling ages and grain size. Given similar grain sizes between samples 205412 and 205415, the age difference could be a result of the difference in structural level (i.e. burial depth), which based on average dip of the structural envelope, is approximately 1 km. Such a large age difference between such structurally proximal samples would logically point to slow cooling rates ( $< 5$  °C  $\text{Ma}^{-1}$ ). This estimate of cooling rate is consistent with

cooling rates calculated from the high-grade rocks in the orogenic hinterland (Raimondo *et al.* 2009, 2010; Walsh *et al.* 2013) but this consistency is not required.

Muscovite in the structurally higher north-western part of the Petermann Nappe Complex (Fig. 3) yields an age of  $598 \pm 3$  Ma from the Dean Quartzite. There are no  $P$ – $T$  estimates for this sequence as it does not preserve mineral assemblages suitable for providing tight  $P$ – $T$  constraints; however, semi-quantitative conditions for metamorphism can be estimated if the assumption of structural continuity between sample localities in Fig. 3 is made. The dip of relic bedding planes in the Dean Quartzite and the metamorphic foliation in the Mesoproterozoic basement sequences range between 38 and 58° in the area to the north of the fold axis, shown in Fig. 3. Based on the average dip of the sequences and the approximate across strike linear distance from the deepest sequences of the Petermann Nappe Complex (section X–Y on Fig. 3), samples 205400 and 205406 could occur between 8 and 10 km higher in the structural section. Based on maximum  $P$ – $T$  conditions of 6–7 kbar and 550–600 °C (Walsh *et al.* submitted), the apparent thermal gradient in the Petermann Orogeny was 26 to 33 °C  $\text{km}^{-1}$  (based on a crustal density of  $\sim 3$   $\text{kg m}^{-3}$ ). Peak metamorphic temperatures of 408 to 220 °C would be expected at the localities of samples 205400 and 205406. These estimated temperatures are equivalent or much lower than the proposed closure temperature of argon diffusion in muscovite (Harrison *et al.* 2009). Therefore, it seems that either muscovite crystallised at temperatures below those required for ‘effective’  $^{40}\text{Ar}$  diffusion, or that they crystallised at approximately 400 °C and underwent minor amounts of diffusion during cooling, and therefore even in a slow cooling system ( $> 5$  °C  $\text{Ma}^{-1}$ ) the timing of  $^{40}\text{Ar}$  closure would be within error of the age of crystallisation.

The age spectrum for sample 205406 displays



what could be interpreted to represent a minor proportion of excess  $^{40}\text{Ar}$  or  $^{39}\text{Ar}$  recoil (Fig. 6b). The older steps are  $> 600$  Ma but the relative amount of  $^{39}\text{Ar}$  that they include is relatively insignificant, as it comprises  $<20\%$  of the age spectrum. The plateau age does not include this portion of the data. Therefore, the derived age is interpreted to represent, within error, the timing of (prograde) neocrystallisation or recrystallisation of metamorphic muscovite at *ca.* 600 Ma. The tectonic interpretation of this age is critically important for understanding that early part of the evolution of the Petermann Orogen.

The interpretation that *ca.* 600 Ma  $^{40}\text{Ar}/^{39}\text{Ar}$  muscovite ages from the structurally highest parts of the sampled fold-thrust belt represent prograde metamorphic ages as a result of crustal thickening (orogenesis), is preferred. This interpretation is consistent with the field observation of structural interleaving and stacking (thickening) that characterises the Petermann Nappe Complex (Flöttmann *et al.* 2004; Scrimgeour *et al.* 1999). The implication is therefore that the crust may have already attained appreciable thickness by 600 Ma. Our interpretation is supported by the record of mass influx of Musgrave Province sediments into the Officer Basin at *ca.* 600 Ma, which suggests that topography existed by 600 Ma (Wade *et al.* 2005). In addition, geochronology from the far north-west of the Musgrave Province (approximately 200 km west of Mt Deering; Fig. 1b), where  $^{40}\text{Ar}/^{39}\text{Ar}$  muscovite and U–Pb zircon rim ages from metasediments and pegmatites give ages of *ca.* 623 Ma, *ca.* 628 Ma and *ca.* 631 Ma (Kirkland *et al.* 2013a; Kirkland *et al.* 2014; Kirkland *et al.* 2011), lends strong support to crustal thickening occurring prior to 600 Ma. All these data together suggest that crustal thickening was underway by this time, and that rocks deeper in the orogen were melting, leading to the crystallisation of pegmatites higher up in the sequence.

#### *Deformation history of the Petermann Orogeny*

Up to now, the timescale of the Petermann Orogeny was more or less restricted to the peak and retrograde/cooling evolution marking the gradual termination of the orogen, over the period *ca.* 575 Ma to 520 Ma (Camacho *et al.* 1997; Gregory *et al.* 2009; Raimondo *et al.* 2009, 2010; Scrimgeour and Close 1999; Walsh *et al.* 2013). With the new geochronological data from the western part of the orogen, the overall timescale for the Petermann Orogeny has been doubled to  $\geq 100$  Myr, to now span *ca.* 630 Ma to *ca.* 520 Ma.

This is a minimum age span as the oldest ages mark time that the orogen had already developed enough to generate prograde metamorphic assemblages, including melting. However, the overall age bracket is significantly older in the foreland region (625 to 545 Ma), relative to the *ca.* 570 to 520 Ma record from the hinterland. The crystallisation of muscovite in the north-western margins of the Petermann Nappe Complex (samples 205400 & 205406) is interpreted to record the timing of deformation and establishment of significant crustal thickness by *ca.* 600 Ma, which is as much as 30 Myr before maximum metamorphic conditions were reached in the hinterland of the orogen (Gregory *et al.* 2009; Raimondo *et al.* 2009, 2010; Scrimgeour and Close 1999; Walsh *et al.* 2013).

Assessing the record of deformation and cooling in the foreland of the orogen in conjunction with the record preserved in the high-grade core of the orogen in detail is difficult given the paucity of geochronological and structural data available, and the large distances between samples. However, there is enough data to at least make some broad interpretations about the assembly of the architecture of the Petermann Orogen. The ages from the orogenic core are appreciably younger than the oldest  $^{40}\text{Ar}/^{39}\text{Ar}$  and U–Pb zircon ages from the foreland fold-thrust belt and NW flanks of the orogen. As such, the available data broadly suggests that the age of tectonic activity gets younger towards the core of the orogen. This is contrary to the

conventional view of contractional orogens and fold-thrust belts where the locus of deformation and exhumation migrates to the foreland (e.g. Ghiglione and Ramos 2005; Gray and Mitra 1999). However, many orogenic systems do not follow this convention and localisation and partitioning of strain, spatially and temporally, is dictated by factors including, but not limited to, the presence of suitably oriented lithospheric structures (De Grave and Buslov 2007; Glorie *et al.* 2011), the modification of lithospheric rheology via thermal heterogeneities (Hand and Sandiford 1999; Sandiford and Hand 1998), the infiltration of fluids (Jamtveit and Austrheim 2010; Miller *et al.* 2002; Yardley 2009) and variation in obliquity of convergence in transpressional orogens (Goscombe *et al.* 2005; Goscombe *et al.* 2003; Goscombe and Gray 2008).

As the pattern of fault reactivation and exhumation within central Australia during the Phanerozoic is largely independent of the presence and orientation of crustal scale structures, Sandiford and Hand (1998) and Hand and Sandiford (1999) argue that lithospheric strength was critically reduced in response to the regime linked to subsidence patterns in intraplate sedimentary basins. Temporal and spatial variations in subsidence resulted in significant variations in the thickness of sedimentary cover and subsequently created lateral thermal heterogeneities in the lithosphere which facilitated localisation of strain. Prior to the Petermann Orogeny the thickest sedimentary cover was at least 4 km and appears to have been in the vicinity of the now exhumed Musgrave Province (Hand and Sandiford 1999). The precise location of the sedimentary depocentre at *ca.* 600 Ma is unknown but plausibly could have been relatively localised, associated with the rift packages of late Mesoproterozoic Bentley Supergroup and equivalents (Evins *et al.* 2010; Howard *et al.* 2011; Scrimgeour *et al.* 1999).

The mechanisms by which deformation might migrate toward the hinterland are

not well understood but a change in the obliquity of transpressional deformation could have assisted in localising strain in the core of the orogen (e.g. Gerbi and West 2007). Transpressional orogens are commonly characterised by strain partitioning between strike-slip- and contraction- dominated deformation (Fossen and Tikoff 1998; Goscombe *et al.* 2003; Holdsworth *et al.* 2002; Lin *et al.* 1998; Oldow *et al.* 1990; Tikoff and Teyssier 1994). This can be manifest as strike-slip-dominated shearing in the hinterland of the orogen, commonly with a major crustal-scale shear zone, with progressively more oblique to high-angle over-thrusting towards and into the foreland (Goscombe *et al.* 2005; e.g. Goscombe *et al.* 2003; Goscombe and Gray 2008). The deformation style in the Petermann Orogen is very similar to a typical transpressional orogen: the northern foreland region is dominated by E–W striking, north-vergent thrusts and upright folding (Flöttmann *et al.* 2004; Raimondo *et al.* 2010; Scrimgeour *et al.* 1999); whereas orogen-parallel crustal scale shear zones in the orogenic core display sub-horizontal stretching lineations that are parallel to acutely oblique to the dominant E–W shear foliation and accommodate large amounts of dextral strike-slip movement (Aitken *et al.* 2009a; Camacho and McDougall 2000). The resultant architecture of the orogen is similar to a transpressional flower structure with a centrally extruded core (Aitken *et al.* 2009a; Camacho and McDougall 2000).

The preservation of younger U–Pb and  $^{40}\text{Ar}/^{39}\text{Ar}$  ages in the core rather than the foreland of the orogen suggest that low-angle strike-slip-dominated tectonism was dominant later in the orogenic cycle or at least for a longer duration. This could imply record a narrowing strain envelope as the orogen evolved towards a low-angle transpressional regime, rather than reflecting contemporaneous strain partitioning for the duration of transpressional deformation (e.g. Gerbi and West 2007).

A shift from high to low angle transpression, or vice-versa, is commonly associated with

a change in obliquity of a converging plate (e.g. Gerbi and West 2007; Goscombe and Gray 2008). However, the intraplate nature of the Petermann Orogeny means there is no obvious indenting plate which might be responsible for variation in obliquity of transpression. Mechanisms which generated stresses and facilitated deformation in the Petermann Orogen are poorly constrained. However, the collision of the Indian plate with the west margin of the Australian plate during the Gondwana supercontinent assembly and subsequent rotation of the West and South Australian Cratons relative to the North Australian Craton may have generated far-field stresses which resulted in intraplate deformation in the Musgrave Province at *ca.* 655 to 550 Ma and a shift in obliquity of transpression during the Petermann Orogeny. (Li and Evans 2011).

The record of crustal thickening as early as 630 Ma in the Petermann Orogeny is contemporaneous with granite emplacement in the Telfer region during the 650 to 611 Ma Miles Orogeny (Bagas 2004; Durocher *et al.* 2003) of the Paterson Orogen in the Rudall Province in north-west Western Australia (Fig. 1a). In addition, regional gravity data shows that structures which coincide with the edges of the Anketell Regional Gravity Ridge are probably associated with the Petermann Orogeny and extend to the northwest into the Paterson Orogen (Bagas 2004; Fraser *et al.* 1976). Therefore, it is plausible that intraplate orogenesis developed contemporaneously in the Musgrave Province as well as the Rudall Province during the late Neoproterozoic, increasing the tectonic footprint of Ediacaran–Cambrian intraplate orogeny in central Australia to >1000 km length scale (Fig. 1a).

The total dataset of Petermann aged geochronology, now including the new high-precision  $^{40}\text{Ar}/^{39}\text{Ar}$  geochronology presented in this study defines a clear spatial pattern regarding the distribution of young (hinterland) versus older ages (foreland) related to burial as well as exhumation. Whereas this total

geochronological dataset remains small relative to the overall size of the Petermann Orogen, the  $^{40}\text{Ar}/^{39}\text{Ar}$  data and interpretations presented here provide impetus for further geochronological and thermochronological studies necessary to assess the patterns of deformation in the Musgrave Province during the Petermann Orogeny and make more informed inferences about the evolution of intraplate orogenic systems.

## CONCLUSIONS

Deformation during the intraplate Petermann Orogeny initiated in the orogenic foreland, resulted in development of a thick-skinned fold-thrust belt that underwent deep burial (up to 20 km) at *ca.* 600 Ma and was followed by modest rates of exhumation and cooling ( $<5^\circ\text{C Ma}^{-1}$ ) until *ca.* 560 Ma. Maximum metamorphic conditions were achieved in the orogenic core at *ca.* 570 Ma, 30 Ma after the record of crustal thickening in the foreland, as the locus of deformation stepped south toward the hinterland. The migration of deformation during transpressional orogenesis could have occurred in response to a shift from a high-angle convergence phase, dominated by foreland-vergent thrusting and the development of the Petermann Nappe Complex, to a low angle convergence phase dominated by strike-slip movement on orogen-parallel crustal scale shear zones. The apparent pattern of deformation observed during the Petermann Orogeny suggests that localisation of strain in intraplate transpressional orogens through time is dependent not only on the presence and distribution of rheological weaknesses but also on the boundary conditions during the generation of far-field stresses.

## ACKNOWLEDGEMENTS

Thanks must go to Traditional Owners of the Warburton–Wingellina–Giles regions and the Ngaanyatjarra Council for access to their lands. Logistical and financial support was provided by the Geological Survey of Western Australia and field assistance by Hugh

Smithies, Raphael Quentin De Gromard and Heather Howard is greatly appreciated. Dr. Masafumi Sudo and an anonymous reviewer are both thanked for providing constructive reviews to improve this manuscript.

## REFERENCES

- AITKEN, A.R.A. & BETTS, P.G. 2008. High-resolution aeromagnetic data over central Australia assist Grenville-era (1300;1100 Ma) Rodinia reconstructions. *Geophys. Res. Lett.*, **35**, L01306, doi: 10.1029/2007gl031563.
- AITKEN, A.R.A., BETTS, P.G. & AILLERES, L. 2009a. The architecture, kinematics, and lithospheric processes of a compressional intraplate orogen occurring under Gondwana assembly: The Petermann orogeny, central Australia. *Lithosphere*, **1**, 343-357, doi: 10.1130/L139.1.
- AITKEN, A.R.A., BETTS, P.G., WEINBERG, R.F. & GRAY, D. 2009b. Constrained potential field modeling of the crustal architecture of the Musgrave Province in central Australia: Evidence for lithospheric strengthening due to crust-mantle boundary uplift. *Journal of Geophysical Research B: Solid Earth*, **114**.
- BAGAS, L. 2004. Proterozoic evolution and tectonic setting of the northwest Paterson Orogen, Western Australia. *Precambrian Research*, **128**, 475-496.
- BALDWIN, S., HARRISON, T.M. & GERALD, J.F. 1990. Diffusion of  $^{40}\text{Ar}$  in metamorphic hornblende. *Contributions to Mineralogy and Petrology*, **105**, 691-703, doi: 10.1007/BF00306534.
- BEAUCHAMP, W., ALLMENDINGER, R.W., BARAZANGI, M., DEMNATI, A., EL ALJI, M. & DAHMANI, M. 1999. Inversion tectonics and the evolution of the High Atlas Mountains, Morocco, based on a geological–geophysical transect. *Tectonics*, **18**, 163-184.
- BIRD, P. 1998. Kinematic history of the Laramide orogeny in latitudes 35–49°N, western United States. *Tectonics*, **17**, 780-801.
- BULL, J.M. & SCRUTTON, R.A. 1992. Seismic reflection images of intraplate deformation, central Indian Ocean, and their tectonic significance. *Journal of the Geological Society*, **149**, 955-966.
- BURCHFIEL, B. & DAVIS, G.A. 1972. Structural framework and evolution of the southern part of the Cordilleran orogen, western United States. *American Journal of Science*, **272**, 97-118.
- BURKE, K. & DEWEY, J. 1973. Plume-generated triple junctions: key indicators in applying plate tectonics to old rocks. *The Journal of Geology*, 406-433.
- BUSLOV, M., DE GRAVE, J., BATALEVA, E. & BATALEV, V.Y. 2007. Cenozoic tectonic and geodynamic evolution of the Kyrgyz Tien Shan Mountains: A review of geological, thermochronological and geophysical data. *Journal of Asian Earth Sciences*, **29**, 205-214.
- CAMACHO, A., COMPSTON, W., MCCULLOCH, M. & MCDUGALL, I. 1997. Timing and exhumation of eclogite facies shear zones, Musgrave Block, central Australia. *Journal of Metamorphic Geology*, **15**, 735-751, doi: 10.1111/j.1525-1314.1997.00053.x.
- CAMACHO, A. & FANNING, C.M. 1995. Some isotopic constraints on the evolution of the granulite and upper amphibolite facies terranes in the eastern Musgrave Block, central Australia. *Precambrian Research*, **71**, 155-181, doi: 10.1016/0301-9268(94)00060-5.
- CAMACHO, A., HENSEN, B.J. & ARMSTRONG, R. 2002. Isotopic test of a thermally driven intraplate orogenic model, Australia. *Geology*, **30**, 887-890, doi:10.1130/0016-7613(2002)030<0887:itoatd>2.0.co;2.
- CAMACHO, A. & MCDUGALL, I. 2000. Intracratonic, strike-slip partitioned transpression and the formation and exhumation of eclogite facies rocks: An example from the Musgrave Block, central Australia. *Tectonics*, **19**, 978-996, doi: 10.1029/1999tc001151.
- CAMACHO, A., MCDUGALL, I., ARMSTRONG, R. & BRAUN, J. 2001. Evidence for shear heating, Musgrave Block, central Australia. *Journal of Structural Geology*, **23**, 1007-1013, doi: 10.1016/S0191-8141(00)00172-3.



- CAMACHO, A., YANG, P. & FREDERIKSEN, A. 2009. Constraints from diffusion profiles on the duration of high-strain deformation in thickened crust. *Geology*, **37**, 755-758, doi: 10.1130/g25753a.1.
- CLOETINGH, S. & VAN WEES, J. 2005. Strength reversal in Europe's intraplate lithosphere: Transition from basin inversion to lithospheric folding. *Geology*, **33**, 285-288.
- COPELAND, P., HARRISON, T.M., KIDD, W.E.A., RONGHUA, X. & YUQUAN, Z. 1987. Rapid early Miocene acceleration of uplift in the Gangdese Belt, Xizang (southern Tibet), and its bearing on accommodation mechanisms of the India-Asia collision. *Earth and Planetary Science Letters*, **86**, 240-252.
- CRUCIANI, G., FRANCESCHELLI, M., ELTER, F.M., PUXEDDU, M. & UTZERI, D. 2008. Petrogenesis of Al-silicate-bearing trondhjemitic migmatites from NE Sardinia, Italy. *Lithos*, **102**, 554-574.
- CUNNINGHAM, D. 2005. Active intracontinental transpressional mountain building in the Mongolian Altai: defining a new class of orogen. *Earth and Planetary Science Letters*, **240**, 436-444.
- DAHL, P.S. 1996. The crystal-chemical basis for Ar retention in micas: inferences from interlayer partitioning and implications for geochronology. *Contributions to Mineralogy and Petrology*, **123**, 22-39, doi: 10.1007/s004100050141.
- DE BRUIJNE, C. & ANDRIESSEN, P. 2002. Far field effects of Alpine plate tectonism in the Iberian microplate recorded by fault-related denudation in the Spanish Central System. *Tectonophysics*, **349**, 161-184.
- DE GRAVE, J. & BUSLOV, M.M. 2007. Distant effects of India-Eurasia convergence and Mesozoic intracontinental deformation in Central Asia: Constraints from apatite fission-track thermochronology. *Journal of Asian Earth Sciences*, **29**, 188-204.
- DE JONG, K., FÉRAUD, G., RUFFET, G., AMOURIC, M. & WIJBRANS, J. 2001. Excess argon incorporation in phengite of the Mulhacén Complex: submicroscopic illitization and fluid ingress during late Miocene extension in the Betic Zone, south-eastern Spain. *Chemical Geology*, **178**, 159-195.
- DEWEY, J.F. & BIRD, J.M. 1970. Mountain belts and the new global tectonics. *Journal of Geophysical Research*, **75**, 2625-2647.
- DEWEY, J.F. & BURKE, K.C. 1973. Tibetan, Variscan, and Precambrian basement reactivation: products of continental collision. *The Journal of Geology*, 683-692.
- DUROCHER, K., KYSER, T., MARLATT, J. & HANLY, A. 2003. New <sup>40</sup>Ar/<sup>39</sup>Ar ages from the central Paterson Orogen, Western Australia. *Australian Journal of Earth Sciences*, **50**, 601-610.
- EDGOOSE, C.J., SCRIMGEOUR, I.R. & CLOSE, D.F. 2004. Geology of the Musgrave Block, Northern Territory. *Northern Territory Geological Survey. Report 15*.
- ELLIS, D.J. & MABOKO, M.A.H. 1992. Precambrian tectonics and the physiochemical evolution of the continental crust. Part I: The gabbro-eclogite transition. *Precambrian Research*, **55**, 491-506.
- EVINS, P.M., SMITHIES, R.H., HOWARD, H.M., KIRKLAND, C.L., WINGATE, M.T.D. & BODORKOS, S. 2010. Devil in the detail; The 1150–1000 Ma magmatic and structural evolution of the Ngaanyatjarra Rift, west Musgrave Province, Central Australia. *Precambrian Research*, **183**, 572-588, doi: 10.1016/j.precamres.2010.02.011.
- FLÖTTMANN, T., HAND, M., CLOSE, D., EDGOOSE, C. & SCRIMGEOUR, I.R. 2004. Thrust tectonic styles of the intracratonic Alice Springs and Petermann Orogenies, central Australia. in *Thrust tectonics and hydrocarbon systems.*, edited by K. McClay, pp. 538-557, *American Association of Petroleum Geologists Memoir*.
- FOSSEN, H. & TIKOFF, B. 1998. Extended models of transpression and transtension, and application to tectonic settings. *Geological Society, London, Special Publications*, **135**, 15-33.
- FRASER, A.R., MOSS, F.J. & TURPIE, A. 1976. Reconnaissance gravity survey of

- Australia. *GEOPHYSICS*, **41**, 1337-1345, doi: doi:10.1190/1.1440683.
- GERBI, C. & WEST, D.P. 2007. Use of U-Pb geochronology to identify successive, spatially overlapping tectonic episodes during Silurian-Devonian orogenesis in south-central Maine, USA. *Geological Society of America Bulletin*, **119**, 1218-1231, doi: 10.1130/b26162.1.
- GHIGLIONE, M.C. & RAMOS, V.A. 2005. Progression of deformation and sedimentation in the southernmost Andes. *Tectonophysics*, **405**, 25-46.
- GLIKSON, A.Y., BALLHAUS, C.G., CLARKE, G.L., SHERATON, J.W., STEWART, A.J. & SUN, S.-S. 1995. Geological framework and crustal evolution of the Giles mafic-ultramafic complex and environs, western Musgrave Block, central Australia. *AGSO Journal of Australian Geology & Geophysics*, **16**, 41-67.
- GLIKSON, A.Y., STEWART, A.J., BALLHAUS, C.G., CLARKE, G.L., FEEKEN, E.H.J., LEVEN, J.H., SHERATON, J.W. & SUN, S.-S. 1996. Geology of the western Musgrave Block, central Australia, with particular reference to the mafic-ultramafic Giles complex. *AGSO Bulletin*, **239**, 41-68.
- GLODNY, J., KÜHN, A. & AUSTRHEIM, H. 2002. Rb/Sr record of fluid-rock interaction in eclogites, Bergen Arcs, Norway. *Geochim Cosmochim Acta*, **66**, A280.
- GLODNY, J., KÜHN, A. & AUSTRHEIM, H. 2008. Diffusion versus recrystallization processes in Rb-Sr geochronology: Isotopic relics in eclogite facies rocks, Western Gneiss Region, Norway. *Geochimica et Cosmochimica Acta*, **72**, 506-525.
- GLORIE, S., DE GRAVE, J., BUSLOV, M., ZHIMULEV, F., STOCKLI, D., BATALEV, V., IZMER, A., VANHAECKE, F. & ELBURG, M. 2011. Tectonic history of the Kyrgyz South Tien Shan (Atbashi-Inylchek) suture zone: The role of inherited structures during deformation and propagation. *Tectonics*, **30**.
- GORCZYK, W., HOBBS, B., GESSNER, K. & GERYA, T. 2013. Intracratonic geodynamics. *Gondwana Research*, **24**, 838-848.
- GOSCOMBE, B., GRAY, D. & HAND, M. 2005. Extrusional tectonics in the core of a transpressional orogen; the Kaoko Belt, Namibia. *Journal of Petrology*, **46**, 1203-1241.
- GOSCOMBE, B., HAND, M. & GRAY, D. 2003. Structure of the Kaoko Belt, Namibia: progressive evolution of a classic transpressional orogen. *Journal of Structural Geology*, **25**, 1049-1081.
- GOSCOMBE, B.D. & GRAY, D.R. 2008. Structure and strain variation at mid-crustal levels in a transpressional orogen: a review of Kaoko Belt structure and the character of West Gondwana amalgamation and dispersal. *Gondwana Research*, **13**, 45-85.
- GRAY, D. & FOSTER, D. 2004.  $^{40}\text{Ar}/^{39}\text{Ar}$  thermochronologic constraints on deformation, metamorphism and cooling/exhumation of a Mesozoic accretionary wedge, Otago Schist, New Zealand. *Tectonophysics*, **385**, 181-210.
- GRAY, M.B. & MITRA, G. 1999. Ramifications of four-dimensional progressive deformation in contractional mountain belts. *Journal of Structural Geology*, **21**, 1151-1160.
- GREGORY, C.J., BUICK, I.S., HERMANN, J. & RUBATTO, D. 2009. Mineral-scale trace element and U-Th-Pb age constraints on metamorphism and melting during the Petermann Orogeny (central Australia). *Journal of Petrology*, **50**, 251-287.
- GROVE, M. & HARRISON, T.M. 1996.  $^{40}\text{Ar}^*$  diffusion in Fe-rich biotite. *American Mineralogist*, **81**, 940-951.
- HAND, M. & SANDIFORD, M. 1999. Intraplate deformation in central Australia, the link between subsidence and fault reactivation. *Tectonophysics*, **305**, 121-140, doi: Doi: 10.1016/s0040-1951(99)00009-8.
- HARRISON, T.M., CÉLÉRIER, J., AIKMAN, A.B., HERMANN, J. & HEIZLER, M.T. 2009. Diffusion of  $^{40}\text{Ar}$  in muscovite. *Geochimica et Cosmochimica Acta*, **73**, 1039-1051.
- HARRISON, T.M., DUNCAN, I. & MCDOUGALL, I. 1985. Diffusion of  $^{40}\text{Ar}$  in biotite: Temperature, pressure and compositional effects. *Geochimica et Cosmochimica Acta*, **49**, 2461-2468.

- HOLDSWORTH, R., TAVARNELLI, E., CLEGG, P., PINHEIRO, R., JONES, R. & MCCAFFREY, K. 2002. Domainal deformation patterns and strain partitioning during transpression: an example from the Southern Uplands terrane, Scotland. *Journal of the Geological Society*, **159**, 401-415.
- HOLFORD, S.P., HILLIS, R.R., HAND, M. & SANDIFORD, M. 2011. Thermal weakening localizes intraplate deformation along the southern Australian continental margin. *Earth and Planetary Science Letters*, **305**, 207-214.
- HOWARD, H., SMITHIES, R., KIRKLAND, C., KELSEY, D., AITKEN, A., WINGATE, M., DE GROMARD, R.Q., SPAGGIARI, C. & MAIER, W. 2015. The burning heart—The Proterozoic geology and geological evolution of the west Musgrave Region, central Australia. *Gondwana Research*, **27**, 64-94.
- HOWARD, H.M., WERNER, M., SMITHIES, R.H., KIRKLAND, C.L., KELSEY, D.L., HAND, M., COLLINS, A., PIRAJNO, F., WINGATE, M.T.D., MAIER, W.D. & RAIMONDO, T. 2011. The geology of the west Musgrave Province and the Bentley Supergroup. — a field guide. *Geological Survey of Western Australia Record 2011/4*, p. **119**.
- JAMIESON, R.A. & BEAUMONT, C. 2013. On the origin of orogens. *Geological Society of America Bulletin*, **125**, 1671-1702.
- JAMTVEIT, B. & AUSTRHEIM, H. 2010. Metamorphism: the role of fluids. *Elements*, **6**, 153-158.
- KENNER, S.J. & SEGALL, P. 2000. A mechanical model for intraplate earthquakes: Application to the New Madrid seismic zone. *Science*, **289**, 2329-2332.
- KIRKLAND, C.L., JOURDAN, F., WINGATE, M.T.D., QUENTIN DE GROMARD, R., HOWARD, H.M. & SMITHIES, R.H. 2013a. 185414: quartzite, Great Central Road; Geochronology Record 1139. *Geological Survey of Western Australia*, **4p**.
- KIRKLAND, C.L., SMITHIES, R.H., WOODHOUSE, A.J., HOWARD, H.M., WINGATE, M.T., BELOUSOVA, E.A., CLIFF, J.B., MURPHY, R.C. & SPAGGIARI, C.V. 2013b. Constraints and deception in the isotopic record; the crustal evolution of the west Musgrave Province, central Australia. *Gondwana Research*, **23**, 759-781.
- KIRKLAND, C.L., WINGATE, M.T.D., QUENTIN DE GROMARD, R., HOWARD, H.M. & SMITHIES, R.H. 2014. 208414: quartzite, Mitika Homestead; Geochronology Record 1205. *Geological Survey of Western Australia*, **6p**.
- KIRKLAND, C.L., WINGATE, M.T.D. & SMITHIES, R.H. 2011. 187175: muscovite–tourmaline pegmatite, Morgan Range; *Geochronology Record 936*; **Geological Survey of Western Australia**, **4p**.
- KOPPERS, A.A.P. 2002. ArArCALC—software for  $^{40}\text{Ar}/^{39}\text{Ar}$  age calculations. *Computers & Geosciences*, **28**, 605-619.
- KORSCH, R.J., GOLEBY, B.R., LEVEN, J.H. & DRUMMOND, B.J. 1998. Crustal architecture of central Australia based on deep seismic reflection profiling. *Tectonophysics*, **288**, 57-69, doi: 10.1016/s0040-1951(97)00283-7.
- KORSCH, R.J. & KOSITCIN, N. 2010. GOMA (Gawler Craton–Officer Basin–Musgrave Province–Amadeus Basin) Seismic and MT Workshop 2010. *GEOSCIENCE AUSTRALIA RECORD 2010/39*.
- KÜHN, A., GLODNY, J., IDEN, K. & AUSTRHEIM, H. 2000. Retention of Precambrian Rb/Sr phlogopite ages through Caledonian eclogite facies metamorphism, Bergen Arc Complex, W-Norway. *Lithos*, **51**, 305-330.
- KUNK, M.J., WINTSCH, R.P., NAESER, C.W., NAESER, N.D., SOUTHWORTH, C.S., DRAKE, A.A. & BECKER, J.L. 2005. Contrasting tectonothermal domains and faulting in the Potomac terrane, Virginia–Maryland—discrimination by  $^{40}\text{Ar}/^{39}\text{Ar}$  and fission-track thermochronology. *Geological Society of America Bulletin*, **117**, 1347-1366, doi: 10.1130/b25599.1.
- LAMBECK, K. & BURGESS, G. 1992. Deep crustal structure of the Musgrave Block, central Australia: Results from teleseismic travel-time anomalies. *Australian Journal of Earth Sciences: An International Geoscience Journal of the*

- Geological Society of Australia*, **39**, 1 - 19.
- LEE, J.Y., MARTI, K., SEVERINGHAUS, J.P., KAWAMURA, K., YOO, H.S., LEE, J.B. & KIM, J.S. 2006. A redetermination of the isotopic abundance of atmospheric Ar. *Geochimica et Cosmochimica Acta*, **70**, 4507-4512.
- LI, Z.-X. & EVANS, D.A. 2011. Late Neoproterozoic 40 intraplate rotation within Australia allows for a tighter-fitting and longer-lasting Rodinia. *Geology*, **39**, 39-42.
- LIN, S., JIANG, D. & WILLIAMS, P.F. 1998. Transpression (or transtension) zones of triclinic symmetry: natural example and theoretical modelling. *Geological Society, London, Special Publications*, **135**, 41-57.
- LINDSAY, J.F. & LEVEN, J.H. 1996. Evolution of a Neoproterozoic to Palaeozoic intracratonic setting, Officer Basin, South Australia. *Basin Research*, **8**, 403-424, doi: 10.1046/j.1365-2117.1996.00223.x.
- LIVACCARI, R.F. 1991. Role of crustal thickening and extensional collapse in the tectonic evolution of the Sevier-Laramide orogeny, western United States. *Geology*, **19**, 1104-1107.
- MABOKO, M.A.H., MCDUGALL, I., ZEITLER, P.K. & WILLIAMS, I.S. 1992. Geochronological evidence for ~530-550 Ma juxtaposition of two Proterozoic metamorphic terranes in the Musgrave Ranges, central Australia. *Australian Journal of Earth Sciences*, **39**, 457-471.
- MARSHAK, S., KARLSTROM, K. & TIMMONS, J.M. 2000. Inversion of Proterozoic extensional faults: An explanation for the pattern of Laramide and Ancestral Rockies intracratonic deformation, United States. *Geology*, **28**, 735-738.
- MILLER, J., BUICK, I., CARTWRIGHT, I. & BARNICOAT, A. 2002. Fluid processes during the exhumation of high-P metamorphic belts. *Mineralogical Magazine*, **66**, 93-119.
- NEIL, E.A. & HOUSEMAN, G.A. 1999. Rayleigh-Taylor instability of the upper mantle and its role in intraplate orogeny. *Geophysical Journal International*, **138**, 89-107, doi: 10.1046/j.1365-246x.1999.00841.x.
- OLDOW, J.S., BALLY, A.W. & LALLEMANT, H.G.A. 1990. Transpression, orogenic float, and lithospheric balance. *Geology*, **18**, 991-994.
- PYSKLYWEC, R.N. & BEAUMONT, C. 2004. Intraplate tectonics: feedback between radioactive thermal weakening and crustal deformation driven by mantle lithosphere instabilities. *Earth and Planetary Science Letters*, **221**, 275-292, doi: 10.1016/s0012-821x(04)00098-6.
- RAIMONDO, T., COLLINS, A.S., HAND, M., WALKER-HALLAM, A., SMITHIES, R.H., EVINS, P.M. & HOWARD, H.M. 2009. Ediacaran intracontinental channel flow. *Geology*, **37**, 291-294, doi: 10.1130/g25452a.1.
- RAIMONDO, T., COLLINS, A.S., HAND, M., WALKER-HALLAM, A., SMITHIES, R.H., EVINS, P.M. & HOWARD, H.M. 2010. The anatomy of a deep intracontinental orogen. *Tectonics*, **29**, TC4024, doi: 10.1029/2009tc002504.
- RAIMONDO, T., HAND, M. & COLLINS, W.J. 2014. Compressional intracontinental orogens: Ancient and modern perspectives. *Earth-Science Reviews*, **130**, 128-153.
- RENNE, P.R., MUNDIL, R., BALCO, G., MIN, K. & LUDWIG, K.R. 2010. Joint determination of  $^{40}\text{K}$  decay constants and  $^{40}\text{Ar}^*/^{40}\text{K}$  for the Fish Canyon sanidine standard, and improved accuracy for  $^{40}\text{Ar}/^{39}\text{Ar}$  geochronology. *Geochimica et Cosmochimica Acta*, **74**, 5349 - 5367.
- SANDIFORD, M. & HAND, M. 1998. Controls on the locus of intraplate deformation in central Australia. *Earth and Planetary Science Letters*, **162**, 97-110, doi: 10.1016/s0012-821x(98)00159-9.
- SANDIFORD, M., HAND, M. & MCLAREN, S. 2001. Tectonic feedback, intraplate orogeny and the geochemical structure of the crust; a central Australian perspective. In: Miller, J.A., Holdsworth, R.E., Buick Ian, S. & Hand, M. (eds.) *Continental reactivation and reworking*. Geological Society, London, Special Publications.
- SCRIMGEOUR, I.R. & CLOSE, D.F. 1999. Regional high-pressure metamorphism during



- intracratonic deformation: the Petermann Orogeny, central Australia. *Journal of Metamorphic Geology*, **17**, 557-572, doi: 10.1046/j.1525-1314.1999.00217.x.
- SCRIMGEOUR, I.R., CLOSE, D.F. & EDGOOSE, C.J. 1999. Petermann Ranges, N.T. 1:250000 Geological Series. *Department of Mines and Energy, Northern Territory Geological Survey. Explanatory Notes SG52-7*.
- SENGÖR, A.C. 1976. Collision of irregular continental margins: implications for foreland deformation of Alpine-type orogens. *Geology*, **4**, 779-782.
- SMITHIES, R., HOWARD, H., KIRKLAND, C., KORHONEN, F., MEDLIN, C., MAIER, W., DE GROMARD, R.Q. & WINGATE, M. 2015. Piggy-back Supervolcanoes—Long-Lived, Voluminous, Juvenile Rhyolite Volcanism in Mesoproterozoic Central Australia. *Journal of Petrology*, egv015.
- SMITHIES, R., KIRKLAND, C., KORHONEN, F., AITKEN, A., HOWARD, H., MAIER, W., WINGATE, M., QUENTIN DE GROMARD, R. & GESSNER, K. 2014. The Mesoproterozoic thermal evolution of the Musgrave Province in central Australia—Plume vs. the geological record. *Gondwana Research*.
- SMITHIES, R.H., HOWARD, H.M., EVINS, P.M., KIRKLAND, C.L., KELSEY, D.E., HAND, M., WINGATE, M.T.D., COLLINS, A.S. & BELOUSOVA, E. 2011. High-Temperature Granite Magmatism, Crust–Mantle Interaction and the Mesoproterozoic Intracontinental Evolution of the Musgrave Province, Central Australia. *Journal of Petrology*, **52**, 931-958, doi: 10.1093/petrology/egr010.
- SMITHIES, R.H., HOWARD, H.M., EVINS, P.M., KIRKLAND, C.L., KELSEY, D.E., HAND, M., WINGATE, M.T.D., COLLINS, A.S., BELOUSOVA, E. & ALLCHURCH, S. 2010. Geochemistry, geochronology and petrogenesis of Mesoproterozoic felsic rocks in the western Musgrave Province of central Australia and implication for the Mesoproterozoic tectonic evolution of the region. *Geological Survey of Western Australia Record 2011/4, Report 106 73*.
- STEPHENSON, R., EGHOLM, D.L., NIELSEN, S.B. & STOVBA, S.M. 2009. Role of thermal refraction in localizing intraplate deformation in southeastern Ukraine. *Nature Geoscience*, **2**, 290-293, doi:
- STÜWE, K. 1997. Effective bulk composition changes due to cooling: a model predicting complexities in retrograde reaction textures. *Contributions to Mineralogy and Petrology*, **129**, 43-52, doi: 10.1007/s004100050322.
- SUN, S.-S., SHERATON, J.W., GLIKSON, A.Y. & STEWART, A.J. 1996. A major magmatic event during 1050-1080 in central Australia and an emplacement age for the Giles Complex. *AGSO Research Newsletter*, **17**, 9-10.
- TIKOFF, B. & TEYSSIER, C. 1994. Strain modeling of displacement-field partitioning in transpressional orogens. *Journal of Structural Geology*, **16**, 1575-1588.
- TUCKER, N.M., HAND, M., KELSEY, D.E. & DUTCH, R.A. 2015. A duality of timescales: Short-lived ultrahigh temperature metamorphism preserving a long-lived monazite growth history in the Grenvillian Musgrave–Albany–Fraser Orogen. *Precambrian Research*, **264**, 204-234.
- VAN HINSBERGEN, D.J., STRAATHOF, G.B., KUIPER, K.F., CUNNINGHAM, W.D. & WIJBRANS, J. 2008. No vertical axis rotations during Neogene transpressional orogeny in the NE Gobi Altai: coinciding Mongolian and Eurasian early Cretaceous apparent polar wander paths. *Geophysical Journal International*, **173**, 105-126.
- WADE, B.P., BAROVICH, K.M., HAND, M., SCRIMGEOUR, I.R. & CLOSE, D.F. 2006. Evidence for early Mesoproterozoic arc magmatism in the Musgrave Block, central Australia: Implications for Proterozoic crustal growth and tectonic reconstructions of Australia. *Journal of Geology*, **114**, 43-63.
- WADE, B.P., HAND, M. & BAROVICH, K.M. 2005. Nd isotopic and geochemical constraints on provenance of sedimentary rocks in the eastern Officer Basin, Australia: implications for the duration of the intracratonic Petermann Orogeny. *Journal of the Geological Society*, **162**, 513-530, doi: 10.1144/0016-764904-001.
- WADE, B.P., KELSEY, D.E., HAND, M. & BAROVICH, K.M. 2008. The Musgrave

- Province; Stitching North, West and South Australia. *Precambrian Research*, **166**, 370-386.
- WALSH, A.K., HAND, M. & KELSEY, D.E. in review. A metamorphic perspective on foreland flexure during intraplate orogeny: evidence for the involvement of weak lithosphere. *Terra Nova*.
- WALSH, A.K., HAND, M. & KELSEY, D.E. submitted. A metamorphic perspective on foreland flexure during intraplate orogeny: evidence for the involvement of weak lithosphere. *Terra Nova*.
- WALSH, A.K., KELSEY, D.E., KIRKLAND, C.L., HAND, M., SMITHIES, R.H., CLARK, C. & HOWARD, H.M. 2014. P–T–t evolution of a large, long-lived, ultrahigh-temperature Grenvillian belt in central Australia. *Gondwana Research*.
- WALSH, A.K., RAIMONDO, T., KELSEY, D.E., HAND, M., PFITZNER, H.L. & CLARK, C. 2013. Duration of high-pressure metamorphism and cooling during the intraplate Petermann Orogeny. *Gondwana Research*, **24**, 969-983.
- WALTER, M.R., VEEVERS, J.J., CALVER, C.R. & GREY, K. 1995. Neoproterozoic stratigraphy of the Centralian Superbasin, Australia. *Precambrian Research*, **73**, 173-195, doi: 10.1016/0301-9268(94)00077-5.
- WARREN, C.J., HANKE, F. & KELLEY, S.P. 2012. When can muscovite  $^{40}\text{Ar}/^{39}\text{Ar}$  dating constrain the timing of metamorphic exhumation? *Chemical Geology*, **291**, 79-86.
- WHITE, R.W. & CLARKE, G.L. 1997. The Role of Deformation in Aiding Recrystallization: an Example from a High-pressure Shear Zone, Central Australia. *J. Petrology*, **38**, 1307-1329, doi: 10.1093/petroj/38.10.1307.
- WINDLEY, B.F., ALEXEIEV, D., XIAO, W., KRÖNER, A. & BADARCH, G. 2007. Tectonic models for accretion of the Central Asian Orogenic Belt. *Journal of the Geological Society*, **164**, 31-47.
- WINGATE, M.T.D., PIRAJNO, F. & MORRIS, P.A. 2004. Warakurna large igneous province: A new Mesoproterozoic large igneous province in west-central Australia. *Geology*, **32**, 105-108.
- XU, B., GROVE, M., WANG, C., ZHANG, L. & LIU, S. 2000.  $^{40}\text{Ar}/^{39}\text{Ar}$  thermochronology from the northwestern Dabie Shan: constraints on the evolution of Qinling–Dabie orogenic belt, east-central China. *Tectonophysics*, **322**, 279-301.
- YARDLEY, B.W. 2009. The role of water in the evolution of the continental crust. *Journal of the Geological Society*, **166**, 585-600.
- ZIEGLER, P.A., CLOETINGH, S. & VAN WEES, J.-D. 1995. Dynamics of intra-plate compressional deformation: the Alpine foreland and other examples. *Tectonophysics*, **252**, 7-59.
- ZOBACK, M.L. 1992. First- and second-order patterns of stress in the lithosphere: The world stress map project. *Journal of Geophysical Research: Solid Earth (1978–2012)*, **97**, 11703-11728.

## *Supporting information*

Supplementary Table 1. Ar-Ar isotope data collected for muscovite, biotite and hornblende samples from the west Musgrave Province (*on pages to follow*)

Ar-Ar isotope data for muscovite sample 205400														
Relative Abundances	36Ar	%1s	37Ar	%1s	38Ar	%1s	39Ar	%1s	40Ar	%1s	Age ± 2s (Ma)	40Ar(r) (%)	39Ar(k) (%)	K/Ca ± 2s
2A24330D	63.00 W	13.660	0.0002241	153.246	0.0000476	22.573	0.0023883	1.805	0.1238029	0.214	584.24 ± 34.93	82.04	0.72	5 ± 14
2A24331D	63.40 W	75.493	0.0000340	845.245	0.0000198	45.956	0.0013687	1.467	0.0635288	0.351	590.65 ± 60.99	92.80	0.41	17 ± 293
2A24332D	63.90 W	58.288	0.0000049	6263.375	0.0000281	32.370	0.0020329	1.363	0.0937146	0.284	596.59 ± 37.04	94.54	0.61	179 ± 22385
2A24333D	64.40 W	77.085	0.0000821	350.810	0.0000327	29.766	0.0020249	1.212	0.0966119	0.265	622.40 ± 36.19	96.01	0.61	11 ± 74
2A24335D	64.90 W	85.245	0.0001560	215.374	0.0000352	30.115	0.0020655	1.224	0.0973611	0.207	614.25 ± 42.21	95.68	0.62	6 ± 25
2A24336D	65.40 W	70.116	0.0001836	171.442	0.0000335	26.296	0.0026977	1.494	0.1245147	0.246	607.07 ± 31.23	96.38	0.81	6 ± 22
2A24337D	65.90 W	90.526	0.0000497	653.279	0.0000469	19.476	0.0030039	1.133	0.1366498	0.233	604.36 ± 28.64	97.27	0.90	26 ± 340
2A24338D	66.40 W	69.980	0.0001284	225.330	0.0000554	17.469	0.0044480	0.709	0.2035988	0.166	611.11 ± 16.95	97.95	1.34	15 ± 67
2A24340D	66.90 W	342.687	0.0004116	84.194	0.0000605	22.317	0.0053179	0.545	0.2368533	0.090	605.32 ± 16.72	99.54	1.60	6 ± 9
2A24341D	67.40 W	33.114	0.0004325	75.811	0.0001982	5.330	0.0147124	0.413	0.6417178	0.069	589.02 ± 6.75	98.43	4.43	15 ± 22
2A24342D	67.80 W	23.503	0.0000529	627.230	0.0008780	2.227	0.0683416	0.387	2.9863985	0.043	595.47 ± 4.11	99.51	20.57	555 ± 6967
2A24343D	68.00 W	47.442	0.0000580	580.600	0.0005268	3.164	0.0402464	0.412	1.7607769	0.054	596.51 ± 4.64	99.60	12.11	298 ± 3463
2M24368D	68.50 W	32.786	0.0000989	517.022	0.0006034	2.763	0.0453156	0.431	1.9862893	0.034	596.26 ± 4.89	99.36	13.64	197 ± 2037
2M24369D	69.00 W	20.699	0.0003450	149.557	0.0003461	4.626	0.0274265	0.478	1.1936826	0.058	587.41 ± 5.98	98.33	8.26	34 ± 102
2M24370D	69.50 W	29.685	0.0001624	329.650	0.0003538	4.378	0.0279920	0.422	1.2270474	0.089	593.13 ± 5.80	98.74	8.43	74 ± 489
2M24371D	70.50 W	9.135	0.0003353	154.644	0.0004871	3.316	0.0357801	0.472	1.5672205	0.075	584.86 ± 5.45	97.20	10.77	46 ± 142
2M24373D	82.00 W	4.732	0.0003640	140.512	0.0006696	1.862	0.0470692	0.335	2.1244500	0.046	585.99 ± 4.35	94.55	14.17	56 ± 156
J = 0.00900500 ± 0.00002431														

Ar-Ar isotope data for muscovite sample 205406														
Relative Abundances	36Ar	%1s	37Ar	%1s	38Ar	%1s	39Ar	%1s	40Ar	%1s	Age ± 2s (Ma)	40Ar(r) (%)	39Ar(k) (%)	K/Ca ± 2s
2A24175D	63.00 W	709.059	0.0000022	199.337	0.0000265	25.151	0.0018409	1.587	0.0824463	0.284	614.51 ± 61.57	100.77	0.45	2 ± 10
2A24176D	64.00 W	68.991	0.0000092	6924.357	0.0000477	14.229	0.0033446	1.066	0.1605185	0.167	623.57 ± 34.86	95.67	0.81	156 ± 21556
2A24177D	65.00 W	92.521	0.0001362	466.901	0.0000842	8.379	0.0059855	0.703	0.2843487	0.146	632.10 ± 19.45	98.22	1.45	19 ± 177
2A24178D	65.50 W	168.187	0.0000476	1342.943	0.0000905	9.553	0.0070744	0.743	0.3562950	0.091	669.41 ± 17.40	99.19	1.71	64 ± 1717
2A24180D	66.00 W	0.0000062	0.0000445	1456.609	0.0000974	10.129	0.0078480	0.607	0.3941514	0.071	669.71 ± 14.86	99.52	1.90	76 ± 2209
2A24181D	66.50 W	0.0000082	190.502	0.0000680	935.950	0.0001247	4.375	0.0105873	0.570	0.5217335	659.19 ± 11.82	99.53	2.57	67 ± 1253
2A24182D	67.00 W	542.067	0.0000263	2497.567	0.0001069	12.198	0.0089198	0.712	0.4287582	0.121	649.31 ± 14.97	100.22	2.16	146 ± 7298
2A24183D	67.50 W	354.608	0.0000045	1411.286	0.0001130	7.777	0.0083073	0.553	0.3931038	0.069	637.80 ± 14.44	99.66	2.01	78 ± 2203
2A24185D	68.00 W	81.041	0.0004054	51.822	0.0001692	3.558	0.0141826	0.513	0.6634408	0.068	631.09 ± 6.70	99.55	3.44	15 ± 16
2A24186D	68.50 W	13.514	0.0002024	88.305	0.0006743	2.849	0.0532860	0.414	2.4361191	0.044	617.52 ± 4.47	99.28	12.91	113 ± 200
2A24187D	69.00 W	16.613	0.0000370	459.966	0.0010058	1.328	0.0792762	0.358	3.5060489	0.028	601.49 ± 3.78	99.49	19.21	922 ± 8480
2A24188D	69.50 W	13.191	0.0001579	115.821	0.0009240	2.198	0.0725031	0.354	3.1854714	0.026	597.41 ± 3.71	99.35	17.57	197 ± 457
2A24204D	70.00 W	51.491	0.0000642	430.161	0.0002709	2.781	0.0207619	0.572	0.9123620	0.045	598.81 ± 6.21	99.61	5.03	139 ± 1196
2A24205D	70.50 W	5.546	0.0000343	888.624	0.0008427	1.424	0.0652121	0.327	2.8922611	0.057	597.77 ± 3.49	98.49	15.81	819 ± 14550
2A24206D	71.00 W	10.384	0.0000107	2728.753	0.0002223	5.699	0.0166996	0.477	0.7569132	0.076	600.44 ± 6.00	96.88	4.05	673 ± 36708
2A24207D	71.50 W	0.0000903	8.191	0.00003366	81.837	0.0001441	3.346	0.0095152	0.527	0.4410031	595.84 ± 7.64	93.89	2.31	12 ± 20
2A24209D	72.00 W	0.0000935	10.035	0.0002480	108.975	0.0000788	11.812	0.0055233	1.001	0.2659034	590.89 ± 15.66	89.51	1.34	10 ± 21
2A24210D	72.50 W	0.0000757	11.161	0.0001917	153.522	0.0000578	7.530	0.0035896	0.946	0.1730913	577.22 ± 19.10	86.95	0.87	8 ± 25
2A24211D	73.00 W	24.335	0.0001739	158.128	0.0000219	22.779	0.0014736	1.616	0.0704354	0.339	581.50 ± 35.64	88.47	0.36	4 ± 12
2A24212D	82.00 W	5.135	0.0003254	96.732	0.0002317	3.763	0.0166677	0.577	0.7841306	0.059	594.81 ± 7.31	92.31	4.04	22 ± 43
J = 0.00900500 ± 0.00002431														



Ar-Ar isotope data for muscovite sample 205412

Relative Abundances	36Ar	%1s	37Ar	%1s	38Ar	%1s	39Ar	%1s	40Ar	%1s	Age ± 2s (Ma)	40Ar(r) (%)	39Ar(r) (%)	K/Ca ± 2s	
4M32223D	4	0.0000135	76.935	0.0015476	65.342	0.0000263	20.286	0.0021521	1.131	0.0980406	0.460	593.99 ± 33.12	103.97	1.64	0.6 ± 0.8
4M32224D	4	0.0000029	372.722	0.0002603	471.610	0.0000443	10.973	0.0031299	1.246	0.1440097	0.538	582.85 ± 26.27	100.62	2.38	5.2 ± 48.8
4M32225D	4	0.0000123	100.330	0.0009410	129.258	0.0006238	3.570	0.0497118	0.527	2.3134222	0.116	584.56 ± 5.62	99.84	37.85	22.7 ± 58.7
4M32226D	4	0.0000052	209.167	0.0013488	78.945	0.0001049	6.422	0.0086113	0.820	0.4033577	0.147	590.37 ± 11.64	100.35	6.56	2.7 ± 4.3
4M32228D	4	0.0000023	459.755	0.0008066	128.443	0.0006030	1.876	0.0477676	0.508	2.1955360	0.044	579.34 ± 5.25	100.03	36.37	25.5 ± 65.4
4M32229D	4	0.0000042	252.872	0.0005910	209.687	0.0001195	7.411	0.0089735	0.632	0.4100127	0.203	577.70 ± 10.07	100.29	6.83	6.5 ± 27.4
4M32230D	4	0.0000070	151.446	0.0018066	62.625	0.0001446	4.459	0.0109787	0.614	0.4995247	0.149	576.04 ± 8.80	100.39	8.36	2.6 ± 3.3
J = 0.00821500 ± 0.00001600															

Ar-Ar isotope data for muscovite sample 205415

Relative Abundances	36Ar	%1s	37Ar	%1s	38Ar	%1s	39Ar	%1s	40Ar	%1s	Age ± 2s (Ma)	40Ar(r) (%)	39Ar(r) (%)	K/Ca ± 2s
2A24216D	0.0000028	306.756	0.0003038	121.981	0.0000290	29.040	0.0021236	1.128	0.0967768	0.511	614.88 ± 30.95	99.10	1.73	3.0 ± 7.3
2A24217D	0.0000061	145.390	0.0001652	235.285	0.0000549	15.582	0.0042527	1.253	0.1806460	0.277	578.61 ± 19.38	98.98	3.47	11.1 ± 52.1
2A24218D	0.0000354	24.998	0.0000721	472.304	0.0002248	5.260	0.0166908	0.657	0.6855252	0.083	559.60 ± 7.40	98.46	13.63	99.6 ± 940.6
2A24220D	0.0000494	17.283	0.0000151	2173.779	0.0006267	2.622	0.0497229	0.438	2.0198786	0.043	558.25 ± 4.40	99.27	40.62	1414.3 ± 61488.5
2A24221D	0.0000331	33.204	0.0003480	95.484	0.0002095	3.827	0.0162526	0.663	0.6640626	0.108	557.32 ± 8.04	98.51	13.28	20.1 ± 38.4
2A24222D	0.0000563	19.166	0.0000441	785.383	0.0001325	6.485	0.0103240	0.727	0.4317879	0.139	556.70 ± 10.28	96.11	8.43	100.7 ± 1581.7
2A24224D	0.0000224	33.347	0.0001008	334.728	0.0000650	14.150	0.0048234	0.883	0.2043054	0.235	565.94 ± 14.12	96.73	3.94	20.6 ± 137.7
2A24225D	0.0000857	11.380	0.0001457	224.041	0.0001327	8.269	0.0097488	0.840	0.4150567	0.136	553.77 ± 10.81	93.83	7.96	28.8 ± 128.9
2M24228D	0.0000232	37.611	0.0002110	169.018	0.0000153	52.721	0.0012741	1.685	0.0570718	0.870	546.55 ± 52.28	87.85	1.04	2.6 ± 8.8
2M24230D	0.0000400	21.693	0.0002620	83.834	0.0000206	41.420	0.0011635	1.221	0.0594181	0.300	563.71 ± 54.23	79.88	0.95	1.9 ± 3.2
224231D	0.0000705	12.128	0.0002326	76.294	0.0000144	39.724	0.0010853	2.075	0.0636175	0.389	544.80 ± 59.94	66.88	0.89	2.0 ± 3.1
224232D	0.0000709	13.259	0.0000236	903.832	0.0000317	15.525	0.0014596	1.716	0.0803372	0.248	560.68 ± 48.74	73.64	1.19	26.7 ± 481.8
2A24248D	0.0001070	10.992	0.0003483	52.320	0.0000702	10.514	0.0034988	0.707	0.1716828	0.134	553.49 ± 24.94	81.37	2.86	4.3 ± 4.5
J = 0.00900500 ± 0.00002431														

Ar-Ar isotope data for muscovite sample 205417

Relative Abundances	36Ar [V]	%1s	37Ar [V]	%1s	38Ar [V]	%1s	39Ar [V]	%1s	40Ar [V]	%1s	Age ± 2s (Ma)	40Ar(r) (%)	39Ar(k) (%)	K/Ca ± 2s
4M32139D	4	0.000095	62.634	0.0001524	583.058	0.0000308	16.153	0.0015084	1.879	0.0713508	0.643	573.58 ± 32.08	2.63	4.3 ± 49.6
4M32140D	4	0.000047	134.502	0.0001420	79.226	0.0000443	10.631	0.0007139	1.436	0.1201830	0.401	555.87 ± 20.94	4.73	1.0 ± 1.6
4M32141D	4	0.000016	379.135	0.00014632	65.431	0.0000385	13.147	0.0020075	1.205	0.0898858	0.551	564.64 ± 23.73	3.50	0.6 ± 0.8
4M32143D	4	0.0000386	17.734	0.0020872	45.112	0.0002308	4.413	0.0178523	0.582	0.7720085	0.244	542.71 ± 6.44	31.15	3.7 ± 3.3
4M32144D	4	0.000009	728.619	0.0013806	57.868	0.0002428	3.312	0.0174452	0.606	0.7485930	0.084	545.93 ± 6.25	30.44	5.4 ± 6.3
4M32145D	4	0.0000036	181.846	0.0000096	9357.975	0.0000442	13.699	0.0030604	1.248	0.1303697	0.364	546.43 ± 18.66	5.34	136.9 ± 25624.4
4M32147D	4	0.0000037	171.056	0.0006256	112.472	0.0000181	28.771	0.0015966	1.422	0.0679839	0.703	549.46 ± 29.96	101.55	1.1 ± 2.5
4M32148D	4	0.0000047	120.919	0.0010838	103.816	0.0000078	77.430	0.0009669	2.423	0.0421406	1.117	570.63 ± 46.22	103.55	0.4 ± 0.8
4M32149D	4	0.0000018	328.678	0.0003725	220.589	0.0000054	90.418	0.0010756	1.544	0.0472346	1.018	551.99 ± 39.84	98.94	1.2 ± 5.5
4M32150D	4	0.0000000	23909.956	0.0009144	63.963	0.0000151	35.716	0.0014399	1.370	0.0635893	0.741	558.96 ± 32.82	99.89	0.7 ± 1.5
4M32152D	4	0.0000057	101.547	0.0018909	63.963	0.0000206	23.636	0.0019429	2.090	0.0834438	0.568	554.74 ± 28.34	101.84	0.4 ± 0.6
4M32153D	4	0.0000003	3025.542	0.0000543	1771.812	0.0000002	2256.892	0.0006498	3.189	0.0279450	1.604	548.49 ± 88.57	100.30	5.1 ± 182.2
4M32154D	4	0.0000050	122.973	0.0007221	154.323	0.0000228	19.951	0.0019980	1.274	0.0885436	0.523	568.97 ± 23.93	101.61	1.2 ± 3.7
4M32155D	4	0.0000136	52.872	0.0008040	94.441	0.0000075	55.938	0.0009365	1.931	0.0412002	1.102	603.36 ± 53.52	109.66	0.5 ± 0.9
4M32157D	4	0.0000026	232.730	0.0010894	91.539	0.0000279	17.287	0.0016340	1.591	0.0707665	0.719	556.38 ± 29.31	101.22	0.6 ± 1.2
4M32158D	4	0.0000096	63.576	0.0000541	1730.038	0.0000082	62.534	0.0004872	1.785	0.0207172	2.175	605.68 ± 84.19	113.89	3.9 ± 134.0

J = 0.00821500 ± 0.00001600

Ar-Ar isotope data for biotite sample 205417

Relative Abundances	36Ar [V]	%1s	37Ar [V]	%1s	38Ar [V]	%1s	39Ar [V]	%1s	40Ar [V]	%1s	Age ± 2s (Ma)	40Ar(r) (%)	39Ar(k) (%)	K/Ca ± 2s
4M32130D	4	0.0000093	49.995	0.0012061	67.032	0.0000285	16.274	0.0018704	1.703	0.0857215	0.238	560.90 ± 23.16	2.10	1 ± 1
4M32131D	4	0.0000204	33.316	0.0002588	397.596	0.0000301	20.078	0.0023489	1.426	0.1089047	0.389	555.35 ± 23.60	2.63	4 ± 31
4M32132D	4	0.0000626	13.604	0.0013516	69.179	0.0001788	6.979	0.0126269	0.654	0.5792390	0.136	562.34 ± 7.81	96.79	4 ± 6
4M32133D	4	0.0000553	17.872	0.0006155	138.903	0.0006797	2.843	0.0514512	0.394	2.3015000	0.087	562.37 ± 4.10	99.28	36 ± 100
4M32135D	4	0.0000184	39.484	0.0002256	419.903	0.0001799	5.725	0.0131833	0.863	0.5909273	0.207	562.33 ± 9.29	99.07	25 ± 211
4M32136D	4	0.0000205	32.629	0.0003833	240.368	0.0001066	8.460	0.0072745	0.740	0.3278369	0.202	560.28 ± 9.53	8.15	8 ± 39
4M32137D	4	0.0000011	565.792	0.0007669	125.496	0.0000043	152.611	0.0004554	3.067	0.0198831	0.553	548.29 ± 95.98	98.64	0 ± 1

J = 0.00821500 ± 0.00001600

Ar-Ar isotope data for biotite sample 205414

Relative Abundances	36Ar	%1s	37Ar	%1s	38Ar	%1s	39Ar	%1s	40Ar	%1s	Age ± 2s (Ma)	40Ar(r) (%)	39Ar(k) (%)	K/Ca ± 2s
2A24249D	67.00 W	0.0003602	5.016	0.0003147	176.998	0.0004609	3.416	0.0299806	0.500	1.0300139	440.74 ± 6.04	89.56	2.73	41 ± 145
2A24250D	67.30 W	0.0000501	24.745	<b>0.0002792</b>	197.032	0.0002236	5.825	0.0147210	0.699	0.5499911	510.20 ± 8.77	97.28	1.34	<b>23 ± 89</b>
2A24252D	67.60 W	0.0000588	17.622	<b>0.0003654</b>	151.113	0.0002598	5.573	0.0190526	0.483	0.7140179	512.77 ± 5.97	97.54	1.74	<b>22 ± 68</b>
2A24253D	67.90 W	0.0000462	25.174	<b>0.0002192</b>	256.601	0.0003188	3.014	0.0247274	0.450	0.9410129	524.24 ± 5.36	98.53	2.25	<b>49 ± 249</b>
2A24254D	68.10 W	0.0000539	18.634	<b>0.0000344</b>	1610.909	0.0004421	4.561	0.0337362	0.573	1.3065688	533.39 ± 5.73	98.77	3.08	<b>422 ± 13606</b>
2A24256D	68.30 W	0.0000563	17.525	0.0000579	958.746	0.0004774	3.878	0.0332813	0.379	1.2943992	535.03 ± 4.14	98.70	3.03	<b>247 ± 4738</b>
2A24257D	68.50 W	0.0000908	13.247	<b>0.0002053</b>	273.562	0.0005183	3.120	0.0375012	0.420	1.4523442	530.40 ± 4.52	98.13	3.42	<b>79 ± 430</b>
2A24258D	68.70 W	0.000627	15.925	<b>0.0001247</b>	439.995	0.0003316	3.822	0.0243746	0.469	0.9416682	528.70 ± 5.26	98.01	2.22	<b>84 ± 740</b>
2A24260D	69.00 W	0.0001752	7.668	<b>0.0001120</b>	501.587	0.0005529	2.670	0.0414636	0.400	1.5846419	517.68 ± 4.33	96.70	3.78	<b>159 ± 1597</b>
2A24261D	69.30 W	0.0002244	5.970	0.0001406	394.348	0.0006543	2.721	0.0492944	0.445	1.8602802	510.64 ± 4.47	96.40	4.49	151 ± 1189
2A24262D	69.60 W	0.0001776	7.352	0.0001122	4540.516	0.0006652	3.030	0.0497156	0.394	1.8830871	515.91 ± 4.05	97.18	4.53	1753 ± 159173
2A24264D	70.00 W	0.0002784	5.391	0.0002810	200.259	0.0008816	2.015	0.0620747	0.511	2.3146641	505.38 ± 4.87	96.41	5.66	95 ± 380
2A24265D	70.50 W	0.0002865	6.387	0.0007155	80.242	0.0009376	2.869	0.0689403	0.369	2.5712186	506.69 ± 3.81	96.67	6.28	41 ± 66
2A24266D	71.00 W	0.0004022	5.720	0.0005429	104.167	0.0016410	2.916	0.1221253	0.373	4.6210897	516.46 ± 3.63	97.40	11.13	97 ± 202
2A24268D	72.00 W	0.0005104	4.795	0.0010151	54.763	0.0031938	1.013	0.2372875	0.335	9.1032688	526.98 ± 3.17	98.33	21.63	101 ± 110
2A24269D	72.50 W	0.0003382	5.414	0.0016675	32.971	0.0021568	1.828	0.1633591	0.340	6.2894152	528.94 ± 3.23	98.40	14.89	42 ± 28
2A24270D	82.00 W	0.0002252	6.387	0.0003041	182.163	0.0011172	1.514	0.0854164	0.374	3.3498072	535.54 ± 3.69	97.99	7.79	121 ± 440

J = 0.000900500 ± 0.00002431

Ar-Ar isotope data for biotite sample 195365

Relative Abundances	36Ar	%1s	37Ar	%1s	38Ar	%1s	39Ar	%1s	40Ar	%1s	Age ± 2s (Ma)	40Ar(r) (%)	39Ar(k) (%)	K/Ca ± 2s
2A24037D	66.00 W	0.0000252	28.856	0.0000595	260.392	0.0000026	289.660	0.0007262	2.017	0.0327336	490.09 ± 76.15	77.00	0.31	5.2 ± 27.3
2A24043D	67.00 W	0.0000765	11.122	0.0006065	26.367	0.0001061	6.030	0.0073096	0.611	0.3333617	583.84 ± 10.24	93.16	3.16	5.2 ± 2.7
2A24044D	67.50 W	0.0000071	97.632	0.0000096	1758.561	0.0000337	17.897	0.0022712	1.778	0.1017125	599.65 ± 28.12	97.90	0.98	101.7 ± 3577.9
2A24045D	68.00 W	0.0000173	44.401	<b>0.0001229</b>	132.238	0.0000672	10.910	0.0052286	0.707	0.2382702	608.22 ± 12.54	97.83	2.26	<b>18.3 ± 48.4</b>
2A24046D	68.50 W	0.0000447	14.957	<b>0.0001451</b>	108.625	0.0001063	6.421	0.0095028	0.826	0.4258259	594.52 ± 9.77	96.86	4.11	<b>28.2 ± 61.2</b>
2A24048D	69.00 W	0.0000791	8.865	0.0002151	79.236	0.0001986	6.074	0.0147481	0.755	0.6653700	595.83 ± 8.39	96.45	6.38	29.5 ± 46.7
2A24049D	69.50 W	0.0000915	9.034	0.0002773	80.341	0.0003179	3.374	0.0233149	0.602	1.0355822	592.68 ± 5.31	97.36	10.09	36.2 ± 58.1
2A24050D	69.80 W	0.0000954	8.820	0.0006172	26.763	0.0003693	2.586	0.0279398	0.602	1.2245323	587.59 ± 6.43	97.68	12.10	19.5 ± 10.4
2A24051D	70.00 W	0.0000611	12.979	0.0003019	57.183	0.0002341	5.293	0.0164344	0.490	0.7211360	587.13 ± 5.99	97.47	7.11	23.4 ± 26.8
2A24053D	70.20 W	0.0000462	15.876	0.0001914	89.231	0.0002807	2.227	0.0206102	0.398	0.8944855	586.67 ± 4.78	98.46	8.92	46.3 ± 82.6
2A24054D	70.50 W	0.0000529	11.368	0.0005113	34.414	0.0001894	3.724	0.0144791	0.729	0.6241211	578.27 ± 7.82	97.47	6.27	12.2 ± 8.4
2A24055D	70.80 W	0.0000532	17.508	0.0003617	43.885	0.0003844	3.680	0.0285348	0.505	1.2539541	594.35 ± 5.67	98.73	12.35	33.9 ± 29.8
2A24056D	71.20 W	0.0000191	38.598	0.0001685	113.749	0.0001284	5.256	0.0092213	0.512	0.4078749	596.98 ± 7.66	98.60	3.99	23.5 ± 53.5
2A24071D	72.00 W	0.0000855	14.108	<b>0.0000026</b>	8546.702	0.0005674	2.681	0.0444859	0.455	1.9861928	602.32 ± 5.03	98.71	19.26	<b>7372.0 ± 1260133.2</b>
2A24072D	72.50 W	0.0000355	16.403	<b>0.0000328</b>	596.760	0.0000689	9.601	0.0046993	0.868	0.2132895	591.36 ± 12.40	95.03	2.03	<b>61.5 ± 734.2</b>
2A24073D	81.00 W	0.0000601	10.095	<b>0.0000795</b>	283.609	0.0000220	25.266	0.0014883	1.948	0.0808610	581.25 ± 34.61	77.80	0.64	<b>8.0 ± 45.7</b>

J = 0.000900500 ± 0.00002431

Ar-Ar isotope data for hornblende sample 195316

Relative Abundances	36Ar	%1s	37Ar	%1s	38Ar	%1s	39Ar	%1s	40Ar	%1s	Age $\pm$ 2s (Ma)	40Ar/(r) (%)	39Ar/(k) (%)	K/Ca $\pm$ 2s
2A24074D	65.00 W	0.0001993	0.0004086	62.958	0.0000424	14.244	0.0002064	6.480	0.1369611	0.187	2664.20 $\pm$ 214.23	56.58	0.13	0.217 $\pm$ 0.275
2A24076D	67.00 W	0.0000497	0.0001644	131.618	0.0000142	36.469	0.0001712	6.329	0.0460168	0.281	1750.57 $\pm$ 241.35	67.77	0.11	0.447 $\pm$ 1.179
2A24077D	68.00 W	0.0000564	0.0007303	32.079	0.0000167	24.840	0.0003720	2.992	0.0593033	0.306	1276.37 $\pm$ 115.11	71.69	0.24	0.219 $\pm$ 0.141
2A24078D	69.00 W	0.0001376	0.0021817	12.222	0.0000465	12.435	0.0012227	1.705	0.2225823	0.094	1531.79 $\pm$ 48.96	81.62	0.78	0.241 $\pm$ 0.059
2A24079D	70.00 W	0.0002493	0.0440255	2.671	0.0001969	3.746	0.0099231	0.387	1.1279986	0.049	1214.94 $\pm$ 7.89	93.73	6.34	0.097 $\pm$ 0.005
2A24081D	70.30 W	0.0000870	0.0455777	2.552	0.0001629	5.810	0.0096334	1.070	0.8749306	0.056	1059.03 $\pm$ 18.12	97.47	6.16	0.091 $\pm$ 0.005
2A24082D	70.60 W	0.0001800	0.1939530	2.414	0.0006494	2.071	0.0394003	0.457	3.6091770	0.045	1078.31 $\pm$ 7.68	98.96	25.18	0.087 $\pm$ 0.004
2A24083D	70.80 W	0.0000863	0.1200948	2.491	0.0003803	3.140	0.0249152	0.567	2.2996625	0.062	1087.34 $\pm$ 9.64	99.32	15.92	0.089 $\pm$ 0.005
2A24084D	71.00 W	0.0000859	0.1133184	2.458	0.0003783	3.400	0.0231713	0.513	2.1461070	0.012	1089.64 $\pm$ 8.63	99.25	14.81	0.088 $\pm$ 0.004
2A24085D	71.20 W	0.0000279	0.0303396	2.737	0.0000891	8.032	0.0060701	0.503	0.5660701	0.035	1093.06 $\pm$ 10.73	98.98	3.88	0.086 $\pm$ 0.005
2A24086D	71.60 W	0.0000495	0.0707465	2.527	0.0002267	3.238	0.0144135	0.569	1.3315281	0.121	1088.26 $\pm$ 9.89	99.34	9.21	0.087 $\pm$ 0.005
2A24101D	72.00 W	0.0000842	0.0450065	2.538	0.0001684	8.525	0.0095057	0.566	0.8464319	0.055	1043.37 $\pm$ 11.45	97.48	6.08	0.091 $\pm$ 0.005
2A24102D	72.50 W	0.0000418	0.0204044	2.980	0.0000693	19.781	0.0040013	0.950	0.3671276	0.100	1064.12 $\pm$ 22.35	97.07	2.56	0.084 $\pm$ 0.005
2A24103D	81.00 W	0.0001519	0.0589393	2.565	0.0002058	8.130	0.0117187	0.887	1.1078106	0.047	1082.25 $\pm$ 16.32	96.35	7.49	0.085 $\pm$ 0.005
2A24104D	82.00 W	0.0000639	0.0093909	4.201	0.0000487	27.438	0.0017358	1.134	0.1745615	0.181	1072.99 $\pm$ 45.12	89.52	1.11	0.079 $\pm$ 0.007

J = 0.00900500  $\pm$  0.0002431

Ar-Ar isotope data for hornblende sample 205373

Relative Abundances	36Ar	%1s	37Ar	%1s	38Ar	%1s	39Ar	%1s	40Ar	%1s	Age $\pm$ 2s (Ma)	40Ar/(r) (%)	39Ar/(k) (%)	K/Ca $\pm$ 2s
2A23983D	64.00 W	0.0001179	0.0003350	63.116	0.0000330	19.359	0.0001458	24.345	0.0959150	0.526	2811.04 $\pm$ 713.54	63.34	0.24	0.1868 $\pm$ 0.2528
2A23984D	67.20 W	0.0000310	0.0001958	111.599	0.0000151	37.529	0.0000714	49.174	0.0391528	0.926	2818.60 $\pm$ 1442.12	76.42	0.12	0.1566 $\pm$ 0.3821
2A23985D	67.70 W	0.0000127	0.0002235	96.165	0.0000164	35.832	0.0000439	80.224	0.0252208	1.439	3044.97 $\pm$ 2403.20	85.01	0.07	0.0841 $\pm$ 0.2109
2A23986D	68.20 W	0.0001005	0.0004345	50.082	0.0000275	25.810	0.0001244	28.096	0.3374187	0.139	5674.14 $\pm$ 972.39	91.12	0.20	0.1229 $\pm$ 0.1412
2A23987D	68.70 W	0.0000650	0.0002367	96.446	0.0000135	43.048	0.0000739	47.154	0.1146063	0.346	4571.18 $\pm$ 1574.08	83.09	0.12	0.1338 $\pm$ 0.2875
2A23989D	69.20 W	0.0001436	0.0011264	21.644	0.0000381	25.172	0.0001815	20.102	0.7647171	0.095	6506.09 $\pm$ 708.27	94.40	0.30	0.0690 $\pm$ 0.0408
2A24004D	69.70 W	0.0001399	0.0032569	5.603	0.0000328	30.216	0.0005843	3.540	0.4518482	0.083	3594.30 $\pm$ 112.53	90.82	0.95	0.0768 $\pm$ 0.0102
2A24005D	70.20 W	0.0001239	0.0214770	2.692	0.0000773	9.689	0.0037792	1.376	0.6085680	0.050	1556.28 $\pm$ 30.89	94.21	6.17	0.0754 $\pm$ 0.0046
2A24006D	70.70 W	0.0002630	0.1184363	2.416	0.0003635	2.566	0.0207447	0.475	2.1014615	0.030	1143.35 $\pm$ 8.86	96.74	33.85	0.0750 $\pm$ 0.0037
2A24007D	70.90 W	0.0000965	0.0469493	2.594	0.0001499	10.377	0.0081978	0.684	0.7463669	0.078	1054.96 $\pm$ 12.51	96.67	13.38	0.0748 $\pm$ 0.0040
2A24009D	71.10 W	0.0000639	0.0136220	3.560	0.0000459	18.059	0.0022177	0.757	0.2427747	0.146	1172.64 $\pm$ 23.44	92.61	3.62	0.0697 $\pm$ 0.0051
2A24010D	71.30 W	0.0001089	0.0720972	2.487	0.0002046	6.258	0.0121549	0.654	1.1538784	0.060	1097.63 $\pm$ 11.63	97.71	19.83	0.0722 $\pm$ 0.0037
2A24011D	71.50 W	0.0001184	0.0483323	2.588	0.0001007	12.094	0.0050644	0.783	0.4918573	0.080	1083.59 $\pm$ 16.36	93.64	8.24	0.0448 $\pm$ 0.0024
2A24012D	71.70 W	0.0000252	0.0048220	5.964	0.0000076	101.688	0.0003204	4.646	0.0317299	0.854	955.11 $\pm$ 187.94	77.55	0.52	0.0283 $\pm$ 0.0043
2A24014D	72.00 W	0.0000462	0.0153536	2.980	0.0000169	42.318	0.0007241	2.139	0.0725957	0.190	1017.35 $\pm$ 83.19	82.77	1.17	0.0200 $\pm$ 0.0015
2A24015D	81.00 W	0.0002100	0.2719889	2.388	0.0005047	2.021	0.0051218	0.582	1.0158564	0.029	999.28 $\pm$ 39.81	39.94	8.08	0.0078 $\pm$ 0.0004
2A24016D	82.00 W	0.0001461	0.0105736	3.297	0.0000367	22.754	0.0002710	4.498	0.0626449	0.251	935.48 $\pm$ 254.30	31.79	0.43	0.0107 $\pm$ 0.0012
2A24017D	65.00 W	0.0001904	0.0012623	12.777	0.0000748	12.141	0.0016627	1.278	0.2223289	0.105	1154.00 $\pm$ 44.54	74.47	2.72	0.5661 $\pm$ 0.1454

J = 0.00900500  $\pm$  0.0002431



Ar-Ar isotope data for hornblende sample 195377

Relative Abundances	36Ar	%1s	37Ar	%1s	38Ar	%1s	39Ar	%1s	40Ar	%1s	Age ± 2s (Ma)	40Ar(r) (%)	39Ar(k) (%)	K/Ca ± 2s
2A24106D	67.00 W	0.0003262	4.245	0.0009502	23.989	0.0000775	17.157	0.0007121	2.834	0.4588445	3096.94 ± 90.49	78.79	0.09	0.322 ± 0.156
2A24107D	67.50 W	0.0000634	16.088	0.0001373	129.386	0.0000217	57.612	0.0003867	5.251	0.2447253	3305.20 ± 164.24	92.27	0.05	1.210 ± 3.135
2A24108D	68.00 W	0.0000793	10.631	0.0006227	29.016	0.0000239	50.668	0.0005473	3.139	0.3110449	3146.83 ± 97.08	92.41	0.07	0.378 ± 0.220
2A24109D	69.00 W	0.0001468	7.093	0.0250693	2.795	0.0002133	8.139	0.0104405	0.578	1.7130881	1610.39 ± 12.99	97.56	1.37	0.179 ± 0.010
2A24111D	69.30 W	0.0000827	12.668	0.0699339	2.567	0.0005009	3.352	0.0277400	0.437	2.6975146	1129.05 ± 7.63	99.30	3.63	0.170 ± 0.009
2A24112D	69.50 W	0.0001229	10.819	0.1606565	2.445	0.0011478	1.881	0.0641537	0.355	6.2361358	1131.47 ± 6.12	99.63	8.40	0.171 ± 0.008
2A24113D	69.60 W	0.0000587	17.312	0.0650315	2.603	0.0004931	3.317	0.0261010	0.536	2.5447451	1133.11 ± 9.28	99.53	3.42	0.172 ± 0.009
2A24114D	69.80 W	0.0001550	6.961	0.2286791	2.448	0.0016323	1.470	0.0889670	0.342	8.8170823	1148.40 ± 5.94	99.69	11.65	0.167 ± 0.008
2A24117D	70.00 W	0.0000165	92.860	0.0216176	3.243	0.0001787	5.736	0.0089392	0.455	0.8456522	1108.79 ± 11.80	99.63	1.17	0.178 ± 0.012
2A24118D	70.30 W	0.0003776	10.459	0.5681078	2.485	0.0040680	1.423	0.2247790	0.346	21.6704024	1125.17 ± 5.91	99.70	29.43	0.170 ± 0.009
2A24119D	70.40 W	0.0002688	10.972	0.3953219	2.493	0.0027168	1.556	0.1519401	0.389	14.5503569	1119.42 ± 6.63	99.68	19.89	0.165 ± 0.008
2A24120D	70.40 W	0.0000183	95.905	0.0395630	2.755	0.0002524	3.971	0.0149278	0.437	1.3947206	1100.43 ± 9.56	99.85	1.95	0.162 ± 0.009
2A24122D	70.50 W	0.0000147	113.030	0.0291242	3.333	0.0002060	4.171	0.0105631	0.526	0.9860821	1099.42 ± 12.03	99.80	1.38	0.156 ± 0.011
2A24123D	70.60 W	0.0000075	216.061	0.0092184	4.872	0.0000716	10.630	0.0035286	0.956	0.3333116	1107.07 ± 28.90	99.56	0.46	0.164 ± 0.016
2A24124D	71.00 W	0.0000564	28.091	0.1084044	2.533	0.0007518	2.620	0.0425882	0.412	4.0096420	1106.35 ± 7.15	99.81	5.58	0.169 ± 0.009
2A24125D	71.50 W	0.0000680	27.137	0.0792692	2.542	0.0005137	2.027	0.0277933	0.465	2.6027536	1099.38 ± 8.48	99.48	3.64	0.150 ± 0.008
2A24127D	72.00 W	0.0000552	29.886	0.0392011	2.694	0.0002339	4.489	0.0118946	0.453	1.1133654	1093.77 ± 10.52	98.81	1.56	0.130 ± 0.007
2A24128D	72.50 W	0.0000362	24.508	0.0336443	2.727	0.0001966	4.246	0.0109805	0.463	1.0373202	1104.69 ± 8.80	99.23	1.44	0.140 ± 0.008
2A24129D	81.00 W	0.0001621	6.105	0.1107145	2.557	0.0006123	2.693	0.0323943	0.457	3.0687005	1102.95 ± 7.78	98.73	4.24	0.126 ± 0.007
2A24130D	82.00 W	0.0000722	9.056	0.0157905	2.993	0.0001089	8.594	0.0044800	0.979	0.4400910	1104.75 ± 17.98	95.40	0.59	0.122 ± 0.008

J = 0.00900500 ± 0.00002431

Ar-Ar isotope data for biotite sample 195379

Relative Abundances	36Ar	%1s	37Ar	%1s	38Ar	%1s	39Ar	%1s	40Ar	%1s	Age ± 2s (Ma)	40Ar(r) (%)	39Ar(k) (%)	K/Ca ± 2s
2A24017D	65.00 W	0.0001878	8.415	0.0009843	36.172	0.0000700	16.341	0.0016541	1.646	0.2219917	1160.53 ± 56.29	74.78	1.91	0.722 ± 0.523
2A24019D	66.50 W	0.0000286	48.276	0.0000961	363.031	0.0000113	86.520	0.0006350	3.698	0.0452226	754.88 ± 146.13	81.12	0.74	2.841 ± 20.626
2A24020D	68.00 W	0.0001258	12.979	0.0016847	21.138	0.0000865	12.489	0.0047718	0.634	0.2712563	658.86 ± 24.12	86.21	5.53	1.218 ± 0.515
2A24021D	68.50 W	0.0000976	17.339	0.0093566	5.172	0.0001116	8.874	0.0044845	0.679	0.3389502	874.45 ± 24.46	91.63	5.19	0.206 ± 0.021
2A24025D	69.00 W	0.0001090	14.317	0.0276153	2.962	0.0001069	6.595	0.0052193	1.015	0.5630267	1178.04 ± 23.25	94.63	6.02	0.081 ± 0.005
2A24026D	69.50 W	0.0001470	11.393	0.1098022	2.397	0.0002841	3.320	0.0167095	0.559	1.9011239	1258.57 ± 11.31	98.18	19.26	0.065 ± 0.003
2A24027D	69.70 W	0.0000946	17.252	0.1142826	2.437	0.0002404	7.436	0.0163485	0.505	1.1055517	848.82 ± 9.20	98.31	18.84	0.061 ± 0.003
2A24029D	69.90 W	0.0000382	40.150	0.0297023	2.940	0.0000578	14.449	0.0043031	1.066	0.2609758	766.45 ± 26.38	96.59	4.96	0.062 ± 0.004
2A24030D	70.10 W	0.0000434	38.969	0.0352607	2.909	0.0000718	10.548	0.0050431	0.698	0.3132915	783.08 ± 22.97	96.81	5.81	0.061 ± 0.004
2A24031D	70.30 W	0.0000414	36.288	0.0194064	3.395	0.0000425	17.942	0.0030608	1.117	0.1904363	767.58 ± 34.29	94.36	3.53	0.068 ± 0.005
2A24032D	70.80 W	0.0000709	22.821	0.0329706	2.742	0.0000861	10.449	0.0050106	0.826	0.3458084	836.99 ± 22.72	94.68	5.78	0.065 ± 0.004
2A24034D	71.50 W	0.0001384	7.566	0.0810408	2.446	0.0002029	4.585	0.0122987	0.556	0.8242249	825.36 ± 9.11	95.81	14.18	0.065 ± 0.003
2A24035D	72.50 W	0.0001276	7.360	0.0278525	2.608	0.0001144	5.983	0.0060558	0.661	0.3686474	726.62 ± 12.84	90.30	6.99	0.093 ± 0.005
2A24036D	81.00 W	0.0000912	9.705	0.0066624	3.054	0.0000340	19.794	0.0010979	1.908	0.0936697	792.06 ± 56.31	71.54	1.27	0.071 ± 0.005

J = 0.00900500 ± 0.00002431



# Chapter 5

This chapter is prepared for submission as:

Walsh, A. K., Hand, M., Taylor, R. & Clark, C., Kelsey, D. E. 2014. Duration of elevated thermal conditions in the deep crust during intracratonic orogeny





---

# Duration of elevated thermal conditions in the deep crust during intracratonic orogeny

---

## ABSTRACT

In the deep-crustal core of the Petermann Orogen in central Australia, mylonitic shear zones and felsic gneisses from outside shear zones developed kyanite-garnet-bearing metamorphic mineral assemblages indicative of  $P$ – $T$  conditions of 10.5–11.5 kbar and 650–700 °C. A U–Pb monazite age of  $586 \pm 4$  Ma constrains the timing of mylonitisation and recrystallisation in the mid–lower crust. Rutile in mylonitic zones and adjacent wall rocks yield U–Pb ages of  $528 \pm 16$  Ma and  $532 \pm 10$  Ma respectively. Diffusion-driven compositional zoning preserved in garnet–biotite pairs that formed during metamorphism that grew in the same rock indicates an average cooling rate of  $\leq 5$  °C Ma<sup>−1</sup>. Together, the geochronological and cooling rate data suggest that the timescale of thermal perturbations above ~600 °C in the lower crust were at least 40 Myr. Metamorphic assemblages developed in the rocks surrounding the shear zones indicate that elevated temperatures in the core of the orogen were driven by regional conductive heating, rather than localised shear as suggested in previous models for the thermal character of the orogenic core. The spatially restricted growth of high-grade metamorphic mineral assemblages in the core of the orogen, within shear zones and also as local domains in rocks outside shear zones, reflects partitioning of strain in residual lower intracratonic crust.

---

## INTRODUCTION

Intraplate deformation commonly accompanies plate margin processes such as collision (e.g. Marshak, *et al.*, 2000; Sandiford, *et al.*, 2004; Cloetingh & Van Wees, 2005; Raimondo, *et al.*, 2014). An increasing ability to understand and view deep crustal processes have provided important insight into the physical architecture of modern intraplate orogens such as Tien Shan and Altai in central Asia (e.g. Cunningham, 2005; Buslov, *et al.*, 2007; Windley, *et al.*, 2007; Van Hinsbergen, *et al.*, 2008), the Sevier–Laramide Orogen, western North America (e.g. Livaccari, 1991; Bird, 1998; Marshak, *et al.*, 2000), Atlas Mountains, northern Africa (e.g. Beauchamp, *et al.*, 1999) and the Spanish Central System, Iberia (e.g. De Bruijne & Andriessen, 2002).

The initiation of intraplate orogens is becoming increasingly understood although a variety of mechanisms are considered to be effective in localising deformation in continental interiors, including (e.g. Sandiford & Hand, 1998; Neil & Houseman, 1999; Sandiford, *et al.*, 2001; Pysklywec & Beaumont, 2004; Raimondo, *et al.*, 2009; Stephenson, *et al.*, 2009; Raimondo, *et al.*, 2010; Holford, *et al.*, 2011; Raimondo, *et al.*, 2014; Walsh, *et al.*, in review). It is

evident that mechanisms which might promote deformation and metamorphism in intraplate orogens have different implications for the thermo-mechanical state of the lithosphere and the duration of orogenesis. Therefore, the duration and rates of deformation, metamorphism, exhumation and cooling provide insight into the mechanisms which initiate intraplate orogens and control their thermal and mechanical evolution. To this end, here we quantify the duration and physical conditions of metamorphism to further understand the thermo-mechanical evolution of the Ediacaran–Cambrian aged Petermann Orogeny in central Australia

The Petermann Orogeny in central Australia is example of ancient intraplate orogeny and involves magnitudes of crustal thickening, shortening and exhumation comparable to both plate margin orogenic systems, and intraplate systems such as Tien Shan in central Asia (Flöttmann, *et al.*, 2004; Raimondo, *et al.*, 2014). It is best described as a north-vergent transpressive shear system that reworks mostly Mesoproterozoic ultra-hot metamorphic gneisses of the Musgrave Province (Maboko, *et al.*, 1992; Camacho & McDougall, 2000; Flöttmann, *et al.*, 2004; Aitken, *et al.*, 2009a; Aitken, *et al.*, 2009b;

Walsh, *et al.*, in press). A near complete crustal section is preserved from transitional eclogite (12 to 14 kbar) facies deep crustal rocks in the core of the orogen (south), to pumpellyite-actinolite facies rocks in the northern foreland basin (Camacho, *et al.*, 1997; White & Clarke, 1997; Scrimgeour, *et al.*, 1999; Camacho, *et al.*, 2001; Raimondo, *et al.*, 2009; Raimondo, *et al.*, 2010; Walsh, *et al.*, in review). Despite the excellent preservation of high-grade metamorphic shear zone-hosted assemblages across the orogen, the application of modern metamorphic and geochronological tools has been limited, primarily due to land access limitations. However, the Petermann Orogen has been the focus of numerous studies to understand the thermal and mechanical evolution of the system by investigating the timing, duration and physical conditions of metamorphism and deformation (Camacho, *et al.*, 1997; e.g. Camacho, *et al.*, 2001; Camacho, *et al.*, 2009; Gregory, *et al.*, 2009; Raimondo, *et al.*, 2009; Raimondo, *et al.*, 2010; Walsh, *et al.*, 2013; Walsh, *et al.*, in review; Walsh, *et al.*, submitted). It is evident from these studies that the orogen preserves a spatially and temporally complex record of the thermal and mechanical evolution. Initial deformation and crustal thickening is argued to have developed in comparatively weak lithosphere, reflecting a regionally elevated thermal regime (Sandiford & Hand, 1998; Hand & Sandiford, 1999; Walsh, *et al.*, in review; Walsh, *et al.*, submitted), potentially caused by sedimentary cover creating thermal blanketing of high-heat-producing granitic crust (approximately  $4 \mu\text{W m}^{-3}$ ) that was localised in the mid-upper crust (Sandiford & Hand, 1998; Hand & Sandiford, 1999; Sandiford & McLaren, 2002; McLaren, *et al.*, 2003). The development of a deep ( $\sim 10$  km) and narrow foreland basin, a thick ( $\geq 20$  km) basement-involved (thick-skinned) foreland fold-thrust belt and the exhumation of the core of the orogen via lateral extrusion (channel flow) reflect continued orogenic evolution in a mechanically weak lithosphere associated with elevated temperatures (Raimondo, *et al.*, 2009; Raimondo, *et al.*, 2010; Walsh, *et al.*, in review).

However, in contrast to this notion of a (hot/warm) weak lithosphere across the Petermann Orogen is the presence of comparatively

low geothermal gradient rocks ( $\sim 9^\circ\text{C km}^{-1}$ ;  $350^\circ\text{C}$ , 12 kbar) in the axial core, in which low temperatures are deduced based on the interpretation that Ar–Ar isotopic systems have failed to reset (Camacho, *et al.*, 1997; Camacho & McDougall, 2000). Within this core, mylonitic shear zones that host transitional-eclogite facies rocks and voluminous pseudotachylites (Lin, *et al.*, 2005) define Petermann-aged metamorphism. Mesoproterozoic granulites to the south of the orogenic core are largely unaffected by Petermann-aged reworking. To explain the presence of ‘cold’, transitional eclogite facies rocks and pseudotachylites as well as their spatially restricted occurrence, the heat source for Petermann-aged tectonism has been argued to be shear heating (Camacho, *et al.*, 2001). Tectonism (i.e. burial, metamorphism and exhumation) associated with shear heating is argued to be rapid—of the order of 1 M.yr—within regionally cold and strong lithosphere (Camacho, *et al.*, 2009). Such an interpretation has been reinforced through using compositional zoning profiles in garnet from the core of the orogen to estimate/constrain cooling rates and the preservation of pre orogenic ages in low-T thermochronometers (Camacho, *et al.*, 2001; Camacho, *et al.*, 2009). Therefore, the Petermann Orogen preserves a seemingly paradoxical record of tectonism in warm, weak lithosphere as well as in cold, strong lithosphere.

To investigate the seemingly paradoxical thermal setting of tectonism, we have used garnet-bearing samples from the core of the orogen (Amata region) to revisit and constrain: 1) the timescale of metamorphism via cooling rates estimated from compositional zoning profiles in garnet and from rutile and in situ monazite U–Pb geochronology; and 2) the thermal gradient of metamorphism via calculated  $P$ – $T$  pseudosections from rocks inside shear zones to assess the applicability of shear heating being the primary heat source for metamorphism during the Petermann Orogeny. We find that rocks within and outside shear zones both preserve a record of high-pressure metamorphism and that the orogenic core appears to have cooled slowly ( $< 5^\circ\text{C Ma}^{-1}$ ). Temperatures  $> 500$ – $600^\circ\text{C}$  occurred in the deep crust over a timescale of approximately  $\geq 50$  M.yr, supporting the notion that the crust/

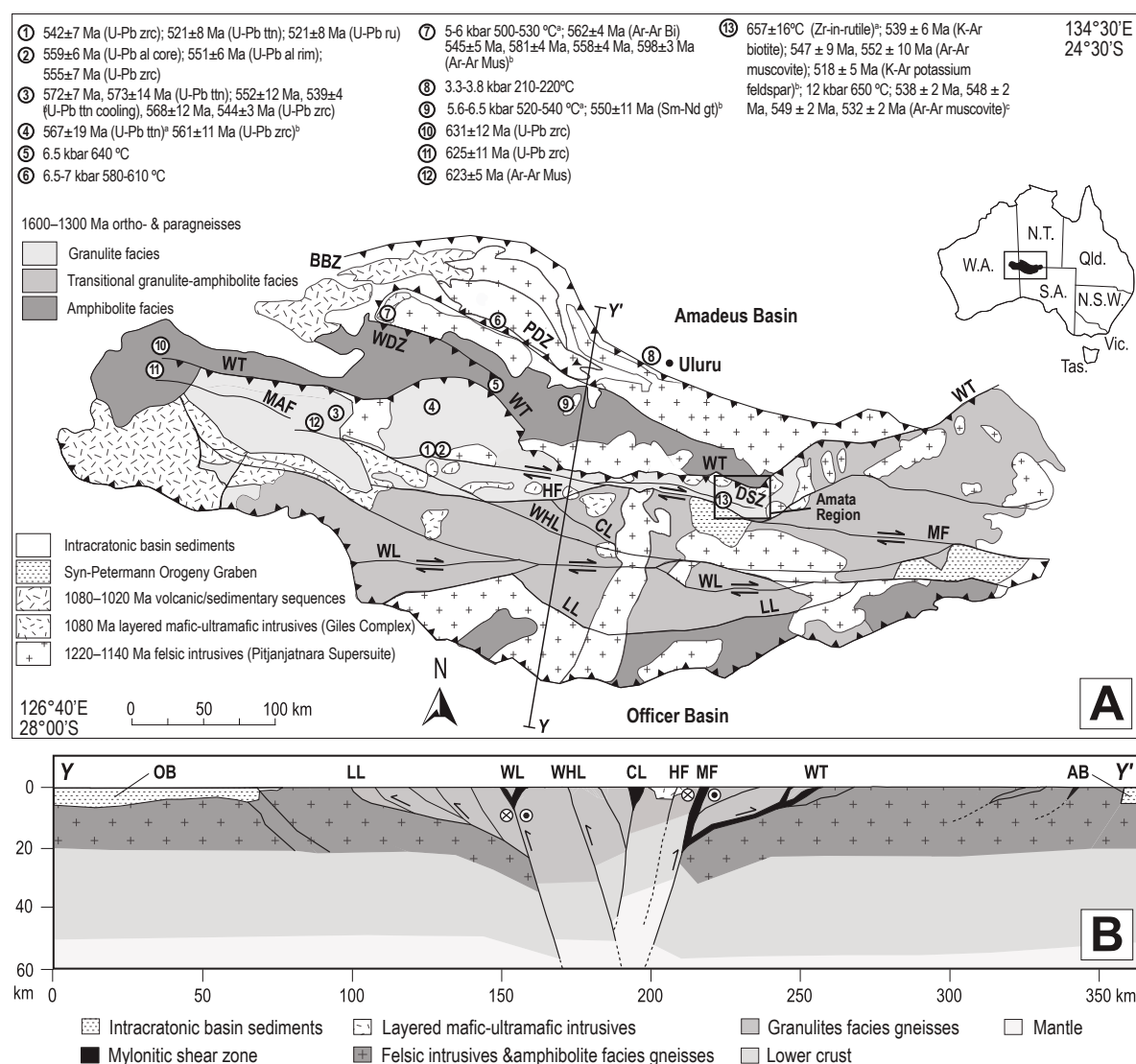


**Figure 1.** Regional solid geology map of the Musgrave Province. The locations of key E-W trending fault structures of the Petermann Orogen, previously collected geochronological data and accompanying P–T constraints and the location of structural collected by previous workers. Boxed area is area of Figure 2 Modified from Edgoose et al. (2004), Raimondo et al. (2010) and Aitken et al. (2009). (b) Schematic cross section (Y–Y') across the central Musgrave Block. Highlights the overall crustal-scale dextral transpressive shear system, involving significant Moho displacement and deep exhumation along the Woodroffe Thrust/ Mann Fault. Modified from Aitken et al. (2009). Abbreviations: AB, Amadeus Basin; BBZ, Bloods Back Thrust Zone; CL, Caroline Lineament; HF, Hinckley Fault; LL, Lindsay Lineament; MAF, Mount Aloysius Fault; MF, Mann Fault; OB, Officer Basin; PDZ, Piltardi Detachment Zone; WDZ, Wankari Detachment Zone; WHL, Wintiginna-Hinckley Lineament; WL, Wintiginna lineament; WT, Woodroffe Thrust. References for locations: 1. (Walsh, et al., 2013); 2. (Gregory, et al., 2009); 3. (Raimondo, et al., 2009; Raimondo, et al., 2010); 4<sup>a</sup>. (Walsh, et al., 2013), <sup>b</sup> (Scrimgeour, et al., 1999); 5. (Scrimgeour, et al., 1999); 6. (Walsh, et al., in review); 7.<sup>a</sup>(Walsh, et al., in review), <sup>b</sup>(Walsh, et al., submitted); 8. (Walsh, et al., in review); 9. <sup>a</sup>(Walsh, et al., in review) <sup>b</sup> (Scrimgeour, et al., 1999); 10. (Kirkland, et al., 2014); 11. (Kirkland, et al., 2011); 12. (Kirkland, et al., 2013); 13. <sup>a</sup> (Camacho, et al., 2009), <sup>b</sup> (Camacho, et al., 1997), <sup>c</sup>(Camacho & McDougall, 2000).

lithosphere was regionally warm, at least over this portion of the evolution of the orogen. The metamorphic and geochemical/isotopic record provides invaluable information about the thermo-mechanical evolution of intraplate orogens, the ability of residual crust to rework and the initiation and termination of intraplate orogens.

## GEOLOGICAL SETTING

The Musgrave Province (Fig. 1) is an east-west trending Mesoproterozoic basement province that outcrops over approximately 120,000 km<sup>2</sup>, straddling the Northern Territory, South Australia and Western Australia borders in central Australia (Camacho & McDougall, 2000; Aitken & Betts, 2008). The Musgrave Province is bounded by the Neoproterozoic to Palaeozoic sedimentary rocks of the Amadeus, Officer, Canning and Perdika Basins (e.g. Walter, *et al.*, 1995).

The Musgrave Province records a complex deformational, metamorphic and magmatic history during the Grenvillian period, spanning *c.* 1345 to 1050 Ma (Glikson, *et al.*, 1995; Sun, *et al.*, 1996; Edgoose, *et al.*, 2004; Wade, *et al.*, 2008; Evins, *et al.*, 2010; Smithies, *et al.*, 2011; Howard, *et al.*, 2014; Smithies, *et al.*, 2014; Walsh, *et al.*, in press). The Grenvillian metamorphic and geochronological record is dominated by long-lived, ultrahot geothermal gradient metamorphism between *c.* 1260 and 1110 Ma (Smithies, *et al.*, 2011; Walsh, *et al.*, in press). Voluminous magmatic (many now gneissic) and volcanic rocks occupy approximately 50 to 60% of total outcrop throughout the province (Glikson, *et al.*, 1996; Camacho, *et al.*, 2002; Wade, *et al.*, 2008; Evins, *et al.*, 2010; Smithies, *et al.*, 2010; Howard, *et al.*, 2011; Smithies, *et al.*, 2011). Numerous dykes of the Amata Dolerite suite cross-cuts much of the central Musgrave Province and are genetically related to co-eval plume-sourced dykes in the south and north Australian cratons (Zhao & McCulloch, 1993; Zhao, *et al.*, 1994; Glikson, *et al.*, 1996). The Amata Dolerite gives Sm–Nd mineral-whole rock and baddelyite U–Pb ages of *ca.* 820 Ma (Zhao, *et al.*, 1994; Glikson, 1996).

The modern day east-west orientation of the Musgrave Province is a strong function

of the overprinting, intraplate Ediacaran to Cambrian-aged Petermann Orogeny (Camacho, *et al.*, 1997; Wade, *et al.*, 2008; Aitken, *et al.*, 2009a; Aitken, *et al.*, 2009b; Raimondo, *et al.*, 2010). The Petermann Orogeny led to the present-day geophysical architecture of the Musgrave Province via the development of major E–W striking faults that penetrate the crust and upper mantle (Korsch, *et al.*, 1998; Aitken, *et al.*, 2009a). The most significant of these structures are the Mann Fault and the Woodroffe Thrust, between which occurs the exposed high-pressure (12 to 14 kbar) core of the Petermann Orogen (Fig. 1). The Woodroffe Thrust is a shallow south-dipping mylonite and pseudotachylite-bearing zone up to 3 km thick (Camacho, *et al.*, 1995; Lin, *et al.*, 2005) that offsets the Moho by approximately 20 km (Lambeck & Burgess, 1992; Camacho & Fanning, 1995; Aitken, *et al.*, 2009a; Korsch & Kositsin, 2010).

Top-to-the-north tectonic transport along the Woodroffe Thrust, coupled with antithetic movement on the Mann Fault system, facilitated the exhumation of lower-crustal granulite-facies gneisses from approximately 40 km depth and the emplacement of a crustal wedge in the orogenic core (Camacho, *et al.*, 1997; Scrimgeour & Close, 1999; Raimondo, *et al.*, 2010). In the western part of the orogen this led to the development of >100 km-scale basement-cored nappes and thick-skinned thrust sheets that transported the orogenic core towards a deeply depressed foreland (Scrimgeour, *et al.*, 1999; Edgoose, *et al.*, 2004; Flöttmann, *et al.*, 2004; Walsh, *et al.*, in review).

Sequential cross-section restorations indicate that north-vergent shortening during the Petermann Orogeny exceeded 150 km and was accommodated by significant crustal thickening (Flöttmann, *et al.*, 2004). Thermobarometric constraints from the exposed orogenic core indicate apparent geothermal gradients of  $\sim 17^{\circ}\text{C km}^{-1}$  (12–14 kbar and 700–750 °C), which are attained immediately north of the western parts of the Mann Ranges (White & Clarke, 1997; Scrimgeour & Close, 1999; Raimondo, *et al.*, 2009; Raimondo, *et al.*, 2010). More eastern parts of the orogenic core record sub-eclogitic facies mineral assemblages in shear zones with lower geothermal gradients of  $15^{\circ}\text{C km}^{-1}$  ( $\sim 12$



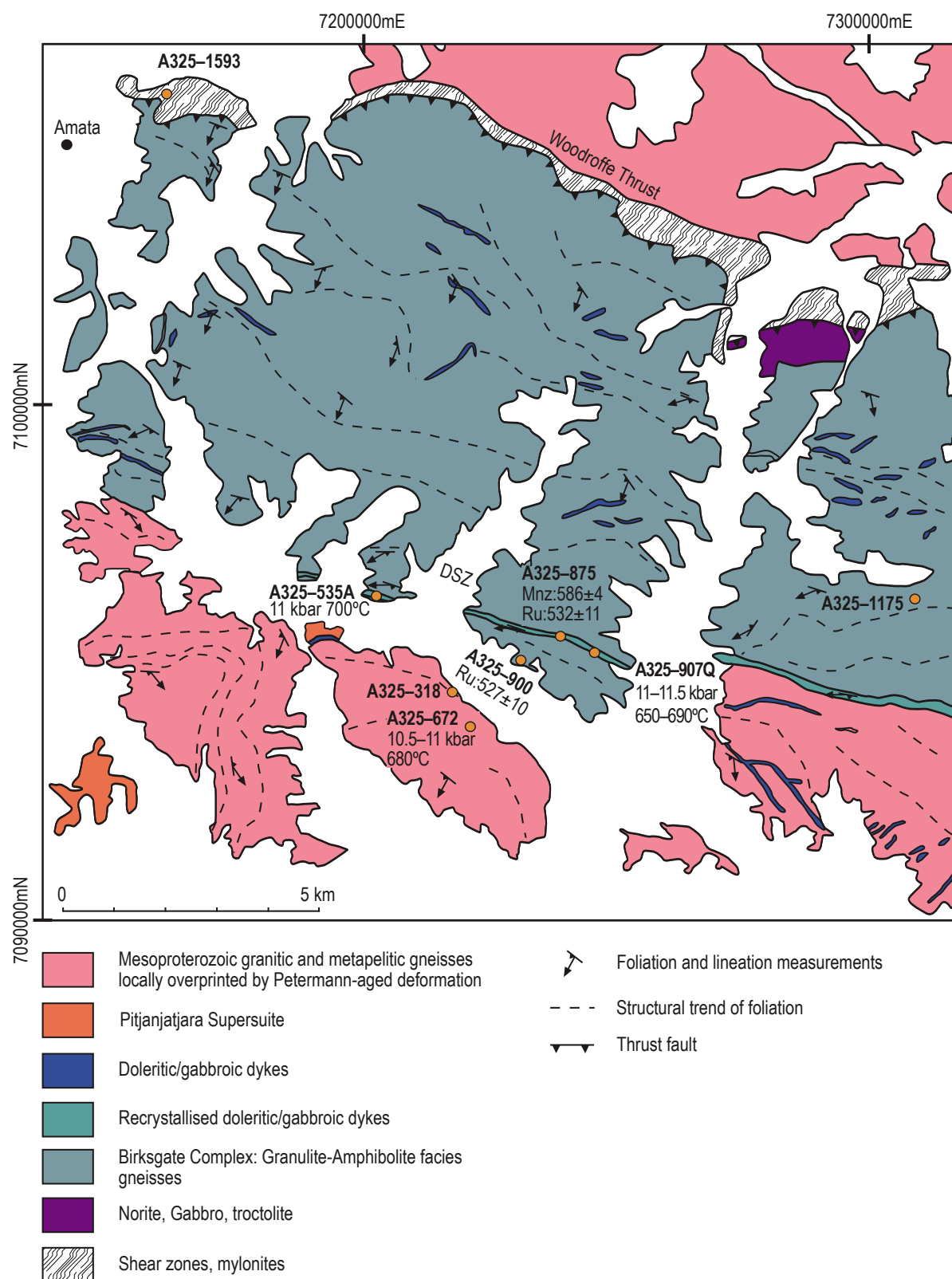


**Figure 2.** Outcropping geology of the Amata region highlighting the distribution of differentiated lithological units, shear zones and structural trends based on foliation and lineation measurements (Geological Survey of South Australia). Precise extent of the Davenport Shear Zone (DSZ) is undefined as deformation is discretely recorded in some areas, sample 325–875 is located in the centre of the DSZ shear. Orange circles represent samples of this study. All GPS coordinates are presented in text.

kbar 600–650 °C; Ellis & Maboko, 1992; Camacho, *et al.*, 1997). However, rocks outside of shear zones preserve only partially reset Rb–Sr and Ar–Ar ages and are characterised by cold–intermediate thermal conditions of <350 °C in the deep crust. Temperatures of > 600 °C in the shear zones are interpreted to have been generated by shear heating (Camacho & McDougall, 2000). Toward the foreland to the north (Fig. 1), relatively elevated apparent geothermal gradients of ~30 °C km<sup>-1</sup> (6–7 kbar and 600–650 °C) are recorded in the thick-skinned fold-thrust belt (Scrimgeour & Close, 1999; Walsh, *et al.*, in review). At the orogenic margin burial metamorphism of syn-orogenic sequences in the foreland basin reached ~3 kbar and 200–220 °C, reflecting the deep flexural response of weak lithosphere during orogeny (Walsh, *et al.*, in review).

The earliest recorded metamorphism associated with the Petermann Orogeny is recorded in the foreland fold-thrust belt on the northern flank of the orogen (Fig. 1) which was substantially thickened by 598 ± 3 Ma (40Ar–39Ar Muscovite crystallisation age; Walsh, *et al.*, submitted). In the western part of the orogenic core (Fig. 1), high-pressure metamorphism (10–14 kbar, 670–730 °C) occurred between 575 and 560 Ma based on the U–Pb dating of zircon and titanite (Scrimgeour & Close, 1999; Raimondo, *et al.*, 2009; Raimondo, *et al.*, 2010). Early stages of cooling and exhumation of the orogen are recorded in the foreland by <sup>40</sup>Ar–<sup>39</sup>Ar muscovite cooling ages ranging between 581 ± 4 and 545 ± 5 Ma (Fig. 1; Walsh, *et al.*, submitted). In the western part of the orogen regional exhumation and cooling were associated with north-vergent lower-crustal channel flow that facilitated exhumation of the high-grade core of the orogen (Raimondo, *et al.*, 2009; Raimondo, *et al.*, 2010). In response to regional cooling, U–Pb zircon and allanite crystallised from partial melts in migmatitic, ductile shear zones between 559 ± 6 and 542 ± 7 Ma (Gregory, *et al.*, 2009; Walsh, *et al.*, 2013). U–Pb titanite and rutile and <sup>40</sup>Ar/<sup>39</sup>Ar muscovite ages record continued exhumation of the core of the orogen, which was associated with slow (0.9 to 4.8 °C Ma<sup>-1</sup>), protracted cooling until *ca.* 500 Ma (Camacho & Fanning, 1995; Camacho, *et al.*, 1997; Walsh, *et al.*, 2013). The overall thermal and deformational

evolution of the Petermann Orogeny is therefore described as a slowly evolving continuous orogenic cycle, consistent with conventional models of collisional orogeny at plate margins (Raimondo, *et al.*, 2014).

In contrast, Camacho *et al.* (2009) used garnet diffusion profiles in garnet from lower crustal shear zones in the Davenport Shear Zone, in the eastern part of the orogen to investigate the duration of deformation at sub-eclogite facies conditions. Zoning profiles in relic Mesoproterozoic garnet grains from mylonites developed in response to recrystallization and neocrystallisation of plagioclase over very short timescales (*ca.* 1 Myr). Additionally, the incomplete resetting of Ar–Ar in relict potassium feldspar and Rb–Sr system in shear zone wall rocks is considered to reflect a short-lived thermal event (Camacho, *et al.*, 2009). Short timescales for deformation and elevated temperatures as well as strong strain partitioning into shear zones is consistent with the proposal that shear heating was the dominant source of heating during the Petermann Orogeny (Camacho, *et al.*, 2009). Invoking shear heating as metamorphic driver implies that the crust was not wholly characterised by elevated temperatures and therefore was cold and strong (Camacho, *et al.*, 2009). Abundant pseudotaclyite in the eastern part of the orogenic core reinforces the idea that the crust was strong. However, in many instances pseudotachylite is largely unrecrystallised and structurally late, suggesting it may have developed late in the orogenic cycle (Lin, *et al.*, 2005). Ultimately, the drivers of metamorphism during the Petermann Orogeny are poorly understood, largely because of different views about the thermal duration.

## GEOLOGY OF THE AMATA REGION

The Amata region of the central Musgrave Ranges represents part of axial core of the Petermann Orogen and exposes Mesoproterozoic granitic gneisses and *ca.* 800 Ma dolerite dykes of the Amata Suite. Petermann-aged overprinting deformation in the Amata Region is dominated by east–west striking shear zones ranging from km to cm scale, which developed at sub-eclogite facies conditions. Three major shear zones outcrop in the region; 1) the Woodroffe Thrust (Fig.



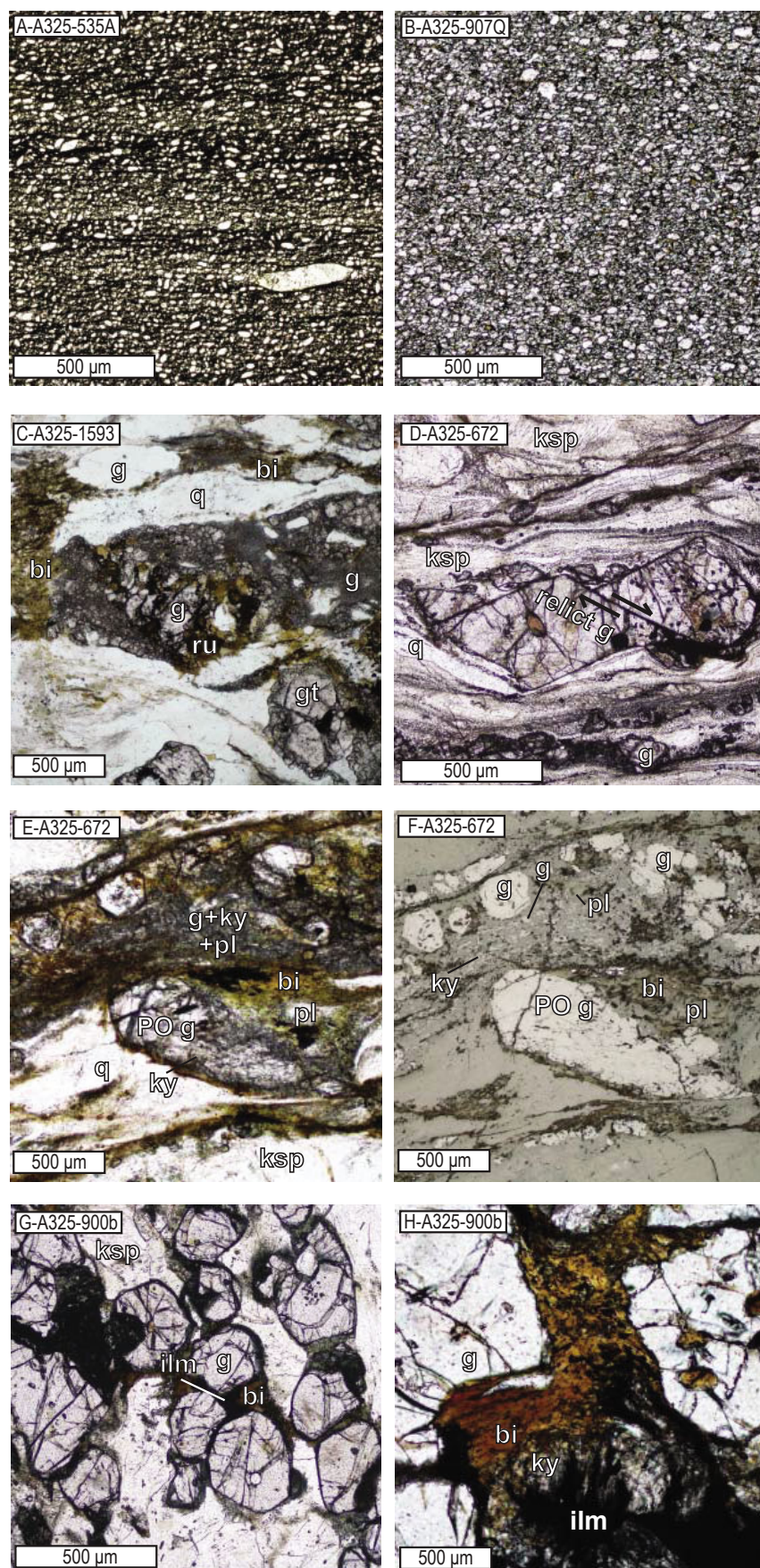


**Figure 3.** Thin section photos of samples used for U–Pb geochronology and/or P–T pseudosections. a and b). Samples 325-535A and 325-907Q. Dolerite dyke now comprised of a recrystallised matrix of fine-grained garnet, clinopyroxene, hornblende, plagioclase and rutile. c) Mylonitic metapelite sample

325–1593. Neoproterozoic garnet (~500  $\mu\text{m}$ ) in contact with biotite and rutile. Very fine-grained garnet (~20–50  $\mu\text{m}$ ) is interpreted to represent mechanical redistribution of medium–coarse grained garnet during mylonitisation. d) Mylonitic metapelite sample 325–672. Coarse-grained garnet in contact with quartz and potassium feldspar interpreted to be Mesoproterozoic. Mylonitisation during the Petermann Orogeny caused commonly observed fracturing and shearing of garnet. e) Sample 325–672 contains small domains of recrystallised Petermann-aged mineral assemblages. Garnet in direct contact with plagioclase, kyanite and biotite is interpreted as a Petermann-aged mineral association. Fine-grained kyanite occurs included in biotite and garnet and in a fine-grained matrix with plagioclase and garnet. f) Reflected light photo of the same area of sample 325–672, more clearly illustrating the distribution of fine-grained garnet, kyanite, biotite and plagioclase. g) Metapelitic gneiss sample 325–900b. Medium–coarse grained garnet separated by biotite and ilmenite. Garnet-biotite pairs are suitable for investigating the diffusional exchange of Fe–Mg during cooling. h) Metapelitic gneiss sample 325–900b. Kyanite included and in contact with biotite suggests biotite is Petermann-aged.

2); 2) the Mann Fault to the south, which is poorly exposed and; 3) the Davenport Shear Zone (Fig. 2), which is up to 500 metres wide and is dominated by mylonitised granitic gneiss, dolerite dykes of the Amata Suite and orthopyroxene-bearing granites (Camacho, *et al.*, 1997). Mylonitisation resulted in extensive recrystallization of Mesoproterozoic wall rocks and dolerite of the Amata Suite during the Petermann Orogeny. Gneisses marginal to the shear zone dominantly preserve coarse-grained Mesoproterozoic mineral assemblages which commonly comprise garnet, sillimanite, spinel, magnetite, perthite and quartz for metapelites and orthopyroxene, clinopyroxene, plagioclase, ilmenite and magnetite for mafic rocks (Collerson, 1972; Camacho, *et al.*, 2001). The effect of the Petermann Orogeny overprint was to replace sillimanite with kyanite and locally grow biotite in pelitic compositions and the growth of garnet, albitic plagioclase and hornblende in mafic compositions. The Davenport Shear Zone and the surrounding rocks are the focus of this study.

## PETROGRAPHY

The samples used in this study are legacy samples from the PhD collection of Collerson (1972). The samples are all garnet-bearing and were chosen in order to provide the most robust constraints on the  $P$ – $T$  conditions as well as potential cooling rates. In the choice of samples for  $P$ – $T$  calculations, a criterion was the identification of garnet grains that were newly formed during Petermann-aged deformation, as opposed to old (Mesoproterozoic) reworked garnet grains, as this affords the best

opportunity to characterise the Petermann-aged metamorphism. To investigate cooling rates, garnet-biotite samples from kyanite-bearing samples outside the Davenport Shear Zone were targeted to avoid garnet that has been mechanically milled during mylonitisation.

### A325-535, 907Q

These samples are from the Davenport Shear Zone (52J 719964mE 7096322mS, 52J 724090mE 7095147mS). The rock has a well-defined mylonitic fabric and as such the grain size is mostly very fine (< 50  $\mu\text{m}$ ). The mineralogy is dominated by a homogenous distribution of fine-grained garnet, clinopyroxene, hornblende, plagioclase, quartz and rutile (Fig. 3a, b).

### A325-875A

This sample is from the Davenport Shear Zone (723558mE 7095342mS). The rock has a well-defined mylonitic fabric and is dominated by coarse-grained porphyroclasts of garnet and potassium feldspar. Fine-grained rutile and monazite are common in the mylonitic fabric and in close proximity to garnet although are rarely included in porphyroclastic garnet (Fig. 4).

### A325-1175, 1593, 318

These samples are from mylonitic zones in the Amata/Davenport Shear Zone region (1175; 52J 478131mE 7101875mS, 1593; 401298mE 7085212mS, 318; 52k 496800mE 7077616mS). All samples have a well-defined mylonitic fabric and are dominated by coarse-grained porphyroclasts of garnet and potassium



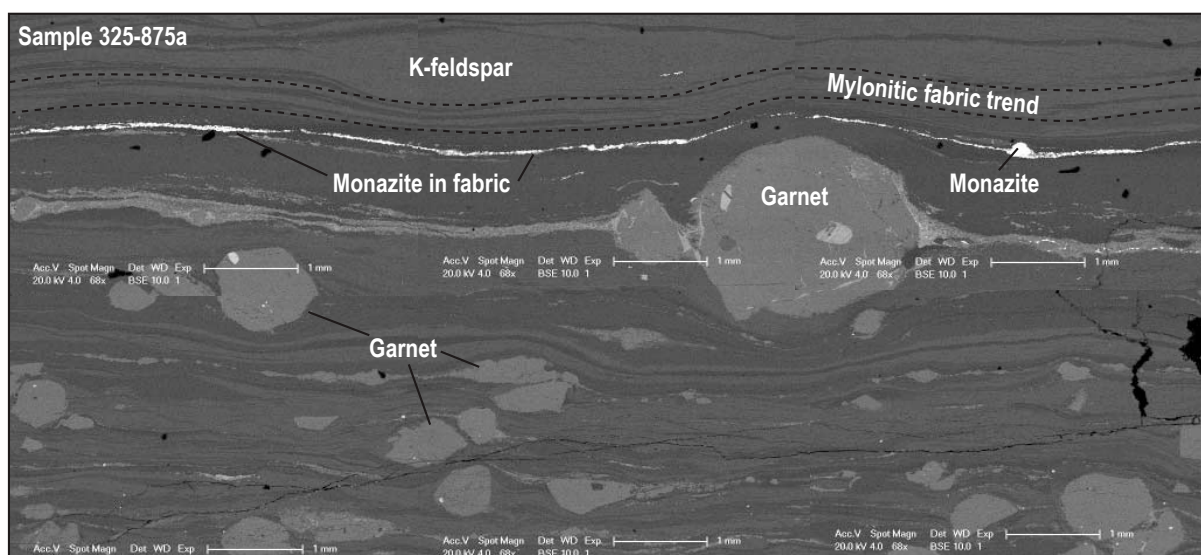


**Figure 4.** Backscattered electron images taken on the Scanning Electron Microscope for mylonitic metapelite sample a325–875a used for in-situ U–Pb monazite geochronology. Monazite was recrystallised within the mylonitic fabric (highlighted) during deformation and metamorphism of the Davenport Shear Zone during the Petermann Orogeny.

feldspar. Biotite is commonly in contact with garnet and fine-grained kyanite, magnetite quartz and plagioclase. Fine-grained rutile most commonly occurs in contact with fine-grained garnet (Fig. 3c).

### A325-672

This sample is from a shear zone ~ 3 km south of the Davenport shear zone (721626 mE 7093406 mS). The rock is a granitic gneiss dominated by coarse-grained porphyroclasts of garnet and potassium feldspar. Coarse-grained garnet commonly has inclusions of quartz and K-feldspar and is commonly sheared post-crystallisation (Fig. 3d). Fine-grained anhedral garnet commonly occurs in narrow bands which likely formed during mechanical breakdown and redistribution during mylonitisation (Fig. 3e, f). Small domains (~9 mm<sup>2</sup>) contain fine-medium-grained porphyroblastic garnet in contact with fine-grained plagioclase, K-feldspar, biotite and quartz (Fig. 3e, f). Foliated fine-grained acicular kyanite is intergrown with quartz, K-feldspar and plagioclase and is also included in garnet (Fig. 3f). Fine-grained magnetite is ubiquitous. Garnet in these domains exhibits no obvious accommodation of strain due to mylonitisation. These isolated domains are extremely localised in terms of their spatial development and macroscopically

the rock is coarse-grained gneiss interpreted to be relict from Mesoproterozoic granulite-facies metamorphism. Only in thin section is there evidence for kyanite-garnet-biotite-plagioclase assemblages. Kyanite-bearing assemblages are inconsistent with the very high geothermal gradients associated with Grenvillian tectonism but are consistent with the existing estimates of the *P–T* conditions of metamorphism during the Petermann Orogeny (Ellis & Maboko, 1992; Camacho, *et al.*, 1997; White & Clarke, 1997; Scrimgeour & Close, 1999; Raimondo, *et al.*, 2010).

### A325-900b

This sample is from 2 km south of the Davenport Shear Sone (Fig. 2). The rock is gneissic and is dominated by coarse-grained porphyroclasts of garnet and perthitic potassium feldspar. Biotite is exclusively fine-grained and locally intergrown with kyanite (Fig. 3g, h), is commonly in contact with and separates clusters of garnet and is rarely associated with anhedral ilmenite (Fig. 3h).

## PHASE EQUILIBRIA MODELLING

Three samples from the orogenic core in the Amata region were chosen for metamorphic modelling. Samples A325-535 and A325-907Q are recrystallised, mylonitic mafic dykes from inside the Davenport Shear Zone and

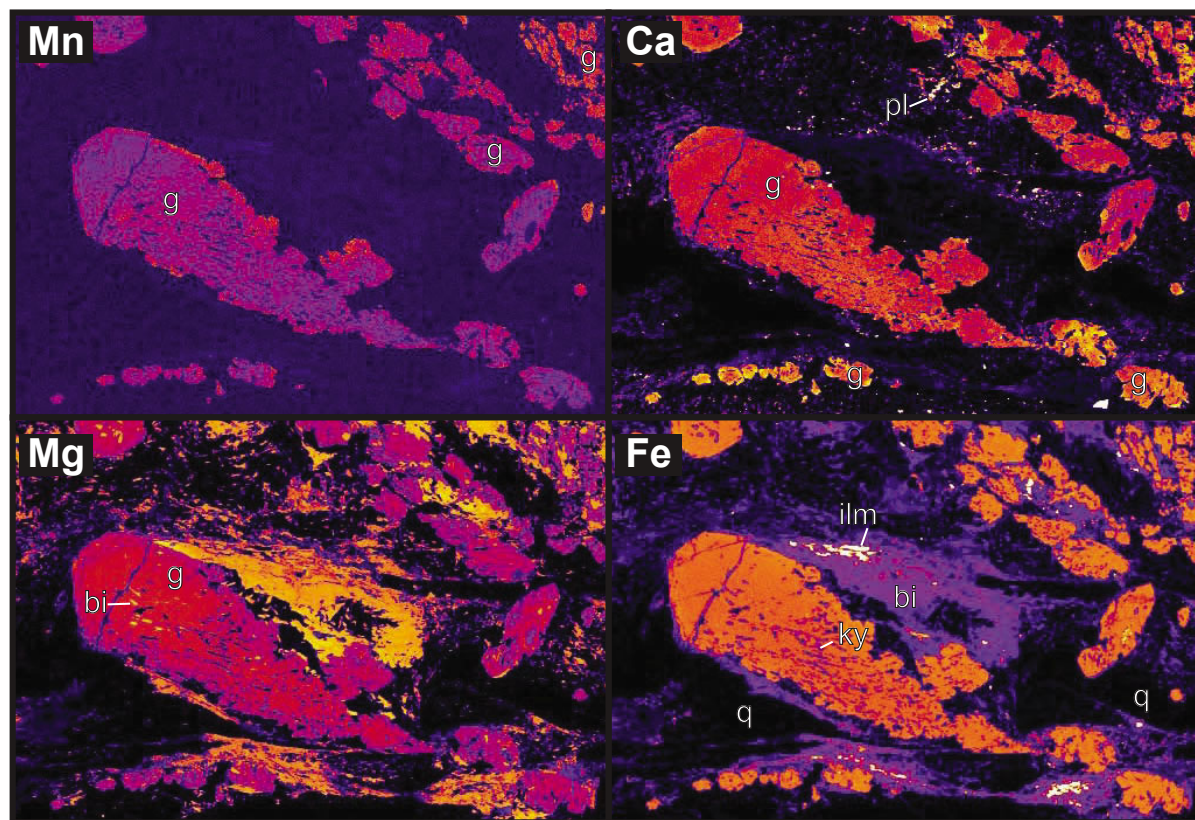


**Figure 5.** Electron microprobe element maps (Fe, Mg, Mn & Ca) for sample 325–672. As the distribution of Petermann-aged metamorphic minerals is heterogeneous and isolated in small domains in metapelitic gneisses, the image is used in combination with mineral composition data to construct a bulk composition for a  $P$ – $T$  pseudosection.

were selected as they are reported to record transitional granulite to eclogite facies mineral assemblages (Camacho *et al.*, 1997; 2009). Sample A325-672 is lower-strain pelitic gneiss from outside the Davenport Shear Zone and was selected because it preserve evidence of kyanite growth, consistent with mineral growth under thermal gradient conditions previously ascribed to the Petermann Orogeny (Camacho, *et al.*, 1997; White & Clarke, 1997; Scrimgeour & Close, 1999; Raimondo, *et al.*, 2010).

Bulk compositions for metamorphic modelling of texturally homogeneous samples A325-535 and A325-907Q were determined via whole-rock XRF analysis at Amdel Laboratories, Adelaide.  $\text{Fe}^{3+}/\text{Fe}^{2+}$  was measured via wet chemistry. For sample A325-672 in which new mineral growth is restricted to very local domains, by the combination of point counting and EMPA (Fig. 5). Bulk compositions are presented as oxide wt% in Table 1.  $P$ – $T$  pseudosections were calculated using Theriak-Domino (De Capitani & Petrakakis, 2010)

using the internally consistent thermodynamic dataset of Holland & Powell (1998; dataset tcds55 November 2003 update), compiled as HPDT.bs for use in Theriak-Domino, and the following  $a$ – $x$  models: garnet and biotite (White, *et al.*, 2007), clinopyroxene (Diener *et al.*, 2007), amphibole (Diener, *et al.*, 2007), spinel and magnetite (White, *et al.*, 2002), K-feldspar and plagioclase (Holland & Powell, 2003), epidote/clinozoisite (Holland & Powell, 1998) and ilmenite (White, *et al.*, 2000). Mafic samples were modelled using the chemical component system  $\text{NaO}$ – $\text{CaO}$ – $\text{FeO}$ – $\text{Mg}_2\text{O}$ – $\text{Al}_2\text{O}_3$ – $\text{SiO}_2$ – $\text{H}_2\text{O}$ – $\text{Ti}_2\text{O}$ – $\text{Fe}_2\text{O}_3$ . Potassium ( $\text{K}_2\text{O}$ ) and manganese ( $\text{MnO}$ ) were not modelled as there are no K-bearing minerals are present and the Mn content of garnet is negligible.  $\text{K}_2\text{O}$  was included when modelling the pelitic sample A325-672 as biotite is present.

#### A325-535

The interpreted peak assemblage of garnet–



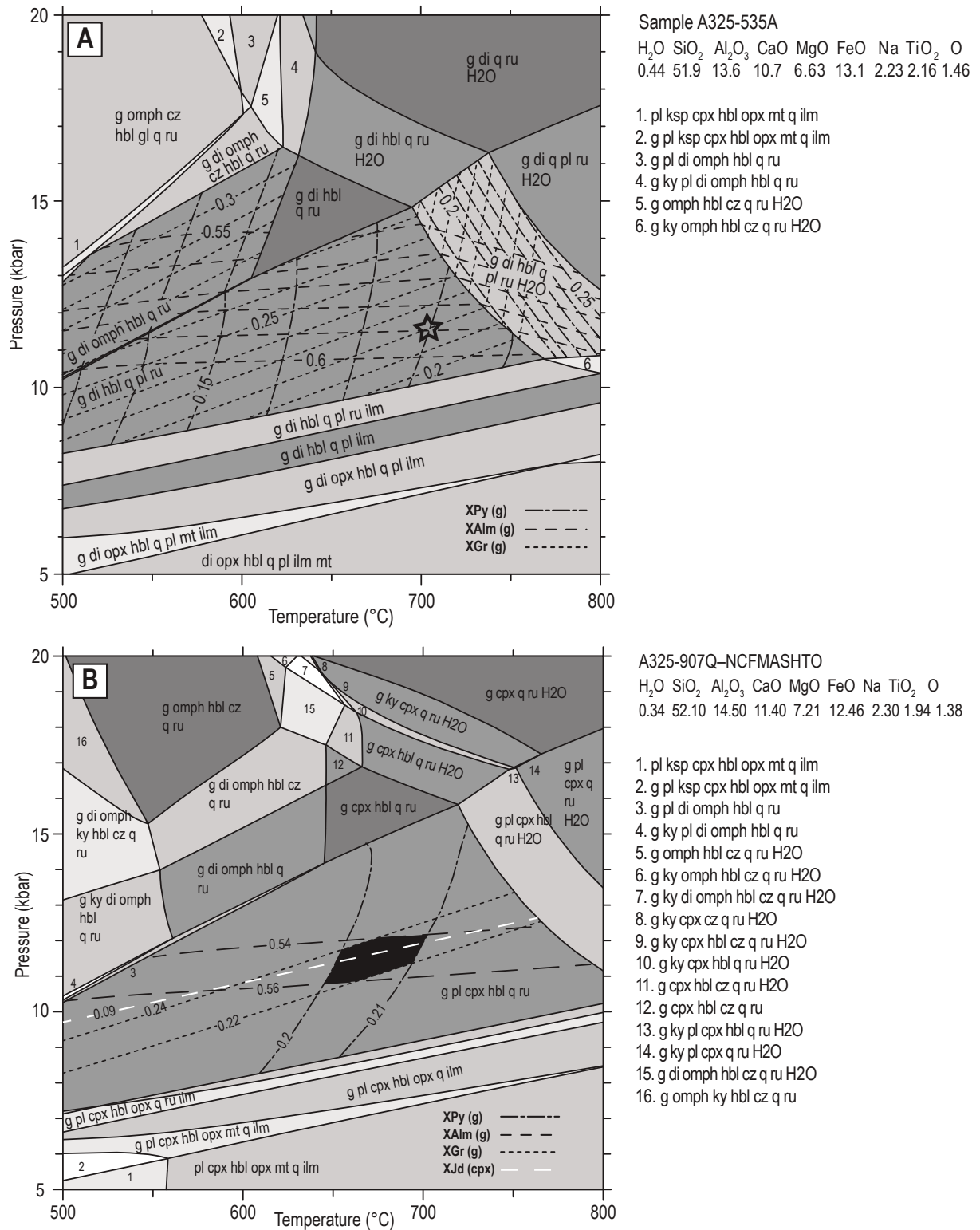


**Figure 6.**  $P$ – $T$  pseudosections calculated in the component system NCFMASHTO for mafic samples that were recrystallised during Petermann-aged deformation in the Davenport Shear Zone. a) sample a325–535.  $P$ – $T$  conditions of the development of a peak metamorphic assemblage of garnet, diopsidic clinopyroxene, hornblende, quartz, plagioclase and rutile are deduced using the composition of garnet to be 10.5–12 kbar and 630–670  $^{\circ}\text{C}$ . b) sample a325–907Q.  $P$ – $T$  conditions of the development of a peak metamorphic assemblage of garnet, diopsidic clinopyroxene, hornblende, quartz, plagioclase and rutile are deduced using the composition of garnet and clinopyroxene to be 10.5–12 kbar and 630–700  $^{\circ}\text{C}$ . As samples come from the same location;  $P$ – $T$  estimates of sample 325–535 are overlain (white dashed outline) in a ‘venn diagram’ approach to produce a more precise constraint of 10.5–11.5 kbar and 640–660  $^{\circ}\text{C}$ .

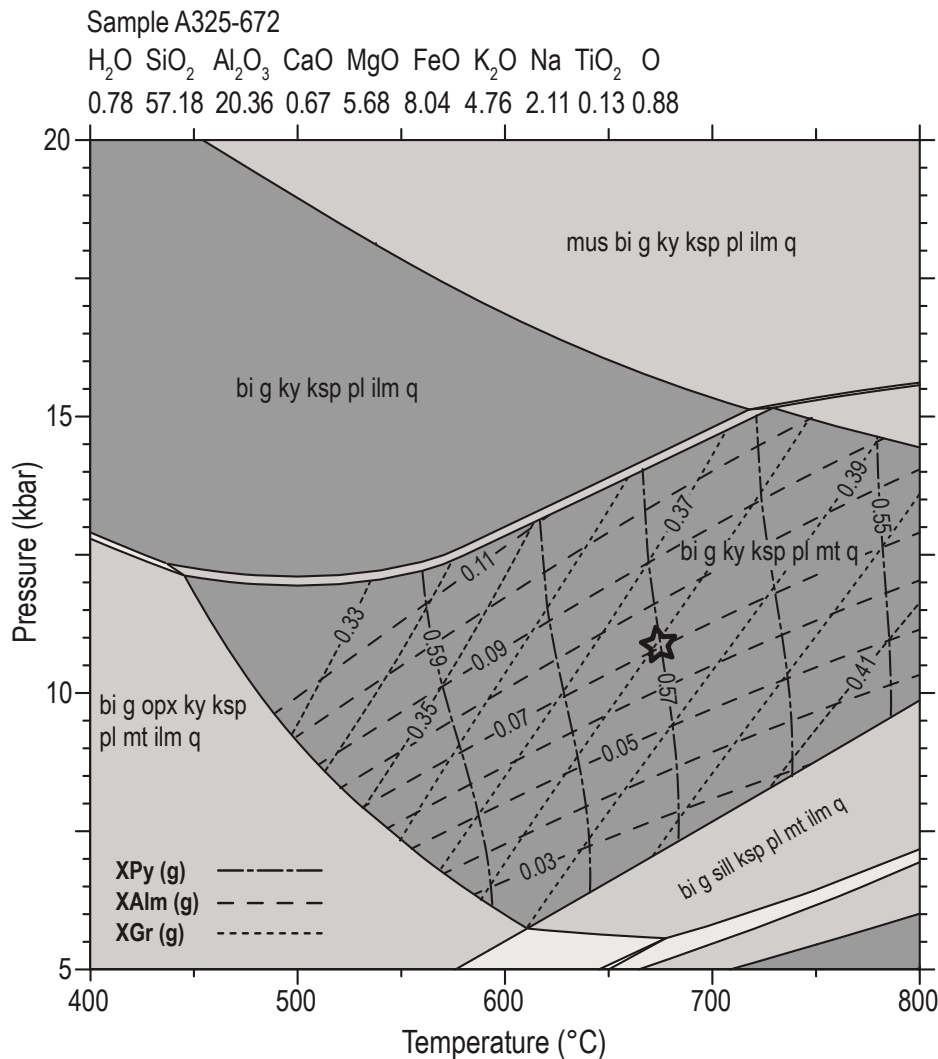


**Figure 7.** P–T pseudosections calculated in the component system NCKFMASHTO for metapelitic sample a325–672 that was recrystallised during Petermann-aged. P–T conditions of the development of a peak metamorphic assemblage of biotite, garnet, kyanite, potassium feldspar, quartz, plagioclase and magnetite are deduced using the composition of garnet to be 10–12 kbar and ~630–730 °C.

clinopyroxene–hornblende–plagioclase–quartz–rutile is modelled to occur at temperatures below 750 °C and between 8 and 15 kbar (Fig. 5a). *P–T* conditions are more precisely constrained by the composition of garnet. Measured garnet rims have a compositional range of  $X_{alm} = 0.58–0.60$ ,  $X_{py} = 0.17–0.18$  and  $X_{gr} = 0.21–0.23$ , which is modelled at 11 kbar and 700 °C (Fig. 6a).

#### A325-907Q

The interpreted peak assemblage of garnet–clinopyroxene–hornblende–plagioclase–quartz–rutile is modelled to occur at temperatures below 750 °C and between 8 and 15 kbar (Fig. 6b). *P–T* conditions are more precisely constrained by the composition of

garnet and clinopyroxene. Measured garnet rims have a compositional range of  $X_{alm} = 0.54–0.56$ ,  $X_{py} = 0.2–0.21$  and  $X_{gr} = 0.22–0.24$ , which is modelled at 10.5 to 12 kbar and 630 to 700 °C. The jadeite  $X_{jd} (Na-Fe^{3+})/(Na + (Na-Fe^{3+}) + Ca)$  component of clinopyroxene ranges between 0.08 and 0.10 and further constrains pressure to between 11 and 11.5 kbar (Fig. 6b). As samples come from the same location; *P–T* estimates of sample 325–535 are overlain (white dashed outline) in a ‘venn diagram’ approach to produce a more precise constraint of 10.5–11.5 kbar and 640–660 °C (Fig. 7b).

#### A325-672

The interpreted peak assemblage of biotite–garnet–kyanite–plagioclase–quartz–magnetite



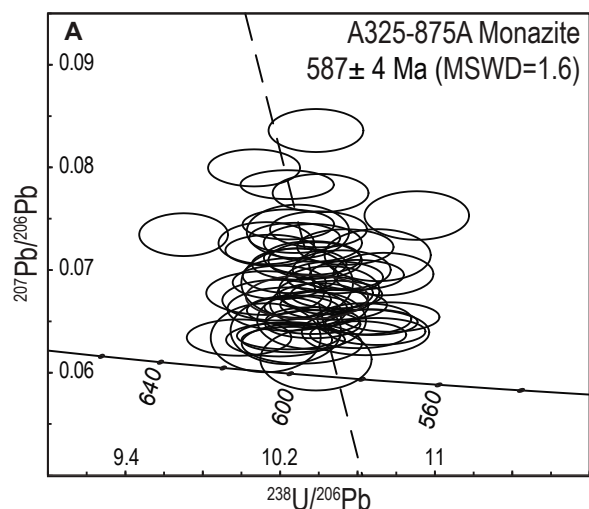


**Figure 8.** LA-ICPMS U-Pb monazite geochronology for metapelite sample a325–875. Age of  $587 \pm 4$  Ma is a calculated lower intercept. Upper intercept is anchored to common Pb composition of Stacey & Kramers (1975).

is modelled to occur at temperatures above 500 °C and between 6 and 15 kbar (Fig. 6). Measured garnet has a compositional range of  $X_{alm} = 0.56$ – $0.57$ ,  $X_{py} = 0.37$ – $0.39$  and  $X_{gr} = 0.06$ – $0.08$ , which is modelled at 10–12 kbar and 620–730 °C (Fig. 7).

### Summary

In the Amata area Petermann Orogeny-related metamorphic mineral assemblages in the three samples record peak  $P$ – $T$  conditions of 10.5–11.5 kbar and 650–700 °C. This equates to an apparent thermal gradient range of approximately 56–66 °C kbar<sup>-1</sup>.

### U-Pb GEOCHRONOLOGY

Samples inside and outside the Davenport Shear Zone containing monazite and/or rutile were targeted for U–Pb geochronology with the aim of constraining the timing and potentially the timescale of metamorphism and residence of rock at temperatures above approximately 600 °C (Vry & Baker 2006), which is the approximate closure temperature of the rutile U–Pb system. Monazite is uncommon and only sample A325–875A contained enough grains to analyse via *in-situ* LA-ICP-MS. Samples A325–875, 1175, 1593, 318 and 900B contain rutile and were analysed via SHRIMP. All isotope data is

contained in Table 4 and individual sample ages are provided in Table 5.

### LA-ICP-MS methods

U–Pb analysis of *in-situ* monazite for sample A325–875A was conducted using a New Wave 213 nm Nd–YAG laser in a He-ablation atmosphere connected to an Agilent 7500cs ICP–MS at the University of Adelaide following the method of Payne *et al.* (2008). Ablation of monazites was done with a frequency of 5 Hz and a spot size of 15 µm was used. The total acquisition time of each analysis was 90 s. This included 40 s of background measurement, 10 s of the laser firing with the shutter closed to allow for beam stabilisation and 40 s of sample ablation. Isotopes measured were <sup>204</sup>Pb, <sup>206</sup>Pb, <sup>207</sup>Pb and <sup>238</sup>U for 10, 15, 30 and 15 ms, respectively. Monazite data were reduced using ‘Glitter’ (Van Achterbergh, *et al.*, 2001; Griffin, *et al.*, 2008). The monazite standard MAdel was used to monitor systematic drift (TIMS normalisation data: <sup>207</sup>Pb/<sup>206</sup>Pb =  $491.0 \pm 2.7$  Ma, <sup>206</sup>Pb/<sup>238</sup>U =  $518.37 \pm 0.99$  Ma and <sup>207</sup>Pb/<sup>235</sup>U =  $513.13 \pm 0.19$  Ma: updated from Payne *et al.* (2008) with additional TIMS analyses. The accuracy of the corrected data was verified using in-house standards 94-222/Bruna-NW (*c.* 450 Ma: Payne *et al.*, 2008). Within Glitter an uncertainty of 1% is assigned to the age of the normalising standard.

### SHRIMP methods

Rutile grains were separated from crushed rock samples by conventional heavy liquid and magnetic methods. Rutile grains of varying morphologies were hand-picked for each sample and mounted in epoxy resin discs. The grains were then ground to approximately half their diameter to expose a representative section through the grain using a combination of polishing cloths. Prior to SHRIMP analysis the mounts were cleaned and coated with 500 nm of high purity gold that produced a resistivity of 10–20 Ω across the disc.

U–Pb–Th analysis of rutile was conducted using the SHRIMP-II facility at the John De Laeter Centre for Mass Spectrometry, Curtin University, Perth. Detailed SHRIMP operating procedures for rutile are outlined by Taylor *et al.* (2011). For all analyses a beam diameter of

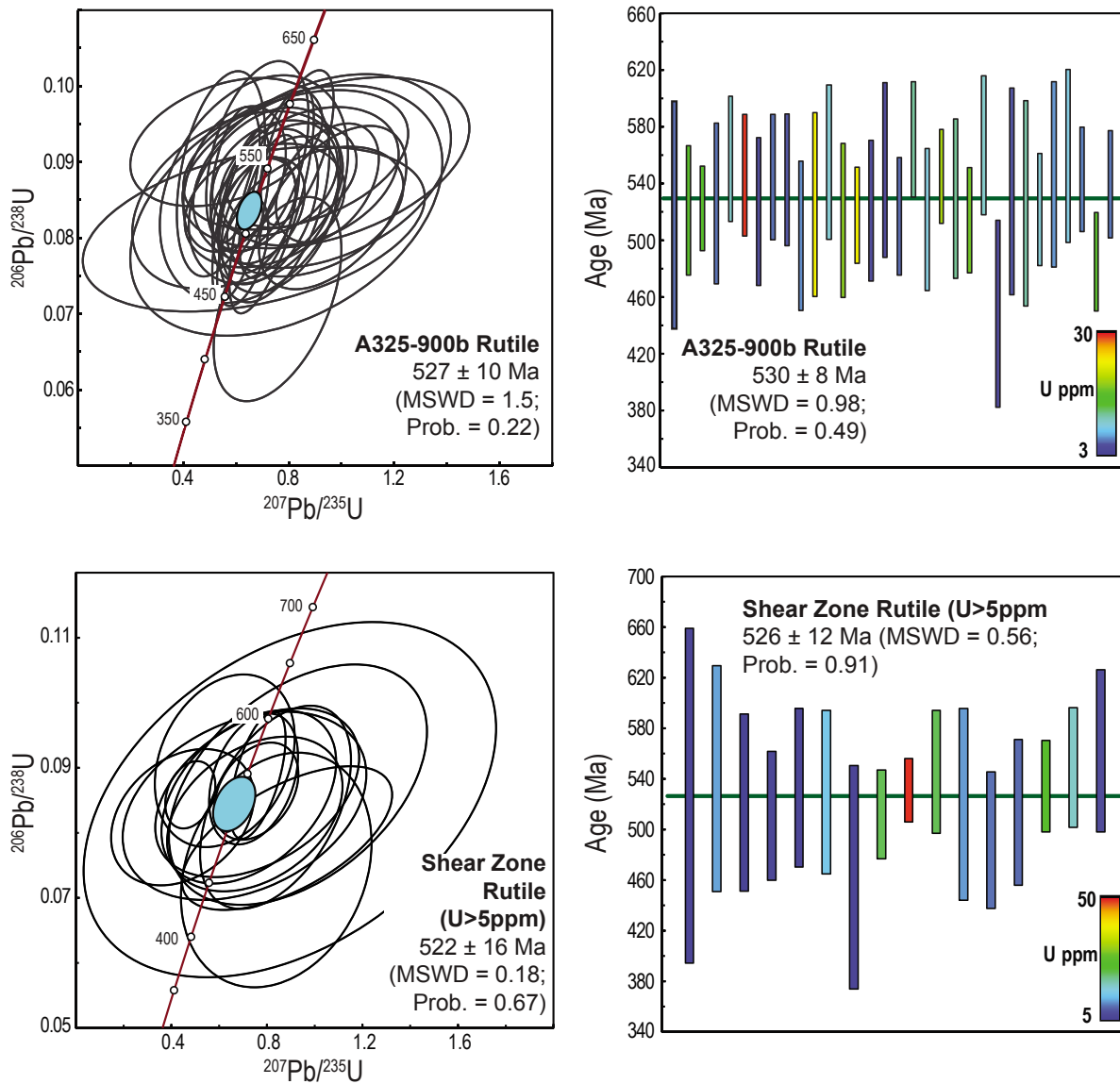


**Figure 9.** SHRIMP U–Pb rutile geochronology. a) Concordia plot for sample a325–900b. b) Weighted average plot for sample a325–900b. Concentration of Uranium is plotted to illustrate the large individual errors are due to the number low-U analyses. c) Concordia plot for shear zone samples 325–1593, 875 & 318. Analyses for all samples commonly contained < 5 ppm Uranium. A representative plot is generated using pooled analyses containing > 5 ppm uranium. b) Weighted average plot for the same analyses. Concentration of uranium (ppm) is plotted

30  $\mu\text{m}$  was used. Prior to each analysis, the spot was rastered for 2 minutes at 120 nA to remove the gold coating and reduce surficial common lead and other sources of contamination. As rutile does not contain radiogenic  $^{208}\text{Th}$ , the  $^{208}\text{Pb}$ -common lead correction was applied to all rutile samples. U–Pb fractionation was corrected using the covariation between  $\text{Pb}^+/\text{U}^+$  and  $\text{UO}^+/\text{U}^+$  determined by analyses of rutile standard WHQ with an age of 2625 Ma (Taylor, *et al.*, 2011). Data was reduced using SQUID 2 software and plotted using Isoplot

3.66 (Ludwig, 2001, 2003).

## RESULTS

### Monazite

Seventy six analyses from 42 monazite grains from sample A325–875A were collected in situ via LA–ICP–MS over two sessions. Monazite grains are commonly tabular to elongate, and range in size from 20  $\mu\text{m}$  to 500  $\mu\text{m}$  and are most commonly located in trails along the same orientation as the dominant mylonitic

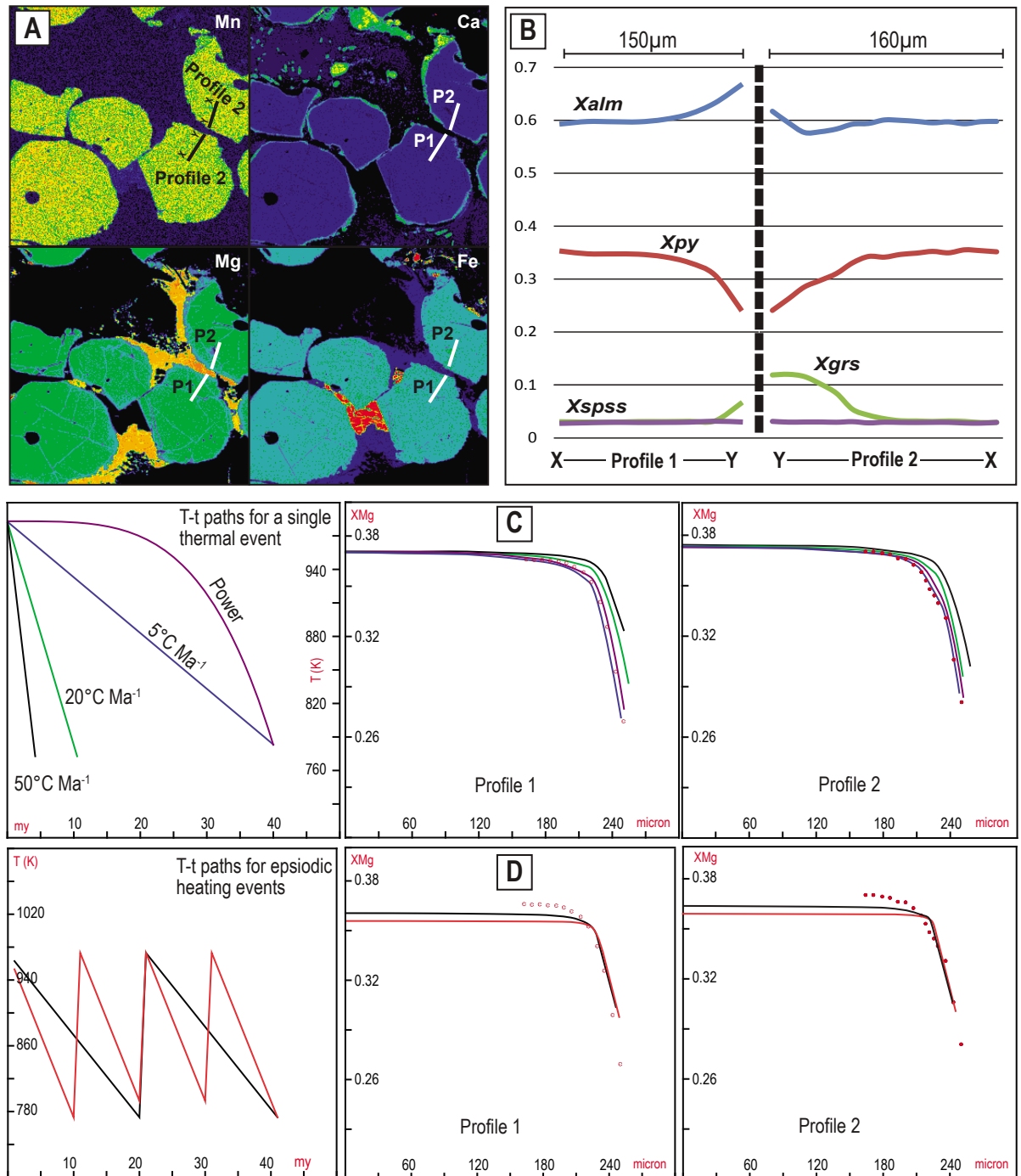


**Figure 10.** Modelling of garnet diffusion produced using software package THERMAL HISTORY of Robl et al. (2007). a) Electron microprobe (EMP) maps (Fe, Mg, Mn & Ca) of sample a325–900b. The location of measured EMP profiles used to investigate element zoning are shown on each map. B) Measured EMP element profiles.  $X_{alm} = (Fe/Fe+Mg+Mn+Ca)$ ,  $X_{py} = (Mg/Fe+Mg+Mn+Ca)$ ,  $X_{spss} = (Mn/Fe+Mg+Mn+Ca)$ ,  $X_{grs} = (Ca/Fe+Mg+Mn+Ca)$ . c) Modelled profiles vs measured  $X_{Mg}$  (Red dots represent measured composition) for different temperature-time histories based on a single cooling event. d) Modelled profiles vs measured  $X_{Mg}$  for different temperature-time histories based on multiple heating and cooling events.

fabric (Fig. 4). Subtle zoning is uncommonly observed via backscatter-electron imagery using a scanning electron microscope. A total of 23 analyses were discarded on the basis of

anomalous spikes in the  $^{204}\text{Pb}$  signal, which were exclusively associated with cracks visible on the grain surface. When modelled on the Stacey-Kramers crustal Pb composition

(Stacey & Kramers, 1975), a total of 53 analyses from 42 grains yields an intercept age of  $587 \pm 4$  Ma with MSWD=1.6 (Fig. 8).

### Rutile

Rutile from samples A325–875, 1175, 1593 and 318, from shear zones in the Amata region, commonly have very low concentrations of uranium (typically < 2 ppm) and high concentrations of common lead. It should be noted that due to the low number of analyses and the large individual spot errors, calculated MSWD values are unrealistically low. As there is low statistical variance between shear zone samples, rutile data are pooled together and data which have uranium concentrations > 5 ppm ( $n=16$ ) yield a concordia age of  $528 \pm 16$  Ma (MSWD = 0.63; probability = 0.42) and a weighted average age of  $526 \pm 12$  Ma (Fig. 9; MSWD = 0.56; probability = 0.91).

Rutile grains from sample 900B (low strain outside shear zones) contain comparably high concentrations of U (> 5 ppm) resulting in reduced uncertainty. 32 analyses from 32 grains yield a concordia age of  $527 \pm 10$  Ma (MSWD = 1.2; probability = 0.27).

## DIFFUSION MODELLING

Compositional zoning profiles preserved in garnet caused by retrograde, re-equilibration diffusion can be used to calculate estimates of the cooling rate of the terrain (e.g. Hauzenberger, *et al.*, 2005; Robl, *et al.*, 2007; Cutts, *et al.*, 2011; Forbes, *et al.*, 2012). This information is particularly useful when coupled with geochronological data. Garnet is well known to diffusively exchange Fe and Mg with other Fe-Mg-bearing reservoirs such as biotite as rocks cool from temperatures above (or around) approximately 600–700 °C (e.g. Grant & Weiblen, 1971; Fitzsimons & Harley, 1994; Pattison & Bégin, 1994; Pattison, *et al.*, 2003) and thus preserve compositions at the rim that do not correspond to the peak of metamorphism. Models simulating retrograde Fe-Mg exchange between garnet and biotite can be used to calculate compositional zoning profiles for a specified cooling rate and size and abundance of garnet (relative to biotite) that can be directly compared to measured garnet compositional profiles to thus constrain predict the cooling rate during retrograde

diffusional exchange in rocks. Estimates of the rate of cooling are only relevant to the period during which retrograde diffusional exchange of Fe and Mg occurs and cannot be used to extrapolate to the entire retrograde/cooling history of the rock.

Sample A325–900b (Fig. 3g, h) is modelled in preference to mylonitic rocks of the Davenport Shear Zone to avoid garnet that has undergone grain size reduction during deformation, which creates a significant disconnect between the thermal history of the orogen and an individual rock. The timing of garnet growth in sample 325–900b is unequivocal although it is assumed that coarse-grained garnet in contact with perthitic K-feldspar is Mesoproterozoic in age. Although there is no way to determine the absolute age of the biotite involved in diffusion with garnet, biotite in sample 900B is commonly intergrown with acicular fine-grained kyanite (Fig. 3h) and therefore is interpreted to be Petermann-aged. Regardless, peak metamorphic temperatures between 650 and 700 °C will facilitate intragranular diffusion of major elements, specifically iron and magnesium, and coupled exchange in the presence of biotite (Carlson, 2006).

Measured garnet element profiles from sample 900B are used to evaluate the potential duration of diffusion and rate of cooling. Garnet grains exhibit mostly flat zoning profiles with compositional variation occurring within ~50 µm of the rim (Fig. 10a, b). Almandine content increases rimward from 0.59–0.67, with pyrope content decreasing rimward from 0.36–0.24. Grossular content increases at the rim from 0.04–0.11, although calcium zoning appears patchy, perhaps reflecting the slow diffusion of calcium in garnet. Spessartine zoning is flat.

Garnet diffusion and cooling rates in the central Musgrave Province are modelled using the software THERMAL HISTORY (Robl, *et al.*, 2007). The software utilises diffusive Fe–Mg exchange by comparing measured diffusion profiles against theoretical profiles of garnet and biotite. Diffusion constants of Ganguly *et al.* (1998) are used. Starting temperatures between 680 and 700 °C were estimated from  $P$ – $T$  calculations for nearby sample A325–672 and  $X_{\text{Mg}}$  biotite values between 0.69 and 0.67 were measured from garnet-adjacent



biotite in sample A325–900b. Volumes of biotite and garnet were fixed at 0.2 and 0.8 respectively. Garnet compositional zoning profiles developed in sample A325–900B can be reproduced by simple linear cooling at  $5\text{ }^{\circ}\text{C Ma}^{-1}$  between 700 and 500  $^{\circ}\text{C}$  over a period of 40 Myr (Fig. 10). For a single cooling rate, a combination of  $X_{\text{Mg}}$  and starting temperatures can provide a non-unique solution to satisfy the modelled  $X_{\text{Mg}}$  of the garnet. However, the shape of the diffusion profile in garnet is fundamentally controlled by the cooling rate (Robl, *et al.*, 2007). Thermal histories involving multiple heating and cooling events are modelled, however, they do not reproduce the observed zoning profiles (Fig. 10d).

## DISCUSSION

### *Timing of metamorphism and footprint of elevated temperatures*

The growth and preservation of metamorphic mineral assemblages reflects the physical and thermal conditions of metamorphism as well as the ability of the crust to record changes in pressure and temperature, i.e. the ‘fertility’ of the crust. Additionally, the apparent geothermal gradient of metamorphism is instructive in terms of predicting heat sources that drive metamorphism.  $P$ – $T$  conditions of 10.5–11.5 kbar and 650–700  $^{\circ}\text{C}$  deduced from shear zones in the Amata area of the Petermann orogenic core indicate that apparent geothermal gradients are of the range 57–66  $^{\circ}\text{C kbar}^{-1}$  (Fig 6 & 7). Such values suggest that the thermal conditions in the Petermann Orogeny crust are analogous to those associated with ‘normal’ crust and are consistent with previous estimates from the western orogenic core (e.g. White & Clarke, 1997; Raimondo, *et al.*, 2010).

In the Davenport Shear Zone, monazite is dominantly located within the mylonitic fabric (Fig. 4), therefore, monazite is interpreted to have recrystallised during mylonitisation and shear zone movement. Whereas temperatures of  $\sim 700\text{ }^{\circ}\text{C}$  are predicted by the equilibrium mineral assemblages preserved in the Davenport Shear Zone, there is no requirement that a U–Pb age of  $586 \pm 4\text{ Ma}$  (Fig. 8) must represent peak metamorphic temperatures, although high temperatures would promote recrystallization. This U–Pb

age could alternatively reflect the cessation of Pb diffusion in monazite and be interpreted to represent cooling. The Pb closure temperature of monazite is typically considered to be approximately equivalent to that of zircon (e.g. Cherniak, *et al.*, 2004), though in highly deformed/strained rocks such as mylonites, it is not clear that monazite closure temperature will remain approximately  $>900\text{ }^{\circ}\text{C}$  (e.g. Kelsey, *et al.*, 2003; Wawrzenitz, *et al.*, 2012).

However, timing of monazite recrystallization in the Davenport Shear Zone at  $586 \pm 4\text{ Ma}$  is similar to the timing of metamorphism and crustal thickening in the foreland fold thrust belt at 600–590 Ma (Walsh *et al.*, 2015) and partial melting associated with peak metamorphism in the western part of the orogen, as recorded by U–Pb titanite and zircon ages of  $\sim 570$  (Raimondo *et al.*, 2009; 2010). Therefore, it is plausible that recrystallisation in shear zones in the east was accompanied by temperatures approaching  $\sim 700\text{ }^{\circ}\text{C}$ .

Though phase equilibria results do not precisely constrain the temperature of rutile growth (Fig. 6 & 7), peak metamorphic temperatures are 680–700  $^{\circ}\text{C}$ —higher than the U–Pb closure temperature of rutile, which is known to be around 600–620  $^{\circ}\text{C}$  for medium–slow cooling rates ( $1\text{--}10\text{ }^{\circ}\text{C Ma}^{-1}$ ) for grains 10–100  $\mu\text{m}$  in radius (Mezger, *et al.*, 1989; Vry & Baker, 2006; Cherniak, *et al.*, 2007; Luvizotto, *et al.*, 2009; Warren, *et al.*, 2012). Therefore, U–Pb rutile ages of *ca.* 525 Ma in the Davenport Shear Zone (Fig. 8) are interpreted to be cooling ages.

Wall rocks to shear zones in the Amata area do not preserve the development of pervasive metamorphic mineral assemblages during the Petermann Orogeny (e.g. Camacho & McDougall, 2000). The extent of Petermann-aged metamorphic mineral growth in metapelitic gneisses is limited to the replacement of sillimanite by kyanite and the growth of biotite (e.g. Fig. 3). Therefore, given the low variance of the developed mineral assemblages, it is challenging to precisely model the metamorphic conditions using  $P$ – $T$  pseudosections. However, temperatures outside of shear zones can be investigated based on the resetting of the U–Pb isotope system in rutile (Fig. 9) and the diffusional response of garnet-biotite pairs (Fig. 10).

A U–Pb rutile age of  $527 \pm 10$  Ma (Fig. 9) from sample 900b is statistically identical to rutile ages from shear zones in the Amata area. In addition, U–Pb cooling ages from titanite and rutile from the western part of the orogen return similar results that range 540 to 500 Ma (Raimondo, *et al.*, 2009; Raimondo, *et al.*, 2010; Walsh, *et al.*, 2013). Temperatures in excess of 600 °C are usually required to reset the U–Pb isotope system in rutile (Vry & Baker, 2006). Factors such fluid–rock interaction, recrystallisation, strain variation and grain size reduction may additionally seek to promote or impede the resetting of the U–Pb isotope system, although the absolute effects of these processes are unconstrained and difficult to identify in U–Pb data (e.g. Schaltegger, *et al.*, 1999; Townsend, *et al.*, 2001; Carson, *et al.*, 2002; Seydoux, *et al.*, 2002). Sample 325–900b contains a low abundance of biotite (1–2%; Fig. 3g) and limited evidence for recrystallisation or grain size reduction and therefore, it is interpreted that temperature was a more important factor in controlling isotopic resetting. Based on the resetting of the U–Pb isotope system in rutile, temperatures in rocks outside shear zones were elevated above ~600 °C.

Major element profiles in garnet consistent with Fe–Mg coupled exchange between garnet and biotite support elevated temperatures outside of shear zones. Diffusional profiles are most accurately reproduced by a thermal histories which involves cooling from initial temperatures 700° C, supporting the interpretation of temperatures  $\geq 600$  °C outside of shear zones during the Petermann Orogeny.

#### *Duration of metamorphism*

The timescale of elevated crustal temperatures is a function of combination of factors including the duration and type of heat source(s) responsible for the thermal structure of the crust, tectonic setting, particle path vectors of an analysed rock, erosion rate and thermo-physical properties of rocks such as thermal diffusivity. The duration of orogenic-scale metamorphism is unlikely to be entirely recorded by a single rock as there is no necessity the heat source will follow a common  $P$ – $T$ – $t$  path. Therefore, a single rock will record at least a minimum duration of orogenic scale metamorphism. The application

of U–Pb geochronology to multiple minerals in the same rock/outcrop is increasingly being utilised to investigate the timing and duration of tectonic and metamorphic processes including crustal melting, fluid–rock interaction, duration of high temperature metamorphism, and timing of deformation fabrics (e.g. Zeh, *et al.*, 2003; McFarlane, *et al.*, 2006; Kelsey, *et al.*, 2008; Janots, *et al.*, 2009; Högdahl, *et al.*, 2012; Korhonen, *et al.*, 2013; Rubatto, *et al.*, 2013). In medium to high temperature (>600 °C) metamorphic systems the combination of U–Pb monazite and rutile geochronology can be used to investigate the timescale and rate of the high-temperature section of the cooling history (e.g. Terry, *et al.*, 2000; Kylander-Clark, *et al.*, 2008; Warren, *et al.*, 2011; Warren, *et al.*, 2012).

Regardless of the interpretation of monazite ages (i.e. growth vs cooling), one interpretation is that monazite ages at least 40 Myr older than rutile ages imply that the crust resided at temperatures >600 °C for a minimum timescale of 40 Myr. If monazite grew from the peak of metamorphism and simple, linear cooling is assumed, the cooling rate over the interval 600–700 °C is constrained to be ~3 °C Ma<sup>-1</sup>. If monazite ages represent cooling, then the cooling rate based on the age difference will be faster. Geochronological data does not constrain the rate of burial or heating and therefore cannot directly constrain the timescale over which peak metamorphic temperatures were sustained but it does indicate that if a single cycle of heating is assumed, crustal temperatures remained >600 °C for >40 Myr. An alternative hypothesis is that heating and metamorphism was episodic and short lived. Future interrogation of the timing of deformation and metamorphism with a systematic approach, e.g. U–Pb monazite geochronology, could resolve episodes of deformation but the currently available data set supports a single cycle of metamorphism during intraplate orogeny.

Modelled zoning profiles in garnet (Fig. 10), which developed in low-strain rocks in response to cooling-driven coupled Fe–Mg exchange with biotite are more consistent with a thermal history that involves a single cycle of heating followed by cooling at a rate of  $\leq 5$  °C Ma<sup>-1</sup>. Thermal histories which involve repeated cycles of heating and

cooling analogous to a hypothetical episodic thermal regime do not accurately replicate the observed element profiles developed during diffusion (Fig. 10).

The results of U–Pb geochronology and diffusion modelling indicate that cooling rates are slow enough to allow for the deep crust residing at elevated temperatures, under ‘normal’ geothermal gradient conditions, for a period of time that is on the order of tens of millions of years.

#### *Drivers for metamorphism*

The conclusions regarding the thermal duration of the Petermann Orogeny, based on U–Pb geochronology,  $P$ – $T$  pseudosections and diffusion modelling, are inconsistent with previous suggestions that elevated temperatures were localised to shear zones, thermal durations were approximately 1 Myr in shear zones and that the primary driver for metamorphism was shear heating (Camacho, *et al.*, 2009). Previous temperature estimates outside of shear zones of ~350 °C were based on the lack of resetting of both the K–Ar isotopic system in biotite and potassium feldspar and Rb–Sr in biotite (Camacho, *et al.*, 1997; Camacho & McDougall, 2000; Camacho, *et al.*, 2001; Camacho, *et al.*, 2009). The key information is the preservation of older age steps in the K–Ar or  $^{40}\text{Ar}/^{39}\text{Ar}$  spectra, or the calculation of Rb–Sr ages  $\gg$  600 Ma (Camacho, *et al.*, 1997; Camacho & McDougall, 2000). In potassium feldspar from non-mylonitic samples, age steps older than known Petermann-aged deformation (*ca.* 600 Ma) in the  $^{39}\text{Ar}$  signal are interpreted to represent incomplete resetting and used to invoke temperatures  $<$  400 °C. Whereas incorporation of excess argon is uncommon in potassium feldspar lattice, fluid inclusions are extremely effective at concentrating excess argon (Turner & Songshan, 1992; Arnaud & Kelley, 1995; Esser, *et al.*, 1997; De Jong, *et al.*, 2001; Kelley, 2002). Potassium feldspar in effectively anhydrous metapelitic granulites from the Amata region commonly display fluid inclusions (Camacho, 1997). Therefore, in addition to the possibility of excess argon in fluid inclusions, transport of excess argon out of potassium feldspar and along grain boundaries would be severely limited even over millions of years given the highly compatible nature

of argon in fluids or melt (Scaillet, *et al.*, 1995; Scaillet, 1996; Kelley, 2002). Therefore an alternative interpretation is that the small percentage (e.g. 5–15 %; Camacho & McDougall, 2000) of the  $^{39}\text{Ar}$  signal older than 600 Ma reflects the analysis of minor amounts of excess argon probably concentrated in fluid inclusions. This would permit an interpretation that potassium feldspar was reset and the restriction of temperatures to ~350 °C outside of shear zones is not necessary.

Similar patterns of isotopic resetting can be observed in the record of Rb–Sr system where a biotite age of *ca.* 1000 Ma is preserved from a sample outside of a shear zone and is interpreted to reflect low ambient temperatures (Camacho, *et al.*, 2001). Similar patterns of resetting of Rb–Sr ages are observed in the Marun-Keu complex and the Western Gneiss Terrane (Kühn, *et al.*, 2000; Glodny, *et al.*, 2008), where former granulite terranes (now anhydrous), are reworked to eclogite in zones where fluid–rock interaction occurs. Whereas eclogitised zones preserve Rb–Sr ages reflecting reworking, the Rb–Sr isotope system in anhydrous granulite has not been reset (Glodny, *et al.*, 2002). Therefore fluid–rock interaction is viewed as vital mechanism in facilitating Sr diffusion and patterns of isotopic resetting. If factors other than temperature are considered then the preservation of an older age outside of shear zones in the Amata region could also reflect the lack of fluid ingress into the granulitic wall rock rather than solely reflect large temperature variations between shear zones and wall rock.

The short durations of elevated temperatures (*ca.* 1 Myr) suggested by Camacho *et al.* (2009) are based on the preservation of older ages in potassium feldspar from inside the Davenport Shear Zone and additionally, narrow calcium diffusion profiles developed during the recrystallization and neocrystallisation of plagioclase at the expense of garnet during mylonitisation in shear zones. Diffusion is suggested to be facilitated by dislocation creep (Camacho, *et al.*, 2009) as volume diffusion coefficients are significantly low and would not allow diffusion to occur on such time scales (c.f. Spear *et al.* 1991, Keller *et al.* 2006). The interpretation that dislocation creep was the mechanism that facilitated calcium diffusion appears to be consistent



with the growth of fine-grained, calcium-rich garnet separating relict garnet and plagioclase (e.g. Camacho *et al.*, 2009). However, the growth of fine-grained calcic garnet would have consumed significant amounts of calcium liberated during recrystallisation of albitic plagioclase. Therefore, the ability of coarse-grained relic garnet to develop zoning profiles could be limited by the consumption of calcium by Petermann-aged garnet and not necessarily by short time scales. Modelling of mylonitic rocks from shear zones in the region present additional complications as the potential for removal of the exterior of garnet during mylonitisation may result in the preservation of unrealistically narrow compositional zoning profiles. Regardless, the garnet modelling of Camacho *et al.* (2009) concludes that deformation in shear zones is short-lived and does not necessitate short durations of elevated temperatures.

The interpretation of U–Pb geochronology and garnet–biotite diffusion modelling from rocks outside shear zones is that thermal gradients were regionally elevated and therefore that the crust overall was warmer than previously suggested in the axial core of the orogen.

#### *Thermo-mechanical evolution of the Petermann Orogen*

Initiation of intraplate orogenesis in central Australia is fundamentally controlled by the rheological properties of the Pre-Petermann Orogeny lithosphere, such that strain was accommodated and localised in the Musgrave Province at ~600 Ma (Walsh, *et al.*, submitted). The rheological weakness of the Musgrave Province could be due to inherent but local structural weaknesses in overall strong lithosphere (Braun & Shaw, 2001; Camacho, *et al.*, 2002). It is not clear that any of the E–W trending structures that dominate and define the strike trend of the Musgrave Province existed prior to the commencement of the Petermann Orogeny as older (Grenvillian) fabrics are not orientated in an E–W direction. However, inherent structural weakness could explain the relatively localised deformation in the orogenic core that is dominated by more or less un-reworked granulite facies rocks. Localisation of orogeny in intraplate lithosphere is also considered to be greatly affected by pervasive thermal weakening

(Sandiford & Hand, 1998; Hand & Sandiford, 1999; Raimondo, *et al.*, 2014; Walsh, *et al.*, in review).

Insight into the possible rheology of lithosphere prior to and in the early stages of orogenesis can be gained with a consideration of the distribution of heat production in the orogen. Mid-crustal granites from the Petermann Nappe Complex (Fig. 1; foreland fold-thrust belt) and north of the Woodroffe Thrust have high average heat production values at 600 Ma of  $4.13 \pm 0.55 \mu\text{W m}^{-3}$  ( $n=58$ ) and  $4.3 \mu\text{W m}^{-3}$  respectively (Sandiford, *et al.*, 2001; Sandiford & McLaren, 2002). Granulite-facies gneisses in the hinterland to the south of the Mann Fault represent the lower crust and have an average heat production at 600 Ma of  $0.911 \pm 0.06 \text{ mW}^{-3}$  ( $n=430$ ). This implies that the heat production maximum was contained in mid- and probably upper-crustal granites. Comparatively lower radiogenic heat production in residual lower crustal (>25 km) rocks probably reflects significant loss of incompatible elements to higher crustal levels through geochemical differentiation of the crust (Bea, 1996; Bea & Montero, 1999; Villaseca, *et al.*, 2003; Villaseca, *et al.*, 2007) occurring by melting and melt loss during Grenvillian-aged, ultrahot thermal gradient metamorphism (Walsh, *et al.*, in press). Therefore, the integrated strength of lithosphere was plausibly strongly affected by the weakening induced by high radiogenic heat-producing granitic rocks in the mid (and upper) crust (Sandiford, *et al.*, 2001; Sandiford & McLaren, 2002; McLaren, *et al.*, 2003), in conjunction with the insulating effects of a thick sedimentary cover (Sandiford & Hand, 1998; Hand & Sandiford, 1999; Stephenson, *et al.*, 2009). The record of pervasive ductile metamorphism in the western part of the orogenic core (Mann Ranges/Bates regions) and the development of a thick-skinned fold-thrust belt at around 600 Ma and deep flexural response of the foreland basin to the north might reflect strain partitioning into areas of greater weakness in the orogen (Walsh, *et al.*, in review; Walsh, *et al.*, submitted).

Patterns of deformation in the east contrast this, where strain is partitioned into more discrete, localised zones i.e. crustal scale faults and foreland development is limited, implying that lithosphere was comparatively strong



in the east. The deduction that metamorphic temperatures of 650–700 °C were achieved across the core of the orogen between 590 and 570 Ma, implies that lithospheric strength was not solely dependent on temperature. It is ultimately unclear what controls the variation in lithospheric strength in the Petermann Orogen, although regions of ductile deformation, including migmatitic shear zones, are considered to represent the migration of metamorphic fluids generated by dehydration of hydrous minerals during metamorphism (Cartwright & Buick, 2000; Gregory, *et al.*, 2009; Raimondo, *et al.*, 2009; Raimondo, *et al.*, 2010). The addition of fluids may have facilitated locally pervasive metamorphism in a dominantly anhydrous residual lower crust that was otherwise unresponsive to periods of elevated temperatures and deformation during intraplate orogeny.

Such strongly residual lower crust became an increasingly important factor during the cooling and exhumation of the orogen (e.g. Sandiford, *et al.*, 2001). The organisation of the majority of crustal radiogenic heat production into the mid and upper crust implies that exhumation and erosion of the orogen resulted in a dramatic reduction of the heat production of the system. The progressive reduction in crustal heat production would have modified the long-term mechanical structure of the lithosphere, leading to a progressive increase in the integrated strength of lithosphere via cooling (Sandiford, *et al.*, 2001; Sandiford & McLaren, 2002; McLaren, *et al.*, 2003). Exhumation of the mantle lithosphere along major shear zones additionally promoted long-term lithospheric strengthening (Sandiford, *et al.*, 2001; Sandiford & McLaren, 2002; Aitken, *et al.*, 2009b). In such a scenario the evolution of the orogen was fundamentally controlled by the progressive modification of the thermal and rheological stratification of pre-Petermann lithosphere.

In this context, it is possible that as the orogen progresses to a colder state, that pseudotachylites and shear heating become an increasingly important way for the orogen to keep deforming (e.g. Camacho, *et al.*, 2001; Lin, *et al.*, 2005; Camacho, *et al.*, 2009). It is envisaged that as the system becomes colder, deformation will become increasingly localised, as the presence of

structurally-late pseudotachylites within the orogenic core demonstrate. The absolute ages of pseudotachylites are not known from the Musgrave Province; however, it is instructive to note that the pseudotachylites remain glassy (Lin, *et al.*, 2005). Tectonic (or volcanic) glass is extremely susceptible to recrystallisation, which may imply that for the glassy pseudotachylite to survive, the regional thermal structure of the Musgrave/Petermann crust was cold enough to prevent recrystallisation. A scenario whereby the rheology of the lithosphere progressively changes from weak and hot to strong and cold in response to progressive denudation/removal of high-heat-producing crust is able to resolve the apparently paradoxical record of warm, weak vs cold, strong lithosphere that occurs in the Petermann Orogen.

## CONCLUSIONS

Long-lived elevated temperatures in the axial core of the orogen were achieved independently of relative accumulation of strain, reinforcing the notion that the Petermann Orogen was associated with extended duration of conductively driven regional metamorphism rather than thermal events generated by shear heating. Removal of the crustal heat production during erosion shifted lithosphere towards a cold and strong state where deformation became brittle and metamorphic temperatures were low.

## ACKNOWLEDGEMENTS

Thanks must go to Alfredo Camacho for inspiring some very thought provoking discussions regarding the complex geological history of the Petermann Orogen!

## REFERENCES

- Aitken, A. R. A. & Betts, P. G., 2008. High-resolution aeromagnetic data over central Australia assist Grenville-era (1300;1100 Ma) Rodinia reconstructions. *Geophys. Res. Lett.*, 35(1), L01306.
- Aitken, A. R. A., Betts, P. G. & Ailleres, L., 2009a. The architecture, kinematics, and lithospheric processes of a compressional intraplate orogen occurring under Gondwana assembly: The Petermann

- orogeny, central Australia. *Lithosphere*, 1(6), 343-357.
- Aitken, A. R. A., Betts, P. G., Weinberg, R. F. & Gray, D., 2009b. Constrained potential field modeling of the crustal architecture of the Musgrave Province in central Australia: Evidence for lithospheric strengthening due to crust-mantle boundary uplift. *Journal of Geophysical Research B: Solid Earth*, 114(12).
- Arnaud, N. & Kelley, S. P., 1995. Evidence for excess argon during high pressure metamorphism in the Dora Maira Massif (western Alps, Italy), using an ultra-violet laser ablation microprobe  $^{40}\text{Ar}$ - $^{39}\text{Ar}$  technique. *Contributions to Mineralogy and Petrology*, 121(1), 1-11.
- Bea, F., 1996. Residence of REE, Y, Th and U in granites and crustal protoliths; Implications for the chemistry of crustal melts. *Journal of Petrology*, 37, 521-552.
- Bea, F. & Montero, P., 1999. Behavior of accessory phases and redistribution of Zr, REE, Y, Th, and U during metamorphism and partial melting of metapelites in the lower crust: An example from the Kinzigite Formation of Ivrea-Verbano, NW Italy. *Geochimica et Cosmochimica Acta*, 63, 1133-1153.
- Beauchamp, W., Allmendinger, R. W., Barazangi, M., Demnati, A., El Alji, M. & Dahmani, M., 1999. Inversion tectonics and the evolution of the High Atlas Mountains, Morocco, based on a geological-geophysical transect. *Tectonics*, 18(2), 163-184.
- Bird, P., 1998. Kinematic history of the Laramide orogeny in latitudes 35–49 N, western United States. *Tectonics*, 17(5), 780-801.
- Braun, J. & Shaw, R., 2001. A thin-plate model of Palaeozoic deformation of the Australian lithosphere; implications for understanding the dynamics of intracratonic deformation. In: *Continental reactivation and reworking*. (eds Miller, J. A., Holdsworth, R. E., Buick Ian, S. & Hand, M.) Special Publications, Geological Society, London.
- Buslov, M., De Grave, J., Bataleva, E. & Batalev, V. Y., 2007. Cenozoic tectonic and geodynamic evolution of the Kyrgyz Tien Shan Mountains: A review of geological, thermochronological and geophysical data. *Journal of Asian Earth Sciences*, 29(2), 205-214.
- Camacho, A., 1997. An isotopic study of deep-crustal orogenic processes, Musgrave Block, central Australia. Unpub. Ph.D. Thesis, Australian National University, Canberra.
- Camacho, A., Compston, W., McCulloch, M. & McDougall, I., 1997. Timing and exhumation of eclogite facies shear zones, Musgrave Block, central Australia. *Journal of Metamorphic Geology*, 15(6), 735-751.
- Camacho, A. & Fanning, C. M., 1995. Some isotopic constraints on the evolution of the granulite and upper amphibolite facies terranes in the eastern Musgrave Block, central Australia. *Precambrian Research*, 71(1-4), 155-181.
- Camacho, A., Hensen, B. J. & Armstrong, R., 2002. Isotopic test of a thermally driven intraplate orogenic model, Australia. *Geology*, 30(10), 887-890.
- Camacho, A. & McDougall, I., 2000. Intracratonic, strike-slip partitioned transpression and the formation and exhumation of eclogite facies rocks: An example from the Musgrave Block, central Australia. *Tectonics*, 19(5), 978-996.
- Camacho, A., McDougall, I., Armstrong, R. & Braun, J., 2001. Evidence for shear heating, Musgrave Block, central Australia. *Journal of Structural Geology*, 23(6-7), 1007-1013.
- Camacho, A., Vernon, R. H. & Fitz Gerald, J. D., 1995. Large volumes of anhydrous pseudotachylyte in the Woodroffe Thrust, eastern Musgrave Ranges, Australia. *Journal of Structural Geology*, 17(3), 371-383.
- Camacho, A., Yang, P. & Frederiksen, A., 2009. Constraints from diffusion profiles on the duration of high-strain deformation in thickened crust. *Geology*, 37(8), 755-758.
- Carlson, W. D., 2006. Rates of Fe, Mg, Mn, and Ca diffusion in garnet. *American*

- Mineralogist, 91(1), 1-11.
- Carson, C. J., Ague, J. J., Grove, M., Coath, C. D. & Harrison, T. M., 2002. U–Pb isotopic behaviour of zircon during upper-amphibolite facies fluid infiltration in the Napier Complex, east Antarctica. *Earth and Planetary Science Letters*, 199(3–4), 287-310.
- Cartwright, I. & Buick, I. S., 2000. Fluid generation, vein formation and the degree of fluid-rock interaction during decompression of high-pressure terranes: the Schistes Lustres, Alpine Corsica, France. *Journal of Metamorphic Geology*, 18, 607-624.
- Cherniak, D. J., Manchester, J. & Watson, E. B., 2007. Zr and Hf diffusion in rutile. *Earth and Planetary Science Letters*, 261(1-2), 267-279.
- Cherniak, D. J., Watson, E. B., Grove, M. & Harrison, T. M., 2004. Pb diffusion in monazite: a combined RBS/SIMS study. *Geochimica et Cosmochimica Acta*, 68(4), 829-840.
- Cloetingh, S. & Van Wees, J., 2005. Strength reversal in Europe's intraplate lithosphere: Transition from basin inversion to lithospheric folding. *Geology*, 33(4), 285-288.
- Collerson, K. D., 1972. High grade metamorphic and structural relationships near Amata, Musgrave Ranges, central Australia. Unpub. Ph.D. Thesis, University of Adelaide.
- Cunningham, D., 2005. Active intracontinental transpressional mountain building in the Mongolian Altai: defining a new class of orogen. *Earth and Planetary Science Letters*, 240(2), 436-444.
- Cutts, K. A., Hand, M., Kelsey, D. E. & Strachan, R. A., 2011. P–T constraints and timing of Barrovian metamorphism in the Shetland Islands, Scottish Caledonides: implications for the structural setting of the Unst ophiolite. *Journal of the Geological Society*, 168(6), 1265-1284.
- De Bruijne, C. & Andriessen, P., 2002. Far field effects of Alpine plate tectonism in the Iberian microplate recorded by fault-related denudation in the Spanish Central System. *Tectonophysics*, 349(1), 161-184.
- De Capitani, C. & Petrakakis, K., 2010. The computation of equilibrium assemblage diagrams with Theriak/Domino software. *American Mineralogist*, 95(7), 1006-1016.
- De Jong, K., Féraud, G., Ruffet, G., Amouric, M. & Wijbrans, J., 2001. Excess argon incorporation in phengite of the Mulhacén Complex: submicroscopic illitization and fluid ingress during late Miocene extension in the Betic Zone, south-eastern Spain. *Chemical Geology*, 178(1), 159-195.
- Diener, J. F. A., Powell, R., White, R. W. & Holland, T. J. B., 2007. A new thermodynamic model for clino- and orthoamphiboles in the system Na<sub>2</sub>O–CaO–FeO–MgO–Al<sub>2</sub>O<sub>3</sub>–SiO<sub>2</sub>–H<sub>2</sub>O–O. *Journal of Metamorphic Geology*, 25(6), 631-656.
- Edgoose, C. J., Scrimgeour, I. R. & Close, D. F., 2004. Geology of the Musgrave Block, Northern Territory. Northern Territory Geological Survey. Report 15.
- Ellis, D. J. & Maboko, M. A. H., 1992. Precambrian tectonics and the physiochemical evolution of the continental crust. Part I: The gabbro-eclogite transition. *Precambrian Research*, 55, 491-506.
- Esser, R., McIntosh, W., Heizler, M. & Kyle, P., 1997. Excess argon in melt inclusions in zero-age anorthoclase feldspar from Mt. Erebus, Antarctica, as revealed by the <sup>40</sup>Ar/<sup>39</sup>Ar method. *Geochimica et Cosmochimica Acta*, 61(18), 3789-3801.
- Evins, P. M., Smithies, R. H., Howard, H. M., Kirkland, C. L., Wingate, M. T. D. & Bodorkos, S., 2010. Devil in the detail; The 1150–1000 Ma magmatic and structural evolution of the Ngaanyatjarra Rift, west Musgrave Province, Central Australia. *Precambrian Research*, 183(3), 572-588.
- Fitzsimons, I. C. W. & Harley, S. L., 1994. The influence of retrograde cation-exchange on granulite P–T estimates and a convergence technique for the recovery of peak metamorphic conditions. *Journal of Petrology*, 35(2), 543-576.
- Flöttmann, T., Hand, M., Close, D., Edgoose,

- C. & Scrimgeour, I. R., 2004. Thrust tectonic styles of the intracratonic Alice Springs and Petermann Orogenies, central Australia. in *Thrust tectonics and hydrocarbon systems.*, edited by K. McClay, pp. 538-557, American Association of Petroleum Geologists Memoir.
- Forbes, C. J., Giles, D., Jourdan, F., Sato, K., Omori, S. & Bunch, M., 2012. Cooling and exhumation history of the northeastern Gawler Craton, South Australia. *Precambrian Research*, 200, 209-238.
- Ganguly, J., Cheng, W. J. & Chakraborty, S., 1998. Cation diffusion in aluminosilicate garnets: experimental determination in pyrope-almandine diffusion couples. *Contributions to Mineralogy and Petrology*, 131(2-3), 171-180.
- Glikson, A. Y., A. J. Stewart, C. G. Ballhaus, G. L. Clarke, E. H. J. Feeken, J. H. Leven, J. W. Sheraton, and S. S. Sun 1996. Geology of the western Musgrave Block, central Australia, with particular reference to the mafic-ultramafic Giles Complex. *GSO Bulletin* 239(206).
- Glikson, A. Y., Ballhaus, C. G., Clarke, G. L., Sheraton, J. W., Stewart, A. J. & Sun, S.-S., 1995. Geological framework and crustal evolution of the Giles mafic-ultramafic complex and environs, western Musgrave Block, central Australia. *AGSO Journal of Australian Geology & Geophysics*, 16, 41-67.
- Glikson, A. Y., Stewart, A. J., Ballhaus, C. G., Clarke, G. L., Feeken, E. H. J., Leven, J. H., Sheraton, J. W. & Sun, S.-S., 1996. Geology of the western Musgrave Block, central Australia, with particular reference to the mafic-ultramafic Giles complex. *AGSO Bulletin*, 239, 41-68.
- Glodny, J., Kühn, A. & Austrheim, H., 2002. Rb/Sr record of fluid-rock interaction in eclogites, Bergen Arcs, Norway. *Geochim Cosmochim Acta*, 66(S1), A280.
- Glodny, J., Kühn, A. & Austrheim, H., 2008. Diffusion versus recrystallization processes in Rb-Sr geochronology: Isotopic relics in eclogite facies rocks, Western Gneiss Region, Norway. *Geochimica et Cosmochimica Acta*, 72(2), 506-525.
- Grant, J. A. & Weiblen, P. W., 1971. Retrograde zoning in garnet near the second sillimanite isograd. *American Journal of Science*, 270(4), 281-296.
- Gregory, C. J., Buick, I. S., Hermann, J. & Rubatto, D., 2009. Mineral-scale trace element and U-Th-Pb age constraints on metamorphism and melting during the Petermann Orogeny (central Australia). *Journal of Petrology*, 50(2), 251-287.
- Griffin, W., Powell, W., Pearson, N. & O'Reilly, S., 2008. GLITTER: data reduction software for laser ablation ICP-MS. *Laser Ablation-ICP-MS in the Earth Sciences. Mineralogical Association of Canada Short Course Series*, 40, 204-207.
- Hand, M. & Sandiford, M., 1999. Intraplate deformation in central Australia, the link between subsidence and fault reactivation. *Tectonophysics*, 305(1-3), 121-140.
- Hauzenberger, C. A., Robl, J. & Stuwe, K., 2005. Garnet zoning in high pressure granulite-facies metapelites, Mozambique belt, SE-Kenya: constraints on the cooling history. *European Journal of Mineralogy*, 17(1), 43-55.
- Högdahl, K., Majka, J., Sjöström, H., Nilsson, K. P., Claesson, S. & Konečný, P., 2012. Reactive monazite and robust zircon growth in diatexites and leucogranites from a hot, slowly cooled orogen: implications for the Palaeoproterozoic tectonic evolution of the central Fennoscandian Shield, Sweden. *Contributions to Mineralogy and Petrology*, 163(1), 167-188.
- Holford, S. P., Hillis, R. R., Hand, M. & Sandiford, M., 2011. Thermal weakening localizes intraplate deformation along the southern Australian continental margin. *Earth and Planetary Science Letters*, 305(1), 207-214.
- Holland, T. & Powell, R., 2003. Activity-composition relations for phases in petrological calculations: an asymmetric multicomponent formulation. *Contributions to Mineralogy and Petrology*, 145(4), 492-501.
- Holland, T. J. B. & Powell, R., 1998. An



- internally consistent thermodynamic data set for phases of petrological interest. *Journal of Metamorphic Geology*, 16(3), 309-343.
- Howard, H., Smithies, R., Kirkland, C., Kelsey, D., Aitken, A., Wingate, M., de Gromard, R. Q., Spaggiari, C. & Maier, W., 2014. The burning heart-the Proterozoic geology and geological evolution of the west Musgrave Region, central Australia. *Gondwana Research*.
- Howard, H. M., Werner, M., Smithies, R. H., Kirkland, C. L., Kelsey, D. L., Hand, M., Collins, A., Pirajno, F., Wingate, M. T. D., Maier, W. D. & Raimondo, T., 2011. The geology of the west Musgrave Province and the Bentley Supergroup. — a field guide. *Geological Survey of Western Australia Record 2011/4*, p. 119. (ISBN 978-1-74168-379-0).
- Janots, E., Engi, M., Rubatto, D., Berger, A., Gregory, C. & Rahn, M., 2009. Metamorphic rates in collisional orogeny from in situ allanite and monazite dating. *Geology*, 37(1), 11-14.
- Kelley, S., 2002. Excess argon in K-Ar and Ar-Ar geochronology. *Chemical Geology*, 188(1-2), 1-22.
- Kelsey, D. E., Clark, C. & Hand, M., 2008. Thermobarometric modeling of zircon and monazite growth in melt-bearing systems: examples using model metapelitic and metapsammitic granulites. *Journal of Metamorphic Geology*, 26, 199-212.
- Kelsey, D. E., Powell, R., Wilson, C. J. L. & Steele, D. A., 2003. (Th+U)-Pb monazite ages from Al-Mg-rich metapelites, Rauer Group, East Antarctica. *Contributions to Mineralogy and Petrology*, 146, 326-340.
- Kirkland, C. L., Jourdan, F., Wingate, M. T. D., Quentin de Gromard, R., Howard, H. M. & Smithies, R. H., 2013. 185414: quartzite, Great Central Road; *Geochronology Record 1139*. Geological Survey of Western Australia, 4p.
- Kirkland, C. L., Wingate, M. T. D., Quentin de Gromard, R., Howard, H. M. & Smithies, R. H., 2014. 208414: quartzite, Mitika Homestead; *Geochronology Record 1205*. Geological Survey of Western Australia, 6p.
- Kirkland, C. L., Wingate, M. T. D. & Smithies, R. H., 2011. 187175: muscovite-tourmaline pegmatite, Morgan Range; *Geochronology Record 936*. Geological Survey of Western Australia, 4p.
- Korhonen, F., Clark, C., Brown, M., Bhattacharya, S. & Taylor, R., 2013. How long-lived is ultrahigh temperature (UHT) metamorphism? Constraints from zircon and monazite geochronology in the Eastern Ghats orogenic belt, India. *Precambrian Research*, 234, 322-350.
- Korsch, R. J., Goleby, B. R., Leven, J. H. & Drummond, B. J., 1998. Crustal architecture of central Australia based on deep seismic reflection profiling. *Tectonophysics*, 288(1-4), 57-69.
- Korsch, R. J. & Kositsin, N., 2010. GOMA (Gawler Craton-Officer Basin-Musgrave Province-Amadeus Basin) Seismic and MT Workshop 2010. *Geoscience Australia record 2010/39*.
- Kühn, A., Glodny, J., Iden, K. & Austrheim, H., 2000. Retention of Precambrian Rb/Sr phlogopite ages through Caledonian eclogite facies metamorphism, Bergen Arc Complex, W-Norway. *Lithos*, 51(4), 305-330.
- Kylander-Clark, A. R. C., Hacker, B. R. & Mattinson, J. M., 2008. Slow exhumation of UHP terranes: Titanite and rutile ages of the Western Gneiss Region, Norway. *Earth and Planetary Science Letters*, 272(3-4), 531-540.
- Lambeck, K. & Burgess, G., 1992. Deep crustal structure of the Musgrave Block, central Australia: Results from teleseismic travel-time anomalies. *Australian Journal of Earth Sciences: An International Geoscience Journal of the Geological Society of Australia*, 39(1), 1 - 19.
- Lin, A., Maruyama, T., Aaron, S., Michibayashi, K., Camacho, A. & Kano, K.-i., 2005. Propagation of seismic slip from brittle to ductile crust: Evidence from pseudotachylyte of the Woodroffe thrust, central Australia. *Tectonophysics*, 402(1),

- 21-35.
- Livaccari, R. F., 1991. Role of crustal thickening and extensional collapse in the tectonic evolution of the Sevier-Laramide orogeny, western United States. *Geology*, 19(11), 1104-1107.
- Luvizotto, G., Zack, T., Meyer, H., Ludwig, T., Triebold, S., Kronz, A., Münker, C., Stockli, D., Prowatke, S. & Klemme, S., 2009. Rutile crystals as potential trace element and isotope mineral standards for microanalysis. *Chemical Geology*, 261(3), 346-369.
- Maboko, M. A. H., McDougall, I., Zeitler, P. K. & Williams, I. S., 1992. Geochronological evidence for ~530-550 Ma juxtaposition of two Proterozoic metamorphic terranes in the Musgrave Ranges, central Australia. *Australian Journal of Earth Sciences*, 39(4), 457-471.
- Marshak, S., Karlstrom, K. & Timmons, J. M., 2000. Inversion of Proterozoic extensional faults: An explanation for the pattern of Laramide and Ancestral Rockies intracratonic deformation, United States. *Geology*, 28(8), 735-738.
- McFarlane, C. R. M., Connelly, J. N. & Carlson, W. D., 2006. Contrasting response of monazite and zircon to a high-T thermal overprint. *Lithos*, 88, 135-149.
- McLaren, S., Sandiford, M., Hand, M., Neumann, N., Wyborn, L. & Bastrakova, I., 2003. The hot southern continent: heat flow and heat production in Australian Proterozoic terranes. *Geological Society of America Special Papers*, 372, 157-167.
- Mezger, K., Hanson, G. N. & Bohlen, S. R., 1989. High-precision UPb ages of metamorphic rutile: application to the cooling history of high-grade terranes. *Earth and Planetary Science Letters*, 96(1-2), 106-118.
- Neil, E. A. & Houseman, G. A., 1999. Rayleigh-Taylor instability of the upper mantle and its role in intraplate orogeny. *Geophysical Journal International*, 138(1), 89-107.
- Pattison, D. R. M. & Bégin, N. J., 1994. Zoning patterns in orthopyroxene and garnet in granulites: implications for geothermometry. *Journal of Metamorphic Geology*, 12, 387-410.
- Pattison, D. R. M., Chacko, T., Farquhar, J. & McFarlane, C. R. M., 2003. Temperatures of granulite-facies metamorphism: constraints from experimental phase equilibria and thermobarometry corrected for retrograde exchange. *Journal of Petrology*, 44, 867-900.
- Payne, J. L., Hand, M., Barovich, K. M. & Wade, B. P., 2008. Temporal constraints on the timing of high-grade metamorphism in the northern Gawler Craton: implications for assembly of the Australian Proterozoic. *Australian Journal of Earth Sciences*, 55(5), 623-640.
- Pysklywec, R. N. & Beaumont, C., 2004. Intraplate tectonics: feedback between radioactive thermal weakening and crustal deformation driven by mantle lithosphere instabilities. *Earth and Planetary Science Letters*, 221(1-4), 275-292.
- Raimondo, T., Collins, A. S., Hand, M., Walker-Hallam, A., Smithies, R. H., Evins, P. M. & Howard, H. M., 2009. Ediacaran intracontinental channel flow. *Geology*, 37(4), 291-294.
- Raimondo, T., Collins, A. S., Hand, M., Walker-Hallam, A., Smithies, R. H., Evins, P. M. & Howard, H. M., 2010. The anatomy of a deep intracontinental orogen. *Tectonics*, 29(4), TC4024.
- Raimondo, T., Hand, M. & Collins, W. J., 2014. Compressional intracontinental orogens: Ancient and modern perspectives. *Earth-Science Reviews*, 130(0), 128-153.
- Robl, J., Hergarten, S., Stüwe, K. & Hauzenberger, C., 2007. THERMAL HISTORY: A new software to interpret diffusive zoning profiles in garnet. *Computers & Geosciences*, 33(6), 760-772.
- Rubatto, D., Chakraborty, S. & Dasgupta, S., 2013. Timescales of crustal melting in the Higher Himalayan Crystallines (Sikkim, Eastern Himalaya) inferred from trace element-constrained monazite and zircon chronology. *Contributions to Mineralogy and Petrology*, 165(2), 349-372.

- Sandiford, M. & Hand, M., 1998. Controls on the locus of intraplate deformation in central Australia. *Earth and Planetary Science Letters*, 162(1-4), 97-110.
- Sandiford, M., Hand, M. & McLaren, S., 2001. Tectonic feedback, intraplate orogeny and the geochemical structure of the crust; a central Australian perspective. In: *Continental reactivation and reworking*. (eds Miller, J. A., Holdsworth, R. E., Buick Ian, S. & Hand, M.) Special Publications, Geological Society, London.
- Sandiford, M. & McLaren, S., 2002. Tectonic feedback and the ordering of heat producing elements within the continental lithosphere. *Earth and Planetary Science Letters*, 204(1-2), 133-150.
- Sandiford, M., Wallace, M. & Coblenz, D., 2004. Origin of the in situ stress field in south-eastern Australia. *Basin Research*, 16(3), 325-338.
- Scaillet, B., Pichavant, M. & Roux, J., 1995. Experimental crystallization of leucogranite magmas. *Journal of Petrology*, 36(3), 663-705.
- Scaillet, S., 1996. Excess<sup>40</sup>Ar transport scale and mechanism in high-pressure phengites: A case study from an eclogitized metabasite of the Dora-Maira nappe, western Alps. *Geochimica et Cosmochimica Acta*, 60(6), 1075-1090.
- Schaltegger, U., Fanning, C. M., Gunther, D., Maurin, J. C., Schulmann, K. & Gebauer, D., 1999. Growth, annealing and recrystallization of zircon and preservation of monazite in high-grade metamorphism: conventional and in-situ U-Pb isotope, cathodoluminescence and microchemical evidence. *Contributions to Mineralogy and Petrology*, 134(2-3), 186-201.
- Scrimgeour, I. R. & Close, D. F., 1999. Regional high-pressure metamorphism during intracratonic deformation: the Petermann Orogeny, central Australia. *Journal of Metamorphic Geology*, 17(5), 557-572.
- Scrimgeour, I. R., Close, D. F. & Edgoose, C. J., 1999. Petermann Ranges, N.T. 1:250000 Geological Series. Department of Mines and Energy, Northern Territory Geological Survey. Explanatory Notes SG52-7.
- Seydoux, G. A. M., Paquette, J. L., Wiedenbeck, M., Montel, J. M. & Heinrich, W., 2002. Experimental resetting of the U-Th-Pb systems in monazite. In: *Chemistry and physics of accessory minerals; crystallisation, transformation and geochronological applications*. (eds Poitrasson, F., Schaltegger, U. & Hancher John, M.).
- Smithies, R., Kirkland, C., Korhonen, F., Aitken, A., Howard, H., Maier, W., Wingate, M., Quentin de Gromard, R. & Gessner, K., 2014. The Mesoproterozoic thermal evolution of the Musgrave Province in central Australia—Plume vs. the geological record. *Gondwana Research*.
- Smithies, R. H., Howard, H. M., Evins, P. M., Kirkland, C. L., Kelsey, D. E., Hand, M., Wingate, M. T. D., Collins, A. S. & Belousova, E., 2011. High-Temperature Granite Magmatism, Crust–Mantle Interaction and the Mesoproterozoic Intracontinental Evolution of the Musgrave Province, Central Australia. *Journal of Petrology*, 52(5), 931-958.
- Smithies, R. H., Howard, H. M., Evins, P. M., Kirkland, C. L., Kelsey, D. E., Hand, M., Wingate, M. T. D., Collins, A. S., Belousova, E. & Allchurch, S., 2010. Geochemistry, geochronology and petrogenesis of Mesoproterozoic felsic rocks in the western Musgrave Province of central Australia and implication for the Mesoproterozoic tectonic evolution of the region. *Geological Survey of Western Australia Record 2011/4*, Report 106 73.
- Stacey, J. S. & Kramers, J. D., 1975. Approximation of terrestrial lead isotope evolution by a two-stage model. *Earth and Planetary Science Letters*, 26(2), 207-221.
- Stephenson, R., Egholm, D. L., Nielsen, S. B. & Stovba, S. M., 2009. Role of thermal refraction in localizing intraplate deformation in southeastern Ukraine. *Nature Geoscience*, 2(4), 290-293.
- Sun, S.-S., Sheraton, J. W., Glikson, A. Y. & Stewart, A. J., 1996. A major magmatic

- event during 1050-1080 in central Australia and an emplacement age for the Giles Complex. AGSO Research Newsletter, 17, 9-10.
- Taylor, R., Clark, C. & Reddy, S. M., 2011. The effect of grain orientation on secondary ion mass spectrometry (SIMS) analysis of rutile. *Chemical Geology* (in review).
- Terry, M. P., Robinson, P., Hamilton, M. A. & Jercinovic, M. J., 2000. Monazite geochronology of UHP and HP metamorphism, deformation, and exhumation Nordøyane, Western Gneiss Region, Norway. *American Mineralogist*, 85(11-12), 1651-1664.
- Townsend, K. J., Miller, C. F., D'Andrea, J. L., Ayers, J. C., Harrison, T. M. & Coath, C. D., 2001. Low temperature replacement of monazite in the Ireteba granite, Southern Nevada: geochronological implications. *Chemical Geology*, 172(1-2), 95-112.
- Turner, G. & Songshan, W., 1992. Excess argon, crustal fluids and apparent isochrons from crushing K-feldspar. *Earth and planetary science letters*, 110(1), 193-211.
- Van Achterbergh, E., Ryan, C. G., Jackson, S. E. & Griffin, W. L., 2001. Data reduction software for LA-ICP-MS. In: *Laser-ablation-ICPMS in the earth sciences; principles and applications*. (ed Sylvester Paul, J.), Mineralogical Association of Canada. Ottawa, ON, Canada. 2001.
- Van Hinsbergen, D. J., Straathof, G. B., Kuiper, K. F., Cunningham, W. D. & Wijbrans, J., 2008. No vertical axis rotations during Neogene transpressional orogeny in the NE Gobi Altai: coinciding Mongolian and Eurasian early Cretaceous apparent polar wander paths. *Geophysical Journal International*, 173(1), 105-126.
- Villaseca, C., Martín Romera, C., De la Rosa, J. & Barbero, L., 2003. Residence and redistribution of REE, Y, Zr, Th and U during granulite-facies metamorphism: behaviour of accessory and major phases in peraluminous granulites of central Spain. *Chemical geology*, 200(3), 293-323.
- Villaseca, C., Orejana, D. & Paterson, B. A., 2007. Zr-LREE rich minerals in residual peraluminous granulites, another factor in the origin of low Zr-LREE granitic melts? *Lithos*, 96(3), 375-386.
- Vry, J. K. & Baker, J. A., 2006. LA-MC-ICPMS Pb-Pb dating of rutile from slowly cooled granulites: Confirmation of the high closure temperature for Pb diffusion in rutile. *Geochimica et Cosmochimica Acta*, 70(7), 1807-1820.
- Wade, B. P., Kelsey, D. E., Hand, M. & Barovich, K. M., 2008. The Musgrave Province; Stitching North, West and South Australia. *Precambrian Research*, 166, 370-386.
- Walsh, A. K., Hand, M. & Kelsey, D. E., in review. A metamorphic perspective on foreland flexure during intraplate orogeny: evidence for the involvement of weak lithosphere. *Terra Nova*.
- Walsh, A. K., Hand, M., Kelsey, D. E., Jourdan, F. & Smithies, R. H., submitted. Crustal thickening in the Petermann Orogeny prior to 600 Ma; evidence from  $^{40}\text{Ar}/^{39}\text{Ar}$  geochronology and implications for spatial patterns of reworking in intraplate orogens. *Journal of the Geological Society*.
- Walsh, A. K., Kelsey, D. E., Kirkland, C. L., Hand, M., Smithies, R. H., Clark, C. & Howard, H. M., in press. P-T-t evolution of a large, long-lived, ultrahigh-temperature Grenvillian belt in central Australia. *Gondwana Research*.
- Walsh, A. K., Raimondo, T., Kelsey, D. E., Hand, M., Pfitzner, H. L. & Clark, C., 2013. Duration of high-pressure metamorphism and cooling during the intraplate Petermann Orogeny. *Gondwana Research*, 24(3-4), 969-983.
- Walter, M. R., Veevers, J. J., Calver, C. R. & Grey, K., 1995. Neoproterozoic stratigraphy of the Centralian Superbasin, Australia. *Precambrian Research*, 73(1-4), 173-195.
- Warren, C. J., Grujic, D., Cottle, J. M. & Rogers, N. W., 2012. Constraining cooling histories: rutile and titanite chronology and diffusion modelling in NW Bhutan. *Journal of Metamorphic Geology*, 30(2), 113-130.
- Warren, C. J., Grujic, D., Kellett, D. A., Cottle, J., Jamieson, R. A. & Ghalley, K. S.,



2011. Probing the depths of the India-Asia collision: U-Th-Pb monazite chronology of granulites from NW Bhutan. *Tectonics*, 30(2), TC2004.
- Wawrzenitz, N., Krohe, A., Rhede, D. & Romer, R. L., 2012. Dating rock deformation with monazite: The impact of dissolution precipitation creep. *Lithos*, 134–135(0), 52–74.
- White, R. W. & Clarke, G. L., 1997. The Role of Deformation in Aiding Recrystallization: an Example from a High-pressure Shear Zone, Central Australia. *J. Petrology*, 38(10), 1307–1329.
- White, R. W., Powell, R. & Clarke, G. L., 2002. The interpretation of reaction textures in Fe-rich metapelitic granulites of the Musgrave Block, central Australia: constraints from mineral equilibria calculations in the system  $K_2O$ -FeO-MgO- $Al_2O_3$ - $SiO_2$ - $H_2O$ - $TiO_2$ - $Fe_2O_3$ . *Journal of Metamorphic Geology*, 20, 41–55.
- White, R. W., Powell, R. & Holland, T. J. B., 2007. Progress relating to calculation of partial melting equilibria for metapelites. *Journal of Metamorphic Geology*, 25(5), 511–527.
- White, R. W., Powell, R., Holland, T. J. B. & Worley, B. A., 2000. The effect of  $TiO_2$  and  $Fe_2O_3$  on metapelitic assemblages at greenschist and amphibolite facies conditions: mineral equilibria calculations in the system  $K_2O$ -FeO-MgO- $Al_2O_3$ - $SiO_2$ - $H_2O$ - $TiO_2$ - $Fe_2O_3$ . *Journal of Metamorphic Geology*, 18, 497–511.
- Windley, B. F., Alexeiev, D., Xiao, W., Kröner, A. & Badarch, G., 2007. Tectonic models for accretion of the Central Asian Orogenic Belt. *Journal of the Geological Society*, 164(1), 31–47.
- Zeh, A., Williams, I. S., Bratz, H. & Millar, I. L., 2003. Different age response of zircon and monazite during the tectono-metamorphic evolution of a high grade paragneiss from the Ruhla Crystalline Complex, central Germany. *Contributions to Mineralogy and Petrology*, 145(6), 691–706.
- Zhao, J.-X. & McCulloch, M. T., 1993. Sm-Nd mineral isochron ages of Late Proterozoic dyke swarms in Australia: evidence for two distinctive events of mafic magmatism and crustal extension. *Chemical Geology*, 109, 341–354.
- Zhao, J., McCulloch, M. T. & Korsch, R. J., 1994. Characterisation of a plume-related approximately 800 Ma magmatic event and its implications for basin formation in central-southern Australia. *Earth and Planetary Science Letters*, 121(3–4), 349–367.

## Supporting information

Analysis_#	$^{207}\text{Pb}/^{235}\text{U}$	$\pm 1\sigma$	$^{206}\text{Pb}/^{238}\text{U}$	$\pm 1\sigma$	rho	$^{206}\text{Pb}/^{238}\text{U}$ age (Ma)	$\pm 1\sigma$ (Ma)
875a	0.8846	0.01631	0.09666	0.0014	0.785551	595	8
875b	0.83868	0.01629	0.0937	0.00138	0.758254	577	8
875c	0.84589	0.01823	0.09403	0.00142	0.700727	579	8
875d	0.89727	0.0252	0.09566	0.00157	0.584375	589	9
875e	0.88859	0.01764	0.09532	0.00142	0.750425	587	8
875f	0.88297	0.0233	0.09613	0.00155	0.61103	592	9
875g	0.90478	0.01851	0.09437	0.00143	0.740694	581	8
875h	0.94228	0.02121	0.09633	0.00148	0.682558	593	9
875i	0.92032	0.02654	0.09342	0.00158	0.586483	576	9
875j	0.89409	0.02257	0.09316	0.00148	0.629335	574	9
875k	0.9521	0.02514	0.09169	0.0015	0.619565	566	9
875l	0.98803	0.02857	0.09716	0.00165	0.587295	598	10
875m	2.71433	0.04816	0.11825	0.00184	0.876986	721	11
875n	1.00211	0.02007	0.09763	0.00149	0.762028	601	9
875o	1.10982	0.02521	0.09629	0.0015	0.685788	593	9
875p	0.98131	0.0197	0.09732	0.00147	0.752411	599	9
875q	1.56704	0.03014	0.09962	0.00153	0.798513	612	9
875r	1.09524	0.02362	0.09935	0.00155	0.723425	611	9
875s	0.97697	0.02009	0.09851	0.0015	0.740478	606	9
875t	0.96595	0.02244	0.09644	0.00156	0.696304	594	9
875u	0.93398	0.0212	0.09753	0.00155	0.700157	600	9
875v	1.04387	0.02545	0.10308	0.00161	0.640634	632	9
875w	0.94661	0.02083	0.09646	0.00154	0.72553	594	9
875x	0.98851	0.02433	0.09873	0.00159	0.654315	607	9
875y	0.94499	0.02002	0.0971	0.00152	0.738903	597	9
875z	1.02658	0.02291	0.09607	0.00151	0.704299	591	9
875aa	0.91781	0.02199	0.09507	0.00151	0.66292	585	9
875bb	0.91141	0.01971	0.0954	0.0015	0.72706	587	9
875cc	0.94525	0.02099	0.0949	0.00148	0.702311	584	9
875dd	0.8869	0.01879	0.09736	0.00152	0.736904	599	9
875ee	0.98076	0.02187	0.09617	0.00153	0.713454	592	9
875ff	0.83758	0.01783	0.09286	0.00145	0.733524	572	9
875gg	0.82837	0.01708	0.09431	0.00146	0.750813	581	9
875hh	0.86539	0.0176	0.09645	0.00149	0.759597	594	9
875ii	0.86061	0.01802	0.09644	0.00151	0.747776	594	9
875jj	0.93028	0.02055	0.09808	0.00153	0.706176	603	9
875kk	0.89509	0.02014	0.09585	0.0015	0.695515	590	9
875ll	1.05492	0.02063	0.09769	0.00152	0.795635	601	9
875mm	0.8249	0.01698	0.09346	0.00145	0.753713	576	9
11i	0.86334	0.03414	0.09876	0.00183	0.468585	607	11
11j	0.86397	0.03306	0.09776	0.0018	0.48118	601	11
11k	0.88798	0.03398	0.0959	0.00177	0.482319	590	10
11l	0.92328	0.0342	0.09816	0.0018	0.495046	604	11
11m	1.1741	0.04672	0.11404	0.00218	0.480398	696	13
11n	1.04295	0.04291	0.10597	0.00203	0.465605	649	12
11o	0.92113	0.0344	0.0972	0.0018	0.495871	598	11
11p	1.05464	0.03707	0.11344	0.00206	0.516634	693	12
20h	0.81391	0.03048	0.09629	0.00176	0.488082	593	10

20i	0.86638	0.02915	0.0965	0.00173	0.53283	594	10
20j	0.98882	0.02539	0.10206	0.00185	0.705945	627	11
27aa	0.85597	0.01884	0.09762	0.00168	0.781894	601	10
27bb	0.87548	0.02245	0.10012	0.00179	0.697208	615	11
34a	0.85483	0.02096	0.09809	0.00174	0.723457	603	10
34b	0.87655	0.01979	0.09545	0.00166	0.770306	588	10
34c	0.8668	0.01966	0.09784	0.0017	0.766069	602	10
34d	0.84896	0.01824	0.09739	0.00167	0.798113	599	10
4b	0.90812	0.0242	0.09821	0.00179	0.683951	604	11
4c	1.03091	0.02643	0.10176	0.00185	0.709118	625	11
27a	1.32422	0.03902	0.13122	0.00268	0.693119	795	15
27b	1.24438	0.03079	0.10736	0.00209	0.786769	657	12
27c	0.85424	0.02354	0.09615	0.00189	0.713323	592	11
4a	1.03778	0.03271	0.10116	0.00209	0.655484	621	12
11a	1.01698	0.02484	0.09955	0.00192	0.789625	612	11
11b	0.92294	0.02649	0.09879	0.00196	0.691249	607	12
11c	0.89152	0.02581	0.09768	0.00195	0.68956	601	11
20c	0.90335	0.01907	0.10112	0.00189	0.885381	621	11
27d	1.21393	0.03521	0.12544	0.00254	0.698112	762	15
11d	0.8284	0.0255	0.09397	0.00192	0.663761	579	11
11e	0.84016	0.024	0.09697	0.00193	0.69674	597	11
20e	0.97146	0.0224	0.11078	0.0021	0.822119	677	12
11f	0.89829	0.02609	0.09672	0.00195	0.694162	595	11
11g	0.86019	0.02467	0.09438	0.00189	0.698244	581	11
20f	0.87377	0.01887	0.10025	0.00188	0.868358	616	11
11h	0.92265	0.02566	0.09848	0.00196	0.71563	606	12
27e	0.9639	0.021	0.10819	0.00204	0.865477	662	12
20g	1.00169	0.02299	0.11204	0.00213	0.828325	685	12

Supplementary Table 1. LA-ICPMS U-Pb monazite geochronological data collected for sample a325-875a

total 206Pb cts /sec	total 207Pb cts /sec	total 208Pb cts /sec	207Pb /206Pb	208Pb /206Pb	206Pb /254	206Pb /270	8-corr 204Pb /206Pb	% 206Pb	ppm U	ppm Th	8-corr ppm 206Pb	232Th /238U	(3) 206Pb /238U Age	(3) 238U /206Pb b	(3) 207Pb /206Pb	(3) 235U /238U	(3) 206Pb /238U	err. corr.	
Spot			±%	±%	±%	±%	±%					±%	±%	±%	±%	±%	±%	±%	
1593-1.1	41	11.4	21.3	16	8.1	0.28	0.53	8.5	0.307	6.4	0.210	5.1	0.041	11.75	0.077	0.90	0.0851	13	0.40
1593-2.1	47	9.1	15.0	20	0.19	0.81	0.307	2.2	0.373	3.6	0.194	4.4	0.007	11.44	0.077	0.93	0.0874	9	0.44
1593-3.1	47	7.5	11.8	22	0.15	0.37	0.25	8.4	0.373	2.2	0.200	1.9	0.006	11.44	0.048	0.63	0.0954	56	0.43
1593-4.1	24	4.5	7.6	26	0.18	0.86	0.30	9.2	0.281	2.9	0.182	4.5	0.008	11.88	0.061	0.71	0.0842	7	0.33
1593-5.1	40	5.7	9.7	41	0.14	0.70	0.25	7.4	0.130	7.9	0.160	3.7	0.006	12.13	0.039	0.45	0.0825	5	0.30
1593-6.1	32	5.6	9.2	25	0.17	7.2	0.29	9.6	0.131	4.5	0.170	2.3	0.004	11.60	0.061	0.76	0.0862	6	0.41
1593-7.1	23	6.2	12.6	23	0.27	6.2	0.56	7.2	0.164	8.4	0.207	2.9	0.007	11.18	0.053	0.66	0.0895	15	0.48
1593-8.1	25	7.5	14.1	21	0.27	4.0	0.56	11.7	0.139	5.6	0.205	4.5	0.019	11.18	0.053	0.66	0.0895	15	0.48
1593-9.1	82	12.6	19.7	19	0.15	7.4	0.23	11.3	0.192	1.4	0.171	2.2	0.006	11.68	0.062	0.69	0.0894	639	0.64
1593-10.1	25	5.4	8.8	27	0.21	6.2	0.35	3.9	0.114	2.4	0.151	2.5	0.009	11.45	0.062	0.73	0.0856	6	0.40
318C-1.1	9	3.9	8.8	28	0.40	8.2	0.95	4.6	0.179	10.6	0.283	8.6	0.023	10.11	0.049	0.84	0.0743	10	0.23
318C-2.1	23	16.5	44.4	16	0.70	4.6	1.90	2.5	0.537	3.6	0.709	8.1	0.054	10.11	0.049	0.84	0.0743	10	0.23
318C-3.1	13	5.1	10.2	20	0.41	4.4	0.84	7.5	0.210	10.9	0.239	10.0	0.023	12.17	0.134	0.22	0.0989	34	0.28
318C-4.1	10	6.1	14.0	27	0.63	4.5	1.50	4.2	0.287	4.9	0.446	9.7	0.040	12.17	0.134	0.22	0.0989	34	0.28
318C-5.1	117	13.4	18.3	19	0.11	4.6	0.15	6.7	0.274	1.3	0.166	2.7	0.003	12.10	0.057	0.65	0.0827	118	0.56
318C-6.1	7	4.5	11.2	23	0.68	6.0	1.74	5.1	0.194	9.0	0.495	7.5	0.046	12.10	0.057	0.65	0.0827	118	0.56
318C-7.1	244	17.1	18.3	35	0.07	4.8	0.07	7.1	0.152	3.7	0.155	2.0	0.001	11.65	0.041	0.48	0.0859	180	0.61
318C-8.1	13	5.2	11.0	24	0.41	8.9	0.81	4.8	0.175	9.3	0.232	10.6	0.021	12.04	0.117	1.34	0.0831	26	0.30
318C-9.1	18	4.7	7.8	38	0.24	11.3	0.44	4.2	0.243	3.3	0.215	3.2	0.017	12.04	0.076	1.00	0.0956	13	0.15
318C-10.1	9	6.2	15.4	21	0.72	4.6	1.82	4.2	0.299	5.1	0.605	6.5	0.048	11.32	0.061	0.75	0.0883	5	0.35
1175-1.1	90	9.7	10.6	28	0.11	5.2	0.12	8.2	0.282	1.5	0.174	2.9	0.003	11.98	0.076	0.88	0.0835	8	0.47
1175-2.1	22	4.9	8.3	30	0.22	6.7	0.38	7.0	0.139	2.9	0.173	3.1	0.009	11.91	0.072	0.84	0.0840	8	0.47
1175-3.1	62	12.5	20.8	22	0.20	4.6	0.34	6.8	0.126	7.2	0.169	2.6	0.004	12.62	0.081	0.89	0.0792	6	0.60
1175-4.1	42	8.7	14.5	22	0.21	6.7	0.34	12.0	0.105	4.1	0.158	1.9	0.008	12.62	0.081	0.89	0.0792	6	0.60
1175-5.1	19	5.6	11.1	27	0.28	7.9	0.58	9.6	0.159	8.3	0.186	3.5	0.014	12.73	0.055	0.75	0.0829	26	0.53
1175-6.1	32	4.3	5.6	58	0.13	9.4	0.16	15.1	0.302	2.6	0.169	2.3	0.004	12.06	0.066	0.75	0.0829	6	0.36
1175-7.1	121	12.5	12.8	20	0.10	5.5	0.10	12.0	0.154	1.1	0.160	1.1	0.002	11.57	0.064	0.76	0.0864	4	0.35
1175-7.2	74	9.1	11.5	58	0.12	2.9	0.15	15.1	0.133	4.1	0.163	1.5	0.004	11.25	0.062	0.76	0.0889	4	0.58
1175-8.1	10	2.9	5.2	33	0.28	5.6	0.51	12.4	0.157	8.9	0.205	4.5	0.015	10.91	0.097	1.23	0.0916	20	0.63
1175-9.1	42	5.5	8.8	33	0.13	6.5	0.21	6.9	0.235	4.7	0.183	3.7	0.005	10.98	0.050	0.62	0.0911	6	0.27
825A-1.1	14	2.4	4.1	50	0.16	12.6	0.27	14.3	0.126	5.8	0.167	3.4	0.007	11.71	0.050	0.45	0.0854	20	0.37
825A-2.1	3	1.8	3.8	41	0.52	14.5	1.13	19.1	0.199	7.9	0.305	8.8	0.029	11.54	0.142	1.69	0.0866	43	0.72
825A-3.1	18	5.4	11.1	41	0.29	6.6	0.61	6.1	0.150	2.9	0.288	10.3	0.016	11.15	0.125	0.71	0.0897	12	0.41
825A-4.1	3	1.8	3.6	38	0.62	9.1	1.28	8.2	0.338	17.8	0.362	17.3	0.033	13.69	0.280	2.28	0.1150	35	0.49
825A-5.1	3	1.4	2.8	100	0.44	9.4	0.96	9.3	0.414	24.9	0.246	10.2	0.030	8.70	0.135	2.19	0.0637	60	0.56
825A-6.1	3	1.7	3.2	29	0.58	9.9	1.18	9.2	0.148	8.8	0.560	13.4	0.047	13.34	0.225	2.02	0.0652	78	0.55
825A-7.1	3	1.9	4.8	71	0.70	9.8	2.03	9.0	0.187	22.0	0.218	7.7	0.053	96.28	4.719	-6.76	0.0104	1741	0.73
825A-8.1	5	2.3	5.2	50	0.47	7.6	1.08	10.7	0.208	12.0	0.555	10.8	0.061	16.29	0.055	1.07	0.0614	48	0.66
825A-9.1	4	2.6	5.8	50	0.65	7.3	1.50	11.0	0.164	6.9	0.555	10.8	0.061	9.32	0.079	1.17	0.1073	181	0.75
825A-10.1	215	120.9	285.7	5	0.57	2.6	1.35	3.9	0.474	4.7	0.262	5.0	0.036	20.33	0.033	0.22	0.0492	138	0.68

Errors are 1-sigma; Pb and Pb<sup>210</sup> indicate the common and radiogenic portions, respectively.

Error in standard calibration was 0.39% (not included in above errors but required when comparing data from different mounts).

(1) Common Pb corrected using measured 204Pb.

(2) Common Pb corrected by assuming 206Pb/238U/235U age-concordance

(3) Common Pb corrected by assuming 206Pb/238U/235U age-concordance

Errors are 1-sigma; Pb and Pb' indicate the common and radiogenic portions, respectively.

Error in standard calibration was 0.39% (not included in above errors but required when comparing data from different mounts).

(1) Common Pb corrected using measured 204Pb.

(2) Common Pb corrected by assuming 206Pb/238U-207Pb/235U age-concordance

(3) Common Pb corrected by assuming 206Pb/238U-208Pb/232Th age-concordance

Supplementary Table 2. SHRIMP U-Pb rutile geochronological data collected for mylonite samples 325-1593, 325-318, 325-1175, 325-875a



Supplementary Table 3. SHRIMP U-Pb rutile geochronological data collected for sample 325-900b

Spot	total 206Pb cts /sec	total 207Pb cts /sec	total 208Pb cts /sec	207Pb /206Pb ±%	208Pb /206Pb ±%	206Pb /254 ±%	206Pb /270 ±%	8-corr 204Pb /206Pb ±%	% 206Pb <sub>c</sub>	ppm U	ppm Th	8-corr 206Pb <sup>*</sup>	232Th /238U ±%	(1) 206Pb /238U Age
900B-1.1	20	3.3	5.1	0.160	11.4	0.122	6.5	0.00635	11.34	5.0	-0.00266	0.36	-5.5E-4	491 ±41
900B-2.1	88	17.8	35.2	0.201	6.8	0.260	4.8	0.01032	18.58	19.4	0.31294	1.17	-1.7E-2	15
900B-3.1	68	5.2	2.8	0.076	3.8	0.242	5.0	0.00095	1.70	13.8	-0.00161	1.00	-1.2E-4	25
900B-4.1	50	3.7	2.5	0.074	7.1	0.113	6.2	0.00117	2.09	14.1	-0.00134	1.02	-9.8E-5	25
900B-5.1	70	7.1	7.2	0.097	12.2	0.428	2.3	0.00247	4.38	21.8	0.05024	1.88	-2.4E-3	54
900B-6.1	23	2.8	4.1	0.117	10.9	0.325	3.7	0.00442	7.91	5.2	-0.00065	0.38	-1.3E-4	35
900B-7.1	35	3.7	4.1	0.103	12.9	0.234	2.8	0.00251	4.47	9.5	-0.00077	0.74	-8.4E-5	35
900B-8.1	104	7.4	5.6	0.067	3.6	0.049	1.7	0.00122	2.18	28.9	0.32855	2.19	-1.2E-2	18
900B-9.1	17	2.3	2.8	0.140	6.2	0.122	3.8	0.00401	7.17	3.6	-0.00055	0.26	-1.6E-4	36
900B-10.1	23	2.4	1.7	0.100	10.7	0.277	3.5	0.00193	3.44	5.1	-0.00247	0.39	-5.0E-4	18
900B-11.1	21	1.9	2.3	0.090	6.6	0.260	3.7	0.00279	4.97	4.1	-0.00111	0.31	-2.8E-4	25
900B-12.1	22	3.1	4.1	0.127	17.0	0.316	3.8	0.00479	8.57	5.8	-0.00144	0.40	-2.6E-4	25
900B-13.1	84	7.3	5.3	0.086	7.2	0.351	3.6	0.00152	2.72	23.2	-0.00836	1.69	-3.7E-4	85
900B-14.1	28	3.6	4.3	0.127	13.1	0.359	3.4	0.00355	6.33	9.2	-0.00101	0.71	-1.1E-4	35
900B-15.1	72	4.8	2.5	0.067	3.8	0.297	4.4	0.00088	1.58	17.6	-0.00135	1.26	-7.9E-5	31
900B-16.1	101	7.6	4.0	0.073	7.4	0.239	4.2	0.00088	1.57	23.3	-0.00062	1.67	-2.7E-5	41
900B-17.1	16	1.4	1.0	0.083	7.6	0.359	4.6	0.00152	2.72	3.6	-0.00063	0.26	-1.8E-4	35
900B-18.1	14	1.7	1.7	0.114	13.3	0.350	7.8	0.00266	4.75	3.3	-0.00140	0.25	-4.4E-4	25
900B-19.1	31	3.7	3.7	0.118	9.3	0.300	5.5	0.00280	5.00	4.9	-0.00132	0.35	-2.8E-4	20
900B-20.1	50	4.7	6.4	0.090	12.2	0.308	2.5	0.00309	5.50	11.1	-0.00264	0.88	-2.5E-4	18
900B-21.1	43	3.7	2.4	0.086	8.2	0.206	6.1	0.00132	2.37	8.7	-0.00103	0.62	-1.2E-4	25
900B-22.1	60	5.2	2.8	0.084	9.4	0.355	2.3	0.00118	2.10	18.8	-0.00379	1.43	-2.1E-4	20
900B-23.1	44	4.1	4.0	0.093	9.9	0.368	2.7	0.00224	4.01	11.2	0.02202	0.82	2.0E-3	51
900B-24.1	81	6.2	4.2	0.078	6.1	0.130	9.4	0.00125	2.23	16.9	0.05366	1.20	3.3E-3	37
900B-25.1	48	3.6	1.2	0.074	4.5	0.412	2.7	0.00058	1.04	9.5	-0.00180	0.75	-1.9E-4	20
900B-26.1	18	2.4	2.9	0.132	6.0	0.258	4.2	0.00390	7.01	3.3	-0.00090	0.20	-2.9E-4	25
900B-27.1	23	2.0	1.6	0.080	14.2	0.259	3.4	0.00161	2.87	4.1	-0.00235	0.30	-6.0E-4	16
900B-28.1	51	3.9	1.9	0.076	4.4	0.323	7.4	0.00093	1.67	10.7	-0.00125	0.78	-1.2E-4	27
900B-29.1	31	2.7	2.2	0.085	11.8	0.332	3.2	0.00168	3.00	9.2	-0.00081	0.66	-9.1E-5	35
900B-30.1	29	2.2	2.1	0.072	6.7	0.321	5.7	0.00187	3.33	6.0	-0.00062	0.45	-1.1E-4	42
900B-31.1	40	3.0	2.0	0.072	7.7	0.326	2.7	0.00119	2.12	8.5	0.01256	0.66	-1.5E-3	73
900B-32.1	31	2.5	2.0	0.079	9.6	0.243	2.9	0.00116	2.08	5.5	-0.00142	0.42	-2.6E-4	20
900B-33.1	67	5.4	3.8	0.080	3.7	0.168	11.1	0.00148	2.66	13.7	-0.00145	0.92	-1.1E-4	20
900B-34.1	26	2.7	2.4	0.107	5.4	0.145	8.8	0.00201	3.59	5.2	-0.00161	0.39	-3.2E-4	21

Errors are 1-sigma; Pb<sub>c</sub> and Pb<sup>\*</sup> indicate the common and radiogenic portions, respectively.

Error in standard calibration was 0.64% (not included in above errors but required when comparing data from different mounts).

(1) Common Pb corrected using measured 204Pb.

(2) Common Pb corrected by assuming 206Pb/238U-207Pb/235U age-concordance

(3) Common Pb corrected by assuming 206Pb/238U-208Pb/232Th age-concordance

(2) 206Pb /238U Age	(3) 206Pb /238U Age	(3) 207Pb /206Pb Age	208 corr % Dis- cor- dant	(1) 238U /206Pb* ±%	(1) 207Pb* /235U ±%	(1) 206Pb* /238U ±%	err corr	(3) 238U /206Pb* ±%	(3) 207Pb* /206Pb* ±%	(3) 207Pb* /235U ±%	(3) 206Pb* /238U ±%	err. corr.
511 ±35	518 ±40	888 ±590	+43	12.64	8.7	0.023	235	0.25	0.791	8.7	0.04	0.38
440 ±31	437 ±40	176 ±770	-154	13.85	8.5	0.074	59	0.74	0.072	8.5	0.14	0.32
518 ±23	521 ±23	699 ±117	+26	11.94	4.6	0.059	15	0.68	0.0837	4.6	0.29	0.55
523 ±15	522 ±15	501 ±204	-4	11.88	3.0	0.055	21	0.63	0.0841	3.0	0.14	0.34
616 ±26	617 ±30	628 ±423	+2	9.90	4.3	0.066	25	0.91	0.1010	4.3	0.17	0.32
530 ±23	526 ±28	273 ±584	-96	11.27	4.7	0.086	26	1.06	0.0888	4.7	0.18	0.37
552 ±20	557 ±22	822 ±415	+34	11.36	4.3	0.046	57	0.55	0.0880	4.3	0.07	0.38
552 ±21	546 ±21	149 ±134	-278	11.57	4.1	0.031	32	0.37	0.0864	4.1	0.13	0.48
504 ±20	520 ±26	1281 ±199	+62	12.91	7.1	0.017	311	0.18	0.0775	7.1	0.02	0.51
535 ±22	544 ±22	998 ±304	+47	11.10	4.2	0.090	17	1.11	0.0901	4.2	0.24	0.32
548 ±22	542 ±23	158 ±292	-253	10.98	4.2	0.079	16	0.99	0.0911	4.2	0.25	0.36
503 ±24	503 ±26	516 ±866	+3	12.64	5.9	0.036	120	0.40	0.0791	5.9	0.05	0.47
521 ±30	525 ±32	735 ±215	+30	11.93	5.9	0.054	22	0.62	0.0838	5.9	0.26	0.38
544 ±24	555 ±27	1094 ±442	+51	11.40	5.1	0.056	58	0.68	0.0877	5.1	0.09	0.40
516 ±27	514 ±27	375 ±124	-38	11.86	5.4	0.067	4	0.78	0.0843	5.4	0.82	0.66
516 ±17	518 ±17	618 ±196	+17	12.17	3.4	0.046	22	0.53	0.0822	3.4	0.15	0.36
519 ±24	521 ±25	650 ±228	+21	11.35	5.1	0.098	16	1.19	0.0881	5.1	0.30	0.40
538 ±30	549 ±31	1086 ±407	+52	12.24	7.9	0.005	1075	0.06	0.0817	7.9	0.01	0.34
504 ±19	517 ±21	1155 ±280	+57	11.72	4.0	0.096	18	1.12	0.0853	4.0	0.22	0.39
581 ±19	571 ±20	-100 ±622	+704	10.78	3.7	0.045	43	0.58	0.0927	3.7	0.08	0.36
509 ±25	515 ±25	837 ±225	+40	12.09	5.1	0.064	21	0.72	0.0827	5.1	0.23	0.41
540 ±17	545 ±17	831 ±249	+36	11.50	3.3	0.055	25	0.66	0.0870	3.3	0.13	0.28
528 ±26	529 ±28	608 ±338	+13	11.70	5.1	0.060	29	0.70	0.0855	5.1	0.18	0.34
513 ±18	514 ±19	583 ±178	+12	12.00	3.7	0.063	13	0.72	0.0833	3.7	0.26	0.39
562 ±25	567 ±25	798 ±113	+30	10.83	4.5	0.069	9	0.88	0.0923	4.5	0.46	0.61
437 ±29	448 ±33	1108 ±229	+62	13.14	6.9	0.119	13	1.25	0.0761	6.9	0.47	0.49
536 ±37	534 ±36	456 ±460	-18	10.96	7.1	0.099	18	1.25	0.0912	7.1	0.37	0.32
523 ±36	526 ±36	702 ±131	+26	11.91	7.1	0.053	22	0.61	0.0839	7.1	0.31	0.73
520 ±19	522 ±20	643 ±361	+20	12.09	4.3	0.046	47	0.52	0.0827	4.3	0.09	0.28
555 ±32	546 ±33	-81 ±286	+811	11.79	6.5	0.009	279	0.11	0.0848	6.5	0.02	0.39
562 ±29	559 ±30	394 ±238	-44	11.58	5.8	0.014	155	0.17	0.0864	5.8	0.04	0.42
541 ±19	543 ±18	668 ±267	+20	11.47	3.8	0.055	29	0.67	0.0872	3.8	0.13	0.28
484 ±17	485 ±17	534 ±122	+10	12.98	3.8	0.047	25	0.50	0.0770	3.8	0.15	0.49
526 ±18	539 ±19	1168 ±152	+56	11.31	3.8	0.089	16	1.09	0.0884	3.8	0.23	0.41

Supplementary Table 4. Electron microprobe data for P-T modelling for sample A325-535a

<b>A325-535a</b>	Cpx	Cpx	Cpx	Gt	Gt	Gt	Pl	Hb	Ttn
SiO <sub>2</sub>	52.89	53.25	54.55	37.07	37.61	38.13	64.18	41.19	30.69
TiO <sub>2</sub>	0.31	0.12	0.13	0.06	0.06	0.04	0.08	0.27	37.19
Al <sub>2</sub> O <sub>3</sub>	3.90	2.70	2.88	21.17	21.24	21.22	21.82	15.50	1.91
Cr <sub>2</sub> O <sub>3</sub>	0.06	0.12	0.02	0.00	0.03	0.00	0.00	0.00	0.00
FeO	9.01	9.52	7.66	27.21	26.18	27.05	0.27	22.76	0.93
MnO	0.04	0.00	0.07	0.46	0.61	0.44	0.02	0.34	0.03
MgO	11.84	11.79	11.99	4.76	3.09	4.89	0.00	6.85	0.00
ZnO	0.15	0.13	0.13	0.05	0.00	0.00	0.13	0.00	0.00
CaO	18.69	19.43	19.89	7.85	11.09	8.27	2.76	10.15	27.51
Na <sub>2</sub> O	2.37	2.61	1.99	0.00	0.04	0.06	9.71	0.41	0.24
K <sub>2</sub> O	0.13	0.01	0.00	0.00	0.01	0.01	0.14	0.35	0.01
Total	99.39	99.68	99.31	98.63	99.96	100.11	99.11	97.82	98.51
No. Oxygens	6.00	6.00	6.00	12.00	12.00	12.00	8.00	23	5
Si	1.96	1.97	2.03	2.94	2.96	2.98	2.86	6.15	1.01
Ti	0.01	0.00	0.00	0.00	0.00	0.00	0.00	0.03	0.92
Al	0.17	0.12	0.13	1.98	1.97	1.95	1.15	2.73	0.07
Cr	0.00	0.00	0.00	0.00	0.00	0.00	0.00	0.00	0.00
Fe <sup>3+</sup>	0.06	0.12	0.00	0.12	0.11	0.10	0.00	0.84	0.00
Fe <sup>2+</sup>	0.21	0.17	0.24	1.68	1.61	1.67	0.01	2.00	0.03
Mn <sup>2+</sup>	0.00	0.00	0.00	0.03	0.04	0.03	0.00	0.04	0.00
Mg	0.65	0.65	0.66	0.56	0.36	0.57	0.00	1.52	0.00
Zn	0.00	0.00	0.00	0.00	0.00	0.00	0.00	0.00	0.00
Ca	0.74	0.77	0.79	0.67	0.93	0.69	0.13	1.62	0.97
Na	0.17	0.19	0.14	0.00	0.01	0.01	0.84	0.12	0.02
K	0.01	0.00	0.00	0.00	0.00	0.00	0.01	0.07	0.00
Sum	4	4	4	8.00	8.00	8	5	15.1262	3.03
X <sub>Fe</sub> (gt)	--	--	--	0.75	0.82	0.75	--	--	--
p(alm)	--	--	--	0.57	0.55	0.56	--	--	--
p(py)	--	--	--	0.13	0.07	0.14	--	--	--
p(grs)	--	--	--	0.23	0.32	0.23	--	--	--
p(spss)	--	--	--	0.01	0.01	0.01	--	--	--
p(kho)	--	--	--	0.06	0.06	0.05	--	--	--
p(jad)	0.12	0.09	0.14	--	--	--	--	--	--
p(diop)	0.62	0.64	0.63	--	--	--	--	--	--
p(hed)	0.20	0.17	0.23	--	--	--	--	--	--
p(aeg)	0.05	0.09	0.00	--	--	--	--	--	--

Supplementary Table 5. Electron microprobe data for P-T modelling for sample A325-907Q

<b>A325-907Q</b>	Cpx	Cpx	Cpx	Gt	Pl	Gt	Hb
SiO <sub>2</sub>	52.32	53.08	52.30	38.23	64.06	38.27	42.19
TiO <sub>2</sub>	0.17	1.12	0.20	0.05	0.02	0.12	0.27
Al <sub>2</sub> O <sub>3</sub>	3.93	3.11	5.04	21.52	21.43	21.79	14.90
Cr <sub>2</sub> O <sub>3</sub>	0.14	0.12	0.06	0.00	0.00	0.15	0.00
FeO	7.31	7.62	7.52	25.48	0.48	22.00	22.41
MnO	0.02	0.02	0.00	0.61	0.02	1.06	0.34
MgO	12.05	12.53	11.61	5.80	0.01	8.10	5.76
ZnO	0.05	0.08	0.15	0.03	0.12	0.00	0.00
CaO	19.66	19.72	19.17	8.47	2.96	6.76	11.15
Na <sub>2</sub> O	2.84	2.69	3.06	0.02	10.36	0.02	0.41
K <sub>2</sub> O	0.01	0.01	0.03	0.00	0.26	0.02	0.35
Total	98.5	100.1	99.14	100.21	99.72	98.29	97.78
No. Oxygens	6	6	6	12	8	12	23
Si	1.94	1.94	1.93	2.96	2.85	2.98	6.33
Ti	0.00	0.03	0.01	0.00	0.00	0.01	0.03
Al	0.17	0.13	0.22	1.97	1.12	2.00	2.64
Cr	0.00	0.00	0.00	0.00	0.00	0.01	0.00
Fe <sup>3+</sup>	0.14	0.10	0.14	0.11	0.00	0.03	0.57
Fe <sup>2+</sup>	0.09	0.13	0.09	1.54	0.02	1.40	2.25
Mn <sup>2+</sup>	0.00	0.00	0.00	0.04	0.00	0.07	0.04
Mg	0.67	0.68	0.64	0.67	0.00	0.94	1.29
Zn	0.00	0.00	0.00	0.00	0.00	0.00	0.00
Ca	0.78	0.77	0.76	0.70	0.14	0.56	1.79
Na	0.20	0.19	0.22	0.00	0.89	0.00	0.12
K	0.00	0.00	0.00	0.00	0.01	0.00	0.07
Total cations	4	4	4	8	5	8	15.725
X <sub>Fe</sub> (gt)	--	--	--	0.70	--	0.60	--
p(alm)	--	--	--	0.52	--	0.47	--
p(py)	--	--	--	0.17	--	0.30	--
p(grs)	--	--	--	0.24	--	0.19	--
p(spss)	--	--	--	0.01	--	0.02	--
p(kho)	--	--	--	0.05	--	0.01	--
p(jad)	0.11	0.11	0.13	--	--	--	--
p(diop)	0.70	0.68	0.68	--	--	--	--
p(hed)	0.09	0.13	0.10	--	--	--	--
p(aeg)	0.09	0.08	0.08	--	--	--	--



Supplementary Table 6. Electron microprobe data for P-T modelling for sample A325-672

<b>A325-672</b>	gt	bi	ksp	pl	mt	ky
SiO <sub>2</sub>	39.725	38.361	65.196	67.585	0.080	36.925
TiO <sub>2</sub>	0.001	1.025	0.004	0.000	0.034	0.002
Al <sub>2</sub> O <sub>3</sub>	22.386	16.921	18.272	22.028	0.053	62.105
Cr <sub>2</sub> O <sub>3</sub>	0.016	0.000	0.000	0.000	0.000	0.000
FeO	24.194	11.521	0.191	0.087	89.794	0.877
MnO	0.374	0.033	0.000	0.000	0.001	0.000
MgO	12.139	17.361	0.000	0.000	0.024	0.011
CaO	1.601	0.018	0.000	1.648	0.002	0.007
Na <sub>2</sub> O	0.022	0.047	0.779	8.774	0.012	0.000
K <sub>2</sub> O	0.001	9.586	15.471	1.021	0.096	0.019
<b>Total</b>	100.46	94.87	99.91	101.14	90.10	99.95
<b>No. Oxygens</b>	12	11	8	8	4	5
Si	2.990	2.815	3.007	2.921	0.004	1.001
Ti	0.000	0.057	0.000	0.000	0.001	0.000
Al	1.986	1.463	0.993	1.122	0.003	1.984
Cr	0.001	0.000	0.000	0.000	0.000	0.000
Fe <sup>3+</sup>	--	--	--	--	--	--
Fe <sup>2+</sup>	1.523	0.707	0.007	0.003	3.978	0.020
Mn <sup>2+</sup>	0.024	0.002	0.000	0.000	0.000	0.000
Mg	1.362	1.899	0.000	0.000	0.002	0.000
Ca	0.129	0.001	0.000	0.076	0.000	0.000
Na	0.003	0.007	0.070	0.735	0.001	0.000
K	0.000	0.897	0.910	0.056	0.006	0.001
<b>Total Cations</b>	8.018	7.849	4.987	4.914	3.997	3.007
xFe	0.519	0.271	--	--	0.999	--
p(alm)	0.492	--	--	--	--	--
p(py)	0.429	--	--	--	--	--
p(grs)	0.043	--	--	--	--	--
p(spss)	0.008	--	--	--	--	--
p(kho)	0.027	--	--	--	--	--
<i>sum gt propns</i>	1	--	--	--	--	--
p(abh)	--	--	0.071	0.847	--	--
p(an)	--	--	0	0.088	--	--
p(san)	--	--	0.929	0.065	--	--
<i>check fsp proport</i>	--	--	1	1	--	--
p(herc)	--	--	--	--	0.000	--
p(sp)	--	--	--	--	0.001	--
p(mt)	--	--	--	--	0.998	--
p(usp)	--	--	--	--	0.001	--
<i>sum mt propns</i>	--	--	--	--	1	--

Supplementary Table 7. Electron microprobe data for garnet diffusion modelling for sample A325-900b

A325-900b																		
Mineral																		
ID number	gt t1-1	gt t1-2	gt t1-3	gt t1-4	gt t1-5	gt t1-6	gt t1-7	gt t1-8	gt t1-9	gt t1-10	gt t1-11	gt t1-12	gt t1-13	gt t1-14	gt t1-15	gt t1-16	gt t1-17	gt t1-18
SiO2	39.29	39.14	39.35	39.13	39.28	39.4	39.36	39.37	39.38	39.21	39.24	39.07	39.3	39.2	39.52	33.8	39.22	39.22
TiO2	0.01	0.01	0.03	0.05	0.03	0.05	0.03	0.04	0.04	0.04	0.03	0.04	0.03	0.04	0.04	0.04	0.05	0.07
Al2O3	22.3	22.18	22.34	22.12	22.19	22.32	22.25	22.15	22.29	22.06	22.18	22.1	22.1	22.22	22.49	21.59	22.01	22.1
Cr2O3	0	0	0	0	0	0	0	0	0	0	0	0	0	0	0	0	0	0
FeO	27.52	27.61	27.78	27.55	27.62	27.85	27.86	27.86	27.98	27.85	27.87	27.97	27.8	27.77	28.14	23.66	28.08	28.08
MnO	1.36	1.31	1.42	1.38	1.35	1.3	1.3	1.36	1.39	1.35	1.34	1.34	1.38	1.34	1.35	1.17	1.37	1.34
MgO	9.48	9.49	9.5	9.41	9.36	9.48	9.25	9.32	9.36	9.52	9.31	9.28	9.34	9.35	9.17	8.8	9.22	9.06
ZnO	0	0	0	0	0	0	0	0	0	0	0	0	0	0	0	0	0	0
CaO	1.12	1.13	1.14	1.14	1.12	1.13	1.11	1.08	0.11	1.09	1.09	1.09	1.08	1.1	1.08	0.99	1.11	1.12
Na2O	0.01	0.01	0	0	0	0	0	0.41	0	0	0	0	0	0	0	0	0	0
K2O	0	0	0	0	0	0	0	0	0	0	0	0	0	0	0	0	0	0
Total	101.09	100.88	101.56	100.78	100.95	101.53	101.16	101.59	100.55	101.12	101.06	100.89	101.03	101.02	101.79	90.05	101.06	100.99
No. Oxygens	12	12	12	12	12	12	12	12	12	12	12	12	12	12	12	12	12	12
Si	2.99	2.99	2.98	2.99	3.00	2.99	3.00	2.98	3.02	2.99	2.99	2.99	3.00	2.99	3.00	2.87	2.99	3.00
Ti	0.00	0.00	0.00	0.00	0.00	0.00	0.00	0.00	0.00	0.00	0.00	0.00	0.00	0.00	0.00	0.00	0.00	0.00
Al	2.00	1.99	2.00	1.99	2.00	2.00	2.00	1.97	2.01	1.98	1.99	1.99	1.99	2.00	2.01	2.16	1.98	1.99
Cr	0.00	0.00	0.00	0.00	0.00	0.00	0.00	0.00	0.00	0.00	0.00	0.00	0.00	0.00	0.00	0.00	0.00	0.00
Fe3+	0.02	0.03	0.03	0.02	0.01	0.02	0.00	0.13	0.00	0.04	0.02	0.03	0.01	0.02	0.00	0.10	0.02	0.00
Fe2+	1.73	1.73	1.73	1.74	1.76	1.74	1.78	1.63	1.79	1.73	1.76	1.76	1.76	1.75	1.78	1.58	1.77	1.79
Mn2+	0.09	0.08	0.09	0.09	0.09	0.08	0.08	0.09	0.09	0.09	0.09	0.09	0.09	0.09	0.09	0.08	0.09	0.09
Mg	1.08	1.08	1.07	1.07	1.06	1.07	1.05	1.05	1.07	1.08	1.06	1.06	1.06	1.06	1.04	1.11	1.05	1.03
Zn	0.00	0.00	0.00	0.00	0.00	0.00	0.00	0.00	0.00	0.00	0.00	0.00	0.00	0.00	0.00	0.00	0.00	0.00
Ca	0.09	0.09	0.09	0.09	0.09	0.09	0.09	0.09	0.01	0.09	0.09	0.09	0.09	0.09	0.09	0.09	0.09	0.09
Na	0.00	0.00	0.00	0.00	0.00	0.00	0.00	0.06	0.00	0.00	0.00	0.00	0.00	0.00	0.00	0.00	0.00	0.00
K	0.00	0.00	0.00	0.00	0.00	0.00	0.00	0.00	0.00	0.00	0.00	0.00	0.00	0.00	0.00	0.00	0.00	0.00
Total cations (	8.00	8.00	8.00	8.00	8.00	8.00	8.00	8.00	8.00	8.00	8.00	8.00	8.00	8.00	8.00	8.00	8.00	8.00
X(Fe(gt)	0.62	0.62	0.62	0.62	0.62	0.62	0.63	0.61	0.63	0.62	0.62	0.62	0.62	0.62	0.63	0.59	0.63	0.63
X(alm)	0.58	0.58	0.58	0.58	0.59	0.58	0.59	0.57	0.61	0.58	0.59	0.59	0.59	0.59	0.60	0.55	0.59	0.60
X(py)	0.35	0.34	0.34	0.35	0.35	0.35	0.35	0.30	0.36	0.34	0.34	0.34	0.35	0.35	0.35	0.34	0.34	0.34
X(grs)	0.03	0.03	0.03	0.03	0.03	0.03	0.03	0.03	0.00	0.03	0.03	0.03	0.03	0.03	0.03	0.03	0.03	0.03
X(spss)	0.03	0.03	0.03	0.03	0.03	0.03	0.03	0.03	0.03	0.03	0.03	0.03	0.03	0.03	0.03	0.03	0.03	0.03
X(kho)	0.01	0.02	0.02	0.01	0.00	0.01	0.00	0.06	0.00	0.02	0.01	0.02	0.01	0.01	0.00	0.05	0.01	0.00

[illegible]

Supplementary Table 7. Electron microprobe data for garnet diffusion modelling for sample A325-900b (continued)

A325-900b		gt	gt	gt
Mineral	ID number	t2-14	t2-15	t2-16
SiO2		39.34	39.16	38.99
TiO2		0.09	0.14	0.18
Al2O3		22.71	22.01	22.12
Cr2O3		0	0	0
FeO		26.7	27.71	27.62
MnO		1.27	1.31	1.35
MgO		8.47	8.22	7.57
ZnO		0	0	0
CaO		1.74	2.77	3.88
Na2O		0	0	0
K2O		0	0	0
Total		100.32	101.32	101.71
No. Oxygens		12	12	12
Si		3.02	2.99	2.97
Ti		0.01	0.01	0.01
Al		2.06	1.98	1.99
Cr		0.00	0.00	0.00
Fe3+		0.00	0.02	0.04
Fe2+		1.72	1.75	1.72
Mn2+		0.08	0.08	0.09
Mg		0.97	0.94	0.86
Zn		0.00	0.00	0.00
Ca		0.14	0.23	0.32
Na		0.00	0.00	0.00
K		0.00	0.00	0.00
Total cations (		8.00	8.00	8.00
Xfe(gt)		0.64	0.65	0.67
X(alm)		0.59	0.58	0.58
X(py)		0.33	0.30	0.27
X(grs)		0.05	0.08	0.11
X(spss)		0.03	0.03	0.03
X(kho)		0.00	0.01	0.02



---

# Chapter 6

---



---

## Summary and conclusions

---

### Thesis summary and conclusions

This thesis attempts to develop an understanding of 1) how the thermomechanical properties of lithosphere controls both the architecture of orogenic belts and the distribution of metamorphism and deformation during orogeny and 2) how orogeny modifies the physical properties of the crust and the implications for future reworking events. In the preceding chapters, the metamorphic and structural record of orogeny in the Musgrave Province, central Australia, was investigated in order to address the principle aims of this thesis. The following discussion summarises the key outcomes and presents a concise summary of the thermo-mechanical evolution of lithosphere in the Musgrave Province throughout Ediacaran–Cambrian intraplate orogeny and the significant role Grenvillian-aged metamorphism played in modifying the crust.

1. *Determine the physical conditions and duration of high-T Grenvillian-aged metamorphism and investigate the crustal and tectonic processes leading to high temperatures in the Musgrave Province*

**Chapter 1** presents petrologic forward modelling and Zr-in-rutile thermometry that indicates peak metamorphic mineral assemblages developed at thermally extreme conditions of approximately 1000 °C and ~7–8 kbar. Combined with SIMS (SHRIMP) and LA-ICP-MS U–Pb monazite geochronology this data indicates approximately 150 Myr of perturbed thermal conditions between 1263 and 1111 Ma. Such long-lived UHT conditions are exceptionally rare in the metamorphic rock record and indicate the crust is able to generate and maintain extreme thermal conditions for long periods. The metamorphic  $P$ – $T$  information presented is used to make several interpretations relevant to the generation of

sustained UHT conditions; 1) the crust was not overly thickened (~30km); 2) apparent thermal gradients are very high (25–35 °C km<sup>-1</sup>) and 3) cooling rates from UHT conditions were very slow as the crust had no exhumation driver given its topographic neutrality. On the basis of the above interpretations we propose that UHT metamorphism was associated with an extensional regime and that the Musgrave Province was in a back-arc environment from *ca.* 1330 Ma to at least 1100 Ma. Long-lived UHT metamorphism and in particular melting processes resulted in the crust evolving to become exceptionally residual and anhydrous in nature, rendering it largely infertile to further metamorphism.

Despite a thorough and methodical analysis the assertion that the entirety of the Musgrave Province experienced UHT metamorphic conditions is contentious given our sample set is largely collected from the western half of the belt. A similar approach/logic presented in chapter 1 could be applied to the eastern section of the orogen (South Australia) to gain a more complete view of the spatial footprint of UHT metamorphism. This will allow a critical investigation of the hypothesis that tectonic setting of the Musgrave Province during the Grenvillian resembled an extensional back-arc system. This hypothesis has significant implications for the paleo-geographic reconstruction of continental Australia.

The conclusion that high temperatures were sustained for a long duration is based on the extended span of U–Pb monazite growth ages from *ca.* 1270–1100 Ma. This interpretation is critically assessed in Chapter 1 as it has significant implications for the behaviour of the monazite in high-grade metamorphic terrains. That monazite can be extremely resistive to resetting even when exposed to such high temperatures for long durations ( $\geq 80$  Myr) is converse to conventional views regarding the

ability of monazite to readily diffuse lead (Pb) at temperatures above  $\sim 800$  °C. This apparent disagreement with the established literature could arise due to an incomplete understanding of factors which might facilitate or inhibit diffusion in monazite, other than temperature, such as the presence/absence of melt. Future work in high-grade metamorphic terrains should focus on critically examining the U–Pb monazite record and ideally additional experimental studies on monazite diffusion that more closely resemble natural rock systems.

2. *To obtain precise geochronological constraints on deformation, metamorphism and exhumation/cooling from both the orogenic foreland and hinterland to evaluate the spatial and temporal patterns of deformation during intraplate reworking.*

**Chapters 2, 4 and 5** present geochronological and thermobarometric (P–T pseudosections and trace-element thermometry) datasets that are collected from metamorphic sequences that cover a crustal section from upper-crustal levels exposed in the foreland fold-thrust belt to the deeply exposed lower crust in the Mann Ranges and Amata Region to the south. A range of geochronometers are coupled with metamorphic *P–T* information to extract various parts of the orogenic evolution and from early stages of burial to late stages of cooling and exhumation of the axial core of the orogen.

**Chapter 4** presents  $^{40}\text{Ar}/^{39}\text{Ar}$  data and a muscovite crystallisation age of  $598 \pm 3$  Ma recorded in low-grade schist constrains the earliest metamorphism associated with the burial of the Musgrave Province during the Petermann Orogeny. **Chapter 5** investigates deep crustal shear zones and the development of monazite constrains the timing of metamorphism in the lower crustal shear zones (10–12 kbar, 600–700 °C) and the host country rock at  $586 \pm 4$  Ma. In response to heating and/or minor decompression of the orogen

partial melting in high-grade (10–12 kbar, 650 °C) ductile shear zones, which were the focus of **Chapter 2**, is recorded by zircon growth at  $542 \pm 7$  Ma (U–Pb). Early stages of cooling and exhumation of the orogen is recorded in the foreland by  $^{40}\text{Ar}/^{39}\text{Ar}$  muscovite and biotite cooling ages ranging between  $581 \pm 4$  and  $545 \pm 5$  Ma in amphibolite facies schists (5–7 kbar, 500–600 °C). U–Pb titanite and rutile ages record continued exhumation of the core of the orogen between *ca.* 540 and 500 Ma which was associated with slow cooling ( $< 5$  °C  $\text{Ma}^{-1}$ ).

The resultant pattern of deformation, metamorphism and exhumation is not uncommon in transpressional orogens although the preservation of overall younger U–Pb and  $^{40}\text{Ar}/^{39}\text{Ar}$  ages in the core rather than the foreland of the orogen do warrant discussion. This pattern could suggest that low-angle strike-slip-dominated tectonism was dominant later in the orogenic cycle or at least for a longer duration. This could imply record a narrowing strain envelope as the orogen evolved towards a low-angle transpressional regime, rather than reflecting contemporaneous strain partitioning for the duration of transpressional deformation.

Our ability to understand strain patterns during intraplate reworking in the Musgrave Province is hindered by the sparse coverage of data compared to the exposure of the orogen. Additional high-precision geochronology, principally from the hinterland of the orogen although extracting Petermann-aged geochronology from the axial core of the orogen is a difficult objective due to the discrete nature of reworking.

3. *To investigate the mechanical strength of the pre-Petermann Orogeny lithosphere*

**Chapter 3** uses *P–T* data to evaluate the extent of burial in the foreland basin and foreland fold-thrust belt. This information is used to determine the architecture of the Petermann Orogen foreland and make an assessment of



the mechanical strength of the lithosphere during the onset of intraplate orogeny.  $P$ – $T$  estimates from burial metamorphic assemblages which developed in a syn-orogenic foreland conglomerate indicate that burial of the foreland basin was at least 10 km, a depth rarely recorded in continental foreland basins.  $P$ – $T$  estimates from the Petermann Nappe Complex indicate that Neoproterozoic sequences were buried up to 20 km during the development of a thick skinned fold-thrust belt.

The deep burial and thickening of the foreland occurred as orogenic loading resulted in dramatic flexure of the lithosphere. A key implication of this deduction is that the lithosphere must have been mechanically weak in order to accommodate deep and narrow flexure. It is not clear what caused lithospheric weaknesses in central Australia but the notion that the pre-Petermann Orogeny lithosphere was weak is consistent with the notion that intraplate deformation is localised within areas of comparative weakness.

However, the interpretation that the lithosphere was regionally weak is inconsistent with the brittle and discrete style of deformation and metamorphism observed in the eastern portion of the orogen, implying that the lithosphere is strong. The absence of a developed fold-thrust belt and/or foreland basin in the foreland to the eastern part of the orogen suggests that the Petermann Orogen is characterised by areas of varying lithospheric strength. The presence of large high-heat producing granitic suites might have caused long-term crustal heating in regions of emplacement and promoted localised weakening in the western part of the orogen. This could suggest that orogeny was initiated in these weak regions with widespread orogeny occurring subsequently. Advection of fluids, strain softening or compositional variation could have additionally contributed to the distribution of lithospheric weakening and subsequent deformation during the Petermann orogeny. The apparently contrasting record of

deformation is further investigated in **Chapter 5**.

4. *Assess drivers for metamorphism by investigating the duration, timing and spatial footprint of high-grade metamorphism in the core of the orogen.*

**Chapters 2, 3 and 4** provide strong arguments that the Petermann Orogeny was characterised by a regionally elevated thermal regime which involved deep burial, pervasive ductile deformation, partial melting and slow cooling. These observations are consistent with conductive heating in a collisional orogen and a cooling history controlled by unroofing of the orogen. However, it is clear that the record of deformation and metamorphism is contrasting in the eastern part of the orogen. Based on the deformation style, previous workers concluded that shear was the dominant mechanism by which elevated temperatures in the orogen were achieved. **Chapter 5** provides analysis of the physical conditions and duration of metamorphism in shear zones and the surrounding country rock in the central Petermann Orogen to test the viability of shear heating as a driver for metamorphism.

The most significant outcome of metamorphic analysis in the central orogenic core is that both rocks inside shear zones and those distal (~5km) to shear zones record metamorphic temperatures approximately 700 °C. This deduction indicates that high metamorphic temperatures were not restricted to shear zones and therefore shear heating does not solely provide a mechanism to achieve regionally elevated temperatures during the Petermann Orogeny. The timing of monazite crystallisation in shear zones at 590 Ma is considered to approximately represent peak temperatures (700 °C) whereas rutile ages of ~530 Ma constrain cooling to temperatures of 550–600 °C. If metamorphism/deformation is not episodic, it implies that cooling is slow and that lower crustal residence times were at least an order of magnitude longer than permitted by shear heating (~1 Ma).

Based on the combination of geochronological and metamorphic analysis presented in **Chapters 2–5**, we conclude that the Petermann Orogeny was characterised by long-lived, conductively driven high-pressure (10–11 kbar), medium-temperature (~700 °C) metamorphism achieved between 600 and 570 Ma.

5. *To critically evaluate the thermomechanical state of the lithosphere prior to, during and post Petermann orogeny.*

The deductions and interpretations presented in **Chapters 2–5** provide valuable insight into the thermomechanical environment during intraplate orogeny in central Australia. The thermomechanical state of the pre-Petermann Orogeny lithosphere is impossible to measure although it must have been significantly weak enough to localise major intraplate deformation. The development of a thick-skinned foreland fold-thrust belt and a deep, narrow foreland basin at 600 Ma suggests that the early stages of orogenesis, as recorded in the western part of the orogen, occurred in relatively weak lithosphere. In contrast, the eastern part of the orogen did not develop a significant foreland basin or a fold thrust belt despite the approximately coeval deformation and metamorphism recorded in the orogenic core (~590 Ma). The significant weakening of the western part of the orogen could reflect the distribution of heat production in the crust.

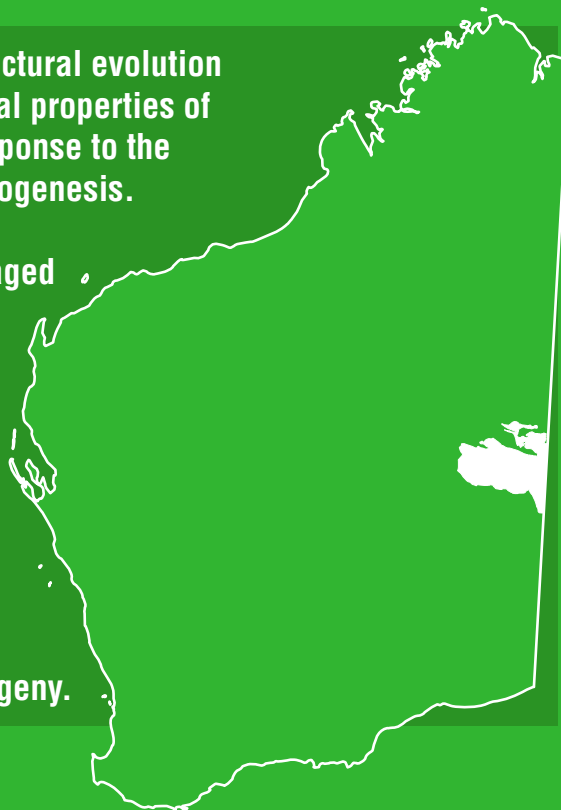
The presence of large volumes of high-heat producing mid-crustal granites in the western part of the orogen could have caused long-term crustal heating and promoted localised weakening and facilitated deep burial of the north-western foreland.

Cooling and exhumation of the orogen will act to modify the thermo-mechanical state of the orogen until termination. The organisation of the majority of crustal radiogenic heat production into the mid and upper crust implies that exhumation and erosion of the orogen during its evolution progressively removed the high-heat producing layers, dramatically reducing the heat production of the orogenic system. The progressive reduction in crustal heat production would have modified the long-term mechanical structure of the lithosphere, leading to a progressive increase in the integrated strength of lithosphere via cooling. It is envisaged that as the system becomes colder and stronger, deformation will become increasingly localised, as the presence of brittle structures, including pseudotachylites, within the orogenic core demonstrate. In summary, a scenario whereby the rheology of the lithosphere progressively changes from weak to strong in response to progressive denudation/removal of high-heat-producing crust is able to resolve the apparently paradoxical record of warm, weak vs cold, strong lithosphere that occurs in the Petermann Orogen.



This Report outlines the metamorphic and structural evolution of the Musgrave Province, and how the physical properties of crustal lithosphere change through time in response to the metamorphic processes which occur during orogenesis.

The Report explores the role that Grenvillian-aged high-temperature metamorphic events played in providing the lithospheric framework for younger Ediacaran–Cambrian crustal reworking. The mechanical response of the lithosphere to this crustal reworking, within an intraplate setting, is also explored to evaluate the importance of inherited lithospheric thermal and mechanical properties and more broadly, the thermo-mechanical evolution of intraplate orogeny.



Further details of geological products and maps produced by the Geological Survey of Western Australia are available from:

Information Centre

Department of Mines and Petroleum

100 Plain Street

EAST PERTH WA 6004

Phone: (08) 9222 3459 Fax: (08) 9222 3444

[www.dmp.wa.gov.au/GSWApublications](http://www.dmp.wa.gov.au/GSWApublications)